Université de Montréal

Cytokinesis in the mouse preimplantation embryo

Mechanism and consequence of failure

Par

Lia Mara Gomes Paim

Centre de Recherche du Centre Hospitalier de l'Université de Montréal

Faculté de Médecine

Thèse présentée en vue de l'obtention du grade de *Philosophiae Doctor (Ph.D.)*

en Sciences Biomédicales, option Médecine Expérimentale

Janvier 2022

Université de Montréal

Centre de Recherche du Centre Hospitalier de l'Université de Montréal

Faculté de Médecine

Cette thèse intitulée

Cytokinesis in the mouse preimplantation embryo

Mechanism and consequence of failure

Présentée par

Lia Mara Gomes Paim

A été évaluée par un jury composé des personnes suivantes

Gilles Hickson, Ph.D.
Président-rapporteur

Greg FitzHarris, Ph.D.
Directeur de recherche

Jean-Claude Labbé, Ph.D.
Membre du jury

Susanne Bechstedt, Ph.D.
Examinatrice externe

Résumé

Essentiel au maintien d'un organisme sain, la division cellulaire est un processus biologique composée de deux phases : la mitose et la cytokinèse. Au cours de la mitose, un fuseau mitotique bipolaire est assemblé et les chromosomes s'alignent au niveau de la plaque métaphasique par l'attachement des kinétochores aux microtubules du fuseau. Une fois les chromosomes alignés, les chromatides sœurs sont séparées par les microtubules pendant l'anaphase et sont ségréguées entre les cellules filles. La cytokinèse est initiée peu après le début de l'anaphase, marquant ainsi la fin de la division cellulaire en séparant le cytoplasme en deux nouvelles cellules filles. Une exécution précise de la mitose et de la cytokinèse est essentielle pour le maintien de l'intégrité du génome. L'échec de l'un de ces processus affecte la fidélité génétique. Les erreurs de ségrégation des chromosomes durant la mitose peuvent entraîner un gain ou une perte de chromosomes entiers, appelé aneuploïdie. Tandis que l'échec de la cytokinèse conduit à la formation d'une cellule binucléée avec un génome entièrement dupliqué, appelé tétraploïdie. Dans les cellules somatiques, la tétraploïdie peut conduire à l'arrêt du cycle cellulaire, à la mort cellulaire, ou provoquer une instabilité chromosomique (CIN), favorisant ainsi la prolifération de cellules avec un potentiel tumorigène. Par conséquent, il est essentiel de bien comprendre la régulation et les causes potentielles de l'échec de la cytokinèse en particulier dans le contexte des systèmes multicellulaires comme l'embryon. En effet, dans ces systèmes, la réduction progressives de la taille des cellules coïncident avec les principaux évènements du développement. De plus, la binucléation est fréquemment observée dans les cliniques de fertilité chez les embryons humains. Cependant, l'impact de la binucléation sur les divisions préimplantatoires demeure inexpliqué à ce jour.

Afin de déterminer les conséquences de la tétraploïdie, nous avons utilisé l'embryon de souris pour modèle et réalisé des expériences d'immunofluorescence à haute résolution et une imagerie sur cellules vivantes. Nous avons découvert que la tétraploïdie chez les embryons de souris provoque une CIN et l'aneuploïdie par un mécanisme différent de celui des cellules somatiques. Dans les cellules somatiques, la formation des fuseaux multipolaires causée par des centrosomes surnuméraires est le principal mécanisme conduisant à la tétraploïdie et ainsi, à une CIN. En revanche, chez les embryons de souris, qui ne possèdent pas de centrosomes, la

tétraploïdie ne conduit pas à la formation des fuseaux multipolaires. Les embryons tétraploïdes de souris développent une CIN en raison d'une réduction du renouvellement des microtubules et d'une altération de l'activité de correction d'erreurs dans l'attachement des kinétochores aux microtubules. Ainsi, une mauvaise correction de l'attachement des kinétochores aux microtubules entraîne des niveaux élevés d'erreurs de ségrégation chromosomique. Dans le cadre d'une étude de suivi, nous avons ensuite utilisé des différentes expériences d'imageries sur des cellules vivantes et d'immunofluorescences. Celles-ci furent couplées à des micromanipulations de la taille des cellules, des techniques modifiant l'adhésion cellulaire et des approches de knock-down des protéines pour étudier les mécanismes de régulation de la cytokinèse. Les expériences d'imageries sur cellules vivantes et les micromanipulations du volume cytoplasmique ont démontré que la taille des cellules détermine la vitesse de constriction de l'anneau contractile, c'est-à-dire que la vitesse de constriction devient progressivement plus lente à mesure que la taille des cellules diminue. Cependant, ce phénomène n'a lieu que lorsque les embryons atteignent le stade de 16 cellules ce qui suggère qu'une limite supérieure de vitesse de constriction peut exister pour restreindre l'augmentation de cette vitesse quand les cellules sont trop grandes. La taille des cellules étant un déterminant de la progression de la cytokinèse, nos expériences de knock-down des protéines ont, de plus, démontré que la formation de la polarité cellulaire a un impact négatif sur l'assemblage et la constriction de l'anneau contractile dans les cellules externes au stade de morula. Plus précisément, nous avons constaté que la polarité limite le recrutement des composants de la cytokinèse spécifiquement d'un côté de l'anneau contractile, provoquant ainsi un déséquilibre de l'ingression du sillon de clivage et réduisant la vitesse de constriction dans les cellules externes. Nous spéculons que la polarité cellulaire agit comme un obstacle à la progression de la cytokinèse, rendant ainsi les cellules externes plus sensibles à un échec de la cytokinèse.

Ces études ont démontré un nouveau mécanisme par lequel la tétraploïdie conduit à l'instabilité chromosomique et à l'aneuploïdie chez les embryons. Ainsi un défaut de la dynamique de correction de l'attachement des kinétochores aux microtubules entraîne une mauvaise ségrégation des chromosomes indépendamment à la formation des fuseaux multipolaires. Ce travail a mis en évidence un rôle inhibiteur de la polarité apicale inattendu sur la machinerie cytokinétique. Cette inhibition pourrait fournir une explication mécanistique de l'incidence élevée de la binucléation dans le trophectoderme. Dans l'ensemble, ces résultats contribuent à notre

compréhension du contrôle spatio-temporel de la cytokinèse au cours du développement embryonnaire et fournissent de nouvelles informations mécanistiques sur les origines et les conséquences biologiques de la tétraploïdie chez les embryons préimplantatoires. Les résultats présentés dans cette thèse ont des implications cliniques importantes, puisqu'ils fournissent des preuves définitives que la tétraploïdie générée par un échec de la cytokinèse est délétère pour le développement embryonnaire. Ces travaux mettent ainsi en lumière que la binucléation est un critère de sélection embryonnaire important à considérer lors des traitements de fertilité.

Mots-clés : Embryon; Cytokinèse; Tétraploïdie; Instabilité Chromosomique; Aneuploïdie; Polarité Apicale; Binucléation; Anneau contractile; Chromosomes retardataires; Attachement kinétochore-microtubule.

Abstract

Cell division is comprised of mitosis and cytokinesis and is an essential biological process for the maintenance of healthy organisms. During mitosis, a bipolar spindle is assembled, and the chromosomes are aligned at the metaphase plate via the attachment of kinetochores to spindle microtubules. Once chromosome alignment is achieved, the sister chromatids are pulled apart by the microtubules during anaphase and segregated into the nascent daughter cells. Cytokinesis is initiated after anaphase onset and marks the completion of cell division by partitioning the cytoplasm of the dividing cell into two new daughter cells. Successful and timely completion of both mitosis and cytokinesis is key for the maintenance of genome integrity, and failure in either one of these processes affects genetic fidelity. Whereas chromosome segregation errors in mitosis can lead to whole chromosome gains or losses, termed aneuploidy, cytokinesis failure leads to the formation of a binucleated cell with an entirely duplicated genome, termed tetraploidy. In somatic cells, tetraploidy can either lead to cell cycle arrest and death or cause chromosomal instability (CIN), thereby promoting the proliferation of cells with high tumorigenic potential. Therefore, understanding cytokinesis regulation and the potential causes of cytokinesis failure is key, especially in the context of multicellular embryonic systems, wherein progressive cell size reductions coincide with developmental transitions. Moreover, binucleation is frequently observed in human embryos in fertility clinics, and whether binucleation impacts early divisions remains elusive.

To elucidate the consequences of tetraploidy, we used the mouse embryo as a model and employed high-resolution immunofluorescence and live-cell imaging experiments. We found that tetraploidy in mouse embryos causes CIN and aneuploidy by a mechanism distinct from that of somatic cells. Whereas in somatic cells multipolar spindle formation caused by supernumerary centrosomes is the major mechanism by which tetraploidy leads to CIN, in mouse embryos - which are acentriolar – tetraploidy does not lead to multipolar spindle formation. Instead, mouse tetraploid embryos develop CIN due to reduced microtubule turnover and impaired error correction activity, which prevents the timely resolution of kinetochore-microtubule mis-attachments, thereby leading to high levels of chromosome segregation errors. As a follow-up study, we next employed live imaging and immunofluorescence experiments, coupled with micromanipulations of cell size, cell

adhesion and protein knockdown approaches to investigate the regulatory mechanisms of cytokinesis. Live imaging experiments and micromanipulations of cytoplasmic volume demonstrated that cell size determines the speed of contractile ring constriction i.e., constriction speed becomes progressively slower as the cells decrease in size. However, this phenomenon takes place only when embryos reach the 16-cell stage, suggesting that an upper limit of constriction speed may exist to restrict the scalability of ring constriction to cell size. In addition to cell size being a powerful determinant of cytokinesis progression, our loss-of-function experiments revealed that the emergence of cell polarity negatively impacts contractile ring assembly and constriction in outer cells at the morula stage. More specifically, we found that polarity limits the recruitment of cytokinesis components specifically to one side of the contractile ring, thereby causing unbalanced furrow ingression and reducing constriction speed in outer cells. We speculate that cell polarity may act as an obstacle for cytokinesis progression and render outer cells to be more susceptible to cytokinesis failure.

These studies have revealed a novel mechanism by which tetraploidy leads to chromosomal instability and aneuploidy in embryos, wherein defective kinetochore-microtubule dynamics cause chromosome mis-segregation in a manner independent of multipolar spindle formation. In addition, this work unravelled an unexpected inhibitory role of apical polarity on the cytokinetic machinery that might provide a mechanistic explanation for the high incidences of binucleation in the outer layer of blastocysts. Altogether, these findings contribute to our understanding of the spatiotemporal control of cytokinesis during embryonic development and provide new mechanistic insights into the origins and biological consequences of tetraploidy in preimplantation embryos. The results presented in this thesis have substantial clinical implications, as they provide definitive evidence that tetraploidy generated by cytokinesis failure is deleterious to embryonic development, therefore underlining binucleation as an important embryo selection criterion to be considered during fertility treatments.

Keywords: Embryo; Cytokinesis; Tetraploidy; Chromosomal instability; Aneuploidy; Apical polarity; Binucleation; Contractile ring; Lagging chromosomes; Kinetochore-microtubule attachment.

Table of contents

List of figures

List of acronyms and abbreviations

+TIP	Plus-end tracking proteins
2D	Two-dimensional
3D	Three-dimensional
2N	Diploid
4N	Tetraploid
8N	Octoploid
64N	Tetrahexacontaploid
AKAP450	A-kinase anchoring protein 450
ALIX	ALG-2 interacting protein X
AMOT	Angiomotin
ANCHR	Abscission/NoCut Checkpoint Regulator
ANOVA	Analysis of Variance
APC	Adenomatous Polyposis Coli
APC/C	Anaphase Promoting Complex/Cyclosome
APC10	Anaphase Promoting Complex 10
aPKC ζ	Atypical Protein Kinase C Zeta
ATP	Adenosine Triphosphate
ATPase	Adenosine Triphosphatase
ARF6	ADP ribosylation factor 6
BMK-1	BimC subfamily of kinesin-1
BRCA2	Breast Cancer Type 2
BSA	Bovine Serum Albumin
BUB1	Budding Uninhibited by Benzimidazoles 1
BUB3	Budding Uninhibited by Benzimidazoles 3
BubR1	Budding Uninhibited by Benzimidazoles-Related 1
Ca^{+2}	Calcium cation
CAMKII	Ca^{+2}/calmodulin-dependent protein kinase II

cAMP	Cyclic Adenosine Monophosphate
CAP-D2	Condensin I Complex Subunit D2
CAP-D3	Condensin I Complex Subunit D3
CAP-G	Condensin I Complex Subunit 3
CAP-G2	Condensin II Complex Subunit G2
CAP-H	Condensin Complex Subunit 2
CAP-H2	Condensin Complex Subunit H2
cCaspase3	Cleaved Caspase 3
CDC12	Cell Division Control 12
CDC20	Cell Division Cycle 20
CDC25	Cell Division Cycle 25
CDC25B	Cell Division Cycle 25B
CDC48	Cell Division Control 48
CDH1	Cadherin-1
CDK1	Cyclin Dependent Kinase 1
CDK5RAP2	CDK5 Regulatory Subunit Associated Protein 2
CDX2	Caudal Type Homeobox 2
CENP-A	Centromere Protein A
CENP-C	Centromere Protein C
CENP-E	Centromere Protein E
Cep55	Centrosomal Protein 55
Cep192	Centrosomal Protein 192
cGMP	Cyclic Guanosine Monophosphatase
CHMP4C	Charged Multivesicular Body Protein 4C
CIN	Chromosomal Instability
CO_2	Carbon Dioxide
CPC	Chromosome Passenger Complex
CREST	Calcinosis, Raynaud's Phenomenon, Esophageal Dysmotility, Sclerodactyly, and Telangiectasia.

CSF	Cytostatic Factor
CYK-4	CYtoKinesis Defect
DAB2	Disabled Homolog 2
DMSO	Dimethyl Sulfoxide
DNA	Deoxyribonucleic Acid
dsRNA	Double Stranded Ribonucleic Acid
EB1	End-Binding 1
ECT2	Epithelial Cell Transforming 2
EGFP	Enhanced Green Fluorescent Protein
eIF4G	Eukaryotic Initiation Factor 4G
EPI	Epiblast
ER	Endoplasmic Reticulum
ES cells	Embryonic Stem Cells
ESCRT-I/III	Endosomal Sorting Complexes Required for Transport I/III
Ezr	Ezrin
FGF4	Fibroblast Growth Factor 4
FISH	Fluorescence *in Situ* Hybridisation
FRAP	Fluorescence Recovery After Photobleaching
G1	Gap 1
G2	Gap 2
γ-TURC	γ-Tubulin Ring Complex
GAP	GTPase Activating Proteins
GAP43	Growth Associated Protein 43
GATA4	Transcription factor GATA4 that binds to the consensus sequence 5'-AGATAG-3'
GATA6	Transcription factor GATA6 that binds to the consensus sequence 5'-AGATAG-3'
GCP	γ-Tubulin Complex Protein
GCP3	γ-Tubulin Complex Protein 3
GCP4	γ-Tubulin Complex Protein 4
GCP6	γ-Tubulin Complex Protein 6

GDP	Guanosine Diphosphate
GEF	Guanine Exchange Factor
GFP	Green Fluorescent Protein
GTP	Guanosine Triphosphate
GTPase	Guanosine Triphosphatase
GVBD	Germinal Vesicle Breakdown
H1	Histone H1
H2	Histone H2
H4	Histone H4
H2A	Histone H2A
H2B	Histone H2B
H3K9me3	Histone H3 Lysine 9 Tri-methylation
H3K27me3	Histone H3 Lysine 27 Tri-methylation
hTERT-RPE1	Human Telomerase Reverse Transcriptase-Retinal Epithelial Cell 1
HyD	Hybrid Detector
ICM	Inner Cell Mass
IMARIS	Interactive Microscopy Image Analysis Software
INCENP	Inner Centromere Protein
InsP	Inositol Phosphate
IP3	Inositol Triphosphate
KIF4	Kinesin Family Member 4
KIF2a	Kinesin Family Member 2a
KIF2b	Kinesin Family Member 2b
KMN	Knl1, Mis12 and Ndc80 complexes
kMT	Kinetochore-Microtubule
KNL1	Kinetochore Scaffold 1
KSOM	Potassium-supplemented Simplex Optimised Medium
LATS 1/2	Large Tumour Suppressor Kinase 1/2
LED	Light Emitting Diode

LGL1	Lethal Giant Larvae Protein Homolog 1
LH	Luteinising Hormone
MAD1	Mitotic Arrest Deficiency 1
MAD2	Mitotic Arrest Deficiency 2
MajSat	Major Satellite
MAP	Microtubule Associated Protein
MCAK	Mitotic Centromere-Associated Kinesin
MCC	Mitotic Checkpoint Complex
MDCK	Madin-Darby Canine Kidney Cells
MEL-28	Maternal Effect Lethal 28
MI	Meiosis I
MII	Meiosis II
M^7G	7-Methylguanosine
MKLP1	Mitotic Kinesin-Like Protein 1
MLCK	Myosin Light-Chain Kinase
MN	Micronucleus
MOZART1	Mitotic-Spindle Organizing Protein 1
M-phase	Mitosis
MPF	Maturation Promoting Factor
MPS1	Monopolar Spindle 1
mRNA	Messenger Ribonucleic Acid
MT	Microtubule
MTOC	Microtubule Organising Center
NEBD	Nuclear Envelope Breakdown
NEDD1	Neural Precursor Cell Expressed Developmentally Downregulated 1
NPC	Nuclear Pore Complex
NPPC	Natriuretic Peptide C
NPR1	Natriuretic Peptide Receptor 1
NuMA	Nuclear Mitotic Apparatus Protein

Nup153	Nucleoporin 153
Nup107-160	Nucleoporin 107-160
OCT4	Octamer-binding Transcription Factor 4
PABP	Poly(A)-binding Protein
PAGFP	Photoactivatable Green Fluorescent Protein
PARD3	Partitioning Defective 3 Homolog
PARD6B	Partitioning Defective 6 Homolog Beta
PBS	Phosphate-Buffered Saline
PCM	Pericentriolar Material
PCNA	Proliferating Cell Nuclear Antigen
PDE3A	Phosphodiesterase 3A
PDGFRα	Platelet-Derived Growth Factor Receptor Alpha
PE	Primitive Endoderm
PFA	Paraformaldehyde
PGS	Preimplantation Genetic Screening
PI3/Akt	Phosphoinositide 3/Protein Kinase B
PIP	Phosphatidylinositol
PKA	Protein Kinase A
PLCζ	Phospholipase C ζ
PLK1	Polo-like Kinase 1
PLK4	Polo-like Kinase 4
PRKC ζ/ι	Protein Kinase C ζ/ι
PKC ι	Protein Kinase C ι
PKC ζ	Protein Kinase C ζ
PMT	Photomultiplier Detector
Rac1	Ras-Related C3 Botulinum Toxin Substrate 1
RanGTP	GTP-Binding Nuclear Protein Ran
REF-52	Rat Embryo Fibroblast 52
RFP	Red Fluorescent Protein

RNA	Ribonucleic Acid
RNAi	Ribonucleic Acid Interference
RhoA	Ras Homolog Family Member A
Rho kinases	Ras Homolog Kinases
Rock 1/2	Rho-Associated Protein Kinase
RZZ	Rod–Zw10–Zwilch Complex
SAC	Spindle Assembly Checkpoint
SEM	Standard Error of Mean
shRNA	Short Hairpin Ribonucleic Acid
Scc1	Sister Chromatin Cohesion Protein 1
Scc3	Sister Chromatin Cohesion Protein 3
SMC	Structural Maintenance of Chromosomes
Smc1	Structural Maintenance of Chromosomes Protein 1
Smc3	Structural Maintenance of Chromosomes Protein 3
SNP	Single Nucleotide Polymorphism
S-phase	Synthesis Phase
SOX2	SRY-Box Transcription Factor 2
SOX17	SRY-Box Transcription Factor 17
TALE	Transcription Activator-like Effector
TE	Trophectoderm
TEAD4	TEA Domain Transcription Factor 4
TGC	Trophoblast Giant Cells
TPX2	Targeting Protein for Xklp2
UBCH10	Ubiquitin-Conjugating Enzyme H10
UPR	Unfolded Protein Response
VPC	Vulval Precursor Cells
VPS4	Vacuolar Protein Sorting-Associated Protein 4A
YAP1	Yes-Associated Protein Homolog 1
ZGA	Zygotic Genome Activation

To my beloved husband, Arturo

Aos meus amados pais e irmã, Cecilia, Jorge e Ana

Acknowledgements

When I first arrived in Canada to start my Ph.D., I could never have imagined how fortunate I would be to have such a supportive network throughout this path. There are so many people who have, one way or another, contributed to my reaching this point and, although it is hard to include everything in just a few paragraphs, I will do my best to acknowledge all of those who have provided me with support during this time.

Firstly, I would like to thank all my mentors who have guided me during these years. My supervisor, Greg FitzHarris. Thank you for giving me the opportunity to perform research in your lab and for providing me with the guidance not only to develop high quality research, but also to think critically and communicate my research. I am also immensely grateful for your trust and for your constant support in my career development. My Ph.D. committee, Gilles Hickson and Richard Bertrand, who have always encouraged me and provided amazing feedback on my research during our meetings, and now Gilles for reviewing my work as my thesis jury. I would also like to extend my gratitude to the other members of my thesis jury, Jean-Claude Labbé and Susanne Bechstedt for reviewing my work.

I would also like to thank my colleagues at the CRCHUM, past and current, with whom I had the pleasure not only to work with on a daily basis but also to share stimulating conversations, 'coffee breaks', 5-7s, conference dinners and etc. The past lab members: Shoma Nakagawa, for his invaluable guidance during my first few months as a Ph.D. student, for thoroughly teaching me every single technique in the lab, from embryo collection to all kinds of micromanipulation and confocal imaging. Jenna Haverfield, Angus Macaulay and Cayetana Vázquez-Diez who all helped me a lot during my training, but also with whom I shared good moments, laughs and stimulating conversations. The present lab members: Filip Vasilev, Lin Yin, Henry Brennan-Craddock, Karolína Kravériková, Aleksandar Mihajlović, who are all kind and amazing colleagues to work with and also with whom I shared many enjoyable and relatable moments. Gaudeline Rémillard-Labrosse, who not only makes sure that we don't accidentally burn down the lab and that we have everything we need to work, but also genuinely cares about those around her and makes us feel welcomed. I am especially grateful to Adélaïde Allais, with whom I drank a lot of coffee at 10am every day (at least before the pandemic!). But not only that, for being there to talk both about

serious and not so serious stuff. For your company, your help in many situations, your advice and for the pleasure of working with you. A big thanks also goes to the past and present members of the Sarfati and Hébert/Dieudé labs for the enjoyable company and to Aurélie Cleret-Buhot for invaluable microscopy assistance.

This work would of course not have been possible without the support of the funding agencies. I am grateful for the Fonds de Recherche du Québec – Santé for awarding me with a doctoral scholarship and for the Université de Montréal for providing me with scholarships for exemption of supplementary tuition fees and recognition awards throughout these years. I would also like to extend my gratitude to the Réseau Québécois en Reproduction and the Centre de Recherche en Reproduction et Fertilité of the Université de Montréal for all the opportunities to share my research and for providing a friendly environment for discussions and networking.

Finally, the most important source of strength, love and support during these years comes from my family. I am infinitely grateful to my husband Arturo, who truly supports me in every possible way and every single day, who believes in my potential, helps me overcome fears and insecurities and encourages me to follow my dreams. ¡Tu apoyo y amor es lo que me llena de fuerza para seguir! Um imenso obrigada vai à minha família no Brasil que estiverem sempre ao meu lado e apoiaram toda e qualquer decisão que eu fiz, por mais difícil que fosse. Meus pais, Cecilia e Jorge, que se preocupam com todos os detalhes, estão sempre presentes e dão tudo de si para nos verem bem, além de sempre se manterem próximos, mesmo que a distância seja grande. Minha irmã, Ana, que sempre me fez ver o mundo e as situações com uma perspectiva positiva e me motiva a seguir meus objetivos. Meu sobrinho, Vinicius, que sempre vai ter um lugar especial no meu coração. ¡Gracias por todo! Obrigada por tudo!

Chapter 1 - Introduction

1.1 Preimplantation development

Preimplantation development in mammals is triggered by fertilisation of the egg by the sperm and subsequent formation of a zygote (or 1-cell embryo) that is encapsulated by a glycoprotein shell termed the zona pellucida and contains two pronuclei (**Figure 1**). In mouse embryos, each parental pronucleus undergoes DNA replication simultaneously, and upon mitotic entry, the maternal and paternal chromosomes fuse prior to cytokinesis to form a single metaphase plate. Following anaphase entry, the embryo completes the first cell division and ultimately forms a 2-cell embryo in which each blastomere contains a single diploid nucleus. As the embryo travels along the oviduct, a sequence of cell divisions takes place, each of which doubles the cell numbers while simultaneously reducing cell size in half (**Figure 1**). At the late 8-cell stage, the embryo undergoes the first major morphogenetic event, termed compaction, whereby increased cell-cell adhesion driven by enrichment of E-cadherin at the basolateral domain causes the blastomeres to become less individualised and more flattened (**Figure 1**). This takes place concomitantly with the emergence of cell polarity, in which an enrichment of polarity proteins at the apical and basal surfaces of each blastomere marks the beginning of lineage differentiation. At the 16-cell stage, the morula embryo is now composed of two cell populations: outer blastomeres that further differentiate into the trophectoderm which is essential for implantation and contribute for the formation of the placenta; and inner blastomeres, most of which will later differentiate to become the foetus (**Figure 1**). The transition between the morula and blastocyst stage is characterised by the formation of a cavity filled with fluid termed the blastocoel, which is surrounded by the trophectoderm and houses a cluster of inner cells termed the inner cells mass (ICM) (**Figure 1**). The following sections will describe the main events of preimplantation development, starting from oogenesis and fertilisation until lineage differentiation in the blastocyst.

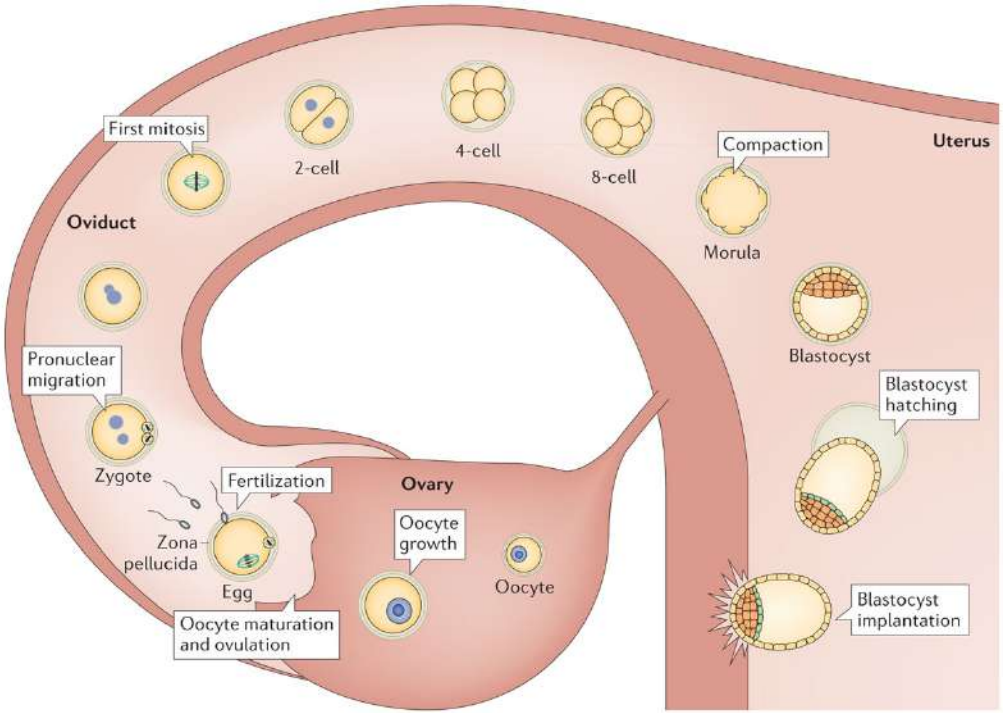

Figure 1. – Overview of preimplantation development.

Egg fertilisation by the sperm takes place after ovulation and forms a zygote containing one maternal and one paternal pronucleus. This is followed by sequential cell divisions that take place as the embryo travels through the oviduct, during which cell number increases concomitantly with progressive reductions of cell size. At the late 8-cell stage, the first identifiable morphogenetic event occurs, termed compaction, concomitantly with the emergence of apical polarity. The subsequent cell divisions from the 8- to 16-cell stage generate two cell populations within the embryo: inner and outer cells which will further contribute to the inner cell mass and trophectoderm lineages, respectively. Finally, a fluid-filled cavity develops inside the embryo forming the blastocyst which further hatches to implant onto the uterine wall. Adapted from Clift and Schuh 2013[1].

1.1.1 Oogenesis and fertilisation

The germ line of mammalian females is composed of differentiated oogenic germ cells arrested at prophase of meiosis I. These highly specialized cells are capable of maintaining meiotic arrest for variable periods of time depending on the species: ~54-60h in *Caenorhabditis elegans*, months in mice and years in women[2]. The prophase I arrest allows the oocyte to grow in size in order to stockpile macromolecules and maternal mRNA to be able to support meiotic maturation, fertilisation and embryonic development. Maintenance of prophase I arrest in the oocyte requires high levels of cyclic AMP (cAMP) which regulates the arrest by acting through protein kinase A (PKA) to maintain the catalytic subunit of the maturation-promoting factor (MPF) CDK1 kinase

in a phosphorylated inactive form (**Figure 2A**). The prophase arrest is thought to be maintained by a combination of intrinsic and extrinsic signals mediated by the oocyte itself and the surrounding cumulus cells, respectively. Cumulus cells are in close contact with the oocyte via gap junctions, and the inhibitory signals that promote the arrest are thought to be transmitted through these gap junctions and the follicular fluid[2, 3]. The molecular mechanism by which cumulus cells contribute to the prophase arrest involves the inhibition of cAMP degradation via cyclic GMP (cGMP) activity[3]. Cyclic GMP synthesis in cumulus cells is promoted by the exchange from GTP to GMP via the membrane-associated guanylyl cyclase natriuretic peptide receptor (NPR2), which is stimulated by signalling from C-type natriuretic peptide (NPPC) originating from mural granulosa cells[4]. Subsequently, cGMP is transported from cumulus cells to the oocyte via gap junctions where it inhibits PDE3A, the main cAMP phosphodiesterase, thereby ensuring that cAMP remains active and functional[4] (**Figure 2A**).

As opposed to somatic cells that have alternating phases of DNA replication and chromosome segregation, meiosis is characterised by two successive rounds of division without intervening S-phase. The first meiotic division is initiated in response to luteinising hormone (LH) signalling from the pituitary gland and is characterised by nuclear envelope breakdown (also termed germinal vesicle breakdown in oocytes – GVBD). LH is recognised by G-protein coupled receptors and decreases cGMP levels in granulosa cells thereby closing gap junctions between cumulus cells and oocytes leading to a drop in intra-oocyte cGMP levels[5, 6]. This drop in cGMP levels induces the activation of PDE3A and further hydrolysis of cAMP, which enables activation of CDK1 via its dephosphorylation and thus entry into M-phase[7]. Upon GVBD, the first meiotic spindle is assembled and, in conjunction with the attached chromosomes, the metaphase I spindle migrates towards the cortex of the oocyte where anaphase I takes place. Prior to anaphase I, CDK1 activity increases drastically during metaphase I, and when all bivalents are properly attached to the spindle microtubules, the APC/C alongside with CDC20 induces ubiquitin-mediated degradation of securin and cyclin B1, which then promotes the cleavage of cohesins by separase and a further decline in CDK1 activity, allowing chromosome segregation and anaphase to progress until the first polar body is extruded[8].

Following polar body extrusion, CDK1 activity is quickly re-established, the oocytes progress through prometaphase II rapidly and again become arrested, this time in metaphase II.

This second cell cycle arrest is distinct to the prophase arrest of immature oocytes as it requires high CDK1 activity which ensures that chromosomes remain aligned in the metaphase spindle without progressing through anaphase. The exact mechanisms that promote the metaphase II arrest are yet to be fully elucidated, however micromanipulation experiments using frog eggs performed by Masui and Market in 1971 demonstrated that this arrest is most likely mediated by cytoplasmic components, which they referred to as the cytostatic factor (CSF)[9]. First, they found that injecting the cytoplasm from MII arrested eggs into immature oocytes can trigger entry into meiosis even in the absence of hormonal stimuli, and second, when injected into 2-cell embryos, the cytoplasm from MII eggs causes a cell cycle arrest, characterised by the presence of a metaphase spindle and high levels of CDK1 activity[9]. The complete molecular composition of the CSF has not been fully elucidated, but the pathways related to the CSF are thought to act via inhibition of the APC/C, and evidence in *Xenopus* eggs suggest that a pathway dependent on Mos/MEK/MAPK/$p30^{Rsk}$ might be responsible for the MII arrest[10, 11, 12, 13, 14], although evidence in mice suggests that $p30^{Rsk}$ is not essential for the MII arrest[15]. Alternatively, the protein Erp1/Emi2 has been identified as another potential component of the CSF that induces the MII arrest presumably due to its ability to inhibit the APC/C[16]. The idea that Erp1/Emi2 might be a component of the CSF was substantiated by the observation that Erp1/Emi2 depletion induces premature release from MII arrest and that endogenous Erp1/Emi2 is rapidly destroyed upon Ca^{2+}-induced egg activation[16].

The trigger to overcome the CSF-induced metaphase II arrest comes from signalling mediated by sperm entry during fertilisation. The event known as "egg activation" is characterised by completion of meiosis II, release of cortical granules and translation of the maternal mRNA. Initial insights into this mechanism were described in 1907, when Loeb observed that changes in the composition of the fertilising media were sufficient for the initiation of development[17]. This observation has been subsequently attributed to periodical changes in Ca^{+2} concentration upon egg activation[18]. These repetitive increases in intracellular [Ca^{+2}] are thought to be triggered by phospholipase Cζ (PLCζ) which is a soluble protein delivered by the sperm. Each oscillation is generated by a release in Ca^{+2} from the endoplasmic reticulum mediated by inositol 1,4,5-triphosphate (InsP) and further influx of extracellular Ca^{+2} [19] (**Figure 2B**). One consequence of Ca^{+2} release is the exocytosis of cortical granules, which are secretory organelles derived from the Golgi complex[20] and this phenomenon is responsible for blocking polyspermy through zona

pellucida modifications[20]. Following egg activation, the maternal and paternal chromatin that remain in the newly formed zygote undergo decondensation and assemble two physically individualised haploid pronuclei, which subsequently undergo DNA replication independently and do not interact until after mitotic entry, in which the parental genome merges by fusing the two mitotic spindles[21].

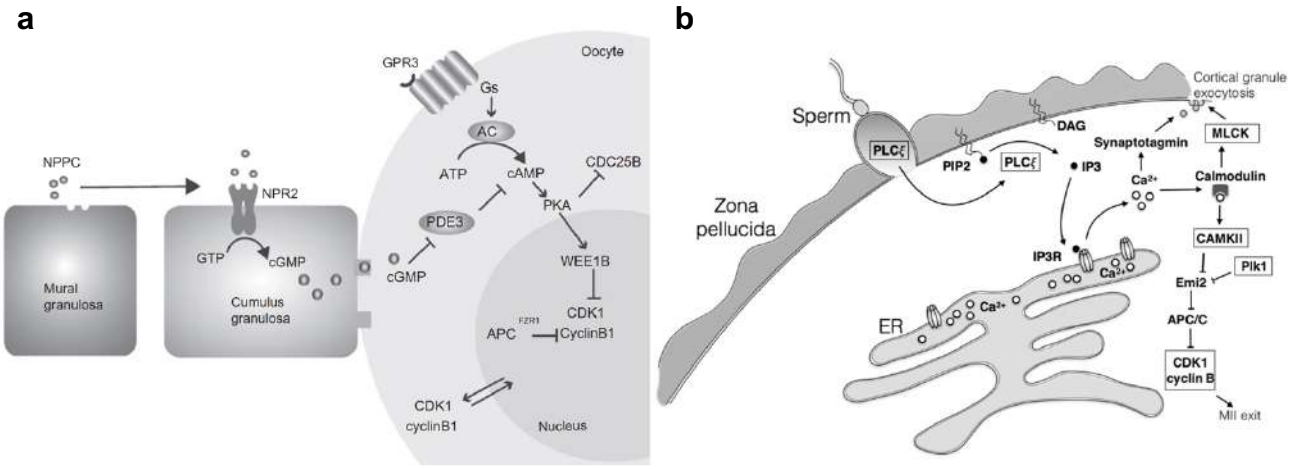

Figure 2. – Molecular pathways of prophase arrest and events triggered by fertilisation.

(a) *G-protein linked receptors (GPR3) stimulate adenylate cyclase (AC) to produce cAMP which promotes PKA activity. The cumulus cells contribute to the maintenance of cAMP levels by producing cGMP from NPR2 in response to NPPC signalling from mural granulosa cells. High PKA activity (i) inhibits CDK1/Cyclin B in the nucleus and (ii) inhibits the activity of CDC25B. Inhibition of CDK1/Cyclin B activity maintains the arrest until the LH surge. Adapted from Holt et al., 2013[22]. (**b**) Following sperm-oocyte fusion, PLCζ is released in the cytoplasm and facilitates the hydrolysis of inositol 1,4,5-triphosphate (IP3). This molecule then induces Ca^{+2} release from the endoplasmic reticulum (ER) and causes calmodulin activation of CAMKII which inhibits the cytostatic factor Emi2. Inhibition of Emi2 leads to the activation of the APC/C, subsequent degradation of cyclin B and completion of meiosis II. Moreover, Ca^{+2} release also induces cortical granule exocytosis through synaptotagmin and MLCK activity. Adapted from Bury et al., 2016[20].*

1.1.2 The preimplantation cell cycle and zygotic genome activation

The cell cycle can be broadly split into two phases: interphase, which is a long growth period that comprises roughly 95% of cell cycle duration and prepares the cell for entry into the second phase, termed mitotic phase (or M-phase) which is substantially shorter and results in segregation of the newly replicated DNA and formation of two new daughter cells (**for a detailed description of mitosis, refer to section 1.2**). Interphase can be further subdivided into stages known as G1, S and G2 which, unlike M-phase, are not discernible by observable events but can be detected through

the measurement of DNA content. The G1 and G2 stages of the cell cycle are known as gap or growth phases, during which cell size increases concomitantly with transcription of mRNA and synthesis of proteins required for cell division. The S-phase is characterised by high fidelity replication of the chromosomes, whereby the diploid genome increases to a tetraploid status, and the number of centrosomes doubles, which is an essential step for proper spindle assembly during mitosis. Following S-phase, the cell enters the G2 phase during which surveillance mechanisms ensure genome integrity, followed by M-phase, during which the duplicated chromosomes are ultimately separated into two new daughter cells[23]. In certain conditions, exit from M-phase can result in cells entering non-replicative states, including permanent arrests associated with terminal differentiation or senescence or the reversible non-replicative state known as quiescence (G0)[24].

Unlike most somatic cells, the preimplantation embryo progresses through the cell cycle without intervening cell growth and it undergoes a series of cleavages during which cell number increases but cell size reduces in half at each consecutive division[21]. The first two embryonic cell cycles are the longest in preimplantation and can last approximately 18h-20h in total, although the length of each cell cycle phase differs between these two divisions[22, 23, 24, 25, 26]. The first cell cycle is reported to display between 5-12h for G1, 4-7h for S-phase, 1-8h for G2 and 120min for M-phase; whereas the second cell cycle consists of a very short G1 phase (0.5-1.3h), followed by 1-5h of S-phase, a very long G2 phase (12-16h) and a shorter M-phase (70min)[25, 26, 27, 28, 29]. In contrast to the wide variation observed in the initial cell cycles, the later cell cycles starting from the 8-cell stage until the 32- to 64-cell stages are shorter, lasting approximately 12-14h, and more homogeneous, with approximate lengths of 1-2h for G1, 7h for S-phase, 1-5h for G2 and 40-50min for M-phase[30].

During the first few days of development, the cell cycle of the early embryo is devoid of active transcription, and previously stored maternal mRNA donated by the oocyte is the main source of translational information. Low levels of transcription can be detected as early as in the first embryonic division, however full zygotic genome activation (ZGA) is only observed at the G2/M transition of the 2-4cell stage in mice and the 4-8cell stage in humans[31]. Across all species, ZGA is a requirement for embryo development and inhibition of this process causes arrest and morphological abnormalities at different stages of development that vary depending on the species[32]. The factors that determine the timing and regulation of ZGA across species have yet to

be fully elucidated, however a combination of histone modifications that directly impact chromatin accessibility to transcription factors, coupled with active degradation of maternal mRNA are thought to be the key steps for ZGA.

The chromatin is composed of DNA molecules wrapped around nucleosomes, which are the basic unit of DNA packaging, containing approximately 146 DNA base pairs wrapped around octamers of the histone proteins H2A, H2B, H2 and H4. The connection of histone proteins via histone linker proteins such as H1 shapes the heterochromatin, which is transcriptionally inactive, and chromatin remodelling is required to provide greater accessibility for transcription. The most common and well-studied types of chromatin remodelling involve histone N-terminal modifications by the addition of methyl or acetyl tails. In the context of embryonic development, lysine acetylation and lysine (tri)methylation are the two major types of histone modifications responsible for allowing ZGA. Initially, the mouse male pronucleus is characterized by a permissive H4 acetylation allowing the minor wave of ZGA at the 1-cell stage, and this is later modified upon the action of histone deacetylase activity, inducing a transient period of transcriptional repression until the 2-cell stage[33, 34]. Trimethylation of histone H3 at lysines 4 and 27 (H3K4me3 and H3K27me3, respectively) seem to play opposing roles of activation and repression of gene expression even though its effects vary considerably across different species. In mice, the inactive female pronucleus is marked with H3K27me3 and the male pronucleus only acquires this feature towards the end of the first minor wave of genome activation[35]. On the other hand, H3K4me3 – which is generally associated with transcription activation functions - is also found in the female pronucleus, indicating that this modification does not affect mouse ZGA[36].

Concomitant with increased chromatin accessibility, a complementary process that must occur is maternal mRNA clearance, which results in a drastic change in the transcriptional landscape with an elimination of 30-40% of the maternal mRNA and relies on modification of key mRNA features that impact its stability, such as modifications in the length of the 3' poly(A) tail and on 7-methylguanylate (m^7G) capping[32, 37]. The poly(A) tail is responsible for stabilizing the mRNA 3' end as it is bound to poly(A)-binding proteins (PABPs), thereby interacting with eIF4G which is a factor that initiates translation[37]. Accordingly, studies in *D. melanogaster* and *Xenopus laevis* embryos have shown that shortening of the poly(A) tail is a major route for maternal mRNA clearance[38, 39, 40]. In addition to poly(A) tail modifications, m^7G capping is another factor that

determines maternal mRNA clearance due to its role on protection of mRNA from exonucleolytic decay and hydrolysis[37]. Consistent with this, in *Xenopus* embryos, although certain maternal mRNAs have been shown to be deadenylated early after egg fertilisation, full degradation was only observed after decapping activity was detected, indicating that mRNA decapping triggers destabilization of deadenylated mRNAs, although the mechanisms that activate decapping and its exact role in maternal mRNA clearance remain to be fully elucidated[41].

1.1.3 Compaction and polarisation

During preimplantation development, a series of morphogenetic changes culminate in the segregation of cell lineages at the blastocyst stage wherein the trophectoderm (TE, future placenta) and the inner cell mass (ICM) are initially established. Further ICM differentiation generates the epiblast (EPI, future foetus, allantois, yolk sac mesoderm and amnion) and primitive endoderm (PE, future yolk sac endoderm) at the late blastocyst stage. However, the onset of cell fate decisions that determine lineage segregation is preceded by specific morphological events that occur as early as the 8-cell stage, which are essential to determine the transcriptional signature of each cell lineage. Compaction at the late 8-cell stage is the first recognisable morphogenetic event of preimplantation development and is characterised by a sharp change in shape of all eight blastomeres within the embryo, that culminates with formation of the characteristic mulberry-shaped morula (**Figure 3A**). At the early 8-cell stage, all blastomeres are round and individualised, but by the time compaction initiates at the late 8-cell stage, the blastomeres become flat and morphologically indistinguishable, which leads to all blastomeres acquiring a contactless apical surface and a basolateral surface that is in contact with the neighbouring cells (**Figure 3**).

The mechanisms that drive compaction are yet to be fully elucidated, however E-cadherin has been shown to be essential for this process[42, 43, 44, 45, 46]. During compaction, the subcellular localisation of E-cadherin changes from being evenly distributed throughout the plasma membrane to being restricted to sites of cell-cell contact (i.e., the basolateral domain) as adherens junctions are formed[47]. Consistent with the role of E-cadherin on compaction, removal of Ca^{+2} from the culture media[42] – which promotes conformational changes in the extracellular domain that prevent homotypic interactions – and depletion of E-cadherin by treatment with an antibody against E-cadherin[43] both prevent embryo compaction. However, evidence suggest that both maternally

inherited or zygotically encoded E-cadherin alone are sufficient to induce compaction, since compaction is only fully abolished once both maternal and zygotic E-cadherin are depleted simultaneously[44, 45, 46]. Regarding the mechanical forces that mediate compaction, different studies propose distinct mechanisms by which the changes in cell shape are generated and maintained during compaction. The existence of filopodia that emanate from the basolateral surface towards the apical domain at the 8-cell stage has been thought to maintain compaction by intensifying cell contacts in the basolateral domain and promoting tension at the apical domain, thereby ensuring the flat and elongated morphology of blastomeres in a manner dependent on E-cadherin[48]. Alternatively, contractility of the actomyosin cortex has been proposed to initiate compaction via pulsed cortical contractions that increase surface tension within the contact-free apical domain and mediate compaction in a manner independent of E-cadherin[49].

Concomitant with compaction, cell polarisation emerges during the late 8-cell stage, wherein asymmetric distribution of proteins between apical and basolateral membrane domains results in differential inheritance of such factors following cell division, generating daughter cells with distinct functional properties that eventually translate into divergent cell fate decisions (**Figure 3**). Although polarisation takes place concomitantly with compaction, evidence suggests that polarity establishment can occur independently of compaction, since blastomeres devoid of maternal and zygotic E-cadherin[46] and isolated blastomeres that lack cell-cell contacts[50] can still establish apical polarity. However, the structural organisation of the apical domain indeed seems to be influenced by cell-cell contacts, given that the apical domain tends to assemble as far away as possible from sites of cell-cell contact, and polarity establishment is seemingly impossible when blastomeres are completely surrounded by other cells[51], which alludes to an influence of cell contact patterns on the determination of the apical-basal axis. As for the factors that initiate polarity acquisition, redistribution and stabilisation of microvilli mediated by phosphorylation of the protein Ezrin (Ezr) is one of the earliest events that initiate polarity establishment[52]. Early 8-cell blastomeres display an even distribution of microvilli around the plasma membrane and this pattern is subsequently shifted towards the contact-free apical domain once the embryo becomes compacted and microvilli are excluded from the basolateral surface[53]. Accordingly, Ezr localisation follows the patterns of microvilli distribution, with it being initially distributed evenly around the plasma membrane in early 8-cell blastomeres, followed by an accumulation at the apical surface

mediated by phosphorylation at amino acid residue threonine-567, thereby inducing apical accumulation of microvilli[52, 54]. Consistent with the role of Ezr phosphorylation in microvilli redistribution, substitution of the threonine-567 residue by alanine prevents Ezr removal from basolateral surface and microvilli accumulation at the apical surface[52], and evidence suggests that aPKC ζ/λ may be responsible for phosphorylation of Ezr[55].

The shifts in microvilli and Ezr distribution are accompanied by dynamic changes in localisation of polarity proteins. For instance, at the late 8-cell stage, Pard6b and Prkc ζ/ι are redirected from the nucleus and cytoplasm, respectively, to the apical membrane, whereas Emk1 is dragged from the nucleus to the basolateral surface, alongside with members of the Scribble complex and the lethal giant larvae homologue 1 (Lgl1)[56, 57, 58, 59]. These precise mutually exclusive apical and basolateral patterns of protein distribution are dependent on the activity of Rho associated kinases (Rock 1/2), which are downstream effectors of the small GTPase RhoA, and chemical inhibition of these factors leads to mis-localisation of apical and basolateral components and impaired blastocyst formation[57, 60]. In addition, Pard6b, Pard3 and Prkc ζ/ι are also thought to be involved in the formation and maintenance of tight junctions and blastocoel formation, as evidenced by disrupted tight junction formation upon Pard6b and/or Prkc ζ/ι downregulation[61, 62] and by the observation that Pard3 is targeted to tight junctions particularly around the time of cavitation[56]. However, little is known about how the expression of genes that encode for polarity factors is controlled, although evidence suggests that the transcription factor AP-2 g (Tfap2g) mediates the expression of Pard6b. Accordingly, Tfap2g downregulation leads to failure in tight junction formation, polarity defects and disrupted trophectoderm lineage specification, all of which are also attributable to perturbations in Pard6b expression[61, 63].

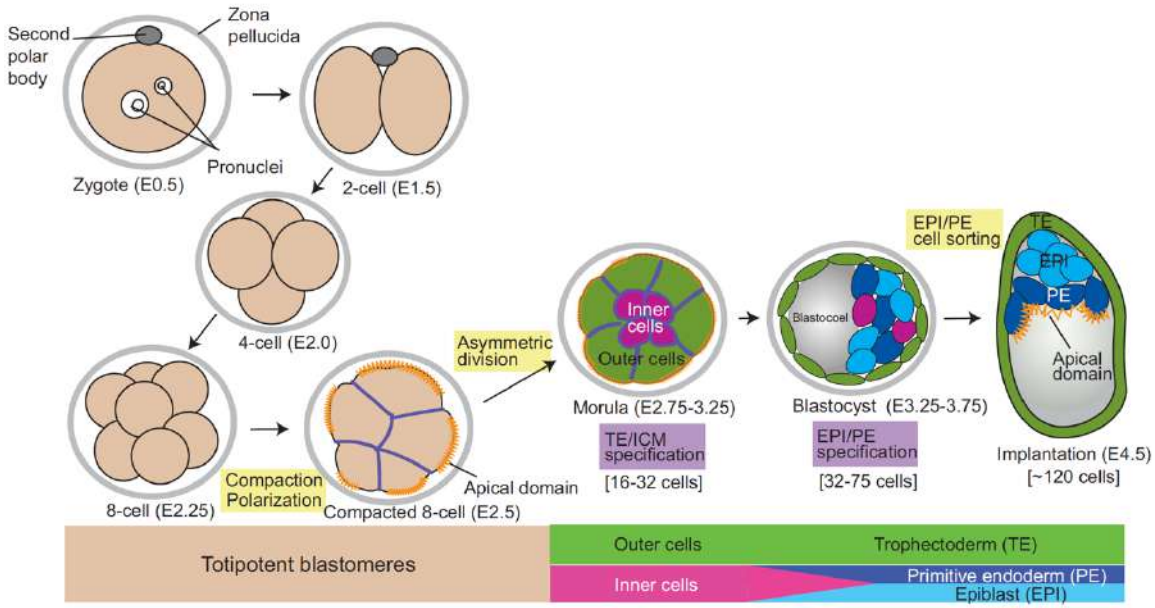

Figure 3. – Main events of mouse preimplantation development.

As the preimplantation embryo travels the oviduct, reductive cell divisions increase cell numbers whilst halving cell size. The late 8-cell stage is characterised by the onset of compaction, during which blastomeres become less individualised and flattened, concomitantly with the emergence of apical polarity, where enrichment of polarity proteins and microvilli at the apical surface marks the beginning of differentiation. Subsequent symmetric and asymmetric cell divisions generate a 16-cell embryo composed of apolar inner cells and polarised outer cells. Early blastocyst formation is marked by onset of blastocoel formation, in which a cavity filled with fluid separates the nascent inner cell mass (ICM) from the trophectoderm (TE), and subsequent cell sorting mechanisms further segregate the two embryonic lineages (primitive endoderm, PE; epiblast, EPI). Adapted from Chazaud and Yamanaka, 2016[64].

1.1.4 Cell position and cell fate determination

At the 16-cell stage, the embryo is composed of two cell populations – inner and outer cells - that are distinct both in terms of position in relation to one another and their function within the embryo (**Figure 3**). The functional differences between these two cell types reside on their distinct fates, with outer cells mostly becoming the trophectoderm and inner cells forming the inner cell mass. Although the detailed mechanisms by which blastomeres acquire their defined positions within the embryo are yet to be fully elucidated, cell division orientation is one of the first determinants of cell position. From the 8-cell stage onwards, two types of cell division can arise depending on whether the apical domain is inherited by both daughter cells or by only one of the daughter cells,

and these two distinct outcomes depend on the orientation of the spindle relative to the apical domain. Symmetric cell divisions are those in which the spindle is orientated perpendicularly to the apical-basolateral axis, and the resulting cell division generates two daughter cells that are seemingly identical in terms of inheritance of apical and basolateral components and occupy an outer position within the embryo (**Figure 4**). In contrast, asymmetric cell divisions are those in which the spindle is oriented parallelly to the apical-basolateral axis, and the resulting daughter cells are different from one another, with one inheriting the basolateral region of the parental cell and acquiring an inner position, and the other retaining the apical surface of the parental cell and remaining in the outer layer[59] (**Figure 4**).

Whether cell division orientation is stochastically determined or whether it is influenced by specific cell intrinsic factors is debatable, however the finding that the relative proportion of inner and outer cells at the 16-cell stage is highly variable among individual embryos argues against the idea that specific regulatory mechanisms drive cell division orientation[65, 66]. On the other hand, a study suggests that nuclear positioning at the 8-cell stage might influence cell division orientation, and nuclei residing closer to the apical surface are more likely to undergo symmetric cell divisions, alluding to the idea that the orientation of cell division might not be entirely randomised[67]. In addition, the size of the apical domain has also been proposed to influence cell division orientation at the 8-cell stage, and blastomeres containing apical domains restricted to a smaller area usually assemble the mitotic spindle in a parallel orientation relative to the apical surface, and therefore, more frequently undergo asymmetric divisions[68]. Interestingly, a recent study has proposed that the factors that influence cell division orientation differ in 8- and 16-cell stage embryos, and whereas 8-cell stage cell divisions are highly influenced by the role of the apical domain on spindle positioning, 16-cell stage cell divisions are more prominently influenced by the flattened shape of outer blastomeres which in turn positions the spindle parallelly to the apical surface[69]. This phenomenon ultimately changes the relative proportions of symmetric and asymmetric cell divisions between 8- and 16-cell embryos, with 8-cell embryos more frequently undergoing asymmetric divisions and 16-cell embryos more often undergoing symmetric divisions[69].

Although cell division orientation is thought to be the most important determinant of cell position in preimplantation development, the observation that some outer blastomeres do not retain the initial position acquired immediately after cell division and instead migrate towards the inner

region of the embryo has led to the realisation that active cell internalisation events might be an independent mechanism that determines cell position irrespective of cell division orientation[70, 71, 72]. These cell internalisation events are thought to arise when spindle positioning is neither perfectly perpendicular nor parallel to the apical-basolateral axis and are instead oblique and thus result in an uneven partitioning of the apical domain between daughter cells, while at the same time allowing the outer location of both cells immediately following cytokinesis[70] (**Figure 4**). This uneven partitioning of the apical domain generates two blastomeres with substantially divergent apical surface area, which in turn leads to internalisation of the less polarised blastomere[49] (**Figure 4**). Why less polarised blastomeres are more likely to be internalised is yet to be fully addressed, but the observation that the apical domain limits the access of myosin at the apical surface and therefore reduces cortical contractility might indicate that less polarised blastomeres accumulate higher levels of cortical myosin, thereby increasing contractility and facilitating cell internalisation due to their increased stiffness[49].

Regardless of whether positioning is determined based on division orientation or by cell internalisation, the cues provided by inner and outer cell position as well as the presence of apical polarity are critical for the first cell fate decision, and landmark work has shown that the Hippo signalling pathway is the molecular link between cell position and fate, wherein Hippo signalling is active in inner cells and suppressed in outer cells from the 16-cell stage onwards[73]. This selective activation of the Hippo pathway requires the activity of the serine/threonine large tumour suppressor kinase 1 and 2 (Lats1/2) exclusively in apolar inner cells, which in turn causes the transcriptional co-activator Yap1 to be phosphorylated and sequestered in the cytoplasm, thereby inhibiting its association with the TEA domain transcription factor 4 (Tead4), a transcription factor required for expression of trophectoderm-related genes[73, 74]. Thus, inhibition of TEAD4-dependent transcription of trophectoderm genes further ensures that ICM-related genes such as Oct4 and Nanog remain actively transcribed. On the other hand, polarised outer cells fail to activate Lats 1/2, which allows Yap1 to retain its nuclear localisation and association with Tead4, thereby enabling the expression of trophectoderm-related genes such as Cdx2[73]. Cdx2 is an essential transcription factor expressed exclusively in outer cells and is essential for trophectoderm specification, as evidenced by the abnormal expression of ICM-specific genes Oct4 and Nanog in the trophectoderm upon Cdx2 deletion[75]. Moreover, Cdx2 and ICM factor Oct3/4 have been shown to interact and

reciprocally inhibit the expression of each other's target genes, and this is thought to be a mechanism that limits their expression to the TE and ICM lineages, respectively[76].

Further studies have shown that Lats1/2 activation is regulated by angiomotin (Amot) and changes in its subcellular localisation are crucial for this process[77, 78]. At the 8-cell stage, Amot is detectable mostly at the apical surface of all blastomeres, and at the 16-cell stage, although outer cells retain an apical localisation of Amot, inner cells diverge from this pattern and Amot is distributed throughout the entire plasma membrane[77, 78]. These differential patterns of Amot localisation between inner and outer cells are thought to be a critical step for the selective activation of the Hippo pathway, since Amot associates with Lats1/2 exclusively at sites of adherens junctions and therefore its activity is restricted to apolar inner cells that are surrounded by cell-cell contacts. In contrast, Amot is sequestered at the apical surface of polarised outer blastomeres, which in turn inhibits its association with Lats1/2, thereby inactivating the Hippo pathway in those cells[78]. Importantly, proper apical localisation of Amot in outer cells is dependent on appropriate establishment of apical and basolateral domains, as evidenced by abnormal localisation of Amot and aberrant Hippo pathway activation in outer cells subjected to disruption of either apical or basolateral domains, indicating that correct Amot localisation is not solely dependent on the presence of a contactless surface[60, 78].

Following the positional and molecular establishment of the ICM during the first cell fate decision, further differentiation of these cells leads to the generation of epiblast and primitive endoderm lineages starting between embryonic days 3.5 and 4 (~32- to 64-cell stage)[64], in what characterises the second cell fate decision (**Figure 3**). The earliest markers of EPI and PE lineages are NANOG and GATA6, respectively, which are present in all blastomeres at the 8-cell stage, but starting at ~32-cell stage, acquire a mutually exclusive 'salt and pepper' pattern of expression, wherein some ICM cells express NANOG and others express GATA6[79]. The mechanism that controls this mutually exclusive pattern of expression is most likely a result of selective mRNA decay, and evidence that NANOG can repress GATA6 expression by binding to the proximal promoter region of the GATA6 gene suggests that these markers can directly interact with one another and therefore regulate EPI and PE lineage specification[80]. In addition, FGF4 signalling has also been associated with lineage specification, and inhibition of this pathway induces all ICM cells to adopt EPI fate[81 82], whereas excessive FGF4 addition leads to commitment of all ICM cells to

PE fate[81]. Mathematical modelling examining EPI/PE specification proposes that NANOG expression in one or a few cells in the early ICM is sufficient to promote an increase in FGF4 secretion[83]. This local increase of extracellular FGF4 concentration stimulates neighbouring cells to acquire PE specification and indicates that heterogeneous propagation of FGF4 could explain the asynchronous salt and pepper pattern of gene expression during EPI/PE lineage specification in the early embryo[83].

Upon specification of EPI/PE lineages, maturation of the PE is further accomplished through the expression of specific markers such as SOX2, SOX17, GATA4, PDGFRα and DAB2. At this point, the cells reach the 'point of no return' (i.e., they are fully committed to their fate), and any experimental manipulation that changes the cell numbers of either lineage is not anymore compensated by the other lineage[64]. Simultaneous to the expression of PE markers, the pluripotency factor OCT4, which is initially expressed in all ICM cells and is required to prevent ICM differentiation into TE, is then downregulated in PE cells at ~embryonic day 4.5[84]. The maturation of the PE is then followed by cell sorting within the ICM to form the two distinct tissues. Although this process is not yet entirely understood, studies have shown that lineage-specific transcription factors can modulate mechanical properties associated with migration, such as cell adhesion, via the expression of lamin 1 and collagen IV in PE cells and promote cell sorting[85, 86]. Moreover, actin inhibition by Cythocalasin D treatment has been shown to disturb cell movements, and different levels of cortical tension among distinct cell types generated by actomyosin network have been proposed to promote cell sorting[87]. Maintenance of cell position upon sorting is thought to be driven by cell polarity, wherein PE cells that migrate towards the blastocoel acquire apical/basolateral polarity, which anchors those cells to the surface thereby preventing further migration[88].

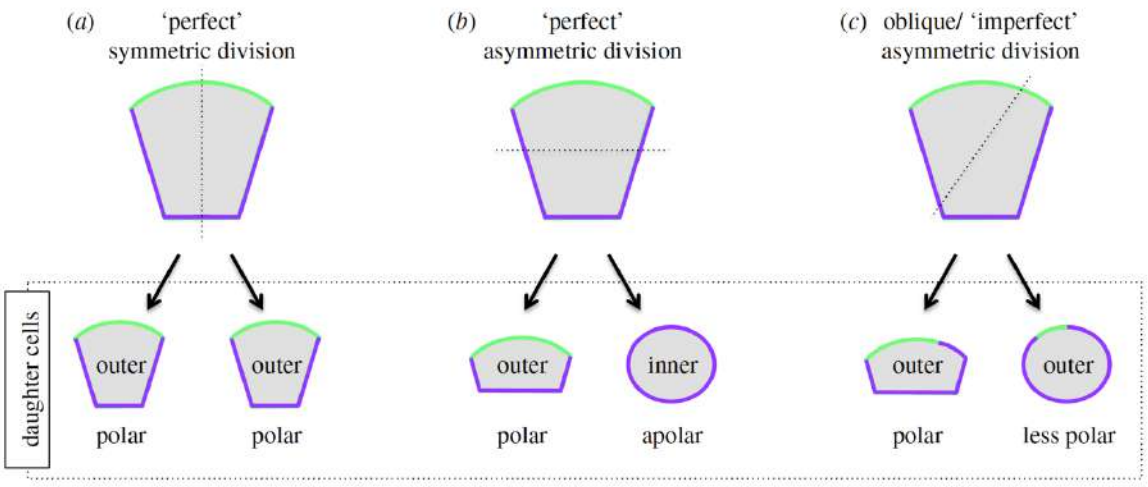

Figure 4. – Determinants of cell position and possible outcomes of polarity inheritance.

*When perfectly symmetric cell divisions take place, two identical polar outer blastomeres are generated **(a)**, whereas perfectly asymmetric cell divisions produce a polar outer blastomere and an apolar inner blastomere **(b)**. When 'oblique' asymmetric cell divisions take place, two initially outer-residing daughter cells are produced both of which contain uneven portions of the apical domain **(c)**. The 'less polarised' outer cell often internalises, most likely due to higher contractility. Green lines = apical domain; purple lines = basolateral domain. Adapted from Mihajlović and Bruce, 2017[59].*

1.2 Mitosis

Cell division is essential for all forms of life and the accuracy of this process is key for the maintenance of a healthy organism. Mitosis is the part of the cell cycle during which replicated chromosomes are separated into two nuclei and is commonly subdivided into five stages: prophase, prometaphase, metaphase, anaphase, and telophase. Prophase is characterised by the onset of chromosome condensation, centrosome separation (in centriolar organisms) and initiation of spindle assembly by mid to late prophase (**Figure 5A**). This is followed by nuclear envelope breakdown, completion of spindle assembly concomitant with capture of chromosomes by microtubules and chromosome congression during the stage known as prometaphase (**Figure 5B**). Chromosome congression further progresses with chromosomes becoming aligned during metaphase, which results in the formation of a symmetric structure named metaphase plate composed of aligned chromosomes and the bipolar fusiform spindle that ensures that chromosomes remain centred (**Figure 5C**). When all chromosomes are perfectly aligned at the metaphase plate, chromosome separation is triggered, wherein sister chromatids detach from one another and

separate, in a process called anaphase (**Figure 5D**). Finally, once the sister chromatids have separated far enough, two new functional nuclei are formed during telophase, so that cytokinesis – the physical separation of the cytoplasm – is initiated. Accuracy during all stages of mitosis is essential, since errors in chromosome segregation often lead to aneuploidy, which can have catastrophic consequences that range from cell cycle arrest and death to the development of cancerous phenotypes.

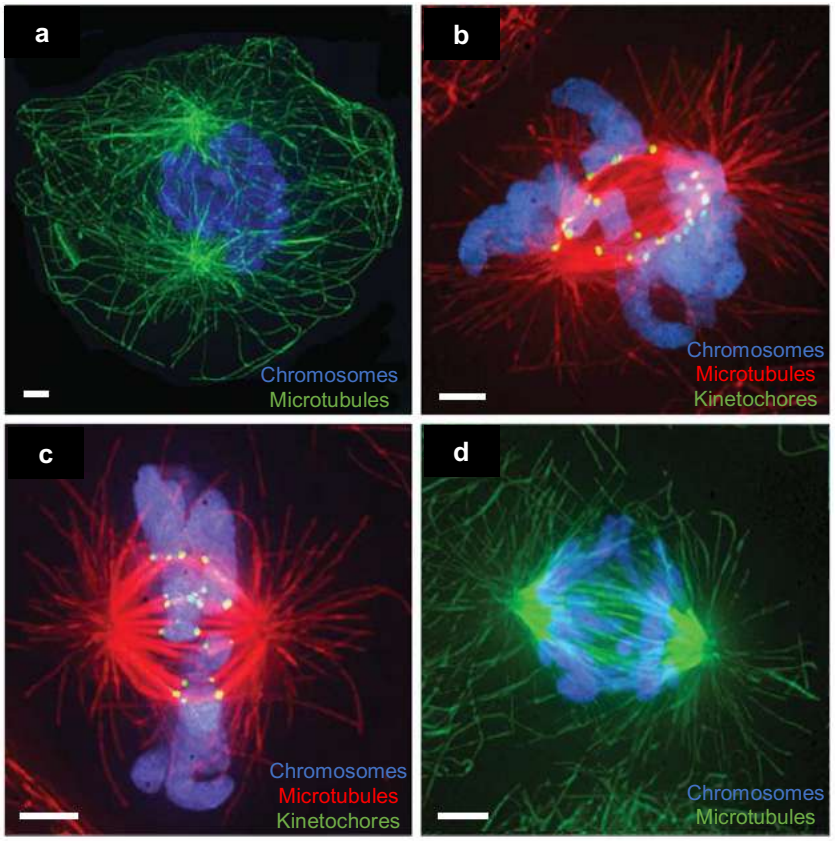

Figure 5. – Overview of mitosis.

*Immunofluorescence images of rat kangaroo Ptk_1 cells during mitosis. During interphase (**a**), the chromosomes start to condense while microtubule nucleation from the centrosomes marks the beginning of spindle assembly. This is followed by nuclear envelope breakdown and completion of spindle assembly during prometaphase (**b**) as the microtubules attach to the chromosomes via the kinetochores. Metaphase (**c**) is characterised by chromosome congression and alignment at the spindle midplane and anaphase (**d**) drives chromosome segregation, wherein individual sister chromatids move towards opposite poles as the spindle elongates. Scale bars = 2µm. Images by Jennifer DeLuca, Department of Biochemistry and Molecular Biology, Colorado State University and adapted from McIntosh, 2016[89].*

1.2.1 Prophase

Mitosis requires dramatic reorganisation of chromosomes. Long before mitosis initiates, the cell prepares for cell division by establishing sister-chromatid cohesion during S-phase. Proper establishment and maintenance of cohesion is essential to ensure that the duplicated sister chromatids are held together and do not drift apart from each other during mitosis. This process is mainly mediated by cohesins, which are protein complexes composed of four subunits: Smc1, Smc3, Scc1 and Scc3. The Smc1 and Smc3 subunits of the cohesin complex are members of the SMC (structural maintenance of chromosomes) family of proteins, and they contain a coiled-coil region flanked by a globular ATPase domain and a dimerization domain, which interact to form a ring-like shaped structure that holds sister chromatids together[90, 91]. The non-SMC subunits of cohesin (Scc1 and Scc3) bind to ATPase domains of Smc1 and Smc3 and lock the ring structure in a closed conformation, most likely via ATP hydrolysis, thereby ensuring that sister chromatids remain in close contact. Sister chromatid cohesion is relieved by proteolytic cleavage of Scc1, which promotes the opening of the ring and allows sister chromatid separation during anaphase[92]. Upon mitotic entry, the onset of chromosome condensation defines the initiation of prophase, and this step is necessary in order to avoid DNA breakage. This is because, immediately after S-phase, sister chromatids pairs are a fragile mass of entangled DNA and protein that are less likely to be safely pulled apart without causing damage. Moreover, uncondensed chromosomes are extremely long, and any attempt to separate such large structures would result in chromatid arms lagging across the midzone during anaphase. Thus, to avoid these damaging consequences, chromosome condensation in animal cells compacts sister chromatids into rod-like structures that are less likely to entangle and are short enough to ensure proper chromosome segregation, resulting in ~10,000-fold decrease in chromosome length[23].

A key component of the process of chromosome condensation is condensin, which is a five-subunit protein complex that is related to the cohesin complex, and is composed of two SMC-family subunits, which form Y-shaped heterodimers with an attached globular ATPase, and three non-SMC subunits[93]. In animal cells, condensin I and II are the two major condensin complexes that mediate chromosome condensation and both contain a SMC heterodimer composed of Smc1 and Smc3 and different non-SMC subunits (condensin I: CAP-D2, CAP-G and CAP-H; condensin II: CAP-D3, CAP-G2 and CAP-H2)[93]. Similar to cohesin, condensin also forms a ring structure

whose closed and open conformation is most likely dependent on cycles of ATP binding and hydrolysis[94]. However, as opposed to cohesin, codensin encircles different parts of the same DNA strand in a single sister chromatid, whereas cohesin encircles DNA from different sister chromatids. Evidence that purified condensin I promotes supercoiling of DNA strand *in vitro* in a manner dependent on ATP[95, 96] and that either depletion of condensin II subunits in human cells[97] or mutations of condensin subunits in fission or budding yeast[98, 99] all lead to defects in chromosome condensation suggests that condensin's enzymatic activity is key to its function *in vivo*. Importantly, the control of both sister chromatid cohesion and chromosome condensation is established primarily by regulation of cohesin and condensin mediated by protein kinases such as cyclin-dependent kinases (Cdk) and Aurora kinases. In vertebrates, cyclin A-Cdk2 complexes are thought to be key for the initiation of chromosome condensation in prophase, and are active in the nucleus in the beginning of mitosis[93]. Moreover, *in vitro* experiments demonstrate that Cdk1 phosphorylates the non-SMC CAP-D2 and CAP-H subunits of condensin I, thereby accelerating chromosome condensation by enhancing condensin's ability to supercoil DNA[100, 101]. The role of Aurora kinases in chromosome condensation is less well established, however loss of Aurora B in *Drosophila melanogaster* causes defects in chromosome structure due to reduced binding of condensin to chromosomes[102]. One potential target of Aurora B during chromosome condensation is histone H3, whose phosphorylation by this kinase correlates with chromosome condensation[102].

Concomitant with chromosome condensation, the nucleoli disperse most likely as a result of condensation of the DNA that had served as nucleolar organiser. Moreover, Cdk1-mediated hyperphosphorylation of components of the nuclear pore complexes and lamin fibers that border the surface of the nuclear envelope drives the dissolution of these components, thereby weakening the nuclear envelope and initiating nuclear envelope breakdown (NEBD)[89]. The precise mechanisms by which NEBD is controlled are not entirely understood, however microtubules of the growing spindle potentially contribute to dispersal of the nuclear envelope by pushing on the envelope[103], and transient increases in cytoplasmic Ca^{+2} mediated by protein kinase C activity have also been associated with envelope dispersal[104]. Prophase is thought to end when the nuclear envelope completely disperses, however in many organisms, the spindle begins to form before NEBD, with dynamic microtubules growing radially from the centrioles (in centriolar organisms). Polo like kinases and the serine/threonine kinase Aurora A further localise to centrosomes and are

essential for the accumulation of γ-tubulin ring complexes that mediate microtubule nucleation at the centrioles[105, 106].

1.2.2 Prometaphase and metaphase

1.2.2.1 Spindle assembly and dynamics

Upon nuclear envelope breakdown, spindle assembly and chromosome congression progress during prometaphase in order to align the chromosomes at the centre, forming the metaphase plate prior to chromosome segregation. The organisation of the spindle as well as how it interacts with chromosomes have been widely investigated and it is well established that the mitotic spindle consists of a bipolar array of microtubules composed of the 6S GTP-binding protein tubulin containing an α and a β-subunit that align to form protofilaments[107] (**Figure 6**). The microtubules are arranged such that their minus ends (the ends of the α-subunits) are embedded within the spindle poles, and their plus ends (the ends of the β-subunits) face outwards from the poles[107]. The plus ends from each spindle side overlap with each other at the centre, resulting in an antiparallel array in the midzone[108]. Microtubule polymerisation is faster at the plus ends and requires the association of GTP-bound α and β-tubulin heterodimers, thereby forming a hollow microtubule[109] (**Figure 6**). The GTP molecules associated with β-tubulin are hydrolysed shortly after their association with the polymerising microtubules, causing conformational changes in the tubulin subunits that lead to microtubule depolymerisation[109] (**Figure 6**). These stochastic cycles of growth and shrinkage characterise the most prominent hallmark of microtubules, termed 'dynamic instability'[110] (**Figure 6**). The overall structure of the spindle requires that a specific population of microtubules (MTs) called kinetochore MTs connect the spindle poles to the sister chromatids by attaching to the kinetochores, thereby forming MT bundles (K-fibers) that directly mediate chromosome segregation during anaphase[109]. The remaining non-kinetochore MTs contribute to spindle architecture, whereas astral MTs emanate outwards from the spindle poles and anchor the spindle within the cytoplasm[109].

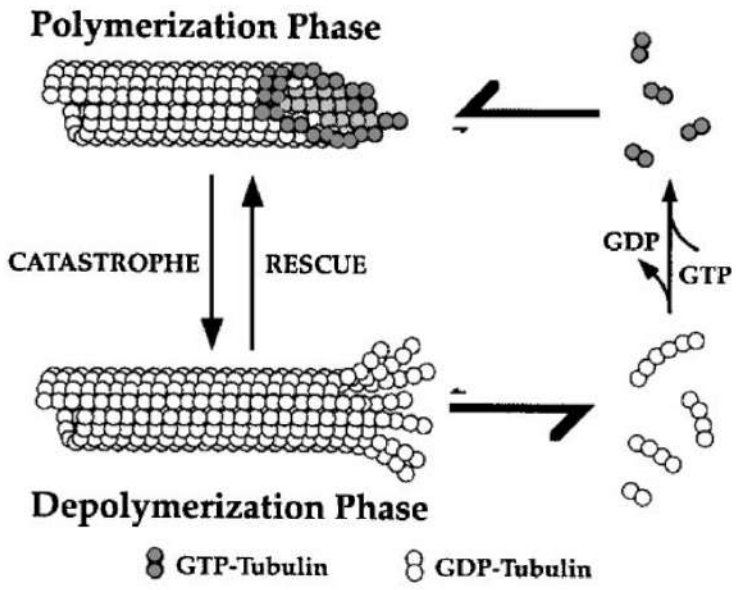

Figure 6. – Microtubule dynamic instability.

The microtubules that form the spindle are composed of GTP-bound to tubulin containing α and β-subunits that align to form protofilaments. Microtubules undergo stochastic cycles of growth and shrinkage, and this property of microtubules is known as dynamic instability. Microtubule polymerisation is faster at the plus end and involves the association of GTP-bound α- and β-tubulin which form a hollow microtubule. The GTP bound to tubulin is subsequently hydrolysed during or soon after polymerisation, and thus depolymerisation at the minus end occurs, wherein GDP-bound tubulin subunits are released. Adapted from Desai & Mitchison, 1997[111].

Spindle architecture is also maintained by microtubule-associated proteins (MAPs), which regulate microtubule nucleation, dynamics, transport, and cross-linking, thereby contributing to the establishment of spindle shape, length as well as its location and orientation. The activity of MAPs can be classified based on their function within the spindle; for instance, microtubule nucleation from MTOCs is usually dependent on γ-tubulin, which in association with γ-tubulin complex proteins GCP3, GCP4, GCP and GCP6, forms a ring-shaped complex (termed γ-TuRC) that is thought to provide a template that interacts with α-tubulin subunits to form the MT lattice[112, 113, 114]. Microtubule dynamics is also regulated by MAPs via a selective stabilisation of specific conformations of tubulin dimers, wherein MT polymerases promote MT growth by stabilising the straight conformation of tubulin assumed when in association with the polymerising microtubule, and MT depolymerases induce MT shrinkage by favouring the curved conformation of tubulin assumed when in isolation[115, 116]. Microtubule dynamics is further regulated by MT plus-end tracking proteins (+TIPs) such as the end-binding protein 1 (EB1), which promotes microtubule

polymerisation by transitioning GTP to GDP-bound tubulin[117, 118]. Finally, molecular motors such as kinesins and dyneins are essential for MT arrangement during mitosis. Kinesins walk along the MT towards the plus ends and contribute to the maintenance of spindle length, promote sliding of antiparallel microtubules, cross-linking of microtubules and regulate microtubule dynamics[119, 120], whereas dynein moves across MTs towards the minus ends and is required for the tethering of MTs to the spindle poles and microtubule sliding[121].

In most cell types, the spindle poles are connected to the centrosomes, the primary microtubule nucleation machinery, which are ~1μm structures composed of a centriole pair surrounded by pericentriolar material (PCM)[122]. During early interphase, a single centrosome is initially present and is subsequently duplicated at the end of S-phase prior to mitotic entry. Upon mitotic entry, the centrosomes separate and move towards opposite spindle poles, where MTs are nucleated in a manner dependent on γ-TuRC activity (**Figure 7B**). Microtubule nucleation is further enhanced by the recruitment of more γ-TuRC[123], and components of the PCM[124]. Other factors are also required for γ-TuRC localisation and MT nucleation at the centrosome, such as NEDD1[125], MOZART1[126], pericentrin[127], AKAP450[128], Cep192[129] and CDK5RAP2[130], whose depletion leads to impaired γ-TuRC localisation, and defects on MT nucleation and spindle formation (**Figure 7B**). Once microtubules are nucleated from the centrosomes, they search their surroundings as they undergo stochastic rounds of growth and shrinkage, travelling varying trajectories due to their inherent dynamic instability before being 'captured' and stabilised by a kinetochore[131, 132]. This mechanism of 'search-and-capture' is thought to be the basis of spindle assembly, and facilitates the incorporation of chromosomes into the spindle during mitosis[127], since the increased nucleation rate from centrosomes and high MT turnover during mitosis allow MTs to scavenge the volume of the cell fast enough to promote chromosome capture.

1.2.2.2 Centrosome-independent spindle assembly mechanisms

The observation that centrosomes can be ablated[133], and that fly cells can survive without centrosomes[134], as well as the fact that certain cell types such as oocytes, plant cells and mouse embryos[135], do not contain centrosomes provided the initial clues that centrosome-independent MT nucleation pathways and spindle assembly mechanisms exist. The precise mechanisms that drive acentriolar spindle assembly are yet to be fully elucidated, however several alternative MT

nucleation pathways have been proposed based on *in vitro* and *in vivo* observations. For instance, evidence that mitotic spindles can be assembled around DNA-coated beads incubated in *Xenopus* egg extracts in the absence of centrosomes indicate that a DNA-dependent microtubule nucleation pathway might exist[136]. Further evidence suggests that the small GTPase Ran is associated with spindle assembly from chromosomes, and *in vitro* experiments have shown that RanGTP induces TPX2 to target Aurora A to the spindle, where it interacts with and phosphorylates the γ-TURC adaptor protein neural precursor cell-expressed developmentally downregulated 1 (NEDD1), promoting microtubule nucleation in the vicinity of the chromatin[137] (**Figure 7D**). Ran-GTP has also been shown to interact with MEL-28 and contribute to microtubule nucleation from chromosomes by regulating γ-TuRC activity[138], as well as to regulate the microtubule depolymerising protein kinesin-13 (Kif2a) [139] (**Figure 7D**).

Alternatively, chromosomes can also regulate microtubule nucleation in the absence of a RanGTP gradient via the chromosome passenger complex (CPC) (**Figure 7C**). The CPC is a group of proteins that localises to the chromosomes during mitosis and ensures the phosphorylation of substrates involved in chromosome condensation, kinetochore-microtubule attachments, activation of the spindle assembly checkpoint and cytokinesis[140]. This group of proteins includes a localisation module which functions to ensure the localisation of the CPC to the centromeres and is composed of the INCENP amino terminus, survivin and borealin; and a kinase module, composed of Aurora B bound to the INCENP C-terminus[140]. Haspin-mediated binding of survivin to phosphorylated histone H3 induces CPC recruitment to the centromeres which drives Aurora B accumulation at this site and its autophosphorylation and subsequent activation[141]. Active Aurora B is responsible for inactivating microtubule depolymerising proteins such as the mitotic centromere-associated kinesin (MCAK), further facilitating microtubule stabilisation and assembly from the chromosomes[141] (**Figure 7C**). Moreover, not only Aurora B concentrates to the centromeres but it also promotes a diffusion gradient over the length of the spindle, which prevents the action of microtubule depolymerising proteins[141]. Therefore, it has been proposed that chromatin-induced microtubule nucleation is driven by two separate pathways: RanGTP from all over the chromatin and the CPC pathway originating from centromeric regions[142] (**Figure 7C and D**). This hypothesis was strengthened by the observation that chromatin beads enriched with CPC lead to local microtubule polymerization in the absence of a RanGTP gradient[142]. Moreover, the

kinetochore itself seems to be able to nucleate microtubules to some extent[143] (**Figure 7F**). In *Drosophila melanogaster* S2 cells, when K-fibers are severed with a laser microbeam, they regrow via microtubule plus-end polymerization at the kinetochore and their minus-ends are subsequently captured by astral microtubules and transported towards the spindle poles by dynein[143]. Moreover, the members of the nuclear pore complex Nup107-160 interact with γ-TURC and recruit it to the kinetochores where they cooperate to promote spindle assembly through microtubule nucleation at the kinetochores[144]. However, it remains unclear whether cells that do not possess astral microtubules, such as the acentriolar oocyte and early mouse embryo, would make use of a kinetochore-mediated microtubule nucleation mechanism, and whether this pathway serves merely as a safety mechanism to ensure proper kinetochore-microtubule attachments or if it is indeed a common microtubule nucleation pathway.

An alternative mechanism of microtubule nucleation whereby microtubules are generated from the body of the spindle has been proposed based on the observation in plant cells that microtubules are nucleated as γ-tubulin-containing branches from an old microtubule template[145], and that growing microtubule plus ends visualised with EB1-GFP are also assembled along the body of the spindle rather than only at centrosomes and chromosomes[146] (**Figure 7E**). This 'microtubule-dependent microtubule nucleation' pathway has been further scrutinised and a genome-wide RNAi screening in *Drosophila* S2 cell lines has identified several genes required for the localisation of γ-tubulin to spindle microtubules, which were termed Augmin complex[147, 148] (**Figure 7E**). Upon knockdown of all components of the Augmin complex, microtubule nucleation is reduced, leading to reduced K-fiber formation, chromosome misalignments and bipolarity defects[147]. In *Xenopus* egg extracts, it has been shown that branching microtubule nucleation depends on γ-tubulin and Augmin and is stimulated by TPX2, which is an effector of RanGTP that plays a role in chromosome-mediated microtubule nucleation[149], however, what regulates the activity of these proteins to induce microtubule nucleation still remains to be determined.

In acentriolar systems, the spindle axis is aligned progressively as the microtubules assemble, as opposed to centriolar cells in which the spindle axis is imposed based on centrosome position prior to NEBD (**Figure 7A**). Therefore, a self-organization model of spindle assembly has been proposed based on the observation that randomly oriented microtubules are organised and

form a spindle through the activity of the plus-end directed motor kinesin-5, inducing the formation of an antiparallel microtubule array, and the minus-end directed motor dynein is responsible for focusing the spindle poles in *Xenopus* egg extracts lacking centrosomes[136] (**Figure 7A**). Moreover, in mouse oocytes, a self-organisation mechanism has also been proposed, wherein MTOCs that are initially scattered through the cytoplasm further congress at the centre of the oocyte and nucleate microtubules in a Ran-dependent manner, resulting in a circular configuration of the chromosomes termed 'microtubule ball'[150]. This array of microtubules is subsequently organised as a bipolar spindle by MTOC clustering at the spindle poles, and this process is mediated by kinesin-5[150]. In addition, the polo-like kinase 4 (Plk4) and Aurora A are also thought to contribute to centrosome-independent microtubule nucleation in mouse oocytes, and chemical inhibition of these kinases perturbs spindle size, bipolarisation and MTOC structure[151]. Moreover, co-inhibition of Aurora A or Plk4 and the Ran signalling pathway further decreases microtubule nucleation, suggesting that these pathways might interact to promote nucleation[151].

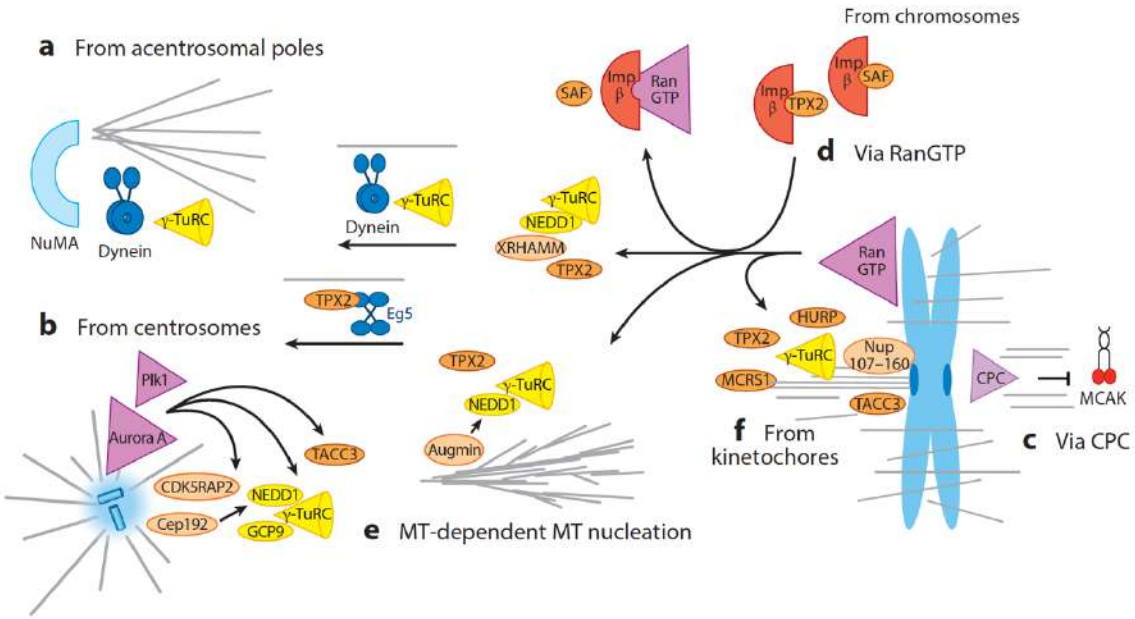

Figure 7. – Summary of spindle assembly mechanisms.

(a) *Although microtubule nucleation from acentrosomal spindle poles is not entirely understood, it is thought to involve a combined action of the cross-linker NuMA and dynein which direct γ-TuRC to the poles. Other mechanisms involving microtubule self-organisation governed by*

kinesin-5 and other kinases such as Plk4 and Aurora A have also been described. ***(b)*** *In most cell types, the spindle poles are connected to centrosomes, to which γ-TuRC is recruited by binding partners NEDD1, GCP9 and centrosomal proteins CDK5RAP2 and Cep192, and mediates microtubule nucleation together with Aurora A and Plk1.* ***(c)*** *Chromosome-dependent spindle assembly can be achieved by the CPC activity, which inhibits MT depolymerases such as MCAK and induce MT formation.* ***(d)*** *Alternatively, RanGTP gradients emanating from chromosomes induce TPX2 to interact with γ-TuRC and other binding partners such as XRHAMM and NEDD1 to promote MT nucleation.* ***(e)*** *Microtubule-dependent spindle assembly involves the activity of TPX2 and augmin, which induce branching microtubule nucleation.* ***(f)*** *The members of the nuclear pore complex Nup107-160 play a less well-known role on microtubule nucleation in the vicinity of kinetochores. Adapted from Petry 2016*[109]*.*

1.2.2.3 Kinetochore-microtubule error correction

One of the main challenges of cell division is the establishment and maintenance of kinetochore-microtubule attachments that allow precise and correct chromosome segregation. Upon NEBD, microtubules can be captured by the kinetochore from almost any angle[152] and the most important task is to ensure that kinetochores from each sister chromatid are attached to microtubules originating from opposite poles, referred to as amphitelic configuration. If a given kinetochore remains attached to microtubules originating from both poles simultaneously (merotelic attachment), or if the kinetochores from both sister chromatids are attached to microtubules emanating from the same pole (syntelic attachment), the likelihood of chromosome segregation error increases, and the resulting daughter cells may acquire inappropriate chromosome numbers, termed aneuploidy, which can cause developmental abnormalities and diseases such as cancer[153]. As such, robust self-organization mechanisms exist to avoid or resolve inappropriate kinetochore-microtubule attachments prior to anaphase onset.

The mechanistic basis for error correction was first postulated by B. Nicklas, who proposed that kinetochore-microtubule attachments are inherently unstable, and that attachment errors are corrected by trial and error[154]. Nicklas proposed that error correction is mediated by repeated cycles of detachment and reattachment of microtubules until the amphitelic configuration is achieved, and that the tension exerted by spindle microtubules from opposite poles on amphitelically-attached sister chromatids acts as a feedback that reinforces the desired orientation (**Figure 8A**). In support to this idea, Nicklas' classic experiments in grasshopper spermatocytes demonstrated that syntelic attachments are only stabilised once tension is artificially applied with a microneedle by pulling the chromosomes from the spindle pole[155]. In somatic cells, a more recent molecular approach has

corroborated Nicklas model of tension-dependent error correction, wherein overexpression of a chromokinesin that causes increased polar ejection of chromosomes led to stabilisation of syntelic attachments[156]. However, although the idea of tension-dependent regulation of error correction has been demonstrated, these experiments were performed in the context of syntelic attachments which are relatively rare in typical mitosis of human cells[153]. Instead, merotelic attachments are more commonly observed and are even more dangerous, since they usually bypass checkpoint signalling and anaphase can start prior to correcting them, often leading to lagging chromosomes and aneuploidy[153, 157, 158].

Theoretically, merotelic attachments could also be corrected by the same tension-dependent mechanism that applies to syntelic attachments, however this would require a relatively large number of incorrectly-attached microtubules to generate sufficient loss of tension to trigger complete microtubule bundle detachment[159]. However, evidence that merotelic attachments are gradually corrected throughout mitosis suggests that tension may modulate kinetochore-microtubule stability in a gradual manner rather than abruptly[160] (**Figure 8B**). Therefore, the tension-dependent model of error correction still raises many questions; for instance, how is error correction regulated such that destabilisation happens specifically in the incorrectly attached microtubule? How many merotelically-attached microtubules are required to induce sufficient loss of tension that triggers correction? And how do kinetochores sort through a large number of microtubule attachments in a timely manner within the short duration of mitosis? A possible explanation is that perhaps some degree of merotely might be tolerated as it might not necessarily cause mis-segregation, however this strategy seems inefficient, since a potential decline in chromosome velocity during anaphase caused by merotelic-attachments could lead to micronuclei formation[159, 161].

Alternative tension-independent mechanisms have thus been explored to further understand error correction. For instance, the geometric constrains imposed by the back-to-back orientation of sister chromatids is thought to favour amphitelic configurations and this, in combination with kinetochore-microtubule turnover, contributes to the establishment and maintenance of properly attached microtubules. This model posits that most improper kinetochore-microtubule attachments are established in early stages of mitosis and that, upon chromosome alignment at metaphase, all kinetochore-microtubules are gradually disassembled as a result of microtubule turnover, thereby

allowing their replacement with new amphitelically-attached microtubules that are favoured due to the geometric constrains of sister chromatid orientation[159, 162] (**Figure 8B**). This is a feasible possibility, since microtubule turnover time in human cells is between 3-7min, which would therefore allow all attached kinetochore-microtubules to be replaced within the timeframe of metaphase (10-20min)[163]. Indeed, overstabilisation of microtubules (i.e., reduced microtubule turnover) is a common feature of cancer cell lines and is associated with increased chromosome segregation errors, presumably due to failure to correct merotelically-attached kinetochore-microtubules, and the accuracy of chromosome segregation is improved by mild destabilisation of microtubules[163, 164]. Nevertheless, the expected rate of mis-segregation for this mechanism is between 10^{-1} to 10^{-2} mis-segregation event per chromosome, which is still relatively high in comparison to the actual rates of mis-segregation of non-cancerous cell lines ($\sim 10^{-4}$)[158, 159], and therefore additional error correction mechanisms must be in place to guarantee proper kinetochore-microtubule attachments.

A key role of the mitotic Aurora kinase B in the regulation of kinetochore-microtubule interactions has been demonstrated in both yeast and human cells, wherein Aurora B phosphorylates kinetochore substrates to promote turnover of kinetochore-microtubules in a manner dependent on the level of tension (i.e., low tension triggers Aurora B phosphorylation of kinetochore substrates and microtubule turnover), thereby playing an essential role in accurate chromosome segregation[165, 166, 167]. Aurora B destabilises attachments by either directly promoting detachment of kinetochore-microtubules, or by promoting catastrophe and depolymerisation of kinetochore-microtubules[166, 168]. How Aurora B activity changes in response to interkinetochore tension has yet to be fully elucidated, but a spatial separation model has been proposed, wherein the amphitelic configuration pulls bi-oriented sister kinetochores away from the inner centromere, where Aurora B is enriched, thereby keeping microtubule binding substrates away from Aurora B phosphorylation activity[165] (**Figure 8C**). This model is consistent with observations that perturbing Aurora B centromeric localisation disrupts the regulation of kinetochore-microtubule attachments[169]. The self-activating capacity of Aurora B has also been proposed to contribute to the establishment and maintenance of the gradient of kinase activity within the kinetochore[170]. Aurora B self-activates at sites of high concentration (inner centromere) and this activity is further spread out through the chromatin by a reaction-diffusion mechanism, thereby inducing the

activation of other chromatin-bound kinase molecules[170, 171]. As the concentration of Aurora B decreases farther away from the inner centromere, this reaction-diffusion mechanism is inhibited by phosphatase activity that switches Aurora B to an inactive state[170]. In summary, although several models have been proposed to explain the dynamics of kinetochore-microtubule error correction and a clear role of Aurora B has been established, the precise molecular pathways that promote error correction and how they sense and interact with interkinetochore tension remain unanswered and are key questions currently under investigation.

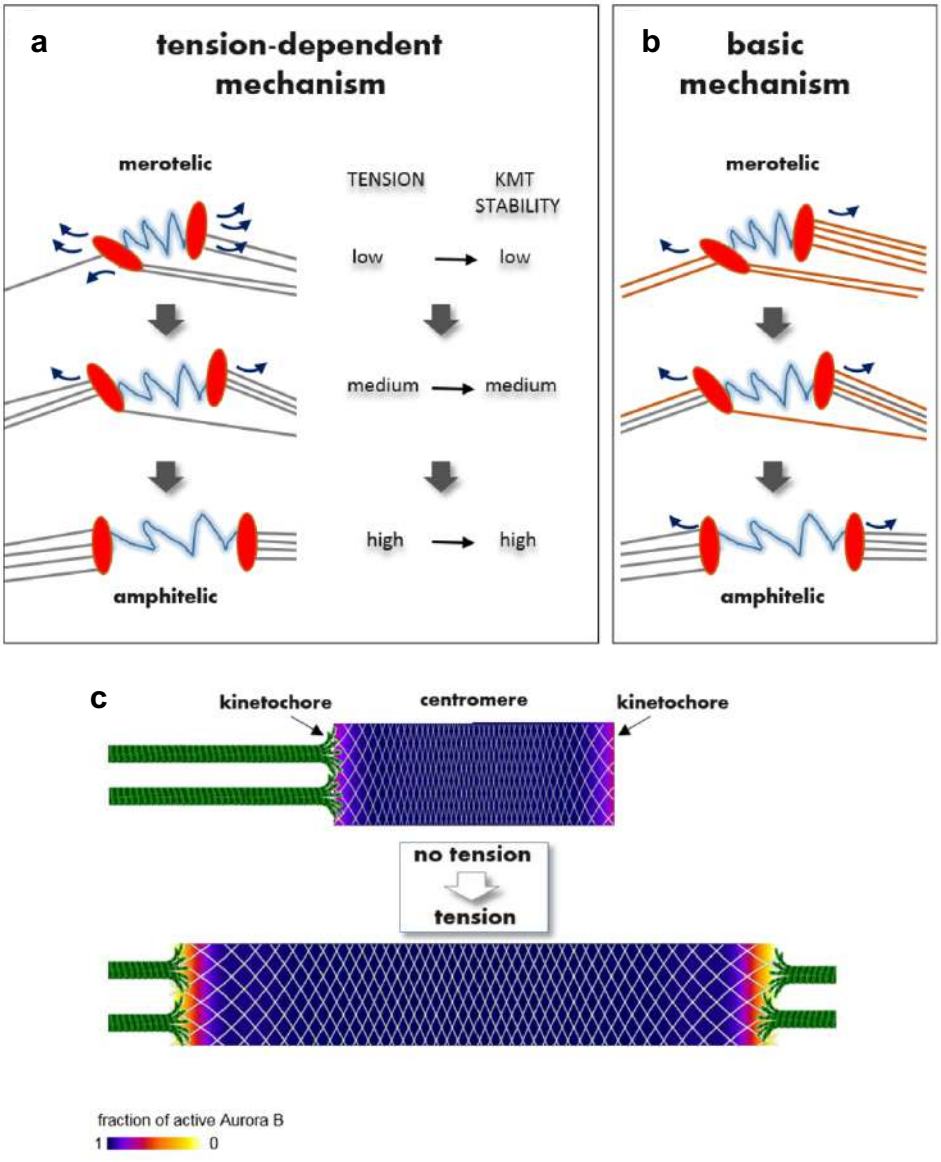

Figure 8. – Proposed models of kinetochore-microtubule error correction.

(a) *The tension-dependent mechanism proposes that low inter-kinetochore tension is the primary signal that induces kinetochore-microtubule turnover, and as new kinetochore-microtubule configurations are formed, the configurations that create higher tension stabilise kinetochore-microtubule attachments.* ***(b)*** *The basic mechanism posits that gradual correction of merotelic attachments proceeds with no change in kinetochore-microtubule turnover rates. In this model, turnover is not dependent on tension and rather, all kinetochore-microtubules eventually detach and are replaced with new microtubules which preferentially attach correctly, due to the back-to-back orientation of sister kinetochores.* ***(c)*** *A theoretical model of how tension modulates Aurora B kinase at the kinetochore proposes that Aurora B activity is optimal when inter-kinetochore tension is low, as it is strongly enriched in the middle of the centromere where it becomes highly active, thereby promoting kinetochore-microtubule turnover. When amphitelic attachments physically stretch the connecting matrix, Aurora B activity remains high within the centromeric heterochromatin, but drops sharply at the outer kinetochore, thereby reducing kinetochore-microtubule turnover. Adapted from Lampson and Grishchuk, 2017*[159].

1.2.2.4 The spindle assembly checkpoint

As detailed in the previous section, accurate chromosome segregation requires the precise alignment of the chromosomes at the metaphase plate and maintenance of kinetochore-microtubule attachments that allow the proper separation of sister chromatids at anaphase. This task is facilitated by the 'spindle assembly checkpoint' (SAC, also known as 'mitotic checkpoint' or 'M-phase checkpoint'), which is a surveillance mechanism that delays anaphase onset until all chromosomes are stably attached to kinetochore-microtubules[172] (**Figure 9**). It is generally accepted that the SAC functions by a mechanism of ON/OFF switch, wherein unattached kinetochores signal the recruitment of SAC complexes that inhibit anaphase onset, and this signalling cascade is relieved once all kinetochores are stably bound to microtubules, thereby allowing anaphase to take place (**Figure 9**). Other mechanistic studies have further suggested that the SAC might instead function as a rheostat, wherein SAC strength might rely not on an 'all-or-nothing' signal but on a threshold amount of Mad2 recruited to unattached kinetochores and consequently, the ability to block the APC/C would ultimately depend on the amount of MCC formed[173]. The downstream target of the SAC is an E3 ubiquitin ligase termed anaphase promoting complex or cyclosome (APC/C), which targets mitotic cyclins for proteolytic degradation, and is activated by two co-factors, Cdc20 and Cdh1[172] (**Figure 9**). Further investigation has identified the 'mitotic checkpoint complex' (MCC), composed of Mad2, BubR1, Bub3 and Cdc20 as the predominant signal generated by the SAC that promotes inhibition of the APC/C in response to unattached kinetochores[174, 175] (**Figure 9**).

An important question is how unattached kinetochores generate the signal that activates the SAC, and although the exact mechanism by which the SAC complex is assembled is still unclear, it is thought that SAC proteins are recruited in a stepwise manner, with Bub1 being one of the earliest components to be recruited in early prophase [176]. In addition, Bub1 is necessary for the recruitment of most of the other SAC components such as BubR1, Bub3, Mad1 and Mad2[176, 177], suggesting that Bub1 links the SAC complex to the outer kinetochore. What mediates Bub1 kinetochore localisation is yet to be fully addressed, however the outer kinetochore KMN network protein KNL1 was shown to directly interact with Bub1 and ensure its ability to support chromosome alignment[178]. Further understanding of how unattached kinetochores recruit the MCC has been possible with the development of the 'Mad2 template model'. This model posits that Mad2 has two distinct conformational configurations: when it is unbound, it adopts an open conformation (O-Mad2), which is then modified by binding to Mad1, in which dislocation of two β-sheets across the face of the protein creates a closed conformation (C-Mad2) that traps Mad1 within its fold[179]. Upon entry in mitosis, the Mad1-C-Mad2 complex is recruited to kinetochores, and the C-Mad2 conformation is further potentiated by dimerization of cytosolic O-Mad2[179]. The O-Mad2 bound to Mad1-C-Mad2 complex further captures Cdc20, acting as a 'prison-like' template that constitutes the first step in MCC assembly and a critical mechanism to indicate that a kinetochore is unattached[179]. In addition, Mps1 kinase has been identified as an important regulator of the Mad2 template mechanism, wherein Mps1 activity promotes the recruitment of the RZZ complex, which in turn recruits Mad1-C-Mad2 early in mitosis[180].

Whereas the assembly of the Mad1-C-Mad2 complex is sufficient to signal the presence of unattached kinetochores, evidence that BubR1 depletion abolishes SAC function without impacting C-Mad2-Cdc20 localisation to unattached kinetochores suggests that BubR1 acts downstream of Mad1-C-Mad2 to delay anaphase onset[181]. Mad2 was initially thought to directly inhibit anaphase onset by binding to Cdc20 and preventing APC/C activation[182], however evidence now indicates that BubR1 is instead a key APC/C inhibitor. The exact mechanism by which BubR1 inhibits the APC/C is not yet known, but evidence that recruitment of Cyclin B1 and securin is reduced upon interaction of the APC/C with the MCC[183] and structural studies dissecting APC/C's binding sites[184] have led to the idea that BubR1 might either cause conformational changes on APC/C that hamper its ability to bind to its substrates, or directly occupy substrate binding sites,

acting as a 'pseudosubstrate'. The 'pseudosubstrate' model was initially supported by evidence that Mad3 (the budding yeast equivalent to BubR1) competes with Cdc20 for substrate binding to APC/C[185], however recent experiments have further demonstrated that Mad3 instead induces a displacement of Cdc20 from the APC/C subunit Apc10, and therefore inhibits the APC/C indirectly by preventing the formation of its substrate-binding site[186].

SAC signalling that promotes inhibition of the APC/C is essential when kinetochores are unattached, however the ability to release the APC/C from inhibition once kinetochore-microtubule attachment is corrected is equally important, and exactly how the binding of microtubules satisfies the SAC remains controversial. Several mechanisms are thought to contribute to SAC silencing once microtubule attachment is achieved. Firstly, removal of Mad1-C-Mad2 from kinetochores is thought to be mediated by a dynein-dependent stripping mechanism once the kinetochore is attached to microtubules, and consistent with this, inhibiting dynein function blocks the removal of Mad1 and Mad2 from kinetochores and inhibits anaphase onset[187]. Secondly, protein phosphatase PP1 antagonises Aurora B kinase and promotes SAC silencing, in a mechanism dependent on chromosome biorientation that stretches the kinetochore and spatially separates Aurora B kinase from PIPs (proteins that interact with protein phosphatase PP1), thereby creating docking sites for the recruitment of PP1 to kinetochores[188]. Finally, disassembly of the MCC is required in order to release Cdc20 so that it can activate the APC/C. A role for p31^{comet} in MCC disassembly has been proposed based on evidence that it associates with MCC during mitosis and that p31^{comet} RNAi increases MCC levels, thereby delaying anaphase[189, 190]. Moreover, *in vitro* experiments demonstrate that p31^{comet} disrupts the MCC in a manner dependent on binding to Mad2[189], although the exact mechanism by which p31^{comet} promotes MCC disassembly remains unclear. In addition to p31^{comet}, ubiquitylation of APC/C substrates such as Cdc20 and BubR1[191, 192] and/or proteasome-mediated degradation have been proposed to direct MCC disassembly. This is substantiated by evidence that an E2 ubiquitin conjugating enzyme (UbcH10) promotes dissociation of MCC components from the APC/C[193], as well as by experiments showing that inhibition of proteasome activity impairs MCC disassembly[194]. In summary, SAC signalling is essential for proper chromosome segregation as it ensures that anaphase onset is delayed in response to unattached kinetochores. However, the exact mechanisms by which unattached kinetochores signal SAC activation, as well as how SAC complexes are released from properly

attached kinetochores once the SAC is satisfied, are all current subjects of investigation and require detailed molecular studies to decipher the complex interactions that drive these pathways.

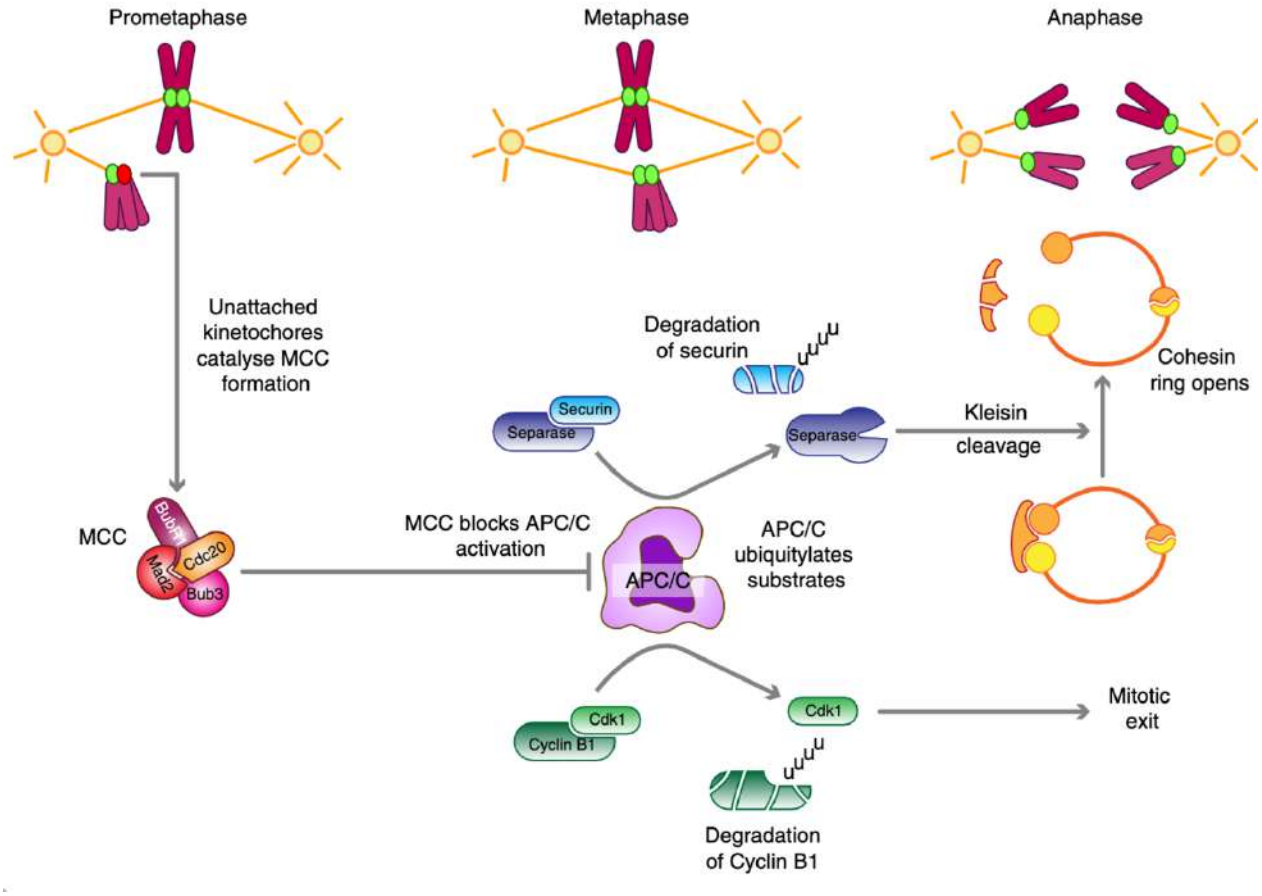

Figure 9. – General principles of the Spindle Assembly Checkpoint.

During prometaphase, unattached kinetochores induce the recruitment of mitotic checkpoint complex (MCC) proteins BubR1, Bub3, Mad2 and Cdc20, thereby causing inhibition of the APC/C. Upon chromosome alignment at metaphase, formation of the MCC is halted, which allows Cdc20 to activate the APC/C and leads to ubiquitylation and subsequent degradation of securin and cyclin B1. Securin degradation releases separase which in turn cleaves the Scc1 kleisin subunit of cohesion, thereby allowing sister chromatid separation at anaphase. Simultaneously, cyclin B1 degradation inactivates Cdk1 and induces mitotic exit. Adapted from Lara-Gonzalez et al. 2012[172].

1.2.2.5 Embryonic cell divisions: peculiarities of spindle assembly and checkpoint signalling

Several clinical reports indicate that human embryos from fertility clinics carry aneuploidies, some of which can arise from meiotic errors[195] - in which case the entire embryo is aneuploid – and

others arising from mitotic errors during embryonic divisions, generating embryos with blastomeres of different ploidy (known as mosaic aneuploidies)[196, 197]. Why the human early embryo is so susceptible to segregation errors has yet to be fully elucidated, however several studies using animal models have shed light into important quirks of embryonic cell divisions, particularly in the modes of spindle assembly, that might explain the propensity of the early embryo to developing aneuploidy. Other specificities of early embryonic divisions indirectly related to spindle assembly *per se* have also been described, for instance, embryo-specific particularities of the error correction pathway and spindle assembly checkpoint, both of which will be discussed further in this section.

One of the most striking characteristics of murine embryonic divisions is the absence of centrioles for most of preimplantation. As discussed in the previous sections (**section 1.2.2.1**), centrioles are the major microtubule organising centres of most mammalian cells which nucleate microtubules for spindle assembly[122]. During mitosis in somatic cells, one centriole pair is inherited by each daughter cell and is subsequently replicated during S-phase to generate the two pairs of centrioles required to sustain pole focusing and spindle assembly during cell division[198, 199]. Oocytes, however, face a challenging situation since the inheritance of an additional centriole pair from the fertilising sperm would mean that the newly formed zygote would have four centriole pairs after the replication phase, and this would necessarily be damaging to cell divisions since centriole overduplication leads to multipolar spindle formation and abnormal chromosome segregation[200, 201, 202]. Thus, to avoid having additional centrioles in the embryo, oocytes from many species including humans[203] degrade their centrioles, and consequently, a single centriole pair is inherited from the sperm upon fertilisation[204, 205]. Intriguingly, in the mouse embryo, in addition to the absence of centrioles in the oocyte, the sperm also degrades its centrioles[206] and this results in most of preimplantation development taking place in the complete absence of bona fide centriolar centrosomes until the ~64-cell stage, when γ-tubulin-labelled centrioles are first detected[135, 207, 208, 209]. Instead, the first few embryonic divisions in the mouse rely entirely on multiple acentriolar MTOCs that are randomly distributed throughout the cytoplasm and self-organise to promote spindle assembly and pole focusing[135, 210, 211].

How spindle assembly is achieved in the acentriolar mouse embryo has naturally been a topic of much investigation, and previous reports have proposed that early embryonic divisions

resemble more the meiosis mode of spindle assembly, and that the shift to classic mitotic cell division occurs gradually as the embryo develops[150, 210]. Similar to the mechanism described in oocyte meiosis I[150], live imaging of mouse embryos expressing the microtubule marker MAP4:EGFP demonstrated that spindle assembly in mouse embryonic divisions was mediated by several cytoplasmic MTOCs which form a transient multipolar spindle that gradually bipolarises by clustering to the poles during mitosis[210] (**Figure 10A**). This self-organisation mechanism progressively changes as the embryo advances to the 8-cell stage, wherein fewer cytoplasmic MTOCs are present, which are assembled directly at the nuclear periphery and along the spindle, generating more focused spindle poles and a more characteristic mitotic spindle[210] (**Figure 10A**). On the other hand, a more recent study using SiR Tubulin as a marker for MTOCs and spindle has demonstrated that even as early as the 2-cell stage, mouse embryos display very few MTOCs localised to the perinuclear region, that cluster to the poles upon mitotic entry and quickly generate a bipolar spindle, with no sign of multipolar intermediates[212]. Why these studies report different modes of spindle assembly is unclear, but these discrepancies may be explained by potential artifacts introduced by the overexpression of MAP4:EGFP, a microtubule associated protein that is essential for microtubule polymerisation.

Further insight into the mechanisms of spindle assembly was provided by evidence that Plk4 - a key protein responsible for centriole duplication in centriolar cells[213] - is essential for spindle bipolarisation in mouse embryos, Plk4 depletion leading to monopolar spindle formation and cytokinesis failure[214], highlighting the unusual roles of mitotic proteins in early embryos. Moreover, kinesin-5 (which is a microtubule motor essential for spindle bipolarisation during oocyte meiosis I) has been shown to be critical for the maintenance of spindle bipolarity only during the first three embryonic divisions but not in later divisions[215], providing another example of gradual shifts from oocyte-like to somatic-like mechanisms of spindle assembly. Interestingly, although centrioles emerge at the blastocyst stage, dynamic tracking of microtubule growth using EB1 comet assays demonstrated that the blastocyst stage embryo continues to lack canonical microtubule-organising ability during interphase[135], suggesting that centriole-independent spindle assembly mechanisms may still be in place even after centrioles emerge. In this context, the Augmin complex was shown to be important for MTOC focusing in blastocyst stage mouse

embryos[216], and it is thus possible that alternative spindle assembly pathways may remain active later in development.

Another challenge faced by the developing embryo is the dramatic changes in cell size that occur at each cell division, and how spindle length is determined and maintained during these reductive cell divisions is still puzzling. Interestingly, studies of spindle scaling in mouse embryos demonstrated that the spindle in 1-cell stage embryos is substantially shorter than the diameter of the cell itself[210, 217], which suggests that the mechanism controlling spindle length at this stage is most likely generated by intrinsic features of microtubule dynamics, rather than extrinsic signals such as cell boundary sensing. On the other hand, from the 2-cell stage onwards, the spindle more closely approaches the size of the cell at each cell division, suggesting that extrinsic signals may regulate spindle length at this point[210, 217], similarly to other invertebrate model systems[218, 219]. The requirement of extrinsic signals for spindle length regulation in embryos has been scrutinised by studies of artificial reduction of cell size, in which it was shown that moderate reductions of cell size at early stages of development has little effect upon spindle length, whereas reduction of cell size at later stages (4- and 8-cell stage) shortens spindle length[210]. This is consistent with divergent mechanisms of spindle length regulation at different stages of development, and it is possible that spindle length regulation at the 1-cell stage relies more heavily on meiosis-like regulatory mechanisms, especially considering that the spindle in the first mitotic division is proportionally smaller than in the second division[210, 217].

In addition to progressive changes in cell size, the early embryo is also faced with key morphogenetic events that determine cell position and cell fate specification, such as dramatic changes in cell-cell adhesion patterns that drive compaction and the emergence of apical and basolateral polarity at the late 8-cell stage[64] (**see also section 1.1.3**). Intriguingly, recent evidence has shown that these events are not only an essential part of the developmental programme but also influence spindle positioning and division plane specification by interacting with the assembling spindle[68, 69]. The apical domain was found to influence spindle positioning at the 8-cell stage in mouse embryos by attracting and clustering MTOCs at the subapical region, thereby creating a strong bias towards asymmetric segregation of the apical domain in the majority of 8-cell blastomeres and thus generating the first pool of inner blastomeres[68] (**Figure 10B**). Interestingly, further comparisons between 8- and 16-cell stage divisions have demonstrated that whereas spindle

positioning at the 8-cell stage is highly influenced by the apical domain, at the 16-cell stage, the distinctively flattened shape of outer cells overcomes the orientation cues from the apical domain and instead, the spindles are frequently oriented circumferentially, thereby creating a strong bias towards the symmetric segregation of the apical domain[69] (**Figure 10B**). Elegant manipulation experiments have corroborated these observations by showing that when 16-cell blastomeres are released from the cell shape asymmetry by individualisation of blastomeres, the axis of division is guided by the apical domain and asymmetric cell divisions are prevalent[69]. On the other hand, when shape asymmetries are induced in 8-cell blastomeres by artificially compressing the blastomeres, the role of the apical domain is overshadowed by the role of cell shape, and consequently, symmetric cell divisions become more prevalent[69]. This direct influence of apical polarity and cell shape on spindle positioning and division plane specification has thus been proposed to be a robust mechanism of tissue patterning that ensures that appropriate proportions of inner and outer cells are generated throughout development[69] (**Figure 10B**).

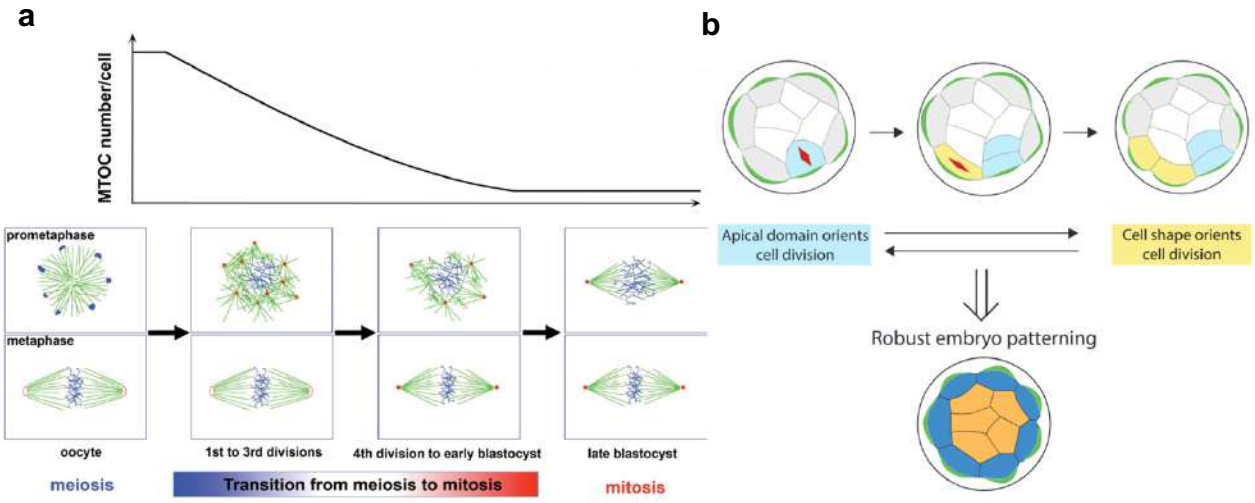

Figure 10. – Dynamics of acentriolar spindle assembly in mouse oocytes and embryos and developmental determinants of spindle orientation.

(a) *The transition from meiotic to mitotic cell division is characterised by gradual changes in MTOC organisation and spindle assembly dynamics in early mouse embryos. The first three acentriolar mitotic divisions largely resemble meiotic divisions, wherein several initially scattered cytoplasmic MTOCs gradually cluster at the poles to bipolarise the spindle. The subsequent divisions from the 8-cell stage until early blastocyst still rely on multiple cytoplasmic MTOCs, but*

*these MTOCs are more focused at the spindle poles and form a sharper bipolar spindle. Centriole-dependent spindle assembly is first detected at the late blastocyst stage, where two focused centrosomes assemble a typical bipolar mitotic spindle. Adapted from Courtois et al., 2012[210]. **(b)** At the 8-cell stage, the apical domain is the major determinant of cell division orientation, whereby clustering of MTOCs in the subapical region favours asymmetric cell divisions, where apical polarity components are asymmetrically inherited by the nascent daughter cells. In contrast, at the 16-cell stage, the flattened shape of outer cells overcomes the influence of the apical domain, and consequently, symmetric cell divisions are more prevalent. This 'tug-of-war' between apical polarity and cell shape is thought to be responsible for robust tissue patterning and cell allocation in the early embryo. Adapted from Niwayama et al., 2019[69].*

In addition to the idiosyncrasies of spindle assembly during early development, several lines of evidence have demonstrated that key surveillance mechanisms that are essential for chromosome segregation fidelity function differently in embryos, and may be compromised or even absent, potentially contributing to the high incidence of aneuploidy. As discussed in more detail in section 1.2.2.3, the kinetochore-microtubule error correction machinery acts on individual mis-attached kinetochores by recruiting microtubule depolymerising factors that destabilise improperly attached microtubules, thereby permitting the attachment of new properly attached microtubules[159]. In canonical somatic cell divisions, this mechanism relies on members of the Chromosomal Passenger Complex (CPC), composed of Aurora kinase B, INCENP, Survivin and Borealin, which localise to centromeres during mitosis and further recruit microtubule depolymerising factors such as MCAK and KIF2B[159]. Interestingly, recent evidence has shown that a less well-characterised isoform of Aurora kinase (Aurora kinase C) is not only more abundant than Aurora B in mouse and human embryos at early stages[220, 221], but also seems to play a more important role in embryo development, as evidenced by substantially reduced blastocyst formation rates upon Aurora kinase C knockout, whereas Aurora kinase B knockout resulted in normal development to blastocyst stage[222]. In addition, immunofluorescence experiments have demonstrated that the localisation patterns of CPC components in human zygotes are distinct to that of somatic cells, namely, CPC proteins were not confined to the inner centromere region as is the case in later stages of development and somatic cells, and the expected centromeric enrichment of phosphorylated histone H3 was not observed in zygotes[223]. Further investigation is required to fully elucidate the relative roles of Aurora kinases in early embryos and how they regulate downstream CPC components to modulate chromosome segregation in this environment. Another key remaining question is whether and how these particular roles of Aurora kinases may impact chromosome

segregation fidelity in early embryos and whether this could provide at least part of the explanation for the high incidence of aneuploidy during development.

The spindle assembly checkpoint (SAC) is another pathway that has been widely studied in oocytes and embryos, and recent evidence suggest that this important surveillance mechanism might not be robust enough in early divisions to adequately prevent chromosome mis-segregation. As detailed in section 1.2.2.4, the SAC operates to arrest cells in metaphase in the presence of unattached kinetochores[172]. This is mediated by the recruitment of SAC proteins such as MPS1, MAD1, MAD2, BUB1, BUB3 and BubR1 to unattached kinetochores, which subsequently catalyse the production of the mitotic checkpoint complex (MCC) and inhibition of the APC/C, thereby preventing the degradation of securin and cohesin cleavage and delaying anaphase onset[172]. Given the importance of this mechanism for chromosome segregation dynamics, the absence of SAC activity has been considered as a potential explanation for the high levels of mis-segregation and aneuploidy in embryos and, consistent with this notion, SAC components transcript levels were found to be low in human embryos[224]. Contrastingly, evidence that cell divisions in human embryos can be arrested by treatment with the spindle poison nocodazole indicate that the SAC might in fact be functional[225]. However, several lines of evidence suggest that the SAC may operate in distinct ways during early development. For instance, in mouse oocytes, it was shown that the SAC not only surveys unattached kinetochores, but also promotes meiotic arrest in response to DNA damage[226, 227, 228]. In addition, a role of cell size on the stringency of the SAC has been revealed in studies of *C. elegans* embryos. More specifically, it was shown that the SAC was weak in early embryonic divisions, when cell size is larger, and becomes increasingly more robust as cells get smaller[229]. Subsequent micromanipulation experiments in mouse oocytes have further reinforced the relationship of cell size to SAC efficiency by demonstrating that smaller cells are more efficient in sensing severely misaligned chromosomes than larger cells[230, 231]. Interestingly, a recent study of early embryonic cell divisions in mice have shown that although SAC components are efficiently recruited to misaligned chromosomes, anaphase onset is still triggered prior chromosome re-alignment, and most importantly, this mismatch between SAC signalling and metaphase arrest was not dependent on cell size, as artificial reduction of cell size did not influence the SAC's ability to induce mitotic arrest[232]. This inability to sustain a metaphase arrest in response to misaligned chromosomes has thus been proposed, at least partially, as a contributing factor for the development

of aneuploidy in early embryos[232]. Altogether, these studies briefly illustrate the mysterious nature of embryonic mitoses and open the doors to a myriad of research yet to be performed in order to integrate our knowledge of the unusual mechanisms of spindle assembly in the early embryo, and how they might impact essential surveillance mechanisms that are meant to safeguard the genome.

1.2.3 Anaphase and telophase

Once all chromosomes are properly aligned at the metaphase plate and kinetochores are stably attached, SAC components are released from kinetochores and APC/C activation triggers securin-mediated activation of separase, which in turn cleaves sister chromatid cohesin, thereby allowing anaphase onset. Anaphase is characterised by the movement of sister chromatids to opposite poles of the cell, and this is followed by telophase, in which the nuclear envelope is reassembled around each segregated chromatin mass. The first stage of anaphase is referred to as anaphase A, wherein sister chromatids move towards the spindle poles, whereas the second stage of anaphase (anaphase B) is characterised by an increase in separation between spindle poles accompanied by spindle elongation[89]. These two distinct phases of anaphase commonly occur sequentially from A to B, but in some cases, such as in mouse oocytes[233], anaphase B occurs prior to anaphase A. During both phases of anaphase, changes in microtubule length and motion are essential and thus, microtubule dynamics and motor proteins are involved[89].

The dynamics and motions of spindle microtubules during anaphase have been investigated using, for instance, photoactivatable tubulin fluorescence[162], electron microscopy[234] and speckle microscopy[235], and these approaches have contributed to the understanding that two major forces act on chromosomes during anaphase A. Two mechanistic models have been proposed to explain chromosome motion and microtubule depolymerisation during anaphase A. In the Pacman mechanism, microtubule plus-end depolymerisation at the kinetochore generates force that moves the chromosomes towards the poles, in a manner similar as if chromosomes 'chew' their way toward the poles[236, 237] (**Figure 11**). On the other hand, the poleward flux mechanism proposes instead that microtubule depolymerisation occurs at the minus-end, thereby dragging chromosomes towards the poles[162, 237, 238] (**Figure 11**). In some species such as yeast, the Pacman plus-end microtubule depolymerisation mechanism has been shown to be the only driver of anaphase A[239], but it has become increasingly clear that in many other organisms, both microtubule poleward flux

and the Pacman plus-end depolymerisation mechanism act in combination to promote chromosome movement[233, 234, 235] (**Figure 11**). Microtubule molecular motors such as dynein[240] and kinesin-14[241] have been implicated in directing poleward movement of chromosomes as kinetochore-microtubules depolymerise. However, experiments showing that minus end-directed motors are dispensable for poleward movement in fission and budding yeast[242] have highlighted differences in the dependency of molecular motors among different species and conditions.

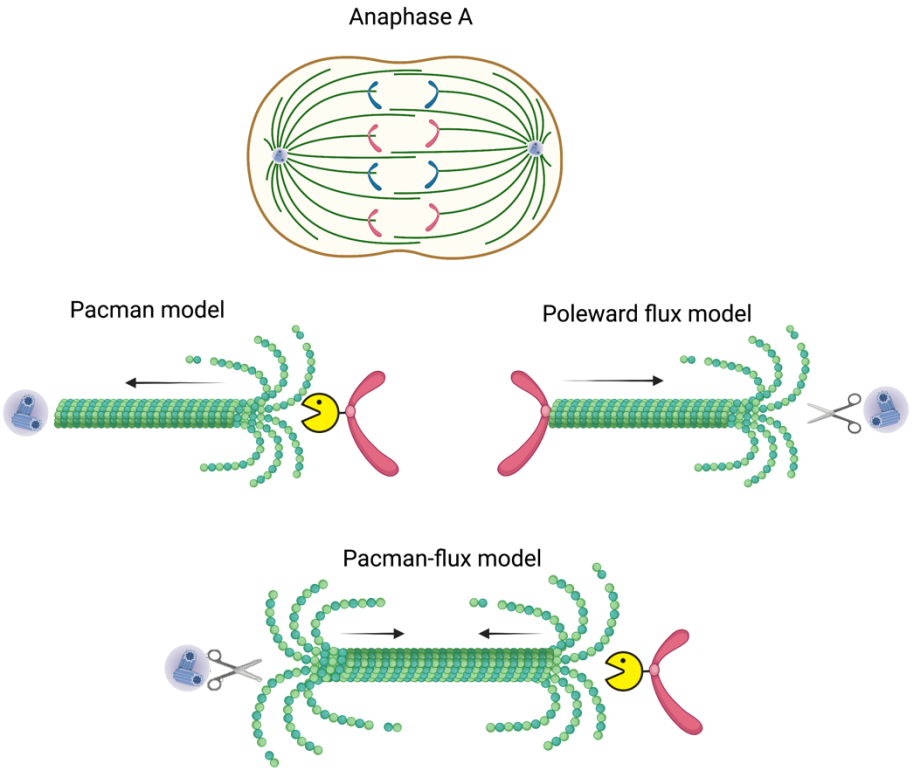

Figure 11. – Proposed models of chromosome poleward movement during anaphase.

During anaphase A, the sister chromatids separate and move towards the spindle poles along kinetochore-associated microtubule bundles (top). Two models were initially proposed to explain chromosome movements during anaphase A. In the Pacman model (middle, left), depolymerisation of microtubule plus-ends at the kinetochore mediates chromosome movement towards the spindle poles. In the poleward flux model, minus-end microtubule depolymerisation at the centrosome drags the chromosomes towards the spindle poles (middle, right). More recently, evidence suggest that both mechanisms act in combination in most organisms, wherein simultaneous microtubule depolymerisation at the plus- and minus-ends promotes chromosome poleward movement, in a model known as Pacman-flux (bottom). Figure created with BioRender.com

During anaphase B, relative sliding of overlapping non-kinetochore interpolar microtubules accompanies spindle pole separation[243], in a manner dependent on plus-end directed motors, such

as kinesin-5[244]. During anaphase A, these kinesins drive flux by pushing interpolar microtubules towards the poles, however in anaphase B, at least in *Drosophila melanogaster* embryos, minus-end depolymerisation is substantially decreased, allowing kinesin-5 motors located at the midzone to push the spindle poles apart[245]. Interestingly, experiments in *C. elegans* embryos demonstrated that, as opposed to other systems, BMK-1 (the *C. elegans* homolog of kinesin-5) is not essential for spindle pole separation, and instead might act as a brake that slows down spindle elongation in anaphase, as evidenced by an increase in the rate of pole separation in *bmk-1* deletion mutants, highlighting substantial inter-species differences in microtubule dynamics during anaphase[246]. In addition, experiments in fungi have further demonstrated that dynein interaction with astral microtubules might exert forces at the spindle to promote anaphase B, as evidenced by the decline in pole separation rates dynein deletion mutants[247]. The activity of many of the proteins involved in microtubule dynamics during anaphase A and B is controlled by cyclin-dependent kinases, and this is highlighted by experiments demonstrating that expression of nondegradable cyclin B mutants results in abnormal anaphase A chromosome movements and defects in anaphase B spindle elongation[248]. This is thought to be mediated by mis-localisation of the Aurora B-INCENP complex, given that expression of non-degradable cyclin B mutants blocks Aurora B-INCENP midzone localisation[249]. Transfer of Aurora B from kinetochores during metaphase to the midzone during anaphase is thought to be essential for chromosome movement[249]. This is because Aurora B is essentially involved in microtubule destabilisation during mitosis and thus, when sister chromatids separate during anaphase, loss of tension could potentially trigger Aurora B activation and microtubule destabilisation at a time when the spindle must be extremely stable, and therefore removal of Aurora B from kinetochores might circumvent this problem. Consistent with this idea, weakened kinetochore-microtubule attachments arise when Cdk dephosphorylation, and consequently removal of Aurora B from kinetochores, is prevented[249].

As anaphase progresses, Cdk activity continues to decrease while chromosomes contract, most likely as a result of renewed condensin activity. Further association of inner nuclear envelope proteins and lamins to the still condensed chromosomes is followed by fusion of these proteins and assembly of a new nuclear envelope, in what characterises telophase. Subsequently, nuclear pore complexes start to reassemble allowing the communication between the nucleoplasm and cytoplasm, and at the same time, chromatin decondensation begins, thereby forming new nucleoli

that mediate transcription during the new cell cycle. The major mechanism driving telophase is dephosphorylation of Cdk substrates as a result of APC^{Cdc20}-mediated cyclin destruction alongside with Cdk inactivation, and telophase is not achieved when Cdk inactivation is prevented[250]. Another important component of telophase is Cdc48, which is an ATPase responsible for protein remodelling, and is required for spindle disassembly, chromosome decondensation, nuclear envelope assembly and for the targeting of ubiquitinated proteins to proteasome-mediated destruction[251, 252]. Spindle disassembly is an integral step of telophase, and is also largely dependent on dephosphorylation of Cdk targets such as the minus-end cross-linking protein NuMA, as well as destruction of protein kinases Plk and Aurora A, and the kinesin-7 CENP-E which is thought to allow microtubule detachment from kinetochores[89]. Further nuclear envelope assembly is mediated by activity of the small GTPase Ran, which is required for the recruitment of nuclear pore complex components and nuclear membrane vesicles to the chromosome surface[253]. Completion of the final steps of mitosis produces a pair of genetically identical daughter nuclei in a shared cytoplasm, and the complex events that follow ensure the physical separation of the cytoplasm, in the process known as cytokinesis.

1.3 Cytokinesis

Cytokinesis is initiated after anaphase onset and completes cell division by partitioning the cytoplasm of the dividing cell into two new daughter cells. Successful and timely cytokinesis completion is key for the maintenance of genome integrity and its failure leads to binucleation, wherein a whole genome doubling event (also termed tetraploidy) arises as a result of two individual nuclei being housed within a single cell. As described in detail in the following sections, cytokinesis in animal cells is orchestrated by a series of intricate steps that initiate with signalling from the anaphase midzone which mediates the assembly and constriction of an equatorial actomyosin contractile ring. As constriction progresses, the actomyosin contractile ring interacts with the anaphase spindle midzone to form a midbody that directs abscission – the final cut of the plasma membrane of the nascent cells.

1.3.1 How it all starts: signalling from the anaphase spindle midzone

In mitotic cells, an actomyosin contractile ring (also termed cleavage furrow) is assembled precisely in the cell equator after anaphase to ensure proper partitioning of the dividing cell.

Accurate placing of the cleavage furrow is the first major step to assure the fidelity of cytokinesis, and in animal cells, the anaphase spindle is the major source of positional information for contractile ring assembly[254, 255]. The absolute requirement of the anaphase spindle for furrow positioning has been first demonstrated by landmark micromanipulation studies of echinoderm eggs[256] and sea urchin embryos[257], wherein artificial translocation of the spindle during anaphase resulted in regression of the original furrow and formation of a new furrow above the spindle midzone. Moreover, mechanistic studies of *Xenopus* embryos[258, 259] have shown that the anaphase spindle directs the formation of a narrow equatorial zone of active RhoA – a GTPase from the Rho family that is activated via the exchange of GDP for GTP mediated by guanine nucleotide exchange factors (GEFs) and inactivated by GTPase-activating proteins (GAPs) – which further recruits effector proteins for contractile ring assembly such as formins, Rho kinase and citron kinase[255] (**Figure 12A**). The mechanistic details of how the anaphase spindle specifies the equatorial zone of active RhoA are not entirely understood, however it is generally thought that opposing activities of the spindle midzone and astral microtubules at the spindle poles act concomitantly to restrict RhoA activation to a narrow equatorial zone[260].

The anaphase spindle midzone is composed of an array of antiparallel microtubules that are organised such that their plus ends are interdigitated with the plus ends of microtubules of opposing orientation, facing the centre of the spindle in what has been termed the central spindle, which serves as a scaffold for the recruitment of cytokinesis components and is populated by key molecular players such as PRC1, kinesin-4 (KIF4), the chromosomal passenger complex (CPC) component Aurora B, the centralspindlin complex and Polo like kinase 1 (Plk1)[255, 261] (**Figure 12A**). In the vicinity of the central spindle, binding of the cross-linker PRC1 with the microtubule motor KIF4 ensures the antiparallel microtubule orientation and prevents microtubule growth at the plus ends[262]. Simultaneously, the CPC component Aurora B phosphorylates the centralspindlin component kinesin-6 (MKLP1) and promotes its recruitment to the midzone[263, 264, 265]. The two major roles of centralspindlin in contractile ring assembly involve the interaction of its CYK-4 subunit with cytokinesis components: first, CYK-4 N-terminus scaffolds the recruitment of the Rho GEF Ect2 to the central spindle which is then loaded to the adjacent plasma membrane[255, 266] and second, the CYK-4 GAP domain plays a role in the maintenance of the equatorial zone of active RhoA, although evidence diverges on whether it promotes RhoA activation[267] or inactivation[268].

The roles of Plk1 in central spindle and cleavage furrow formation are less well understood, but it is thought that Plk1 assists on spindle elongation during late anaphase by indirectly inhibiting KIF4[269].

In addition to the role of the spindle midzone on cytokinesis, seminal work by Rappaport in binucleated sand dollar eggs has shown that the adjacent asters from two individualised spindles are sufficient to form a cleavage furrow even in the absence of a central spindle[270], bringing into light the idea that astral microtubules are also major determinants of cleavage furrow formation. More recently, observations that aster microtubules that had been physically separated from the remaining spindle using laser ablation can independently assemble two individual cleavage furrows[271] and that astral microtubules negatively regulate myosin recruitment to their vicinity[272] support the idea that two mechanistically distinct pathways act simultaneously to restrict contractile ring assembly and ingression to the cell equator: the positive signal that emanates from the spindle midzone recruiting cytokinesis components to the equator is contrasted by a negative signal arising from the asters that prevents the accumulation of cytokinesis components at the poles leading to a relative enrichment at the cell equator. Consistent with this idea, laser or chemical ablation of astral microtubules leads to a broader zone of active RhoA in sea urchin embryos[273], raising the possibility that astral microtubules restrict active RhoA from spreading outside of the cell equator by ensuring that a fixed amount of RhoA is recruited, however more detailed molecular studies are required to understand how asters determine the equatorial zone of RhoA and cleavage furrow formation.

1.3.2 Contractile ring ultrastructure and constriction dynamics

Upon specification of the equatorial zone of active RhoA, cytokinesis progression is mediated by the constriction of a narrow contractile ring composed mainly of actin filaments, myosin-II bipolar filaments and septin filaments, Anillin and proteins that regulate actin nucleation, capping, polymerisation, disassembly, and cross-linking, all of which populate the cell equator beneath the plasma membrane. Anillin – a filament cross-linker – plays a major role in contractile ring assembly and maintenance as it binds to all three filaments at the contractile ring and to the membrane thereby contributing to the anchorage of the ring to the plasma membrane[255] (**Figure 12B-C**). Much effort has been devoted to dissecting the structural composition of the contractile

ring and how these molecular players mediate constriction and, although much is yet to be elucidated, it has become clear that the spatiotemporal regulation of furrow ingression diverges substantially depending on the organism in question.

For instance, in the fission yeast (*Schizosaccharomyces pombe*), contractile ring assembly is initiated during interphase and the plane of division is determined by the position of the nucleus, whereby an Anillin-like protein (Mid1/Mid2) is broadly distributed in the cell equator and forms membrane-bound nodes that further recruit myosin-II and the formin Cdc12 during mitosis, thereby mediating actin nucleation[254]. A mathematical model proposes that progressive condensation of the nodes promotes the narrowing of the ring by a mechanism of search, capture, pull and release in which actin filaments are captured by myosin-II in neighbouring nodes, pulling them together and causing the ring to coalesce, while simultaneous dynamic remodelling of node interactions causes its release from actin, preventing the generation of clumps[274]. This is consistent with evidence that altering the actin-severing activity of cofilin causes node clumping[275]. An alternative model of contractile ring organisation has been proposed in fission yeast, in which Cdc12 concentrates in a limited number of nodes rather than uniformly across the ring, thereby preventing the overaccumulation of actin and node clumping[255].

In contrast to *S. pombe*, cytokinesis in metazoans is coupled with anaphase onset, but it is still unclear whether a similar search, capture, pull and release mechanism is also present. In *C. elegans* embryos, it has been demonstrated that the initial zone of active RhoA that is assembled as a broad equatorial band around the cell equator is followed by a folding of the RhoA band towards the embryo interior which places the plasma membrane in a back-to-back orientation, and contractile ring proteins accumulate at the tip of the furrow[276], however the ultrastructural organisation of contractile ring proteins is much less known. It has been previously proposed that the contractile ring might be organised as a sarcomere-like structure similar to muscle cells, in which intercalated actin and myosin filaments would promote constriction by sliding[277], however organisation of actin into sarcomere-like structures has not been reproducibly observed by electron microscopy[278]. A recently proposed model for the ultrastructural organisation of the contractile ring and constriction dynamics predicts that the ring is organised as functionally individualised "contractile units" each of which exerts force independently to promote constriction[279], and this model is substantiated by evidence in *C. elegans* embryos that partial damage of the contractile

ring by laser ablation does not prevent constriction of the remaining intact ring[280] and by observations in sea urchin embryos[281] and HeLa cells[282] that myosin II filaments are organised into small regularly spaced individualised clusters, as opposed to disorganised interconnected arrays (**for more details on the contractile unit model refer to section 1.3.3**).

The mechanics of force generation in contractile rings during constriction is a subject of much investigation, and several physical models have been proposed to address the questions of how contractile stress is generated and what forces resist ring constriction. A long-standing model proposes that force generation in contractile rings is mostly promoted by myosin sliding, similar to muscle contraction mechanisms[283]. However, evidence suggests that actin filament turnover might also act as a force generating factor independently of myosin sliding, and that the essential function of myosin might be its cross-linking activity rather than sliding, which would promote ring constriction by accelerating actin disassembly[284, 285]. Actin treadmilling has also been proposed to play a role in force generation during constriction, whereby the motion caused by actin polymerisation and depolymerisation at opposite ends mediates ring remodelling and constriction[283]. Moreover, an alternative model predicts that tight cross-linking of actin filaments generates a homogeneous contractile ring that constricts in a manner dependent on filament turnover[286]. In contrast to the contractile forces generated within the ring, resistance from the plasma membrane is required during constriction to maintain contractile ring structure and avoid its collapse. An elegant work in isolated fission yeast contractile rings has demonstrated that resistance is dependent on the anchoring of the barbed-ends of actin filaments to the plasma membrane that enables the maintenance of tension during cytokinesis[287]. Although many biophysical and mathematical models have been developed to understand ring constriction dynamics, much is yet to be elucidated with regards to the force generating and resistance factors that promote tension and drive the intricate process of ring constriction.

1.3.3 The final cut: abscission

Abscission is the final step of cytokinesis, and it directs the physical separation of the two new daughter cells with the assistance of a densely packed midbody derived from remodelling of the spindle midzone, which further matures to form an intercellular bridge (**Figure 12D-E**). Electron microscopy observations of the midbody demonstrate that this structure is composed of a central

disc of electron dense material populated by microtubules oriented parallelly to one another[288]. During contractile ring constriction, maturation of the midbody is mediated by central spindle components that are partitioned into three groups and redirected to the midbody in a manner dependent on Plk1 activity[289]. The first group is composed of KIF4 and PRC1 which remain in close association with midzone microtubules in the centre of the midbody; the second group includes centralspindlin and Ect2 which are dissociated from microtubules and colocalise with anillin, RhoA, ARF6 and Cep55 to form the midbody ring; and the third group is composed of CENP-E, MKLP1 and Aurora B which are distributed along tightly packed midbody microtubules occupying the regions that flank the midbody core, forming what is termed midbody flank[289].

As ring constriction progresses, contractile ring components such as anillin, septins, citron kinase and RhoA are redirected to form the midbody ring, and different studies have elucidated additional functions of contractile ring components, distinct to those related to constriction, that contribute to successful abscission[289, 290, 291, 292]. For instance, in *Drosophila melanogaster* S2 cells, anillin has been shown to be essential for anchoring of the plasma membrane to the midbody ring, and anillin-depleted S2 cells fail to maintain stable intercellular bridges, eventually undergoing abscission failure[291, 292]. This essential role of anillin in midbody ring formation and maintenance is most likely related to its ability to cross-link actin and membrane-associated septin filaments, given that an anillin truncation lacking the septin-interacting domain causes midbody ring instability and regression[291]. Similarly, citron kinase has been shown to be essential for proper distribution of anillin and RhoA in the midbody ring, and cells devoid of citron kinase display a disorganised distribution of anillin and RhoA during early stages of abscission and are eventually excluded from the midbody ring as it matures[290].

Upon furrow ingression, the presence of microtubules prevents the contractile ring from cutting through the plasma membrane to separate the daughter cells and a distinct membrane-associated filament system independent of actomyosin termed the ESCRT complex has been shown to direct abscission by driving the narrowing of the intercellular bridge concomitantly with depolymerisation of midzone microtubules[293] (**Figure 12D-E**). The ESCRT complex was initially identified as being responsible for membrane scission during viral budding and vesicle budding, whereby the proteins ESCRT-I and ALIX recruit ESCRT-III, which in turn mediates scission by formation of a spiral membrane-associated polymer that is subsequently disassembled by the

ATPase VSP4[293]. In the context of abscission, Cep55 is the major responsible for ESCRT recruitment[294], and work in HeLa[295] and MDCK cells[296] have demonstrated that ESCRT-I and ESCRT-III are sequentially recruited to the intercellular bridge, forming a pair of overlapping rings that are further followed by VSP4 to the abscission site, which coincides with subsequent loss of midbody microtubules and cell separation. Disassembly of midbody microtubules is suggested to be the rate-limiting step for completion of abscission and is thought to be driven by ESCRT-III-mediated recruitment of microtubule depolymerising enzyme spastin[295].

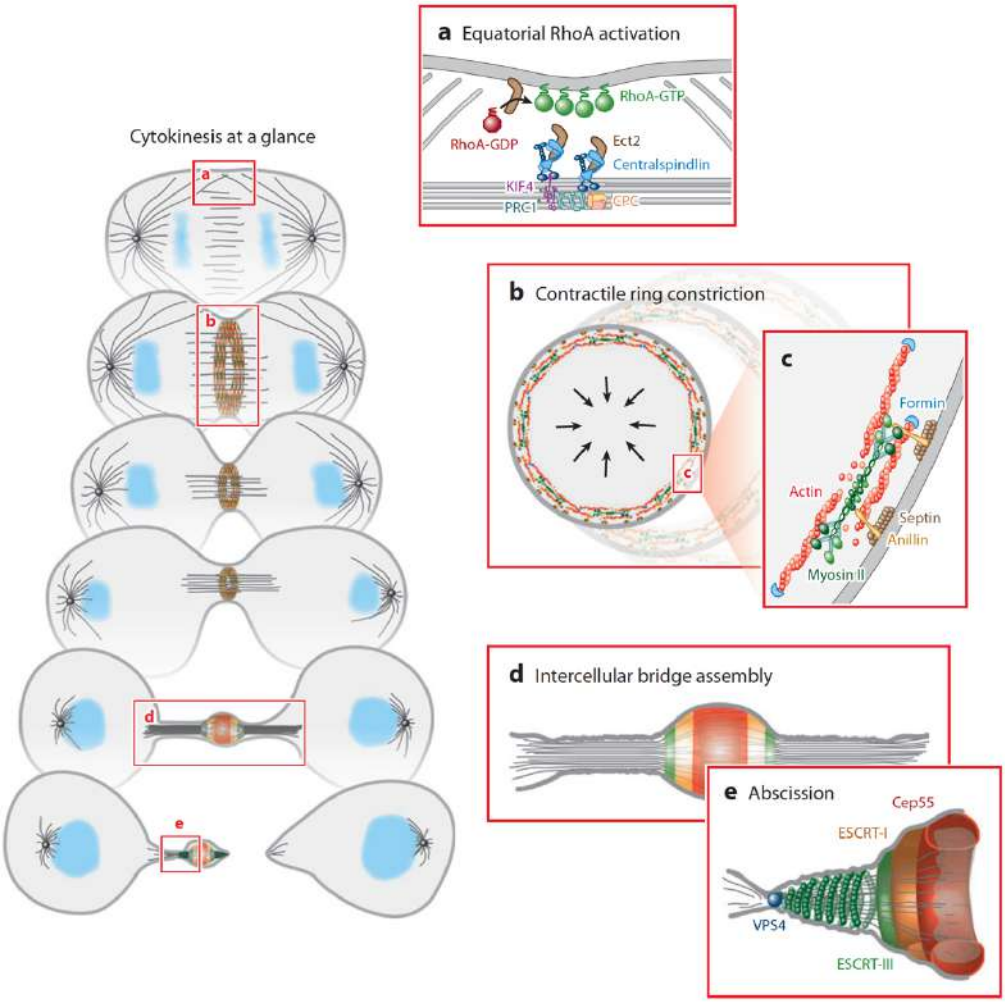

Figure 12. – Summary of cytokinesis events in animal cells.

(a) *Cytokinesis is initiated with signalling from the anaphase spindle midzone and astral microtubules to generate a narrow zone of active RhoA restricted to the cell equator. The central spindle, which consists of overlapping microtubules, further recruits the Rho GEF Ect2 and loads it into the plasma membrane, where it activates RhoA.* ***(b and c)*** *Upon RhoA activation, a contractile ring composed of formin-nucleated actin filaments, myosin II, membrane-associated septin filaments and the filament cross-linker anillin is assembled, and subsequent ring constriction mediates the physical separation of the dividing cell.* ***(d and e)*** *As ring constriction progresses, the spindle midzone matures to form the midbody, which organises the intercellular bridge, and subsequent recruitment of specialised ESCRT-III filaments promotes abscission by catalysing membrane scission to generate the nascent daughter cells. Adapted from Green et al. 2012*[255].

1.3.4 Cell size variations and constriction speed: the contractile unit model

An intriguing feature of ring constriction dynamics detected in many different model systems is that the rate of constriction is approximately constant during cytokinesis despite progressively decreasing ring perimeter[279, 283, 284, 297]. Interestingly, work in *C. elegans* embryos has dissected this property of contractile rings in detail by demonstrating that the constant rate of constriction is proportional to initial ring perimeter at cytokinesis onset, and that contractile rings harbouring a larger starting perimeter constrict faster than those with smaller starting perimeter, thereby allowing cells of different sizes to complete cytokinesis in approximately the same amount of time[279] (**Figure 13**). Based on this property of ring constriction dynamics, a model was proposed that suggests that contractile rings are composed of individualised force-generating units of fixed initial size distributed around the contractile ring, and that the number of contractile units in a given ring is dependent on starting perimeter, with larger rings containing more units than smaller rings[279, 280] (**Figure 13**). This model also predicts that constriction is mediated by the shortening of contractile units rather than by the loss of individual units, given that anillin, myosin and septins were shown to progressively disassemble in proportion to ring perimeter decrease[279] (**Figure 13**).

Subsequent work in filamentous fungi *Neurospora crassa* of varying sizes further supported the contractile unit model by providing evidence that larger rings constricted faster than smaller rings; however, the mechanism by which constriction speed is controlled differs in *N. crassa*, and instead of a progressive loss of cytokinesis components as was the case in *C. elegans*, the amount of myosin was shown to be constant throughout constriction[297]. Rather, the initial concentration of myosin at cytokinesis onset was proportional to initial ring perimeter[297]. Interestingly, work in *C. elegans* vulval precursor cells (VPCs) - which halve in size at each division but maintain constant height due to the flattened aspect of the tissue - support the idea that the rate of constriction is

determined by initial ring perimeter, however this property was not dependent on overall cell size *per se*, and was instead dependent on division plane dimensions, given that the initial ring perimeter in VPCs was roughly constant despite decreasing cell size as a result of the cells being flat[298]. These studies provide support to the contractile unit model of ring constriction and suggest that this mechanism is conserved in different cell types within the same species and among other species.

Further studies have set out to investigate the biophysical properties and mechanics of ring constriction, taking into account the current notion that contractile rings are compartmentalised. For instance, laser ablation experiments in *C. elegans* embryos have shown that severing the contractile ring causing it to snap open does not lead to complete ring disassembly and instead, recruitment of cytokinesis components to the site of damage allows the gap to be completely repaired and temporarily increases the speed of constriction, ensuring that cytokinesis duration is similar to that of uncut rings[280]. Moreover, causing the contractile ring to remain continuously open by performing successive cuts did not stop constriction from taking place, and instead the remainder of the intact ring was able to constrict irrespective of the damaged portion, corroborating the notion that the contractile ring is composed of functionally individualised components[299]. A recent analysis of cortical flow has expanded the contractile unit model by introducing the idea that coupling of cortical flow and ring disassembly contributes to the maintenance of constriction rate[300]. In this model, the opposing effects of polar relaxation and cortical compression near the ring drive new cortex to be pulled towards the contractile ring during cytokinesis, thereby allowing cortical myosin to be loaded into the ring, while at the same time, continuous disassembly of previously loaded myosin provides a balance between loss and accumulation, and ensure the maintenance of a constant constriction speed[300]. In summary, the contractile unit model has been thoroughly characterised in non-mammalian systems and elegant work has provided support to this model. Further studies using mammalian models are required to address whether this mechanism is conserved among other species and how the contractile ring adapts to complex cellular environments and developmental transitions.

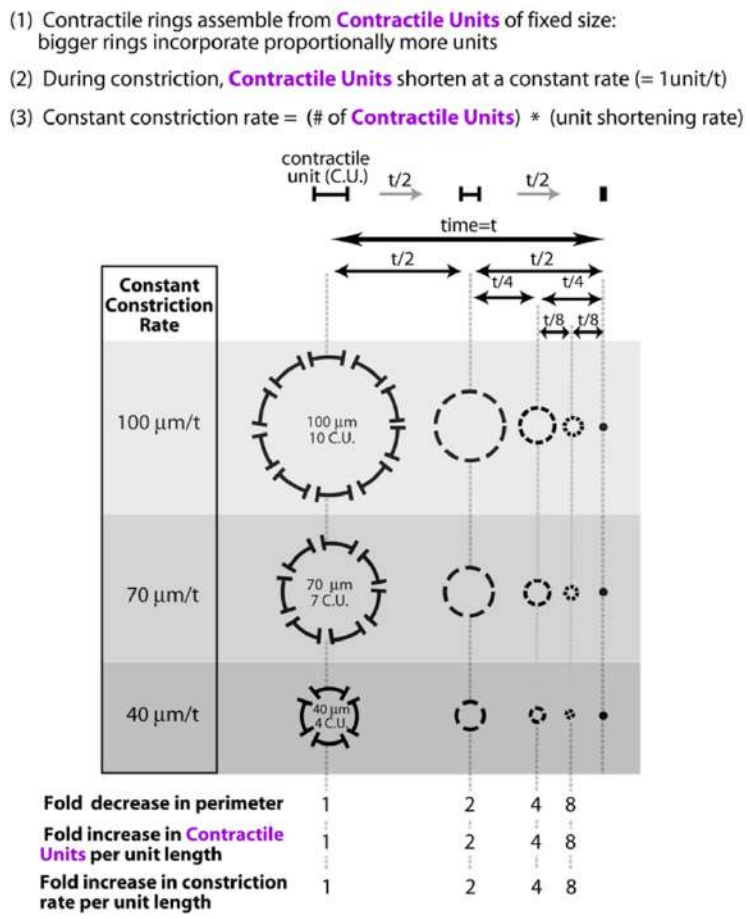

Figure 13. – Proposed model of cell size-dependent constriction speed determination.

A "contractile unit" model has been proposed in C. elegans to explain the scalability of contractile ring constriction speed according to cell size[279]. In this model, contractile units of fixed size are assembled onto the ring at cytokinesis onset and, as a result, bigger rings incorporate more contractile units than smaller rings. As cytokinesis progresses, contractile units shorten at a constant rate and thus, rings that initiate cytokinesis with a larger perimeter and contain more contractile units constrict proportionally faster than smaller rings composed of fewer units. The result of this organisation is a perfect scalability of constriction speed to cell size, which culminates in cytokinesis duration being the same independently of cell size. Adapted from Carvalho et al, 2009[279].

1.3.5 The abscission checkpoint

An interesting recent discovery pertaining to abscission is the existence of a checkpoint machinery responding to cytokinetic stress, termed 'NoCut' response or abscission checkpoint that can cause a delay in abscission completion for many hours[301]. The abscission checkpoint was initially associated with the presence of chromatin bridges[302] that remain trapped in the intercellular bridge (**Figure 14**); however recent work has shown that other insults can also trigger an abscission arrest[303, 304, 305]. For instance, high tension in the intercellular bridge has been associated with

delayed abscission, and reduction of tension by restricting cell migration and contractility or by laser ablation of the intercellular bridge rapidly induce abscission[303]. Moreover, defective nuclear pore complex (NPC) assembly has also been shown to activate the abscission checkpoint, and depletion of the NPC protein Nup153 triggers an Aurora B-dependent abscission arrest[304]. Finally, DNA replication stress has been associated with activation of the abscission checkpoint, as cells displaying DNA damage foci as a result of under-replication take substantially longer to complete abscission[305].

The detailed molecular mechanisms surrounding the abscission checkpoint are still a subject of much investigation, however evidence suggests that persistent Aurora kinase B activation, mediated by CPC components INCENP, Survivin and Borealin, is the first major signal that triggers the delay in abscission associated with cytokinetic stress[302] (**Figure 14**). Subsequent association of the Abscission/NoCut Checkpoint Regulator (ANCHR) and CHMP4C to VSP4 causes VSP4 inhibition and delay of abscission[306]. Interestingly, ANCHR depletion leads to furrow regression only in cells displaying chromatin bridges[306], providing further support that an abscission-specific machinery mediates a surveillance mechanism to prevent errors. Further work is required to identify whether other insults can trigger the abscission checkpoint; whether this checkpoint is conserved among different cell types and species; and to assess the physiological relevance of the abscission checkpoint, as well as its potential role in furrow regression events that cause binucleation.

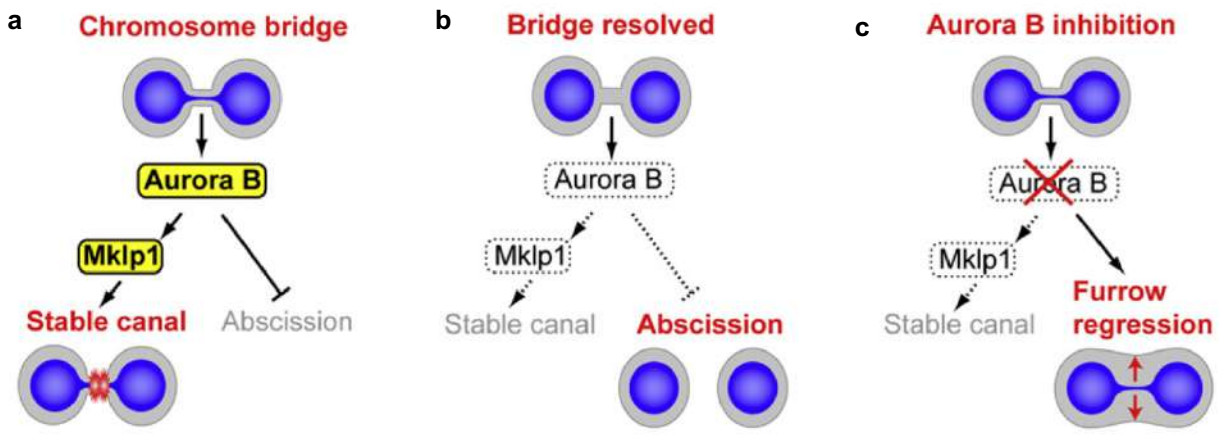

Figure 14. – Model for Aurora B-dependent abscission checkpoint.

(a) *The formation of chromosome bridges at anaphase induces prolonged Aurora B activity to post-telophase stages, thereby leading to phosphorylation of Mklp1, stabilisation of the intercellular bridge and delayed abscission.* ***(b)*** *Upon resolution of the chromosome bridge and removal of the chromatin from the cleavage furrow, Aurora B is inactivated, leading to destabilisation of the intercellular bridge and successful abscission completion.* ***(c)*** *Chemical inhibition of Aurora B in cells displaying chromatin bridges leads to destabilisation of the intercellular bridge and furrow regression, resulting in tetraploidy. Adapted from Steigemann et al. 2009*[302].

1.4 Tetraploidy

As described in the paragraphs above, cytokinesis is an intricate step of cell division and requires precise coordination of different cellular structures and processes that promote timely and successful cell separation, initiating from signalling from the spindle and astral microtubules, cortical remodelling, and further detection of mitotic or mechanical errors that can be harmful for future generations. Certainly, errors at any stage of the process can lead to failure of cytokinesis and thus generate a binucleated cell containing two entirely diploid nuclei instead of one, in what is known as tetraploidy. The following sections will detail the origins and consequences of tetraploidy in different cell types. Tetraploidy can occur as a normal part of physiological processes, and certain cell types and tissues are thought to take advantage of their tetraploid genome to optimise metabolic activity. In contrast, unscheduled tetraploidisation can either trigger a cell cycle arrest and apoptosis or, in certain conditions, lead to persistent chromosome segregation errors and tumorigenesis. Furthermore, although tetraploidy is generally incompatible with embryo development, its adverse effects on cell fate are used as a convenient laboratory technique for the generation of transgenic mice.

1.4.1 Physiological tetraploidisation

Most mammals are diploid – meaning that each cell contains two sets of chromosomes (2N); the only exception being the red vizcacha rat (*Tympanoctomys barrera*) and close relatives which contain four sets of chromosomes (4N, i.e. tetraploid)[307]. The maintenance of a diploid genome content is essential for survival of mammalian species, and the occurrence of tetraploidy in mammals is associated with spontaneous abortions[308] and early lethality[309]. Given that tetraploidy

appears to have severe deleterious consequences that are incompatible with proper development, it is perhaps surprising that high levels of polyploidy can be found in certain mammalian tissues. At least three specialized cell types are well known to have varying degrees of polyploidy: trophoblast giant cells (TGCs)[310, 311, 312, 313], megakaryocytes[314] and hepatocytes[315, 316, 317]. Less well characterised cells that display polyploidy are skeletal muscle, osteoclasts, lactating mammary gland cells, urothelium, mesothelium, Purkinje neurons and cardiomyocytes[310, 318].

Trophoblast giant cells are a result of differentiation of trophoblast stem cells in the placenta and are characterised by high levels of polyploidy with DNA content ranging from 8N to 64N[310, 313]. These cells are considered the only characterized mammalian cell type to undergo endoreplication - a process by which cells undergo multiple rounds of DNA replication without intervening mitosis and cytokinesis[313]. The mechanism by which TGCs undergo constant rounds of polyploidisation initiates with deprivation of fibroblast growth factor 4 (FGF4)[312]. Inhibition of FGF4 signalling pathway induces the expression of the Cdk inhibitor p57[312] and reduces the translation of Cyclin B, thereby blocking mitotic entry. This cycle is maintained by constant oscillations between Cdk2/CycE and p57 levels, which induces alternations between S-phase and G-phase[311]. Because no mitosis takes place, the resulting cell exists S-phase with replicated chromatids that are not separate and remain as a single polyploid nucleus. Whether endoreplication is the only route by which TGCs are generated or whether cytokinesis failure events may also contribute to TGC emergence is unclear.

Differently than TGCs, megakaryocytes achieve polyploidisation by cytokinesis failure, reaching a DNA content of up to 64N or higher depending on stress conditions[314]. Prior to cytokinesis failure, megakaryocytes progress through mitosis normally, initiating anaphase and cytokinesis, however furrow ingression is defective, leading to cytokinesis failure, most likely due to suboptimal levels of Cdk1/CycB activity and premature degradation of Cyclin B, thereby generating a single polyploid cell[310, 319, 320]. Interestingly, unlike it would be expected for a cell that undergoes cytokinesis failure, polyploid megakaryocytes are not binucleated or multinucleated; and this is due to additional karyokinesis abnormalities that lead to persistent nuclear bridges and incomplete separation of the two nuclei, thereby providing the characteristic bi/multilobulated appearance of megakaryocytes[314, 321].

In the case of hepatocytes, polyploidisation initiates within the first three weeks after birth, in which the proportion of diploid cells decreases and binucleated cells emerge[315]. In both humans

and rats, the proportion of binucleated cells can reach between 30% and 40% in the adult liver[315]. The mechanisms by which binucleated hepatocytes arise have not been entirely elucidated, but it is believed that binucleation takes place as a result of either cytokinesis failure[315, 316] or cell fusion in cases of liver disease[317]. In rats, it has been shown that cytokinesis failure during liver growth is triggered by a rise in insulin signalling during suckling-to-weaning transition and that the PI3/Akt pathway regulates cytokinesis by controlling the cytoskeleton network and inhibiting furrow ingression[316], however further studies are required to fully understand the molecular mechanisms by which cytokinesis failure and/or cell fusion arises in hepatocytes.

Given that polyploidy (or tetraploidy) is known to cause developmental defects, a reasonable question is what are the benefits of programmed polyploidy in TGCs, megakaryocytes and hepatocytes? There is no definitive answer to this question so far, however one hypothesis is that polyploidisation in cells with high metabolic rates (such as hepatocytes and TGCs) would provide a means to redirect energy usage from cell division and membrane synthesis towards gene duplication and protein synthesis, thereby increasing the metabolic capacity of the tissue as a whole[310]. Alternatively, a mechanism of 'ploidy reversal' has been shown to occur in polyploid hepatocytes, wherein the formation of multipolar spindles during polyploid cell divisions results in multidirectional anaphases that produce daughter cells containing highly diverse genetic content[322]. This mechanism is thought to provide an evolutionary advantage to towards the maintenance of genetic diversity and adaptation of liver tissues to xenobiotic or nutritional injury[322].

In the case of megakaryocytes, although its main function is platelet production rather than metabolism, it is reasonable to think that polyploidy would also be advantageous. Polyploidisation by cytokinesis failure enables megakaryocytes to enlarge their cytoplasm to up to 100µm diameter[323]. This cellular enlargement coupled with membrane modifications and high production of granules and organelles allows for the production of platelet-specific proteins and eventually release of up to ~3,000 platelets from a single 32N megakaryocyte[310, 323]. Therefore, polyploidisation in megakaryocytes might provide an efficient way to direct energy expenditure to membrane modifications and organelle synthesis, thereby maximising the production and release of platelets into the bloodstream.

1.4.2 Unscheduled tetraploidisation

Although tolerated under certain physiological circumstances, most often than not polyploidisation is deleterious and incompatible with proper development. Among human spontaneous miscarriages, polyploidy (triploidy and/or tetraploidy) constitutes around 20% of miscarriages with chromosomal abnormalities, which represent ~10% of total miscarriages[324, 325, 326, 327]. Moreover, in certain somatic cells, the potential for cell transformation induced by tetraploidy has been demonstrated as evidenced by the development of tumours in mice injected with tetraploid cells[328, 329]. Several molecular pathways are known to act throughout the cell cycle to prevent the generation of cells with deviant DNA contents. For instance, the alternation between DNA replication and mitosis is tightly regulated by cyclin-dependent kinases (Cdks) to ensure that mitosis only initiates when the DNA has been entirely and correctly replicated[310]. Moreover, two types of checkpoints – the DNA damage checkpoint and the spindle assembly checkpoint (SAC) – ensure that the genome remains intact and allows the separation of only correctly aligned sister chromatids, respectively[310]. It is, therefore, logical that defects in any of these control mechanisms or even inherent features of specific cell types might allow the generation of cells with aberrant DNA content with potential for damaging consequences.

In the case of tetraploidy, three main mechanisms are known to cause unscheduled tetraploidisation: virus-induced cell fusion, mitotic slippage (sometimes referred to as endomitosis) and cytokinesis failure. Cell fusion is a common feature of cells infected with viruses of the herpes, paramyxo and poxvirus groups, although cell fusion independent of active viral infection has also been described in cells exposed to large doses of inactivated versions of the Sendai virus[330]. These two types of cell fusion events are mechanistically distinct; whereas cell fusion caused by ongoing infections requires intracellular replication of the virus and synthesis of viral proteins that induce membrane fusion, cell fusion by inactivated Sendai virus is essentially a laboratory technique developed for cells cultured *in vitro* in the presence of extremely large amounts of inactivated viruses that does not require viral replication and protein synthesis and instead, relies on the presence of glycoproteins associated with the viral membrane envelope that have fusion activity[330, 331].

Tetraploidy can also arise by mitotic slippage, in which cells exit mitosis without completing chromosome segregation, by escaping a SAC-mediated metaphase arrest[324]. The SAC

acts to prevent anaphase onset in the presence of unattached kinetochores by preventing APC/C-mediated proteolysis of Cyclin B[332]. Mitotic slippage takes place when cells that have been arrested in metaphase for too long escape the SAC-mediated arrest without intervening anaphase and cytokinesis, and thus reassemble the nuclear envelope with a tetraploid genome[333]. Although the mechanisms by which mitotic slippage takes place have not been entirely elucidated, a progressive reduction of MAD2 at the kinetochore seems to play a role in promoting a gradual weakening of the SAC that enables the APC/C^{CDC20} to degrade Cyclin B and allows for mitotic exit even without intervening anaphase[333, 334].

Finally, cytokinesis failure is a third mechanism by which tetraploidy can arise. Cytokinesis failure can occur by mechanisms including the trapping of bulk chromatin[288] or single chromosomes[335] in the vicinity of the cleavage furrow, or specific genetic alterations and mutations that lead to cytokinesis failure. For instance, overexpression of Eg5[336], Mad2[337], Aurora A[338], defects in the gene that encodes for the protein adenomatous polyposis coli (APC)[339] and deficiency in the tumour suppressor gene BRCA2[340] all result in cytokinesis failure and lead to accumulation of tetraploid cells.

1.4.3 The tetraploidy checkpoint

Most cells possess surveillance mechanisms (i.e. checkpoints) to ensure the integrity of the genome and proper segregation of chromosomes. Although the robustness of these checkpoints varies depending on the type of cell and organism, it is well established that cells have checkpoints for all phases of the cell cycle: G1, S-phase, G2 and M-phase. In general, checkpoints during G1 and G2 phases act to ensure the repair of damaged DNA prior to progression to S-phase and mitosis, respectively. The intra S-phase checkpoint causes inhibition of DNA replication in response to genotoxic insults. And the M-phase checkpoint, also known as spindle assembly checkpoint, is responsible for mediating the correct attachment of kinetochores and microtubules to ensure chromosome segregation fidelity. An additional checkpoint, termed tetraploidy checkpoint, has been proposed to exist based on evidence that a p53-dependent G1 arrest is observed when cytokinesis failure is induced by Cytochalasin B treatment in non-transformed rat fibroblasts (REF-52)[341, 342] (**Figure 15A**). The existence of a tetraploidy checkpoint was further contested by evidence that three different non-transformed cell lines (hTERT-RPE1, REF-52 and human

primary fibroblasts) failed to display a G1 arrest caused by tetraploidisation when the dose of Cytochalasin B used to induce cytokinesis failure was reduced 20 times, or when Blebbistatin was used as an alternative means of inducing cytokinesis failure[343]. Thus, it has been further suggested that the G1 arrest previously observed in REF-52 cells could have been caused by disorganisation of the actin cytoskeleton induced by high doses of Cytochalasin B that could lead to activation of the p53 cell cycle arrest pathway, rather than by tetraploidy itself[343].

Alternatively, it is possible that the tetraploidy checkpoint may be an indirect effect of other cellular abnormalities related to tetraploidy that trigger the p53-mediated arrest. For instance, supernumerary centrosomes generated by cytokinesis failure have been shown to activate the Hippo tumour suppressor pathway via interaction with kinase Lats2, which in turn stabilises p53 thereby inducing cell cycle arrest of RPE-1 tetraploid cells[344] (**Figure 15A**). Moreover, binucleated cells that progress through the following mitosis with abnormal multipolar spindles are more likely to undergo subsequent p53-mediated G1 arrest than those that divide with normal bipolar spindles[345]. This evidence supports the notion that other factors indirectly related to tetraploidy are responsible for inducing a cell cycle arrest. Interestingly, megakaryocytes - in which polyploidy is considered a normal physiological feature - have been shown to bypass the Hippo-p53 mediated arrest[346], raising the possibility that the uncoupling of the Hippo pathway and p53 activation is an evolutionary mechanism to bypass cell cycle arrests.

The checkpoint mediated by tetraploidy (or by cellular abnormalities caused by tetraploidy) has mostly been associated with a G1 arrest, however recent evidence has demonstrated that a G2 arrest can also be triggered when tetraploidy is induced via restriction of substrate adhesion, and in this case, activation of the ATM/ATR pathway is responsible for this arrest[347]. The ATM/ATR pathway is classically involved in the repair of DNA strand breaks, and prolonged activation of this pathway in cells is associated with Cdc25 and p53 phosphorylation and further cell cycle arrest and apoptosis[348]. Therefore, this observation raises an interesting possibility that even when tetraploid cells bypass the G1 arrest, a G2 arrest triggered by DNA damage checkpoint mechanisms could still be in play. Further studies are necessary to fully dissect the mechanisms by which tetraploidy directly or indirectly leads to cell cycle arrests and whether tetraploidy generated by different means (i.e., cytokinesis failure or mitotic slippage) could trigger different checkpoint mechanisms.

1.4.4 Tetraploidy as a steppingstone for tumorigenesis

Many cancer cell lines are highly aneuploid, with chromosome numbers ranging from hypodiploid to hypertetraploid. Most of the aneuploidy generated in cancer cells has been attributed to individual chromosome gains and losses caused by persistent chromosome segregation error (i.e., chromosomal instability, CIN). This CIN phenotype has been proposed to lead to approximately one chromosome gain or loss event in every five cell divisions in colorectal cancer[349], providing a reasonable explanation for the occurrence of near-diploid aneuploidies. However, this frequency of mis-segregation does not explain the near-triploid or near-tetraploid chromosome numbers observed in many cancers given that, at a rate of 1/5 mis-segregation events, a massive amount of cell divisions would be required to generate viable cells with a near-tetraploid genome[310]. Therefore, a second pathway for the generation of tumours with high chromosome numbers has been proposed, whereby an unstable tetraploid intermediate would lead to chromosomal instability[350]. Consistent with this, polyploidy is frequently observed in tumours of all stages and several lines of evidence indicate that tetraploidy occurs commonly as an early step in tumour formation. For instance, accumulation of tetraploid pancreatic cells induced by virus-dependent cell fusion is followed by an increase in aneuploidy and neoplastic tissues[351]. Moreover, tetraploid cells are detected before aneuploidy occurs in the pre-malignant condition Barrett's oesophagus[352, 353, 354] and in early stages of cervical carcinogenesis[355]. But perhaps the most direct evidence of tetraploidy being an early step of tumorigenesis was established when p53-null mammary gland tetraploid cells were transplanted into mice and quickly generated tumours[329].

The mechanisms by which tetraploidy might promote tumorigenesis have been widely studied. Some clues emerged when an association between tetraploidy and CIN was observed in in yeast[356, 357] and mammalian cells[329, 354]. Whereas CIN in diploid or near diploid cells would most likely reduce its fitness and lead to cell death after multiple rounds of chromosome loss, CIN in tetraploids might not cause such deleterious consequences, due to a greater redundancy in chromosomal content caused by genome doubling, which might serve as a buffer for the damaging effects of aneuploidy and allow cells to remain viable even in the presence of chaotic karyotypes[324]. Another possibility is that additional mutations might facilitate the propagation of tetraploid cells. Several reports have suggested that tumour development is triggered by tetraploidy in combination with additional mutations, such as absence of p53[329], overexpression of Mad2[337] or Eg5[336], and it

is thus possible that these mutations may provide a more permissive environment for tetraploid cell divisions, perhaps due to defective checkpoint signalling caused by these mutations. Further investigation is undoubtedly required to elucidate the role of additional mutations on the propagation of tetraploid cells and its tumorigenic potential.

Further studies have elucidated a mechanism underpinning the CIN caused by tetraploidy, wherein the supernumerary centrosomes that originate as a result of the genome doubling event lead to multipolar spindle formation during the following cell divisions[200, 201] (**Figure 15B**). These multipolar spindles often cluster their extra centrosomes enabling the bipolarisation of the spindle[202, 358], but in doing so lead to an accumulation of kinetochore-microtubule mis-attachments that promote chromosome segregation error and increase the likelihood of whole chromosome aneuploidies[200, 201] (**Figure 15B**). In contrast, in budding yeast cells, tetraploidy leads to CIN even in the absence of multipolar spindle formation and instead, altered spindle geometry is thought to cause an accumulation of syntelic kinetochore-microtubule attachments (wherein both sister chromatids are attached to the same spindle pole), thereby driving CIN[356]. An additional mechanism by which tetraploidy drives CIN and aneuploidy in mammalian cells has been shown in our study, wherein tetraploidy causes persistent chromosome mis-segregation by directly altering kinetochore-microtubule error correction efficiency in a manner completely independent of multipolar spindles in acentriolar mouse embryos[359] (**see Chapter 2**).

1.4.5 Tetraploidy in embryos: developmental potential and the tetraploid complementation assay

Complete tetraploidy is generally not compatible with normal embryonic development, as evidenced by the presence of polyploid genomes in approximately 10% of total spontaneous miscarriages[324, 325, 326, 327]. However, rare instances of tetraploid live births have been described although the infants display severe developmental abnormalities such as spina bifida, skeletal and cartilaginous defects, organ hypoplasia and facial dysmorphologies as well as limited lifespan[299, 309], indicating that tetraploidy can occur in embryos and threatens normal development and life. Similarly, tetraploidy in mouse embryos is also incompatible with normal development, with most embryos not developing to term and those that do, display severe abnormalities[360, 361, 362]. Perhaps one of the most striking adverse effects of tetraploidy in embryos - and possibly the main reason

why tetraploid embryos have low post-implantation developmental potential - is its impact on inner cell mass formation (**Figure 15C**). Notably, tetraploid embryos are able to develop to the blastocyst stage but only 56% display a clear inner cell mass expressing pluripotency markers such as OCT4, whereas 44% display a complete absence of inner cell mass and develop into an empty trophectoderm sphere[363] (**Figure 15C; see also Discussion**). Whether tetraploidy affects cell fate by directly interfering with the expression of pluripotency genes or whether other effects of tetraploidy on cell numbers might indirectly impact inner cell mass formation are yet to be ascertained, but it has been suggested that a cell cycle delay, elevated levels of apoptosis and a lack of sufficient inner cells at the time of cavitation caused by the halving of cell numbers might all be responsible for the high number of blastocysts devoid of inner cell mass (**see Discussion**)[363, 364, 365].

Interestingly, embryonic tetraploidy was harnessed in the development of a powerful technique, termed tetraploid complementation assay. This assay was established on the grounds that chimeric tetraploid:diploid embryos display distinct lineage potencies, with diploid cells mostly populating embryonic tissues, and tetraploid cells being restricted to extraembryonic tissues[299]. By introducing diploid embryonic stem (ES) cells with a mutation or genotype of interest into a tetraploid embryo generated by either cell fusion or cytokinesis failure, this technique allows for almost complete segregation of descendants of these two cell types and is a powerful tool for the study of the effect of mutations on the embryonic vs extraembryonic tissues and for the generation of transgenic mouse lines, as the foetus proper will be constituted exclusively by the ES cells introduced[299, 366].

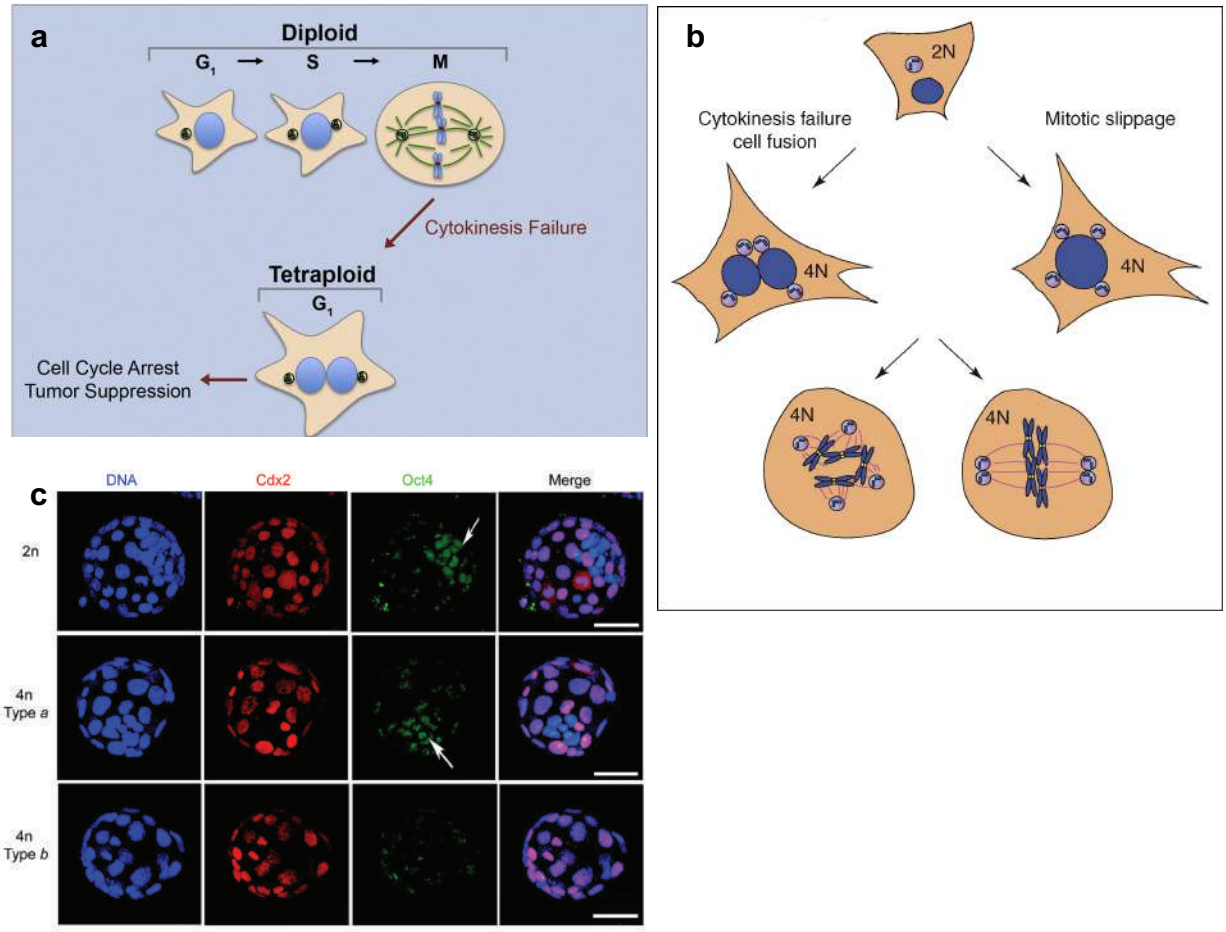

Figure 15. – Outcomes of tetraploidy in somatic cells and embryos.

(a) *In non-transformed somatic cells, tetraploidy caused by cytokinesis failure activates the Hippo pathway component LATS2 by a mechanism dependent on supernumerary centrosomes, which thus stabilises p53 and leads to cell cycle arrest, in a mechanism known as the tetraploidy checkpoint. Figure adapted from Ganem et al. 2014*[344]*.* ***(b)*** *In contrast, somatic cells lacking p53 activity bypass the tetraploidy checkpoint and proliferate with high levels of chromosome segregation error. These segregation errors are caused by multipolar spindles that arise as a result of supernumerary centrosomes. These multipolar spindles can often bipolarise due to centrosome clustering mechanisms, but by doing so increase the rates of chromosome mis-segregation. Figure adapted from Ganem et al. 2007*[367]*.* ***(c)*** *In mouse embryos, tetraploidy allows preimplantation development to the blastocyst stage, but severely impacts inner cell mass (ICM) formation. Tetraploid embryos often display a complete absence of OCT4-labelled ICM cells (third row – 4n type b), although some tetraploid embryos are still able to generate few OCT4-labelled ICM cells (middle row – 4n type a). Figure adapted from Wen et al. 2014*[363]*.*

1.5 The mouse embryo as a model for the study of cytokinesis and tetraploidy

The mouse is a popular experimental model for embryogenesis because it is cost-effective, it is amenable to genetic and biochemical manipulations and has a short gestational period, with implantation occurring only ~4-5 days postcoitum, whereas humans average 9 days and cows 30 days until implantation[368]. Despite its remarkably quick preimplantation period, mouse embryo development still closely resembles that of other mammals and, although the time elapsed between events can vary, the sequence of developmental events from fertilisation to implantation and the morphological characteristics are essentially the same among several mammalian species[368]. For instance, both mouse and human embryos undergo compaction at the morula stage and require similar signalling pathways to form the three distinguishable cell lineages at the late blastocyst stage (epiblast, primitive endoderm and trophectoderm), placing the mouse embryo as a powerful model system for the study of embryogenesis (reviewed in Piliszek et al. 2016[369]). The first attempts to culture mouse embryos *in vitro* with chemically defined media were reported by Whitten in 1956[370], and more than six decades of further research have greatly advanced *in vitro* culture conditions such that mouse embryo culture media nowadays is well optimised, enabling very high rates of development to blastocyst stage and even live births upon transfer to females (reviewed in Summers and Bigger 2003[371]). Importantly, mouse preimplantation embryos are translucent, and this feature combined with optimised culture conditions allows for the assessment of essentially all aspects of preimplantation development *in vitro*, from the timing of cell divisions to cell size and visualisation of developmental transitions.

In addition to its applicability for the study of embryogenesis, the mouse embryo is a remarkably robust system that allows direct and fast morphological and genetic manipulations and provides an opportunity for the study of cell biological processes such as chromosome segregation and cytokinesis. For instance, cell size can be readily and quickly manipulated by micromanipulation approaches such as cytoplasmic removal[232], without intervening effects on subsequent cell divisions. Moreover, protein knockdown approaches have been extensively applied via microinjection of short-hairpin or double-stranded RNAs to abolish developmental events such as apical polarity emergence[61] and cell fate determination[372]. Finally, well-established live cell

imaging approaches that rely on the expression of mRNAs that encode for fluorescently tagged proteins allow for direct visualisation of cell biological events[212, 232]. As detailed in the previous sections, one outstanding question in the field of cytokinesis is how contractile ring assembly and constriction is regulated to account for cell size reductions and developmental changes. Therefore, the flexibility of the mouse embryo in terms of cell size manipulations and protein knockdown approaches provides an opportunity for the development of experimental designs that distinguish between the relative roles of cell size and developmental events on the regulation of cytokinesis.

An obvious question that arises from the subject of cytokinesis regulation is what the consequences of cytokinesis failure are. As detailed in the previous sections, in centriolar somatic cells, cytokinesis failure leads to binucleation (i.e., tetraploidy), which induces chromosomal instability by a mechanism dependent on overduplication of centrioles which impairs spindle assembly, thereby causing segregation errors[200, 201]. One notable difference of the mouse embryo from other mammalian systems is that early embryonic mitotic divisions take place in the complete absence of centrioles, as sperm centrioles are degraded upon egg fertilisation. The PCM component γ-tubulin starts to appear as well-defined foci at the ~32-cell stage[207, 209], but proper centrioles are only detected by the ~64-cell stage[135, 209]. Therefore, the unusual scenario of mouse acentriolar divisions provides a compelling opportunity to address whether tetraploidy can also impact chromosome segregation even in the absence of centrioles, and how this might take place.

The following chapters will address the impacts of tetraploidy on chromosome segregation dynamics as well as the mechanisms that regulate cytokinesis, using the mouse embryo as a model. Chapter 2 will detail experiments that unravel an unexpected mechanism by which tetraploidy causes chromosomal instability in a manner independent of centriole overduplication (**see also Annexe 1**). Chapter 3 will present a novel mechanism by which apical polarity modulates contractile ring assembly and constriction during cytokinesis (**see also Annexe 2**). Chapter 4 will present a hypothesis that proposes that binucleation can arise by mechanistically distinct routes, one that produces viable embryos and one that directly threatens embryo health (**see also Annexe 3**). Finally, Chapter 5 will discuss the findings of this thesis and present the significance of this work for the field of reproductive and cell biology.

Results

Chapter 2 – Tetraploidy causes chromosomal instability in acentriolar mouse embryos

Lia Mara Gomes Paim[1] and Greg FitzHarris[1, 2*]

[1] Centre de Recherche du Centre Hospitalier de l'Université de Montréal, H2X 0A9, Montréal, Canada

[2] Département d'Obstétrique-Gynécologie, Université de Montréal, H3T 1C5, Montréal, Québec, Canada

* Correspondence: greg.fitzharris@umontreal.ca

Citation: Paim, L.M.G., FitzHarris, G. Tetraploidy causes chromosomal instability in acentriolar mouse embryos. Nat Commun 10, 4834 (2019). https://doi.org/10.1038/s41467-019-12772-8

ABSTRACT

Tetraploidisation is considered a common event in the evolution of chromosomal instability (CIN) in cancer cells. The current model for how tetraploidy drives CIN in mammalian cells is that a doubling of the number of centrioles that accompany the genome doubling event leads to multipolar spindle formation and chromosome segregation errors. By exploiting the unusual scenario of mouse blastomeres, which lack centrioles until the ~64-cell stage, we show that tetraploidy can drive CIN by an entirely distinct mechanism. Tetraploid blastomeres assemble bipolar spindles dictated by microtubule organising centres, and multipolar spindles are rare. Rather, kinetochore-microtubule turnover is altered, leading to microtubule attachment defects and anaphase chromosome segregation errors. The resulting blastomeres become chromosomally unstable and exhibit a dramatic increase in whole chromosome aneuploidies. Our results thus reveal an unexpected mechanism by which tetraploidy drives CIN, in which the acquisition of chromosomally-unstable microtubule dynamics contributes to chromosome segregation errors following tetraploidisation.

2.1 Introduction

Cell division is comprised of mitosis and cytokinesis. During mitosis, a bipolar spindle is organised by two centrosomes, each comprising a pair of centrioles surrounded by the pericentriolar material. The spindle segregates sister chromatids by the attachment of kinetochores to microtubules that generate forces to separate the chromatids[1,2]. Following chromosome alignment in metaphase, sister chromatids are segregated during anaphase. In most cells, cytokinesis occurs concomitantly causing the cytoplasm to be partitioned into two daughter cells to house the newly segregated chromosomes[3,4]. Defects in either process can affect genetic fidelity. Whereas chromosome mis-segregation in mitosis can cause gains or losses of whole chromosomes, termed aneuploidy, cytokinesis failure leads to an entirely duplicated genome, termed tetraploidy[5,6].

Importantly, tetraploidy can trigger persistent chromosomal mis-segregation (also known as chromosomal instability; CIN), and therefore drive aneuploidy[5,6]. Indeed, tetraploidy is considered a common steppingstone in tumorigenesis and likely contributes to the high levels of CIN in cancer[5,7–11]. Landmark studies described a mechanism underpinning this phenomenon, wherein the excess of centrioles generated by failed cytokinesis causes multipolar spindles during subsequent mitoses. These multipolar spindles can cluster their extra centrosomes to form a bipolar spindle prior to anaphase, but in doing so increase the likelihood of segregation error and whole-chromosome aneuploidy[9,11–13]. Whether this is the only mechanism by which tetraploidy promotes CIN is unknown.

The early mouse embryo lacks centrioles. Whereas in most mammals the fertilising sperm provides the centrioles[14], in mouse they are eliminated both in the oocyte and the sperm, such that the first several mitoses occur in the complete absence of centrioles, and new centrioles are eventually manufactured de novo in the ~64-cell stage embryo[15–17]. Here we take advantage of this highly unusual scenario to investigate the impact of tetraploidy upon chromosome segregation in an acentriolar setting. By extensive live time-lapse imaging we show that, in the acentriolar mouse embryo, tetraploidy rapidly leads to CIN by a mechanism independent of supernumerary centrosomes.

2.2 Results

2.2.1 Tetraploid mouse embryos are highly chromosomally unstable.

To explore the impact of tetraploidy, we transiently prevented cytokinesis using the actin depolymerising agent Latrunculin B at the 4–8-cell transition, thereby obtaining embryos with four binucleated blastomeres (Fig. 1a, see also the section "Methods"). Herein we refer to the next cell division, in which the four binucleated blastomeres divide to become eight mono-nucleated blastomeres as the 'binucleated division', and the subsequent division as the 'second tetraploid division' (Fig. 1a). In some somatic cells, tetraploidy results in a p53-dependent cell cycle checkpoint that prevents further cell division[18,19]. To assess the impact of tetraploidy in embryos, we allowed binucleated embryos to develop *in vitro* and counted cell numbers 12 and 24h after binucleation using fixed-cell analysis. Embryos developed from the binucleated four-cell stage to become morulae possessing 17.9 ± 1.15 (mean ± SEM, n = 23 embryos) cells 24 h after binucleation, confirming that cell divisions were not critically impeded (Supplementary Fig. 1a, b). Next, we used PCNA:EGFP to visualise cell cycle progression[20]. Nuclear PCNA:EGFP foci were transiently evident in mid-interphase both in the binucleated division and the second tetraploid division, similar to control embryos, indicative of successful progression through S phase (Supplementary Fig. 1c, d). Accordingly, the number of kinetochores, as observed by kinetochore immunostaining in metaphase-arrested embryos, was doubled in Latrunculin-treated embryos as compared to controls (Supplementary Fig. 1e, f). Thus, as suggested previously[21–23], preimplantation mouse embryos fail to mount a tetraploidy-induced cell cycle checkpoint and continue to develop with a doubled genome.

We wondered about the impact of tetraploidy upon chromosome segregation in embryos. Analysis of chromosome segregation dynamics in live H2B:RFP-expressing embryos at the binucleated division revealed that whereas 82% of divisions in control embryos were normal and without obvious defects, segregation defects were common in tetraploid embryos, with only 33% of divisions occurring with no observable defect (Fig. 1b, c). Embryos also displayed segregation defects when cytokinesis failure had been induced with either Cytochalasin B or Blebbistatin (Supplementary Fig. 2a, b). Moreover, embryos undergoing mitosis in the continued presence of the actin inhibitor Latrunculin had few errors (Supplementary Fig. 2c–e), confirming that actin

depolymerisation does not negatively affect chromosome segregation fidelity in the mouse embryo, contrary to the case of mouse oocyte meiosis I[24]. Together, these experiments confirm that the errors observed are attributable to the tetraploid state of the embryos, not the method of inducing tetraploidy. Strikingly, analysis of the second tetraploid division revealed a phenotype very similar to that of the binucleated division, whereas stage-matched controls showed few discernible defects (Fig. 1d, e). Increased abundance of micronuclei, a marker of accumulated chromosome segregation errors[25], was also observed in fixed cell experiments, excluding the possibility that the increased number of errors was somehow related to live imaging (Supplementary Fig. 3). Importantly, ploidy analysis by chromosome spreads at early blastocyst stage revealed that 68.2% of 32-cell stage control embryos contained 40 chromosomes, whereas 31.8% had either chromosome gains or losses (Fig. 1f, g), with chromosome numbers ranging from 38 to 42 (Supplementary Fig. 4a). In contrast, we found that only 24% of 16-cell stage tetraploid embryos maintained a perfect tetraploid genome (80 chromosomes) (Fig. 1f, g), with chromosome numbers ranging from 77 to 83 (Supplementary Fig. 4b). Taken together these experiments reveal that tetraploid mouse embryos continue to divide but become chromosomally unstable during the next few cell divisions.

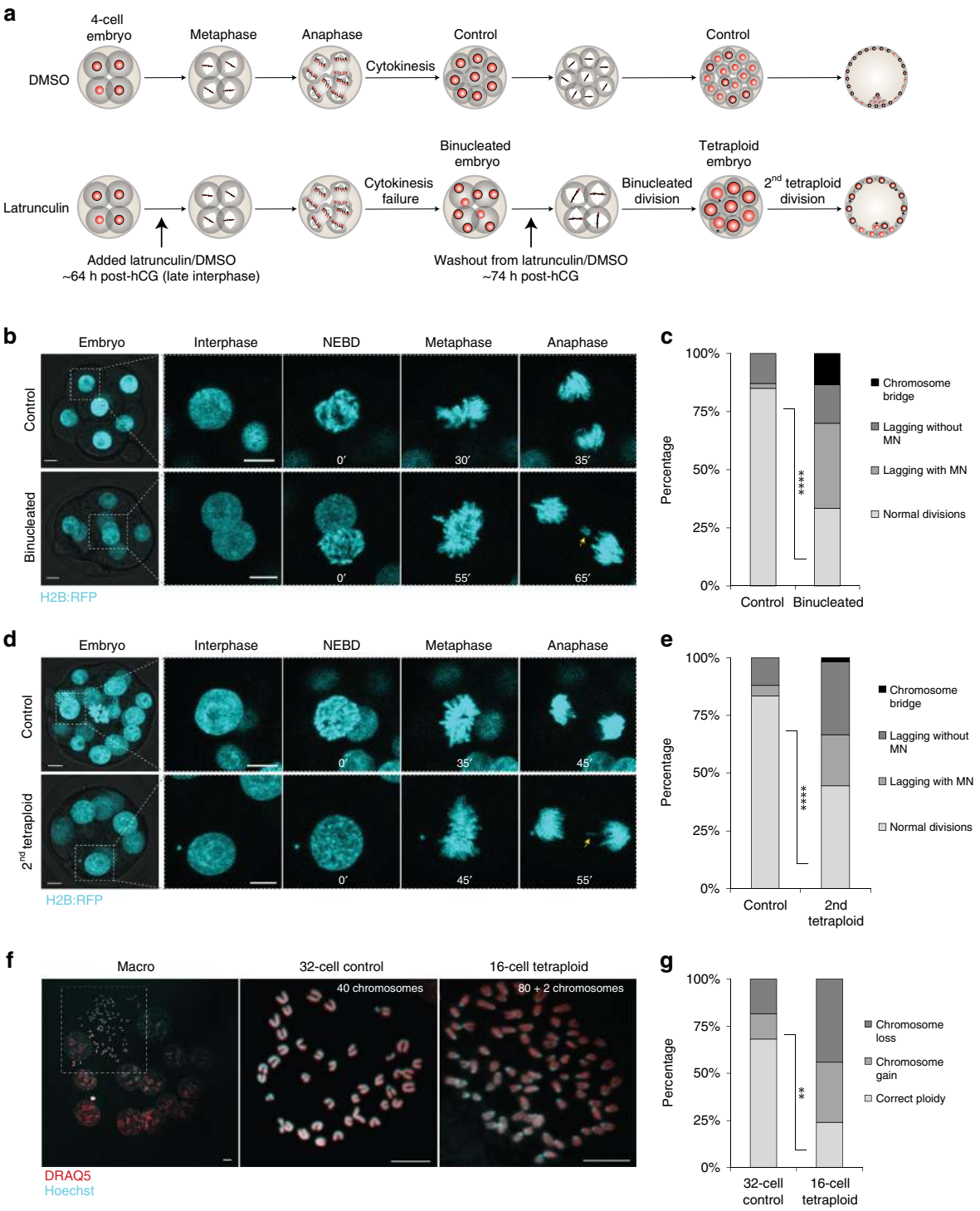

Figure 16. – Tetraploidy leads to chromosomal instability and aneuploidy in the mouse embryo (Figure 1).

a *Scheme illustrating the experimental design applied for the generation of tetraploid embryos.* ***b*** *and* ***d*** *Representative time-lapse images of mitosis in live H2B:RFP-expressing 8-cell control and 4-cell-binucleated* ***b****, 16-cell control and 8-cell tetraploid embryos* ***d****. A lagging chromosome (yellow arrows) can be observed both in the binucleated and second tetraploid divisions.* ***c*** *and* ***e*** *Percentage of cell divisions containing chromosome segregation errors in 8-cell control (n = 47 divisions from seven embryos), 4-cell binucleated embryos (n =30 divisions from eight embryos) ****P < 0.0001 (two-tailed Fisher's exact test)* ***c****; 16-cell control (n = 66 divisions from seven embryos) and 8-cell tetraploid embryos (n = 50 divisions from nine embryos) ****P < 0.0001 (two-tailed Fisher's exact test)* ***e****. Chromosome segregation errors observed included: lagging chromosomes resulting in micronuclei formation (lagging with MN); lagging chromosomes that did not result in micronuclei formation (lagging without MN); and chromosome bridges.* ***f*** *Representative images of chromosome spreads obtained from 32-cell control and 16-cell tetraploid embryos.* ***g*** *Percentage of blastomeres containing whole chromosome gains and losses in 32-cell control (n = 22 spreads) and 16-cell tetraploid embryos (n = 25 spreads) **P = 0.0034 (two-tailed Fisher's exact test). Scale bars= 10 µm. NEBD nuclear envelope breakdown.*

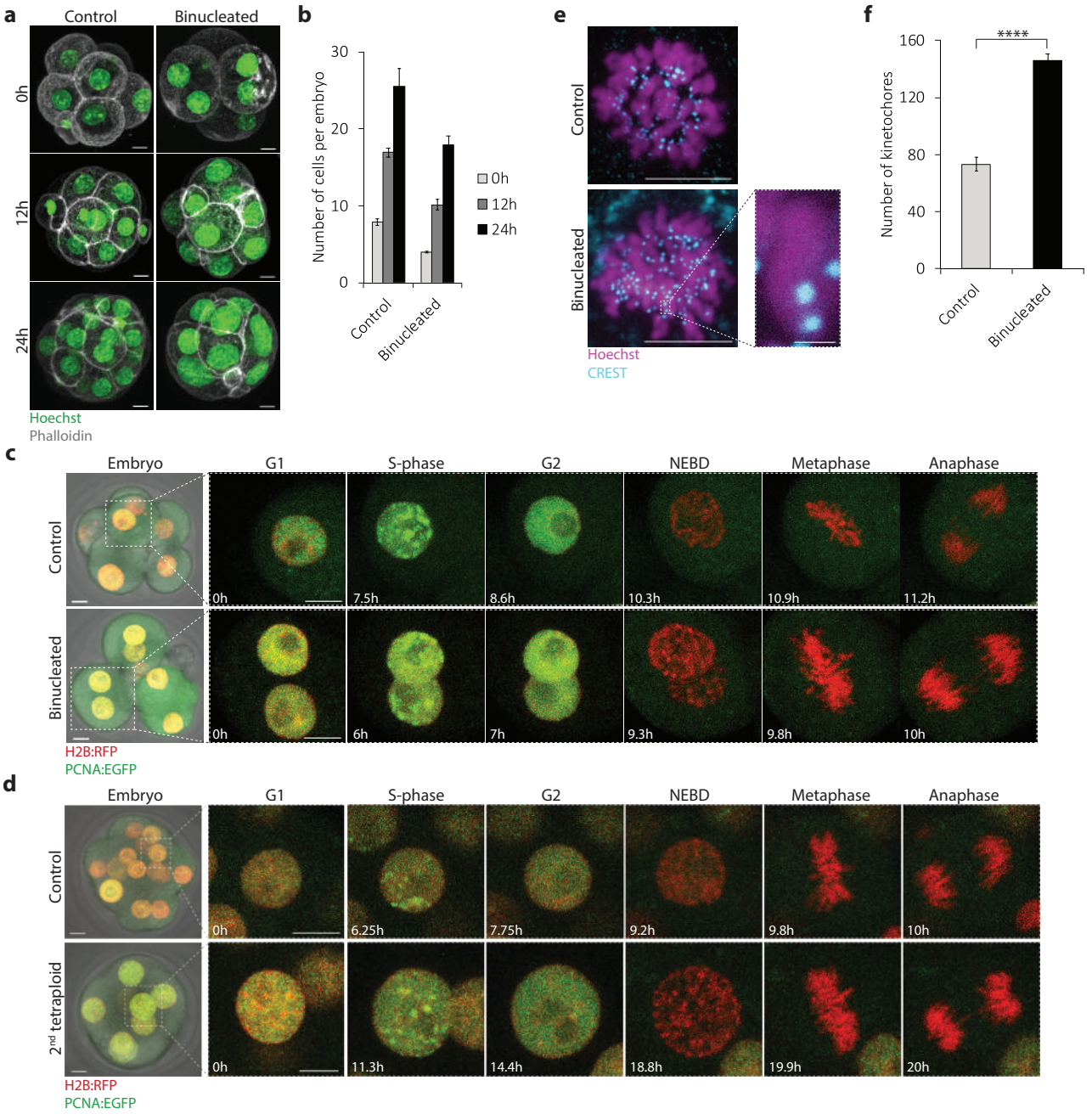

Figure 17. – The mouse embryo lacks a tetraploidy checkpoint (Supplementary Figure 1).

(a) *Representative z-projections of embryos fixed 0h, 12h and 24h after exposure to either Latrunculin B (Binucleated) or DMSO (Control).* ***(b)*** *Quantification of number of cells per embryo 0h, 12h, and 24h after exposure to either DMSO (0h n=34 embryos; 12h n=31 embryos; 24h n=21 embryos) or Latrunculin B (0h n=27 embryos; 12h n=21 embryos; 24h n=23 embryos).* ***(c and d)***

Representative z-projections of 8-cell control, 4-cell binucleated ***(c)****, 16-cell control and 8-cell tetraploid embryos* ***(d)*** *expressing H2B:RFP (red) and PCNA:EGFP (green). Note that S-phase can be identified by the accumulation of PCNA foci at the nucleus demarking DNA replication.* ***(e)*** *Representative z-projections of metaphase-arrested controls and binucleated embryos. Note that treatment with Monastrol induces monopolar spindle formation, allowing for the better visualisation of individual kinetochores.* ***(f)*** *Quantification of number of kinetochores per cell in 8-cell control (n=5 blastomeres) and 4-cell binucleated embryos (n=8 blastomeres) ****P<0.0001 (unpaired, two-tailed t test). Note that this approach allows for an approximation of kinetochore numbers (close to 80 kinetochores in controls and close to 160 kinetochores in tetraploids). Scale bars = 10µm, except for the chromosome zoom in (****e****), where scale bar = 1µm. Error bars represent SEM. NEBD=nuclear envelope breakdown.*

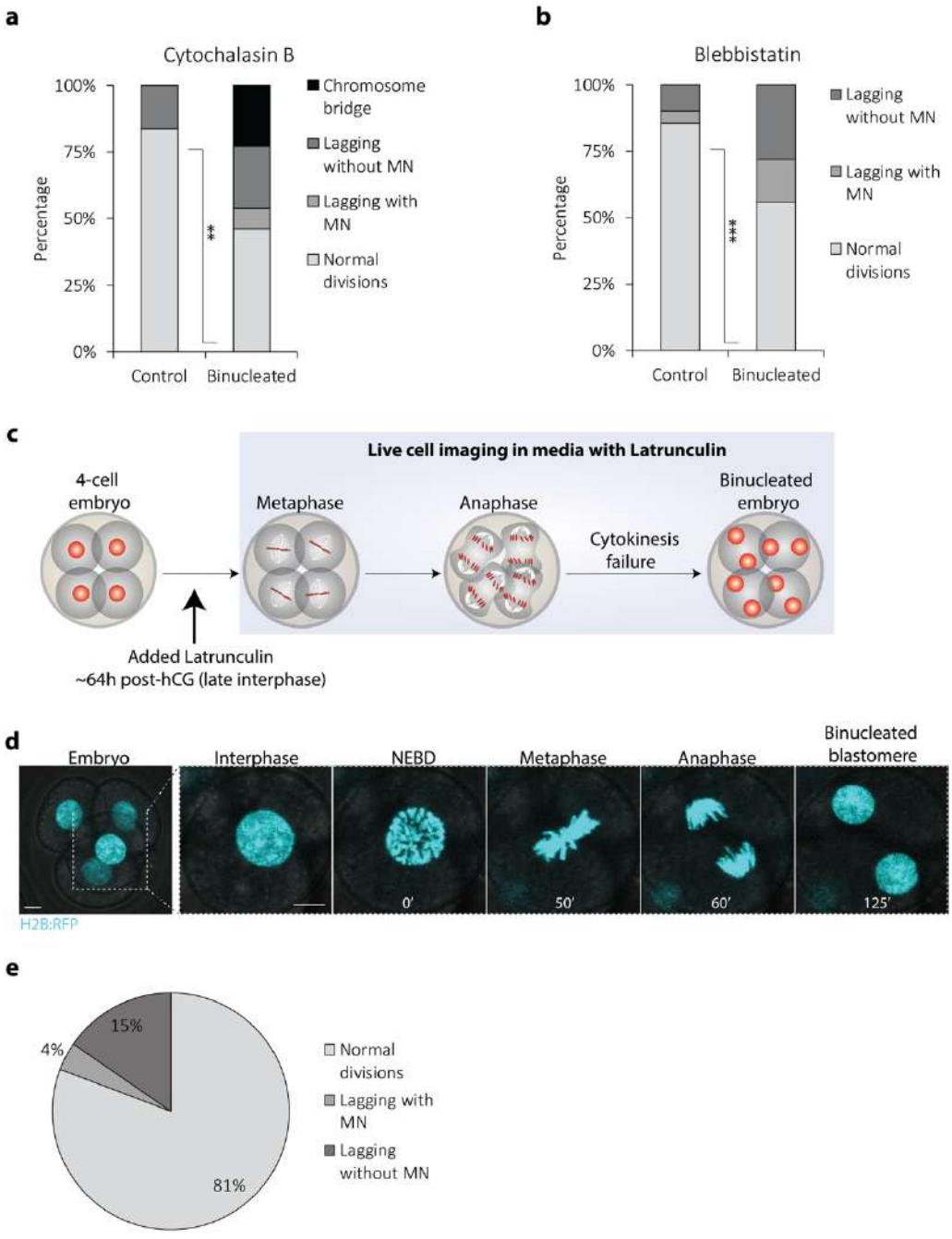

Figure 18. – The chromosome segregation errors observed after Latrunculin-induced binucleation are phenocopied by Cytochalasin B and Blebbistatin (Supplementary Figure 2).

(a and b) *Percentage of chromosome segregation errors in 8-cell control and 4-cell binucleated embryos produced with either Cytochalasin B (control n= 62 divisions from 15 embryos; binucleated n=13 divisions from 7 embryos; **P=0.0072, unpaired, two-tailed Fisher's exact test) or Blebbistatin treatment (control n=90 divisions from 14 embryos; binucleated n=43 divisions*

*from 16 embryos; ***P=0.0004, unpaired, two-tailed Fisher's exact test).* ***(c)*** *Scheme illustrating the experimental design applied to assess the effects of actin depolymerization on chromosome segregation dynamics. 4-cell stage embryos at late interphase were live imaged in the presence of Latrunculin and the rate of chromosome segregation errors was assessed.* ***(d)*** *Representative z-projections of H2B:RFP-expressing 4-cell stage embryos live imaged in media containing Latrunculin B.* ***(e)*** *Percentage of chromosome segregation errors in 4-cell embryos imaged in media containing Latrunculin (n=26 divisions from 9 embryos). Chromosome segregation errors observed included: lagging chromosomes resulting in micronuclei formation (lagging with MN); lagging chromosomes that did not result in micronuclei formation (lagging without MN); and chromosome bridges. Scale bars = 10µm. NEBD=nuclear envelope breakdown.*

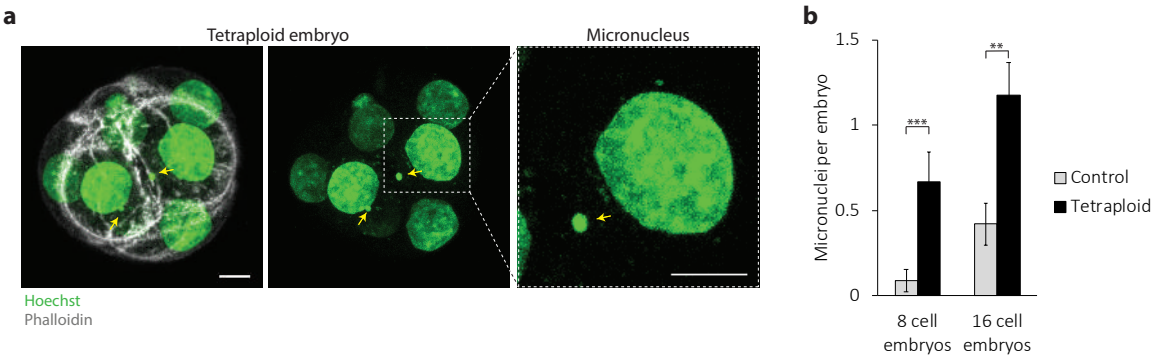

Figure 19. – Tetraploid embryos display high rates of micronuclei (Supplementary Figure 3).

(a) *Representative z-projection of an 8-cell tetraploid embryo with two micronuclei (yellow arrows).* ***(b)*** *Rates of micronuclei per embryo in 8-cell controls (n=34 embryos), 8-cell tetraploid (n=21 embryos, ***P=0.0006, unpaired, two-tailed t test), 16-cell controls (n=31 embryos) and 16-cell tetraploid embryos (n=23 embryos, **P=0.0011, unpaired, two-tailed t test). Scale bars = 10µm. Error bars represent SEM.*

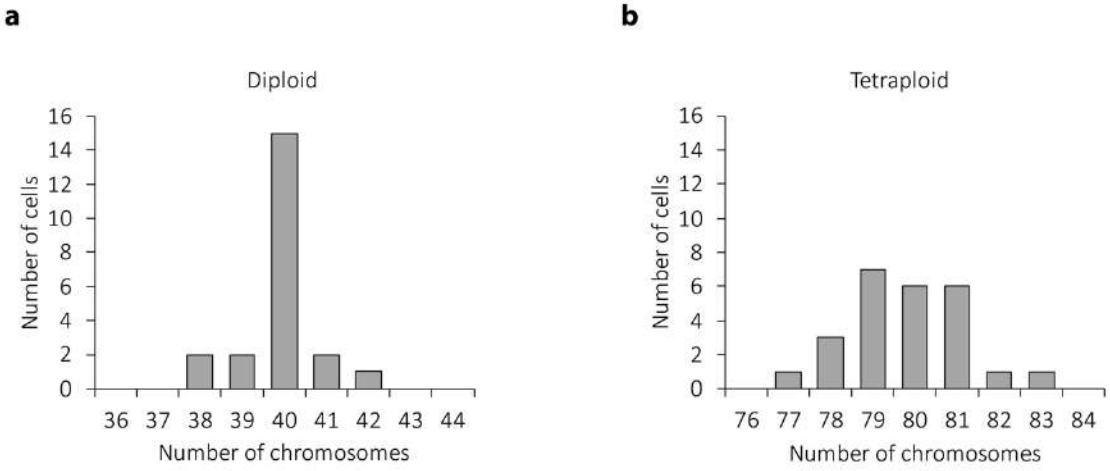

Figure 20. – Tetraploidy causes high levels of aneuploidy (Supplementary Figure 4).

(a) *Histogram demonstrating the distribution of ploidy status in diploid blastomeres (n = 22 spreads).* ***(b)*** *Histogram demonstrating the distribution of ploidy status in tetraploid blastomeres (n= 25 spreads).*

2.2.2 CIN is not attributable to supernumerary centrosomes.

In tetraploid somatic cells caused by cytokinesis failure, supernumerary centrosomes lead to the formation of transiently multipolar spindles that promote segregation errors[9,11]. Preimplantation mouse embryos lack centrioles until ~64-cell stage but achieve spindle assembly between the 4-cell and 32-cell stage by acentriolar microtubule-organising centres (MTOCs)[26]. We therefore set out to simultaneously observe MTOCs, spindles, and chromosome dynamics in tetraploid embryos, using CDK5RAP2:GFP[27,28], SiR Tubulin[29] and H2B:RFP, respectively. During interphase, the majority of normal diploid 8-cell embryos displayed a single clear MTOC close to the nucleus (Fig. 2a; Supplementary Fig. 5c and Supplementary Movie 1). At the onset of nuclear envelope breakdown (NEBD) a new MTOC was assembled such that most diploid embryos displayed a clear CDK5RAP2:GFP-labelled MTOC at each spindle pole at metaphase (Fig. 2a; Supplementary Fig. 5d and Supplementary Movie 1)[16,17]. Analogously, during the binucleated division, 4-cell binucleated embryos typically displayed a single clear MTOC on each nucleus during interphase (Fig. 2b; Supplementary Fig. 5a and c; Supplementary Movie 2). Shortly after NEBD, two new MTOCs were usually assembled such that most binucleated embryos displayed four MTOCs during mitosis (Fig. 2b and Supplementary Fig. 5a, d; Supplementary Movie 2). Interestingly, these four MTOCs usually formed the poles of two completely separate bipolar spindles (Fig. 2b and Supplementary Fig. 5a, b; Supplementary Movies 2, 3). These two spindles rapidly moved towards

each other and fused to form a single bipolar spindle prior to anaphase (Supplementary Movies 2, 3). We measured and tracked the angles between the two spindles from the moment they first established contact until they completely fused (Fig. 2c). Upon contact, the spindles fused by either sliding together or rotating towards each other depending on the initial angle of contact until they eventually became a single bipolar spindle (Fig. 2b, c; Supplementary Fig. 5a, b; Supplementary Movies 2, 3), as observed in Fmn2$^{-/-}$ mouse oocytes[30], *Xenopus* extract spindles in close apposition[31], and in mouse zygotes[32]. Notably however, there was no relationship between the initial angle at which the spindles made contact with each other and the likelihood of developing chromosome segregation errors (Fig. 2c). Moreover, multipolar spindles such as are characteristic in somatic cells with supernumerary centrioles, and associated with segregation error, were rare both in 4-cell binucleated (18.4% of divisions) and 8-cell control embryos (11.4% of divisions). Importantly, we used 3-min acquisitions intervals, which allowed us to confidently distinguish between spindle fusion events and multipolarity. Notably, even in more extreme examples of perpendicular spindle fusion, the two spindles remained distinguishable throughout fusion without neighbouring poles connecting via microtubule bundles (Supplementary Fig. 5a, b; Supplementary Movie 3).

Next, we analysed spindle dynamics in the second tetraploid division which, importantly, begins with a single morphologically normal nucleus containing a tetraploid genome. Similar to 8-cell and 16-cell controls, these cells usually possessed only one major MTOC adjacent to the nucleus and a second major MTOC was assembled at NEBD to enable the generation of a bipolar spindle (Fig. 2d, e; and Supplementary Fig. 5e, f). Though general spindle morphology was not obviously altered as compared to diploid controls, tetraploid blastomeres possessed a wider metaphase plate, presumably as a result of having twice as many chromosomes (Supplementary Fig. 5g, h). Spindle assembly was otherwise morphologically indistinguishable from diploid 8-cell or 16-cell embryos, despite the dramatic increase in segregation errors (Fig. 1d, e), with multipolar spindles again very rare (16-cell control: 9.6% of divisions; 8-cell tetraploid: 16.6% of divisions). Taken together, these observations reveal that CIN observed in the tetraploid mouse embryo cannot be attributed to supernumerary centrioles or multipolar spindles.

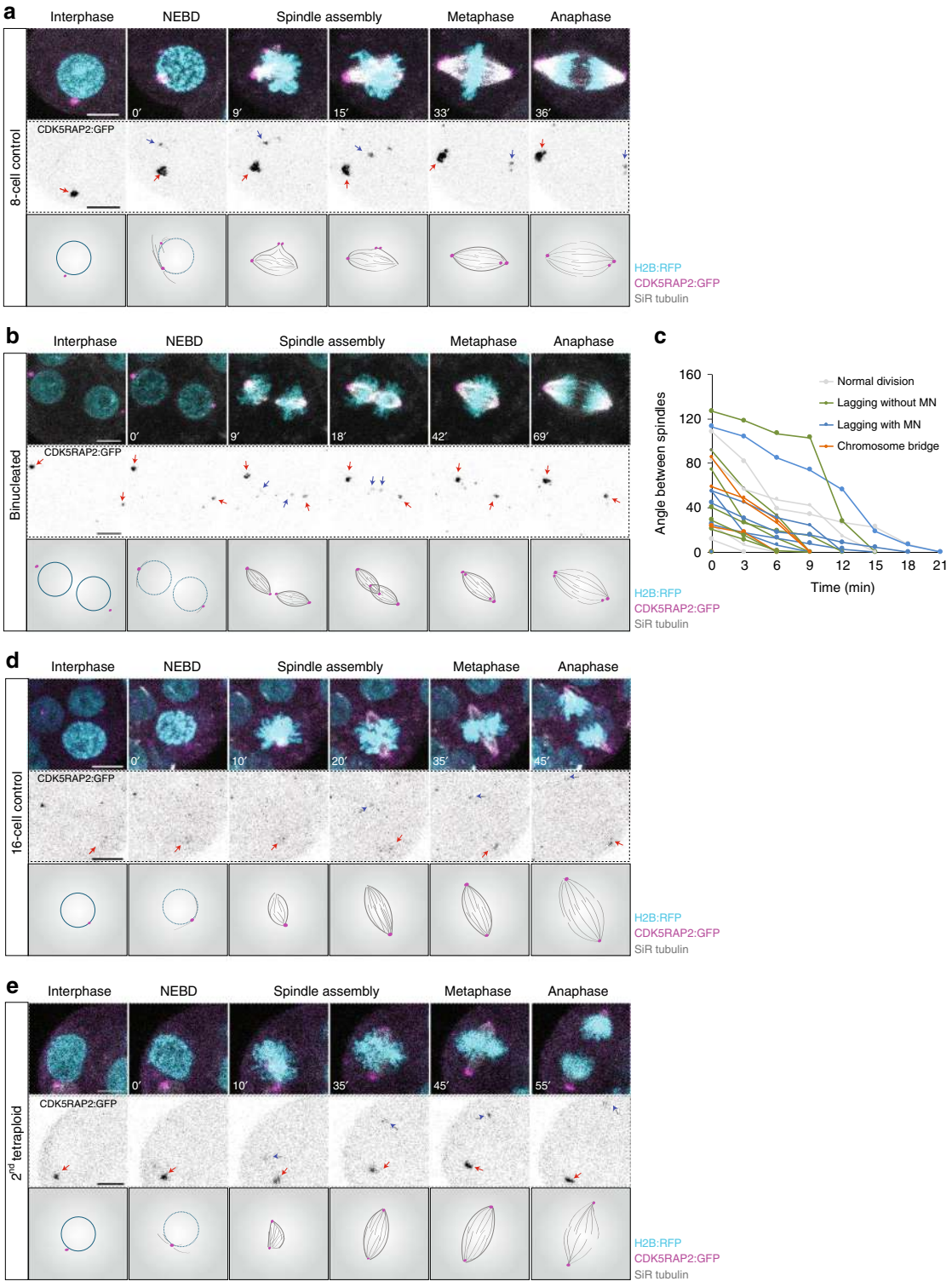

Figure 21. – Chromosomal instability in tetraploid embryos is not attributable to supernumerary centrosomes (Figure 2).

a, ***b***, ***d*** *and* ***e*** *Representative time-lapse images and illustrations of live 8-cell control (**a**), 4-cell binucleated (**b**), 16-cell control (**d**) and 8-cell tetraploid embryos (**e**) labelled with SiR Tubulin (grey) and coexpressing H2B:RFP (cyan) and CDK5RAP2:GFP (magenta and inverted grey). A major microtubule organising centre (MTOC) can be observed in the 8-cell control, 16-cell control and 8-cell tetraploid embryo during interphase (red arrows) and a newly assembled MTOC can be observed during mitosis (blue arrows). In binucleated embryos, two major MTOCs (red arrows) can be observed during interphase and two newly assembled MTOCs (blue arrows) can be observed during mitosis.* ***c*** *Measurements of the angle between the two individualized spindles during the binucleated division. Line colours represent the different types of chromosome segregation events associated with a specific cell division (n =23 divisions from 12 embryos). Chromosome segregation errors observed included: lagging chromosomes resulting in micronuclei formation (lagging with MN); lagging chromosomes that did not result in micronuclei formation (lagging without MN); and chromosome bridges. Scale bars= 10 μm. NEBD nuclear envelope breakdown.*

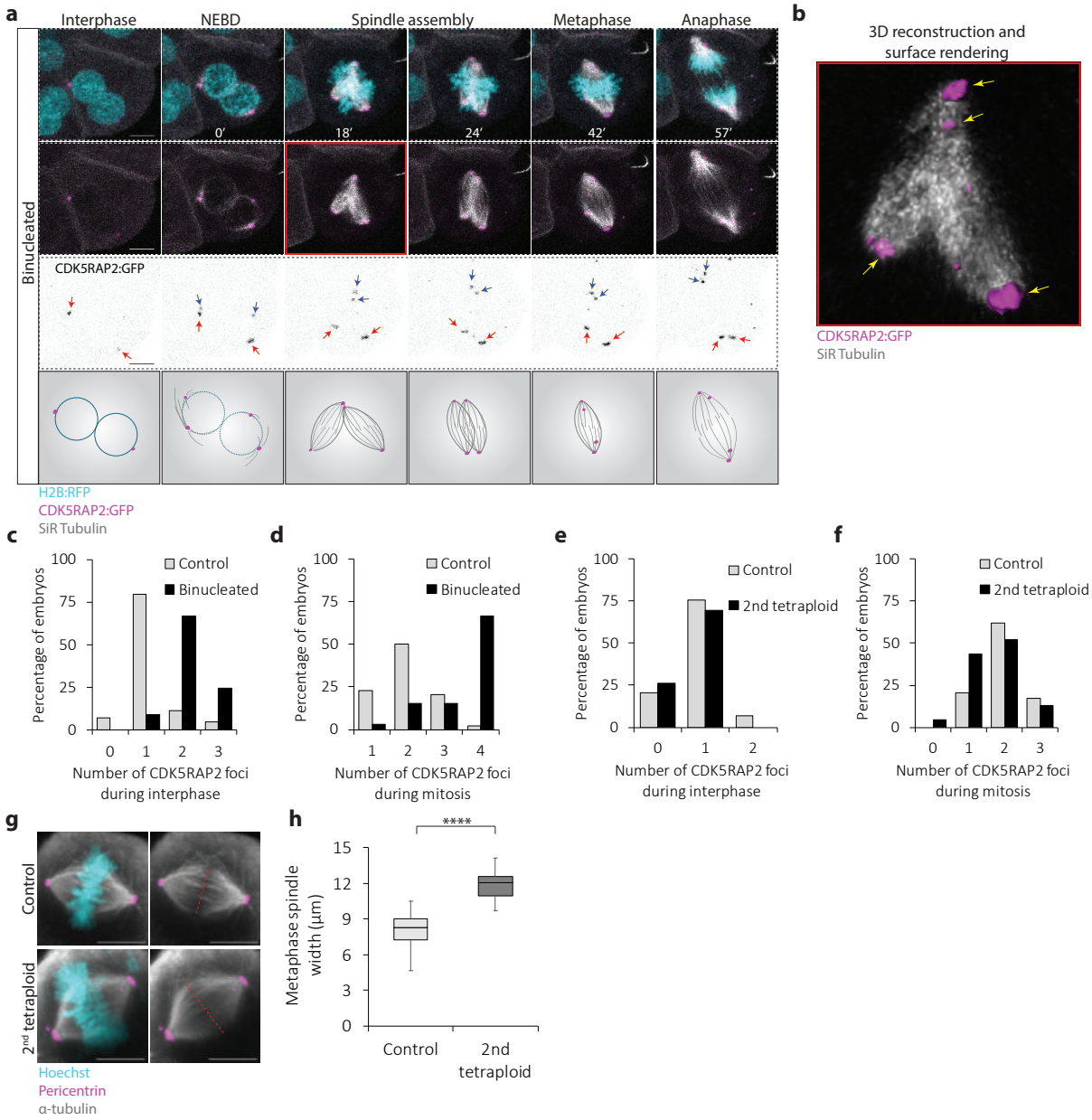

Figure 22. – Spindle assembly and MTOC dynamics in tetraploid embryos (Supplementary Figure 5).

(a) *Representative z-projection and illustrations of a 4-cell binucleated embryo stained with SiR Tubulin (grey) and co-expressing H2B:RFP (cyan) and CDK5RAP2:GFP (magenta and inverted grey) chosen to illustrate an example of perpendicular spindle fusion. Two major microtubule organising centres (MTOCs) (red arrows) can be observed during interphase and two newly assembled MTOCs (blue arrows) can be observed during mitosis.* ***(b)*** *Three-dimensional reconstruction of the spindle fusion event in panel* ***(a)*** *(red square), with a surface rendering*

representation of spindle poles (magenta). Note the presence of four completely individualised spindle poles (yellow arrows), demarking the presence of two independent spindles during fusion. ***(c and d)*** *Quantification of number of CDK5RAP2 foci during interphase* ***(c)*** *and mitosis* ***(d)*** *in 8-cell control (n=44 divisions from 11 embryos) and 4-cell binucleated embryos (n=33 divisions from 14 embryos).* ***(e and f)*** *Quantification of number of CDK5RAP2 foci during interphase* ***(e)*** *and mitosis* ***(f)*** *in 16-cell control (n=29 divisions from 9 embryos) and 8-cell tetraploid embryos (n=24 divisions from 9 embryos).* ***(g)*** *Representative immunofluorescence z-projections of a metaphase spindle of 16-cell control and 8-cell tetraploid embryo.* ***(h)*** *Quantification of metaphase spindle width in 16-cell controls (n= 31 spindles from 15 embryos) and 8-cell tetraploid embryos (n= 27 spindles from 14 embryos) ****P<0.0001 (unpaired, two-tailed t test). Scale bars = 10μm. Where box plots are shown, the centre line represents the median, the bounds of box represent the upper and lower quartiles and the whiskers represent minimum and maximum values. NEBD=nuclear envelope breakdown.*

2.2.3 Spindle assembly checkpoint (SAC) is not abrogated by tetraploidy.

Most cells possess a signalling pathway termed the SAC that serves to prevent chromosome segregation errors by delaying anaphase until all chromosomes are aligned at the metaphase plate and the kinetochores attached to microtubules[33,34]. Notably, recent work has shown that, in early embryos, although misaligned chromosomes/kinetochores also recruit SAC proteins, such as Mad1 and Mad2, SAC signalling is not sufficiently robust to enforce a metaphase arrest[35–37]. We wondered whether the higher rates of error in tetraploid embryos might be attributable to further weakening of the SAC, and thus set out to probe SAC activity in tetraploid embryos. Notably, tetraploidy prolonged mitosis, as observed by increased NEBD-anaphase duration (Fig. 3a, b), suggesting SAC activation. SAC inhibition using the Mps1 inhibitor AZ 3146 reduced the duration of mitosis causing controls and tetraploids to have a similar M-phase duration, indicating that the prolonged mitosis in tetraploids was attributable to the SAC (Fig. 3a, b). Immunofluorescence analysis of the SAC protein Mad2 revealed that the majority of kinetochores exhibited pronounced Mad2 staining shortly after NEBD which was lost as chromosomes aligned, similar to controls (Fig. 3c–e). Similarly, live imaging of tetraploid embryos co-expressing H2B:RFP and MAD1:2EGFP clearly shows MAD1:2EGFP recruitment to kinetochores shortly after NEBD and gradual loss of signal within 30–40 min as chromosomes align at the metaphase plate (Fig. 3f, g). As is the case in normal diploid mouse embryos[36], tetraploid blastomeres frequently failed to wait for full chromosome alignment prior to anaphase onset, underscoring the previously reported inefficiency of SAC in the mouse embryo (Supplementary Fig. 6). Nonetheless, tetraploidy caused a substantial SAC-dependent lengthening of mitosis. Therefore, though we cannot exclude the

possibility of minor impacts of tetraploidy upon the SAC, our experiments fail to uncover a clear weakening of the SAC in tetraploids that might explain the high rate of segregation error.

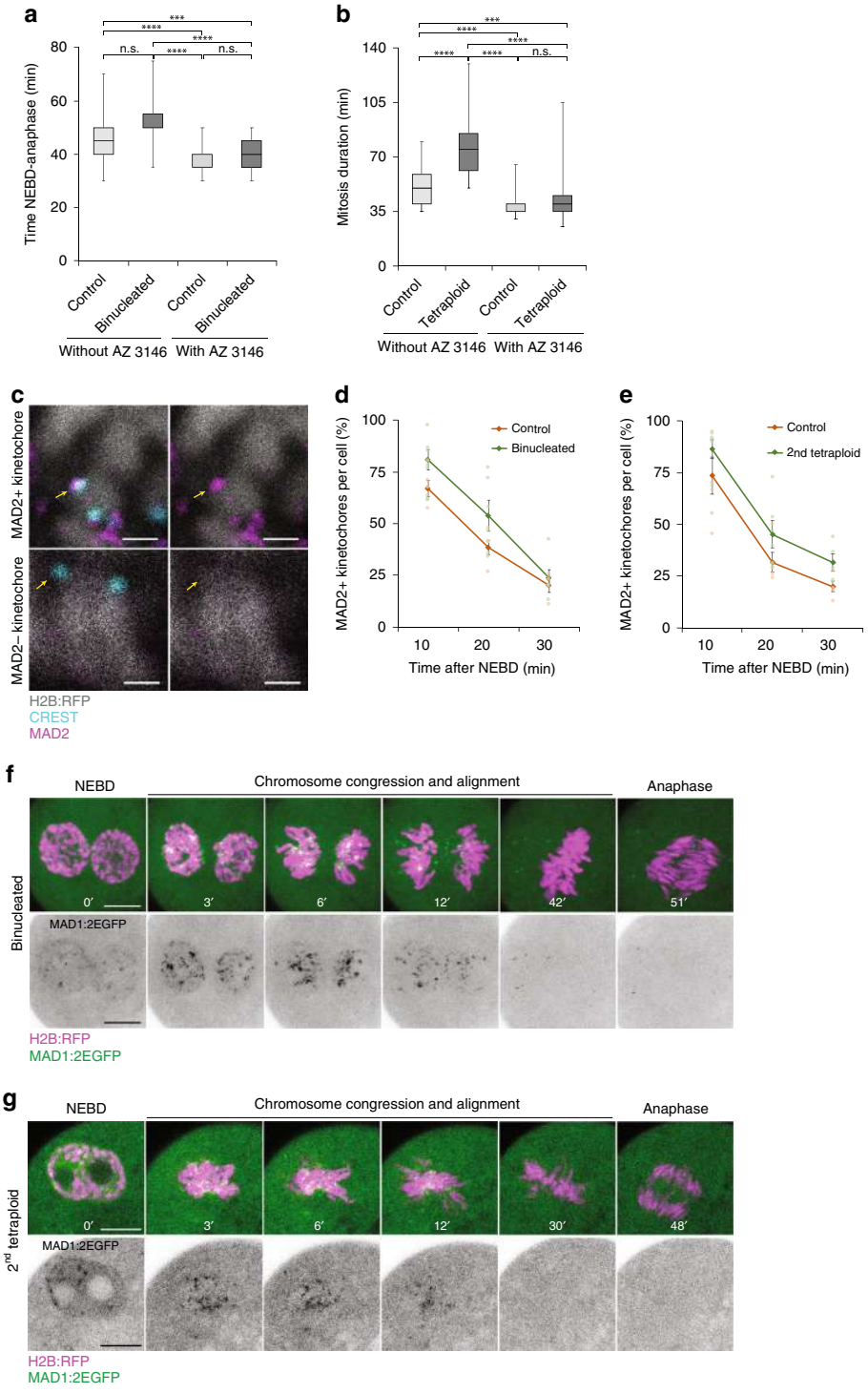

Figure 23. – Spindle assembly checkpoint activity is not abrogated in tetraploid embryos (Figure 3).

a *and* ***b*** *Quantification of mitosis duration in 8-cell control (without AZ 3146 n = 47 divisions from seven embryos; with AZ 3146 n =63 divisions from eight embryos), 4-cell binucleated embryos (without AZ 3146 n = 30 divisions from eight embryos; with AZ 3146 n =54 divisions from 15 embryos) ***P =0.0009; ****P < 0.0001 (unpaired Kruskal–Wallis test with Dunn's test for multiple comparisons)* ***a****; 16-cell control (without AZ 3146 n =61 divisions from seven embryos; with AZ 3146 n =59 divisions from seven embryos) and 8-cell tetraploid embryos (without AZ 3146 n = 50 divisions from nine embryos; with AZ 3146 n = 63 divisions from 12 embryos) ***P= 0.0005; ****P < 0.0001 (unpaired Kruskal–Wallis test with Dunn's test for multiple comparisons)* ***b****.* ***c*** *Representative z-projections of MAD2-positive and MAD2-negative kinetochores demonstrating co-localisation of MAD2 (magenta) and CREST (cyan) in positively stained kinetochores and no colocalization in negatively stained kinetochores.* ***d*** *and* ***e*** *Proportion of MAD2-positive kinetochores in 8-cell control, 4-cell binucleated d, 16-cell control and 8-cell tetraploid embryos* ***e*** *at 10 mins (8-cell control n = 6 blastomeres; 4 cell binucleated n = 6 blastomeres; 16-cell control n = 5 blastomeres; 8-cell tetraploid n = 5 blastomeres), 20 mins (8-cell control n = 5 blastomeres; 4-cell binucleated n =6 blastomeres; 16-cell control n = 5 blastomeres; 8-cell tetraploid n = 6 blastomeres) and 30 mins (8-cell control n =4 blastomeres; 4-cell binucleated n = 6 blastomeres; 16-cell control n = 5 blastomeres; 8-cell tetraploid n = 5 blastomeres) after nuclear envelope breakdown (NEBD). Error bars represent SEM.* ***f*** *and* ***g*** *Representative time-lapse images of live 4-cell binucleated f and 8-cell tetraploid embryos g co-expressing H2B:RFP and MAD1:2EGFP. Note that MAD1:2EGFP signal is clearly observed at the kinetochores shortly after nuclear envelope breakdown (NEBD) and is gradually lost following chromosome alignment at the metaphase plate. Scale bars= 10 μm except for figure c, where scale bars= 1 μm. Where box plots are shown, the centre line represents the median, the bounds of box represent the upper and lower quartiles and the whiskers represent minimum and maximum values.*

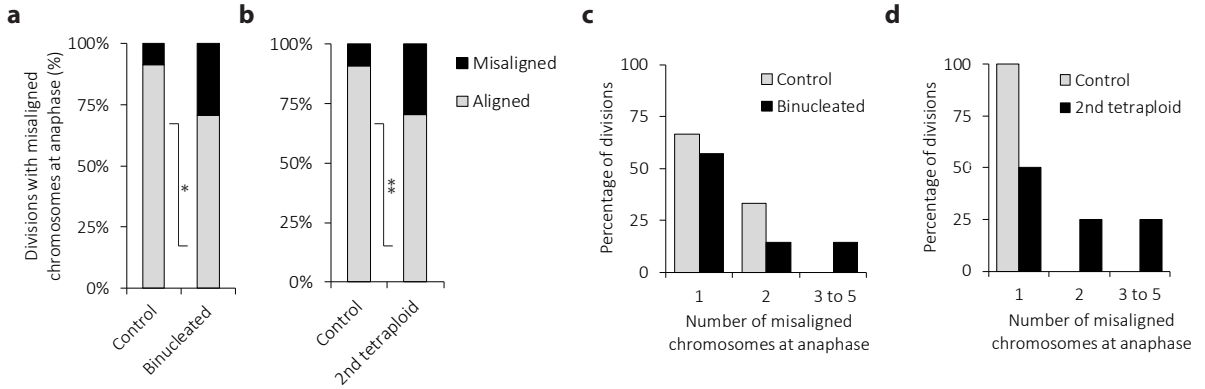

Figure 24. – High frequency of misaligned chromosomes in tetraploid embryos (Supplementary Figure 6).

(a and b) *Percentage of divisions with severely misaligned chromosomes at anaphase onset in 8-cell controls (n= 47 divisions from 7 embryos), 4-cell binucleated embryos (n= 30 divisions from 8 embryos, *P=0.0412, two-tailed Fisher's exact test)* ***(a)****, 16-cell controls (n= 66 divisions from 7 embryos) and 8-cell tetraploid embryos (n= 50 divisions from 9 embryos, **P=0.0012, two-tailed Fisher's exact test)* ***(b)****.* ***(c and d)*** *Quantification of number of severely misaligned chromosomes visible at anaphase onset per cell division in 8-cell controls, 4-cell binucleated embryos* ***(c)****; 16-cell controls and 8-cell tetraploid embryos* ***(d)****.*

2.2.4 Tetraploidy perturbs metaphase chromosome alignment.

To further investigate how tetraploidy leads to lagging chromosomes and chromosome segregation error, we performed a comprehensive analysis of centromere spatiotemporal behaviour in mitosis. Embryos co-expressing H2B:RFP and the centromere label Maj-SatTALE:mClover[38] were imaged in three dimensions at 75 s intervals, and individual centromere pairs were tracked during the second tetraploid division. Our analysis showed no difference in centromere velocity either prior to anaphase onset or during anaphase poleward chromosome movement (Fig. 4a, b), or in the tightness of the metaphase plate (Fig. 4c, d), suggesting that overall behaviour of most chromosomes is not adversely affected in tetraploids. Interestingly, however, we observed that both controls and tetraploid blastomeres displayed chromosomes that, having previously been aligned, displaced from the metaphase plate to become unaligned (Fig. 4e). In controls, these displacement events lasted on average 6.32 ± 1.43 min (n= 16 displacement events; Fig. 4h) during which time the centromeres typically moved between 1.7 and 10.74 μm from the metaphase plate, before returning to full alignment. Importantly, in control blastomeres, chromosomes that became displaced from the metaphase plate returned to full alignment prior to anaphase onset in almost all cases (Fig. 4e, f and h). On the other hand, in tetraploid embryos, chromosome displacement events lasted substantially longer (13.57 ± 2.11min, n =14 displacement events), and in many cases chromosomes failed to completely re-align prior to anaphase onset (Fig. 4e, g, h). Of the misaligned chromosomes at anaphase onset observed in tetraploid embryos, almost all resulted from a chromosome that was previously aligned and became displaced during metaphase. Consistent with our previous results, the majority of tetraploid embryos displayed lagging chromosomes. Importantly, all anaphase laggards arose from previously metaphase-aligned chromosomes, revealing that the elevated frequency of lagging chromosomes in tetraploid embryos is not attributable to failed alignment (Supplementary Fig. 7).

Taken together, these results show that, though overall centromere behaviour and chromosome congression are largely unaltered in tetraploid embryos, a deficiency in maintaining chromosome alignment leads to an increased likelihood of chromosome misalignment at anaphase. However, these misaligned chromosomes do not seem to be the major cause of lagging chromosomes in tetraploid embryos. Rather, similar to somatic[39] and cancer cells[40] lagging chromosomes arise from chromosomes that were correctly aligned at the metaphase plate prior to anaphase onset.

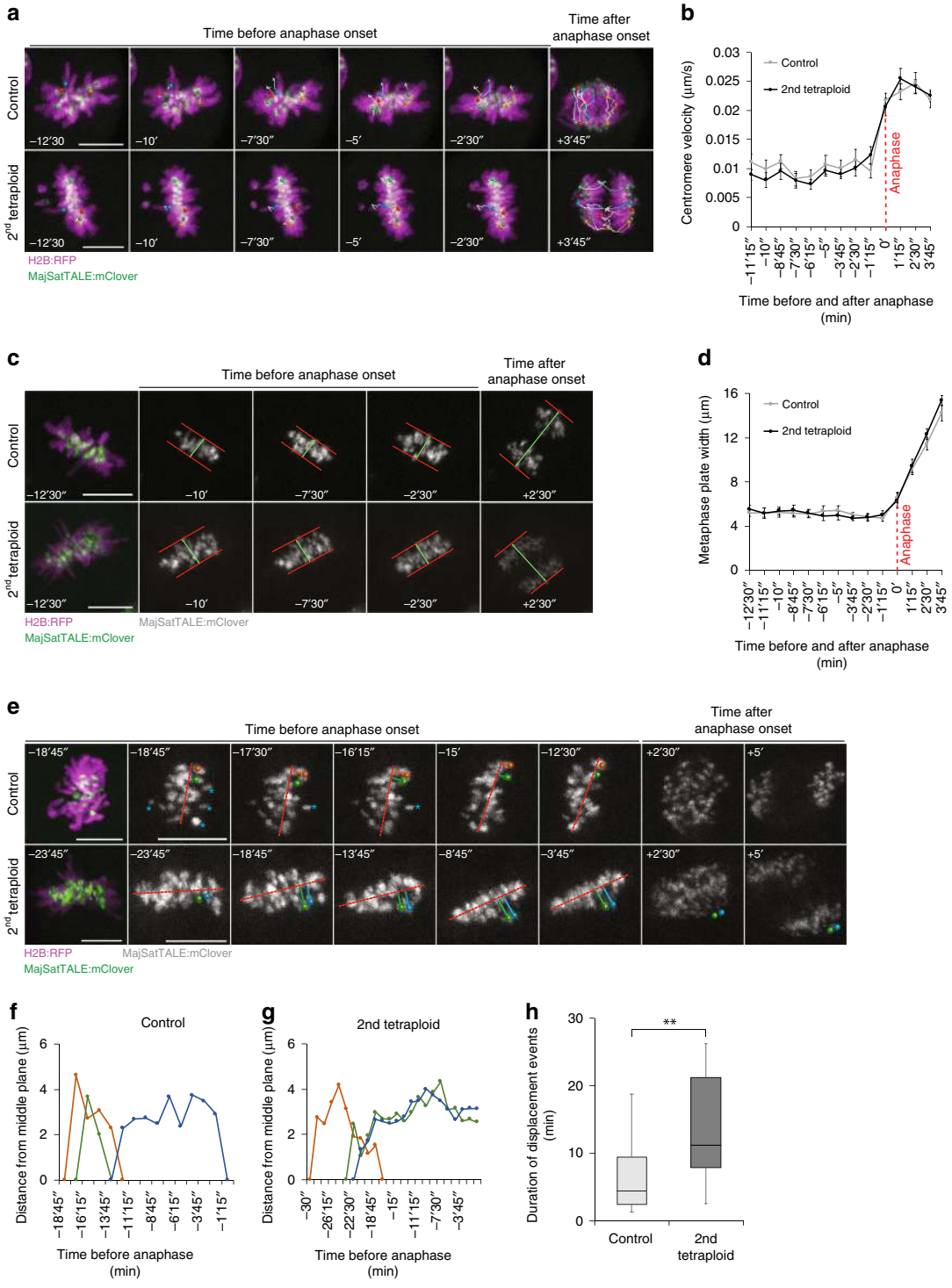

Figure 25. – Tetraploid embryos exhibit chromosome alignment defects (Figure 4).

a *Representative time-lapse images of centromere tracking in 16-cell controls and 8-cell tetraploid embryos co-expressing H2B:RFP and MajSatTALE:mClover. Coloured circles indicate*

centromere pairs that were tracked throughout mitosis and individualised centromeres at anaphase. Coloured lines represent the path covered by the centromere pairs during time. ***b*** *Quantification of average centromere velocity in 16-cell control (n = 24 centromere pairs from five blastomeres) and 8-cell tetraploid embryos (n = 21 centromere pairs from five blastomeres).* ***c*** *Representative time-lapse images of 16-cell control and 8-cell tetraploid embryos co-expressing H2B:RFP and MajSatTALE:mClover, demonstrating the measurements of metaphase plate width throughout mitosis. Red dashed lines indicate the borders of the metaphase plate based on the MajSatTALE:mClover signal. Green lines indicate width measurements.* ***d*** *Quantification of metaphase plate width in 16-cell control (n = 5 blastomeres) and 8-cell tetraploid embryos (n =5 blastomeres). e Representative time-lapse images of 16-cell control and 8-cell tetraploid embryos co-expressing H2B:RFP and MajSatTALE:mClover, demonstrating chromosome displacement events. In the control embryo, two chromosomes (orange and green circles— corresponding to the orange and green lines in figure* ***f****) that were previously aligned become displaced from the middle plane of the metaphase plate (red dashed lines) at mid-mitosis, returning to their original position before anaphase onset. In the tetraploid embryo, the two chromosomes that become displaced (green and blue circles—corresponding to the green and blue lines in figure* ***g****) fail to return to the metaphase plate, resulting in misaligned chromosomes at anaphase onset. Blue asterisks indicate chromosomes that were not yet aligned for the first time during the time sequence shown.* ***f*** *and* ***g*** *Quantification of the distance between centromere pairs and metaphase middle plane in a 16-cell control* ***f*** *and 8-cell tetraploid embryo* ***g****.* ***h*** *Quantification of average duration of displacement events in 16-cell controls (n = 16 displacement events from five blastomeres) and 8-cell tetraploid embryos (n = 14 displacement events from five blastomeres; **P =0.0061, unpaired two-tailed Mann–Whitney test). In the box plot, the centre line represents median, the bounds of box represent upper and lower quartiles and the whiskers represent minimum and maximum values. Scale bars= 10 μm. Error bars represent SEM*

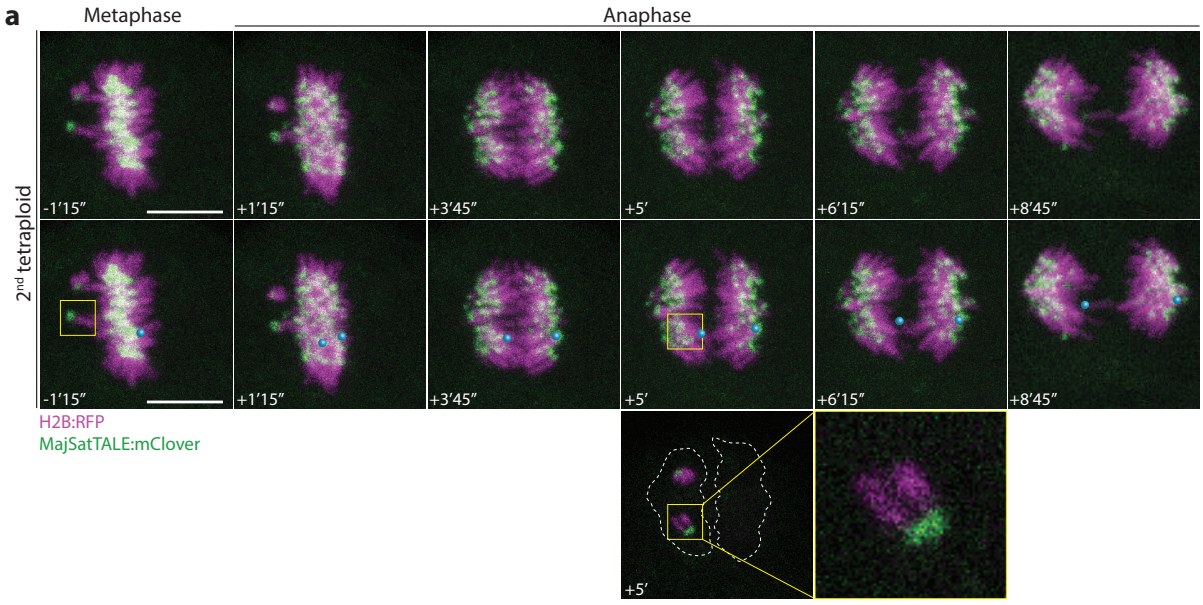

Figure 26. – Lagging chromosomes arise from fully aligned chromosomes (Supplementary Figure 7).

(a) *A time-lapse image of mitosis in an 8-cell tetraploid embryo that exemplifies both anaphase chromosome lagging, and also misalignment at anaphase. Blue circles highlight a sister pair that was aligned at anaphase onset, but which gives rise to a lagging chromosome in anaphase. The yellow box indicates a sister pair that remains misaligned at the time of anaphase onset. The bottom row displays a reduced z-projection to clearly visualise the misaligned chromosome in mid anaphase. Note that both sister chromatids move towards the same spindle pole. Scale bars = 10μm.*

2.2.5 Tetraploidy affects kinetochore microtubule establishment.

During spindle assembly some kinetochore pairs form merotelic attachments in which a single kinetochore simultaneously contacts microtubules (MTs) from both spindle poles. Establishment of correct (amphitelic) chromosome attachment prior to anaphase occurs by correction of previously mis-attached kinetochores, a process that depends upon MT turnover at the kinetochore[41,42]. In cancer cells, CIN is associated with reduced kinetochore–microtubule (kMT) turnover that promotes errors including merotelic attachments that lead to lagging chromosomes and aneuploidy[43]. We directly analysed kMT turnover during the second tetraploid division using fluorescence dissipation after photoactivation of photoactivatable-GFP-tubulin (PAGFP-tubulin)

within the metaphase spindle as previously described[43–45], using SiR Tubulin to select cells with spindles oriented in the plane of imaging (Fig. 5a–c). Strikingly, kMT half-life was substantially increased in tetraploid embryos compared to controls (Fig. 5a–c), indicating reduced kMT turnover. Notably, this increase is similar to that observed when comparing chromosomally unstable to chromosomally stable somatic cells[43]. Non-kinetochore MT half-life and the rate of poleward microtubule flux measured with PAGFP-tubulin, as well as the velocity of microtubule growth events as determined by EB1:EGFP imaging, were all unchanged between tetraploids and controls (Supplementary Fig. 8a–e), revealing that the change in MT dynamics was highly specific to kMT turnover. Importantly, there was no difference in MT turnover when comparing SiR Tubulin stained blastomeres with SiR Tubulin-free blastomeres, ruling out the possibility that the increase in kMT half-life observed in tetraploid embryos could have been induced by potential MTstabilising effects of SiR Tubulin (Supplementary Fig. 8f–h). Highly consistent with a kMT turnover defect, direct comparison of stable kMT attachments in embryos with a classic cold shock approach revealed a far greater proportion of mis-attachments in tetraploid embryos as compared to controls in mid-late prometaphase/metaphase (Fig. 5d, e). Whereas lateral/merotelic attachments were very rare in diploid blastomeres (0.9%), 7% of all attachments observed in tetraploid blastomeres were misattached, at least one kinetochore being misattached in every tetraploid blastomere examined. This is highly consistent with the notion that a single merotelically attached kinetochore is sufficient to cause missegregation[39] and correlates with the elevated rates of lagging chromosomes observed in tetraploids (Fig. 1b–e).

A major determinant of the capacity to maintain kinetochore MT turnover to correct misattachments is the recruitment of the microtubule depolymerising protein mitotic centromere associated kinesin (MCAK)[46,47]. We wondered whether MCAK was sufficiently recruited to the centromere/kinetochore in tetraploid embryos. Using immunofluorescence we found that MCAK was significantly underrepresented at the kinetochore in tetraploid embryos as compared to controls (Fig. 5f, g). This suggests that reduced MT turnover may be downstream of an inability to recruit sufficient MT-turnover-sustaining factors. Consistent with this notion, overexpression of MCAK:GFP substantially and significantly decreased the rates of chromosome segregation errors in tetraploid embryos, when compared to tetraploid embryos expressing GFP alone (Fig. 5h, i), as has also been seen in cancer cells ectopically expressing MCAK[48]. Taken together these data show

that, in tetraploid embryos, kMT turnover is reduced and error correction mechanisms are suppressed, allowing for the accumulation of merotelic attachments that in turn lead to lagging chromosomes, which can be rescued by introducing ectopic MCAK:GFP.

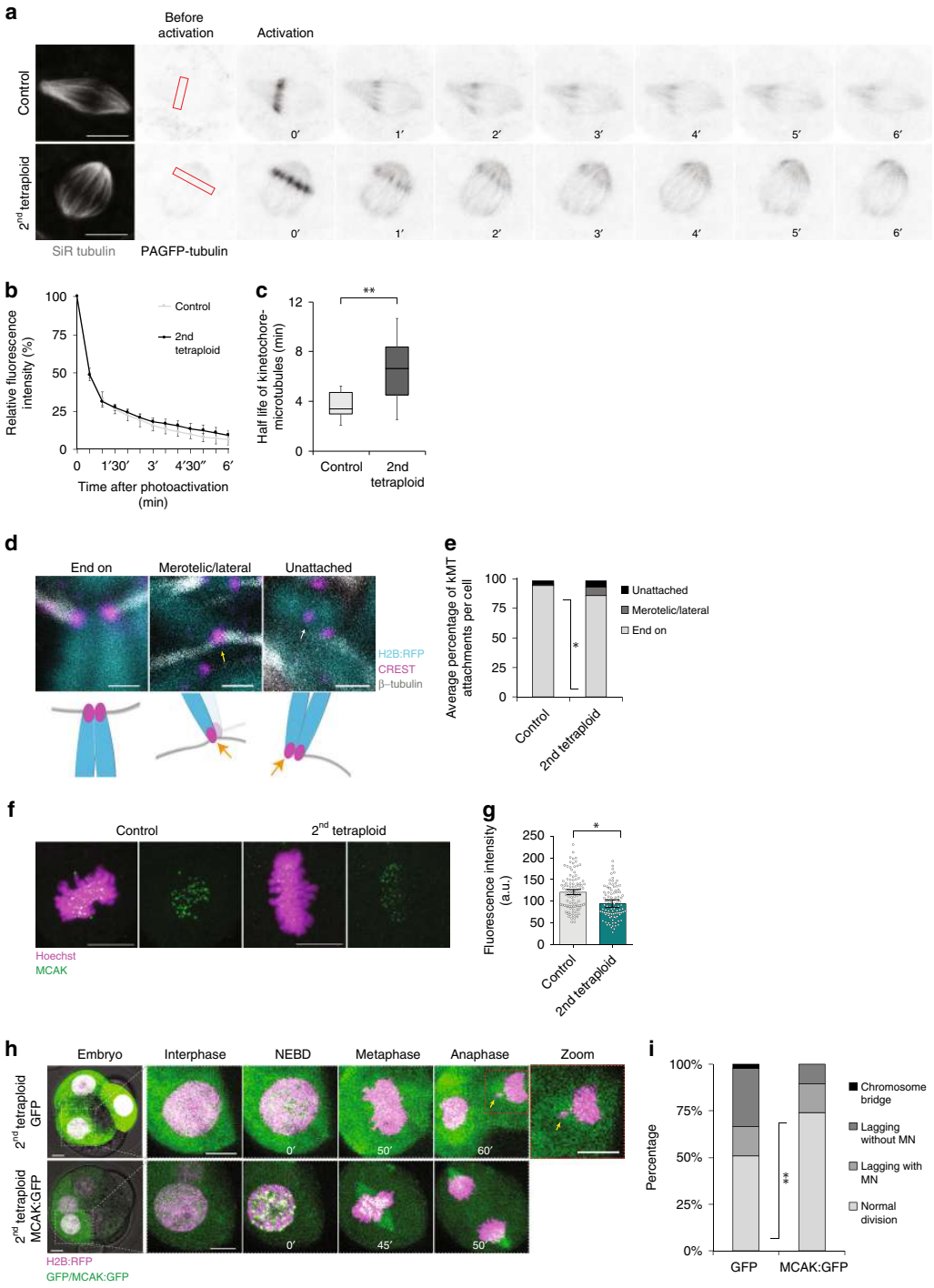

Figure 27. – Error correction mechanisms are defective in tetraploid embryos (Figure 5).

a *PAGFP-tubulin (inverted grey) was photoactivated at a rectangular region across one side of the metaphase spindle (red rectangles) and the time-course for fluorescence decay was monitored. Embryos were labelled with SiR Tubulin (grey) to identify the metaphase spindle.* ***b*** *and* ***c*** *Quantification of fluorescence decay values* ***b*** *and kinetochore microtubule half-life (****c****; **P= 0.008, unpaired, two-tailed t test) in 16-cell control (n = 11 blastomeres) and 8-cell tetraploid embryos (n = 9 blastomeres). In the box plot, the centre line represents median, the bounds of box represent upper and lower quartiles and the whiskers represent minimum and maximum values.* ***d*** *Representative z projections of end-on, merotelic/lateral, and unattached kinetochores at 35 min after nuclear envelope breakdown (NEBD); and scheme illustrating the types of kinetochore–microtubule attachments analysed. Representative images were chosen to demonstrate the different types of attachments. For the merotelic/lateral attachment image, only the merotelically attached kinetochore is in focus (as represented in the illustration by a fainter colour of the sister chromatid).* ***e*** *Average percentage of end-on, merotelic/lateral and unattached kinetochores per cell in 16-cell (n = 189 kinetochores from five blastomeres) control and 8-cell tetraploid embryos (n = 223 kinetochores from five blastomeres; *P= 0.0148, unpaired, two-tailed t test).* ***f*** *Representative z-projections of MCAK immunofluorescence in 16- cell control and 8-cell tetraploid embryos.* ***g*** *Quantification of fluorescence intensity in 16-cell control and 8-cell tetraploid embryos (n= 100 kinetochores from 10 blastomeres per group). Statistical analysis was performed as an inter-embryo comparison using the average from 10 individual kinetochores analysed per blastomere, *P= 0.0223 (unpaired, two-tailed t test).* ***h*** *Representative time-lapse images of 8-cell tetraploid embryos co-expressing H2B:RFP and either GFP or MCAK:GFP. The yellow arrow indicates a lagging chromosome.* ***i*** *Percentage of cell divisions displaying chromosome segregation errors in 8-cell tetraploid embryos co-expressing H2B:RFP and either GFP (n =51 divisions from 16 embryos) or MCAK:GFP (n = 66 divisions from 23 embryos) **P = 0.0093 (two-tailed chi-square). Chromosome segregation errors observed included: lagging chromosomes resulting in micronuclei formation (lagging with MN); lagging chromosomes that did not result in micronuclei formation (lagging without MN); and chromosome bridges. Scale bars = 10 μm, except for d, where scale bars= 1 μm. Error bars represent SEM.*

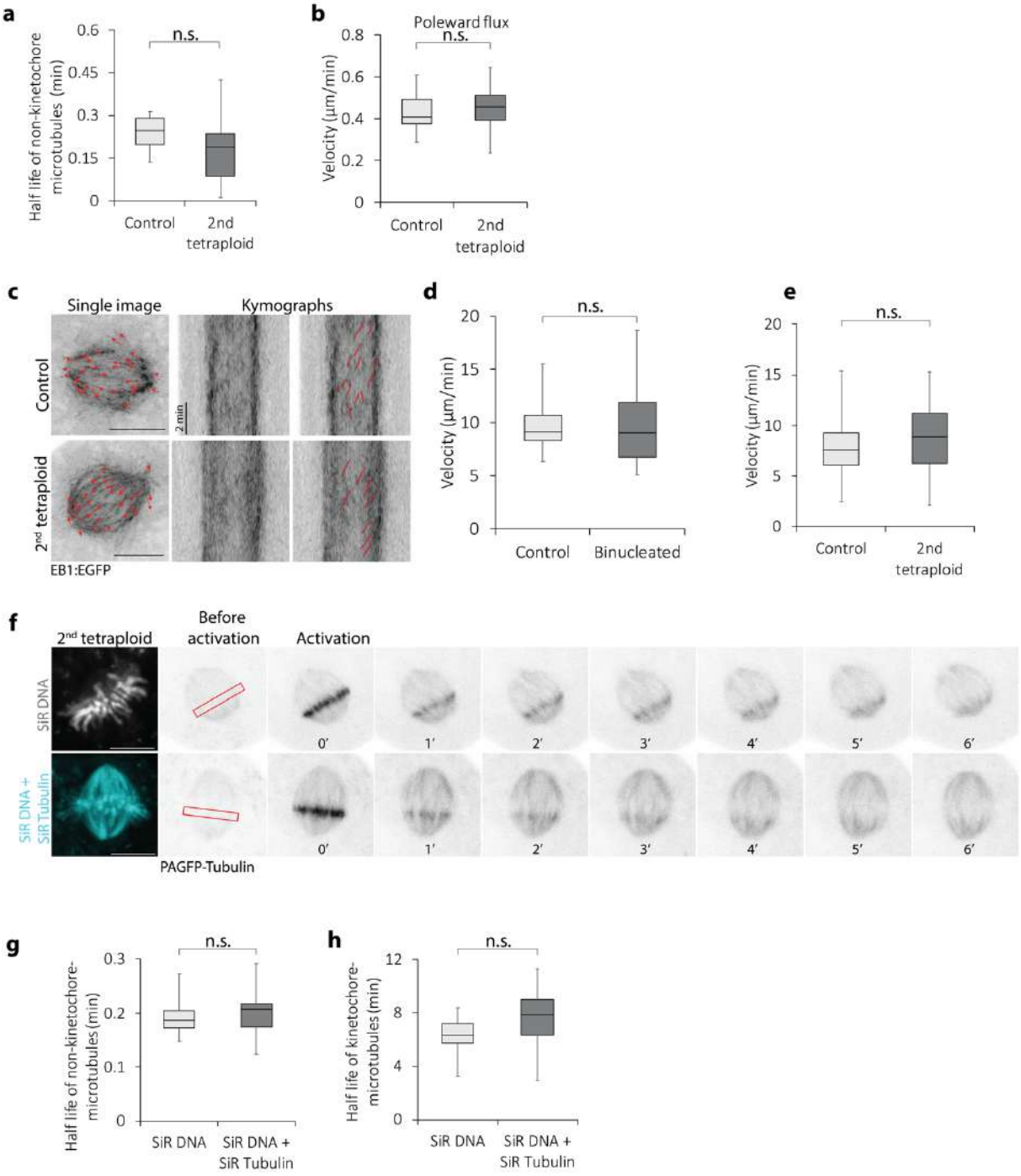

Figure 28. – Non-kinetochore-microtubule half-life, poleward flux and microtubule growth events are unchanged in tetraploid embryos (Supplementary Figure 8).

(a and b) *Quantification of non-kinetochore-microtubule half-life in 16-cell control (n=11 blastomeres) and 8-cell tetraploid embryos (n=9 blastomeres)* ***(a)*** *and poleward flux in 16-cell control (n=11 blastomeres) and 8-cell tetraploid embryos (n=10 blastomeres)* ***(b)*** *(unpaired, two-tailed t test).* ***(c)*** *Representative z-projections and kymographs of control and tetraploid embryos expressing EB1:EGFP.* ***(d and e)*** *Quantification of microtubule growth velocity in 8-cell controls (n=36 tracks from 4 embryos), 4-cell binucleated (n=28 tracks from 3 embryos) (unpaired, two-tailed Mann-Whitney test)* ***(d)****, 16-cell controls (n=76 tracks from 8 embryos) and 8-cell tetraploid embryos (n=58 tracks from 6 embryos) (unpaired, two-tailed t test)* ***(e)****.* ***(f)*** *Representative time-lapse images of PAGFP-tubulin (inverted grey) in 8-cell tetraploid embryos labeled with either SiR DNA (grey) or SiR DNA + SiR Tubulin (cyan).* ***(g and h)*** *Quantification of non-kinetochore-microtubule half-life (unpaired, two-tailed Mann-Whitney test)* ***(g)*** *and kinetochore-microtubule half-life* ***(h)*** *in 8-cell tetraploid embryos labeled with either SiR DNA (n= 10 blastomeres) or SiR DNA + SiR Tubulin (n= 10 blastomeres) (unpaired, two-tailed Mann-Whitney test). Scale bars = 10μm. Where box plots are shown, the centre line represents the median, the bounds of box represent the upper and lower quartiles and the whiskers represent minimum and maximum values.*

2.3 Discussion

Our data show that mouse embryos do not possess a tetraploidy checkpoint but continue to divide and become chromosomally unstable immediately after tetraploidisation (Fig. 1). Why the mouse embryo fails to mount a tetraploidy checkpoint is unclear but may relate to the key role of centrioles in mediating the checkpoint, shown in RPE1 cells[19]. The described mechanism by which tetraploidy leads to CIN in mammalian cells is that the acquisition of supernumerary centrioles/centrosomes leads to the formation of hazardous multipolar spindles that induce segregation errors[5,7,9,11]. That there might be other means by which tetraploidy could cause CIN was alluded to in studies of tetraploid yeast with normal centrosome numbers, where CIN was likely due to the impact of cell size upon spindle geometry[49]. Here we show that mouse blastomeres, which are acentriolar, become highly chromosomally unstable upon tetraploidisation as a result of altered kMT dynamics. Notably, this mechanism is distinct to yeast, where tetraploid spindles have unchanged microtubule dynamics[49]. Our data indicate that reduced kinetochore recruitment of MCAK, a well-characterised MT depolymerizing kinesin, provides at least part of the explanation for the reduced kinetochore MT turnover that underpins misattachments and segregation errors in tetraploid blastomeres. Why MCAK is underrepresented at the kinetochores remains to be determined. Gene expression changes associated with having extra copies of chromosomes[50], and the doubling of kinetochores, could present an overburden on the ability to recruit MCAK. Alternatively, tetraploidy could impact upstream signalling necessary for MCAK recruitment to the kinetochore[51,52], or affect the structure of the kinetochore itself.

Our centromere and chromosome tracking data show that tetraploidy introduces two types of anaphase defects. First, we observed lagging anaphase chromosomes, that arise from fully aligned metaphase chromosomes, and frequently result in a micronucleus. Whereas in somatic cells micronuclei derived from lagging chromosomes are frequently reabsorbed in the next cell cycle, which likely forms the mechanistic basis for chromothripsis[53], we have previously shown that in mouse embryos micronuclei are very rarely reincorporated into the principal nucleus, and repeated micronucleus inheritance necessarily drives aneuploidy[25]. Notably, micronuclei are also unilaterally inherited in tetraploid embryos (Supplementary Fig. 9), thus lagging chromosomes seem certain to contribute to mosaic aneuploidy in the mouse tetraploid embryo. Secondly, we observe chromosomes that fail to align in time for anaphase onset. In some cases, the proximity of the misaligned chromosome to the metaphase plate, paired with imaging resolution limits prevented us from determining whether the two sister chromatids were ultimately correctly segregated. However, in at least one example where we labelled both the chromosome and the centromere in live imaging, both misaligned sister chromatids were seen to migrate to the same spindle pole (Supplementary Fig. 7). Thus, although formally distinguishing the proportional contribution of these two distinct defects to embryo aneuploidy is experimentally challenging, both likely contribute to the elevated rate of aneuploidy in the tetraploid embryo.

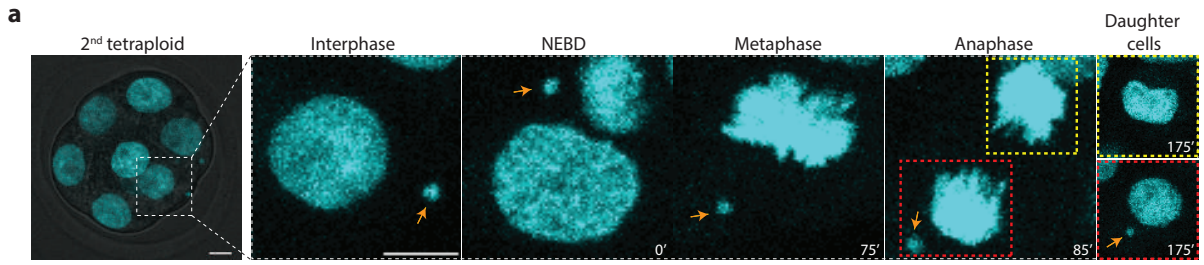

Figure 29. – Unilateral inheritance of micronuclei in tetraploid embryos (Supplementary Figure 9).

(a) *Representative time-lapse images of mitosis in an 8-cell tetraploid embryo. A micronucleus originated from the previous cell division is observed (orange arrows). As anaphase takes place, the micronucleus is inherited by one of the daughter cells (red dashed square) without reincorporation in the principal nucleus, whereas the other daughter cell (yellow dashed square) remains without micronucleus. Note that the micronucleus remained visibly separate from the main*

chromosome mass throughout the process of cell division. The same unilateral inheritance pattern was observed in all 8 mitoses analysed. Scale bars = 10µm. NEBD=nuclear envelope breakdown.

Tetraploidy is common in the early stages of tumorigenesis, and likely contributes to the CIN and aneuploidy associated with some cancers[5–9,54]. Genome doubling is thought to provide a permissive environment for the acquisition of CIN, as chromosome losses are more likely to be tolerated with multiple chromosome copies present[54]. Importantly, our data do not oppose the notion that centriole doubling can be a major driver of CIN, but rather add altered microtubule dynamics as a distinct mechanism that can also confer CIN immediately after tetraploidisation. In tetraploid somatic cells, the extra centrioles are lost after repeated passages[9,55], and it remains to be seen whether an analogous adaptation might occur with microtubule dynamics. Nonetheless our data adds altered MT dynamics to supernumerary centrosomes as two separate defects that emerge rapidly to drive CIN in the first cell cycles following tetraploidisation.

2.4 Methods

2.4.1 Embryo culture and microinjection.

All experiments were performed in accordance with the guidelines for animal experimentation of the Comité Institutionnel de Protections des Animaux (CIPA). All experiments were approved by the Centre de Recherche du Centre Hospitaliaire de l'Université de Montréal (CRCHUM) Comité Institutionnel de Protections des Animaux (CIPA). Protocol number: IP18034GFs. Embryos were harvested from superovulated CD1 female mice (Crl:CD1(ICR) Charles River Laboratories) mated with CD1 male mice, and cultured in KSOM medium (EmbryoMax® KSOM; Millipore, MR-020P-5F) in 5% CO_2 at 37 °C. mRNA was manufactured using Ambion mMessage Machine T3 (AM1348) or T7 (AM1344) according to manufacturer's instructions. Plasmids used were H2B:RFP in pRN4 (gift from Alex McDougall), PCNA:EGFP in pcDNA3.1 + poly(A) (gift from Kazuo Yamagata), CDK5RAP2:GFP in pGEMHE (gift from Tomoya Kitajima), α-tubulin-human:PAGFP in pIRESHyg2 (Addgene, plasmid #12296), EB1:EGFP in pcDNA3.1 + poly(A) (gift from Lynne Cassimeris), MAD1:2EGFP in pIVT (gift from Michael Lampson), MajSatTALE:mClover in pTALYM3 (Addgene, plasmid #47878) and MCAK:GFP (purchased in the pEGFP-C1 vector from Addgene, #pYOY152 and subcloned into pcDNA.3.1/myc-His(–)A). Two-cell embryos were microinjected using a picopump (World Precision Instruments) and

micromanipulators (Narishige) mounted on a Leica DMI4000 inverted microscope[45]. For the experiments in Fig. 3f, the embryos were microinjected at the 4-cell stage. For the experiments in Figs. 3g and 5h, the embryos were microinjected at late 4-cell binucleated stage (equivalent to 8-cell stage).

2.4.2 Drug treatments.

To induce binucleation, late interphase 4-cell stage embryos (~64 h post-hCG) were treated for ~10h with Latrunculin B (5 μM; EMD Millipore, 428020). Embryos that did not display the four blastomeres with two visible nuclei by the end of the incubation period were excluded. Simultaneously, control embryos were treated with 1:1000 DMSO (Sigma Aldrich, D2650). After the incubation period, the embryos were thoroughly washed and cultured in KSOM media. For experiments in Supplementary Fig. 2a, b, either Cytochalasin B (5 μg/mL; Sigma-Aldrich C6762) or Blebbistatin (100 μM; Calbiochem/Millipore, 203391) were used to induce binucleation. For experiments in Supplementary Figs. 1e, f, 5g, h; Figs. 1f, g; 5f, g, the embryos were treated with 25 μM of MG 132 (Calbiochem 474790) to induce a metaphase arrest. For kinetochore counts in Supplementary Fig. 1e, f, after metaphase arrest the embryos were treated with 200 μM of Monastrol (Calbiochem, 475879) to induce monopolar spindle formation and allow better visualisation of individual kinetochores. For the SAC inhibition treatment in Fig. 3a, b, the embryos were live-imaged in the presence of AZ 3146 (Calbiochem, catalogue #531976). For experiments involving PAGFP:tubulin live imaging, embryos were arrested in metaphase using 100 μM of APCin (Tocris, 5747). For the photobleaching control experiments, MII eggs were live-imaged in the presence of 10 μM of Taxol (Paclitaxel; Sigma Aldrich, T402). Spindle labelling in live embryos was performed with a 2 h incubation in 300 nM of SiR Tubulin (Cytoskeleton Inc., CY-SC002). For the experiment in Supplementary Fig. 8f–h, the embryos were either exposed to 1 μM of SiR DNA (Cytoskeleton Inc., CY-SC007) alone for 3 h or to 300 nM of SiR Tubulin for 2 h followed by a 3 h exposure to 1 μM of SiR DNA.

2.4.3 Chromosome spreads.

Chromosome spreads were performed using an air-drying method[56]. Metaphase arrested 32-cell diploid and 16-cell tetraploid embryos were exposed to 1% sodium citrate for 15 min and subsequently transferred to a grease-free slide. Three drops of methanol:acetic acid (3:1) were

applied directly on top of the embryos and the slides were air-dried. For staining, air-dried slides were co-labelled with Hoechst 33342 (Sigma Aldrich, H6024, 1:500) and DRAQ5 (Thermo Fisher Scientific, 62254, 1:250) loaded in FluorSave™ Reagent (Calbiochem, 345789) in order to differentially label the chromosomes and centromeric regions.

2.4.4 Cold shock treatment.

For assessment of kMT attachments in Fig. 5d, e, H2B:RFP-expressing embryos were exposed to a 10 min cold shock treatment in ice cold M2 media (Sigma Aldrich M7167) 35 min after NEBD was observed by live imaging and then immediately fixed.

2.4.5 Immunofluorescence and live imaging.

Embryos were fixed with 4% paraformaldehyde (PFA) in PBS for 40 min followed by 10 min permeabilization using 0.25% Triton X in PBS, and blocked with 3% bovine serum albumin (BSA) in PBS[57]. Where CREST antibodies were used, embryos were fixed with 2% PFA in PBS for 30 min. Where MAD2 antibodies were used, embryos were fixed with 2% PFA in PBS for 15 min. Primary antibodies used were: CREST anti-human (gift from Marvin J. Fritzler 1:100), β-tubulin anti-mouse (Sigma Aldrich catalogue #T4026 1:1000), MCAK anti-rabbit (gift from Duane Compton; 1:1000), pericentrin anti-mouse (BD Biosciences catalogue #611814 1:500), α-tubulin anti-rabbit (Abcam catalogue #AB18251 1:1000) and MAD2 anti-rabbit (Biolegend catalogue #924601; 1:300). Hoechst 33342 (1:1000) was used for DNA labelling. Alexa-labelled secondary antibodies (1:1000) were purchased from ThermoFisher. Alexa Fluor® 555 Phalloidin-conjugated antibody (1:200) was purchased from Invitrogen (A34055). Immunofluorescence imaging was performed on either a Leica SP8 confocal microscope fitted with a 63 x 1.4 numerical aperture oil objective or a Leica SP5 confocal microscope fitted with a 100 x 1.4 numerical aperture oil objective and a HyD detector. Live cell imaging and FDAP was performed on a Leica SP8 confocal microscope fitted with a 20 x 0.75 numerical aperture air objective and a HyD detector and embryos were imaged on KSOM media, placed on a heated stage top incubator with 5% CO_2 supply at 37 °C. For the live imaging experiment performed in Supplementary Fig. 1a, the embryos were imaged in a Zeiss Axio observer, equipped with an Axiocam and Apotome and 20 x 0.8 numerical aperture air objective and LED light. For EB1:EGFP live imaging, embryos were imaged every 2.578 s for 2 min with a 63 x 1.4 numerical aperture oil objective. For live imaging in the presence of either

Taxol (photobleaching control in Fig. 5a–c) or Latrunculin (Supplementary Fig. 2c, d), the embryos were live imaged in Ibidi micro-insert wells mounted in a glass-bottom dish with distilled water and our setup was modified for proper CO_2 supply[58].

2.4.6 Fluorescence dissipation after photoactivation.

Photoactivation was performed by briefly exposing a defined rectangular region of interest positioned across one side of the metaphase spindle to 405-nm laser. Live imaging was performed at 30 s intervals for 15 min. For fluorescence decay curves and half-life analyses, the measurements of fluorescence intensity decay for each blastomere were plotted against time and fitted into a double exponential curve $f(t) = A \times \exp(-k_1 t) + B \times \exp(-k_2 t)$ using the cftool on MATLAB[43,59,60]. In this equation, t represents time; A, the less stable non-kMTs; B, the stable kMTs and k_1 and k_2 represent the decay rates of A and B, respectively. The half-life for each MT population was calculated as $\ln 2/k$. Photobleaching was corrected for each measurement by imaging MII eggs exposed to 10 μM of the MT-stabilising agent Taxol, where MT turnover is minimal. Poleward flux velocity was calculated by determining the distance between the fluorescent mark on the spindle and the corresponding spindle pole at each time point[45,60].

2.4.7 Imaging analysis and statistics.

All image processing and analysis was performed using ImageJ/Fiji[61]. No thresholding or masking was applied to the images and LUT brightness varies linearly. For centromere tracking in Fig. 4a, b, manual tracking was performed using the "Manual Tracking with TrackMate" feature of TrackMate plugin[62] on Fiji. For metaphase plate width measurements in Fig. 4c, d, the distance between two lines drawn across each side of the metaphase plate was measured. The lines were drawn based on the MajSatTALE:mClover fluorescent signal and delimited the area occupied by all aligned chromosomes. Three dimensional reconstructions (Supplementary Fig. 5b; Supplementary Movies 1–3) and surface rendering (Supplementary Fig. 5b and Supplementary Movie 3) were generated using IMARIS 9.3. For MCAK fluorescence intensity analysis in Fig. 5f, g, background-subtracted fluorescence intensity values were obtained from a total of 100 kinetochores analysed from 10 embryos (10 kinetochores per embryo) for each group and statistical analysis was performed as an inter-embryo comparison using the average fluorescence intensity per embryo. All measurements analysed in this study were taken from distinct samples and samples

were not measured repeatedly. Data were analysed using GraphPad Prism 7 software (GraphPad Software, La Jolla, CA, USA, www.graphpad.com). Shapiro–Wilk normality tests were applied where appropriate and either unpaired two-tailed t tests or two-tailed Mann–Whitney tests were applied. Statistical significance was considered when $P < 0.05$.

2.4.8 Reporting summary.

Further information on research design is available in the Nature Research Reporting Summary linked to this article.

2.5 Data availability

The data related to the findings of this study are available within the manuscript and Supplementary Information, or from the corresponding author upon request. The source data underlying Figs. 1c, e, g, 2c, 3a, b, d, e, 4b, d, f, g, h, 5c, e, g, i, Supplementary Figs. 1b, d, 2a, b, e, 3b, 4a, b, 5c, d, 5e, f, h, 6a–d, 8a, b, d, e, g, h are provided as a Source Data file.

2.6 Acknowledgments

Work funded by grants from the Natural Sciences and Engineering Research Council of Canada, Fondation Jean-Louis Lévesque, Canadian Foundation for Innovation and the Canadian Institutes of Health Research. LMGP is supported by a Fonds de Recherche du Québec—Santé Doctoral Scholarship. We thank Gilles Hickson, Jean Claude Labbé, and Aleksandar Mihajlović for comments on the manuscript, Gaudeline Rémillard-Labrosse and Aurélie Cleret-Buhot for excellent technical support.

2.7 Author contributions

L.M.G.P. and G.F. conceptualised the study. L.M.G.P. performed the experiments and analysed the data. L.M.G.P. and G.F. wrote the manuscript.

2.8 Competing interests

The authors declare no competing interests.

Received: 1 February 2019; Accepted: 20 September 2019;

Published online: 23 October 2019

2.9 References

1. Compton, D. A. Spindle assembly in animal cells. Annu. Rev. Biochem. **69**, 95–114 (2000).
2. Heald, R. & Khodjakov, A. Thirty years of search and capture: the complex simplicity of mitotic spindle assembly. J. Cell Biol. **211**, 1103–1111 (2015).
3. Barr, F. A. & Gruneberg, U. Cytokinesis: placing and making the final cut. Cell **131**, 847–860 (2007).
4. Green, R. A., Paluch, E. & Oegema, K. Cytokinesis in animal cells. Annu. Rev. Cell Dev. Biol. **28**, 29–58 (2012).
5. Storchova, Z. & Kuffer, C. The consequences of tetraploidy and aneuploidy. J. Cell Sci. **121**, 3859–3866 (2008).
6. Storchova, Z. & Pellman, D. From polyploidy to aneuploidy, genome instability and cancer. Nat. Rev. Mol. Cell Biol. **5**, 45–54 (2004).
7. Fujiwara, T. et al. Cytokinesis failure generating tetraploids promotes tumorigenesis in p53-null cells. Nature **437**, 1043–1047 (2005).
8. Galipeau, P. C. et al. 17p (p53) allelic losses, 4N (G2/tetraploid) populations, and progression to aneuploidy in Barrett's esophagus. Proc. Natl Acad. Sci. USA **93**, 7081–7084 (1996).
9. Ganem, N. J., Godinho, S. A. & Pellman, D. A mechanism linking extra centrosomes to chromosomal instability. Nature **460**, 278–282 (2009).
10. Pfau, S. J. & Amon, A. Chromosomal instability and aneuploidy in cancer: from yeast to man. EMBO Rep. **13**, 515–527 (2012).
11. Silkworth, W. T., Nardi, I. K., Scholl, L. M. & Cimini, D. Multipolar spindle pole coalescence is a major source of kinetochore mis-attachment and chromosome mis-segregation in cancer cells. PLoS ONE **4**, e6564 (2009).
12. Quintyne, N. J., Reing, J. E., Hoffelder, D. R., Gollin, S. M. & Saunders, W. S. Spindle multipolarity is prevented by centrosomal clustering. Science **307**, 127–129 (2005).
13. Kwon, M. et al. Mechanisms to suppress multipolar divisions in cancer cells with extra centrosomes. Genes Dev. **22**, 2189–2203 (2008).
14. Delattre, M. & Gonczy, P. The arithmetic of centrosome biogenesis. J. Cell Sci. **117**, 1619–1630 (2004).

15. Howe, K. & FitzHarris, G. A non-canonical mode of microtubule organization operates throughout pre-implantation development in mouse. Cell Cycle **12**, 1616–1624 (2013).
16. Gueth-Hallonet, C. et al. Gamma-tubulin is present in acentriolar MTOCs during early mouse development. J. Cell Sci. **105**, 157–166 (1993).
17. Palacios, M. J., Joshi, H. C., Simerly, C. & Schatten, G. Gamma-tubulin reorganization during mouse fertilization and early development. J. Cell Sci. **104**, 383–389 (1993).
18. Andreassen, P. R., Lohez, O. D., Lacroix, F. B. & Margolis, R. L. Tetraploid state induces p53-dependent arrest of nontransformed mammalian cells in G1. Mol. Biol. Cell **12**, 1315–1328 (2001).
19. Ganem, N. J. et al. Cytokinesis failure triggers hippo tumor suppressor pathway activation. Cell **158**, 833–848 (2014).
20. Ueda, J. et al. Heterochromatin dynamics during the differentiation process revealed by the DNA methylation reporter mouse, MethylRO. Stem Cell Rep. **2**, 910–924 (2014).
21. Horii, T. et al. p53 suppresses tetraploid development in mice. Sci. Rep. **5**, 8907 (2015).
22. Eakin, G. S. & Behringer, R. R. Tetraploid development in the mouse. Dev. Dyn. **228**, 751–766 (2003).
23. Eakin, G. S., Hadjantonakis, A. K., Papaioannou, V. E. & Behringer, R. R. Developmental potential and behavior of tetraploid cells in the mouse embryo. Dev. Biol. **288**, 150–159 (2005).
24. Mogessie, B. & Schuh, M. Actin protects mammalian eggs against chromosome segregation errors. Science **357**, https://doi.org/10.1126/science.aal1647 (2017).
25. Vazquez-Diez, C., Yamagata, K., Trivedi, S., Haverfield, J. & FitzHarris, G. Micronucleus formation causes perpetual unilateral chromosome inheritance in mouse embryos. Proc. Natl Acad. Sci. USA **113**, 626–631 (2016).
26. Courtois, A., Schuh, M., Ellenberg, J. & Hiiragi, T. The transition from meiotic to mitotic spindle assembly is gradual during early mammalian development. J. Cell Biol. **198**, 357–370 (2012).
27. Fong, K. W., Choi, Y. K., Rattner, J. B. & Qi, R. Z. CDK5RAP2 is a pericentriolar protein that functions in centrosomal attachment of the gamma-tubulin ring complex. Mol. Biol. Cell **19**, 115–125 (2008).
28. Balboula, A. Z. et al. Haspin kinase regulates microtubule-organizing center clustering and stability through Aurora kinase C in mouse oocytes. J. Cell Sci. **129**, 3648–3660 (2016).

29. Lukinavicius, G. et al. Fluorogenic probes for live-cell imaging of the cytoskeleton. Nat. Methods **11**, 731–733 (2014).
30. Dumont, J. et al. Formin-2 is required for spindle migration and for the late steps of cytokinesis in mouse oocytes. Dev. Biol. **301**, 254–265 (2007).
31. Gatlin, J. C. et al. Spindle fusion requires dynein-mediated sliding of oppositely oriented microtubules. Curr. Biol. **19**, 287–296 (2009).
32. Reichmann, J. et al. Dual-spindle formation in zygotes keeps parental genomes apart in early mammalian embryos. Science **361**, 189–193 (2018).
33. Lara-Gonzalez, P., Westhorpe, F. G. & Taylor, S. S. The spindle assembly checkpoint. Curr. Biol. **22**, R966–R980 (2012).
34. Musacchio, A. The molecular biology of spindle assembly checkpoint signaling dynamics. Curr. Biol. **25**, R1002–R1018 (2015).
35. Bolton, H. et al. Mouse model of chromosome mosaicism reveals lineage specific depletion of aneuploid cells and normal developmental potential. Nat. Commun. **7**, 11165 (2016).
36. Vazquez-Diez, C., Paim, L. M. G. & FitzHarris, G. Cell-size-independent spindle checkpoint failure underlies chromosome segregation error in mouse embryos. Curr. Biol. **29**, 865–873 e863 (2019).
37. Wei, Y. et al. Spindle assembly checkpoint regulates mitotic cell cycle progression during preimplantation embryo development. PLoS ONE **6**, e21557 (2011).
38. Miyanari, Y., Ziegler-Birling, C. & Torres-Padilla, M. E. Live visualization of chromatin dynamics with fluorescent TALEs. Nat. Struct. Mol. Biol. **20**, 1321–1324 (2013).
39. Cimini, D. et al. Merotelic kinetochore orientation is a major mechanism of aneuploidy in mitotic mammalian tissue cells. J. Cell Biol. **153**, 517–527 (2001).
40. Thompson, S. L. & Compton, D. A. Examining the link between chromosomal instability and aneuploidy in human cells. J. Cell Biol. **180**, 665–672 (2008).
41. Lampson, M. A. & Grishchuk, E. L. Mechanisms to avoid and correct erroneous kinetochore-microtubule attachments. Biology **6**, https://doi.org/10.3390/biology6010001 (2017).
42. Salmon, E. D., Cimini, D., Cameron, L. A. & DeLuca, J. G. Merotelic kinetochores in mammalian tissue cells. Philos. Trans. R. Soc. Lond. B Biol. Sci. **360**, 553–568 (2005).
43. Bakhoum, S. F., Genovese, G. & Compton, D. A. Deviant kinetochore microtubule dynamics underlie chromosomal instability. Curr. Biol. **19**, 1937–1942 (2009).

44. Zhai, Y., Kronebusch, P. J. & Borisy, G. G. Kinetochore microtubule dynamics and the metaphase–anaphase transition. J. Cell Biol. **131**, 721–734 (1995).
45. Fitzharris, G. A shift from kinesin 5-dependent metaphase spindle function during preimplantation development in mouse. Development **136**, 2111–2119 (2009).
46. Kline-Smith, S. L., Khodjakov, A., Hergert, P. & Walczak, C. E. Depletion of centromeric MCAK leads to chromosome congression and segregation defects due to improper kinetochore attachments. Mol. Biol. Cell **15**, 1146–1159 (2004).
47. Wordeman, L., Wagenbach, M. & von Dassow, G. MCAK facilitates chromosome movement by promoting kinetochore microtubule turnover. J. Cell Biol. **179**, 869–879 (2007).
48. Bakhoum, S. F., Thompson, S. L., Manning, A. L. & Compton, D. A. Genome stability is ensured by temporal control of kinetochore-microtubule dynamics. Nat. Cell Biol. **11**, 27–35 (2009).
49. Storchova, Z. et al. Genome-wide genetic analysis of polyploidy in yeast. Nature **443**, 541–547 (2006).
50. Stingele, S. et al. Global analysis of genome, transcriptome and proteome reveals the response to aneuploidy in human cells. Mol. Syst. Biol. **8**, 608 (2012).
51. Andrews, P. D. et al. Aurora B regulates MCAK at the mitotic centromere. Dev. Cell **6**, 253–268 (2004).
52. Lan, W. et al. Aurora B phosphorylates centromeric MCAK and regulates its localization and microtubule depolymerization activity. Curr. Biol. **14**, 273–286 (2004).
53. Zhang, C. Z. et al. Chromothripsis from DNA damage in micronuclei. Nature **522**, 179–184 (2015).
54. Davoli, T. & de Lange, T. The causes and consequences of polyploidy in normal development and cancer. Annu. Rev. Cell Dev. Biol. **27**, 585–610 (2011).
55. Baudoin, N. C. et al. Asymmetric clustering of centrosomes defines the early evolution of tetraploid cells. Prepint at https://www.biorxiv.org/content/10.1101/526731v1, https://doi.org/10.1101/526731 (2019).
56. Tarkowski, A. K. An air-drying method for chromosome preparations from mouse eggs. Cytogenetics **5**, 394–400 (1966).
57. FitzHarris, G. Anaphase B precedes anaphase A in the mouse egg. Curr. Biol. **22**, 437–444 (2012).

58. Vazquez-Diez, C. & FitzHarris, G. Correlative live imaging and immunofluorescence for analysis of chromosome segregation in mouse preimplantation embryos. Methods Mol. Biol. **1769**, 319–335 (2018).
59. Zhang, Q. H. et al. Cyclin A2 modulates kinetochore-microtubule attachment in meiosis II. J. Cell Biol. **216**, 3133–3143 (2017).
60. Cimini, D., Wan, X., Hirel, C. B. & Salmon, E. D. Aurora kinase promotes turnover of kinetochore microtubules to reduce chromosome segregation errors. Curr. Biol. **16**, 1711–1718 (2006).
61. Schindelin, J. et al. Fiji: an open-source platform for biological-image analysis. Nat. Methods **9**, 676–682 (2012).
62. Tinevez, J. Y. et al. TrackMate: an open and extensible platform for single particle tracking. Methods **115**, 80–90 (2017).

Chapter 3 – Cell size and polarisation determine cytokinesis furrow ingression dynamics in mouse embryos

Lia Mara Gomes **Paim**[1]; Greg **FitzHarris**[1,2,3*]

[1]Centre de Recherche du Centre Hospitalier de l'Université de Montréal, H2X 0A9, Montréal, QC, Canada

[2]Département d'Obstétrique-Gynécologie, Université de Montréal, H3C 3J7, Montréal, QC, Canada

[3]Département de Pathologie et Biologie Cellulaire, Université de Montréal, H3T 1J4, Montréal, QC, Canada

*Corresponding author: Greg FitzHarris

Email: greg.fitzharris@umontreal.ca

Citation: Paim, L.M.G., FitzHarris, G. Cell size and polarization determine cytokinesis furrow ingression dynamics in mouse embryos. PNAS 119 (12) e2119381119 https://doi.org/10.1073/pnas.2119381119

Author contributions: L.M.G.P. and G.F. designed research; L.M.G.P. performed research; L.M.G.P. and G.F. analyzed data; and L.M.G.P. and G.F. wrote the paper.

The authors declare no competing interest.

Classification: Biological Sciences/Cell Biology

Keywords: Cytokinesis; Cell polarity; Embryo development; Contractile ring; Furrow ingression

3.1 Abstract

Cytokinesis is the final step of cell division during which a contractile ring forms a furrow that partitions the cytoplasm in two. How furrow ingression is spatiotemporally regulated and how it is adapted to complex cellular environments and developmental transitions remain poorly understood. Here, we examine furrow ingression dynamics in the context of the early mouse embryo and find that cell size is a powerful determinant of furrow ingression speed during reductive cell divisions. In addition, the emergence of cell polarity and the assembly of the apical domain in outer cells locally inhibits the recruitment of cytokinesis components and thereby negatively regulates furrow ingression specifically on one side of the furrow. We show that this biasing of cytokinesis is not dependent upon cell–cell adhesion or shape but rather is cell intrinsic and is caused by a paucity of cytokinetic machinery in the apical domain. The results thus reveal that in the mouse embryo cell polarity directly regulates the recruitment of cytokinetic machinery in a cell-autonomous manner and that subcellular organization can instigate differential force generation and constriction speed in different zones of the cytokinetic furrow.

3.2 Significance Statement

The final step of cell division, termed cytokinesis, comprises the constriction of a furrow that divides the cytoplasm to form two daughter cells. Although cytokinesis is well studied in traditional cell systems, how cytokinesis is regulated in complex multicellular settings and during cell-fate decisions is less well understood. Here, using live imaging and physical and molecular interventions, we find that the emergence of cell polarity during mouse embryo morphogenesis dramatically impacts cytokinesis mechanisms. Specifically, the assembly of the apical domain in outer cells locally inhibits the cytokinetic machinery, leading to an unexpected laterally biased cytokinesis.

3.3 Introduction

Cytokinesis is the final step of cell division, a multistep process initiated by signaling from the anaphase spindle midzone that induces the assembly and constriction of an actomyosin ring responsible for partitioning the cytoplasm in two (1, 2). Although many of the molecular players

in furrow constriction have been identified, how furrow ingression is spatiotemporally regulated remains poorly understood. Moreover, little is known about how constriction is adapted to different cell contexts.

While many studies of cytokinesis use cultured cells, valuable insights can be gleaned from complex cellular systems. For instance, in epithelia cell–cell adhesion has been shown to mechanically regulate furrow ingression by anchoring the contractile ring to sites of cell adhesion, thereby restricting constriction on the apical side (3–6). Moreover, apical polarity has been proposed to contribute to furrow ingression positioning and dynamics during asymmetric cell divisions (7, 8), though how polarity controls cytokinesis, and how apical polarity and cell adhesion cooperate to regulate furrow ingression, are not well understood. One outstanding question to which complex systems have generated insight is how the contractile ring is organized and whether contractile forces are generated locally or globally throughout the ring. Interestingly, in the reductive cleavages of Caenorhabditis elegans embryos, it was found that cell-size reductions cause a progressive decline in contractile ring constriction speed (9–12). Based on this, a model was proposed wherein a greater number of locally regulated contractile units in bigger cells causes larger rings to constrict more rapidly than smaller ones (10). However, whether these observations extend to higher eukaryotes and what regulates furrow ingression dynamics in complex mammalian systems remain underexplored.

Here we address these questions in the context of early mouse embryo development, in which progressive cell-size reductions coincide with key morphogenetic events—such as the emergence of cell–cell adhesion patterns, apical polarity establishment, and cell-fate determination. In addition to a strong influence of cell size upon furrow ingression speed, we report that apical polarity limits the recruitment of cytokinesis components specifically on one side of the furrow, which serves as a cell-intrinsic mechanism for generating a laterally based cytokinesis.

3.4 Results

3.4.1 An upper limit to cell-size scaling of furrow ingression in mouse embryos.

Although many of the molecules essential for the constriction of the actomyosin ring that in turn drives furrow ingression are known, what determines the speed of ring constriction is poorly understood. We set out to perform four-dimensional live cell imaging during the 1–2, 2–4, 4–8, 8–16, 16–32, and 32–64 cell divisions in mouse embryos, using GAP43:GFP plasma membrane labeling to measure the perimeter of the contractile ring during furrowing (**Fig. 1 A and B** and see also **SI Appendix, Fig. S1**). The speed at which the cytokinetic furrow constricted ("speed of constriction," expressed as a decrease in furrow perimeter in micrometers per minute) was constant for the majority of the duration of furrow ingression in any given cell, similar to other cells studied (10, 13, 14). We found that constriction speed is similar between the 1–2 and 8–16 cell divisions in mouse embryos (**Fig. 1C**) and, consequently, the duration of cytokinesis (see **Materials and Methods**) decreases between the 1–2 and 8–16 cell divisions (**Fig. 1D**). However, furrowing speed decreased between the 8–16 and 16–32 cell division ($P < 0.05$), with a further nonsignificant decrease in speed observed between the 16–32 and 32–64 cell stages (**Fig. 1 C and D**).

To explore whether the differences in furrow ingression speed we observed from the 8–16 cell stage onward might be due to changing cell size, we first set out to artificially reduce cytoplasmic volume using micromanipulation (**SI Appendix, Fig. S2 A–I** and see **Materials and Methods**). Although furrowing speed was similar between sham-manipulated controls and blastomeres with reduced cytoplasmic size (∼40% reduction by volume) at the 4–8 cell division (sham: 12.22 ± 0.43 μm/min; reduced cytoplasm: 11.78 ± 0.52 μm/min; $P = 0.5222$) (**Fig. 1 E and F**), furrowing speed was substantially reduced in blastomeres undergoing the 8–16 cell division with reduced cytoplasmic size (sham: 11.22 ± 0.55 μm/min; reduced cytoplasm: 8.55 ± 0.30 μm/min; $P = 0.0004$) (**Fig. 1 G and H**). Notably, the distribution of constriction speeds measured in sham-manipulated controls and blastomeres with reduced cytoplasmic size at the 8–16 cell division followed an inverse correlation with initial perimeter at anaphase onset ($R^2 = 0.4930$; **SI Appendix, Fig. S2J**), indicating that cytoplasmic removal impacted furrowing proportional to the amount of cytoplasm removed.

Next, to investigate the impact of increased cell size, we employed an approach we previously developed to increase cell volume while maintaining the correct ploidy and cell division count (15), wherein cytokinesis was blocked at the 2–4 cell stage, and micromanipulation was then employed to remove the additional nucleus, thereby creating an embryo comprising two double-sized four-cell-stage blastomeres (**SI Appendix, Fig. S3**). Analysis of these embryos later in development showed that constriction speed was similar at the 8–16 cell division between sham-manipulated controls (10.63 ± 0.35 μm/min) and double-sized blastomeres (11.52 ± 0.41 μm/min; P = 0.1118) (**Fig. 1 I and J**), consistent with a lack of impact of cell size upon furrowing speed prior to the 16–32 cell stage. Notably however, at the 16–32 cell division, constriction speed was increased in double-sized blastomeres (7.76 ± 0.25 μm/min) as compared to controls (5.44 ± 0.23 μm/min; P < 0.0001; **Fig. 1 K and L**). Thus, increasing or decreasing cytoplasmic volume changes furrowing speed accordingly from the 8–16 cell stage onward. Whether this effect is a direct impact of cell size on the cytokinesis machinery, as previously alluded to in *C. elegans* embryos (10, 12) and *Neurospora crassa* (13), or whether cell size impacts constriction speed indirectly by influencing other cellular systems that affect the cytoskeleton remains to be determined. Nonetheless, this series of experiments suggest that cytokinesis furrowing speed is strongly influenced by cell size from the 8–16 cell stage onward.

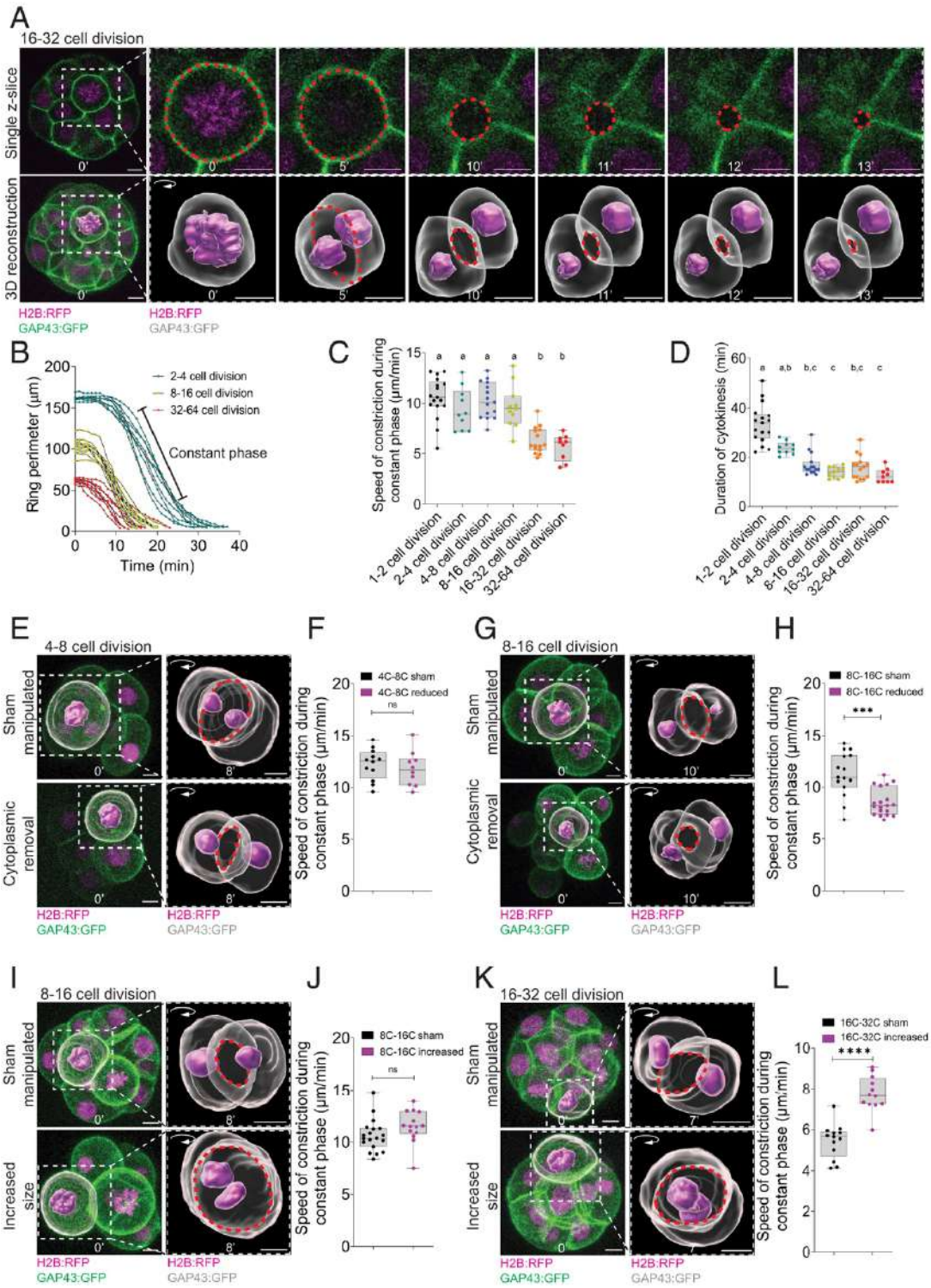

Figure 30. – Cell size determines furrowing speed from the eight-cell stage in mouse embryos. (Figure 1).

(a) *Single z-slice (Top) and three-dimensional reconstructions (Bottom) of a cell undergoing the 16–32 cell division (example shown has 26 cells) coexpressing H2B:RFP (magenta) and GAP43:GFP (green/gray). Red dashed circles indicate where the measurements of contractile ring perimeter were performed.* ***(b)*** *Quantification of contractile ring perimeter in blastomeres undergoing the 2–4 (n = 10 blastomeres from 10 embryos), 8–16 (n = 11 blastomeres from 8 embryos), and 32–64 cell divisions (n = 9 blastomeres from eight embryos). Individual curves represent independent blastomeres.* ***(c and d)*** *Quantification of average speed of ring constriction during the constant phase of perimeter decrease (one-way ANOVA with multiple comparisons)* ***(c)*** *and duration of cytokinesis (Kruskal–Wallis with multiple comparisons)* ***(d)*** *at the 1–2 (n = 17 blastomeres from 17 embryos), 2–4 (n = 10 blastomeres from 10 embryos), 4–8 (n = 15 blastomeres from 12 embryos), 8–16 (n = 11 blastomeres from 8 embryos), 16–32 (n = 15 blastomeres from 11 embryos), and 32–64 cell divisions (n = 9 blastomeres from eight embryos).* ***(e and g*** *and see also* ***SI Appendix, Fig. S2 A–I****) Representative time-lapse three-dimensional reconstruction of a cell in a sham-manipulated and embryo with reduced cytoplasmic size undergoing the 4–8 (example in sham has seven cells and reduced size has six cells)* ***(e)*** *and 8–16 cell divisions (example in sham has 8 cells and reduced size has 13 cells)* ***(g)*** *coexpressing H2B:RFP (magenta) and GAP43:GFP (green/gray).* ***(f and h)*** *Quantification of average speed of constriction at the 4–8 (sham-manipulated n = 12 blastomeres from 11 embryos; cytoplasmic removal n = 10 blastomeres from 9 embryos; two-tailed unpaired t test, P = 0.5222)* ***(f)*** *and 8–16 cell divisions (sham-manipulated n = 15 blastomeres from 8 embryos; cytoplasmic removal n = 19 blastomeres from 10 embryos; two-tailed Mann–Whitney U test, ***P = 0.0004)* ***(h)****.* ***(i and k)*** *Representative time-lapse three-dimensional reconstructions of cells undergoing the 8–16 cell division from sham-manipulated (Top; example shown has 12 cells) or embryos with increased cytoplasmic size (Bottom; example has six cells)* ***(i)*** *and cells undergoing the 16–32 cell division from sham-manipulated (Top; example has 18 cells) or embryos with increased cytoplasmic size (Bottom; example has 13 cells)* ***(k)****.* ***(j and l)*** *Quantification of average speed of constriction of blastomeres from sham-manipulated or embryos with increased cytoplasmic size at the 8–16 (sham n = 19 blastomeres from 11 embryos; increased n = 14 blastomeres from 9 embryos; two-tailed unpaired t test nonsignificant (ns) P = 0.1118* ***(j)*** *and outer blastomeres at 16–32 cell divisions (sham n = 13 blastomeres from 7 embryos; increased n = 12 blastomeres from 9 embryos; two-tailed unpaired t test ****P < 0.0001. Time is shown in minutes, where 0' is anaphase onset. (Scale bars, 10 μm.) In the box plots, the center line represents the median, the bounds of the box represent upper and lower quartiles, the whiskers represent minimum and maximum values, and dots represent independent measurements. In multiple comparison analyses, different letters represent statistical significance at P < 0.05.*

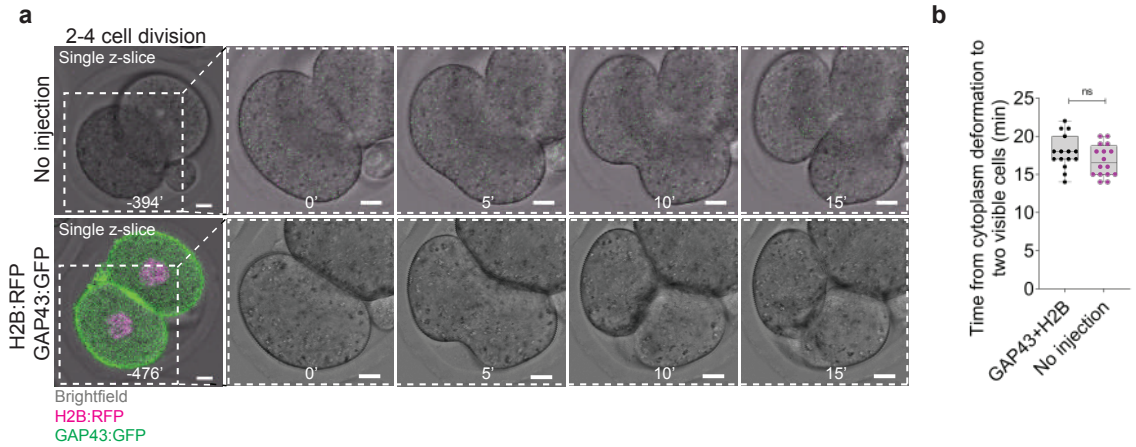

Figure 31. – H2B:RFP and GAP43:GFP imaging does not affect cytokinesis dynamics (Supplementary Figure 1).

(a) *Representative time-lapse images of a cell undergoing the 2-4 cell division from non-injected embryos (top; example shown has 2 cells) or expressing H2B:RFP (magenta) and GAP43:GFP (green) (bottom; example has 2 cells).* ***(b)*** *Quantification of average time from initial cytoplasm deformation until two individualised blastomeres are visible in blastomeres undergoing the 2-4 cell division from embryos without microinjection (n=15 blastomeres from 11 embryos) or microinjected with H2B:RFP and GAP43:GFP (n=16 blastomeres from 14 embryos; two-tailed unpaired t test, P=0.1596). Quantification was performed using only the brightfield channel in both groups for visualisation of cytoplasm deformation and cell separation. Time is shown in minutes, where 0' is the first frame of visible cytoplasm deformation. Scale bars = 10μm. In the box plots, the centre line represents the median, the bounds of the box represent upper and lower quartiles, the whiskers represent minimum and maximum values, and dots represent independent measurements. See also Figure 1.*

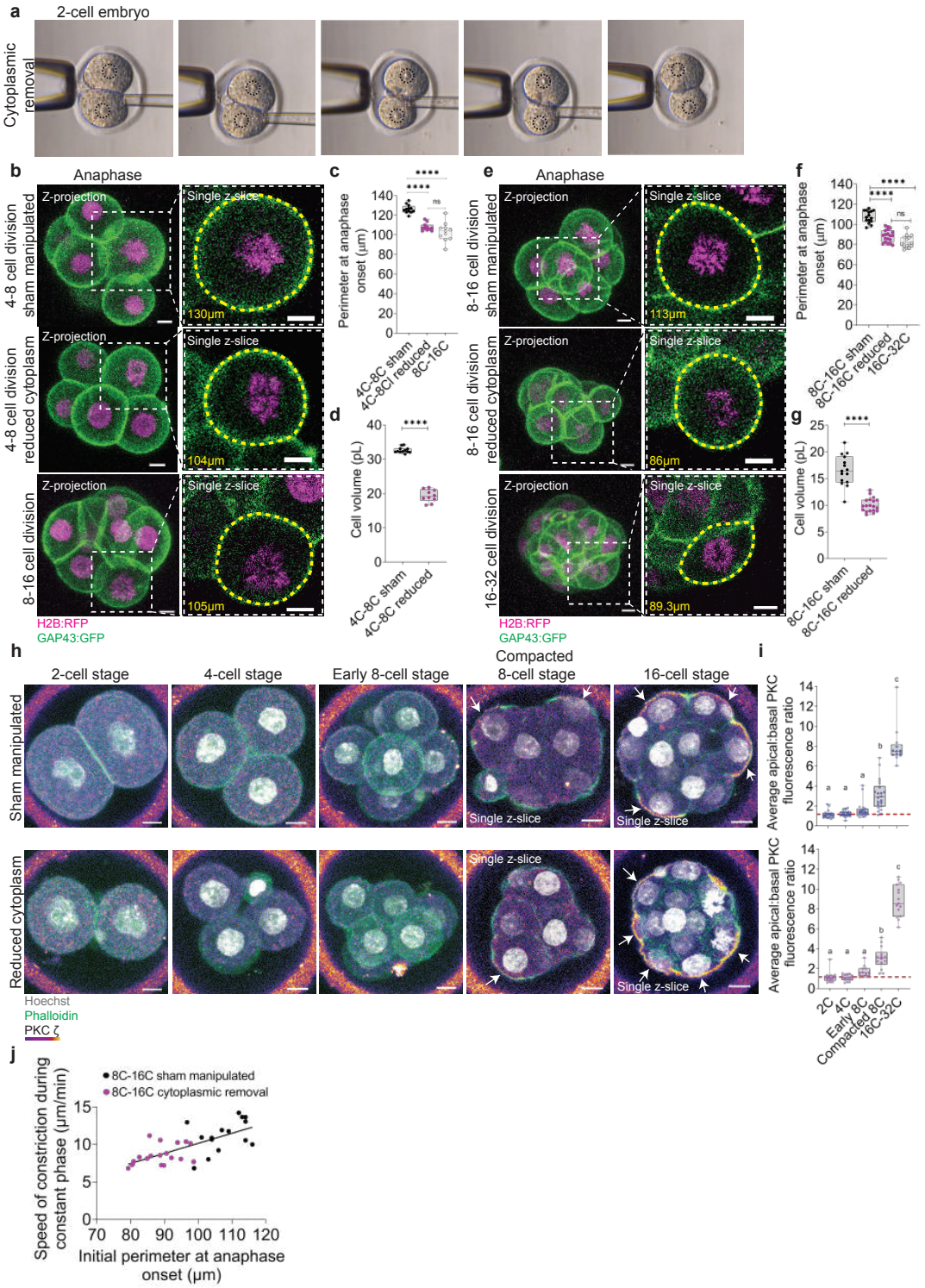

Figure 32. – Cytoplasmic removal to reduce blastomere size (Supplementary Figure 2).

(a) *Representative brightfield timelapse images of cytoplasmic removal procedure in a 2-cell embryo. Dashed black circles indicate the location of the nuclei. Note that upon cytoplasmic removal, cell volume decreases approximately 40%* ***(b and e)*** *Representative z-projections of cells undergoing the 4-8 cell division in sham manipulated embryos (top; example shown has 7 cells), embryos with reduced cytoplasm (middle; example has 5 cells) and a cell undergoing the 8-16 cell division (bottom; example has 8 cells)* ***(b);*** *cells undergoing the 8-16 cell division in sham manipulated embryos (top; example shown has 8 cells), embryos with reduced cytoplasm (middle; example has 9 cells) and a cell undergoing the 16-32 cell division (bottom; example has 22 cells)* ***(e)*** *from embryos co-expressing H2B:RFP (magenta) and GAP43:GFP (green). The yellow dashed lines and values indicate the measurements of cell perimeter at anaphase onset.* ***(c and f)*** *Quantification of average perimeter measured at anaphase onset in sham manipulated embryos at the 4-8 cell transition (n=12 blastomeres from 11 embryos), embryos with reduced cytoplasm at the 4-8 cell transition (n=11 blastomeres from 9 embryos) and embryos at the 8-16 cell transition (n =11 blastomeres from 8 embryos; one-way ANOVA with multiple comparisons, ****P<0.0001, ns P=0.5365)* ***(c);*** *sham manipulated embryos at 8-16 cell transition (n=15 blastomeres from 8 embryos), embryos with reduced cytoplasm at 8-16 cell transition (n=19 blastomeres from 10 embryos) and embryos at the 16-32 cell transition (n=15 blastomeres from 11 embryos; Kruskal-Wallis with multiple comparisons, ****P<0.0001, ns P= 0.1734)* ***(f). (d and g)*** *Quantification of average blastomere volume in sham manipulated embryos at the 4-8 cell transition (n=12 blastomeres from 11 embryos), embryos with reduced cytoplasm at the 4-8 cell transition (n=11 blastomeres from 9 embryos; unpaired t test, ****P<0.0001)* ***(d);*** *sham manipulated embryos at 8-16 cell transition (n=15 blastomeres from 8 embryos), embryos with reduced cytoplasm at 8-16 cell transition (n=19 blastomeres from 10 embryos, unpaired t test ****P<0.0001)* ***(g).*** *The data from 8-16 in* ***(c)*** *and 16-32 cell divisions in* ***(f)*** *was obtained from the same embryos in figure 1B-D.* ***(h)*** *Evidence that polarity emerges at the compacted 8-cell stage even in embryos with reduced cytoplasmic size. Representative immunofluorescence images of 2-cell, 4-cell, early 8-cell, compacted 8-cell and 16-cell stage sham manipulated (top) and embryos with reduced cytoplasm (bottom). Note that apical localization of PKCz is only clearly visible from the compacted 8-cell stage onwards in both sham-manipulated and embryos with reduced cytoplasm (white arrows).* ***(i)*** *Quantification of average apical:basal PKCz fluorescence ratio in sham manipulated (top) 2-cell (n = 17 embryos), 4-cell (n = 20 embryos), early 8-cell (n = 19 embryos), compacted 8-cell (n = 22 embryos) and 16-32 cell stage embryos (n = 13 embryos; One-way ANOVA) and embryos with reduced cytoplasm (bottom) at the 2-cell (n = 17 embryos), 4-cell (n = 15 embryos), early 8-cell (n = 12 embryos), compacted 8-cell (n = 14 embryos) and 16-32 cell stage (n = 15 embryos; One-way ANOVA).* ***(j)*** *Scatterplot demonstrating the distribution of average speed of constriction during constant phase of perimeter decrease relative to the initial perimeter at anaphase onset in sham-manipulated (black dots; n=15 blastomeres from 8 embryos) and embryos with reduced cytoplasm at the 8-16 cell transition (pink dots; n=19 blastomeres from 10 embryos; simple linear regression analysis R2 = 0.4930, slope is significantly non-zero p<0.0001). Scale bars = 10μm. In box plots, the center line represents the median, the bounds of the box represent upper and lower quartiles, the whiskers represent minimum and maximum values, and dots represent independent measurements. In multiple comparison analyses, different letters represent statistical significance at P<0.05. See also Figure 1.*

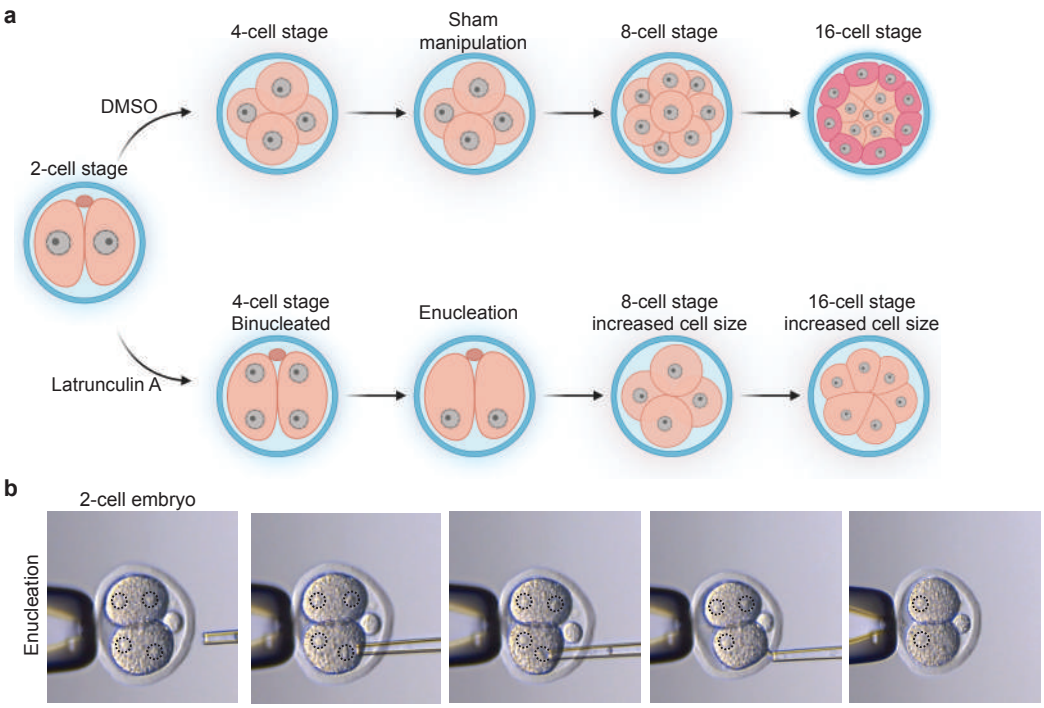

Figure 33. – Procedure to artificially increase blastomere size (Supplementary Figure 3).

(a and b) *Scheme illustrating the experimental design to increase cytoplasmic size. Two-cell embryos were treated Latrunculin A during the 2- to 4-cell transition to generate binucleated embryos. Binucleated embryos were then subjected to micromanipulation to remove one of the extra nuclei generated as a result of cytokinesis failure (enucleation;* ***b****) and allowed to divide to the 8-cell or 16-cell stages prior to live-cell imaging. Figure S3A was created with BioRender. See also Figure 1.*

3.4.2 Apical polarity emergence decreases outer cell constriction speed independently of cell fate.

Early embryonic development is marked not only by lessening cell size but also by well-defined morphogenetic events (**Fig. 2A**). At the 8-cell stage, pulsatile forces generated by the actomyosin cortex coupled with E-cadherin–dependent restriction of contractility away from cell–cell contacts drive the onset of compaction (16, 17). The subsequent cell division gives rise to a 16-cell embryo composed of approximately spherical/cuboidal nonpolarized inner blastomeres, and flatter, polarized outer blastomeres that possess a characteristic apical domain (16, 18–20) (**Fig.**

2A). By the late 16-cell stage, the first cell fate decision is initiated, wherein the transcription factor TEAD4 is expressed in outer cells and induces the expression of the trophectoderm determinant CDX2 exclusively in those cells (16) (**Fig. 2A**). To address whether any of these events might cooperate with cell size to influence furrowing speed in embryos, we first compared furrowing speeds in inner cells and outer cells and found that, both at the 16–32 and 32–64 cell divisions, outer cells had a significantly reduced furrowing speed compared to inner cells (16–32 outer: 5.39 ± 0.15 μm/min; 32–64 outer: 4.71 ± 0.67 μm/min; 16–32 inner: 7.71 ± 0.42 μm/min; 32–64 inner: 6.39 ± 0.24 μm/min; 16–32 P = 0.0004; 32–64 P = 0.0081) (**Fig. 2 B and C**). We wondered whether the slowed furrowing of outer cells might be a result of the different shapes of inner and outer cells, outer cells being predominantly more flattened than inner cells. To test this, we abolished cell adhesion in embryos undergoing the 16–32 cell division using Ca^{+2}-free media (**SI Appendix, Fig. S4A**). Importantly, removal of Ca^{+2} from the culture media did not prevent apical polarity establishment, as evidenced by the enrichment of the polarity marker PKCζ in the apical surface of outer cells (**SI Appendix, Fig. S4 B and C**) and embryos were able to undergo the 16–32C transition (**SI Appendix, Fig. S4 D and E and Movie S1**), but in the absence of cell–cell adherence, all cells adopted a rounded shape. Notably, outer cells still displayed reduced speed of constriction (6.02 ± 0.39 μm/min) as compared to inner cells (7.42 ± 0.27 μm/min; P = 0.0062) (**Fig. 2 D and E**). Thus, the slower furrowing speed of outer cells relative to inner cells is not due to their flattened shape or cell–cell adhesion but is rather due to an intrinsic property of the cells.

We next wondered whether the emergence of cell polarity and the formation of the apical domain might be responsible for the decrease in speed of constriction of outer cells. To address this, we depleted the apical polarity protein PARD6B using short hairpin RNAs (shRNA). PARD6B shRNA efficiently disrupted apical polarity emergence, as evidenced by the absence of the apical domain marker PKCζ (**Fig. 2 F and G**), as previously described (21, 22). Strikingly, following PARD6B depletion, furrowing speed in outer cells increased to a velocity comparable to that of inner cells (7.04 ± 0.23 μm/min vs. 6.65 ± 0.20 μm/min, P = 0.7127) (**Fig. 2 H and I**), suggesting that the emergence of apical polarity in outer cells negatively impacts furrow dynamics. Formation of the apical domain contributes to cell-fate determination in the early embryo by allowing the transcriptional activation of TEAD4 in outer cells at the 16-cell stage (16, 23). Therefore, to determine whether the impact of the apical domain on furrowing speed might relate

to cell fate, we depleted TEAD4 by double-stranded RNA (dsRNA) injections (23) and analyzed the speed of constriction of inner and outer cells at the 16–32 cell division. TEAD4 dsRNA knockdown efficiency was confirmed by the absence of TEAD4 nuclear localization with immunofluorescence (**SI Appendix, Fig. S5 A and B**), as previously described (23), and its depletion did not prevent apical polarity emergence at the 16-cell stage as evidenced by the enrichment of the polarity marker PKCζ in the apical surface of outer cells (**SI Appendix, Fig. S5C**). Notably, outer cells from TEAD4-depleted embryos still displayed reduced speed of constriction (6.98 ± 0.23 μm/min) as compared to inner cells (9.75 ± 0.28 μm/min; P = 0.0022), similar to controls (inner: 9.06 ± 0.35 μm/min; outer: 6.47 ± 0.23 μm/min; P = 0.0010) (**SI Appendix, Fig. S5 D and E**). Thus, the emergence of the apical domain lessens furrowing speed in outer cells independently of the downstream impact on cell fate.

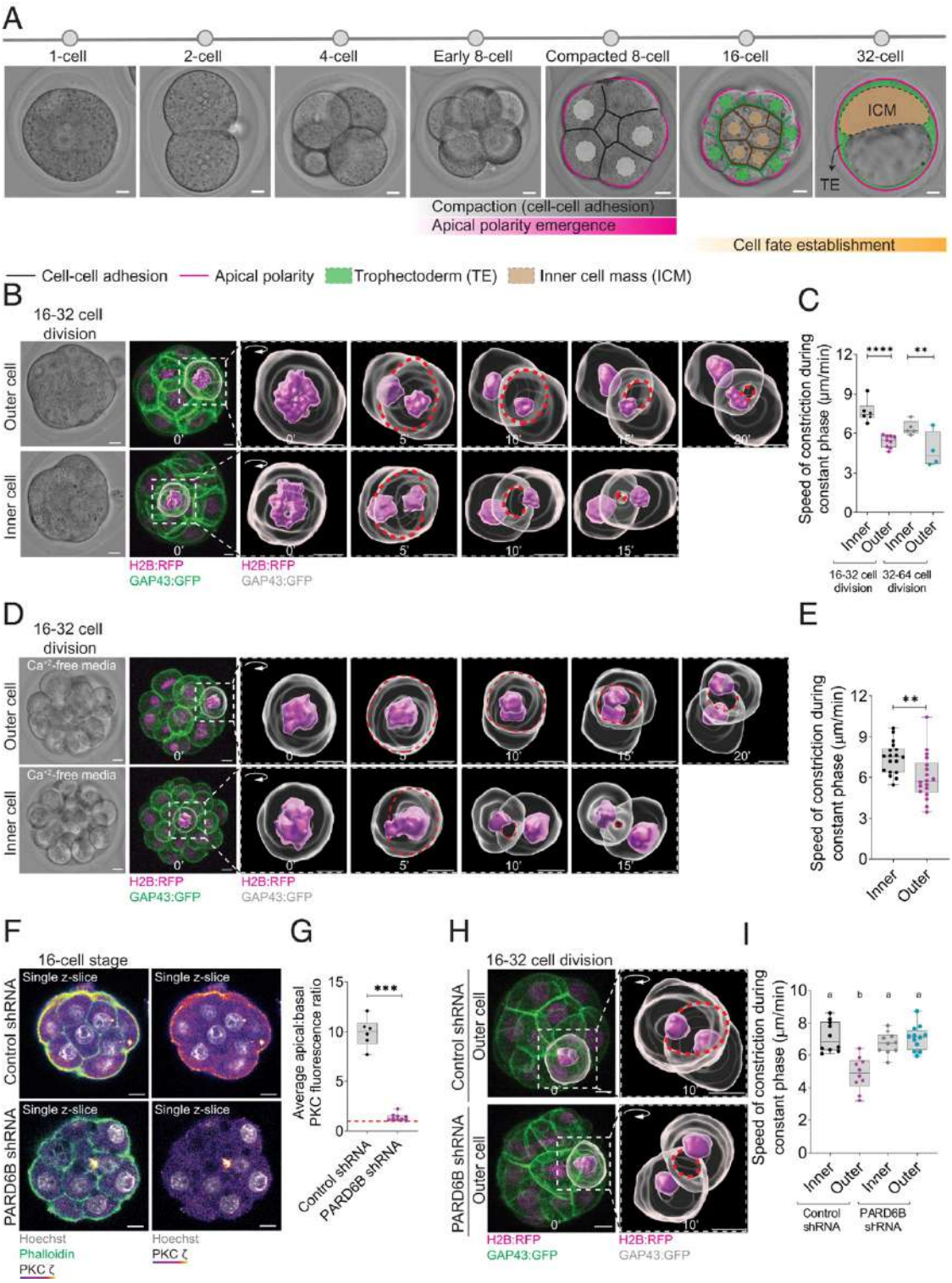

Figure 34. – Apical polarity reduces the speed of constriction of outer cells independently of cell shape and adhesion (Figure 2).

(a) *Illustration of morphogenetic events of mouse preimplantation development. E-cadherin accumulation at the basolateral surface drives compaction at the 8-cell stage, concomitantly with the emergence of apical polarity. The resulting 16-cell embryo displays outer cells that are polarised and flat, and inner cells that are cuboidal and apolar, and undergoes lineage specification, wherein most outer cells are destined to trophectoderm (TE) specification whereas inner cells are directed to the inner cell mass (ICM).* ***(b)*** *Representative brightfield and time-lapse 3D reconstructions of outer and inner cells undergoing the 16-32 cell division (example shown for outer cell has 16 cells and for inner cell has 24 cells) co-expressing H2B:RFP (magenta) and GAP43:GFP (green/grey).* ***(c)*** *Quantification of average speed of constriction of inner and outer cells at 16-32 (inner n=6 blastomeres; outer n=9 blastomeres from 11 embryos) and 32-64 cell divisions (inner n=5 blastomeres; outer n=4 blastomeres from 8 embryos; one-way ANOVA comparing means of preselected columns ****P<0.0001, **P=0.0081). The data quantified in (c) was obtained from the same embryos in figure 1B-D.* ***(d)*** *Representative brightfield and time-lapse 3D reconstructions of outer and inner cells undergoing the 16-32 cell division (example for outer cell has 21 cells and for inner cell has 30 cells) co-expressing H2B:RFP (magenta) and GAP43:GFP (green/grey) cultured in Ca^{+2}-free media.* ***(e)*** *Quantification of average speed of constriction of inner (n=18 blastomeres) and outer blastomeres (n=18 blastomeres from total of 18 embryos; two-tailed unpaired t test, **P=0.0062) undergoing the 16-32 cell division from embryos cultured in Ca+2-free media.* ***(f)*** *Representative immunofluorescence images of 16-cell embryos previously injected with either control shRNA (top) or PARD6B shRNA (bottom).* ***(g)*** *Quantification of average apical:basal PKCζ fluorescence ratio in 16-cell embryos previously injected with either control shRNA (n=6 embryos) or PARD6B shRNA (n=9 embryos; two tailed Mann Whitney test, ***P=0.0004).* ***(h)*** *Representative time-lapse 3D reconstructions of outer blastomeres undergoing the 16-32 cell division from embryos previously injected with control shRNA (top; example has 17 cells) or PARD6B shRNA (bottom; example has 20 cells) and co-expressing H2B:RFP (magenta) and GAP43:GFP (green/grey).* ***(i)*** *Quantification of average speed of constriction of inner and outer blastomeres undergoing the 16-32 cell division from embryos previously injected with control shRNA (inner n=10 blastomeres; outer n=10 blastomeres from a total of 12 embryos) or PARD6B shRNA (inner n=10 blastomeres; outer n=12 blastomeres from a total of 10 embryos; one-way ANOVA with multiple comparisons). Time is shown in minutes, where 0' is anaphase onset. Scale bars = 10μm. In the box plots, the centre line represents the median, the bounds of the box represent upper and lower quartiles, the whiskers represent minimum and maximum values, and dots represent independent measurements.*

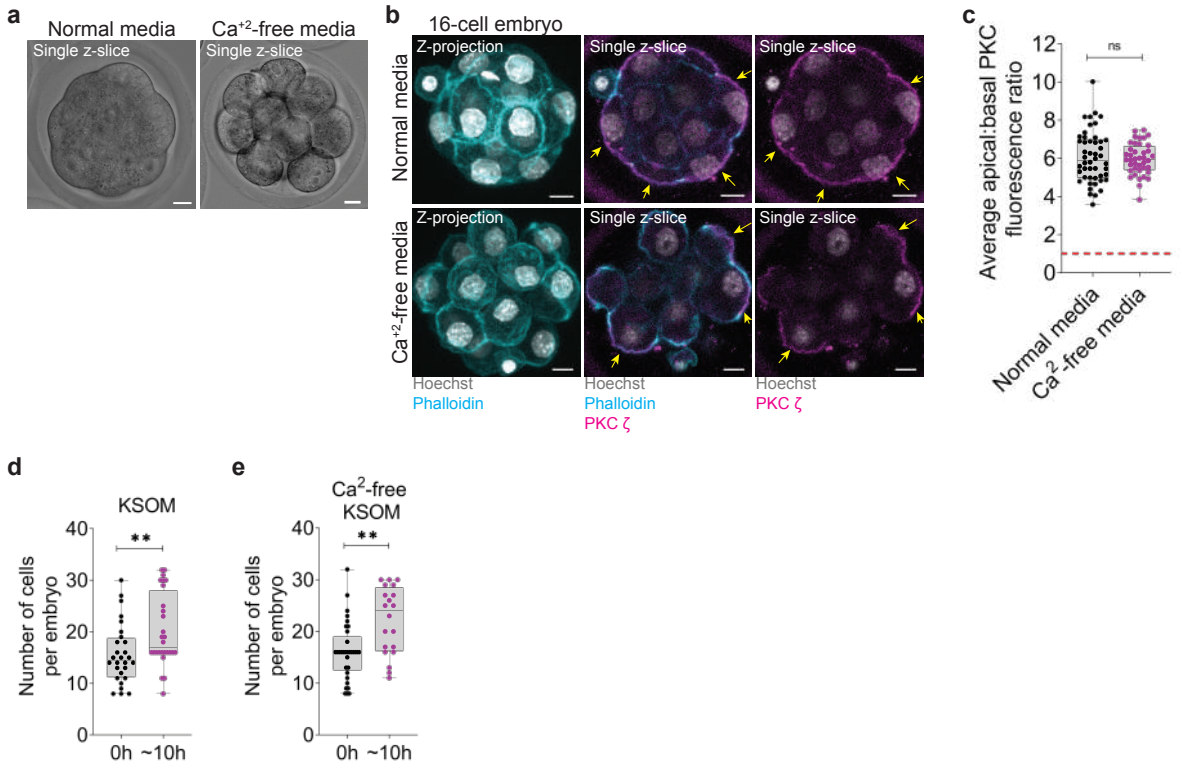

Figure 35. – Embryos treated with Ca+2-free media form apical domains and undergo cell division (Supplementary Figure 4).

(a) *Representative brightfield images of 16-cell embryos exposed to either normal (left) or Ca+2-free media (right). Note that upon treatment with Ca^{+2}-free media, compaction is abolished and all blastomeres have a nearly identical round shape.* ***(b)*** *Representative immunofluorescence images of 16-cell embryos exposed to either normal (top) or Ca^{+2}-free media (bottom). Note that in both groups, the apical domain (PKC ζ staining, magenta) is present in outer cells (yellow arrows).* ***(c)*** *Quantification of average PKC ζ apical:basal fluorescence ratio of outer cells in 16-cell embryos exposed to normal (n=48 embryos) or Ca+2-free media (n=40 embryos; unpaired two-tailed t test, P=0.6809).* ***(d)*** *Quantification of average cell number per embryo before (n=28 embryos) and after ~10h exposure to normal media (n=28 embryos; two-tailed Mann-Whitney test, **P=0.0044).* ***(e)*** *Quantification of average cell number per embryo before (n=33 embryos) and after ~10h exposure to Ca+2-free media (n=20 embryos; two-tailed Mann-Whitney test, **P=0.0010). Scale bars = 10µm. In the box plots, the centre line represents the median, the*

bounds of the box represent upper and lower quartiles, the whiskers represent minimum and maximum values, and dots represent independent measurements. See also Figure 2.

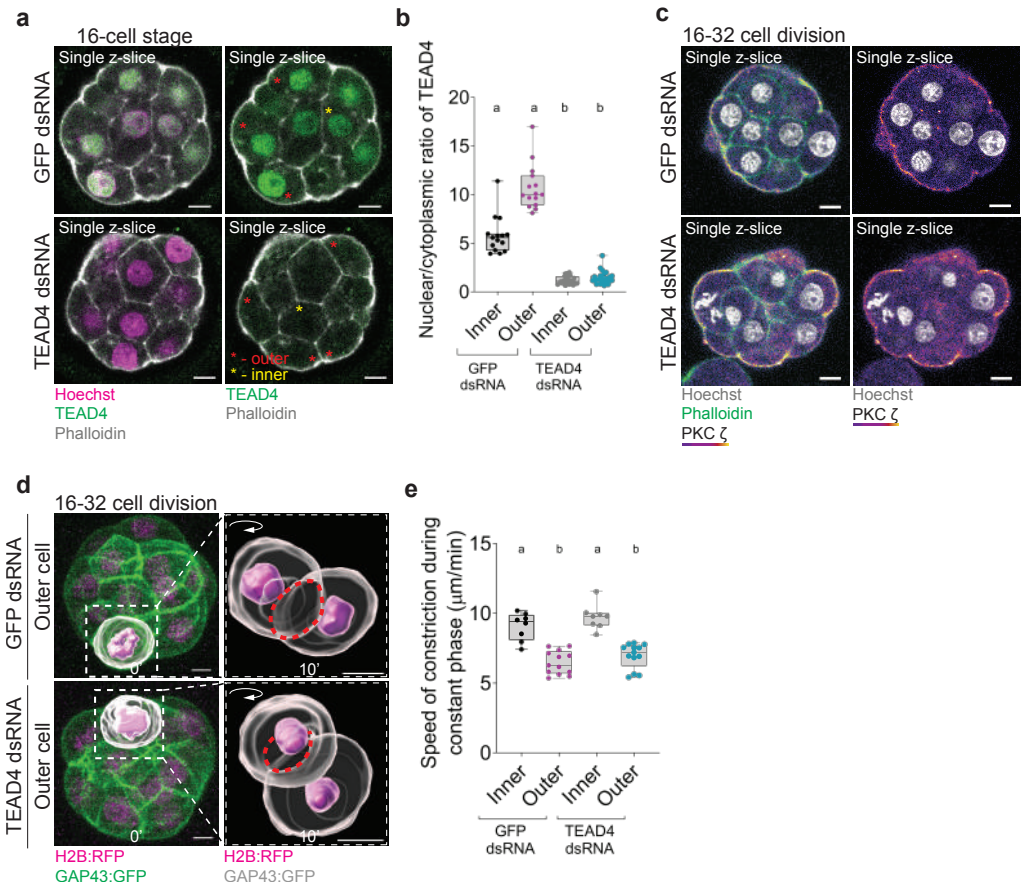

Figure 36. – TEAD4 knockdown does not affect apical polarity emergence and does not alter the speed of constriction of outer cells. (Supplementary Figure 5).

(a) *Representative immunofluorescence images of 16-cell embryos previously injected at the 2-cell stage with either GFP dsRNA (top) or TEAD4 dsRNA (bottom).* ***(b)*** *Quantification of nuclear/cytoplasmic ratio of TEAD4 in 16-cell embryos previously injected with either GFP dsRNA (n=15 embryos) or TEAD4 dsRNA (n=26 embryos; Kruskal-Wallis test with multiple comparisons).* ***(c)*** *Representative immunofluorescence images of embryos undergoing the 16-32 cell division previously injected with either GFP dsRNA (top; example shown has 26 cells) or TEAD4 dsRNA (bottom; example has 25 cells). Note that in both groups, the apical polarity marker PKC ζ (magenta) is present in outer cells.* ***(d)*** *Representative time-lapse 3D reconstructions of outer blastomeres undergoing the 16-32 cell division from embryos previously injected with GFP dsRNA (example has 18 cells) or TEAD4 dsRNA (example has 21 cells) and co-expressing H2B:RFP (magenta) and GAP43:GFP (green/grey).* ***(e)*** *Quantification of average speed of constriction of inner and outer blastomeres undergoing the 16-32 cell division from embryos previously injected with GFP dsRNA (inner n=8 blastomeres; outer n=13 blastomeres from a total*

of 12 embryos) or TEAD4 dsRNA (inner=8 blastomeres; outer n=13 blastomeres from a total of 13 embryos; Kruskal-Wallis with multiple comparisons). Time is shown in minutes, where 0' is anaphase onset. Scale bars = 10μm. In the box plots, the centre line represents the median, the bounds of the box represent upper and lower quartiles, the whiskers represent minimum and maximum values, and dots represent independent measurements. In multiple comparison analyses, different letters represent statistical significance at P<0.05. See also Figure 2.

3.4.3 Apical polarity laterally biases furrow ingression independently of cell adhesion.

In 16–32 cell-stage embryos, outer cell divisions are oriented either circumferentially or radially relative to the surface of the embryo (**Fig. 3A**). Circumferential cell divisions generate two new outer-residing cells immediately after cytokinesis completion, whereas radial cell divisions generate one inner-residing and one outer-residing cell (16, 24–26). Importantly, whereas radial divisions typically cause the apical domain to be asymmetrically inherited by the outer cell, circumferential divisions occur such that the contractile ring cuts through the apical domain and causes it to be symmetrically inherited by both daughter cells (**Fig. 3A**) (18). To better gauge the impact of polarity on cytokinesis in outer cells we therefore examined furrow ingression in relation to division orientation. Analysis of circumferential cell divisions demonstrated that the basal side of the furrow ingressed more quickly than the apical side (**Fig. 3 B–D**, Top), resulting in a total displacement of 17.37 ± 2.30 μm from the basal side and 8.71 ± 0.57 μm from the apical side (**Fig. 3 B–D**, first row; P = 0.0327). Strikingly, this basal-to-apical ingression bias was abolished in circumferential outer cell divisions upon PARD6B knockdown (total displacement apical side: 10.88 ± 0.73 μm; total displacement basal side: 13.28 ± 0.90 μm; P = 0.1514) (**Fig. 3 B–D**, third row and **SI Appendix, Fig. S6**). In contrast, in radial cell divisions both sides of the furrow ingressed similarly both in controls (total displacement side 1: 12.96 μm ± 1.44; total displacement side 2: 12.43 μm ± 1.77; P = 0.8209) as well as in PARD6B-depleted embryos (total displacement side 1: 12.37 μm ± 0.90; total displacement side 2: 13.73 μm ± 1.04; P = 0.9290) (**Fig. 3 B–D**, second and fourth rows and **SI Appendix, Fig. S6**).

A basal-to-apical cytokinesis ingression bias has previously been observed in both *Drosophila melanogaster* and mammalian epithelial cells (3–6, 27). Notably, however, in the case of *D. melanogaster* epithelial cells, cell–cell adhesion drives the bias via mechanical anchorage of

the contractile ring to E-cadherin complexes, thus hampering furrow ingression on the apical side (3–6). Thus, to further probe whether the bias observed in outer blastomeres was indeed caused by an inhibitory effect of the apical domain on the cytokinesis machinery rather than cell–cell adhesion, we analyzed furrow ingression dynamics in circumferentially and radially dividing outer blastomeres at the 16–32 cell transition from embryos relieved of cell–cell adhesion via exposure to Ca^{+2}-free media (**Fig. 3 E–G**). Similarly to our previous results, a basal-to-apical bias of furrow ingression was detected exclusively in circumferentially dividing outer blastomeres of embryos devoid of cell–cell adhesion (total displacement apical side: 10.97 μm ± 0.94; total displacement basal side: 15.91 μm ± 0.98; P = 0.0264) and not in radially dividing blastomeres (total displacement side 1: 15.18 μm ± 0.92; total displacement side 2: 13.36 μm ± 0.65; P = 0.2026) (**Fig. 3 E–G**). We conclude that the overall slowing of ring constriction speed in outer cells is a result of reduced ingression specifically on the apical side during circumferential cell divisions, by a mechanism that is cell-intrinsic and not dependent on cell adhesion or shape.

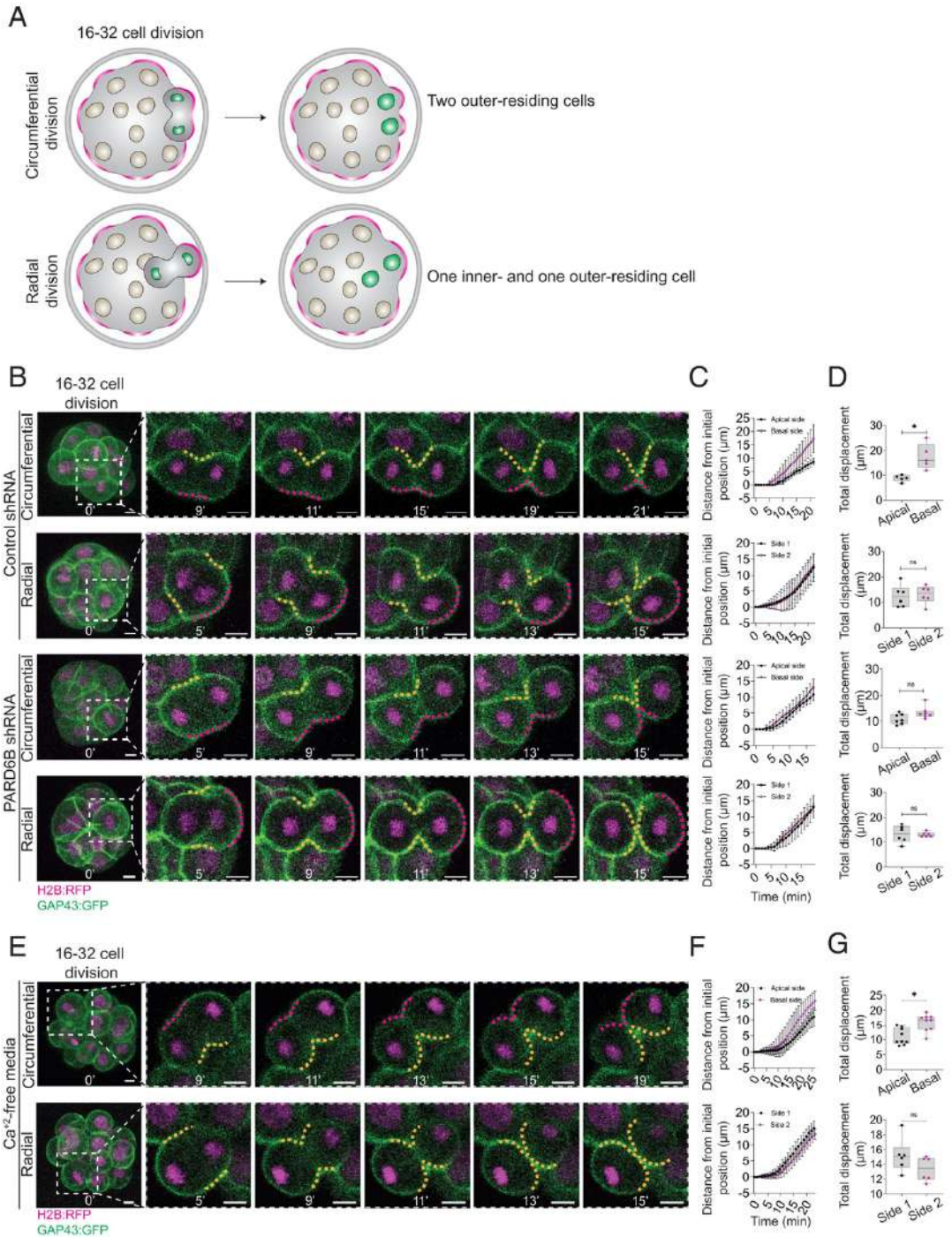

Figure 37. – Apical polarity biases furrow ingression independently of cell adhesion (Figure 3).

(a) *Illustration of cell division orientation in outer cells at the 16–32 cell transition. Outer cells divide either circumferentially, generating two new outer-residing cells, or radially, generating one inner-residing and one outer-residing cell. Note that circumferential cell divisions occur such that the contractile ring cuts through the apical domain and can lead to symmetric inheritance of*

the apical domain. ***(b)*** *Representative time-lapse images of circumferentially and radially dividing blastomeres undergoing the 16–32 cell division from embryos previously injected with either control shRNA (examples shown for both circumferential and radial divisions have 23 cells) or PARD6B shRNA (example shown for circumferential division has 21 cells and for radial has 16 cells) and coexpressing H2B:RFP (magenta) and GAP43:GFP (green). Magenta dashed lines indicate the location of the apical domain, and yellow dashed lines indicate the regions that do not contain an apical domain.* ***(c)*** *Average distance from initial furrow position at anaphase onset in circumferentially or radially dividing blastomeres undergoing the 16–32 cell division from embryos previously injected with control (circumferential: n = 5 blastomeres from five embryos; radial: n = 6 blastomeres from five embryos) or PARD6B shRNA (circumferential: n = 7 blastomeres from five embryos; radial: n = 6 blastomeres from five embryos).* ***(d)*** *Total furrow displacement of blastomeres from embryos in C, dividing circumferentially (control: *P = 0.0327; PARD6B: ns [not significant] P = 0.1514) or radially (control: ns P = 0.8209; PARD6B: ns P = 0.9290; two-tailed paired t tests).* ***(e)*** *Representative time-lapse images of circumferentially and radially dividing blastomeres undergoing the 16–32 cell division from embryos coexpressing H2B:RFP (magenta) and GAP43:GFP (green) and cultured in Ca^{+2}-free media (example shown for circumferential division has 21 cells and for radial has 19 cells). Magenta dashed lines indicate the location of the apical domain, and yellow dashed lines indicate the regions that do not contain an apical domain.* ***(f)*** *Average distance from initial furrow position at anaphase onset in circumferentially (n = 9 blastomeres from eight embryos) or radially dividing blastomeres (n = 6 blastomeres from six embryos) undergoing the 16–32 cell division from embryos cultured in Ca+2-free media.* ***(g)*** *Total furrow displacement of blastomeres from embryos in F, dividing circumferentially (two-tailed paired t test, *P = 0.0264) or radially (two-tailed paired t test, ns P = 0.2026). Time is shown in minutes, where 0′ is anaphase onset. (Scale bars, 10 μm.) In the box plots, the center line represents the median, the bounds of the box represent upper and lower quartiles, the whiskers represent minimum and maximum values, and dots represent independent measurements.*

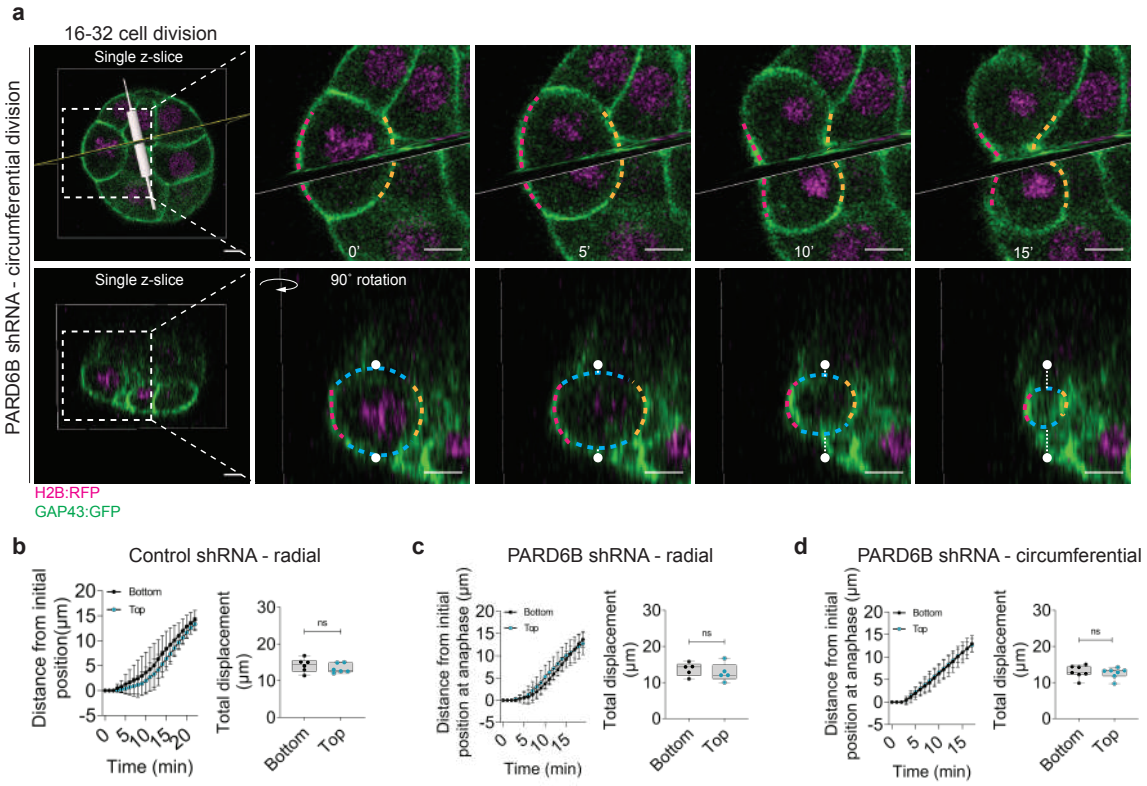

Figure 38. – Three-dimensional analysis of furrow ingression rate (Supplementary Figure 6).

(a) *Representative time-lapse images of a circumferentially-dividing outer blastomere undergoing the 16-32 cell division (example shown has 20 cells) from an embryo previously injected with PARD6B shRNA. In the top row, note that when 2D furrow ingression analysis revealed furrow ingression rate to be approximately equal in both sides of the furrow, the images were rotated 90° in IMARIS and the same analysis was performed using the portions of the furrow that were not originally visible in the 2D plane of image (blue dashed lines).* ***(b-d)*** *Average distance from initial furrow position at anaphase onset and total furrow displacement in radially dividing outer blastomeres undergoing the 16-32 cell division from embryos previously injected with control shRNA (n=6 blastomeres from 5 embryos; two-tailed paired t test, ns P=0.3096)* ***(b)****; radially dividing outer blastomeres undergoing the 16-32 cell division from embryos previously injected with PARD6B shRNA (n=5 blastomeres from 5 embryos; two-tailed paired t test, ns P=0.4402)* ***(c)****; and circumferentially dividing outer blastomeres undergoing the 16-32 cell division from embryos previously injected with PARD6B shRNA (n=7 blastomeres from 5 embryos; two-tailed paired t test, ns P=0.4394)* ***(d)****. Time is shown in minutes, where 0' is anaphase onset. Scale bars = 10µm. In the box plots, the centre line represents the median, the bounds of the box represent upper and lower quartiles, the whiskers represent minimum and maximum values, and dots represent independent measurements. See also Figure 3.*

3.4.4 Apical polarity disrupts the recruitment of furrowing regulators in a cell-autonomous manner.

To understand why the apical domain might slow furrow ingression, we sought to visualize the distribution of cytokinesis components at the contractile ring during cytokinesis in circumferentially dividing outer cells. To do this, we applied a correlative live-fix imaging approach (28, 29), in which we first performed live imaging of control and PARD6B-depleted embryos at the 16–32 cell division expressing H2B:RFP to visualize cytokinesis and then fixed them specifically at midcytokinesis to further perform immunofluorescence of established cytokinesis regulators. Consistent with previous reports (18, 30), a focused apical domain was retained during M-phase in control embryos, as evidenced by the enrichment of polarity protein PKCζ in the apical surface at midcytokinesis (**Fig. 4 A and C**). Strikingly, in control embryos, Anillin and p-Myosin were asymmetrically distributed within the contractile ring, being enriched in regions where it overlapped with the basolateral domain, but substantially decreased where it overlapped with the PKCζ-positive apical domain (apical:basal ratio Anillin: 0.28 ± 0.05; p-Myosin: 0.31 ± 0.05; **Fig. 4 A–D** and **SI Appendix, Fig. S7 A and B**). This asymmetric distribution within the contractile ring was lost upon PARD6B knockdown, wherein the PKCζ-labeled apical domain was no longer evident, and Anillin and p-Myosin became evenly distributed (apical:basal ratio Anillin: 0.86 ± 0.04; p-Myosin: 0.96 ± 0.08; **Fig. 4 A–D; SI Appendix, Fig. S7 A and B**). The sum of fluorescence intensity of both apical and basal sides was similar between control (Anillin: 87.78 ± 16.41 arbitrary units [a.u.]; p-Myosin: 126.6 ± 12.86 a.u.) and PARD6B-depleted embryos (Anillin: 103.9 ± 22.48 a.u. P = 0.6881; p-Myosin: 118.7 ± 15.08 a.u. P = 0.7006; **SI Appendix, Fig. S7 C and D**), suggesting that the impact of polarity emergence was to bias the localization of Anillin and p-Myosin rather than affect their overall levels. To address whether asymmetric distribution of cytokinesis regulators could be mediated by cell adhesion rather than apical polarity, we performed correlative live-fix imaging of embryos at the 16–32 cell division treated with Ca^{+2}-free media to abolish cell adhesion and assessed the levels of Anillin at the contractile ring by immunofluorescence. Notably, Anillin was substantially underrepresented where the contractile ring overlapped with the apical domain and enriched at the basal side (Anillin apical:basal ratio: 0.35 ± 0.04; significant deviation from 1, $P < 0.0001$; **Fig. 4 E and F and SI Appendix, Fig. S7E**). These results corroborate the notion that the inhibitory effect of apical

polarity on the cytokinetic machinery is a cell-autonomous effect that is not dependent on cell–cell contacts (**Fig. 4G**). The asymmetric localization of cytokinesis components was observed exclusively in dividing blastomeres undergoing cytokinesis, whereas interphase localization of Anillin (nuclear) and p-Myosin (undetectable/cytoplasmic) remained unaffected (**Fig. 4 A, C, and E**, third panels), suggesting that the apical domain most likely impacts the localization of cytokinesis components solely during cytokinesis. Thus, the emergence of the apical domain in outer cells prevents accumulation of cytokinesis components including Anillin and p-Myosin during cytokinesis, leading to an unbalanced furrow ingression which is slowed specifically on the apical side.

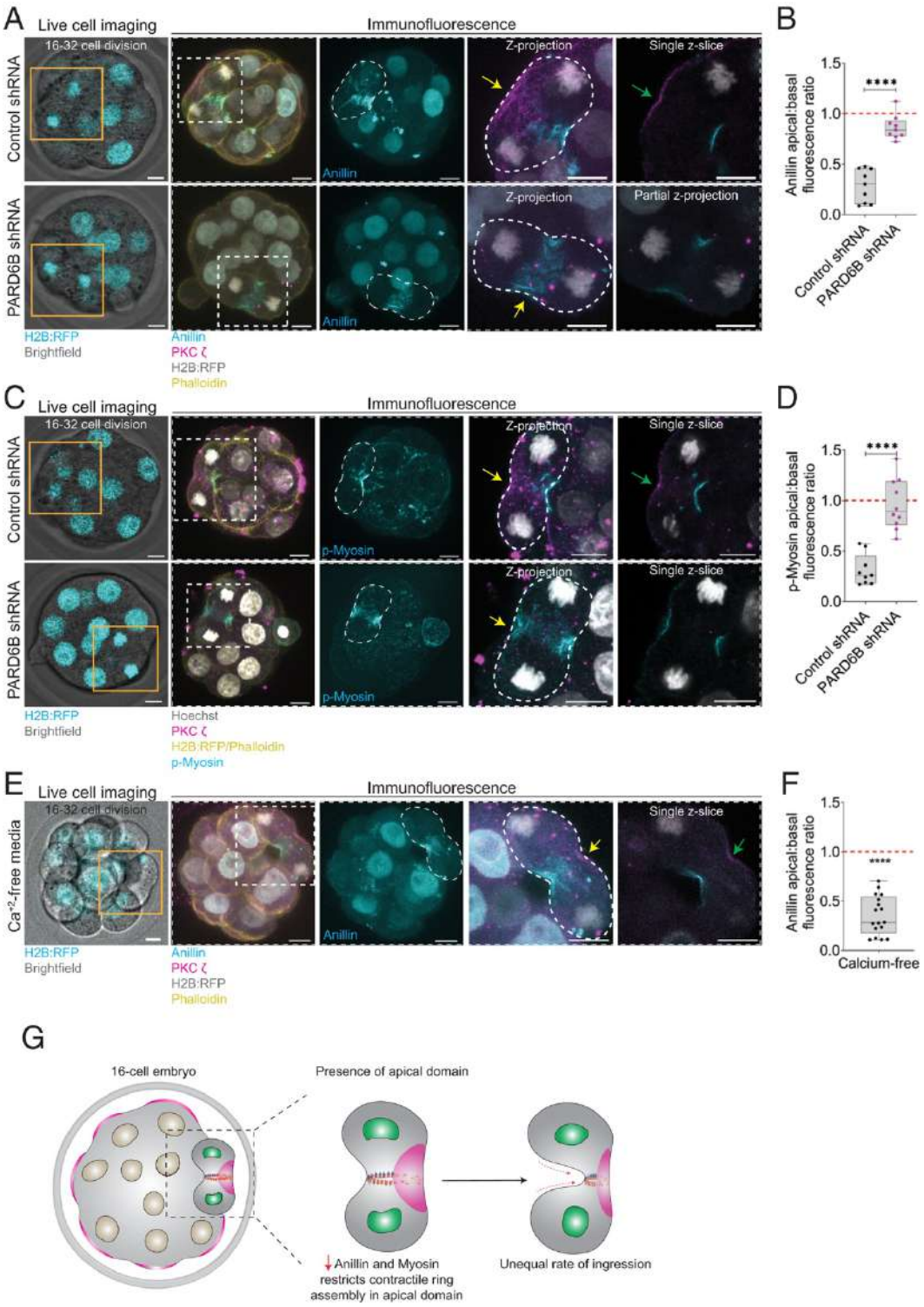

Figure 39. – Apical polarity disrupts the recruitment of furrowing regulators independently of cell adhesion (Figure 4).

(a and c) *Representative live and immunofluorescence images of circumferentially dividing blastomeres undergoing the 16–32 cell division from embryos previously injected with control (example shown in A has 19 cells and in C has 16 cells) or PARD6B shRNA (example shown in A has 16 cells and in C has 16 cells). Note that both Anillin* ***(a)*** *and p-Myosin* ***(c)*** *are underrepresented at the side of contractile ring that overlaps with the apical domain in controls, and this bias is abolished upon PARD6B depletion (yellow arrows). Also note that the apical domain is intact during division in controls (green arrows).* ***(b)*** *Apical:basal fluorescence ratio of Anillin in outer blastomeres undergoing the 16–32 cell division from embryos previously injected with control (n = 9 blastomeres from nine embryos) or PARD6B shRNA (n = 9 blastomeres from nine embryos; unpaired two-tailed t test, ****P < 0.0001).* ***(d)*** *Apical:basal fluorescence ratio of p-Myosin in outer blastomeres undergoing the 16–32 cell division from embryos previously injected with control (n = 9 blastomeres from nine embryos) or PARD6B shRNA (n = 10 blastomeres from 10 embryos; unpaired two-tailed t test, ****P < 0.0001).* ***(e)*** *Representative live and immunofluorescence images of a circumferentially dividing blastomere undergoing the 16–32 cell division from a H2B:RFP-expressing embryo cultured in Ca^{+2}-free media, in which the furrow overlaps with the apical domain (example has 16 cells). Note that Anillin was underrepresented at the apical side (yellow arrow) and the apical domain is intact during division (green arrow).* ***(f)*** *Apical:basal fluorescence ratio of Anillin in outer blastomeres undergoing the 16–32 cell division from embryos cultured in Ca+2-free media (n = 17 blastomeres from 17 embryos, one-sample t test, ****P < 0.0001 significant deviation from 1).* ***(g)*** *Model for local regulation of ring constriction by the apical domain. In intact 16-cell embryos, apical polarity restricts the access of Anillin and p-Myosin to the contractile ring in circumferentially dividing outer cells, thereby slowing furrow ingression specifically on the side of the contractile ring that overlaps with the apical domain. Time is shown in minutes, where 0′ is anaphase onset. (Scale bars, 10 μm.) In the box plots, the center line represents the median, the bounds of the box represent upper and lower quartiles, the whiskers represent minimum and maximum values, and dots represent independent measurements.*

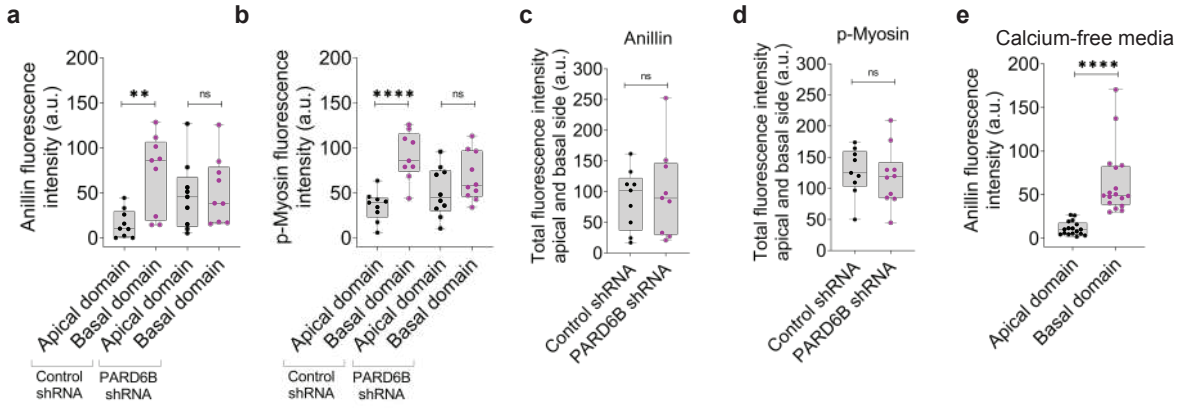

Figure 40. – Anillin and p-Myosin are asymmetrically distributed in outer blastomeres (Supplementary Figure 7).

(a) *Background-subtracted fluorescence intensity of Anillin in apical vs basal sides in outer blastomeres undergoing the 16-32 cell division from embryos previously injected with control (n=9 blastomeres from 9 embryos two-tailed paired t test, **P=0.004) or PARD6B shRNA (n=9 blastomeres from 9 embryos; two-tailed paired t test, P=0.2946).* ***(b)*** *Background-subtracted fluorescence intensity of p-Myosin in apical vs basal sides in outer blastomeres undergoing the 16-32 cell division from embryos previously injected with control (n=9 blastomeres from 9 embryos; two-tailed paired t test, ****P<0.0001) or PARD6B shRNA (n=10 blastomeres from 10 embryos; two-tailed paired t test, P=0.0706).* ***(c)*** *Total (sum) Anillin fluorescence intensity in apical and basal sides of the contractile ring in blastomeres undergoing the 16-32 cell division from embryos previously injected with either control (n = 9 blastomeres from 9 embryos) or PARD6B shRNA (n = 9 blastomeres from 9 embryos; two-tailed unpaired t test, P=0.6881).* ***(d)*** *Total (sum) p-Myosin fluorescence intensity in apical and basal sides of the contractile ring in blastomeres undergoing the 16-32 cell division from embryos previously injected with either control (n = 9 blastomeres from 9 embryos) or PARD6B shRNA (n =10 blastomeres from 10 embryos; two-tailed unpaired t test, P=0.7006).* ***(e)*** *Background-subtracted fluorescence intensity of Anillin in apical vs basal sides in outer blastomeres undergoing the 16-32 cell division from embryos cultured in Ca^{+2}-free media (n= 17 blastomeres from 17 embryos, two-tailed paired Wilcoxon test, ****P<0.0001). In the box plots, the centre line represents the median, the bounds of the box represent upper and lower quartiles, the whiskers represent minimum and maximum values, and dots represent independent measurements. See also Figure 4.*

3.5 Discussion

Exploiting multiple well-characterized developmental transitions in the early mouse embryo, our work delineates two powerful influences on furrow ingression speed, both of which have broad ramifications for our understanding of the mechanism of ring ingression in diverse cell types. First, our data show a strong influence of cell size on furrow ingression from the 8–16 cell division onward. A similar cell-size to cytokinesis speed correlation in *C. elegans* (9–12) and *N. crassa* (13) was previously proposed as evidence that the contractile ring is locally regulated, bigger rings contracting more quickly because they comprise larger numbers of locally regulated units that disassemble during furrowing. Our results extend the relationship between cell size and furrowing speed to the mouse preimplantation embryo. The insensitivity of furrowing speed to cell size from the 1–2 to 8–16 cell divisions suggests an upper limit of cell size beyond which furrowing speed cannot be further scaled up, and it is possible that this upper limit is not reached in one-cell *C. elegans* embryos which are more similar in volume to eight-cell-stage mouse blastomeres. An upper limit has been previously shown to restrict the scaling of spindle length in *Xenopus laevis* (31) and *C. elegans* embryos (32, 33). Given that the speed of chromosome separation and spindle

elongation during anaphase is reduced from the eight-cell stage onward (34), altered furrowing speed may help avoid chromosome segregation error at later developmental stages.

Second, restricted furrowing in the apical domain was found to be the result of limited access of contractile ring components. This effect of the apical domain is independent of its role on cell fate determination, as determined by a lack of effect of TEAD4-knockdown (**SI Appendix, Fig. S5**), and consistent with this we also found a failure in the recruitment of Anillin and p-Myosin to the apical side of the contractile ring in circumferentially dividing blastomeres at the 8–16 cell division, in which apical polarity has already been established but cell fate is not yet determined (**SI Appendix, Fig. S8**). Limited myosin levels at the apical surface have also been observed in nondividing outer blastomeres and are thought to influence cell position and cell fate specification by reducing contractility to limit outer cell internalization and thus ensure adequate proportions of inner and outer blastomeres (35). Although the abundance of cytokinetic components has been previously correlated with ingression speed in asymmetrically ingressing furrows (5, 36, 37), our unexpected discovery that a similar bias in mouse embryos is due to the emergence of the apical domain allowed us to experimentally relieve that bias, and therein show directly that the abundance of Anillin and p-Myosin determines furrow ingression speed. Whether the inhibitory effect of polarity also affects other tissues in the mouse remains to be addressed. Nonetheless this series of experiments provide some of the strongest evidence that cell-autonomous subcellular organization can dictate local regulation of furrow ingression (**Fig. 4G**).

Our data also demonstrate that the inhibitory impact of the apical domain upon furrow ingression is not dependent on cell contacts, as embryos devoid of cell adhesion also display a basal-to-apical ingression bias and reduced Anillin localization to the apical side. This is distinct from previously noted links between furrowing and cell polarity described in *D. melanogaster* polarized epithelial cells, wherein cell adhesion promotes an anchoring of the contractile ring to E-cadherin complexes and reduce furrow ingression at the apical side independently of apical polarity (6). The phenomenon described herein is also distinct from that observed in *C. elegans* zygotes wherein apical PAR proteins promote the retention of Anillin and Septin at the anterior pole during an asymmetric division, possibly as a means to prevent an overload of cytokinesis regulators in the ingressing furrow in the first cell division (7). Why cytokinesis regulators are chased from the apical cortex during cytokinesis in mouse blastomeres remains to be determined, but an intriguing

precedent is found in the observation that ECT2, the GEF responsible for activating cytokinesis master-regulator RhoA, and RhoA downstream effectors Rock1/2 can interact with polarity proteins (38, 39), albeit that whether these interactions might result in an inhibitory effect on cytokinesis components remains to be addressed. Alternatively, unidentified apical domain components may outcompete cytokinesis components for limited membrane binding sites. Our experiments highlight the complexity of furrow ingression regulation and underscore that cellular contexts and asymmetries can have stark impacts upon the mechanisms of cytokinesis.

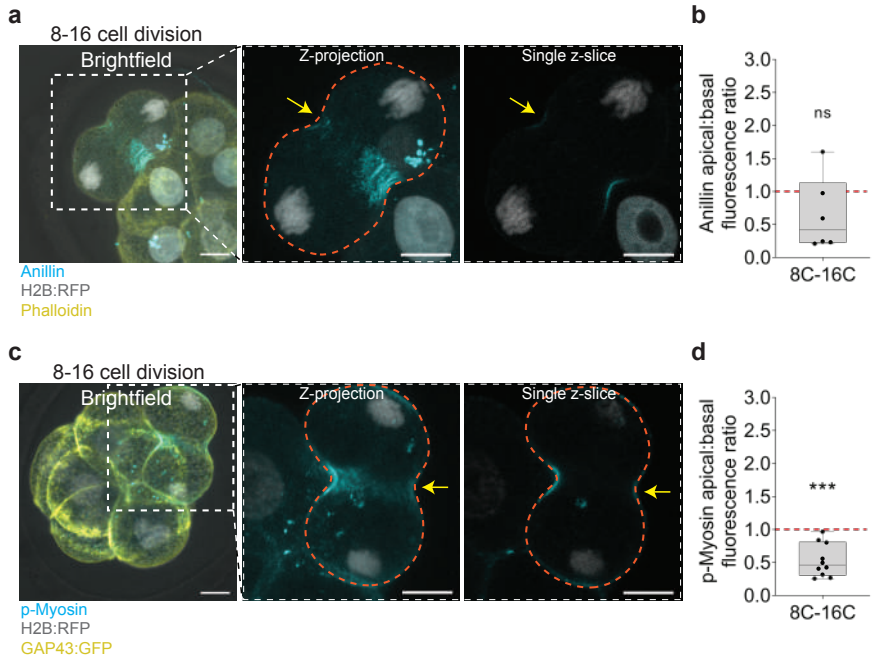

Figure 41. – Anillin and p-Myosin are underrepresented in the apical side of the contractile ring in circumferentially dividing 8-cell blastomeres. (Supplementary Figure 8).

(a and c) *Representative immunofluorescence images of circumferentially dividing blastomeres undergoing the 8-16 cell division (examples shown both in (a) and (c) have 8 cells each). Note that both Anillin* ***(a)*** *and p-Myosin* ***(c)*** *are underrepresented at the side of the contractile ring that overlaps with the apical domain (yellow arrows).* ***(b)*** *Anillin apical:basal fluorescence ratio in blastomeres undergoing the 8-16 cell division (n=6 blastomeres from 6 embryos; one-sample t test, P=0.1762).* ***(d)*** *p-Myosin apical:basal fluorescence ratio in blastomeres undergoing the 8-16 cell division (n=10 blastomeres from 10 embryos; one-sample t test, ***P=0.0003, significant deviation from 1). Scale bars = 10µm. In the box plots, the centre line represents the median, the bounds of the box represent upper and lower quartiles, the whiskers represent minimum and maximum values, and dots represent independent measurements.*

3.6 Materials and Methods

3.6.1 Experimental model

All experiments performed followed the guidelines for animal experimentation and were approved by the Comité Institutionnel de Protection des Animaux of the Centre de Recherche du Centre Hospitalier de l'Université de Montréal (protocol number: IP18034GFs). The female mice used in this study were 2- to 3-mo-old CD1 [Crl:CD1(ICR) 022CD1] and male mice were 3- to 12-mo-old BDF1 (B6D2F1/J 100006). All animals were kept in individually ventilated cages (up to five animals per cage for the females and one animal per cage for the males) at 22 ± 2 °C, 40 to 60% humidity in 12-h light/dark cycles with lights switched on from 6:30 AM to 6:30 PM and food and water available for *ad libitum* consumption.

3.6.2 Embryo collection and culture

Two-cell embryos were harvested from previously superovulated 2- to 3-mo-old female CD1 mice mated with BDF1 male mice, except for the experiment in Fig. 1 A–D (one-cell stage group), in which embryos were harvested at the zygote stage. Embryos were collected in homemade M2 media and cultured in KSOM (MR-020P-5F; EMD Millipore) in 5% CO_2 at 37 °C. For experiments in Figs. 2 D and E, 3 E–G, 4 E and F, and SI Appendix, Fig. S4, 16-cell embryos were exposed to either complete homemade KSOM or Ca^{+2}-free homemade KSOM (SI Appendix, Table S1) during the 16–32 cell division.

3.6.3 Messenger RNA, shRNA and dsRNA production

Messenger RNA (mRNA) was synthesized using Ambion mMessage Machine T3 (AM1348) or SP6 (AM1340) according to the manufacturer's instructions from the following plasmids: H2B:RFP in pRN4 (gift from Alex McDougal, Observatoire Océanologique de Villefranche sur Mer, Villefranche sur Mer, France) and GAP43:GFP in psC2 (gift from Yojiro Yamanaka, McGill University, Montréal, Canada). Knockdown of PARD6B via shRNA and TEAD4 via dsRNA was performed following previously described protocols (21–23). shRNA plasmids were purchased from Millipore Sigma (Control shRNA SHC002; PARD6B shRNA SHCLND-NM_021409

TRCN0000054687) and purified using QIAGEN Miniprep kit (27106). For dsRNA production, a Tead4 specific PCR primer pair including T7-derived RNApol promoters was used to obtain the in vitro transcription template using mouse blastocyst cDNA (sense; TAATACGACTCACTATAGGGTGTTGGAGTTCTCGGCTTTC, antisense; TAATACGACTCACTATAGGGTCGGTAGATGTGGTGCTGAG, T7-promoter underlined) (23). For the control group, a GFP specific dsRNA was produced with PCR primers including a T7 promoter (sense; TAATACGACTCACTATAGGGAGAGTACAAATTTTCTGTCAGTGGAGAGG, antisense; TAATACGACTCACTATAGGGAGATGTATAGTTCATCCATGCCATGTGTA, T7-promoter underlined) (23) using pcDNA3.1 plasmid vector containing a GFP sequence as a template. Tead4 and GFP specific double-stranded RNA synthesis was performed using Ambion mMessage Machine T7 (AM1344) according to the manufacturer's instructions.

3.6.4 Microinjection, cytoplasmic removal, and enucleation.

Cytoplasmic microinjection of mRNAs or dsRNAs in two-cell embryos or zygotes was performed in M2 media (M7167; Sigma) using a picopump (World Precision Instruments) and micromanipulators (Narishige) mounted on a Leica DMI4000 inverted microscope (40). For shRNA microinjections in Figs. 2 F–I, 3 B–D, 4 A–D, and SI Appendix, Figs. S6 and S7, shRNA plasmids were microinjected directly inside both nuclei of two-cell embryos. Prior to microinjection, shRNA plasmids were diluted to 20 ng/μL in homemade microinjection buffer (5 mM Tris pH 7.4 and 0.1 mM ethylenediaminetetraacetic acid) and Fluorescein Dextran 70 kDa (FD70S; Sigma) 0.01 mg/mL was added to the solution to confirm that the shRNA was successfully injected in the nucleus. Cytoplasmic removal in Fig. 1 E–H and SI Appendix, Fig. S2 was performed as previously described (41) and enucleation in Fig. 1 I–L and SI Appendix, Fig. S3 was adapted from a previous report (15). Hydraulic-controlled glass pipettes mounted on a Piezo-electric drill were used to perforate the zona pellucida of embryos and aspirate either the nucleus (for enucleation) or the cytoplasm without perturbing the nucleus. These procedures were performed in M2 media supplemented with Latrunculin A 5 μM (428021; EMD Millipore). After cytoplasmic removal, at the four-cell stage, sham-manipulated blastomeres displayed on average 32.61 ± 0.24 pL of volume, whereas blastomeres with reduced cytoplasmic size displayed 19.31 ±

0.57 pL (SI Appendix, Fig. S2D; average volume reduction of ~40.8%). At the eight-cell stage, sham-manipulated blastomeres displayed on average 16.52 ± 0.74 pL of volume, whereas blastomeres with reduced cytoplasmic size displayed 10.02 ± 0.29 pL (SI Appendix, Fig. S2G; average volume reduction of ~40.4%). Embryos were thoroughly washed through at least 10 drops of KSOM prior to being transferred to and cultured in clean KSOM drops prior to imaging.

3.6.5 Immunofluorescence and live imaging.

Embryos were fixed in 2% paraformaldehyde (P6148; Sigma) diluted in phosphate-buffered saline (PBS) for 20 min followed by 10-min permeabilization using 0.25% Triton X-100 (T9284; Sigma) diluted in PBS and a blocking step with 3% bovine serum albumin (A7906; Sigma) diluted in PBS for either 1 h at 37 °C or overnight at 4 °C (41). Primary antibodies used were PKC ζ anti-mouse 1:100 (sc-17781; Santa Cruz), Anillin anti-rabbit 1:300 (gift from Alisa Piekny, Concordia University, Montréal, Canada); p-Myosin light chain II anti-rabbit 1:100 (3671T; Cell Signaling Technology), and TEAD4 anti-mouse 1:100 (ab58310; Abcam). Hoechst 33342 (1:1,000) (H1399; Invitrogen) was used for DNA labeling and Alexa-labeled secondary antibodies (1:1,000) were purchased from Thermo Fisher. Alexa Fluor 555 Phalloidin (A34055) and Alexa Fluor 647 Phalloidin (A22287) conjugated antibodies (1:200) were purchased from Invitrogen.

Immunofluorescence imaging was performed on a Leica SP8 confocal microscope fitted with a 63× 1.4 numerical aperture oil objective, HyD and PMT detectors and images were acquired using 1.5-µm optical sections and z-stack step size of 1.5 µm. Live imaging was performed on a Leica SP8 confocal microscope fitted with a 20× 0.75 numerical aperture air objective, HyD and PMT detectors and images were acquired with 1-min time intervals using 2.0-µm optical sections and z-stack step size of 2.0 µm. For experiments in Fig. 4, a correlative live and immunofluorescence imaging approach was used as described previously (28), wherein embryos expressing H2B:RFP were subjected to live imaging on either a Leica SP8 confocal microscope fitted with a 20× 0.75 numerical aperture air objective, HyD and PMT detectors or a Zeiss Axio observer equipped with an Axiocam and 20× 0.5 numerical aperture air objective and light-emitting diode light to observe ongoing cell divisions and fixed individually at midcytokinesis (~9 min postanaphase onset) for further immunofluorescence imaging. For all live imaging, embryos were

placed on a heated stage top incubator with 5% CO2 supply at 37 °C and imaged in 3-µL drops of pre-equilibrated KSOM.

3.6.6 Image analysis and interpretation.

Measurements of contractile ring perimeter were performed using IMARIS 9.3 (Bitplane; Oxford Instruments). Using the Oblique Slicer function of IMARIS, the images were slightly rotated and oriented such that the contractile ring was seen from a "face-on" position in a single z-slice and measurements were performed using the Measurement Point function to manually trace the outline of the contractile ring at each timepoint (every 1 min). The contractile ring perimeter was defined as the sum of distances between each Measurement Point outline around the contractile ring. For one-cell embryos, cell divisions always took place such that the contractile ring was parallel from the image plane, and therefore image rotation was deemed not appropriate due to limitations on z-step size resolution that caused deformations on the image and therefore, contractile ring perimeter was calculated based on measurements of ring diameter obtained from a single z-slice and applying the following formula $P=\pi\times d$, where P stands for perimeter, π stands for pi, and d stands for diameter. The duration of cytokinesis was measured as the time between the first frame at which a perimeter decrease was first observed (defined as 5% decrease), until the last frame at which a contractile ring was clearly visible and the perimeter reliably measurable.

Analysis of distance from initial furrow position in Fig. 3 was performed using a single middle z-slice where both sides of the furrow were visible simultaneously. Only blastomeres that were dividing parallel to the coverslip were analyzed. When furrow ingression rate was approximately equal between both sides of the furrow, the images were rotated in IMARIS, and the same analysis was performed using the portions of the furrow that were not visible in the original plane of analysis to confirm that no bias in furrow ingression was present from another plane (SI Appendix, Fig. S6). For measurements of furrow ingression of radial cell divisions in Fig. 3, since no apical and basal sides are present "side 1" was determined as the side of the furrow that was closer to the top of the image in the XY plane and side 2 as the side closer to the bottom of the image.

All experiments involving comparisons of fluorescence intensity between embryos were performed under strictly controlled conditions—simultaneous immunostaining of different

samples, same antibody aliquots, concentrations, temperature, time of incubation, as well as confocal imaging performed simultaneously (on the same day) and with identical imaging settings. All fluorescence intensity measurements were performed using Fiji/ImageJ. Apical:basal fluorescence ratios presented in Figs. 2 F and G and 4 A–F and SI Appendix, Figs. S2 H–I, S4 B and C, and S8 were calculated using apical and basal maximum gray values from a single z-slice. Background-subtracted total fluorescence intensity (Raw Integrated Density) measurements obtained from a single middle z-slice were used for analysis of apical vs. basal levels of Anillin and p-Myosin in SI Appendix, Fig. S7. For confirmation of TEAD4 knockdown efficiency in SI Appendix, Fig. S5 A and B, nuclear:cytoplasmic ratios were calculated using total fluorescence intensity (Raw Integrated Density) measurements in the nucleus or cytoplasm. For analysis of apical vs. basal levels of PKC ζ and confirmation of TEAD4 knockdown, between 2 and 13 inner and outer blastomeres were quantified per embryo in each group and the data displayed is an average per embryo. For cell volume measurements in SI Appendix, Fig. S2 D and G, the areas delineated by the cell membrane (GAP43:GFP) were manually traced and measured in each z-slice in blastomeres prior to mitotic entry and the sum of areas was multiplied by the step size (2 μm) to obtain the volume in cubic micrometers and further converted to picoliters, as previously described (41).

For the live-imaging experiments, circumferential cell divisions were classified as those in which the dividing outer cell generated two new outer-residing cells immediately after cytokinesis completion, whereas radial cell divisions were considered as those in which the dividing outer cell generated one new outer-residing and one new inner-residing cell immediately following cytokinesis completion.

3.6.7 Statistical analysis

All statistical analyses were performed using GraphPad Prism (https://www.graphpad.com/). Shapiro–Wilk normality tests were applied and either parametric or nonparametric statistical tests were applied accordingly. For data encompassing multiple comparisons, either unpaired one-way ANOVA or unpaired Kruskal–Wallis tests corrected for multiple comparisons were applied. For data encompassing two comparisons, either unpaired two-tailed t tests or unpaired two-tailed Mann–Whitney U tests were applied. For analyses of total furrow displacement (Fig. 3 D and G

and SI Appendix, Fig. S6), background-subtracted fluorescence intensity of Anillin and p-Myosin (SI Appendix, Fig. S7), either paired two-tailed t test or paired Wilcoxon test were applied. For analyses in Fig. 4F and SI Appendix, Fig. S8 B and D, one-sample t test was applied for calculations of significant deviation from 1. For SI Appendix, Fig. S2J, simple linear regression analysis was applied. Statistical significance was considered when $P < 0.05$.

3.7 Acknowledgments

This work was funded by grants from the Natural Sciences and Engineering Research Council of Canada, Fondation Jean-Louis Lévesque, Canadian Foundation for Innovation, and the Canadian Institutes of Health Research. L.M.G.P. is supported by a Fonds de Recherche du Québec—Santé Doctoral Scholarship. We thank Drs. Jean-Claude Labbé, Gilles Hickson, and Tim Davies for comments on the manuscript as well as the members of the G.F., Labbé, Hickson, and Gerhold laboratories for constructive discussions. We also thank Gaudeline Rémillard-Labrosse and Aurélie Cleret-Buhot for excellent technical support.

3.8 References

1. F. A. Barr, U. Gruneberg, Cytokinesis: Placing and making the final cut. Cell 131, 847–860 (2007).

2. R. A. Green, E. Paluch, K. Oegema, Cytokinesis in animal cells. Annu. Rev. Cell Dev. Biol. 28, 29–58 (2012).F. A. Barr, U. Gruneberg, Cytokinesis: placing and making the final cut. *Cell* **131**, 847-860 (2007).

3. E. Morais-de-Sá, C. Sunkel, Adherens junctions determine the apical position of the midbody during follicular epithelial cell division. EMBO Rep. 14, 696–703 (2013).

4. C. Thieleke-Matos, D. S. Osório, A. X. Carvalho, E. Morais-de-Sá, Emerging mechanisms and roles for asymmetric cytokinesis. Int. Rev. Cell Mol. Biol. 332, 297–345 (2017).

5. N. Founounou, N. Loyer, R. Le Borgne, Septins regulate the contractility of the actomyosin ring to enable adherens junction remodeling during cytokinesis of epithelial cells. Dev. Cell 24, 242-255 (2013).

6. C. Guillot, T. Lecuit, Adhesion disengagement uncouples intrinsic and extrinsic forces to drive cytokinesis in epithelial tissues. Dev. Cell 24, 227-241 (2013).

7. S. N. Jordan et al., Cortical PAR polarity proteins promote robust cytokinesis during asymmetric cell division. J. Cell Biol. 212, 39-49 (2016).

8. C. Cabernard, K. E. Prehoda, C. Q. Doe, A spindle-independent cleavage furrow positioning pathway. Nature 467, 91-94 (2010).

9. K. G. Bourdages, B. Lacroix, J. F. Dorn, C. P. Descovich, A. S. Maddox, Quantitative analysis of cytokinesis in situ during C. elegans postembryonic development. PLoS One 9, e110689 (2014).

10. A. Carvalho, A. Desai, K. Oegema, Structural memory in the contractile ring makes the duration of cytokinesis independent of cell size. Cell 137, 926-937 (2009).

11. R. N. Khaliullin et al., A positive-feedback-based mechanism for constriction rate acceleration during cytokinesis in Caenorhabditis elegans. eLife 7, e36073 (2018).

12. A. M. Silva et al., Robust gap repair in the contractile ring ensures timely completion of cytokinesis. J. Cell Biol. 215, 789-799 (2016).

13. M. E. Calvert et al., Myosin concentration underlies cell size-dependent scalability of actomyosin ring constriction. J. Cell Biol. 195, 799-813 (2011).

14. X. Ma et al., Nonmuscle myosin II exerts tension but does not translocate actin in vertebrate cytokinesis. Proc. Natl. Acad. Sci. U.S.A. 109, 4509-4514 (2012).

15. E. Tsichlaki, G. FitzHarris, Nucleus downscaling in mouse embryos is regulated by cooperative developmental and geometric programs. Sci. Rep. 6, 28040 (2016).

16. C. Chazaud, Y. Yamanaka, Lineage specification in the mouse preimplantation embryo. Development 143, 1063-1074 (2016).

17. J. L. Maître, R. Niwayama, H. Turlier, F. N ed elec, T. Hiiragi, Pulsatile cell-autonomous contractility drives compaction in the mouse embryo. Nat. Cell Biol. 17, 849-855 (2015).

18. R. Niwayama et al., A tug-of-war between cell shape and polarity controls division orientation to ensure robust patterning in the mouse blastocyst. Dev. Cell 51, 564-574.e6 (2019).

19. M. H. Johnson, J. C. Chisholm, T. P. Fleming, E. Houliston, A role for cytoplasmic determinants in the development of the mouse early embryo? J. Embryol. Exp. Morphol. 97 (suppl.), 97-121 (1986).

20. M. H. Johnson, C. A. Ziomek, Cell interactions influence the fate of mouse blastomeres undergoing the transition from the 16- to the 32-cell stage. Dev. Biol. 95, 211-218 (1983).

21. V. B. Alarcon, Cell polarity regulator PARD6B is essential for trophectoderm formation in the preimplantation mouse embryo. Biol. Reprod. 83, 347-358 (2010).

22. Y. Hirate et al., Polarity-dependent distribution of angiomotin localizes Hippo signaling in preimplantation embryos. Curr. Biol. 23, 1181-1194 (2013).

23. A. I. Mihajlovi c, V. Thamodaran, A. W. Bruce, The first two cell-fate decisions of preimplantation mouse embryo development are not functionally independent. Sci. Rep. 5, 15034 (2015).

24. S. Anani, S. Bhat, N. Honma-Yamanaka, D. Krawchuk, Y. Yamanaka, Initiation of Hippo signaling is linked to polarity rather than to cell position in the pre-implantation mouse embryo. Development 141, 2813–2824 (2014).

25. J. Rossant, P. P. Tam, Blastocyst lineage formation, early embryonic asymmetries and axis patterning in the mouse. Development 136, 701–713 (2009).

26. T. Frum, A. Ralston, "Pluripotency—What does cell polarity have to do with it?" in Cell Polarity in Development and Disease, P. M. Conn, D. W. Houston, Eds. (Elsevier, 2018), chap. 2, pp. 31–60.

27. S. Reinsch, E. Karsenti, Orientation of spindle axis and distribution of plasma membrane proteins during cell division in polarized MDCKII cells. J. Cell Biol. 126, 1509–1526 (1994).

28. C. Vázquez-Diez, G. FitzHarris, Correlative live imaging and immunofluorescence for analysis of chromosome segregation in mouse preimplantation embryos. Methods Mol. Biol. 1769, 319–335 (2018).

29. C. Vázquez-Diez, K. Yamagata, S. Trivedi, J. Haverfield, G. FitzHarris, Micronucleus formation causes perpetual unilateral chromosome inheritance in mouse embryos. Proc. Natl. Acad. Sci. U.S.A. 113, 626–631 (2016).

30. E. Korotkevich et al., The apical domain is required and sufficient for the first lineage segregation in the mouse embryo. Dev. Cell 40, 235–247.e7 (2017).

31. M. W€uhr et al., Evidence for an upper limit to mitotic spindle length. Curr. Biol. 18, 1256–1261 (2008).

32. G. Greenan et al., Centrosome size sets mitotic spindle length in Caenorhabditis elegans embryos. Curr. Biol. 20, 353–358 (2010).

33. Y. Hara, A. Kimura, Cell-size-dependent spindle elongation in the Caenorhabditis elegans early embryo. Curr. Biol. 19, 1549–1554 (2009).

34. K. Yamagata, G. FitzHarris, 4D imaging reveals a shift in chromosome segregation dynamics during mouse pre-implantation development. Cell Cycle 12, 157–165 (2013).

35. J. L. Maître et al., Asymmetric division of contractile domains couples cell positioning and fate specification. Nature 536, 344–348 (2016).

36. A. S. Maddox, L. Lewellyn, A. Desai, K. Oegema, Anillin and the septins promote asymmetric ingression of the cytokinetic furrow. Dev. Cell 12, 827–835 (2007).

37. S. Herszterg, A. Leibfried, F. Bosveld, C. Martin, Y. Bellaiche, Interplay between the dividing cell and its neighbors regulates adherens junction formation during cytokinesis in epithelial tissue. Dev. Cell 24, 256–270 (2013).

38. X. F. Liu, H. Ishida, R. Raziuddin, T. Miki, Nucleotide exchange factor ECT2 interacts with the polarity protein complex Par6/Par3/protein kinase Czeta (PKCzeta) and regulates PKCzeta activity. Mol. Cell. Biol. 24, 6665–6675 (2004).

39. A. I. Mihajlović, A. W. Bruce, Rho-associated protein kinase regulates subcellular localisation of Angiomotin and Hippo-signalling during preimplantation mouse embryo development. Reprod. Biomed. Online 33, 381–390 (2016).

40. G. Fitzharris, A shift from kinesin 5-dependent metaphase spindle function during preimplantation development in mouse. Development 136, 2111–2119 (2009).

41. C. Vázquez-Diez, L. M. G. Paim, G. FitzHarris, Cell-size-independent spindle checkpoint failure underlies chromosome segregation error in mouse embryos. Curr. Biol. 29, 865–873.e3 (2019).

Chapter 4 – The impact of embryo binucleation depends upon its origin

Lia Mara Gomes Paim[1] and Greg FitzHarris[1,2]

[1]Centre de Recherche du Centre Hospitalier de l'Université de Montréal, Montréal, Québec, Canada and

[2]Département d'Obstétrique-Gynécologie, Université de Montréal, Montréal, Québec, Canada

Correspondence should be addressed to G FitzHarris; Email: greg.fitzharris@umontreal.ca

Citation: Paim, L.M.G., FitzHarris, G. The impact of embryo binucleation depends upon its origin. Reproduction 160:1, V1-V4 (2020). https://doi.org/10.1530/REP-20-0188

4.1 Summary

Preimplantation embryos frequently contain binucleated cells, but reports differ as to whether binucleation affects development and whether such embryos should be used clinically. In this Point Of View article, we propose a possible explanation for this disparity: binucleation can arise by distinct routes, one that produces healthy blastomeres and one that directly threatens embryo viability.

4.2 Main text

The success of in vitro fertilisation cycles relies heavily on the choice of the most suitable embryo to be transferred to patients. Despite the emergence in recent years of a myriad of exotic means of embryo testing[373, 374], embryo selection remains mainly based on morphological features observable under the light microscope, such as stage appropriate cell numbers, cytoplasmic fragmentation patterns, and nucleus configuration. Binucleation is the scenario wherein a blastomere within an embryo contains two evenly sized nuclei and is an example of a feature of nuclear morphology that can be seen under a microscope. Note that, in this Point of View article, we refer principally to truly binucleated embryos and not to other types of nuclear aberration such as micronucleation, where cells contain an extra 'mini' nucleus, or multinucleation, where three or

more nuclei are seen in a blastomere. Binucleation is a relatively common phenomenon in human embryos in in vitro fertilisation cycles, with frequencies ranging from 7 to 65% of embryos depending on the stage of development examined (**Hardy et al. 1993, Meriano et al. 2004, Aguilar et al. 2016, Seikkula et al. 2018**). Although it is perhaps intuitive that to have two nuclei in a given cell should be indicative of poor prognosis for the embryo, contrasting and perhaps puzzling results as to the developmental potential and clinical outcomes of these embryos have been reported. Some studies report that the presence of binucleated blastomeres causes decreased developmental potential and implantation rates (**Hardy et al. 1993, Aguilar et al. 2016, Seikkula et al. 2018**). On the other hand, perhaps surprisingly, other reports seem to suggest that embryos containing binucleated blastomeres have relatively normal developmental potential (**Staessen & Van Steirteghem 1998, Meriano et al. 2004**). An explanation for the apparently divergent reports is not apparent, and thus the use of binucleation as a means of embryo selection is not widely implemented. Here, following recent mechanistic studies of cell divisions and nuclear morphology in mouse embryos, we propose that binucleation can originate by two mechanistically distinct routes, depending on whether it occurs at the 2-cell stage or at later stages of development, and that these two routes to binucleation have contrasting implications for embryo health that explain the apparent conflicting reports.

The origins of binucleation in mid-preimplantation development (~16-cell stage) human embryos were studied by Hardy et al. (1993), who found that binucleated blastomeres at the 16-32 cell stage had double the amount of cytoplasm compared to mononucleated counterparts, and thus concluded that binucleated blastomeres arise as a result of a failure of cytokinesis, the final step of cell division. Although other routes to binucleation can be envisaged, such as cell fusion, cytokinesis failure is generally considered the most common route to binucleation in somatic cells, and thus the conclusions of Hardy et al. appear very likely. Cytokinesis failure (or indeed cell fusion) means that the resulting blastomere contains an entire duplicated genome complement (i.e. tetraploid). Consistent with this, complete tetraploidy has been described in spontaneous abortions (**Genest et al. 1995**), as well as in embryos undergoing preimplantation genetic screening (**Bielanska et al. 2002**), and the rare cases of tetraploid live-born infants display severe developmental abnormalities, with a lifespan limited to months (**Stefanova et al. 2010**), indicative that tetraploidy is indeed a feature of early embryo development and poses severe consequences

for fertility and life. Recent mechanistic studies in mouse embryos have uncovered at least two reasons why tetraploid blastomeres in mid- preimplantation development should jeopardise the likelihood of a successful pregnancy. First, it was shown that tetraploidy resulting from cytokinesis failure at the 4–8 cell division increases the rates of chromosome segregation errors and consequently favors the development of further aneuploidy (**Paim & FitzHarris 2019**) (**Fig. 1**). Such errors could lead to the complex and chaotic karyotypes seen in embryo blastomeres which are widely associated with embryonic failure (**Bielanska et al. 2002**). Second, tetraploidy in early mouse embryos has been shown to reduce the number of cells available to form the inner cell mass within the blastocyst that forms the embryo proper (**Eakin et al. 2005, LMG Paim and G FitzHarris, unpublished observations**). Why this decrease in the number of cells takes place is not entirely clear, but it is likely that fewer but larger cells at the time of blastocoel formation reduce the availability of 'inner' cells to form the ICM. Thus, binucleation in later stage embryos likely occurs by cytokinesis failure and threatens embryo viability in at least two ways (**Fig. 1**).

In contrast, a recent examination of the first mitosis (1-cell to 2-cell transition) in mouse leads us to suggest that binucleation at the 2-cell stage in human embryos may arise by an entirely different means. Reichmann et al. (2018) demonstrated that each pronucleus in the mouse zygote originates two spatially separate parental genomes that initially remain individualised during the first mitotic division (**Fig. 1**). As the first mitosis progresses, two independent spindles are assembled (one for each parental genome), which eventually fuse to align the maternal and paternal genome before anaphase. Interestingly, experimentally induced failure to align the two zygotic spindles leads to the formation of perfectly binucleated 2-cell embryos (**Reichmann et al. 2018**) (**Fig. 1**). Although the implications of this were not explored, each nucleus would be haploid and thus each cell should logically be overall diploid. Since binucleated cells can assemble a single spindle and form mononucleated daughter cells (**Paim & FitzHarris 2019**), resulting 4-cell embryos would be expected to be mononucleated, euploid (overall correct chromosome complement), and as such be identical to other 'normal' embryos that were never binucleated (**Fig. 1**). Thus, although it remains to be formally tested, we propose that binucleation at the 2-cell stage under these circumstances likely has minimal impact upon developmental potential.

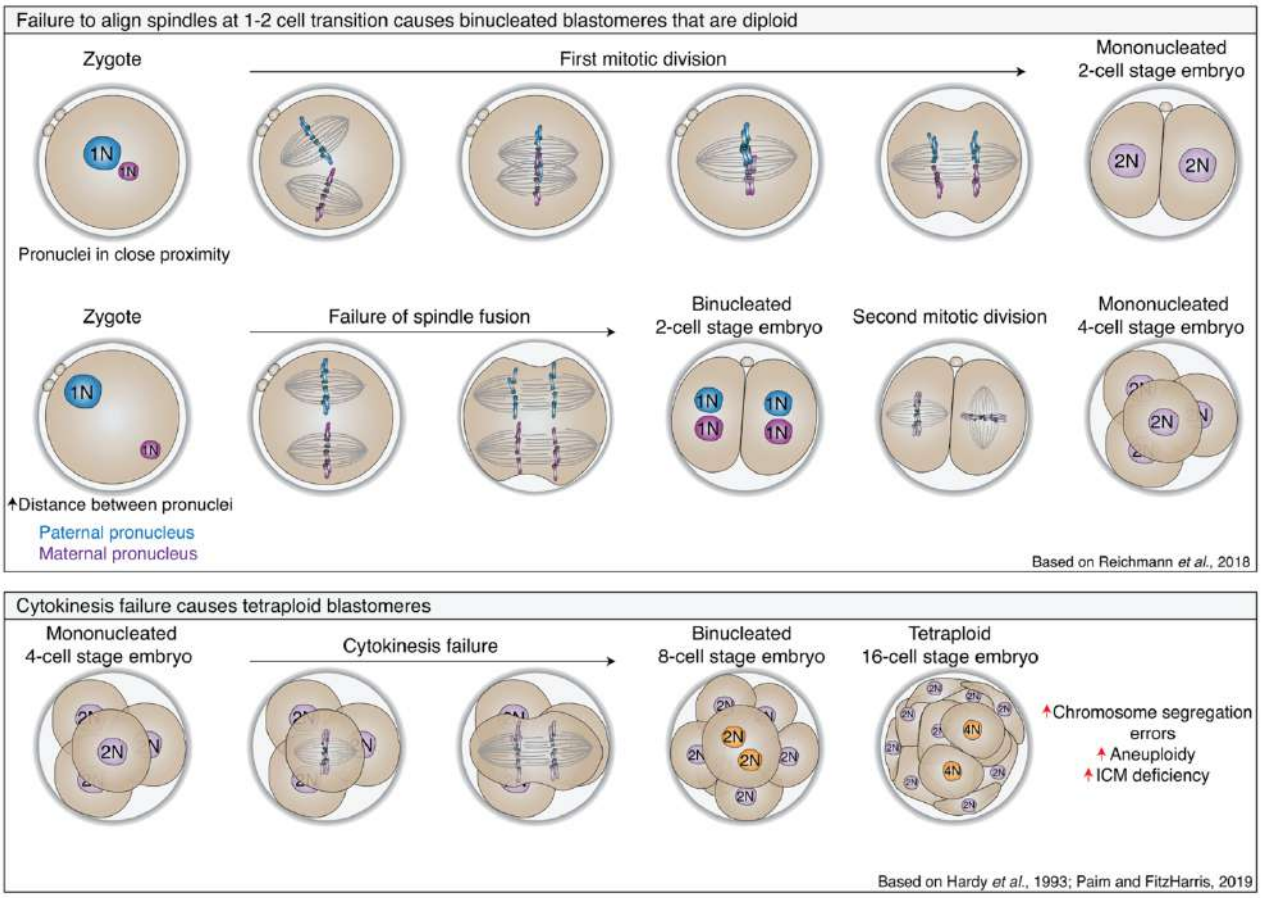

Figure 42. – Two mechanistically distinct modes of binucleation might explain divergent clinical outcomes (Figure 1).

Top panel: At the zygote stage, the paternal and maternal pronuclei are maintained physically separated due to the assembly of two individualized mitotic spindles. Further into the first mitotic division, the spindles fuse such that the parental genome is aligned in a single metaphase plate, allowing cell division to take place, and a diploid mononucleated 2-cell stage embryo is formed. Middle panel: In cases where the two parental pronuclei are too distant from each other, the two individualized spindles fail to fully fuse and cell division takes place without alignment of the parental genomes, resulting in a 2-cell stage embryo with two haploid nuclei. This scenario is likely not deleterious to development, since the resulting 2-cell embryo remains with a diploid genome complement. Bottom panel: Binucleation later in development more likely indicates cytokinesis failure or regression (which may be mistaken optically for cell fusion), which would lead to tetraploidy. This is followed by an increase in the levels of chromosomes segregation errors, allowing for the accumulation of highly aneuploid blastomeres that potentially lead to low implantation rates.

To our knowledge, this explanation to the varied results of clinical binucleation studies mentioned has not previously been proposed. And while the tendency of many clinical studies to group binucleation in conjunction with other forms of nuclear aberration (micronucleation, multinucleation – which themselves very likely have severe consequences for embryo development (**Vazquez-Diez et al. 2016**)) muddies the issue in some cases, close examination of a few key papers lends some support for our proposal. Specifically, Staessen and Van Steirteghem (1998) showed that blastomeres karyotyped at the 3–8 cell stage from embryos previously scored as binucleated at the 2-cell stage are frequently diploid. This strongly supports the notion that the binucleated 2-cell blastomere can be diploid. Perhaps most intriguingly, one study that carefully distinguished binucleated embryos from multinucleated and mononucleated, and then by developmental stage, found that embryos displaying 2/4 binucleated blastomeres at the 4-cell stage never implanted, whereas implantation rates were normal in embryos binucleated at the 2-cell stage (**Aguilar et al. 2016**). The studies described previously (**Staessen & Van Steirteghem 1998, Bielanska et al. 2002**) used karyotyping techniques now considered outdated such as FISH, and further analyses of the ploidy status of binucleated embryos using more reliable modern approaches are certainly warranted. Nevertheless, the findings described by Aguilar et al. (2016), Reichmann et al. (2018), and Paim and FitzHarris (2019) support the notion that binucleation at different stages of development might affect embryo health differently. Therefore, we hypothesise that the discordant conclusions on the impact of binucleation are a result of the different impacts of binucleation at different developmental stages; whereas binucleation in mid- to late-preimplantation development very likely indicates an error of chromosomal content, binucleation at the 2-cell stage may not.

How and why cytokinesis failure comes about, whether a single binucleated/tetraploid blastomere is sufficient to significantly disrupt embryonic development at a given developmental stage, and to what extent embryos can tolerate binucleation/tetraploidy and still give rise to healthy live births, all remain unknown. However, the developments discussed here underscore the importance of foundational molecular research to understand and interpret the biological basis of phenomena observed in the clinic. Non-invasive means of selecting the best embryo(s) for transfer in the clinic remains one of the holy grails of reproductive medicine, and it is our hope that this re-interpretation of the impact of binucleation, paired with improvements in time-lapse microscopy,

may ultimately lead to better paradigms and tools for embryo sorting. Essential in this will be further studies that carefully distinguish the developmental stage at which true binucleation occurs.

4.3 Declaration of interest

G FitzHarris is on the editorial board of Reproduction. G FitzHarris was not involved in the review or editorial process for this paper, on which he is listed as an author. L M Gomes Paim has nothing to disclose.

4.4 Funding

This work did not receive any specific grant from any funding agency in the public, commercial, or not-for-profit sector.

4.5 Author contribution statement

L M G P and G F wrote the manuscript. L M G P produced the figure.

4.6 Acknowledgements

The authors thank Drs Alexander Bruce and Jim Meriano for comments on the manuscript. Work in G F's lab is supported by grants from the Natural Sciences and Engineering Research Council of Canada, Fondation Jean-Louis Lévesque, Canadian Foundation for Innovation, and the Canadian Institutes of Health Research. L M G P is supported by a Fonds de Recherche du Québec – Santé Doctoral Scholarship.

4.7 References

Aguilar J, Rubio I, Munoz E, Pellicer A & Meseguer M 2016 Study of nucleation status in the second cell cycle of human embryo and its impact on implantation rate. *Fertility and Sterility* **106** 291.e2–299.e2. (https://doi.org/10.1016/j.fertnstert.2016.03.036)

Bielanska M, Tan SL & Ao A 2002 Chromosomal mosaicism throughout human preimplantation development in vitro: incidence, type, and relevance to embryo outcome. *Human Reproduction* **17** 413–419. (https://doi.org/10.1093/humrep/17.2.413)

Eakin GS, Hadjantonakis AK, Papaioannou VE & Behringer RR 2005 Developmental potential and behavior of tetraploid cells in the mouse embryo. *Developmental Biology* **288** 150–159. (https://doi. org/10.1016/j.ydbio.2005.09.028)

Genest DR, Roberts D, Boyd T & Bieber FR 1995 Fetoplacental histology as a predictor of karyotype: a controlled study of spontaneous first trimester abortions. *Human Pathology* **26** 201–209. (https://doi. org/10.1016/0046-8177(95)90038-1)

Hardy K, Winston RM & Handyside AH 1993 Binucleate blastomeres in preimplantation human embryos in vitro: failure of cytokinesis during early cleavage. *Journal of Reproduction and Fertility* **98** 549–558. (https://doi.org/10.1530/jrf.0.0980549)

Meriano J, Clark C, Cadesky K & Laskin CA 2004 Binucleated and micronucleated blastomeres in embryos derived from human assisted reproduction cycles. *Reproductive Biomedicine Online* **9** 511–520. (https://doi.org/10.1016/s1472-6483(10)61635-5)

Paim LMG & Fitzharris G 2019 Tetraploidy causes chromosomal instability in acentriolar mouse embryos. *Nature Communications* **10** 4834. (https://doi.org/10.1038/s41467-019-12772-8)

Reichmann J, Nijmeijer B, Hossain MJ, Eguren M, Schneider I, Politi AZ, Roberti MJ, Hufnagel L, Hiiragi T & Ellenberg J 2018 Dual-spindle formation in zygotes keeps parental genomes apart in early mammalian embryos. *Science* **361** 189–193. (https://doi.org/10.1126/science. aar7462)

Seikkula J, Oksjoki S, Hurme S, Mankonen H, Polo-Kantola P & Jokimaa V 2018 Pregnancy and perinatal outcomes after transfer of binucleated or multinucleated frozen-thawed embryos: a case-control study. *Reproductive Biomedicine Online* **36** 607–613. (https://doi. org/10.1016/j.rbmo.2018.02.003)

Staessen C & Van Steirteghem A 1998 The genetic constitution of multinuclear blastomeres and their derivative daughter blastomeres. *Human Reproduction* **13** 1625–1631. (https://doi.org/10.1093/humrep/13.6.1625)

Stefanova I, Jenderny J, Kaminsky E, Mannhardt A, Meinecke P, Grozdanova L & Gillessen-Kaesbach G 2010 Mosaic and complete tetraploidy in live-born infants: two new

patients and review of the literature. *Clinical Dysmorphology* **19** 123–127. (https://doi.org/10.1097/ MCD.0b013e3283353877)

Vazquez-Diez C, Yamagata K, Trivedi S, Haverfield J & Fitzharris G 2016 Micronucleus formation causes perpetual unilateral chromosome inheritance in mouse embryos. *PNAS* **113** 626–631. (https://doi. org/10.1073/pnas.1517628112)

Chapter 5 – Discussion

5.1 Preamble

This thesis presented the results of experiments investigating the regulatory mechanisms of cytokinesis and the impacts of tetraploidy in the early mouse embryo. Firstly, Chapter 2 demonstrated that, even in mouse embryos which lack centrioles, tetraploidy leads to chromosomal instability and aneuploidy as a result of reduced microtubule turnover and impaired error correction activity, which thus increases the rates of chromosome mis-segregation. Chapter 3 showed that in addition to cell size being a powerful regulator of furrow ingression speed in mouse embryos, apical polarity in outer cells directly and locally regulates contractile ring assembly and constriction dynamics in a cell-autonomous manner, potentially increasing the susceptibility of outer cells to cytokinesis failure. Chapter 4 discusses the contrasting clinical data regarding the impacts of binucleation to embryo development and proposes that two distinct routes of binucleation may have opposing impacts on embryo development.

The implications of these findings have been discussed in each chapter in which the experiments were performed. In Chapter 5, I will further elaborate on key topics of interest that come to light from the results described in this thesis, and I will highlight interesting topics that are raised by my work. Firstly, I will discuss the use of mouse embryos for biological studies of cell size scaling (**section 5.2**). I will then elaborate on the mechanisms of local regulation of furrow ingression in mammalian cells (**section 5.3**). Following, I will discuss the potential reasons why tetraploidy impacts kinetochore-microtubule dynamics, and how the absence of checkpoint signalling in embryos may contribute to the proliferation of chromosomally-unstable cells (**section 5.4**). I will then discuss the biological significance of some of the morphological criteria used in fertility clinics for embryo selection (**section 5.5**). In addition to discussing the results presented in Chapters 2, 3 and 4, I will also take the opportunity to present unpublished experiments investigating the mechanisms by which tetraploidy impacts inner cell mass formation in the early mouse embryo (**section 5.6**).

5.2 The mouse embryo as a model for cell size scaling studies

Cells are highly organised systems that rely on compartmentalised organelles to maintain their functions. Each organelle carries out a distinct purpose within cells, and in many cases, organelle activity depends not only on molecular components but on its size. For instance, the mitotic spindle must be sufficiently large in order to accurately attach to all chromosomes during metaphase and to elongate fast enough for timely chromosome segregation during anaphase prior to cytokinesis onset. Moreover, the contractile ring must be large enough to encompass the entirety of cell perimeter and generate sufficient force to drive constriction. On the other hand, organelle size must also not be excessive such that it causes a bioenergetic overburden to the system and therefore, an organelle to cytoplasmic ratio must be achieved to ensure homeostasis. A particular challenge of organelle scaling is faced in specific multicellular systems such as the preimplantation embryo, wherein cell divisions take place without intervening cell growth, and cell size decreases approximately in half at each consecutive division[217]. Therefore, understanding how cellular components and processes scale with declining cell size is a widely investigated topic in the field of cell and developmental biology. In this context, mouse oocytes and embryos have been increasingly used as model systems for the study of cell size scaling due to their tractability and robustness, which allows for direct manipulations of cell size without deleterious effects on cell division, and invaluable cell biological insights have emerged from studies of cell size scaling in mouse.

Several cellular components and biological processes have been shown to be regulated by cell size in different species. For instance, metaphase spindle length was shown to progressively decline with decreasing cell size in mouse embryos from the 2-cell stage onwards, although 1-cell embryos appear to have shorter spindles[217], most likely due to residual "meiosis-like" spindle assembly mechanisms during the first embryonic mitosis[210]. Nuclear scaling has also been shown to depend on cell size in mouse embryos, and direct manipulations of blastomere size demonstrated that a combination of cell size and developmental features control nucleus size in a manner dependent on PKC activity[375]. A related analysis has been performed in *C. elegans* embryos, wherein chromosome length was found to be controlled by cell and nucleus size but not developmental program[376]. Interestingly, recent advances have shown that cell size not only regulates organelle scaling, but also impacts the stringency of checkpoint signalling and the

dynamics of biological processes such as cytokinesis. For instance, the spindle assembly checkpoint was found to become progressively more robust as cells get smaller both in *C. elegans* embryos[229, 377] and mouse oocytes[230, 231], and larger cells were less likely to sustain a SAC-induced metaphase arrest in response to misaligned chromosomes. On the other hand, direct manipulations of cell size have shown that this is not the case in mouse embryos, namely, cell size reductions did not produce significant changes in checkpoint strength in response to misaligned chromosomes[232] (**see also Annexe 4**) . The constriction of the contractile ring during cytokinesis has also been shown to be influenced by cell size, and a cell size-dependent scalability mechanism was shown to mediate a progressive decline in constriction speed during cytokinesis in *C. elegans* embryos[279, 280, 298, 300] and the filamentous fungi *N. crassa*[297]. Our micromanipulation of cytoplasmic size in mouse embryos also reveals a strong influence of cell size in the speed of ring constriction from the 8-cell stage onwards, but not in earlier divisions (1- to 8-cell stage) (**see Chapter 3, Figures 30-33**), suggesting that an upper limit of cell size beyond which constriction speed cannot be scaled up might restrict scalability mechanisms. Interestingly, upper limits of scalability have been observed in other biological processes, such as the scaling of spindle length to cell size in *Xenopus laevis* and *C. elegans* embryos[378, 379], wherein spindle length cannot be scaled up past a certain threshold of cell size[219].

The abovementioned examples only briefly illustrate the existing literature on organelle scaling and indicate that scaling is a widely conserved feature of cells across many organisms and biological processes. The study of cell size scaling is naturally a subject of much curiosity: How do cells 'know' that the spindle must get shorter as cells get smaller, or that the nucleus must be smaller, or that constriction speed must be slower? Moreover, what signals set these upper limits of scalability, which are so widely reported in biology? There has been a myriad of models and hypotheses that propose different mechanisms by which cells could ensure precise organelle scaling. I will describe some of these mechanisms in detail in the next section (**section 5.2.1**), and I will then use the following section (**section 5.2.2**) to relate the findings of this thesis to current models of cell size scalability and propose adapted models to explain our results in the mouse embryo.

5.2.1 Scaling mechanisms of subcellular structures

An intriguing model for organelle scaling is that of **molecular rulers**, where organelle size is determined by the size of a given molecule that guides organelle assembly. Molecular rulers provide a structural scaffold with a determined length and shape, which act as a template for the size of the target organelle[380]. Perhaps one of the most striking examples of molecular rulers setting organelle size is that of gene H protein in bacteriophage λ, which specifies tail length. In this organism, the length of gene H protein (determined by the number of amino acids) directly corresponds to the length of phage tails, with smaller gene H proteins generating shorter tails[381]. Similar molecular rulers have been proposed to regulate the length of injectisome needles used by pathogenic bacteria[382, 383] and actin filament length in myofibrils[384], although the latter has been further questioned in more recent studies[385]. Related to the concept of molecular rulers is that of **molecular gradients**, in which the scaling is set by the sensing of different concentrations of a given molecule within the organelle. One of the clearest examples of molecular gradients is observed in *C. elegans* mitotic spindles, wherein a gradient of the microtubule-associated protein TPXL1 (the *C. elegans* homolog of TPX2) is formed along the microtubules with a maximum at the centrosome, decaying towards the kinetochore[378]. The TPLX1 gradient decay length was shown to directly regulate spindle length, with shorter gradients leading to shorter spindles and vice-versa[378].

Scaling of cellular structures can also be simply determined by direct sensing of cell boundaries[380]. The simplest manifestation of this mechanism is for the structure to assemble directly onto the plasma membrane, such as is the case with the cytokinetic ring which naturally decreases in size as cells get smaller during development[279, 297, 298] (**Chapter 3, Figure 30**). Cell boundary sensing is also an important mechanism for determining the centre of the cell in extremely large organisms, such as the ~1200µm *Xenopus laevis* oocyte and the ~600µm *Danio rerio* oocyte[386, 387]. In these organisms, centrosome-nucleated interphase asters expand to reach the cell boundaries in a dynein-dependent mechanism, and this is thought to ensure that centrosomes are located precisely in the centre of the cell and even determine cleavage plane position[386, 387]. Other size control mechanisms exist considering that the size of a structure is often regulated by the rates of assembly and disassembly. These so-called **dynamic balance models** have been shown to modulate, for instance, microtubule length via the microtubule motor kinesin-8[388, 389]. Kinesin-

8 is a microtubule motor that binds preferentially to the plus-ends of microtubules where it promotes microtubule depolymerisation. The amount of kinesin-8 recruited to microtubules is proportional to microtubule length, and thus the pool of plus end-associated kinesin-8 is higher in longer microtubules, which therefore leads to higher depolymerisation rates in longer microtubules[388, 389]. This in association with size-independent polymerisation mechanisms results in precise maintenance of a defined microtubule length[388, 389]. Although this mechanism accounts for organelle-intrinsic size control, it does not necessarily explain the scaling of organelles with cell size, and other mechanisms that control the rates of assembly and disassembly in a manner dependent on cell size must also exist.

Consistent with this, a related mechanism has been shown to play a role in nucleus size scaling, wherein the levels of free importin α – an essential component of the nuclear import machinery that controls protein trafficking from cytoplasm to nucleus – regulates nucleus size in a manner dependent on cell size, with smaller cells having lower overall cytosolic levels of importin α due to increased sequestration at the membrane, thereby reducing nuclear import and consequently restricting nuclear growth rates[390]. Similarly, importin α has also been shown to regulate spindle scaling by binding to and inhibiting the microtubule destabiliser Kif2a, thereby increasing spindle length[139]. As cells get smaller, this inhibitory activity of importin α upon Kif2a is restricted by sequestration of importin α to the plasma membrane, which thus generates higher levels of free cytosolic Kif2a that promote microtubule depolymerisation, resulting in smaller spindles[139].

Another factor that might affect organelle size is the time taken to assemble/disassemble a particular organelle. In this **timer mechanism**, it is assumed that an organelle that assembles faster or for longer time will be larger than one that assembles more slowly or for shorter time, and any factors that limit the timing of assembly would necessarily affect organelle size[380]. This type of mechanism could make sense in organisms where rapid cell cycle progression places time constraints on the assembly of structures, for instance, during embryonic development. Although this mechanism has not been clearly dissected, evidence in *C. elegans* 1- and 2-cell embryos showing that centrosomes grow exponentially during mitosis until telophase, when they dissemble rapidly and completely, suggest that centrosome size does not reach a stable plateau during early

divisions, as it does later in development[391], and therefore rapid cell cycle progression might restrict organelle growth[380]. Another perspective of scaling is that rather than directly relying on cell size, organelle size may be regulated in response to metabolic demands. This **demand sensing** mechanism seems to exist particularly in the context of mitochondria and ER regulation, although these processes are not necessarily related to cell size changes. For instance, muscle cells respond to increased energy requirements by increasing mitochondria biogenesis rates and consequently mitochondria capacity[380]. A similar mechanism exists during ER proliferation, wherein the unfolded protein response (UPR) machinery senses abnormal accumulations of unfolded or misfolded proteins in the ER lumen, and subsequently promotes lipid biosynthesis and generation of new ER sheets, as well as the transcription of Golgi components[392].

Finally, one of the most largely accepted mechanism of scaling is known as the **limiting component** or **limiting pool** hypothesis, and it posits that the initial amount of a given component determines organelle size. The limiting pool hypothesis assumes that a cell starts with a fixed amount of the essential structural molecule (limiting component) and as the organelle is assembled, this component is exhausted, which thus limits organelle growth and ensures that the final organelle size is directly proportional to the initial amount of this given component[380]. This hypothesis is an attractive explanation for the natural scaling of organelles to cell size as long as the initial concentration of the limiting component is constant across cells of different sizes, meaning that the total amount of limiting components should scale with cell size. The idea of a limiting pool of structural components is the basis for the contractile unit model of contractile ring constriction proposed in *C. elegans*[279, 280] and *N. crassa*[297] wherein a fixed amount of contractile units, determined based on cell size, is assembled at the contractile ring at the onset of cytokinesis and dictates constriction speed[232]. In this case, however, the prediction is that the concentration of the limiting component (most likely cytokinesis components) should be higher in bigger cells in order to provide sufficient contractile forces for the ring to constrict faster. This was found to be the case in *N. crassa*, where the starting concentration of myosin II at the contractile ring was higher in bigger cells, and this was then attributed as the mechanism by which bigger rings constrict faster[297]. Another prediction of the limiting pool hypothesis is that organelle size is responsive to changes in concentration of the limiting component, and evidence for this was shown in size determination of

C. elegans centrosomes[391] and nuclear envelope[390], spindle size in *Xenopus laevis*[218] and constriction speed in *N. crassa*, where mild inhibition of myosin II decreased constriction speed[297].

5.2.2 Proposed models for the scaling of constriction speed in mouse embryos

Given the variety of scaling mechanisms described for several organelles and biological processes, it is exciting to think how the experiments described in this thesis could relate to some of these models and the future directions to be taken that might answer some of the puzzles encountered in our study. We found that constriction speed decreases as cells get smaller from the 8-cell stage onwards in mouse embryos (**Chapter 3, Figure 30**). These findings could readily relate to a limiting pool model, wherein the starting amount of cytokinesis components recruited to the contractile ring progressively decreases as cells get smaller, thereby generating less contractile forces and ultimately decreasing constriction speed. Our micromanipulation of cell size (**Chapter 3, Figures 30E-L**) further reinforces this idea, as cytoplasmic removal could presumably decrease cytosolic levels of certain cytokinesis components to similar levels to that of smaller cells, and thus decrease constriction speed. Although we have not formally compared the levels of cytokinesis components recruited to the contractile ring between the 8- and 32-cell stages (where a cell size-dependent scalability of constriction speed is first detected), I predict that a gradual decline in the concentration of cytokinesis components, coinciding with cell size reductions, would be observed. Moreover, further experiments where the levels of cytokinesis components are carefully manipulated by mild chemical inhibitions or protein knockdown and overexpression approaches will be invaluable to determine whether constriction speed would change in response to different levels of limiting components. Preliminary unpublished experiments from our lab indicate that high levels of Anillin overexpression increase constriction speed in 2-cell stage mouse embryos, suggesting that a limiting component might indeed regulate constriction speed, however, a more careful analysis applying precise modulation of protein levels is necessary.

On the other hand, we also found that from the 1- through 8-cell stages, the mouse embryo reaches an upper limit beyond which constriction speed cannot be scaled up (**Chapter 3, Figures 30**). This might suggest either that large blastomeres cannot synthesise sufficiently high amounts of cytokinesis components to increase constriction speed, or that excessively large cells may become insensitive to changes in the amount of cytokinesis components. Interestingly, we found

found that the amount of Anillin (as measured by fluorescence intensity unit/μm) at the contractile ring is constant from the 2- to 8-cell stages (**Figure 43A-B**) during which the upper limit is detected, pointing towards the prediction that larger blastomeres might not be able to produce enough cytokinesis components to increase constriction speed according to cell size. Why larger cells could have limited amounts of cytokinesis components is unknown but could relate to the fact that the early divisions of the mouse embryo rely almost entirely on maternally inherited RNA for transcription, and full zygotic genome activation occurs only at the late 2-cell stage[31]. It is therefore possible that the first few embryonic divisions occur with suboptimal levels of cytokinesis components produced from maternally inherited RNA, thereby limiting the scalability of constriction speed in large cells, and that optimal levels of cytokinesis components might only be fully synthesised by the ~8-cell stage. If the lack of scalability of constriction speed in large blastomeres is indeed solely related to suboptimal levels of cytokinesis components, then this would imply that artificially increasing the amount of cytokinesis components in larger cells would increase constriction speed. In contrast, if the lack of scalability is related to an overall insensitivity of larger cells to high amounts of cytokinesis components, then one would expect to see no changes in constriction speed upon exogenous overexpression of cytokinesis components. The preliminary experiments mentioned in the previous paragraph which show that Anillin overexpression increases constriction speed in 2-cell embryos suggest that rather than being insensitive to changing concentrations, large cells may simply not synthesise sufficient cytokinesis components to adjust constriction speed. Overall, our data is consistent with a limiting pool model, wherein the amount of cytokinesis components gradually decreases as cells get smaller after the 8-cell stage, thereby driving the progressive decline in constriction speed (**Figure 43C**). On the other hand, in excessively large cells, the amount of limiting component is not scaled up accordingly and thus constriction speed reaches an upper limit, potentially due to suboptimal levels of maternally inherited mRNA transcription prior to zygotic genome activation (**Figure 43C**).

Alternatively, the upper limit of constriction speed could relate to a limited ability of excessively large cells to sense molecular gradients that signal contractile ring assembly from the spindle midzone within the short time frame between anaphase onset and furrow ingression initiation. As detailed in the introductory sections of this thesis (**Chapter 1, section 1.3.1**), the signals that promote contractile ring assembly primarily originate from the anaphase spindle

midzone, where Rho GEFs such as Ect2 are loaded to the adjacent plasma membrane and ensure RhoA activation. Larger cells must cover a long distance between the spindle midzone and the plasma membrane, and it is possible that the midzone-based signals that promote contractile ring assembly might not reach the plasma membrane as quickly and efficiently as in smaller cells (**Figure 43D**). As the anaphase chromosome masses rapidly approach the cell poles during spindle elongation, it is possible that furrow ingression starts when the contractile ring is below its full contractile capacity due to limited assembly of cytokinesis components, thereby halting the scalability of constriction speed in larger cells. If the long distance between the spindle midzone and the plasma membrane indeed was responsible for the lack of scalability in large cells, a prediction would be that the closer the plasma membrane gets to the midzone, the faster constriction speed should be and therefore, it would be expected that the speed of constriction would get progressively faster during cytokinesis as the plasma membrane gets closer to the midzone. Instead, we observed that constriction speed was constant throughout most of cytokinesis (**Chapter 3, Figure 30B**), suggesting that the proximity of cell cortex to spindle midzone might not necessarily correlate with higher constriction speeds. In fact, in *C. elegans* embryos, it was shown that at the very end of cytokinesis, as the contractile ring gets closer to the spindle midzone, there was a substantial decline in constriction speed which was dependent on the presence of midzone microtubules, suggesting that an inhibitory component of the spindle midzone might exist instead[279]. Nevertheless, it is still possible that there might be a threshold distance between the spindle midzone and cell cortex after which constriction speed cannot be scaled up accordingly.

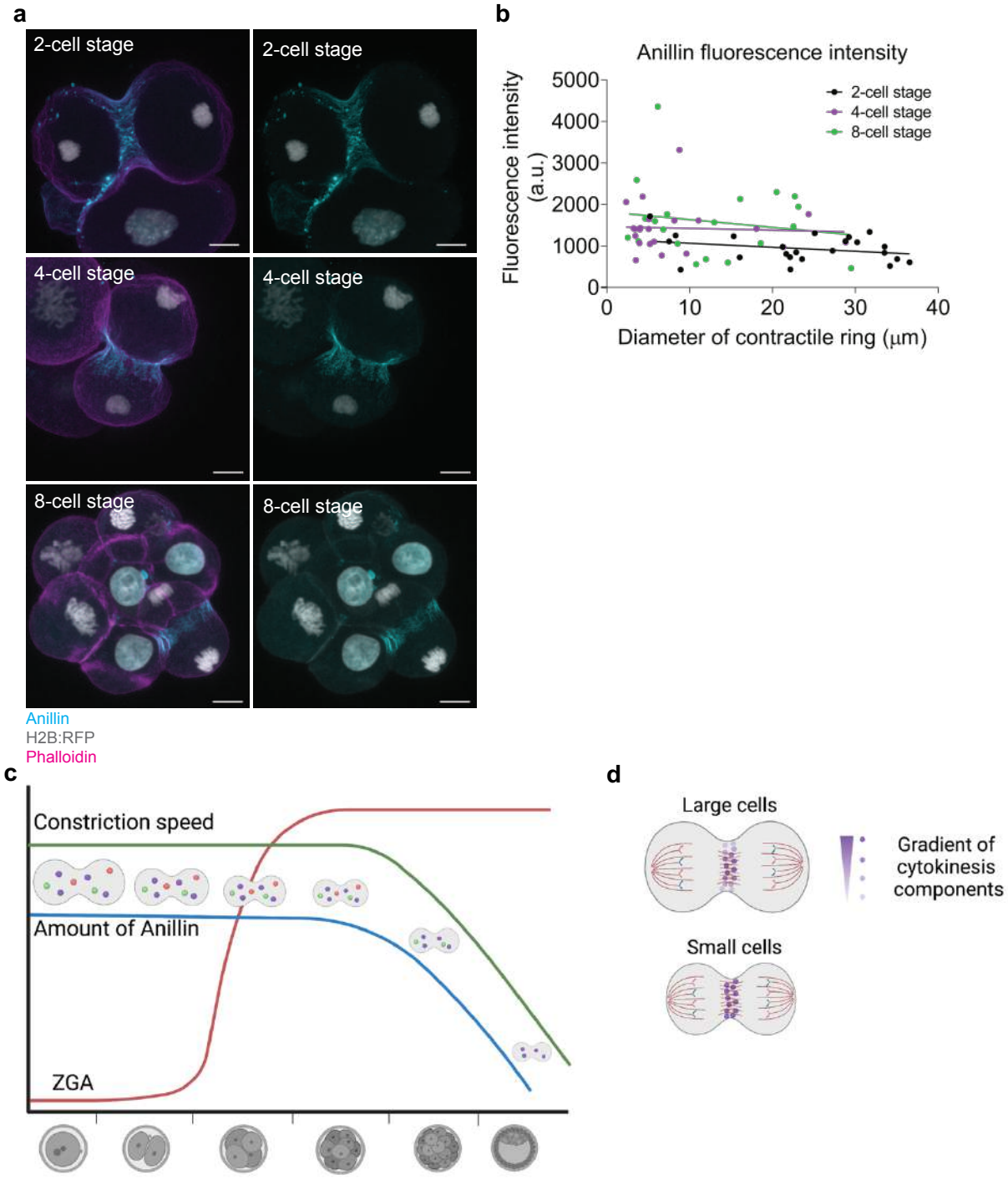

Figure 43. – Proposed mechanisms of cell size-dependent constriction speed regulation in mouse embryos.

(a) *Representative immunofluorescence images of dividing blastomeres at the 2-cell (top panel), 4-cell (middle panel) and 8-cell stages (bottom panel) expressing H2B:RFP and immunostained with Phalloidin (plasma membrane) and Anillin.* ***(b)*** *Quantification of Anillin fluorescence intensity in dividing blastomeres at the 2-cell (23 blastomeres), 4-cell (22 blastomeres) and 8-cell stages (20 blastomeres) at diverse stages of cytokinesis progression, as evidenced by varying contractile ring diameters (X axis). Simple linear regression analysis did not detect statistically significant differences between the slopes (P= 0.8516), indicating that average Anillin fluorescence intensity per µm is unchanged throughout cytokinesis and among different developmental stages. Scales = 10µm.* ***(c)*** *The gradual decline in constriction speed observed after the 8-cell stage (green curve) in mouse embryos may relate to a limiting component model, wherein the amount of cytokinesis components (blue curve) decreases as cells get smaller, thereby decreasing constriction speed. On the other hand, the upper limit of constriction speed observed from the 1- through 8-cell stages may relate to an inability of excessively large blastomeres to synthesise sufficient cytokinesis components to scale constriction speed, potentially due to insufficient maternally inherited mRNA transcription prior to zygotic genome activation (ZGA; red curve).* ***(d)*** *An alternative model for the upper limit of constriction speed is that midzone-based signals that promote contractile ring assembly may not reach the plasma membrane sufficiently fast in large cells due to the long distance between the spindle midzone to the neighbouring cortex, thereby causing the assembly of a contractile ring with suboptimal contractile capacity and preventing scalability. Figures (c) and (d) created with BioRender.com*

Another possibility is that the decline in constriction speed observed after the 8-cell stage might be linked to chromatin- or spindle-based signals, rather than cell size directly. This hypothesis is substantiated by the fact that the change in constriction speed observed after the 8-cell stage in embryos coincides with a decline in the speed of chromosome separation and spindle elongation at anaphase at this stage[217]. Therefore, it is possible that constriction speed is adjusted according to the speed of chromosome separation from the 8-cell stage onwards, in order to avoid chromosome segregation errors. Consistent with a role of chromosomes on cytokinesis regulation, previous work has shown that Aurora B signalling emanating from chromosomes activates the abscission checkpoint in cells containing severely lagging chromosomes or chromatin bridges that remain trapped within the midzone[302]. In addition, work in *D. melanogaster* neuronal stem cells elucidated a mechanism wherein an efflux of myosin from the contractile ring towards the cell poles promotes cortical contractions and cell elongation, thereby facilitating the clearance of trailing chromatid from the midzone[393]. Moreover, during our live imaging experiments, we observed two examples of dividing 8-cell blastomeres displaying severely lagging chromosomes trapped within the midzone, wherein constriction speed was substantially reduced (**Figure 44**). Although this Aurora B-dependent signal was shown to emanate specifically from lagging

chromosomes[302], it is conceivable that other unidentified chromatin-based signals emanating from the chromosome mass during anaphase might influence constriction speed, even in the absence of lagging chromosomes. Further experiments that directly manipulate the speed of chromosome separation during anaphase and simultaneously assess constriction speed will help elucidate the potential role of chromosomes on cytokinesis regulation.

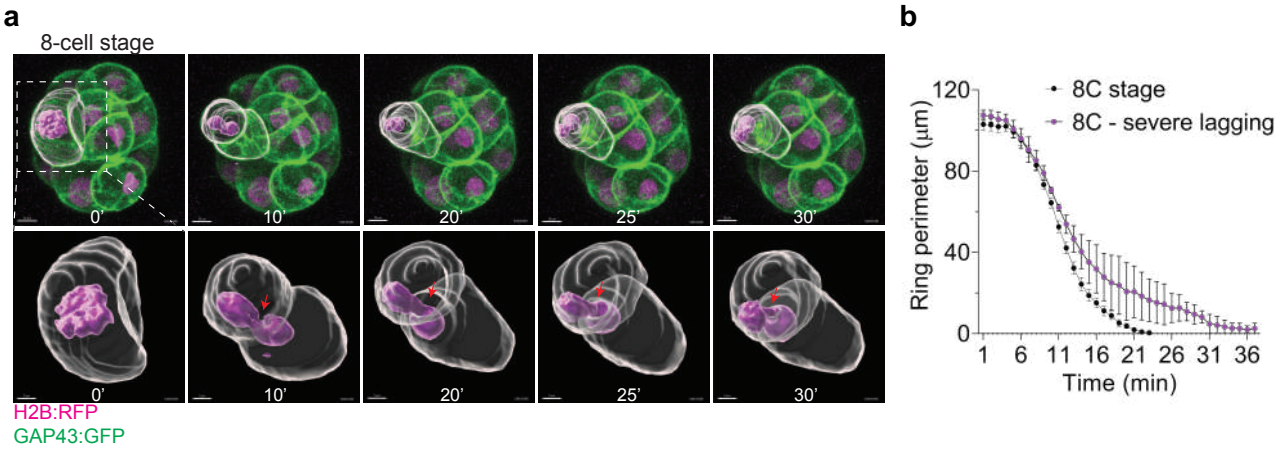

Figure 44. – Contractile ring constriction is slowed in cell divisions harbouring severely lagging chromosomes.

(a) *Representative time-lapse 3D reconstruction of a dividing 8-cell blastomere expressing H2B:RFP (magenta) and GAP43:GFP (green/grey) and harbouring a severely lagging chromosome at anaphase. Note that the lagging chromosome remains trapped in the vicinity of the midzone during cytokinesis (red arrow).* ***(b)*** *Quantification of average ring perimeter during cytokinesis in 8-cell blastomeres (n = 11 blastomeres from 8 embryos) and 8-cell blastomeres containing severely lagging chromosomes (n = 2 blastomeres from 2 embryos). Time is shown in minutes, where 0' refers to anaphase onset. Scales = 10µm.*

5.3 Local regulation of furrow ingression in mammalian cells

One of the most investigated aspects of cytokinesis is how the contractile ring generates forces that promote constriction, and whether the ring functions as a single force-generating structure or by local regulation of independent contractile units. The mechanics of cytokinesis force generation was initially thought to be analogous to muscle contraction mechanisms, wherein sarcomere-like structures comprising intercalated actin and myosin filaments promote constriction by sliding, which results in compression of the sarcomere[394]. The idea of a sarcomere-like mode of contractile

ring constriction has been further put into question, given that a sarcomeric organisation has not been reproducibly observed by electron microscopy[279]. Moreover, muscle contraction takes place in cycles of compression and relaxation without intervening loss of filaments, whereas contractile rings disassemble as they constrict[254]. Alternative models have thus been developed to understand contractile ring constriction and regulation. For instance, in fission yeast, the contractile ring is thought to be organised as actomyosin "nodes" that are assembled during interphase and anchored to the plasma membrane during cytokinesis[395]. Contractility is then generated by myosin-II laterally binding to actin filaments from adjacent nodes and pulling them in opposite directions, thereby creating tension that promotes constriction[395].

Another model has been developed based on experiments in *C. elegans* embryos, which proposes that a fixed number of individualised "contractile units" established at cytokinesis onset is recruited to the contractile ring, and each of these units exerts contractile force independently, thereby driving constriction[279]. Myosin organisation as individualised clusters has been further visualised in contractile rings by super-resolution microscopy in both HeLa cells[282] and isolated sea urchin cortices[281], supporting a model for contractile unit organisation. Importantly, the contractile unit model implies that the ring is an ensemble of functionally individualised structures that could therefore be locally regulated. Consistent with this idea, elegant experiments in *C. elegans* embryos, in which laser ablation was used to create a gap in the contractile ring, demonstrated that the ring does not disintegrate upon severing[280]. Instead, the remainder of the intact ring continues to constrict whilst the gap is repaired[280], strengthening the notion that independent force-generating units promote constriction. Interestingly, a similar phenomenon is observed upon severing of the contractile ring in HeLa cells, but not in fission yeast, where ring constriction is halted during gap repair[396], highlighting the substantial inter-species differences in the mechanics of constriction.

Our finding that apical polarity disrupts furrow ingression specifically on the apical side of the contractile ring without impacting the basal side not only supports the notion that the ring can be locally regulated, but also provides evidence that local regulation occurs naturally in multicellular mammalian systems (**Chapter 3, Figures 37, 39 and 41**). This phenomenon was also shown to be an intrinsic feature of polarised cells rather than an effect of cell shape and/or adhesion (**Chapter 3, Figures 37, 39 and 41**), in contrast to the mechanism described in *D. melanogaster*,

wherein an anchoring of cytokinesis components to sites of cell adhesion causes unbalanced constriction rates in epithelial cells[397]. Apical polarity has been shown to reduce cell contractility and limit outer cell internalisation in mouse embryos, thereby contributing to the maintenance of appropriate amounts of inner and outer cells during development[49]. Future experiments in which measurements of cell contractility and/or elasticity (**see also Annexe 5**) are performed in polarised outer cells specifically during cytokinesis will provide insights into how the apical domain impacts the mechanics of force generation during cytokinesis from a biophysical point of view.

An interesting feature observed in *C. elegans* embryos is that the contractile ring progressively disassembles during constriction without intervening turnover of cytokinesis components[279]. This was shown both by fluorescence recovery after photobleaching (FRAP) experiments, which revealed a slow recovery time of Myosin:GFP after photobleaching, as well as by acute treatment of dividing cells with the actin-binding agent Latrunculin A at mid-cytokinesis, which did not prevent cytokinesis completion[279]. These results, as well as the observation that constriction speed scales with cell size, suggest that the contractile ring is initially built with a fixed amount of contractile units that progressively disassembles during cytokinesis without cytoplasmic exchange, given that disruption of the actin cytoskeleton after contractile ring assembly does not prevent cytokinesis completion[279]. Surprisingly, we obtained opposite results when dividing 4-cell mouse blastomeres were acutely treated with Latrunculin A after cytokinesis onset (**Figure 45**). We observed that addition of Latrunculin A to the media 17 minutes post anaphase onset caused regression of the contractile ring and generated a binucleated blastomere (**Figure 45**), suggesting that active turnover of actin at the ring is required for cytokinesis completion in the mouse, even after the ring has been fully assembled. Furrow regression is also observed in *Arbacia punctulate* eggs treated with Cytochalasin D at midcytokinesis[394]. Interestingly, however, when Cytochalasin D is at late stages of cytokinesis in *A. punctulata* eggs, the furrow frequently arrests, rather than regresses[394], and it would be interesting to address whether a similar mechanism is observed in mouse embryos treated with actin depolymerising agents at different timepoints of cytokinesis. Why actin turnover is required for constriction in mouse but not *C. elegans* blastomeres remains to be elucidated, but might relate to the fact that the scaling of cytokinesis with cell size initiates only from the 8-cell stage in mouse embryos (**Figure 45**), as opposed to the 1-cell stage in *C. elegans* embryos[279]. It is thus possible that if the same experiments were performed with 16-cell

stage mouse embryos, at which the influence of cell size on cytokinesis is first detected (**Chapter 3, Figures 30 and 33**), the results might be similar to those of *C. elegans* embryos, where actin turnover after contractile ring assembly might not be required for constriction.

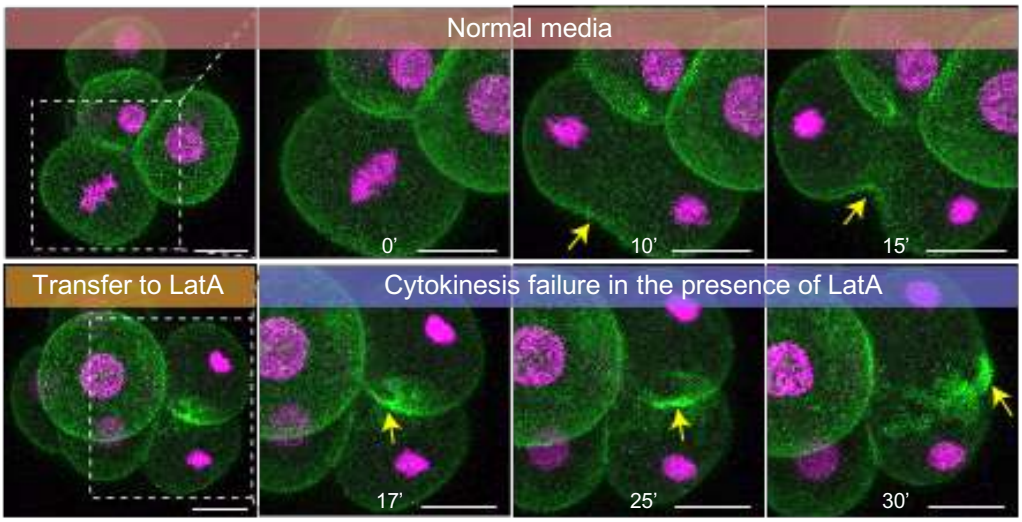

Figure 45. – Inhibition of F-actin polymerisation at mid-cytokinesis prevents cytokinesis completion.

Representative images of a 4-cell stage embryo co-expressing H2B:RFP (magenta) and GAP43:GFP (green). Anaphase was observed with confocal imaging and embryos were transferred to media supplemented with an inhibitor of actin polymerisation (LatA 5µM) ~17min post-anaphase onset. Note that the contractile ring (yellow arrows) regresses upon LatA exposure. Scale bars = 20µm. Time is shown in minutes, where 0' = anaphase onset.

In addition, our observation that lateral constriction is caused by the apical domain limiting the access of Anillin and p-Myosin specifically to the apical side of the contractile ring (**Chapter 3, Figure 39**) alludes that specific subcellular domains might have a direct inhibitory effect on cytokinesis components. How these molecular interactions are established is yet to be addressed, but evidence that ECT2 interacts with the Par6/Par3/aPKC polarity complex and that RhoA downstream effectors Rock1/2 play a role on polarity establishment[60] place ECT2 and Rho-kinases as common components of both polarisation and cytokinesis[398, 399]. A limitation of this argument

is that these interactions must necessarily be inhibitory, given that constriction speed is decreased at the apical side. However, it is still possible that ECT2 and/or Rho-kinases may be repurposed for polarity establishment in polarised cells, thereby limiting their role on contractile ring assembly. Indeed, protein repurposing has been shown to occur in neurons, wherein kinetochore components are re-directed to promote dendritic extension rather than chromosome segregation[400]. Another possibility is that the association of ECT2 and/or Rho-kinases with polarity proteins might confine these components within the polarity complex or cause conformational changes that limit their ability to promote contractile ring assembly, although evidence for these hypotheses are lacking. Alternatively, a recent hypothesis proposes that contractile ring assembly and closure relies on the availability and fine-tuned management of membrane microdomains to which cytokinetic networks are attached[401], and it is thus possible that rather than directly influencing cytokinesis on a molecular level, apical polarity proteins might outcompete cytokinesis components for limited membrane-binding sites. Detailed investigation of protein-protein interactions is necessary and will further enlighten our understanding of how apical polarity proteins regulate the recruitment of cytokinesis components to the contractile ring.

5.4 The mouse embryo as a permissive environment for the development of aneuploidy

Chromosomal instability (CIN) is the phenomenon in which cells persistently mis-segregate chromosomes, thereby increasing the likelihood of whole chromosome gains and losses (i.e., aneuploidy). CIN is a hallmark of tumorigenesis and the disruption of several genes and pathways has been implicated in generating chromosomally-unstable cells, including defects on spindle assembly dynamics, kinetochore-microtubule error correction mechanisms, the SAC and sister chromatid cohesion[402]. Ultimately, defects in either of these processes often results in a common phenotype, which is the presence of merotelic kinetochore-microtubule attachments at anaphase, wherein both sister chromatids are attached to microtubules emanating from both spindle poles. If merotelic attachments are not corrected prior to anaphase onset, the forces exerted by microtubules emanating from both sides of the spindle cause chromosomes to lag behind during anaphase, and this is thought to be a major driver of CIN and aneuploidy[161, 403].

5.4.1 Tetraploidy as a driver of aneuploidy

Genome doubling, or tetraploidisation, which usually arises from cytokinesis failure, can directly impact chromosome segregation fidelity, and therefore drive aneuploidy[324]. Importantly, tetraploidy is considered a steppingstone in tumorigenesis[324, 329] and landmark work has shown that injection of tetraploid cells in p53-null mice can cause cancer[329]. Mechanistic experiments have further elucidated that this phenomenon is a result of supernumerary centrosomes generated upon cytokinesis failure, which cause multipolar spindle formation during subsequent cell divisions. These multipolar spindles are eventually able to cluster their supernumerary centrosomes, but in doing so, increase the formation of merotelic kinetochore-microtubule attachments that cause chromosome mis-segregation and aneuploidy[200, 201, 202, 358]. Similarly to the scenario described in somatic cells, our findings show that tetraploid mouse embryos display high rates of chromosome mis-segregation that lead to aneuploidy later in development (**Chapter 2, Figures 16 and 19**). However, as opposed to somatic cells, we found that this is not attributable to multipolar spindles (**Chapter 2, Figure 21**). Instead, we found that chromosomal instability in tetraploid embryos was caused by reduced kinetochore-microtubule error correction activity, resulting in high proportions of merotelic attachments (**Chapter 2, Figure 27**).

Establishment of amphitelic attachments is mediated by correction of wrongly attached kinetochores prior to anaphase, and this process relies on the activity of microtubule destabilising proteins that promote microtubule turnover at the kinetochore[159, 404]. The use of photoactivatable GFP coupled to tubulin (tubulin:PAGFP) has allowed for the direct analysis of microtubule turnover, which serves as a readout of error correction efficiency[162, 164, 359]. Photoactivatable GFP fluorophores are a variant of the standard GFP molecule from jellyfish, and they display very dim or no fluorescence when illuminated with 488nm wavelength lights, but exhibit up to 100-fold increase in fluorescence when pulsed with UV light[405]. In cells expressing tubulin:PAGFP, a brief exposure of a defined region of interest within the metaphase spindle to UV light will cause local photoactivation of tubulin molecules and a rapid increase in fluorescence intensity (**Chapter 2; Figure 27A-C**)[162, 164, 359]. Given that microtubules within the spindle are constantly undergoing depolymerisation due to microtubule turnover, the fluorescently labelled tubulin molecules are gradually replaced by new unlabelled tubulin, and consequently, the fluorescence intensity within the region of interest gradually decreases (**Chapter 2; Figure 27A-C**)[162, 164, 359]. By measuring the

decline in fluorescence intensity over time, mathematical calculations can be applied to determine microtubule half-life, which essentially translates into how quickly microtubule depolymerisation, and thus microtubule turnover, occurs in that cell (**Chapter 2; Figure 27A-C**)[162, 164, 359]. Elevated microtubule half-life is indicative of overly stable microtubules, most likely caused by reduced error correction activity, and is associated with chromosomal instability in cancer cells[164] and tetraploid embryos (**Chapter 2, Figure 27A-C**)[359]. Most importantly, the finding that the microtubule depolymerising protein MCAK was underrepresented at the kinetochores (**Chapter 2, Figure 27F-G**) and that overexpression of MCAK rescued the rates of lagging chromosomes in tetraploid embryos (**Chapter 2, Figure 27H-I**) further reinforces the notion that impaired error correction activity is a major driver of chromosome mis-segregation caused by tetraploidy.

Why MCAK is underrepresented at the kinetochore of tetraploid embryos is unknown, but the observation that the structural integrity of the kinetochore is unaffected in tetraploid embryos (**Figure 46**) suggests that tetraploidy might instead affect upstream signalling responsible for MCAK recruitment, although evidence for this is lacking. Alternatively, gene expression changes associated with tetraploidy might impact error correction efficiency. In accordance with this hypothesis, transcriptome and proteome analysis of cells containing extra chromosome copies (trisome and tetrasomic) revealed that, whereas transcription levels reflected the chromosome copy number, protein levels were often reduced to diploid levels, particularly for subunits of protein complexes and protein kinases[406]. Moreover, studies of gene expression in tetraploid mouse embryos demonstrated that tetraploidy does not result in a simple doubling of protein and RNA levels, and total RNA levels have been reported to reach maximum 1.45 times that of diploid embryos[407], perhaps as a result of each nucleus in the binucleated blastomere having unequal gene expression levels[408]. It is thus conceivable that imbalanced gene expression might lead to insufficient protein levels in tetraploid embryos, and this might particularly affect protein kinases responsible for error correction, ultimately reducing the effectiveness of this processes. Future experiments in which single-cell RNA sequencing is performed in tetraploid blastomeres will provide invaluable information about the signalling pathways and biological processes affected by tetraploidy.

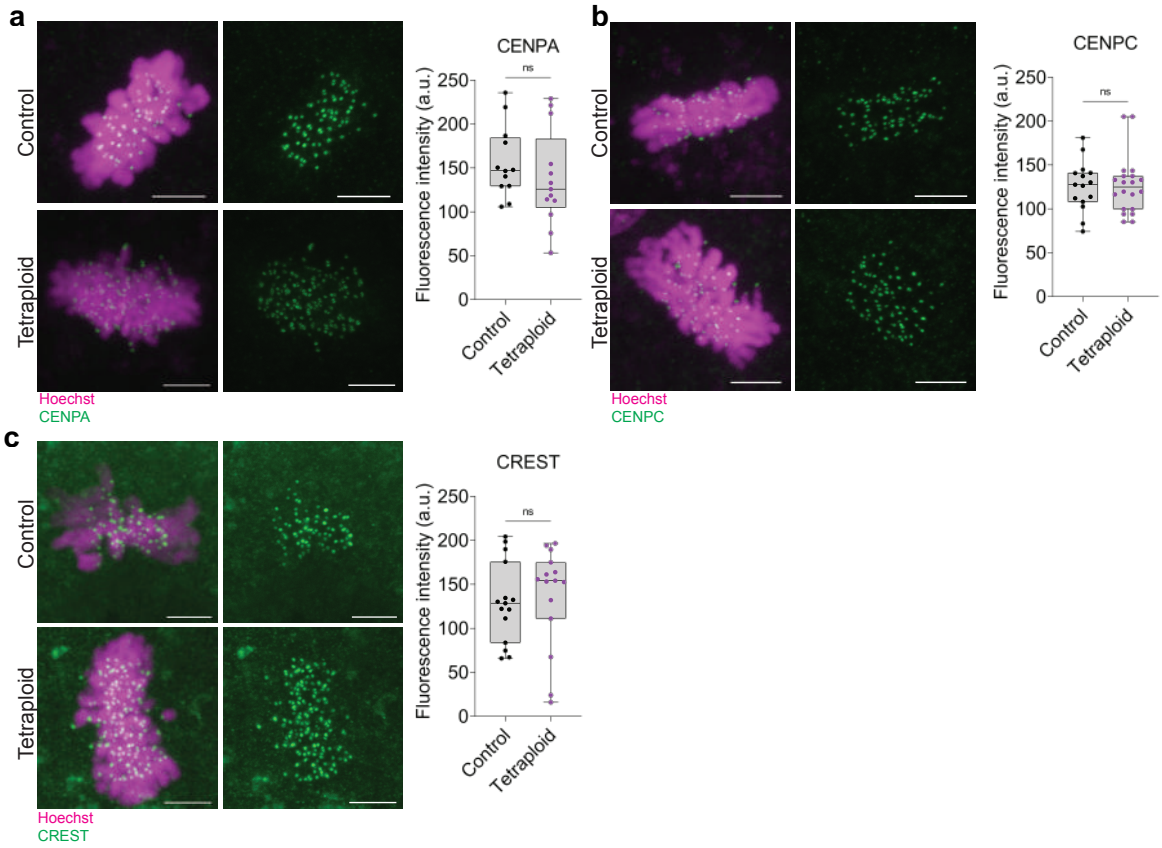

Figure 46. – Kinetochore structure is intact in tetraploid embryos.

(a) *Representative immunofluorescence images of 8-cell diploid (control) and 8-cell tetraploid (tetraploid) metaphase-arrested blastomeres and quantification of background-subtracted CENP-A centromere fluorescence intensity in controls (n = 12 blastomeres) and tetraploid (n = 13 blastomeres; P = 0.3418) blastomeres.* ***(b)*** *Representative immunofluorescence images of 8-cell diploid (control) and 8-cell tetraploid (tetraploid) metaphase-arrested blastomeres and quantification of background-subtracted CENP-C kinetochore fluorescence intensity in controls (n = 15 blastomeres) and tetraploid (n = 20 blastomeres; P = 0.8499) blastomeres.* ***(c)*** *Representative immunofluorescence images of 8-cell diploid (control) and 8-cell tetraploid (tetraploid) metaphase-arrested blastomeres and quantification of background-subtracted CREST kinetochore fluorescence intensity in controls (n = 15 blastomeres) and tetraploid (n = 15 blastomeres; P = 0.4864) blastomeres. Each data point represents an average of 10 kinetochores/centromeres per blastomere. Scale = 5μm.*

Our results also show that acentriolar mouse embryos do not generally assemble multipolar spindles in the divisions following tetraploidisation, and instead the first division following cytokinesis failure is characterised by the assembly of two completely individualised spindles, which subsequently fuse prior to anaphase onset (**Chapter 2, Figures 21 and 22**). Spindle fusion

has been previously shown to occur when two spindles are brought in close apposition in *Xenopus laevis* egg extracts[409]. This process relies on dynein activity and the mechanics of spindle fusion depends on the angle of contact between the poles of each spindle. More specifically, when spindles are oriented parallelly with overlapped poles, they merge by sliding towards each other; whereas, when spindles are orientated perpendicularly, one of the spindles rotates towards the neighbouring spindle prior to merging (referred to as "jackknifing")[409] (**Chapter 2, Figures 21 and 22**). Whether spindle fusion in tetraploid embryos relies on dynein activity remains to be investigated.

Spindle fusion has also been shown to take place as a programmed part of development during the first mitotic division of mouse[410] and bovine[411] embryos, where the zygote is composed of two separate parental pronuclei. In the mouse zygote, which is acentriolar, two completely individualised spindles are initially assembled from cytoplasmic MTOCs, each independently capturing and congressing the paternal and maternal genomes[410]. These two spindles further fuse and align both sets of parental genomes into a single metaphase plate prior to anaphase to ensure proper chromosome segregation and generation of normal mononucleated 2-cell blastomeres[410]. A similar mechanism has since been proposed to occur in bovine zygotes which, as opposed to mouse zygotes, are centriolar[411]. In this case, it was proposed that even in the presence of centrosome-dependent microtubule nucleation mechanisms, dual spindle formation is nevertheless favoured, although the frequency of this phenomenon is relatively low (~30%)[411]. It was also speculated that despite the presence of functional centrosomes, chromosome-mediate microtubule nucleation pathways are the primary route for spindle assembly in bovine zygotes[411], although the evidence for this argument was mainly observational and further mechanistic experiments are lacking.

Importantly, given that spindle fusion seems to be a natural feature of mammalian embryonic development, I find it unlikely that spindle fusion itself may be a contributor to the CIN phenotype of tetraploid embryos observed in our experiments. Instead, it is more plausible that mammalian blastomeres may be properly equipped to undergo spindle fusion without affecting chromosome segregation dynamics. Moreover, the second cell division following tetraploidisation, in which blastomeres assemble a single bipolar spindle, displays similarly high rates of chromosome mis-segregation (**Chapter 2, Figure 16B-E**), indicating that even in the absence of dual spindle formation, tetraploid blastomeres are still highly predisposed to segregation errors. However, further experiments where dual spindle formation and spindle fusion are induced while

maintaining a diploid genome will help distinguish the relative roles of spindle fusion and ploidy on the development of chromosomal instability and aneuploidy.

5.4.2 Absence of checkpoint signalling in mouse embryos

An important observation reported in studies of tetraploidy in somatic cells is that tetraploid cells are only able to proliferate in the absence of normal p53 signalling response[329, 341, 344], and therefore, the role of tetraploidy on the generation of chromosomally-unstable cells is only observable in transformed cell lines or cells in which p53 signalling has been inhibited. Instead, in non-transformed cell lines, tetraploidisation has been shown to induce cell cycle arrest and apoptosis by a mechanism dependent on p53 signalling, and this phenomenon has been termed the 'tetraploidy checkpoint'[341]. Further experiments demonstrated that the tetraploidy checkpoint is induced by a signalling cascade that involves hyperphosphorylation of Rac1 and a decrease in active RhoA mediated by supernumerary centrosomes[344]. This decline in RhoA activity activates the Hippo pathway component Lats2 kinase, which thus phosphorylates, inactivates and excludes YAP from the nucleus and stabilises p53 activity, thereby causing cell cycle arrest[344]. In addition to limiting the proliferation of tetraploid cells, a p53-dependent 'aneuploidy checkpoint' has also been proposed to induce cell cycle arrest and apoptosis in response to whole chromosome gains or losses in somatic cells[412, 413, 414, 415]. In contrast, our experiments show that mouse tetraploid blastomeres activate neither the tetraploidy nor the aneuploidy checkpoint and instead, continue to divide with high levels of aneuploidy and no evidence of cell cycle arrest (**Chapter 2, Figures 16 and 17**).

Although intriguing, the lack of tetraploidy and aneuploidy checkpoints in mouse embryos is not surprising, given that several other surveillance mechanisms are inefficient or even absent in preimplantation stages, reflecting a general inability of embryos to sustain checkpoint signalling. For instance, tetraploid cells within chimeric diploid:tetraploid mouse embryos were shown to be eliminated by p53-mediated apoptosis at post implantation stages, but not earlier[365]. Moreover, previous work has shown that artificial induction of aneuploidy in mouse embryos does not affect early preimplantation development, and aneuploid blastomeres are eliminated by apoptosis only at peri/post implantation stages[416, 417], suggestive of a lack of aneuploidy checkpoint earlier in development. Why tetraploid and aneuploid cells are not eliminated by apoptosis earlier in

development is unclear, but might relate to the fact that p53 activity remains latent until the blastocyst stage in mouse embryos[418], which might thus delay the apoptotic response in early embryos. Consistent with this, we observed an increased percentage of apoptotic cells specifically at the blastocyst stage in tetraploids as compared to diploid embryos (**Figure 50**), and it is therefore plausible that tetraploid blastomeres can proliferate during early embryonic cell cycles due to the late initiation of programmed cell death inherent of preimplantation embryos. Future experiments are necessary to address whether artificial activation of the p53 signalling pathway before blastocyst formation can induce apoptosis of tetraploid and aneuploid blastomeres earlier in development.

Additionally, in early embryos, the Hippo pathway remains inactive during the first four cell divisions, and is activated only from the 16-cell stage onwards exclusively in inner cells, as a part of cell fate determination[64]. Therefore, it is also possible that the role of the Hippo pathway in triggering the tetraploidy checkpoint is restricted in early embryos by developmental constraints that limit its activation to only a subset of blastomeres and only at later stages of development. Consistent with this hypothesis, we detected that Hippo signalling is not activated immediately following tetraploidisation, as evidenced by the presence of nuclear YAP (Hippo pathway inactive) in binucleated 4-cell embryos **(Figure 47)**. Additional experiments that address whether a tetraploidy checkpoint can be induced upon artificial activation of the Hippo pathway might help elucidate why this checkpoint is not present in embryos.

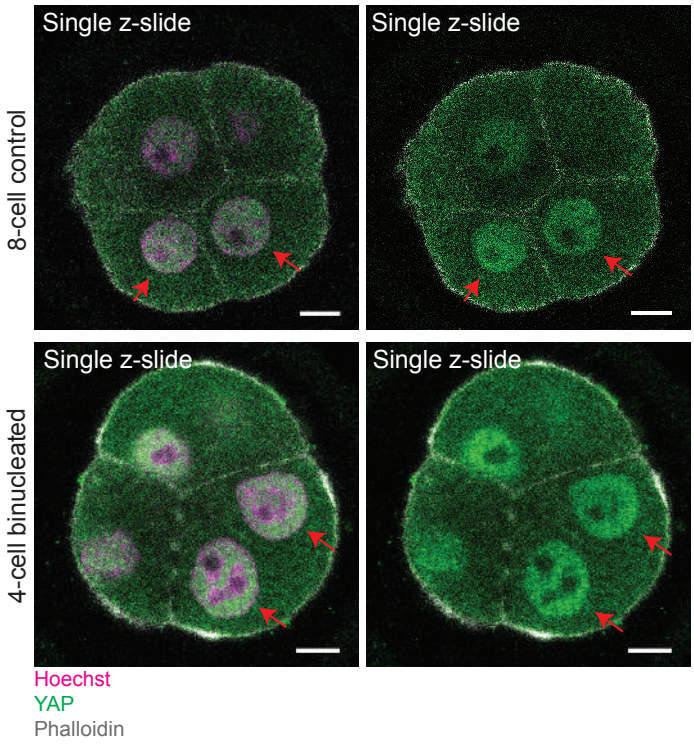

Figure 47. – The Hippo pathway is not activated by tetraploidisation in mouse embryos.

Representative immunofluorescence images of 8-cell controls (top panel) and 4-cell binucleated (bottom panel) embryos. Note the nuclear localisation of the Hippo pathway component YAP (red arrows) both in controls and tetraploid embryos, indicating that mouse embryos do not activate a Hippo-dependent tetraploidy checkpoint in early divisions. Scale = 10µm.

Another major surveillance mechanism shown to be inefficient in mouse embryos is the spindle assembly checkpoint. Previous work has shown that the early mouse embryo fails to maintain a mitotic arrest in response to severely misaligned chromosomes, even though SAC proteins are efficiently recruited to misaligned kinetochores[232] (**see also Annexe 4**). In accordance with this, we found that tetraploid embryos frequently display severely misaligned chromosomes and often proceed through anaphase without chromosome re-alignment, even though SAC proteins are recruited to kinetochores during mitosis (**Chapter 2, Figures 23-26**). Importantly, on one occasion, we observed that a severely misaligned chromosome failed to segregate its sister chromatids and was entirely inherited by a single daughter cell (**Chapter 2, Figure 26**), which necessarily causes aneuploidy. It is likely that this phenomenon takes place more frequently than we were able to detect in our experiments, given that the proximity of misaligned chromosomes to the metaphase plate, coupled with imaging resolution limitations often prevented us from clearly

visualising sister chromatid separation. Thus, it is likely that the inefficiency of SAC response in early embryos further facilitates the proliferation of chromosomally-unstable blastomeres, thereby contributing to aneuploidy.

Ongoing work in our lab has also demonstrated that mouse embryos lack other well-characterised cell cycle checkpoints that are commonly observed in somatic cells. For instance, whereas somatic cells frequently undergo a G1 cell cycle arrest in response to prolonged mitosis duration[419, 420, 421] (i.e., mitotic clock checkpoint), mouse embryos fail to activate the mitotic clock checkpoint in response to prolongation of mitosis and cohesion fatigue (Allais *et al.* unpublished). Moreover, mouse embryos also fail to sustain an abscission checkpoint in response to chromatin bridges that remain trapped within the intercellular bridge (Vasilev *et al.* unpublished) as opposed to somatic cells, which activate an Aurora B-dependent abscission checkpoint in response to lagging chromosomes[302]. Why checkpoints are generally less robust in embryos is unknown, but might relate to the fact that the first few mitotic divisions in the early embryo still resemble meiotic divisions, as was previously reported for spindle assembly mechanisms in mouse embryos[210], and thus the full capacity of checkpoint signalling might only be achieved once the embryo completes the transition to canonical mitotic cell cycle. Moreover, the preimplantation embryo faces a significant challenge which is the need to rapidly increase cell numbers whilst ensuring accurate lineage specification within the short timeframe of ~5 days prior to implantation. Therefore, one possibility is that the general absence of checkpoint signalling would offer an important evolutionary advantage that could guarantee the maximum capacity for rapid cell proliferation. Although suboptimal surveillance mechanisms would almost certainly compromise genetic fidelity, it is possible that the early embryo temporarily tolerates these drawbacks in the interest of generating sufficient cell numbers. In addition, as surveillance mechanisms arise during peri/post implantation stages, any 'abnormal' or unhealthy cells generated during preimplantation stages would presumably get eliminated by canonical checkpoint mechanisms, as was demonstrated for peri/post implantation apoptotic response to tetraploidy[365] and aneuploidy[416, 417] mentioned in the previous paragraph. In summary, although the inherent inability of mouse embryos to sustain cell cycle checkpoints and activate the apoptotic machinery may provide a major evolutionary advantage to guarantee cell proliferation during preimplantation stages, it most likely places the early embryo as a permissive environment for the development of aneuploidy.

5.5 Clinical outcomes of cytokinesis failure and tetraploidy

Successful outcomes of *in vitro* fertilisation cycles rely heavily on proper assessment of embryo quality and selection of the most suitable embryo prior to transfer. The development of sophisticated techniques for embryo testing, such as preimplantation genetic screening (PGS), allowed for the direct assessment of ploidy status in live embryos without substantial impacts on embryo health. The basic principle of PGS is that a small number of blastomeres is removed from the embryo, usually from the trophectoderm layer of blastocysts, and genetic assessments are performed including fluorescent *in situ* hybridisation (FISH), microarrays, single nucleotide polymorphism (SNP) and sequencing analyses to detect chromosomal abnormalities. Whereas PGS is effective in detecting ploidy levels in individual cells, this technique is limited by the fact that only a small proportion of cells is analysed and thus, the results of a single trophectoderm biopsy might not be representative of the whole embryo[422]. Moreover, those cases where mosaic aneuploidies are detected by PGS raise an additional ethical dilemma, given that there is an ongoing debate on whether certain levels of mosaic aneuploidy might still be tolerated and allow normal development in embryos[416] and thus, the decision of whether (and which) mosaic embryos should be transferred is not clear-cut. Therefore, most embryo selection criteria used in fertility clinics still rely on morphological features observed under the light microscope, such as stage-matched cell numbers, cytoplasmic fragmentation, and nucleus configuration[423].

Although morphological selection of embryos has been widely applied during *in vitro* fertilisation cycles, the biological significance of phenotypes commonly scored as abnormal has only recently began to be dissected with cell biological studies. For instance, nucleoli clustering within the zygotic pronuclei is an observable morphological criterion used in fertility clinics as an indicative of embryo health, and a recent study has demonstrated that the degree of nucleoli clustering in zygotic pronuclei might influence chromosome segregation fidelity[424]. Nucleoli clustering was found to be required for parental genome polarisation within the pronuclei, which facilitates genome unification after nuclear envelope breakdown, thereby ensuring proper chromosome segregation[424]. Micro/multinucleation is another feature of human embryos in fertility clinics frequently associated with low embryonic competence, and work from our lab has shown that micronuclei are a major driver of aneuploidy in embryos[425]. Micronuclei were found to emerge from lagging chromosomes at anaphase, and were shown to be persistently inherited by daughter

cells in the following embryonic divisions, thereby leading to aneuploidy[425] (**Chapter 2, Figure 29**). Binucleation is also a common phenomenon of human embryos in *in vitro* fertilisation cycles, and the results described in this thesis further add to our understanding of the clinical significance of binucleation, both in terms of potential causes (**Chapters 3 and 4**) and consequences of binucleation (**Chapters 1 and 4**).

Our finding that apical polarity negatively regulates furrow ingression by preventing the recruitment of cytokinesis components to the apical side (**Chapter 3, Figures 37, 39 and 41**) might indicate that cytokinesis is compromised in polarised cells, thereby increasing their susceptibility to cytokinesis failure. On one hand, this increased susceptibility of trophectoderm cells to binucleation could be seemingly harmless, as programmed cytokinesis failure at peri/post implantation stages could contribute to the generation of specialised binucleated/multinucleated trophoblast giant cells (TGCs), which are an integral part of placental development in several mammalian species and are thought to ensure proper hormone production and maintenance of the feto-maternal interface during foetal development[426, 427]. On the other hand, our results also indicate that unscheduled cytokinesis failure at early preimplantation stages negatively impacts embryo health by increasing aneuploidy rates (**Chapter 2, Figure 16F-G**). Therefore, it is possible that the impact of apical polarity on cytokinesis exclusively in outer cells from the 16-cell stage onwards might be an evolutionary mechanism that facilitates the generation of specialised cell types required for placental development, while at the same time restricting cytokinesis failure from taking place at earlier stages, during which tetraploidisation severely compromises development.

An ongoing debate is whether cytokinesis failure is the only cause of embryo binucleation, and recent studies suggest that other mechanisms unrelated to cytokinesis might also play a role (**see also Chapter 4**)[410]. For instance, failure in parental genome unification during the first zygotic division was found to generate 2-cell binucleated blastomeres that still retain a diploid genome in mouse embryos (**Chapter 4, Figure 42**)[410]. This phenomenon could potentially explain the observation that human blastomeres scored as binucleated at the 2-cell stage are frequently diploid[428]. Interestingly, a recent report contradicts this idea as it shows that the mechanisms of parental genome unification differ substantially between mouse and human zygotes. As opposed to the mouse zygote, in which each parental genome initially assembles two separate spindles at early prometaphase driven by cytoplasmic MTOCs[410] (**Chapter 4, Figure 42**), the human zygote

instead assembles a single bipolar spindle mediated by sperm centrosome microtubule nucleation[429]. Therefore, it is likely that erroneous zygotic divisions might not originate from failure of spindle fusion in humans, and rather might be a result of an inability of sperm centrosomes to properly capture both the maternal and paternal genome[429]. Future live imaging experiments in which human embryonic cell divisions are observed with fluorescently-labelled microtubules, chromosomes and plasma membrane will certainly provide invaluable information regarding the different origins of binucleation.

5.6 Impacts of tetraploidy on inner cell mass formation

In embryos, the adverse effects of tetraploidy go beyond chromosomal instability and aneuploidy, and major impacts of tetraploidy on ICM establishment at the blastocyst stage have been reported[299, 363, 364, 365] (**see also section 1.4.5**). The following paragraphs will detail unpublished experiments performed to address the mechanistic basis of the ICM deficiency phenotype observed in tetraploid embryos. Firstly, we induced tetraploidy by treating mouse embryos with the actin-binding agent Latrunculin during the 4- to 8-cell transition in order to generate binucleated embryos. We then performed immunofluorescence experiments of stage-matched diploid and tetraploid blastocysts with labelled ICM (OCT4 pluripotency marker) to compare the proportion of ICM cells between diploids and tetraploids. Notably, although tetraploid embryos developed to the blastocyst stage, they frequently displayed absent or reduced ICM formation, as evidenced by low proportions of OCT4-labelled inner cells at the blastocyst stage (**Figure 48A-B**), as previously[363].

The exact mechanism by which tetraploidy causes ICM deficiency is unknown, but is thought to be a result of reduced cell numbers at the time of blastocoel formation, given that tetraploid embryos have half the number of blastomeres as compared to stage-matched diploid embryos, as a consequence of cytokinesis failure[363]. During preimplantation development, inner cells are first established during the 8- to 16-cell transition, during which asymmetric cell divisions and cell internalisation events both generate inner cells within the nascent 16-cell stage embryo[59]. The subsequent cell division, from the 16- to 32-cell stage, further increases the pool of inner cells when outer cells undergo another round of asymmetric cell divisions or internalisation events, and the inner cells previously established at the 16-cell stage divide, thus resulting in a 32-cell stage embryo

that undergoes blastocoel formation with a well-established reservoir of inner cells[59]. Our live imaging experiments are consistent with this and demonstrate that diploid ~32-cell embryos undergo blastocoel formation when they have ~27-32 cells (**Figure 48C-D**). Importantly, at this point, a pool of 5-7 inner cells has already been established, which will further contribute to ICM formation (**Figure 48C-D**). In contrast, our experiments also revealed that although tetraploid embryos undergo blastocoel formation chronologically at the same time as stage-matched diploids, they do so when they have less than half the number of cells as diploids (**Figure 48C-D**). More specifically, tetraploid embryos frequently undergo blastocoel formation when they have only between ~8-12 blastomeres and thus, very few or no inner cells have been generated at this point (**Figure 48C-D**). Importantly, this suggests that the simple halving of cell numbers caused by cytokinesis failure might not be the sole contributor to ICM deficiency in tetraploids, and other unrelated mechanisms might further decrease overall cell numbers, thus limiting the number of inner cells generated.

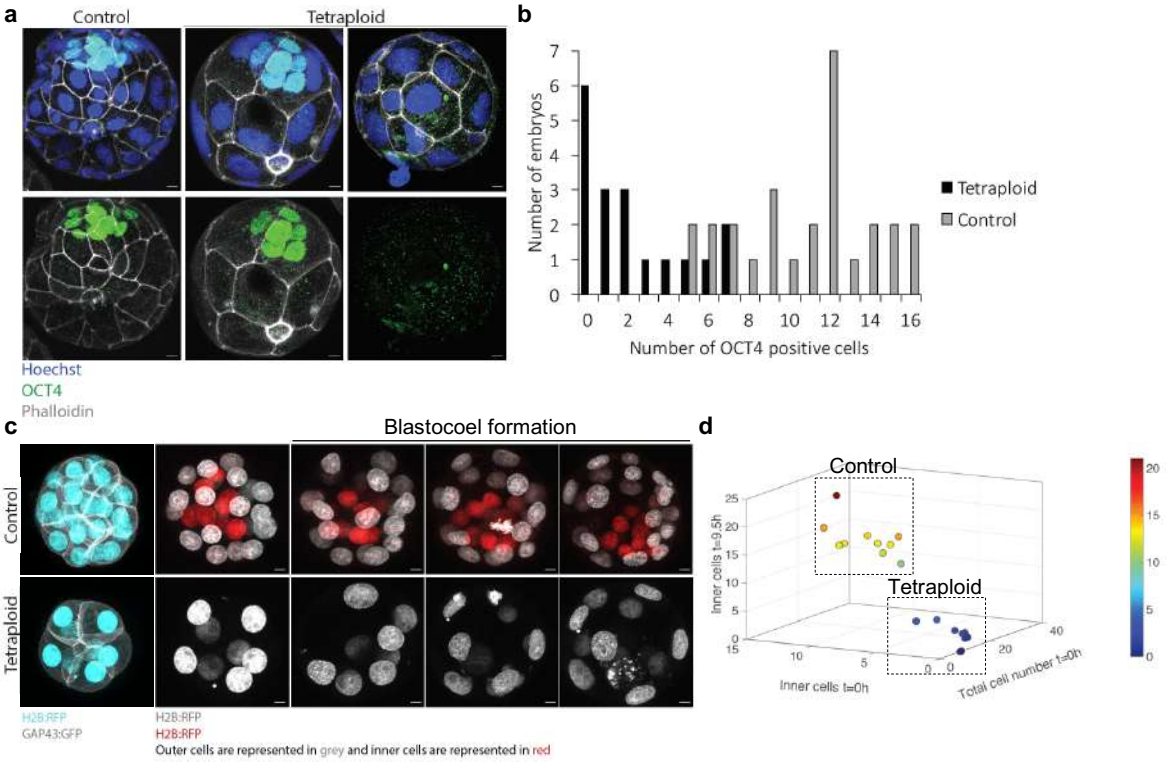

Figure 48. – Tetraploid embryos display inner cell mass deficiency.

(a) *Representative immunofluorescence images of late blastocyst diploid (control) and tetraploid mouse embryos. Note that although OCT4-positive inner cells can be observed in some tetraploid embryos (middle panel), a complete absence of OCT4-labelled inner cells is often detected instead (right panel).* ***(b)*** *Frequency distribution of control (n = 27 embryos) and tetraploid embryos (n = 18 embryos) containing OCT4-positive cells at the late blastocyst stage.* ***(c and d)*** *Representative time-lapse images of diploid control and tetraploid embryos undergoing blastocoel formation (c) and 3D plot correlating the total number of cells at blastocoel formation with the number of inner cells both at the onset of blastocoel formation and at 9.5h after blastocoel formation in control (n = 10 embryos) and tetraploid embryos (n = 9 embryos) (d). Note that tetraploid embryos (blue dots in the 3D plot) frequently initiate blastocoel formation with around ~8-12 cells and, at this point, there are too few or no inner cells to allow for proper inner cell mass formation.*

An important limitation of most tetraploidy studies is the lack of appropriate diploid controls that accurately reflect the number, stage, and size of tetraploid blastomeres. For instance, when binucleation is generated during the 4- to 8-cell division, the resulting tetraploid embryo is, developmentally, at the 8-cell stage, but contains four 4-cell-stage-sized blastomeres (**Figure 49A – top and middle panels**). It is thus challenging to dissociate the relative roles of ploidy and cell size/numbers on the phenotype of ICM deficiency observed in tetraploids. Therefore, to circumvent these limitations and precisely dissociate the relative roles of cell numbers/size and other yet undiscovered effects of tetraploidy on ICM formation, we developed an experimental design to create diploid embryos containing the same number and size of blastomeres as tetraploids. Firstly, we induced binucleation at the 2- to 4-cell transition using the actin-binding agent Latrunculin to promote cytokinesis failure. We then removed one of the nuclei within the binucleated embryo by micromanipulation, resulting in an 'enucleated embryo' that displayed the same number of cells, with similar size and at the same developmental stage as tetraploids, while maintaining a diploid genome (**Figure 49A** – **third panel**).

Strikingly, using this experimental design, we observed that diploid-enucleated embryos were able to generate comparable numbers of ICM cells as diploid sham-manipulated embryos at the blastocyst stage (**Figure 49B-C**), further corroborating the notion that other factors unrelated to a simple halving of cell numbers are responsible for ICM deficiency in tetraploids. Interestingly, tetraploid embryos displayed significantly reduced total number of cells at the blastocyst stage as compared to both diploid-enucleated and diploid sham-manipulated embryos (**Figure 49D**), suggesting that tetraploid blastomeres might either get eliminated later in development or that a cell cycle delay or arrest may contribute to the ICM deficiency in tetraploids. Consistent with this,

we also observed that diploid:tetraploid chimeric embryos developed to the blastocyst stage with a higher proportion of diploid blastomeres than tetraploids, and that their ICM was primarily composed of diploid cells **(Figure 49E-H)**. These sets of experiments suggest that the deficiency in ICM formation in tetraploids may be induced by a cell cycle delay/arrest or by an increase in apoptosis, both of which would ultimately reduce the number of cells at the blastocyst stage, thereby affecting ICM formation.

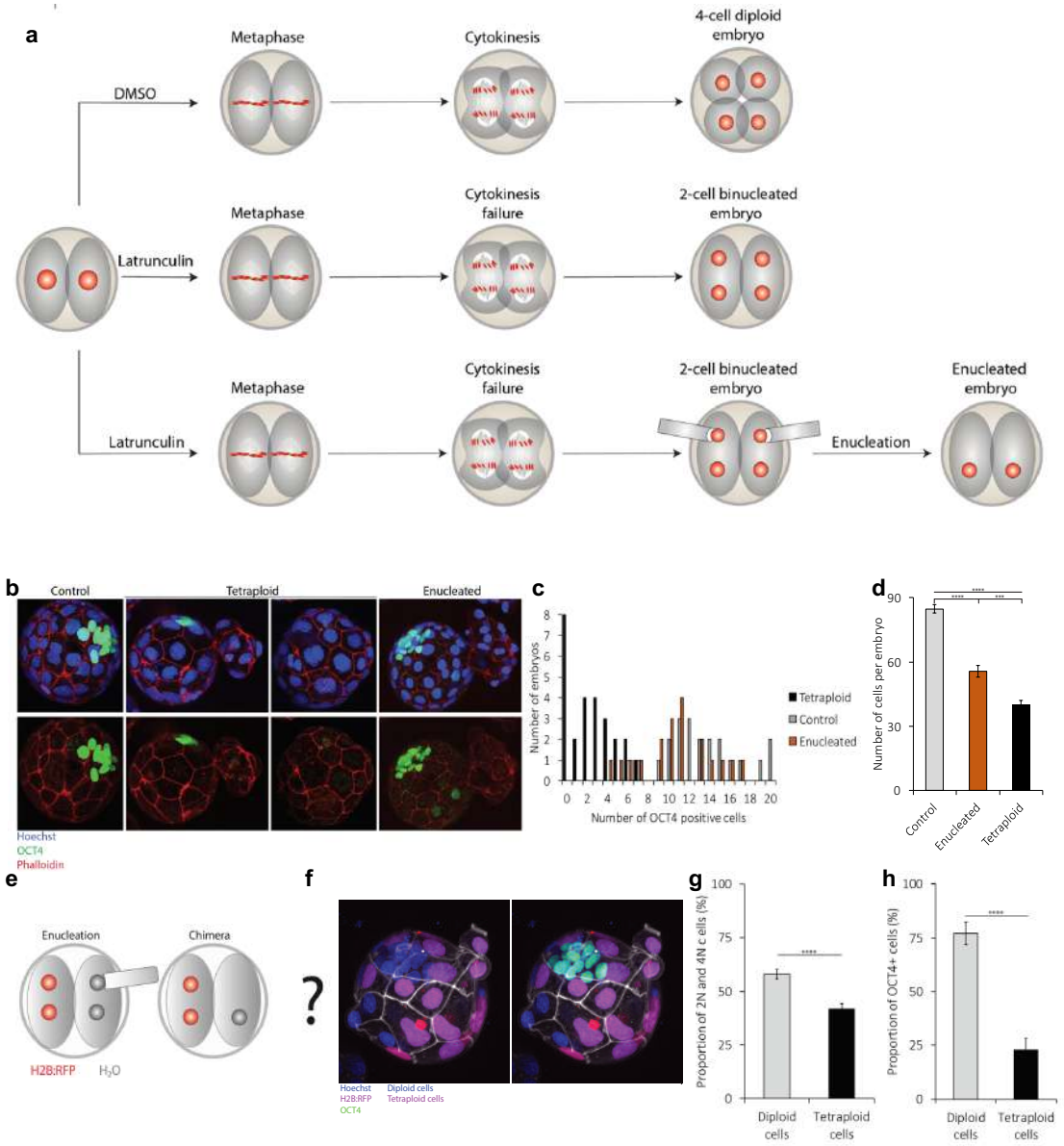

Figure 49. – Inner cell mass deficiency in tetraploid embryos is not attributable solely to low cell numbers.

(a) *Scheme illustrating the experimental design for the creation of 'enucleated-diploid' controls. Embryos at the 2- to 4-cell transition are exposed to either DMSO as a control or Latrunculin for induction of binucleation by cytokinesis failure. Subsequent removal of one of the nuclei within the binucleated embryo is performed by micromanipulation and generates a diploid embryo that is developmentally at the 4-cell stage but contains two 2-cell-sized blastomeres. This approach allows for a direct comparison of diploid and tetraploid embryos without intervening effects of divergent cell numbers, cell sizes or developmental stages.* ***(b)*** *Representative immunofluorescence images of late blastocyst diploid (control), tetraploid and enucleated mouse embryos.* ***(c)*** *Frequency distribution of control (n = 21 embryos), tetraploid (n = 28 embryos) and enucleated embryos (n = 19 embryos) containing OCT4-positive cells at the late blastocyst stage.* ***(d)*** *Total number of cells per embryo of control (n = 21 embryos), tetraploid (n = 28 embryos) and enucleated embryos (n = 19 embryos) at the late blastocyst stage.* ***(e and f)*** *Scheme illustrating the experimental design for the generation of chimeric diploid:tetraploid embryos (e) and representative immunofluorescence images of chimeric diploid:tetraploid embryos at the late blastocyst stage (f). 2-cell embryos containing one blastomere expressing H2B:RFP are exposed to Latrunculin for induction of binucleation. Enucleation is further performed in only one of the blastomeres to remove one of the nuclei and the H2B:RFP fluorescent signal is used to identify the diploid or tetraploid clones.* ***(g)*** *Proportion of diploid (2N) and tetraploid (4N) blastomeres in chimeric embryos (n = 24 embryos; $P < 0.0001$)* ***(h)*** *Proportion of OCT4-positive inner cells in chimeric embryos (n = 24 embryos; $P < 0.0001$).*

We next set out to determine whether high levels of apoptosis and/or a delay in cell cycle progression could be the cause of reduced cell numbers in tetraploid embryos. Immunofluorescence experiments demonstrated that tetraploid blastocysts displayed significantly increased levels of apoptosis as compared to diploid-enucleated, as evidenced by an increased proportion of blastomeres positively labelled for the apoptotic marker cleaved caspase 3 (cCaspase 3) (**Figure 50A-B**). Tetraploid embryo development was previously shown to be suppressed by p53-dependent apoptosis specifically at post implantation stages[365]. Our results suggest that apoptosis may initiate even earlier, potentially as a mechanism to prevent implantation of tetraploid embryos. In addition, live cell imaging experiments of diploid-enucleated and tetraploid embryos also demonstrated that the duration of the cell cycle was increased in tetraploid embryos during the following two divisions after tetraploidisation (**Figure 50C-E**), suggesting that cell cycle delay may also be a contributing factor for the ICM deficiency of tetraploids. A delay in cell cycle progression has been previously reported in mouse tetraploid embryos compared to stage-matched diploid embryos[364], and thus our results further suggest that this phenomenon may not attributable to the differences in cell size/number, and rather is a feature of cells harbouring a tetraploid genome. However, a significant drawback of our experimental design is that diploid-enucleated embryos displayed reduced cell cycle duration as compared to sham-manipulated controls (data

not shown). Thus, it is unclear whether the enucleation procedure itself or other indirect effects of altering nuclear:cytoplasmic ratio in enucleated embryos may have affected cell cycle dynamics in those embryos. Therefore, although our results allude to the idea that a combination of cell cycle delay and increased apoptosis may drive ICM deficiency in tetraploid embryos, alternative experimental designs that allow for the generation of stage and size-matched diploid and tetraploid embryos that are not affected by potential impacts of micromanipulation are required to fully resolve this question.

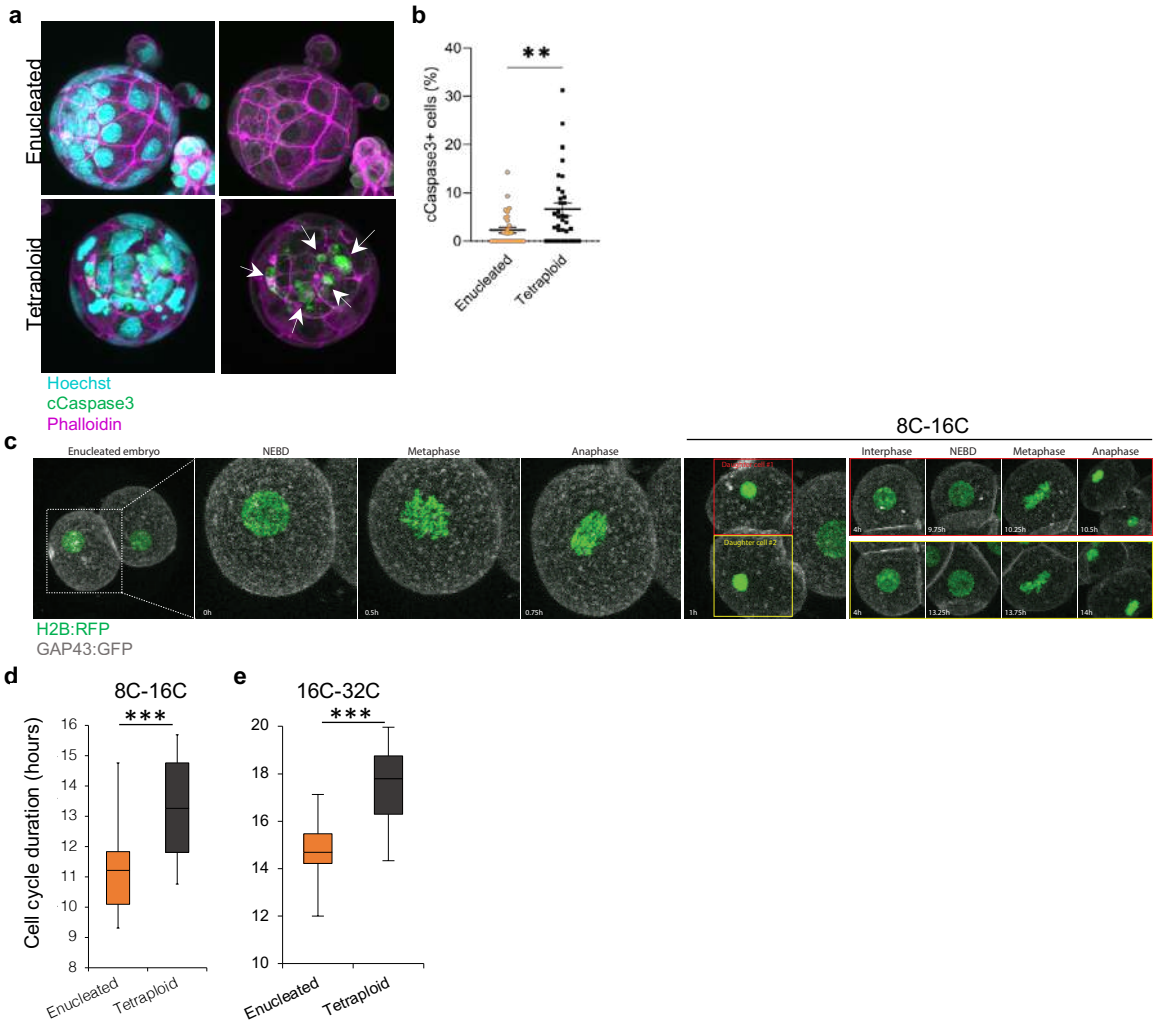

Figure 50. – Inner cell mass deficiency in tetraploid embryos is possibly a result of cell cycle delay and increased apoptosis.

(a) *Representative immunofluorescence images of enucleated and tetraploid embryos at the late blastocyst stage. Note the presence of cleaved caspase 3-positive apoptotic cells in the tetraploid embryo (white arrows).* ***(b)*** *Proportion of cleaved caspase 3-positive apoptotic cells in enucleated (n = 32 embryos) and tetraploid blastocysts (n = 34 embryos; P = 0.0029).* ***(c-e)*** *Representative time-lapse imaging of an enucleated embryo expressing H2B:RFP and GAP43:GFP (c) and quantification of cell cycle duration at the 8- to 16-cell stage (enucleated n = 24 embryos; tetraploid n= 20 embryos; P < 0.0001) (d) and 16- to 32-cell stages (e) (enucleated n = 13 embryos; tetraploid n = 14 embryos; P = 0.0002). Cell cycle duration was measured as the time from anaphase onset to anaphase onset of the subsequent cell division and data is displayed as an average of at least two blastomeres per embryo. Note that 8C-16C and 16C-32C transitions refer to developmental stage rather than cell numbers. Time is shown in hours.*

Overall, our experiments are in line with previous findings that tetraploidy impairs ICM formation in the mouse embryo[299, 363, 364, 365] and are consistent with a model wherein a combination of cell cycle delay and apoptosis may drive this phenotype. Our finding that blastocoel formation occurs in tetraploid embryos when they have too few cells to effectively form an ICM suggests that other factors unrelated to the simple halving of cell numbers caused by cytokinesis failure may affect total cell numbers and consequently ICM formation. In addition, by using a unique experimental design in which the direct effects of tetraploidy upon ICM formation are assessed while removing other important confounding variables such as differences in cell size/numbers and developmental stage between diploids and tetraploids, we found that tetraploidy might impair ICM formation by delaying cell cycle progression and increasing apoptosis. Although potential artifacts of micromanipulation may have played a role on our cell cycle duration results, it would nevertheless be interesting to further investigate the potential causes for the cell cycle delay identified in tetraploids.

Our previous work has shown that the second division following tetraploidisation exhibits a ~20min delay in mitotic duration as compared to that of stage-matched diploid embryos[359] (**Chapter 2, Figure 23B**). Although this ~20min delay certainly contributes to the cell cycle delay in tetraploid embryos, it does not fully account for the ~2.5h prolongation of cell cycle duration reported in our experiments and instead, other interphase-specific effects must also be present. An immediate future direction from these findings would be to use live fluorescent probes that allow for clear visualisation of cell cycle phases, such as PCNA:EGFP[359, 430] (**Chapter 2, Figure 17C-D**), to further identify which phase(s) of the cell cycle are predominantly affected by tetraploidy. An extensively described cause of cell cycle delay is DNA damage, wherein different molecular

pathways either involving p53-dependent cell cycle arrest, or DNA repair machineries can cause delays or arrests in all phases of interphase (G1, S and G2)[431]. Therefore, one possibility is that tetraploid blastomeres undergo replication stress, perhaps due to an overburden of the DNA replication machinery imposed by doubled genome content, thereby leading to DNA damage, and consequently causing a prolongation in interphase duration. One way to address this possibility is by using immunofluorescence staining of DNA damage markers, such as the double-strand break marker γH2AX[425], to compare the levels of DNA damage in diploids and tetraploids. If tetraploid embryos indeed exhibit higher levels of DNA damage than diploids, then it would be interesting to further manipulate the DNA repair machinery by using chemical inhibitors to address whether this could rescue cell numbers and ICM formation in tetraploid embryos.

Another interesting possibility is that the increase in the proportion of apoptotic cells observed in tetraploid blastocysts may reflect a late onset of the tetraploidy checkpoint. As previously described, tetraploid blastomeres do not initially activate the Hippo pathway in response to tetraploidy (**Chapter 5, section 5.4.2, Figure 47**), however, given that Hippo activation is a major determinant of inner cell specification from the 16-cell stage onwards[64], it is possible that its role in triggering the tetraploidy checkpoint is first observed at later stages. It would be interesting to further inhibit Hippo signalling, either chemically or genetically, to address whether this would impact the incidence of apoptosis in tetraploid embryos, although it might be challenging to manipulate Hippo signalling without disturbing overall embryo health and cell fate. Nevertheless, future experiments that address whether cell numbers and ICM formation can be rescued in tetraploid embryos upon artificial suppression of apoptosis might provide invaluable insights into the mechanisms of embryonic failure caused by tetraploidy.

5.7 Concluding remarks

Cytokinesis is a critical step of cell division and is essential for the maintenance of genomic fidelity. Understanding cytokinesis regulation is key, as its failure leads to the formation of a single binucleated cell with a tetraploid genome which, in somatic cells, can lead to two distinct fates: cell cycle arrest and apoptosis[341, 342, 344] or chromosomal instability and aneuploidy[200, 201, 324]. Moreover, binucleation is also relatively common in human embryos from *in vitro* fertilisation clinics, however whether and how this phenotype negatively impacts embryo development, as well

as the mechanisms that might lead to the formation of binucleated blastomeres had not been fully elucidated. In this thesis, I applied high resolution imaging techniques as well as precise manipulations of cell size, cell adhesion, and protein levels to investigate the regulatory mechanisms of cytokinesis and the consequences of failure in the early mouse embryo. I uncovered that a subset of cells within the preimplantation embryo may be more susceptible to cytokinesis failure due to unexpected effects of the developmental machinery on contractile ring assembly. More specifically, mechanistic experiments revealed that outer cell apical polarity limits the recruitment of cytokinesis components locally at the apical side of the contractile ring. I also found that upon cytokinesis failure, the tetraploid embryo rapidly develops aneuploidy by a mechanism distinct to that of somatic cells, wherein altered kinetochore-microtubule dynamics causes high rates of chromosome mis-segregation. These findings greatly contribute to our knowledge of cell biology, as they provide mechanistic insights into the spatiotemporal control of cytokinesis and unravel a novel mechanism by which tetraploidy causes chromosomal instability. In addition, this work has a direct clinical implication as it provides evidence that binucleation may be a potential cause of pregnancy failures in fertility clinics. In the long term, I hope that the results presented in this thesis will be helpful to embryologists and clinicians working in fertility clinics to select the best embryos to be transferred back to the patients, and ultimately increase the chances of a successful pregnancies.

References

1. Clift D, Schuh M. Restarting life: fertilization and the transition from meiosis to mitosis. *Nat Rev Mol Cell Biol* **14**, 549-562 (2013).

2. Arur S. Signaling-Mediated Regulation of Meiotic Prophase I and Transition During Oogenesis. *Results Probl Cell Differ* **59**, 101-123 (2017).

3. Jaffe LA, Egbert JR. Regulation of Mammalian Oocyte Meiosis by Intercellular Communication Within the Ovarian Follicle. *Annu Rev Physiol* **79**, 237-260 (2017).

4. Clarke HJ. Regulation of germ cell development by intercellular signaling in the mammalian ovarian follicle. *Wiley Interdiscip Rev Dev Biol*, (2017).

5. Vaccari S, Weeks JL, 2nd, Hsieh M, Menniti FS, Conti M. Cyclic GMP signaling is involved in the luteinizing hormone-dependent meiotic maturation of mouse oocytes. *Biol Reprod* **81**, 595-604 (2009).

6. Liu L, Kong N, Xia G, Zhang M. Molecular control of oocyte meiotic arrest and resumption. *Reprod Fertil Dev* **25**, 463-471 (2013).

7. Norris RP*, et al.* Cyclic GMP from the surrounding somatic cells regulates cyclic AMP and meiosis in the mouse oocyte. *Development* **136**, 1869-1878 (2009).

8. Jin F*, et al.* Cdc20 is critical for meiosis I and fertility of female mice. *PLoS Genet* **6**, e1001147 (2010).

9. Masui Y, Markert CL. Cytoplasmic control of nuclear behavior during meiotic maturation of frog oocytes. *J Exp Zool* **177**, 129-145 (1971).

10. Sagata N, Watanabe N, Vande Woude GF, Ikawa Y. The c-mos proto-oncogene product is a cytostatic factor responsible for meiotic arrest in vertebrate eggs. *Nature* **342**, 512-518 (1989).

11. Watanabe N, Hunt T, Ikawa Y, Sagata N. Independent inactivation of MPF and cytostatic factor (Mos) upon fertilization of Xenopus eggs. *Nature* **352**, 247-248 (1991).

12. Haccard O*, et al.* Induction of metaphase arrest in cleaving Xenopus embryos by MAP kinase. *Science* **262**, 1262-1265 (1993).

13. Kosako H, Gotoh Y, Nishida E. Mitogen-activated protein kinase kinase is required for the mos-induced metaphase arrest. *J Biol Chem* **269**, 28354-28358 (1994).

14. Bhatt RR, Ferrell JE, Jr. The protein kinase p90 rsk as an essential mediator of cytostatic factor activity. *Science* **286**, 1362-1365 (1999).

15. Dumont J, Umbhauer M, Rassinier P, Hanauer A, Verlhac MH. p90Rsk is not involved in cytostatic factor arrest in mouse oocytes. *J Cell Biol* **169**, 227-231 (2005).

16. Schmidt A*, et al.* Xenopus polo-like kinase Plx1 regulates XErp1, a novel inhibitor of APC/C activity. *Genes Dev* **19**, 502-513 (2005).

17. Loeb J. On the Chemical Character of the Process of Fertilization and Its Bearing Upon the Theory of Life Phenomena. *Science* **26**, 425-437 (1907).

18. Miyazaki S, Hashimoto N, Yoshimoto Y, Kishimoto T, Igusa Y, Hiramoto Y. Temporal and spatial dynamics of the periodic increase in intracellular free calcium at fertilization of golden hamster eggs. *Dev Biol* **118**, 259-267 (1986).

19. Haverfield J*, et al.* Ca(2+) dynamics in oocytes from naturally-aged mice. *Sci Rep* **6**, 19357 (2016).

20. Bury L, Coelho PA, Glover DM. From Meiosis to Mitosis: The Astonishing Flexibility of Cell Division Mechanisms in Early Mammalian Development. *Curr Top Dev Biol* **120**, 125-171 (2016).

21. Palmer N, Kaldis P. Regulation of the Embryonic Cell Cycle During Mammalian Preimplantation Development. *Curr Top Dev Biol* **120**, 1-53 (2016).

22. Holt JE, Lane SI, Jones KT. The control of meiotic maturation in mammalian oocytes. *Curr Top Dev Biol* **102**, 207-226 (2013).

23. Morgan D. *The cell cycle: Principles of control.* New Science Press Ltd. (2007).

24. Matson JP, Cook JG. Cell cycle proliferation decisions: the impact of single cell analyses. *FEBS J* **284**, 362-375 (2017).

25. Abramczuk J, Sawicki W. Pronuclear synthesis of DNA in fertilized and parthenogenetically activated mouse eggs. *Exp Cell Res* **92**, 361-371 (1975).

26. Howlett SK, Bolton VN. Sequence and regulation of morphological and molecular events during the first cell cycle of mouse embryogenesis. *J Embryol Exp Morphol* **87**, 175-206 (1985).

27. Krishna M, Generoso WM. Timing of sperm penetration, pronuclear formation, pronuclear DNA synthesis, and first cleavage in naturally ovulated mouse eggs. *J Exp Zool* **202**, 245-252 (1977).

28. Molls M, Zamboglou N, Streffer C. A comparison of the cell kinetics of pre-implantation mouse embryos from two different mouse strains. *Cell Tissue Kinet* **16**, 277-283 (1983).

29. Bolton VN, Oades PJ, Johnson MH. The relationship between cleavage, DNA replication, and gene expression in the mouse 2-cell embryo. *J Embryol Exp Morphol* **79**, 139-163 (1984).

30. Smith RK, Johnson MH. Analysis of the third and fourth cell cycles of mouse early development. *J Reprod Fertil* **76**, 393-399 (1986).

31. Latham KE, Schultz RM. Embryonic genome activation. *Front Biosci* **6**, D748-759 (2001).

32. Lee MT, Bonneau AR, Giraldez AJ. Zygotic genome activation during the maternal-to-zygotic transition. *Annu Rev Cell Dev Biol* **30**, 581-613 (2014).

33. Christians E, Campion E, Thompson EM, Renard JP. Expression of the HSP 70.1 gene, a landmark of early zygotic activity in the mouse embryo, is restricted to the first burst of transcription. *Development* **121**, 113-122 (1995).

34. Davis W, Jr., De Sousa PA, Schultz RM. Transient expression of translation initiation factor eIF-4C during the 2-cell stage of the preimplantation mouse embryo: identification by mRNA differential display and the role of DNA replication in zygotic gene activation. *Dev Biol* **174**, 190-201 (1996).

35. Santos F, Peters AH, Otte AP, Reik W, Dean W. Dynamic chromatin modifications characterise the first cell cycle in mouse embryos. *Dev Biol* **280**, 225-236 (2005).

36. Lepikhov K, Walter J. Differential dynamics of histone H3 methylation at positions K4 and K9 in the mouse zygote. *BMC Dev Biol* **4**, 12 (2004).

37. Yartseva V, Giraldez AJ. The Maternal-to-Zygotic Transition During Vertebrate Development: A Model for Reprogramming. *Curr Top Dev Biol* **113**, 191-232 (2015).

38. Semotok JL, Cooperstock RL, Pinder BD, Vari HK, Lipshitz HD, Smibert CA. Smaug recruits the CCR4/POP2/NOT deadenylase complex to trigger maternal transcript localization in the early Drosophila embryo. *Curr Biol* **15**, 284-294 (2005).

39. Weidmann CA, Raynard NA, Blewett NH, Van Etten J, Goldstrohm AC. The RNA binding domain of Pumilio antagonizes poly-adenosine binding protein and accelerates deadenylation. *RNA* **20**, 1298-1319 (2014).

40. Nakamura A, Sato K, Hanyu-Nakamura K. Drosophila cup is an eIF4E binding protein that associates with Bruno and regulates oskar mRNA translation in oogenesis. *Dev Cell* **6**, 69-78 (2004).

41. Gillian-Daniel DL, Gray NK, Astrom J, Barkoff A, Wickens M. Modifications of the 5' cap of mRNAs during Xenopus oocyte maturation: independence from changes in poly(A) length and impact on translation. *Mol Cell Biol* **18**, 6152-6163 (1998).

42. Ducibella T, Anderson E. The effects of calcium deficiency on the formation of the zonula occludens and blastocoel in the mouse embryo. *Dev Biol* **73**, 46-58 (1979).

43. Winkel GK, Ferguson JE, Takeichi M, Nuccitelli R. Activation of protein kinase C triggers premature compaction in the four-cell stage mouse embryo. *Dev Biol* **138**, 1-15 (1990).

44. Larue L, Ohsugi M, Hirchenhain J, Kemler R. E-cadherin null mutant embryos fail to form a trophectoderm epithelium. *Proc Natl Acad Sci U S A* **91**, 8263-8267 (1994).

45. De Vries WN*, et al.* Maternal beta-catenin and E-cadherin in mouse development. *Development* **131**, 4435-4445 (2004).

46. Stephenson RO, Yamanaka Y, Rossant J. Disorganized epithelial polarity and excess trophectoderm cell fate in preimplantation embryos lacking E-cadherin. *Development* **137**, 3383-3391 (2010).

47. Vestweber D, Gossler A, Boller K, Kemler R. Expression and distribution of cell adhesion molecule uvomorulin in mouse preimplantation embryos. *Dev Biol* **124**, 451-456 (1987).

48. Fierro-Gonzalez JC, White MD, Silva JC, Plachta N. Cadherin-dependent filopodia control preimplantation embryo compaction. *Nat Cell Biol* **15**, 1424-1433 (2013).

49. Maitre JL*, et al.* Asymmetric division of contractile domains couples cell positioning and fate specification. *Nature* **536**, 344-348 (2016).

50. Johnson MH, Ziomek CA. The foundation of two distinct cell lineages within the mouse morula. *Cell* **24**, 71-80 (1981).

51. Johnson MH, Ziomek CA. Induction of polarity in mouse 8-cell blastomeres: specificity, geometry, and stability. *J Cell Biol* **91**, 303-308 (1981).

52. Dard N, Louvet-Vallee S, Santa-Maria A, Maro B. Phosphorylation of ezrin on threonine T567 plays a crucial role during compaction in the mouse early embryo. *Dev Biol* **271**, 87-97 (2004).

53. Reeve WJ, Ziomek CA. Distribution of microvilli on dissociated blastomeres from mouse embryos: evidence for surface polarization at compaction. *J Embryol Exp Morphol* **62**, 339-350 (1981).

54. Louvet S, Aghion J, Santa-Maria A, Mangeat P, Maro B. Ezrin becomes restricted to outer cells following asymmetrical division in the preimplantation mouse embryo. *Dev Biol* **177**, 568-579 (1996).

55. Liu H*, et al.* Atypical PKC, regulated by Rho GTPases and Mek/Erk, phosphorylates Ezrin during eight-cell embryocompaction. *Dev Biol* **375**, 13-22 (2013).

56. Vinot S, Le T, Ohno S, Pawson T, Maro B, Louvet-Vallee S. Asymmetric distribution of PAR proteins in the mouse embryo begins at the 8-cell stage during compaction. *Dev Biol* **282**, 307-319 (2005).

57. Kono K, Tamashiro DA, Alarcon VB. Inhibition of RHO-ROCK signaling enhances ICM and suppresses TE characteristics through activation of Hippo signaling in the mouse blastocyst. *Dev Biol* **394**, 142-155 (2014).

58. Hirate Y, Hirahara S, Inoue K, Kiyonari H, Niwa H, Sasaki H. Par-aPKC-dependent and -independent mechanisms cooperatively control cell polarity, Hippo signaling, and cell positioning in 16-cell stage mouse embryos. *Dev Growth Differ* **57**, 544-556 (2015).

59. Mihajlovic AI, Bruce AW. The first cell-fate decision of mouse preimplantation embryo development: integrating cell position and polarity. *Open Biol* **7**, (2017).

60. Mihajlovic AI, Bruce AW. Rho-associated protein kinase regulates subcellular localisation of Angiomotin and Hippo-signalling during preimplantation mouse embryo development. *Reprod Biomed Online* **33**, 381-390 (2016).

61. Alarcon VB. Cell polarity regulator PARD6B is essential for trophectoderm formation in the preimplantation mouse embryo. *Biol Reprod* **83**, 347-358 (2010).

62. Dard N, Le T, Maro B, Louvet-Vallee S. Inactivation of aPKClambda reveals a context dependent allocation of cell lineages in preimplantation mouse embryos. *PLoS One* **4**, e7117 (2009).

63. Cao Z, Carey TS, Ganguly A, Wilson CA, Paul S, Knott JG. Transcription factor AP-2gamma induces early Cdx2 expression and represses HIPPO signaling to specify the trophectoderm lineage. *Development* **142**, 1606-1615 (2015).

64. Chazaud C, Yamanaka Y. Lineage specification in the mouse preimplantation embryo. *Development* **143**, 1063-1074 (2016).

65. Fleming TP. A quantitative analysis of cell allocation to trophectoderm and inner cell mass in the mouse blastocyst. *Dev Biol* **119**, 520-531 (1987).

66. Dard N, Louvet-Vallee S, Maro B. Orientation of mitotic spindles during the 8- to 16-cell stage transition in mouse embryos. *PLoS One* **4**, e8171 (2009).

67. Ajduk A, Biswas Shivhare S, Zernicka-Goetz M. The basal position of nuclei is one pre-requisite for asymmetric cell divisions in the early mouse embryo. *Dev Biol* **392**, 133-140 (2014).

68. Korotkevich E*, et al.* The Apical Domain Is Required and Sufficient for the First Lineage Segregation in the Mouse Embryo. *Dev Cell* **40**, 235-247 e237 (2017).

69. Niwayama R*, et al.* A Tug-of-War between Cell Shape and Polarity Controls Division Orientation to Ensure Robust Patterning in the Mouse Blastocyst. *Dev Cell* **51**, 564-574 e566 (2019).

70. Anani S, Bhat S, Honma-Yamanaka N, Krawchuk D, Yamanaka Y. Initiation of Hippo signaling is linked to polarity rather than to cell position in the pre-implantation mouse embryo. *Development* **141**, 2813-2824 (2014).

71. Samarage CR*, et al.* Cortical Tension Allocates the First Inner Cells of the Mammalian Embryo. *Dev Cell* **34**, 435-447 (2015).

72. Watanabe T, Biggins JS, Tannan NB, Srinivas S. Limited predictive value of blastomere angle of division in trophectoderm and inner cell mass specification. *Development* **141**, 2279-2288 (2014).

73. Nishioka N*, et al.* The Hippo signaling pathway components Lats and Yap pattern Tead4 activity to distinguish mouse trophectoderm from inner cell mass. *Dev Cell* **16**, 398-410 (2009).

74. Nishioka N*, et al.* Tead4 is required for specification of trophectoderm in pre-implantation mouse embryos. *Mech Dev* **125**, 270-283 (2008).

75. Strumpf D*, et al.* Cdx2 is required for correct cell fate specification and differentiation of trophectoderm in the mouse blastocyst. *Development* **132**, 2093-2102 (2005).

76. Niwa H*, et al.* Interaction between Oct3/4 and Cdx2 determines trophectoderm differentiation. *Cell* **123**, 917-929 (2005).

77. Leung CY, Zernicka-Goetz M. Angiomotin prevents pluripotent lineage differentiation in mouse embryos via Hippo pathway-dependent and -independent mechanisms. *Nat Commun* **4**, 2251 (2013).

78. Hirate Y*, et al.* Polarity-dependent distribution of angiomotin localizes Hippo signaling in preimplantation embryos. *Curr Biol* **23**, 1181-1194 (2013).

79. Chazaud C, Yamanaka Y, Pawson T, Rossant J. Early lineage segregation between epiblast and primitive endoderm in mouse blastocysts through the Grb2-MAPK pathway. *Dev Cell* **10**, 615-624 (2006).

80. Singh AM, Hamazaki T, Hankowski KE, Terada N. A heterogeneous expression pattern for Nanog in embryonic stem cells. *Stem Cells* **25**, 2534-2542 (2007).

81. Yamanaka Y, Lanner F, Rossant J. FGF signal-dependent segregation of primitive endoderm and epiblast in the mouse blastocyst. *Development* **137**, 715-724 (2010).

82. Kang M, Piliszek A, Artus J, Hadjantonakis AK. FGF4 is required for lineage restriction and salt-and-pepper distribution of primitive endoderm factors but not their initial expression in the mouse. *Development* **140**, 267-279 (2013).

83. Bessonnard S*, et al.* Gata6, Nanog and Erk signaling control cell fate in the inner cell mass through a tristable regulatory network. *Development* **141**, 3637-3648 (2014).

84. Palmieri SL, Peter W, Hess H, Scholer HR. Oct-4 transcription factor is differentially expressed in the mouse embryo during establishment of the first two extraembryonic cell lineages involved in implantation. *Dev Biol* **166**, 259-267 (1994).

85. Niakan KK*, et al.* Sox17 promotes differentiation in mouse embryonic stem cells by directly regulating extraembryonic gene expression and indirectly antagonizing self-renewal. *Genes Dev* **24**, 312-326 (2010).

86. Gerbe F, Cox B, Rossant J, Chazaud C. Dynamic expression of Lrp2 pathway members reveals progressive epithelial differentiation of primitive endoderm in mouse blastocyst. *Dev Biol* **313**, 594-602 (2008).

87. Meilhac SM, Adams RJ, Morris SA, Danckaert A, Le Garrec JF, Zernicka-Goetz M. Active cell movements coupled to positional induction are involved in lineage segregation in the mouse blastocyst. *Dev Biol* **331**, 210-221 (2009).

88. Moore R, Cai KQ, Escudero DO, Xu XX. Cell adhesive affinity does not dictate primitive endoderm segregation and positioning during murine embryoid body formation. *Genesis* **47**, 579-589 (2009).

89. McIntosh JR. Mitosis. *Cold Spring Harb Perspect Biol* **8**, (2016).

90. Michaelis C, Ciosk R, Nasmyth K. Cohesins: chromosomal proteins that prevent premature separation of sister chromatids. *Cell* **91**, 35-45 (1997).

91. Sumara I, Vorlaufer E, Gieffers C, Peters BH, Peters JM. Characterization of vertebrate cohesin complexes and their regulation in prophase. *J Cell Biol* **151**, 749-762 (2000).

92. Haering CH, Schoffnegger D, Nishino T, Helmhart W, Nasmyth K, Lowe J. Structure and stability of cohesin's Smc1-kleisin interaction. *Mol Cell* **15**, 951-964 (2004).

93. Hirano T. Condensins: organizing and segregating the genome. *Curr Biol* **15**, R265-275 (2005).

94. Hirano M, Hirano T. Positive and negative regulation of SMC-DNA interactions by ATP and accessory proteins. *EMBO J* **23**, 2664-2673 (2004).

95. Kimura K, Hirano T. ATP-dependent positive supercoiling of DNA by 13S condensin: a biochemical implication for chromosome condensation. *Cell* **90**, 625-634 (1997).

96. Bazett-Jones DP, Kimura K, Hirano T. Efficient supercoiling of DNA by a single condensin complex as revealed by electron spectroscopic imaging. *Mol Cell* **9**, 1183-1190 (2002).

97. Ono T, Fang Y, Spector DL, Hirano T. Spatial and temporal regulation of Condensins I and II in mitotic chromosome assembly in human cells. *Mol Biol Cell* **15**, 3296-3308 (2004).

98. Freeman L, Aragon-Alcaide L, Strunnikov A. The condensin complex governs chromosome condensation and mitotic transmission of rDNA. *J Cell Biol* **149**, 811-824 (2000).

99. Sutani T, Yuasa T, Tomonaga T, Dohmae N, Takio K, Yanagida M. Fission yeast condensin complex: essential roles of non-SMC subunits for condensation and Cdc2 phosphorylation of Cut3/SMC4. *Genes Dev* **13**, 2271-2283 (1999).

100. Kimura K, Rybenkov VV, Crisona NJ, Hirano T, Cozzarelli NR. 13S condensin actively reconfigures DNA by introducing global positive writhe: implications for chromosome condensation. *Cell* **98**, 239-248 (1999).

101. Kimura K, Hirano M, Kobayashi R, Hirano T. Phosphorylation and activation of 13S condensin by Cdc2 in vitro. *Science* **282**, 487-490 (1998).

102. Giet R, Glover DM. Drosophila aurora B kinase is required for histone H3 phosphorylation and condensin recruitment during chromosome condensation and to organize the central spindle during cytokinesis. *J Cell Biol* **152**, 669-682 (2001).

103. Beaudouin J, Gerlich D, Daigle N, Eils R, Ellenberg J. Nuclear envelope breakdown proceeds by microtubule-induced tearing of the lamina. *Cell* **108**, 83-96 (2002).

104. Steinhardt RA, Alderton J. Intracellular free calcium rise triggers nuclear envelope breakdown in the sea urchin embryo. *Nature* **332**, 364-366 (1988).

105. Lane HA, Nigg EA. Antibody microinjection reveals an essential role for human polo-like kinase 1 (Plk1) in the functional maturation of mitotic centrosomes. *J Cell Biol* **135**, 1701-1713 (1996).

106. Hannak E, Kirkham M, Hyman AA, Oegema K. Aurora-A kinase is required for centrosome maturation in Caenorhabditis elegans. *J Cell Biol* **155**, 1109-1116 (2001).

107. Brinkley W. Microtubules: a brief historical perspective. *J Struct Biol* **118**, 84-86 (1997).

108. Inoue S. Cell division and the mitotic spindle. *J Cell Biol* **91**, 131s-147s (1981).

109. Petry S. Mechanisms of Mitotic Spindle Assembly. *Annu Rev Biochem* **85**, 659-683 (2016).

110. Mitchison T, Kirschner M. Dynamic instability of microtubule growth. *Nature* **312**, 237-242 (1984).

111. Desai A, Mitchison TJ. Microtubule polymerization dynamics. *Annu Rev Cell Dev Biol* **13**, 83-117 (1997).

112. Moritz M, Zheng Y, Alberts BM, Oegema K. Recruitment of the gamma-tubulin ring complex to Drosophila salt-stripped centrosome scaffolds. *J Cell Biol* **142**, 775-786 (1998).

113. Murphy SM*, et al.* GCP5 and GCP6: two new members of the human gamma-tubulin complex. *Mol Biol Cell* **12**, 3340-3352 (2001).

114. Zheng Y, Wong ML, Alberts B, Mitchison T. Nucleation of microtubule assembly by a gamma-tubulin-containing ring complex. *Nature* **378**, 578-583 (1995).

115. Ayaz P, Ye X, Huddleston P, Brautigam CA, Rice LM. A TOG:alphabeta-tubulin complex structure reveals conformation-based mechanisms for a microtubule polymerase. *Science* **337**, 857-860 (2012).

116. Nogales E, Wang HW. Structural mechanisms underlying nucleotide-dependent self-assembly of tubulin and its relatives. *Curr Opin Struct Biol* **16**, 221-229 (2006).

117. Honnappa S*, et al.* An EB1-binding motif acts as a microtubule tip localization signal. *Cell* **138**, 366-376 (2009).

118. Maurer SP, Cade NI, Bohner G, Gustafsson N, Boutant E, Surrey T. EB1 accelerates two conformational transitions important for microtubule maturation and dynamics. *Curr Biol* **24**, 372-384 (2014).

119. Welburn JP. The molecular basis for kinesin functional specificity during mitosis. *Cytoskeleton (Hoboken)* **70**, 476-493 (2013).

120. Kapitein LC, Peterman EJ, Kwok BH, Kim JH, Kapoor TM, Schmidt CF. The bipolar mitotic kinesin Eg5 moves on both microtubules that it crosslinks. *Nature* **435**, 114-118 (2005).

121. Tanenbaum ME, Vale RD, McKenney RJ. Cytoplasmic dynein crosslinks and slides anti-parallel microtubules using its two motor domains. *Elife* **2**, e00943 (2013).

122. Boveri T. Zellen-Studien. *Jena, Gustav Fischer*, (1907).

123. Khodjakov A, Rieder CL. The sudden recruitment of gamma-tubulin to the centrosome at the onset of mitosis and its dynamic exchange throughout the cell cycle, do not require microtubules. *J Cell Biol* **146**, 585-596 (1999).

124. Martinez-Campos M, Basto R, Baker J, Kernan M, Raff JW. The Drosophila pericentrin-like protein is essential for cilia/flagella function, but appears to be dispensable for mitosis. *J Cell Biol* **165**, 673-683 (2004).

125. Haren L, Remy MH, Bazin I, Callebaut I, Wright M, Merdes A. NEDD1-dependent recruitment of the gamma-tubulin ring complex to the centrosome is necessary for centriole duplication and spindle assembly. *J Cell Biol* **172**, 505-515 (2006).

126. Hutchins JR*, et al.* Systematic analysis of human protein complexes identifies chromosome segregation proteins. *Science* **328**, 593-599 (2010).

127. Zimmerman WC, Sillibourne J, Rosa J, Doxsey SJ. Mitosis-specific anchoring of gamma tubulin complexes by pericentrin controls spindle organization and mitotic entry. *Mol Biol Cell* **15**, 3642-3657 (2004).

128. Gillingham AK, Munro S. The PACT domain, a conserved centrosomal targeting motif in the coiled-coil proteins AKAP450 and pericentrin. *EMBO Rep* **1**, 524-529 (2000).

129. Gomez-Ferreria MA*, et al.* Human Cep192 is required for mitotic centrosome and spindle assembly. *Curr Biol* **17**, 1960-1966 (2007).

130. Choi YK, Liu P, Sze SK, Dai C, Qi RZ. CDK5RAP2 stimulates microtubule nucleation by the gamma-tubulin ring complex. *J Cell Biol* **191**, 1089-1095 (2010).

131. Heald R, Khodjakov A. Thirty years of search and capture: The complex simplicity of mitotic spindle assembly. *J Cell Biol* **211**, 1103-1111 (2015).

132. Kirschner M, Mitchison T. Beyond self-assembly: from microtubules to morphogenesis. *Cell* **45**, 329-342 (1986).

133. Khodjakov A, Cole RW, Oakley BR, Rieder CL. Centrosome-independent mitotic spindle formation in vertebrates. *Curr Biol* **10**, 59-67 (2000).

134. Basto R*, et al.* Flies without centrioles. *Cell* **125**, 1375-1386 (2006).

135. Howe K, FitzHarris G. A non-canonical mode of microtubule organization operates throughout pre-implantation development in mouse. *Cell Cycle* **12**, 1616-1624 (2013).

136. Heald R*, et al.* Self-organization of microtubules into bipolar spindles around artificial chromosomes in Xenopus egg extracts. *Nature* **382**, 420-425 (1996).

137. Scrofani J, Sardon T, Meunier S, Vernos I. Microtubule nucleation in mitosis by a RanGTP-dependent protein complex. *Curr Biol* **25**, 131-140 (2015).

138. Yokoyama H*, et al.* The nucleoporin MEL-28 promotes RanGTP-dependent gamma-tubulin recruitment and microtubule nucleation in mitotic spindle formation. *Nat Commun* **5**, 3270 (2014).

139. Wilbur JD, Heald R. Mitotic spindle scaling during Xenopus development by kif2a and importin alpha. *Elife* **2**, e00290 (2013).

140. Carmena M, Wheelock M, Funabiki H, Earnshaw WC. The chromosomal passenger complex (CPC): from easy rider to the godfather of mitosis. *Nat Rev Mol Cell Biol* **13**, 789-803 (2012).

141. Prosser SL, Pelletier L. Mitotic spindle assembly in animal cells: a fine balancing act. *Nat Rev Mol Cell Biol* **18**, 187-201 (2017).

142. Maresca TJ, Groen AC, Gatlin JC, Ohi R, Mitchison TJ, Salmon ED. Spindle assembly in the absence of a RanGTP gradient requires localized CPC activity. *Curr Biol* **19**, 1210-1215 (2009).

143. Maiato H, Rieder CL, Khodjakov A. Kinetochore-driven formation of kinetochore fibers contributes to spindle assembly during animal mitosis. *J Cell Biol* **167**, 831-840 (2004).

144. Mishra RK, Chakraborty P, Arnaoutov A, Fontoura BM, Dasso M. The Nup107-160 complex and gamma-TuRC regulate microtubule polymerization at kinetochores. *Nat Cell Biol* **12**, 164-169 (2010).

145. Murata T*, et al.* Microtubule-dependent microtubule nucleation based on recruitment of gamma-tubulin in higher plants. *Nat Cell Biol* **7**, 961-968 (2005).

146. Mahoney NM, Goshima G, Douglass AD, Vale RD. Making microtubules and mitotic spindles in cells without functional centrosomes. *Curr Biol* **16**, 564-569 (2006).

147. Goshima G, Mayer M, Zhang N, Stuurman N, Vale RD. Augmin: a protein complex required for centrosome-independent microtubule generation within the spindle. *J Cell Biol* **181**, 421-429 (2008).

148. Goshima G*, et al.* Genes required for mitotic spindle assembly in Drosophila S2 cells. *Science* **316**, 417-421 (2007).

149. Petry S, Groen AC, Ishihara K, Mitchison TJ, Vale RD. Branching microtubule nucleation in Xenopus egg extracts mediated by augmin and TPX2. *Cell* **152**, 768-777 (2013).

150. Schuh M, Ellenberg J. Self-organization of MTOCs replaces centrosome function during acentrosomal spindle assembly in live mouse oocytes. *Cell* **130**, 484-498 (2007).

151. Bury L*, et al.* Plk4 and Aurora A cooperate in the initiation of acentriolar spindle assembly in mammalian oocytes. *J Cell Biol*, (2017).

152. Nicklas RB, Ward SC. Elements of error correction in mitosis: microtubule capture, release, and tension. *J Cell Biol* **126**, 1241-1253 (1994).

153. Cimini D. Merotelic kinetochore orientation, aneuploidy, and cancer. *Biochim Biophys Acta* **1786**, 32-40 (2008).

154. Nicklas RB. How cells get the right chromosomes. *Science* **275**, 632-637 (1997).

155. Nicklas RB, Koch CA. Chromosome micromanipulation. 3. Spindle fiber tension and the reorientation of mal-oriented chromosomes. *J Cell Biol* **43**, 40-50 (1969).

156. Cane S, Ye AA, Luks-Morgan SJ, Maresca TJ. Elevated polar ejection forces stabilize kinetochore-microtubule attachments. *J Cell Biol* **200**, 203-218 (2013).

157. Cimini D, Fioravanti D, Salmon ED, Degrassi F. Merotelic kinetochore orientation versus chromosome mono-orientation in the origin of lagging chromosomes in human primary cells. *J Cell Sci* **115**, 507-515 (2002).

158. Thompson SL, Compton DA. Examining the link between chromosomal instability and aneuploidy in human cells. *J Cell Biol* **180**, 665-672 (2008).

159. Lampson MA, Grishchuk EL. Mechanisms to Avoid and Correct Erroneous Kinetochore-Microtubule Attachments. *Biology (Basel)* **6**, (2017).

160. Cimini D, Moree B, Canman JC, Salmon ED. Merotelic kinetochore orientation occurs frequently during early mitosis in mammalian tissue cells and error correction is achieved by two different mechanisms. *J Cell Sci* **116**, 4213-4225 (2003).

161. Thompson SL, Compton DA. Chromosome missegregation in human cells arises through specific types of kinetochore-microtubule attachment errors. *Proc Natl Acad Sci U S A* **108**, 17974-17978 (2011).

162. Zhai Y, Kronebusch PJ, Borisy GG. Kinetochore microtubule dynamics and the metaphase-anaphase transition. *J Cell Biol* **131**, 721-734 (1995).

163. Bakhoum SF, Thompson SL, Manning AL, Compton DA. Genome stability is ensured by temporal control of kinetochore-microtubule dynamics. *Nat Cell Biol* **11**, 27-35 (2009).

164. Bakhoum SF, Genovese G, Compton DA. Deviant kinetochore microtubule dynamics underlie chromosomal instability. *Curr Biol* **19**, 1937-1942 (2009).

165. Liu D, Vader G, Vromans MJ, Lampson MA, Lens SM. Sensing chromosome bi-orientation by spatial separation of aurora B kinase from kinetochore substrates. *Science* **323**, 1350-1353 (2009).

166. Welburn JP*, et al.* Aurora B phosphorylates spatially distinct targets to differentially regulate the kinetochore-microtubule interface. *Mol Cell* **38**, 383-392 (2010).

167. Salimian KJ*, et al.* Feedback control in sensing chromosome biorientation by the Aurora B kinase. *Curr Biol* **21**, 1158-1165 (2011).

168. Sarangapani KK, Akiyoshi B, Duggan NM, Biggins S, Asbury CL. Phosphoregulation promotes release of kinetochores from dynamic microtubules via multiple mechanisms. *Proc Natl Acad Sci U S A* **110**, 7282-7287 (2013).

169. Wang F*, et al.* Histone H3 Thr-3 phosphorylation by Haspin positions Aurora B at centromeres in mitosis. *Science* **330**, 231-235 (2010).

170. Zaytsev AV*, et al.* Bistability of a coupled Aurora B kinase-phosphatase system in cell division. *Elife* **5**, e10644 (2016).

171. Yasui Y*, et al.* Autophosphorylation of a newly identified site of Aurora-B is indispensable for cytokinesis. *J Biol Chem* **279**, 12997-13003 (2004).

172. Lara-Gonzalez P, Westhorpe FG, Taylor SS. The spindle assembly checkpoint. *Curr Biol* **22**, R966-980 (2012).

173. Collin P, Nashchekina O, Walker R, Pines J. The spindle assembly checkpoint works like a rheostat rather than a toggle switch. *Nat Cell Biol* **15**, 1378-1385 (2013).

174. Fang G. Checkpoint protein BubR1 acts synergistically with Mad2 to inhibit anaphase-promoting complex. *Mol Biol Cell* **13**, 755-766 (2002).

175. Tang Z, Bharadwaj R, Li B, Yu H. Mad2-Independent inhibition of APCCdc20 by the mitotic checkpoint protein BubR1. *Dev Cell* **1**, 227-237 (2001).

176. Johnson VL, Scott MI, Holt SV, Hussein D, Taylor SS. Bub1 is required for kinetochore localization of BubR1, Cenp-E, Cenp-F and Mad2, and chromosome congression. *J Cell Sci* **117**, 1577-1589 (2004).

177. Sharp-Baker H, Chen RH. Spindle checkpoint protein Bub1 is required for kinetochore localization of Mad1, Mad2, Bub3, and CENP-E, independently of its kinase activity. *J Cell Biol* **153**, 1239-1250 (2001).

178. Kiyomitsu T, Obuse C, Yanagida M. Human Blinkin/AF15q14 is required for chromosome alignment and the mitotic checkpoint through direct interaction with Bub1 and BubR1. *Dev Cell* **13**, 663-676 (2007).

179. De Antoni A*, et al.* The Mad1/Mad2 complex as a template for Mad2 activation in the spindle assembly checkpoint. *Curr Biol* **15**, 214-225 (2005).

180. Hewitt L*, et al.* Sustained Mps1 activity is required in mitosis to recruit O-Mad2 to the Mad1-C-Mad2 core complex. *J Cell Biol* **190**, 25-34 (2010).

181. Hardwick KG, Johnston RC, Smith DL, Murray AW. MAD3 encodes a novel component of the spindle checkpoint which interacts with Bub3p, Cdc20p, and Mad2p. *J Cell Biol* **148**, 871-882 (2000).

182. Li Y, Gorbea C, Mahaffey D, Rechsteiner M, Benezra R. MAD2 associates with the cyclosome/anaphase-promoting complex and inhibits its activity. *Proc Natl Acad Sci U S A* **94**, 12431-12436 (1997).

183. Herzog F*, et al.* Structure of the anaphase-promoting complex/cyclosome interacting with a mitotic checkpoint complex. *Science* **323**, 1477-1481 (2009).

184. da Fonseca PC*, et al.* Structures of APC/C(Cdh1) with substrates identify Cdh1 and Apc10 as the D-box co-receptor. *Nature* **470**, 274-278 (2011).

185. Burton JL, Solomon MJ. Mad3p, a pseudosubstrate inhibitor of APCCdc20 in the spindle assembly checkpoint. *Genes Dev* **21**, 655-667 (2007).

186. Chao WC, Kulkarni K, Zhang Z, Kong EH, Barford D. Structure of the mitotic checkpoint complex. *Nature* **484**, 208-213 (2012).

187. Howell BJ*, et al.* Cytoplasmic dynein/dynactin drives kinetochore protein transport to the spindle poles and has a role in mitotic spindle checkpoint inactivation. *J Cell Biol* **155**, 1159-1172 (2001).

188. Lesage B, Qian J, Bollen M. Spindle checkpoint silencing: PP1 tips the balance. *Curr Biol* **21**, R898-903 (2011).

189. Westhorpe FG, Tighe A, Lara-Gonzalez P, Taylor SS. p31comet-mediated extraction of Mad2 from the MCC promotes efficient mitotic exit. *J Cell Sci* **124**, 3905-3916 (2011).

190. Hagan RS*, et al.* p31(comet) acts to ensure timely spindle checkpoint silencing subsequent to kinetochore attachment. *Mol Biol Cell* **22**, 4236-4246 (2011).

191. Nilsson J, Yekezare M, Minshull J, Pines J. The APC/C maintains the spindle assembly checkpoint by targeting Cdc20 for destruction. *Nat Cell Biol* **10**, 1411-1420 (2008).

192. Choi E, Choe H, Min J, Choi JY, Kim J, Lee H. BubR1 acetylation at prometaphase is required for modulating APC/C activity and timing of mitosis. *EMBO J* **28**, 2077-2089 (2009).

193. Reddy SK, Rape M, Margansky WA, Kirschner MW. Ubiquitination by the anaphase-promoting complex drives spindle checkpoint inactivation. *Nature* **446**, 921-925 (2007).

194. Visconti R, Palazzo L, Grieco D. Requirement for proteolysis in spindle assembly checkpoint silencing. *Cell Cycle* **9**, 564-569 (2010).

195. Nagaoka SI, Hassold TJ, Hunt PA. Human aneuploidy: mechanisms and new insights into an age-old problem. *Nat Rev Genet* **13**, 493-504 (2012).

196. Fragouli E, Wells D. Aneuploidy in the human blastocyst. *Cytogenet Genome Res* **133**, 149-159 (2011).

197. Coonen E*, et al.* Presence of chromosomal mosaicism in abnormal preimplantation embryos detected by fluorescence in situ hybridisation. *Hum Genet* **94**, 609-615 (1994).

198. Loncarek J, Khodjakov A. Ab ovo or de novo? Mechanisms of centriole duplication. *Mol Cells* **27**, 135-142 (2009).

199. Nigg EA, Raff JW. Centrioles, centrosomes, and cilia in health and disease. *Cell* **139**, 663-678 (2009).

200. Ganem NJ, Godinho SA, Pellman D. A mechanism linking extra centrosomes to chromosomal instability. *Nature* **460**, 278-282 (2009).

201. Silkworth WT, Nardi IK, Scholl LM, Cimini D. Multipolar spindle pole coalescence is a major source of kinetochore mis-attachment and chromosome mis-segregation in cancer cells. *PLoS One* **4**, e6564 (2009).

202. Kwon M*, et al.* Mechanisms to suppress multipolar divisions in cancer cells with extra centrosomes. *Genes Dev* **22**, 2189-2203 (2008).

203. Sathananthan AH*, et al.* Centrioles in the beginning of human development. *Proc Natl Acad Sci U S A* **88**, 4806-4810 (1991).

204. Szollosi D, Calarco P, Donahue RP. Absence of centrioles in the first and second meiotic spindles of mouse oocytes. *J Cell Sci* **11**, 521-541 (1972).

205. Mikeladze-Dvali T*, et al.* Analysis of centriole elimination during C. elegans oogenesis. *Development* **139**, 1670-1679 (2012).

206. Sathananthan AH. Mitosis in the human embryo: the vital role of the sperm centrosome (centriole). *Histol Histopathol* **12**, 827-856 (1997).

207. Calarco-Gillam PD, Siebert MC, Hubble R, Mitchison T, Kirschner M. Centrosome development in early mouse embryos as defined by an autoantibody against pericentriolar material. *Cell* **35**, 621-629 (1983).

208. Schatten H, Schatten G, Mazia D, Balczon R, Simerly C. Behavior of centrosomes during fertilization and cell division in mouse oocytes and in sea urchin eggs. *Proc Natl Acad Sci U S A* **83**, 105-109 (1986).

209. Gueth-Hallonet C*, et al.* gamma-Tubulin is present in acentriolar MTOCs during early mouse development. *J Cell Sci* **105 (Pt 1)**, 157-166 (1993).

210. Courtois A, Schuh M, Ellenberg J, Hiiragi T. The transition from meiotic to mitotic spindle assembly is gradual during early mammalian development. *J Cell Biol* **198**, 357-370 (2012).

211. Maro B. Fertilization and the cytoskeleton in the mouse. *Bioessays* **3**, 18-21 (1985).

212. Macaulay AD, Allais A, FitzHarris G. Chromosome dynamics and spindle microtubule establishment in mouse embryos. *FASEB J* **34**, 8057-8067 (2020).

213. Arquint C, Nigg EA. The PLK4-STIL-SAS-6 module at the core of centriole duplication. *Biochem Soc Trans* **44**, 1253-1263 (2016).

214. Coelho PA*, et al.* Spindle formation in the mouse embryo requires Plk4 in the absence of centrioles. *Dev Cell* **27**, 586-597 (2013).

215. Fitzharris G. A shift from kinesin 5-dependent metaphase spindle function during preimplantation development in mouse. *Development* **136**, 2111-2119 (2009).

216. Watanabe S, Shioi G, Furuta Y, Goshima G. Intra-spindle Microtubule Assembly Regulates Clustering of Microtubule-Organizing Centers during Early Mouse Development. *Cell Rep* **15**, 54-60 (2016).

217. Yamagata K, FitzHarris G. 4D imaging reveals a shift in chromosome segregation dynamics during mouse pre-implantation development. *Cell Cycle* **12**, 157-165 (2013).

218. Good MC, Vahey MD, Skandarajah A, Fletcher DA, Heald R. Cytoplasmic volume modulates spindle size during embryogenesis. *Science* **342**, 856-860 (2013).

219. Wuhr M*, et al.* Evidence for an upper limit to mitotic spindle length. *Curr Biol* **18**, 1256-1261 (2008).

220. Avo Santos M*, et al.* A role for Aurora C in the chromosomal passenger complex during human preimplantation embryo development. *Hum Reprod* **26**, 1868-1881 (2011).

221. Li W*, et al.* Differential regulation of H3S10 phosphorylation, mitosis progression and cell fate by Aurora Kinase B and C in mouse preimplantation embryos. *Protein Cell* **8**, 662-674 (2017).

222. Schindler K, Davydenko O, Fram B, Lampson MA, Schultz RM. Maternally recruited Aurora C kinase is more stable than Aurora B to support mouse oocyte maturation and early development. *Proc Natl Acad Sci U S A* **109**, E2215-2222 (2012).

223. van de Werken C*, et al.* Chromosome segregation regulation in human zygotes: altered mitotic histone phosphorylation dynamics underlying centromeric targeting of the chromosomal passenger complex. *Hum Reprod* **30**, 2275-2291 (2015).

224. Wells D*, et al.* Expression of genes regulating chromosome segregation, the cell cycle and apoptosis during human preimplantation development. *Hum Reprod* **20**, 1339-1348 (2005).

225. Jacobs K, Van de Velde H, De Paepe C, Sermon K, Spits C. Mitotic spindle disruption in human preimplantation embryos activates the spindle assembly checkpoint but not apoptosis until Day 5 of development. *Mol Hum Reprod* **23**, 321-329 (2017).

226. Collins JK, Lane SIR, Merriman JA, Jones KT. DNA damage induces a meiotic arrest in mouse oocytes mediated by the spindle assembly checkpoint. *Nat Commun* **6**, 8553 (2015).

227. Lane SIR*, et al.* DNA damage induces a kinetochore-based ATM/ATR-independent SAC arrest unique to the first meiotic division in mouse oocytes. *Development* **144**, 3475-3486 (2017).

228. Marangos P*, et al.* DNA damage-induced metaphase I arrest is mediated by the spindle assembly checkpoint and maternal age. *Nat Commun* **6**, 8706 (2015).

229. Galli M, Morgan DO. Cell Size Determines the Strength of the Spindle Assembly Checkpoint during Embryonic Development. *Dev Cell* **36**, 344-352 (2016).

230. Kyogoku H, Kitajima TS. Large Cytoplasm Is Linked to the Error-Prone Nature of Oocytes. *Dev Cell* **41**, 287-298 e284 (2017).

231. Lane SIR, Jones KT. Chromosome biorientation and APC activity remain uncoupled in oocytes with reduced volume. *J Cell Biol* **216**, 3949-3957 (2017).

232. Vazquez-Diez C, Paim LMG, FitzHarris G. Cell-Size-Independent Spindle Checkpoint Failure Underlies Chromosome Segregation Error in Mouse Embryos. *Curr Biol* **29**, 865-873 e863 (2019).

233. FitzHarris G. Anaphase B precedes anaphase A in the mouse egg. *Curr Biol* **22**, 437-444 (2012).

234. Mitchison T, Evans L, Schulze E, Kirschner M. Sites of microtubule assembly and disassembly in the mitotic spindle. *Cell* **45**, 515-527 (1986).

235. Maddox P, Desai A, Oegema K, Mitchison TJ, Salmon ED. Poleward microtubule flux is a major component of spindle dynamics and anaphase a in mitotic Drosophila embryos. *Curr Biol* **12**, 1670-1674 (2002).

236. Gorbsky GJ, Sammak PJ, Borisy GG. Chromosomes move poleward in anaphase along stationary microtubules that coordinately disassemble from their kinetochore ends. *J Cell Biol* **104**, 9-18 (1987).

237. Sharp DJ, Rogers GC. A Kin I-dependent Pacman-flux mechanism for anaphase A. *Cell Cycle* **3**, 707-710 (2004).

238. Mitchison TJ. Polewards microtubule flux in the mitotic spindle: evidence from photoactivation of fluorescence. *J Cell Biol* **109**, 637-652 (1989).

239. Maddox PS, Bloom KS, Salmon ED. The polarity and dynamics of microtubule assembly in the budding yeast Saccharomyces cerevisiae. *Nat Cell Biol* **2**, 36-41 (2000).

240. Sharp DJ, Rogers GC, Scholey JM. Cytoplasmic dynein is required for poleward chromosome movement during mitosis in Drosophila embryos. *Nat Cell Biol* **2**, 922-930 (2000).

241. Tanaka K, Kitamura E, Kitamura Y, Tanaka TU. Molecular mechanisms of microtubule-dependent kinetochore transport toward spindle poles. *J Cell Biol* **178**, 269-281 (2007).

242. Grishchuk EL, McIntosh JR. Microtubule depolymerization can drive poleward chromosome motion in fission yeast. *EMBO J* **25**, 4888-4896 (2006).

243. McIntosh JR, McDonald KL, Edwards MK, Ross BM. Three-dimensional structure of the central mitotic spindle of Diatoma vulgare. *J Cell Biol* **83**, 428-442 (1979).

244. Sharp DJ, Yu KR, Sisson JC, Sullivan W, Scholey JM. Antagonistic microtubule-sliding motors position mitotic centrosomes in Drosophila early embryos. *Nat Cell Biol* **1**, 51-54 (1999).

245. Brust-Mascher I, Civelekoglu-Scholey G, Kwon M, Mogilner A, Scholey JM. Model for anaphase B: role of three mitotic motors in a switch from poleward flux to spindle elongation. *Proc Natl Acad Sci U S A* **101**, 15938-15943 (2004).

246. Saunders AM, Powers J, Strome S, Saxton WM. Kinesin-5 acts as a brake in anaphase spindle elongation. *Curr Biol* **17**, R453-454 (2007).

247. Fink G, Schuchardt I, Colombelli J, Stelzer E, Steinberg G. Dynein-mediated pulling forces drive rapid mitotic spindle elongation in Ustilago maydis. *EMBO J* **25**, 4897-4908 (2006).

248. Parry DH, O'Farrell PH. The schedule of destruction of three mitotic cyclins can dictate the timing of events during exit from mitosis. *Curr Biol* **11**, 671-683 (2001).

249. Parry DH, Hickson GR, O'Farrell PH. Cyclin B destruction triggers changes in kinetochore behavior essential for successful anaphase. *Curr Biol* **13**, 647-653 (2003).

250. Wheatley SP, Hinchcliffe EH, Glotzer M, Hyman AA, Sluder G, Wang Y. CDK1 inactivation regulates anaphase spindle dynamics and cytokinesis in vivo. *J Cell Biol* **138**, 385-393 (1997).

251. Cao K, Nakajima R, Meyer HH, Zheng Y. The AAA-ATPase Cdc48/p97 regulates spindle disassembly at the end of mitosis. *Cell* **115**, 355-367 (2003).

252. Hetzer M, Meyer HH, Walther TC, Bilbao-Cortes D, Warren G, Mattaj IW. Distinct AAA-ATPase p97 complexes function in discrete steps of nuclear assembly. *Nat Cell Biol* **3**, 1086-1091 (2001).

253. Walther TC*, et al.* RanGTP mediates nuclear pore complex assembly. *Nature* **424**, 689-694 (2003).

254. Pollard TD, O'Shaughnessy B. Molecular Mechanism of Cytokinesis. *Annu Rev Biochem* **88**, 661-689 (2019).

255. Green RA, Paluch E, Oegema K. Cytokinesis in animal cells. *Annu Rev Cell Dev Biol* **28**, 29-58 (2012).

256. Rappaport R. Repeated furrow formation from a single mitotic apparatus in cylindrical sand dollar eggs. *J Exp Zool* **234**, 167-171 (1985).

257. Bement WM, Benink HA, von Dassow G. A microtubule-dependent zone of active RhoA during cleavage plane specification. *J Cell Biol* **170**, 91-101 (2005).

258. Kishi K, Sasaki T, Kuroda S, Itoh T, Takai Y. Regulation of cytoplasmic division of Xenopus embryo by rho p21 and its inhibitory GDP/GTP exchange protein (rho GDI). *J Cell Biol* **120**, 1187-1195 (1993).

259. Drechsel DN, Hyman AA, Hall A, Glotzer M. A requirement for Rho and Cdc42 during cytokinesis in Xenopus embryos. *Curr Biol* **7**, 12-23 (1997).

260. D'Avino PP, Savoian MS, Glover DM. Cleavage furrow formation and ingression during animal cytokinesis: a microtubule legacy. *J Cell Sci* **118**, 1549-1558 (2005).

261. Euteneuer U, McIntosh JR. Polarity of midbody and phragmoplast microtubules. *J Cell Biol* **87**, 509-515 (1980).

262. Bieling P, Telley IA, Surrey T. A minimal midzone protein module controls formation and length of antiparallel microtubule overlaps. *Cell* **142**, 420-432 (2010).

263. Guse A, Mishima M, Glotzer M. Phosphorylation of ZEN-4/MKLP1 by aurora B regulates completion of cytokinesis. *Curr Biol* **15**, 778-786 (2005).

264. Douglas ME, Davies T, Joseph N, Mishima M. Aurora B and 14-3-3 coordinately regulate clustering of centralspindlin during cytokinesis. *Curr Biol* **20**, 927-933 (2010).

265. Kaitna S, Mendoza M, Jantsch-Plunger V, Glotzer M. Incenp and an aurora-like kinase form a complex essential for chromosome segregation and efficient completion of cytokinesis. *Curr Biol* **10**, 1172-1181 (2000).

266. Su KC, Takaki T, Petronczki M. Targeting of the RhoGEF Ect2 to the equatorial membrane controls cleavage furrow formation during cytokinesis. *Dev Cell* **21**, 1104-1115 (2011).

267. Loria A, Longhini KM, Glotzer M. The RhoGAP domain of CYK-4 has an essential role in RhoA activation. *Curr Biol* **22**, 213-219 (2012).

268. Jantsch-Plunger V*, et al.* CYK-4: A Rho family gtpase activating protein (GAP) required for central spindle formation and cytokinesis. *J Cell Biol* **149**, 1391-1404 (2000).

269. Hu CK, Coughlin M, Field CM, Mitchison TJ. KIF4 regulates midzone length during cytokinesis. *Curr Biol* **21**, 815-824 (2011).

270. Rappaport R. Experiments concerning the cleavage stimulus in sand dollar eggs. *J Exp Zool* **148**, 81-89 (1961).

271. Bringmann H, Hyman AA. A cytokinesis furrow is positioned by two consecutive signals. *Nature* **436**, 731-734 (2005).

272. Werner M, Munro E, Glotzer M. Astral signals spatially bias cortical myosin recruitment to break symmetry and promote cytokinesis. *Curr Biol* **17**, 1286-1297 (2007).

273. von Dassow G, Verbrugghe KJ, Miller AL, Sider JR, Bement WM. Action at a distance during cytokinesis. *J Cell Biol* **187**, 831-845 (2009).

274. Vavylonis D, Wu JQ, Hao S, O'Shaughnessy B, Pollard TD. Assembly mechanism of the contractile ring for cytokinesis by fission yeast. *Science* **319**, 97-100 (2008).

275. Chen Q, Pollard TD. Actin filament severing by cofilin is more important for assembly than constriction of the cytokinetic contractile ring. *J Cell Biol* **195**, 485-498 (2011).

276. Lewellyn L, Carvalho A, Desai A, Maddox AS, Oegema K. The chromosomal passenger complex and centralspindlin independently contribute to contractile ring assembly. *J Cell Biol* **193**, 155-169 (2011).

277. Schroeder TE. Dynamics of the contractile ring. *Soc Gen Physiol Ser* **30**, 305-334 (1975).

278. Maupin P, Pollard TD. Arrangement of actin filaments and myosin-like filaments in the contractile ring and of actin-like filaments in the mitotic spindle of dividing HeLa cells. *J Ultrastruct Mol Struct Res* **94**, 92-103 (1986).

279. Carvalho A, Desai A, Oegema K. Structural memory in the contractile ring makes the duration of cytokinesis independent of cell size. *Cell* **137**, 926-937 (2009).

280. Silva AM*, et al.* Robust gap repair in the contractile ring ensures timely completion of cytokinesis. *J Cell Biol* **215**, 789-799 (2016).

281. Henson JH*, et al.* The ultrastructural organization of actin and myosin II filaments in the contractile ring: new support for an old model of cytokinesis. *Mol Biol Cell* **28**, 613-623 (2017).

282. Fenix AM*, et al.* Expansion and concatenation of non-muscle myosin IIA filaments drive cellular contractile system formation during interphase and mitosis. *Mol Biol Cell*, (2016).

283. Biron D, Alvarez-Lacalle E, Tlusty T, Moses E. Molecular model of the contractile ring. *Phys Rev Lett* **95**, 098102 (2005).

284. Zumdieck A, Kruse K, Bringmann H, Hyman AA, Julicher F. Stress generation and filament turnover during actin ring constriction. *PLoS One* **2**, e696 (2007).

285. Ma X*, et al.* Nonmuscle myosin II exerts tension but does not translocate actin in vertebrate cytokinesis. *Proc Natl Acad Sci U S A* **109**, 4509-4514 (2012).

286. Carlsson AE. Contractile stress generation by actomyosin gels. *Phys Rev E Stat Nonlin Soft Matter Phys* **74**, 051912 (2006).

287. Wang S, O'Shaughnessy B. Anchoring of actin to the plasma membrane enables tension production in the fission yeast cytokinetic ring. *Mol Biol Cell* **30**, 2053-2064 (2019).

288. Mullins JM, Biesele JJ. Terminal phase of cytokinesis in D-98s cells. *J Cell Biol* **73**, 672-684 (1977).

289. Hu CK, Coughlin M, Mitchison TJ. Midbody assembly and its regulation during cytokinesis. *Mol Biol Cell* **23**, 1024-1034 (2012).

290. Gai M*, et al.* Citron kinase controls abscission through RhoA and anillin. *Mol Biol Cell* **22**, 3768-3778 (2011).

291. Kechad A, Jananji S, Ruella Y, Hickson GR. Anillin acts as a bifunctional linker coordinating midbody ring biogenesis during cytokinesis. *Curr Biol* **22**, 197-203 (2012).

292. Echard A, Hickson GR, Foley E, O'Farrell PH. Terminal cytokinesis events uncovered after an RNAi screen. *Curr Biol* **14**, 1685-1693 (2004).

293. Guizetti J, Gerlich DW. ESCRT-III polymers in membrane neck constriction. *Trends Cell Biol* **22**, 133-140 (2012).

294. Morita E*, et al.* Human ESCRT and ALIX proteins interact with proteins of the midbody and function in cytokinesis. *EMBO J* **26**, 4215-4227 (2007).

295. Guizetti J*, et al.* Cortical constriction during abscission involves helices of ESCRT-III-dependent filaments. *Science* **331**, 1616-1620 (2011).

296. Elia N, Sougrat R, Spurlin TA, Hurley JH, Lippincott-Schwartz J. Dynamics of endosomal sorting complex required for transport (ESCRT) machinery during cytokinesis and its role in abscission. *Proc Natl Acad Sci U S A* **108**, 4846-4851 (2011).

297. Calvert ME*, et al.* Myosin concentration underlies cell size-dependent scalability of actomyosin ring constriction. *J Cell Biol* **195**, 799-813 (2011).

298. Bourdages KG, Lacroix B, Dorn JF, Descovich CP, Maddox AS. Quantitative analysis of cytokinesis in situ during C. elegans postembryonic development. *PLoS One* **9**, e110689 (2014).

299. Eakin GS, Behringer RR. Tetraploid development in the mouse. *Dev Dyn* **228**, 751-766 (2003).

300. Khaliullin RN*, et al.* A positive-feedback-based mechanism for constriction rate acceleration during cytokinesis in Caenorhabditis elegans. *Elife* **7**, (2018).

301. Nahse V, Christ L, Stenmark H, Campsteijn C. The Abscission Checkpoint: Making It to the Final Cut. *Trends Cell Biol* **27**, 1-11 (2017).

302. Steigemann P*, et al.* Aurora B-mediated abscission checkpoint protects against tetraploidization. *Cell* **136**, 473-484 (2009).

303. Lafaurie-Janvore J*, et al.* ESCRT-III assembly and cytokinetic abscission are induced by tension release in the intercellular bridge. *Science* **339**, 1625-1629 (2013).

304. Mackay DR, Makise M, Ullman KS. Defects in nuclear pore assembly lead to activation of an Aurora B-mediated abscission checkpoint. *J Cell Biol* **191**, 923-931 (2010).

305. Mackay DR, Ullman KS. ATR and a Chk1-Aurora B pathway coordinate postmitotic genome surveillance with cytokinetic abscission. *Mol Biol Cell* **26**, 2217-2226 (2015).

306. Thoresen SB*, et al.* ANCHR mediates Aurora-B-dependent abscission checkpoint control through retention of VPS4. *Nat Cell Biol* **16**, 550-560 (2014).

307. Gallardo MH, Bickham JW, Honeycutt RL, Ojeda RA, Kohler N. Discovery of tetraploidy in a mammal. *Nature* **401**, 341 (1999).

308. Genest DR, Roberts D, Boyd T, Bieber FR. Fetoplacental histology as a predictor of karyotype: a controlled study of spontaneous first trimester abortions. *Hum Pathol* **26**, 201-209 (1995).

309. Stefanova I*, et al.* Mosaic and complete tetraploidy in live-born infants: two new patients and review of the literature. *Clin Dysmorphol* **19**, 123-127 (2010).

310. Davoli T, de Lange T. The causes and consequences of polyploidy in normal development and cancer. *Annu Rev Cell Dev Biol* **27**, 585-610 (2011).

311. Hattori N, Davies TC, Anson-Cartwright L, Cross JC. Periodic expression of the cyclin-dependent kinase inhibitor p57(Kip2) in trophoblast giant cells defines a G2-like gap phase of the endocycle. *Mol Biol Cell* **11**, 1037-1045 (2000).

312. Ullah Z, Kohn MJ, Yagi R, Vassilev LT, DePamphilis ML. Differentiation of trophoblast stem cells into giant cells is triggered by p57/Kip2 inhibition of CDK1 activity. *Genes Dev* **22**, 3024-3036 (2008).

313. Ullah Z, Lee CY, Lilly MA, DePamphilis ML. Developmentally programmed endoreduplication in animals. *Cell Cycle* **8**, 1501-1509 (2009).

314. Mazzi S, Lordier L, Debili N, Raslova H, Vainchenker W. Megakaryocyte and polyploidization. *Exp Hematol* **57**, 1-13 (2018).

315. Celton-Morizur S, Desdouets C. Polyploidization of liver cells. *Adv Exp Med Biol* **676**, 123-135 (2010).

316. Celton-Morizur S, Merlen G, Couton D, Margall-Ducos G, Desdouets C. The insulin/Akt pathway controls a specific cell division program that leads to generation of binucleated tetraploid liver cells in rodents. *J Clin Invest* **119**, 1880-1887 (2009).

317. Duncan AW*, et al.* Ploidy reductions in murine fusion-derived hepatocytes. *PLoS Genet* **5**, e1000385 (2009).

318. Derks W, Bergmann O. Polyploidy in Cardiomyocytes: Roadblock to Heart Regeneration? *Circ Res* **126**, 552-565 (2020).

319. Geddis AE, Fox NE, Tkachenko E, Kaushansky K. Endomitotic megakaryocytes that form a bipolar spindle exhibit cleavage furrow ingression followed by furrow regression. *Cell Cycle* **6**, 455-460 (2007).

320. Lordier L*, et al.* Megakaryocyte endomitosis is a failure of late cytokinesis related to defects in the contractile ring and Rho/Rock signaling. *Blood* **112**, 3164-3174 (2008).

321. Lordier L*, et al.* Presence of a defect in karyokinesis during megakaryocyte endomitosis. *Cell Cycle* **11**, 4385-4389 (2012).

322. Duncan AW*, et al.* The ploidy conveyor of mature hepatocytes as a source of genetic variation. *Nature* **467**, 707-710 (2010).

323. Patel SR, Hartwig JH, Italiano JE, Jr. The biogenesis of platelets from megakaryocyte proplatelets. *J Clin Invest* **115**, 3348-3354 (2005).

324. Storchova Z, Kuffer C. The consequences of tetraploidy and aneuploidy. *J Cell Sci* **121**, 3859-3866 (2008).

325. Carr DH, Gedeon MM. Q-banding of chromosomes in human spontaneous abortions. *Can J Genet Cytol* **20**, 415-425 (1978).

326. Hassold T*, et al.* A cytogenetic study of 1000 spontaneous abortions. *Ann Hum Genet* **44**, 151-178 (1980).

327. Jia CW*, et al.* Aneuploidy in Early Miscarriage and its Related Factors. *Chin Med J (Engl)* **128**, 2772-2776 (2015).

328. Duelli DM, Padilla-Nash HM, Berman D, Murphy KM, Ried T, Lazebnik Y. A virus causes cancer by inducing massive chromosomal instability through cell fusion. *Curr Biol* **17**, 431-437 (2007).

329. Fujiwara T, Bandi M, Nitta M, Ivanova EV, Bronson RT, Pellman D. Cytokinesis failure generating tetraploids promotes tumorigenesis in p53-null cells. *Nature* **437**, 1043-1047 (2005).

330. Poste G. Mechanisms of virus-induced cell fusion. *Int Rev Cytol* **33**, 157-252 (1972).

331. Knutton S. The mechanism of virus-induced cell fusion. *Micron* **9**, 133-154 (1978).

332. Musacchio A, Salmon ED. The spindle-assembly checkpoint in space and time. *Nat Rev Mol Cell Biol* **8**, 379-393 (2007).

333. Brito DA, Rieder CL. Mitotic checkpoint slippage in humans occurs via cyclin B destruction in the presence of an active checkpoint. *Curr Biol* **16**, 1194-1200 (2006).

334. Lok TM, Wang Y, Xu WK, Xie S, Ma HT, Poon RYC. Mitotic slippage is determined by p31(comet) and the weakening of the spindle-assembly checkpoint. *Oncogene* **39**, 2819-2834 (2020).

335. Shi Q, King RW. Chromosome nondisjunction yields tetraploid rather than aneuploid cells in human cell lines. *Nature* **437**, 1038-1042 (2005).

336. Castillo A, Morse HC, 3rd, Godfrey VL, Naeem R, Justice MJ. Overexpression of Eg5 causes genomic instability and tumor formation in mice. *Cancer Res* **67**, 10138-10147 (2007).

337. Sotillo R*, et al.* Mad2 overexpression promotes aneuploidy and tumorigenesis in mice. *Cancer Cell* **11**, 9-23 (2007).

338. Meraldi P, Honda R, Nigg EA. Aurora-A overexpression reveals tetraploidization as a major route to centrosome amplification in p53-/- cells. *EMBO J* **21**, 483-492 (2002).

339. Caldwell CM, Green RA, Kaplan KB. APC mutations lead to cytokinetic failures in vitro and tetraploid genotypes in Min mice. *J Cell Biol* **178**, 1109-1120 (2007).

340. Daniels MJ, Wang Y, Lee M, Venkitaraman AR. Abnormal cytokinesis in cells deficient in the breast cancer susceptibility protein BRCA2. *Science* **306**, 876-879 (2004).

341. Andreassen PR, Lohez OD, Lacroix FB, Margolis RL. Tetraploid state induces p53-dependent arrest of nontransformed mammalian cells in G1. *Mol Biol Cell* **12**, 1315-1328 (2001).

342. Margolis RL, Lohez OD, Andreassen PR. G1 tetraploidy checkpoint and the suppression of tumorigenesis. *J Cell Biochem* **88**, 673-683 (2003).

343. Uetake Y, Sluder G. Cell cycle progression after cleavage failure: mammalian somatic cells do not possess a "tetraploidy checkpoint". *J Cell Biol* **165**, 609-615 (2004).

344. Ganem NJ*, et al.* Cytokinesis failure triggers hippo tumor suppressor pathway activation. *Cell* **158**, 833-848 (2014).

345. Kuffer C, Kuznetsova AY, Storchova Z. Abnormal mitosis triggers p53-dependent cell cycle arrest in human tetraploid cells. *Chromosoma* **122**, 305-318 (2013).

346. Roy A*, et al.* Uncoupling of the Hippo and Rho pathways allows megakaryocytes to escape the tetraploid checkpoint. *Haematologica* **101**, 1469-1478 (2016).

347. De Santis Puzzonia M, Gonzalez L, Ascenzi S, Cundari E, Degrassi F. Tetraploid cells produced by absence of substrate adhesion during cytokinesis are limited in their proliferation and enter senescence after DNA replication. *Cell Cycle* **15**, 274-282 (2016).

348. Hayashi MT, Karlseder J. DNA damage associated with mitosis and cytokinesis failure. *Oncogene* **32**, 4593-4601 (2013).

349. Lengauer C, Kinzler KW, Vogelstein B. Genetic instability in colorectal cancers. *Nature* **386**, 623-627 (1997).

350. Shackney SE*, et al.* Model for the genetic evolution of human solid tumors. *Cancer Res* **49**, 3344-3354 (1989).

351. Ornitz DM, Hammer RE, Messing A, Palmiter RD, Brinster RL. Pancreatic neoplasia induced by SV40 T-antigen expression in acinar cells of transgenic mice. *Science* **238**, 188-193 (1987).

352. Barrett MT, Pritchard D, Palanca-Wessels C, Anderson J, Reid BJ, Rabinovitch PS. Molecular phenotype of spontaneously arising 4N (G2-tetraploid) intermediates of neoplastic progression in Barrett's esophagus. *Cancer Res* **63**, 4211-4217 (2003).

353. Maley CC. Multistage carcinogenesis in Barrett's esophagus. *Cancer Lett* **245**, 22-32 (2007).

354. Galipeau PC*, et al.* 17p (p53) allelic losses, 4N (G2/tetraploid) populations, and progression to aneuploidy in Barrett's esophagus. *Proc Natl Acad Sci U S A* **93**, 7081-7084 (1996).

355. Olaharski AJ*, et al.* Tetraploidy and chromosomal instability are early events during cervical carcinogenesis. *Carcinogenesis* **27**, 337-343 (2006).

356. Storchova Z*, et al.* Genome-wide genetic analysis of polyploidy in yeast. *Nature* **443**, 541-547 (2006).

357. Mayer VW, Aguilera A. High levels of chromosome instability in polyploids of Saccharomyces cerevisiae. *Mutat Res* **231**, 177-186 (1990).

358. Quintyne NJ, Reing JE, Hoffelder DR, Gollin SM, Saunders WS. Spindle multipolarity is prevented by centrosomal clustering. *Science* **307**, 127-129 (2005).

359. Paim LMG, FitzHarris G. Tetraploidy causes chromosomal instability in acentriolar mouse embryos. *Nat Commun* **10**, 4834 (2019).

360. Snow MH. Tetraploid mouse embryos produced by cytochalasin B during cleavage. *Nature* **244**, 513-515 (1973).

361. Snow MH. Embryonic development of tetraploid mice during the second half of gestation. *J Embryol Exp Morphol* **34**, 707-721 (1975).

362. Tarkowski AK, Witkowska A, Opas J. Development of cytochalasin in B-induced tetraploid and diploid/tetraploid mosaic mouse embryos. *J Embryol Exp Morphol* **41**, 47-64 (1977).

363. Wen D, Saiz N, Rosenwaks Z, Hadjantonakis AK, Rafii S. Completely ES cell-derived mice produced by tetraploid complementation using inner cell mass (ICM) deficient blastocysts. *PLoS One* **9**, e94730 (2014).

364. Eakin GS, Hadjantonakis AK, Papaioannou VE, Behringer RR. Developmental potential and behavior of tetraploid cells in the mouse embryo. *Dev Biol* **288**, 150-159 (2005).

365. Horii T, Yamamoto M, Morita S, Kimura M, Nagao Y, Hatada I. p53 suppresses tetraploid development in mice. *Sci Rep* **5**, 8907 (2015).

366. Tam PP, Rossant J. Mouse embryonic chimeras: tools for studying mammalian development. *Development* **130**, 6155-6163 (2003).

367. Ganem NJ, Storchova Z, Pellman D. Tetraploidy, aneuploidy and cancer. *Curr Opin Genet Dev* **17**, 157-162 (2007).

368. DePamphilis ML. Preface. *Curr Top Dev Biol* **120**, xiii-xxi (2016).

369. Piliszek A, Grabarek JB, Frankenberg SR, Plusa B. Cell fate in animal and human blastocysts and the determination of viability. *Mol Hum Reprod* **22**, 681-690 (2016).

370. Whitten WK. Culture of tubal mouse ova. *Nature* **177**, 96 (1956).

371. Summers MC, Biggers JD. Chemically defined media and the culture of mammalian preimplantation embryos: historical perspective and current issues. *Hum Reprod Update* **9**, 557-582 (2003).

372. Mihajlovic AI, Thamodaran V, Bruce AW. The first two cell-fate decisions of preimplantation mouse embryo development are not functionally independent. *Sci Rep* **5**, 15034 (2015).

373. Braude P, Pickering S, Flinter F, Ogilvie CM. Preimplantation genetic diagnosis. *Nat Rev Genet* **3**, 941-953 (2002).

374. Lu L, Lv B, Huang K, Xue Z, Zhu X, Fan G. Recent advances in preimplantation genetic diagnosis and screening. *J Assist Reprod Genet* **33**, 1129-1134 (2016).

375. Tsichlaki E, FitzHarris G. Nucleus downscaling in mouse embryos is regulated by cooperative developmental and geometric programs. *Sci Rep* **6**, 28040 (2016).

376. Ladouceur AM, Dorn JF, Maddox PS. Mitotic chromosome length scales in response to both cell and nuclear size. *J Cell Biol* **209**, 645-651 (2015).

377. Gerhold AR, Poupart V, Labbe JC, Maddox PS. Spindle assembly checkpoint strength is linked to cell fate in the Caenorhabditis elegans embryo. *Mol Biol Cell* **29**, 1435-1448 (2018).

378. Greenan G, Brangwynne CP, Jaensch S, Gharakhani J, Julicher F, Hyman AA. Centrosome size sets mitotic spindle length in Caenorhabditis elegans embryos. *Curr Biol* **20**, 353-358 (2010).

379. Hara Y, Kimura A. Cell-size-dependent spindle elongation in the Caenorhabditis elegans early embryo. *Curr Biol* **19**, 1549-1554 (2009).

380. Reber S, Goehring NW. Intracellular Scaling Mechanisms. *Cold Spring Harb Perspect Biol* **7**, (2015).

381. Katsura I. Determination of bacteriophage lambda tail length by a protein ruler. *Nature* **327**, 73-75 (1987).

382. Journet L, Agrain C, Broz P, Cornelis GR. The needle length of bacterial injectisomes is determined by a molecular ruler. *Science* **302**, 1757-1760 (2003).

383. Wagner S, Stenta M, Metzger LC, Dal Peraro M, Cornelis GR. Length control of the injectisome needle requires only one molecule of Yop secretion protein P (YscP). *Proc Natl Acad Sci U S A* **107**, 13860-13865 (2010).

384. Labeit S*, et al.* Evidence that nebulin is a protein-ruler in muscle thin filaments. *FEBS Lett* **282**, 313-316 (1991).

385. Castillo A, Nowak R, Littlefield KP, Fowler VM, Littlefield RS. A nebulin ruler does not dictate thin filament lengths. *Biophys J* **96**, 1856-1865 (2009).

386. Wuhr M, Tan ES, Parker SK, Detrich HW, 3rd, Mitchison TJ. A model for cleavage plane determination in early amphibian and fish embryos. *Curr Biol* **20**, 2040-2045 (2010).

387. Mitchison T, Wuhr M, Nguyen P, Ishihara K, Groen A, Field CM. Growth, interaction, and positioning of microtubule asters in extremely large vertebrate embryo cells. *Cytoskeleton (Hoboken)* **69**, 738-750 (2012).

388. Varga V, Helenius J, Tanaka K, Hyman AA, Tanaka TU, Howard J. Yeast kinesin-8 depolymerizes microtubules in a length-dependent manner. *Nat Cell Biol* **8**, 957-962 (2006).

389. Leduc C, Padberg-Gehle K, Varga V, Helbing D, Diez S, Howard J. Molecular crowding creates traffic jams of kinesin motors on microtubules. *Proc Natl Acad Sci U S A* **109**, 6100-6105 (2012).

390. Levy DL, Heald R. Nuclear size is regulated by importin alpha and Ntf2 in Xenopus. *Cell* **143**, 288-298 (2010).

391. Decker M*, et al.* Limiting amounts of centrosome material set centrosome size in C. elegans embryos. *Curr Biol* **21**, 1259-1267 (2011).

392. Travers KJ, Patil CK, Wodicka L, Lockhart DJ, Weissman JS, Walter P. Functional and genomic analyses reveal an essential coordination between the unfolded protein response and ER-associated degradation. *Cell* **101**, 249-258 (2000).

393. Montembault E*, et al.* Myosin efflux promotes cell elongation to coordinate chromosome segregation with cell cleavage. *Nat Commun* **8**, 326 (2017).

394. Schroeder TE. The contractile ring. II. Determining its brief existence, volumetric changes, and vital role in cleaving Arbacia eggs. *J Cell Biol* **53**, 419-434 (1972).

395. O'Shaughnessy B, Thiyagarajan S. Mechanisms of contractile ring tension production and constriction. *Biophys Rev* **10**, 1667-1681 (2018).

396. Wollrab V, Thiagarajan R, Wald A, Kruse K, Riveline D. Still and rotating myosin clusters determine cytokinetic ring constriction. *Nat Commun* **7**, 11860 (2016).

397. Guillot C, Lecuit T. Adhesion disengagement uncouples intrinsic and extrinsic forces to drive cytokinesis in epithelial tissues. *Dev Cell* **24**, 227-241 (2013).

398. Liu XF, Ohno S, Miki T. Nucleotide exchange factor ECT2 regulates epithelial cell polarity. *Cell Signal* **18**, 1604-1615 (2006).

399. Liu XF, Ishida H, Raziuddin R, Miki T. Nucleotide exchange factor ECT2 interacts with the polarity protein complex Par6/Par3/protein kinase Czeta (PKCzeta) and regulates PKCzeta activity. *Mol Cell Biol* **24**, 6665-6675 (2004).

400. Cheerambathur DK*, et al.* The Kinetochore-Microtubule Coupling Machinery Is Repurposed in Sensory Nervous System Morphogenesis. *Dev Cell* **48**, 864-872 e867 (2019).

401. Carim SC, Kechad A, Hickson GRX. Animal Cell Cytokinesis: The Rho-Dependent Actomyosin-Anilloseptin Contractile Ring as a Membrane Microdomain Gathering, Compressing, and Sorting Machine. *Front Cell Dev Biol* **8**, 575226 (2020).

402. Thompson SL, Bakhoum SF, Compton DA. Mechanisms of chromosomal instability. *Curr Biol* **20**, R285-295 (2010).

403. Cimini D, Howell B, Maddox P, Khodjakov A, Degrassi F, Salmon ED. Merotelic kinetochore orientation is a major mechanism of aneuploidy in mitotic mammalian tissue cells. *J Cell Biol* **153**, 517-527 (2001).

404. Salmon ED, Cimini D, Cameron LA, DeLuca JG. Merotelic kinetochores in mammalian tissue cells. *Philos Trans R Soc Lond B Biol Sci* **360**, 553-568 (2005).

405. Patterson GH, Lippincott-Schwartz J. A photoactivatable GFP for selective photolabeling of proteins and cells. *Science* **297**, 1873-1877 (2002).

406. Stingele S, Stoehr G, Peplowska K, Cox J, Mann M, Storchova Z. Global analysis of genome, transcriptome and proteome reveals the response to aneuploidy in human cells. *Mol Syst Biol* **8**, 608 (2012).

407. Eglitis MA, Wiley LM. Tetraploidy and early development: effects on developmental timing and embryonic metabolism. *J Embryol Exp Morphol* **66**, 91-108 (1981).

408. Petzoldt U. Developmental profile of glucose phosphate isomerase allozymes in parthenogenetic and tetraploid mouse embryos. *Development* **112**, 471-476 (1991).

409. Gatlin JC*, et al.* Spindle fusion requires dynein-mediated sliding of oppositely oriented microtubules. *Curr Biol* **19**, 287-296 (2009).

410. Reichmann J*, et al.* Dual-spindle formation in zygotes keeps parental genomes apart in early mammalian embryos. *Science* **361**, 189-193 (2018).

411. Schneider I, de Ruijter-Villani M, Hossain MJ, Stout TAE, Ellenberg J. Dual spindles assemble in bovine zygotes despite the presence of paternal centrosomes. *J Cell Biol* **220**, (2021).

412. Hinchcliffe EH*, et al.* Chromosome missegregation during anaphase triggers p53 cell cycle arrest through histone H3.3 Ser31 phosphorylation. *Nat Cell Biol* **18**, 668-675 (2016).

413. Li M*, et al.* The ATM-p53 pathway suppresses aneuploidy-induced tumorigenesis. *Proc Natl Acad Sci U S A* **107**, 14188-14193 (2010).

414. Santaguida S*, et al.* Chromosome Mis-segregation Generates Cell-Cycle-Arrested Cells with Complex Karyotypes that Are Eliminated by the Immune System. *Dev Cell* **41**, 638-651 e635 (2017).

415. Thompson SL, Compton DA. Proliferation of aneuploid human cells is limited by a p53-dependent mechanism. *J Cell Biol* **188**, 369-381 (2010).

416. Bolton H*, et al.* Mouse model of chromosome mosaicism reveals lineage-specific depletion of aneuploid cells and normal developmental potential. *Nat Commun* **7**, 11165 (2016).

417. Singla S, Iwamoto-Stohl LK, Zhu M, Zernicka-Goetz M. Autophagy-mediated apoptosis eliminates aneuploid cells in a mouse model of chromosome mosaicism. *Nat Commun* **11**, 2958 (2020).

418. Jin XL, Chandrakanthan V, Morgan HD, O'Neill C. Preimplantation embryo development in the mouse requires the latency of TRP53 expression, which is induced by a ligand-activated PI3 kinase/AKT/MDM2-mediated signaling pathway. *Biol Reprod* **80**, 286-294 (2009).

419. Lanni JS, Jacks T. Characterization of the p53-dependent postmitotic checkpoint following spindle disruption. *Mol Cell Biol* **18**, 1055-1064 (1998).

420. Lambrus BG*, et al.* A USP28-53BP1-p53-p21 signaling axis arrests growth after centrosome loss or prolonged mitosis. *J Cell Biol* **214**, 143-153 (2016).

421. Uetake Y, Sluder G. Prolonged prometaphase blocks daughter cell proliferation despite normal completion of mitosis. *Curr Biol* **20**, 1666-1671 (2010).

422. Gleicher N, Orvieto R. Is the hypothesis of preimplantation genetic screening (PGS) still supportable? A review. *J Ovarian Res* **10**, 21 (2017).

423. Magli MC, Jones GM, Lundin K, van den Abbeel E. Atlas of human embryology: from oocytes to preimplantation embryos. Preface. *Hum Reprod* **27 Suppl 1**, i1 (2012).

424. Cavazza T*, et al.* Parental genome unification is highly error-prone in mammalian embryos. *Cell* **184**, 2860-2877 e2822 (2021).

425. Vazquez-Diez C, Yamagata K, Trivedi S, Haverfield J, FitzHarris G. Micronucleus formation causes perpetual unilateral chromosome inheritance in mouse embryos. *Proc Natl Acad Sci U S A* **113**, 626-631 (2016).

426. Hoffman LH, Wooding FB. Giant and binucleate trophoblast cells of mammals. *J Exp Zool* **266**, 559-577 (1993).

427. Wooding FB. The role of the binucleate cell in ruminant placental structure. *J Reprod Fertil Suppl* **31**, 31-39 (1982).

428. Staessen C, Van Steirteghem A. The genetic constitution of multinuclear blastomeres and their derivative daughter blastomeres. *Hum Reprod* **13**, 1625-1631 (1998).

429. Kai Y, Kawano H, Yamashita N. First mitotic spindle formation is led by sperm centrosome-dependent MTOCs in humans. *Reproduction* **161**, V19-V22 (2021).

430. Ueda J*, et al.* Heterochromatin dynamics during the differentiation process revealed by the DNA methylation reporter mouse, MethylRO. *Stem Cell Reports* **2**, 910-924 (2014).

431. Dasika GK, Lin SC, Zhao S, Sung P, Tomkinson A, Lee EY. DNA damage-induced cell cycle checkpoints and DNA strand break repair in development and tumorigenesis. *Oncogene* **18**, 7883-7899 (1999).

Annexe 1

The following is the published version of Chapter 2 of this thesis, published in the journal Nature Communications in 2019.

nature COMMUNICATIONS

ARTICLE

https://doi.org/10.1038/s41467-019-12772-8 OPEN

Tetraploidy causes chromosomal instability in acentriolar mouse embryos

Lia Mara Gomes Paim[1] & Greg FitzHarris[1,2*]

Tetraploidisation is considered a common event in the evolution of chromosomal instability (CIN) in cancer cells. The current model for how tetraploidy drives CIN in mammalian cells is that a doubling of the number of centrioles that accompany the genome doubling event leads to multipolar spindle formation and chromosome segregation errors. By exploiting the unusual scenario of mouse blastomeres, which lack centrioles until the ~64-cell stage, we show that tetraploidy can drive CIN by an entirely distinct mechanism. Tetraploid blastomeres assemble bipolar spindles dictated by microtubule organising centres, and multipolar spindles are rare. Rather, kinetochore-microtubule turnover is altered, leading to microtubule attachment defects and anaphase chromosome segregation errors. The resulting blastomeres become chromosomally unstable and exhibit a dramatic increase in whole chromosome aneuploidies. Our results thus reveal an unexpected mechanism by which tetraploidy drives CIN, in which the acquisition of chromosomally-unstable microtubule dynamics contributes to chromosome segregation errors following tetraploidisation.

[1] Centre de Recherche du Centre Hospitalier de l'Université de Montréal, H2X 0A9 Montreal, QC, Canada. [2] Département d'Obstétrique-Gynécologie, Université de Montréal, H3T 1C5 Montreal, QC, Canada. *email: greg.fitzharris@umontreal.ca

Cell division is comprised of mitosis and cytokinesis. During mitosis, a bipolar spindle is organised by two centrosomes, each comprising a pair of centrioles surrounded by the pericentriolar material. The spindle segregates sister chromatids by the attachment of kinetochores to microtubules that generate forces to separate the chromatids[1,2]. Following chromosome alignment in metaphase, sister chromatids are segregated during anaphase. In most cells, cytokinesis occurs concomitantly causing the cytoplasm to be partitioned into two daughter cells to house the newly segregated chromosomes[3,4]. Defects in either process can affect genetic fidelity. Whereas chromosome mis-segregation in mitosis can cause gains or losses of whole chromosomes, termed aneuploidy, cytokinesis failure leads to an entirely duplicated genome, termed tetraploidy[5,6].

Importantly, tetraploidy can trigger persistent chromosomal mis-segregation (also known as chromosomal instability; CIN), and therefore drive aneuploidy[5,6]. Indeed, tetraploidy is considered a common steppingstone in tumorigenesis and likely contributes to the high levels of CIN in cancer[5,7–11]. Landmark studies described a mechanism underpinning this phenomenon, wherein the excess of centrioles generated by failed cytokinesis causes multipolar spindles during subsequent mitoses. These multipolar spindles can cluster their extra centrosomes to form a bipolar spindle prior to anaphase, but in doing so increase the likelihood of segregation error and whole-chromosome aneuploidy[9,11–13]. Whether this is the only mechanism by which tetraploidy promotes CIN is unknown.

The early mouse embryo lacks centrioles. Whereas in most mammals the fertilising sperm provides the centrioles[14], in mouse they are eliminated both in the oocyte and the sperm, such that the first several mitoses occur in the complete absence of centrioles, and new centrioles are eventually manufactured de novo in the ~64-cell stage embryo[15–17]. Here we take advantage of this highly unusual scenario to investigate the impact of tetraploidy upon chromosome segregation in an acentriolar setting. By extensive live time-lapse imaging we show that, in the acentriolar mouse embryo, tetraploidy rapidly leads to CIN by a mechanism independent of supernumerary centrosomes.

Results

Tetraploid mouse embryos are highly chromosomally unstable. To explore the impact of tetraploidy, we transiently prevented cytokinesis using the actin depolymerising agent Latrunculin B at the 4–8-cell transition, thereby obtaining embryos with four binucleated blastomeres (Fig. 1a, see also the section "Methods"). Herein we refer to the next cell division, in which the four binucleated blastomeres divide to become eight mono-nucleated blastomeres as the 'binucleated division', and the subsequent division as the 'second tetraploid division' (Fig. 1a). In some somatic cells, tetraploidy results in a p53-dependent cell cycle checkpoint that prevents further cell division[18,19]. To assess the impact of tetraploidy in embryos, we allowed binucleated embryos to develop in vitro and counted cell numbers 12 and 24 h after binucleation using fixed-cell analysis. Embryos developed from the binucleated four-cell stage to become morulae possessing 17.9 ± 1.15 (mean ± SEM, $n = 23$ embryos) cells 24 h after binucleation, confirming that cell divisions were not critically impeded (Supplementary Fig. 1a, b). Next, we used PCNA:EGFP to visualise cell cycle progression[20]. Nuclear PCNA:EGFP foci were transiently evident in mid-interphase both in the binucleated division and the second tetraploid division, similar to control embryos, indicative of successful progression through S phase (Supplementary Fig. 1c, d). Accordingly, the number of kinetochores, as observed by kinetochore immunostaining in metaphase-arrested embryos, was doubled in Latrunculin-treated embryos as compared to controls (Supplementary Fig. 1e, f). Thus, as suggested previously[21–23], preimplantation mouse embryos fail to mount a tetraploidy-induced cell cycle checkpoint and continue to develop with a doubled genome.

We wondered about the impact of tetraploidy upon chromosome segregation in embryos. Analysis of chromosome segregation dynamics in live H2B:RFP-expressing embryos at the binucleated division revealed that whereas 82% of divisions in control embryos were normal and without obvious defects, segregation defects were common in tetraploid embryos, with only 33% of divisions occurring with no observable defect (Fig. 1b, c). Embryos also displayed segregation defects when cytokinesis failure had been induced with either Cytochalasin B or Blebbistatin (Supplementary Fig. 2a, b). Moreover, embryos undergoing mitosis in the continued presence of the actin inhibitor Latrunculin had few errors (Supplementary Fig. 2c–e), confirming that actin depolymerisation does not negatively affect chromosome segregation fidelity in the mouse embryo, contrary to the case of mouse oocyte meiosis I[24]. Together, these experiments confirm that the errors observed are attributable to the tetraploid state of the embryos, not the method of inducing tetraploidy. Strikingly, analysis of the second tetraploid division revealed a phenotype very similar to that of the binucleated division, whereas stage-matched controls showed few discernible defects (Fig. 1d, e). Increased abundance of micronuclei, a marker of accumulated chromosome segregation errors[25], was also observed in fixed cell experiments, excluding the possibility that the increased number of errors was somehow related to live imaging (Supplementary Fig. 3). Importantly, ploidy analysis by chromosome spreads at early blastocyst stage revealed that 68.2% of 32-cell stage control embryos contained 40 chromosomes, whereas 31.8% had either chromosome gains or losses (Fig. 1f, g), with chromosome numbers ranging from 38 to 42 (Supplementary Fig. 4a). In contrast, we found that only 24% of 16-cell stage tetraploid embryos maintained a perfect tetraploid genome (80 chromosomes) (Fig. 1f, g), with chromosome numbers ranging from 77 to 83 (Supplementary Fig. 4b). Taken together these experiments reveal that tetraploid mouse embryos continue to divide but become chromosomally unstable during the next few cell divisions.

CIN is not attributable to supernumerary centrosomes. In tetraploid somatic cells caused by cytokinesis failure, supernumerary centrosomes lead to the formation of transiently multipolar spindles that promote segregation errors[9,11]. Preimplantation mouse embryos lack centrioles until ~64-cell stage but achieve spindle assembly between the 4-cell and 32-cell stage by acentriolar microtubule-organising centres (MTOCs)[26]. We therefore set out to simultaneously observe MTOCs, spindles, and chromosome dynamics in tetraploid embryos, using CDK5RAP2:GFP[27,28], SiR Tubulin[29] and H2B:RFP, respectively. During interphase, the majority of normal diploid 8-cell embryos displayed a single clear MTOC close to the nucleus (Fig. 2a; Supplementary Fig. 5c and Supplementary Movie 1). At the onset of nuclear envelope breakdown (NEBD) a new MTOC was assembled such that most diploid embryos displayed a clear CDK5RAP2:GFP-labelled MTOC at each spindle pole at metaphase (Fig. 2a; Supplementary Fig. 5d and Supplementary Movie 1)[16,17]. Analogously, during the binucleated division, 4-cell binucleated embryos typically displayed a single clear MTOC on each nucleus during interphase (Fig. 2b; Supplementary Fig. 5a and c; Supplementary Movie 2). Shortly after NEBD, two new MTOCs were usually assembled such that most binucleated embryos displayed four MTOCs during mitosis (Fig. 2b and Supplementary Fig. 5a, d; Supplementary Movie 2). Interestingly,

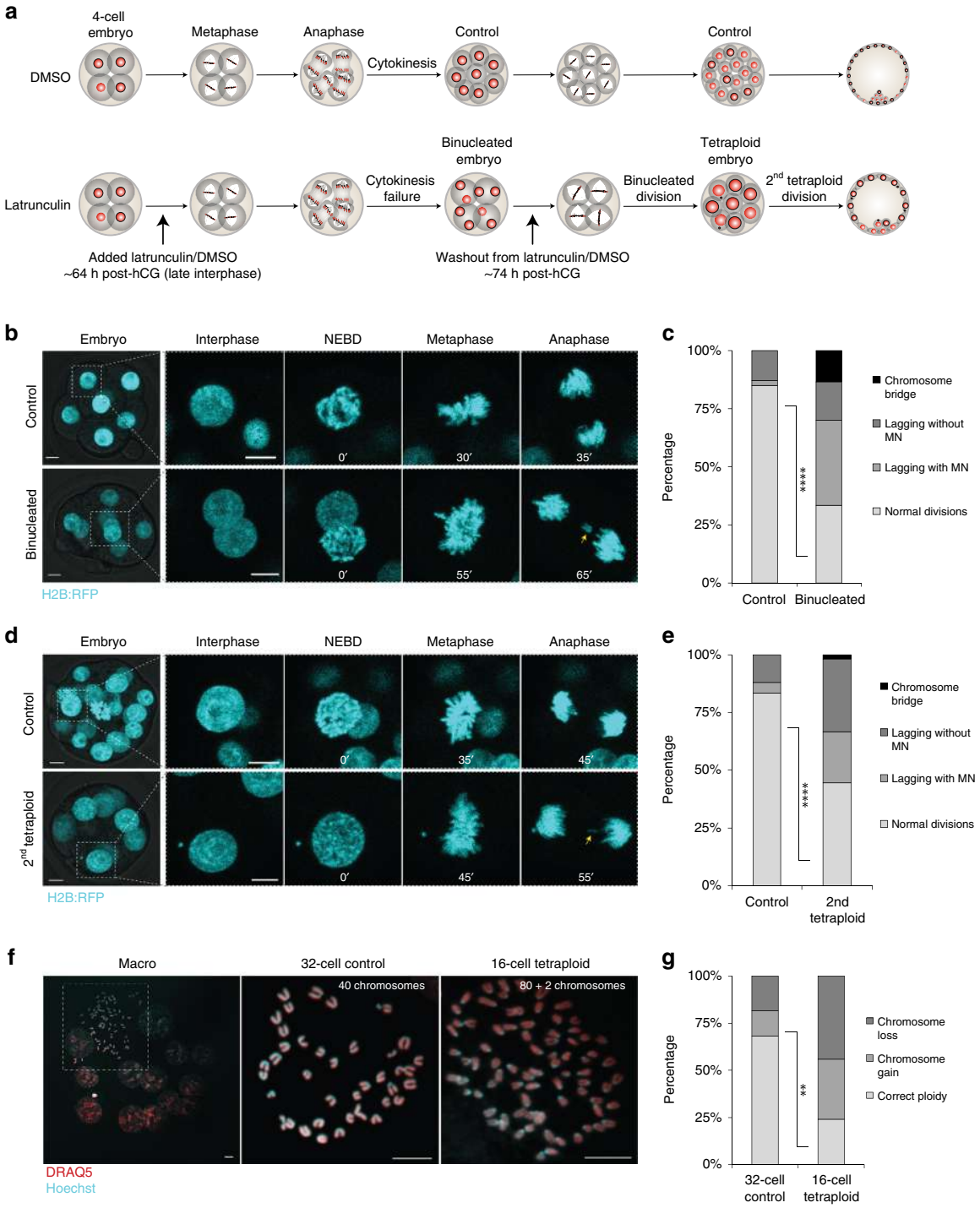

Fig. 1 Tetraploidy leads to chromosomal instability and aneuploidy in the mouse embryo. **a** Scheme illustrating the experimental design applied for the generation of tetraploid embryos. **b** and **d** Representative time-lapse images of mitosis in live H2B:RFP-expressing 8-cell control and 4-cell binucleated **b**, 16-cell control and 8-cell tetraploid embryos **d**. A lagging chromosome (yellow arrows) can be observed both in the binucleated and second tetraploid divisions. **c** and **e** Percentage of cell divisions containing chromosome segregation errors in 8-cell control ($n = 47$ divisions from seven embryos), 4-cell binucleated embryos ($n = 30$ divisions from eight embryos) $^{****}P < 0.0001$ (two-tailed Fisher's exact test) **c**; 16-cell control ($n = 66$ divisions from seven embryos) and 8-cell tetraploid embryos ($n = 50$ divisions from nine embryos) $^{****}P < 0.0001$ (two-tailed Fisher's exact test) **e**. Chromosome segregation errors observed included: lagging chromosomes resulting in micronuclei formation (lagging with MN); lagging chromosomes that did not result in micronuclei formation (lagging without MN); and chromosome bridges. **f** Representative images of chromosome spreads obtained from 32-cell control and 16-cell tetraploid embryos. **g** Percentage of blastomeres containing whole chromosome gains and losses in 32-cell control ($n = 22$ spreads) and 16-cell tetraploid embryos ($n = 25$ spreads) $^{**}P = 0.0034$ (two-tailed Fisher's exact test). Scale bars = 10 μm. NEBD nuclear envelope breakdown

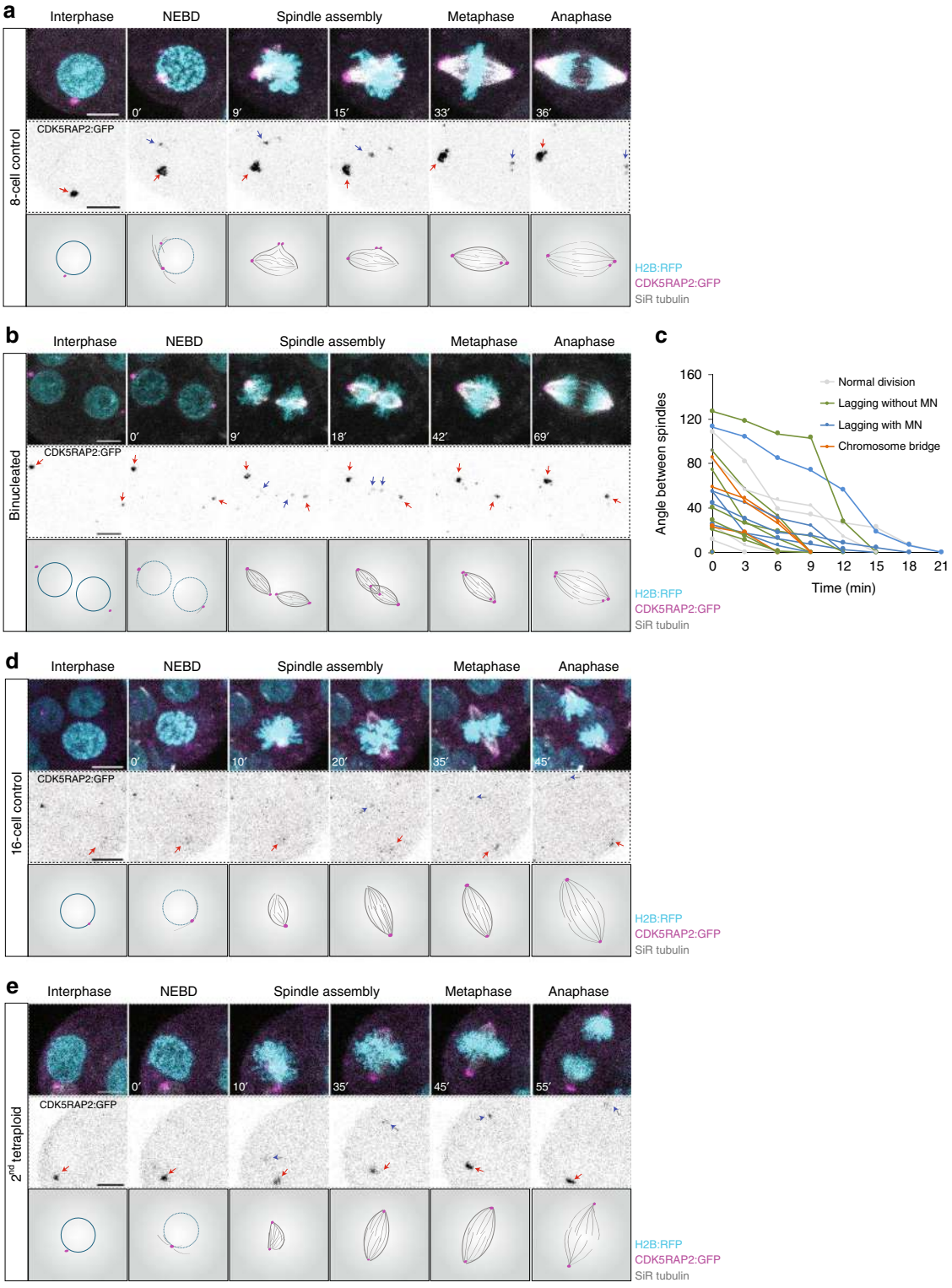

Fig. 2 Chromosomal instability in tetraploid embryos is not attributable to supernumerary centrosomes. **a**, **b**, **d** and **e** Representative time-lapse images and illustrations of live 8-cell control (**a**), 4-cell binucleated (**b**), 16-cell control (**d**) and 8-cell tetraploid embryos (**e**) labelled with SiR Tubulin (grey) and co-expressing H2B:RFP (cyan) and CDK5RAP2:GFP (magenta and inverted grey). A major microtubule organising centre (MTOC) can be observed in the 8-cell control, 16-cell control and 8-cell tetraploid embryo during interphase (red arrows) and a newly assembled MTOC can be observed during mitosis (blue arrows). In binucleated embryos, two major MTOCs (red arrows) can be observed during interphase and two newly assembled MTOCs (blue arrows) can be observed during mitosis. **c** Measurements of the angle between the two individualised spindles during the binucleated division. Line colours represent the different types of chromosome segregation events associated with a specific cell division ($n = 23$ divisions from 12 embryos). Chromosome segregation errors observed included: lagging chromosomes resulting in micronuclei formation (lagging with MN); lagging chromosomes that did not result in micronuclei formation (lagging without MN); and chromosome bridges. Scale bars = 10 μm. NEBD nuclear envelope breakdown

these four MTOCs usually formed the poles of two completely separate bipolar spindles (Fig. 2b and Supplementary Fig. 5a, b; Supplementary Movies 2, 3). These two spindles rapidly moved towards each other and fused to form a single bipolar spindle prior to anaphase (Supplementary Movies 2, 3). We measured and tracked the angles between the two spindles from the moment they first established contact until they completely fused (Fig. 2c). Upon contact, the spindles fused by either sliding together or rotating towards each other depending on the initial angle of contact until they eventually became a single bipolar spindle (Fig. 2b, c; Supplementary Fig. 5a, b; Supplementary Movies 2, 3), as observed in Fmn2$^{-/-}$ mouse oocytes[30], Xenopus extract spindles in close apposition[31], and in mouse zygotes[32]. Notably however, there was no relationship between the initial angle at which the spindles made contact with each other and the likelihood of developing chromosome segregation errors (Fig. 2c). Moreover, multipolar spindles such as are characteristic in somatic cells with supernumerary centrioles, and associated with segregation error, were rare both in 4-cell binucleated (18.4% of divisions) and 8-cell control embryos (11.4% of divisions). Importantly, we used 3-min acquisitions intervals, which allowed us to confidently distinguish between spindle fusion events and multipolarity. Notably, even in more extreme examples of perpendicular spindle fusion, the two spindles remained distinguishable throughout fusion without neighbouring poles connecting via microtubule bundles (Supplementary Fig. 5a, b; Supplementary Movie 3).

Next, we analysed spindle dynamics in the second tetraploid division which, importantly, begins with a single morphologically normal nucleus containing a tetraploid genome. Similar to 8-cell and 16-cell controls, these cells usually possessed only one major MTOC adjacent to the nucleus and a second major MTOC was assembled at NEBD to enable the generation of a bipolar spindle (Fig. 2d, e; and Supplementary Fig. 5e, f). Though general spindle morphology was not obviously altered as compared to diploid controls, tetraploid blastomeres possessed a wider metaphase plate, presumably as a result of having twice as many chromosomes (Supplementary Fig. 5g, h). Spindle assembly was otherwise morphologically indistinguishable from diploid 8-cell or 16-cell embryos, despite the dramatic increase in segregation errors (Fig. 1d, e), with multipolar spindles again very rare (16-cell control: 9.6% of divisions; 8-cell tetraploid: 16.6% of divisions). Taken together, these observations reveal that CIN observed in the tetraploid mouse embryo cannot be attributed to supernumerary centrioles or multipolar spindles.

Spindle assembly checkpoint (SAC) is not abrogated by tetraploidy. Most cells possess a signalling pathway termed the SAC that serves to prevent chromosome segregation errors by delaying anaphase until all chromosomes are aligned at the metaphase plate and the kinetochores attached to microtubules[33,34]. Notably, recent work has shown that, in early embryos, although misaligned chromosomes/kinetochores also recruit SAC proteins, such as Mad1 and Mad2, SAC signalling is not sufficiently robust to enforce a metaphase arrest[35–37]. We wondered whether the higher rates of error in tetraploid embryos might be attributable to further weakening of the SAC, and thus set out to probe SAC activity in tetraploid embryos. Notably, tetraploidy prolonged mitosis, as observed by increased NEBD-anaphase duration (Fig. 3a, b), suggesting SAC activation. SAC inhibition using the Mps1 inhibitor AZ 3146 reduced the duration of mitosis causing controls and tetraploids to have a similar M-phase duration, indicating that the prolonged mitosis in tetraploids was attributable to the SAC (Fig. 3a, b). Immunofluorescence analysis of the SAC protein Mad2 revealed that the majority of kinetochores exhibited pronounced Mad2 staining shortly after NEBD which was lost as chromosomes aligned, similar to controls (Fig. 3c–e). Similarly, live imaging of tetraploid embryos co-expressing H2B:RFP and MAD1:2EGFP clearly shows MAD1:2EGFP recruitment to kinetochores shortly after NEBD and gradual loss of signal within 30–40 min as chromosomes align at the metaphase plate (Fig. 3f, g). As is the case in normal diploid mouse embryos[36], tetraploid blastomeres frequently failed to wait for full chromosome alignment prior to anaphase onset, underscoring the previously reported inefficiency of SAC in the mouse embryo (Supplementary Fig. 6). Nonetheless, tetraploidy caused a substantial SAC-dependent lengthening of mitosis. Therefore, though we cannot exclude the possibility of minor impacts of tetraploidy upon the SAC, our experiments fail to uncover a clear weakening of the SAC in tetraploids that might explain the high rate of segregation error.

Tetraploidy perturbs metaphase chromosome alignment. To further investigate how tetraploidy leads to lagging chromosomes and chromosome segregation error, we performed a comprehensive analysis of centromere spatiotemporal behaviour in mitosis. Embryos co-expressing H2B:RFP and the centromere label MajSatTALE:mClover[38] were imaged in three dimensions at 75 s intervals, and individual centromere pairs were tracked during the second tetraploid division. Our analysis showed no difference in centromere velocity either prior to anaphase onset or during anaphase poleward chromosome movement (Fig. 4a, b), or in the tightness of the metaphase plate (Fig. 4c, d), suggesting that overall behaviour of most chromosomes is not adversely affected in tetraploids. Interestingly, however, we observed that both controls and tetraploid blastomeres displayed chromosomes that, having previously been aligned, displaced from the metaphase plate to become unaligned (Fig. 4e). In controls, these displacement events lasted on average 6.32 ± 1.43 min ($n = 16$ displacement events; Fig. 4h) during which time the centromeres typically moved between 1.7 and 10.74 µm from the metaphase plate, before returning to full alignment. Importantly, in control blastomeres, chromosomes that became displaced from the metaphase plate returned to full alignment prior to anaphase onset in almost all cases (Fig. 4e, f and h). On the other hand, in tetraploid embryos, chromosome displacement events lasted substantially longer (13.57 ± 2.11 min, $n = 14$ displacement events), and in many cases chromosomes failed to completely re-align prior to anaphase onset (Fig. 4e, g, h). Of the misaligned chromosomes at anaphase onset observed in tetraploid embryos, almost all resulted from a chromosome that was previously aligned and became displaced during metaphase. Consistent with our previous results, the majority of tetraploid embryos displayed lagging chromosomes. Importantly, all anaphase laggards arose from previously metaphase-aligned chromosomes, revealing that the elevated frequency of lagging chromosomes in tetraploid embryos is not attributable to failed alignment (Supplementary Fig. 7).

Taken together, these results show that, though overall centromere behaviour and chromosome congression are largely unaltered in tetraploid embryos, a deficiency in maintaining chromosome alignment leads to an increased likelihood of chromosome misalignment at anaphase. However, these misaligned chromosomes do not seem to be the major cause of lagging chromosomes in tetraploid embryos. Rather, similar to somatic[39] and cancer cells[40] lagging chromosomes arise from chromosomes that were correctly aligned at the metaphase plate prior to anaphase onset.

Tetraploidy affects kinetochore microtubule establishment. During spindle assembly some kinetochore pairs form merotelic

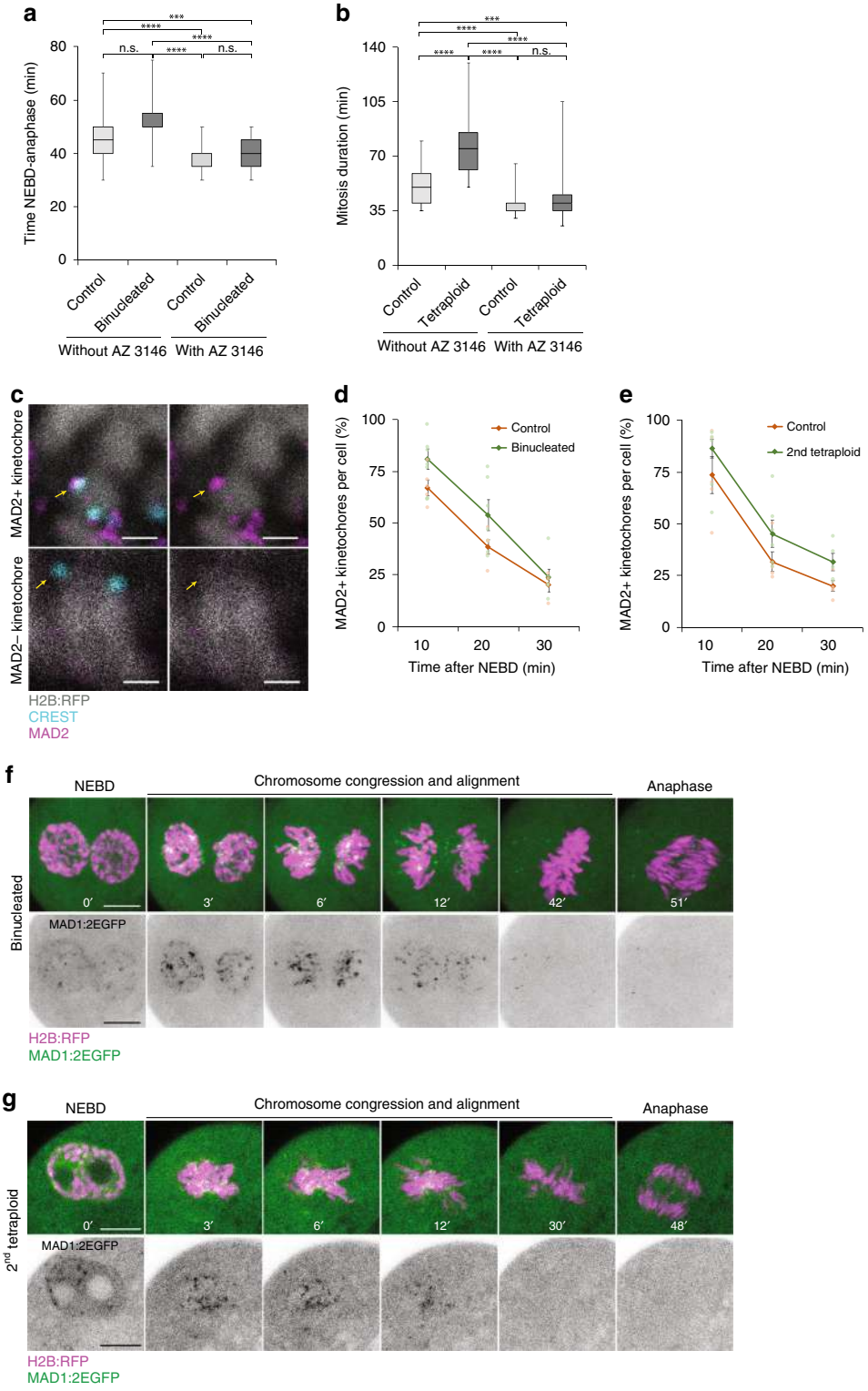

attachments in which a single kinetochore simultaneously contacts microtubules (MTs) from both spindle poles. Establishment of correct (amphitelic) chromosome attachment prior to anaphase occurs by correction of previously mis-attached kinetochores, a process that depends upon MT turnover at the kinetochore[41,42]. In cancer cells, CIN is associated with reduced kinetochore–microtubule (kMT) turnover that promotes errors including merotelic attachments that lead to lagging chromosomes and aneuploidy[43]. We directly analysed kMT turnover during the second tetraploid division using fluorescence dissipation after photoactivation of photoactivatable-GFP-tubulin (PAGFP-tubulin) within the metaphase spindle as previously described[43–45], using SiR Tubulin to select cells with spindles oriented in the plane of imaging (Fig. 5a–c). Strikingly, kMT half-life was substantially increased in tetraploid embryos compared to controls (Fig. 5a–c), indicating reduced kMT turnover. Notably, this increase is similar to that observed when comparing chromosomally unstable to chromosomally stable somatic cells[43]. Non-kinetochore MT half-life and the rate of poleward microtubule flux measured with PAGFP-tubulin, as well as the velocity

Fig. 3 Spindle assembly checkpoint activity is not abrogated in tetraploid embryos. **a** and **b** Quantification of mitosis duration in 8-cell control (without AZ 3146 $n = 47$ divisions from seven embryos; with AZ 3146 $n = 63$ divisions from eight embryos), 4-cell binucleated embryos (without AZ 3146 $n = 30$ divisions from eight embryos; with AZ 3146 $n = 54$ divisions from 15 embryos) $^{***}P = 0.0009$; $^{****}P < 0.0001$ (unpaired Kruskal–Wallis test with Dunn's test for multiple comparisons) **a**; 16-cell control (without AZ 3146 $n = 61$ divisions from seven embryos; with AZ 3146 $n = 59$ divisions from seven embryos) and 8-cell tetraploid embryos (without AZ 3146 $n = 50$ divisions from nine embryos; with AZ 3146 $n = 63$ divisions from 12 embryos) $^{***}P = 0.0005$; $^{****}P < 0.0001$ (unpaired Kruskal–Wallis test with Dunn's test for multiple comparisons) **b**. **c** Representative z projections of MAD2-positive and MAD2-negative kinetochores demonstrating co-localisation of MAD2 (magenta) and CREST (cyan) in positively stained kinetochores and no co-localisation in negatively stained kinetochores. **d** and **e** Proportion of MAD2-positive kinetochores in 8-cell control, 4-cell binucleated **d**, 16-cell control and 8-cell tetraploid embryos **e** at 10 mins (8-cell control $n = 6$ blastomeres; 4-cell binucleated $n = 6$ blastomeres; 16-cell control $n = 5$ blastomeres; 8-cell tetraploid $n = 5$ blastomeres), 20 mins (8-cell control $n = 5$ blastomeres; 4-cell binucleated $n = 6$ blastomeres; 16-cell control $n = 5$ blastomeres; 8-cell tetraploid $n = 6$ blastomeres) and 30 mins (8-cell control $n = 4$ blastomeres; 4-cell binucleated $n = 6$ blastomeres; 16-cell control $n = 5$ blastomeres; 8-cell tetraploid $n = 5$ blastomeres) after nuclear envelope breakdown (NEBD). Error bars represent SEM. **f** and **g** Representative time-lapse images of live 4-cell binucleated **f** and 8-cell tetraploid embryos **g** co-expressing H2B:RFP and MAD1:2EGFP. Note that MAD1:2EGFP signal is clearly observed at the kinetochores shortly after nuclear envelope breakdown (NEBD) and is gradually lost following chromosome alignment at the metaphase plate. Scale bars = 10 μm except for figure **c**, where scale bars = 1 μm. Where box plots are shown, the centre line represents the median, the bounds of box represent the upper and lower quartiles and the whiskers represent minimum and maximum values

of microtubule growth events as determined by EB1:EGFP imaging, were all unchanged between tetraploids and controls (Supplementary Fig. 8a–e), revealing that the change in MT dynamics was highly specific to kMT turnover. Importantly, there was no difference in MT turnover when comparing SiR Tubulin-stained blastomeres with SiR Tubulin-free blastomeres, ruling out the possibility that the increase in kMT half-life observed in tetraploid embryos could have been induced by potential MT-stabilising effects of SiR Tubulin (Supplementary Fig. 8f–h). Highly consistent with a kMT turnover defect, direct comparison of stable kMT attachments in embryos with a classic cold shock approach revealed a far greater proportion of mis-attachments in tetraploid embryos as compared to controls in mid-late prometaphase/metaphase (Fig. 5d, e). Whereas lateral/merotelic attachments were very rare in diploid blastomeres (0.9%), 7% of all attachments observed in tetraploid blastomeres were mis-attached, at least one kinetochore being misattached in every tetraploid blastomere examined. This is highly consistent with the notion that a single merotelically attached kinetochore is sufficient to cause missegregation[39] and correlates with the elevated rates of lagging chromosomes observed in tetraploids (Fig. 1b–e).

A major determinant of the capacity to maintain kinetochore MT turnover to correct misattachments is the recruitment of the microtubule depolymerising protein mitotic centromere-associated kinesin (MCAK)[46,47]. We wondered whether MCAK was sufficiently recruited to the centromere/kinetochore in tetraploid embryos. Using immunofluorescence we found that MCAK was significantly underrepresented at the kinetochore in tetraploid embryos as compared to controls (Fig. 5f, g). This suggests that reduced MT turnover may be downstream of an inability to recruit sufficient MT-turnover-sustaining factors. Consistent with this notion, overexpression of MCAK:GFP substantially and significantly decreased the rates of chromosome segregation errors in tetraploid embryos, when compared to tetraploid embryos expressing GFP alone (Fig. 5h, i), as has also been seen in cancer cells ectopically expressing MCAK[48]. Taken together these data show that, in tetraploid embryos, kMT turnover is reduced and error correction mechanisms are suppressed, allowing for the accumulation of merotelic attachments that in turn lead to lagging chromosomes, which can be rescued by introducing ectopic MCAK:GFP.

Discussion

Our data show that mouse embryos do not possess a tetraploidy checkpoint but continue to divide and become chromosomally unstable immediately after tetraploidisation (Fig. 1). Why the mouse embryo fails to mount a tetraploidy checkpoint is unclear but may relate to the key role of centrioles in mediating the checkpoint, shown in RPE1 cells[19]. The described mechanism by which tetraploidy leads to CIN in mammalian cells is that the acquisition of supernumerary centrioles/centrosomes leads to the formation of hazardous multipolar spindles that induce segregation errors[5,7,9,11]. That there might be other means by which tetraploidy could cause CIN was alluded to in studies of tetraploid yeast with normal centrosome numbers, where CIN was likely due to the impact of cell size upon spindle geometry[49]. Here we show that mouse blastomeres, which are acentriolar, become highly chromosomally unstable upon tetraploidisation as a result of altered kMT dynamics. Notably, this mechanism is distinct to yeast, where tetraploid spindles have unchanged microtubule dynamics[49]. Our data indicate that reduced kinetochore recruitment of MCAK, a well-characterised MT depolymerising kinesin, provides at least part of the explanation for the reduced kinetochore MT turnover that underpins misattachments and segregation errors in tetraploid blastomeres. Why MCAK is underrepresented at the kinetochores remains to be determined. Gene expression changes associated with having extra copies of chromosomes[50], and the doubling of kinetochores, could present an overburden on the ability to recruit MCAK. Alternatively, tetraploidy could impact upstream signalling necessary for MCAK recruitment to the kinetochore[51,52], or affect the structure of the kinetochore itself.

Our centromere and chromosome tracking data show that tetraploidy introduces two types of anaphase defects. First, we observed lagging anaphase chromosomes, that arise from fully aligned metaphase chromosomes, and frequently result in a micronucleus. Whereas in somatic cells micronuclei derived from lagging chromosomes are frequently reabsorbed in the next cell cycle, which likely forms the mechanistic basis for chromothripsis[53], we have previously shown that in mouse embryos micronuclei are very rarely reincorporated into the principal nucleus, and repeated micronucleus inheritance necessarily drives aneuploidy[25]. Notably, micronuclei are also unilaterally inherited in tetraploid embryos (Supplementary Fig. 9), thus lagging chromosomes seem certain to contribute to mosaic aneuploidy in the mouse tetraploid embryo. Secondly, we observe chromosomes that fail to align in time for anaphase onset. In some cases, the proximity of the misaligned chromosome to the metaphase plate, paired with imaging resolution limits prevented us from determining whether the two sister chromatids were ultimately correctly segregated. However, in at least one example where we labelled both the chromosome and the centromere in live imaging, both misaligned sister chromatids were seen to migrate to

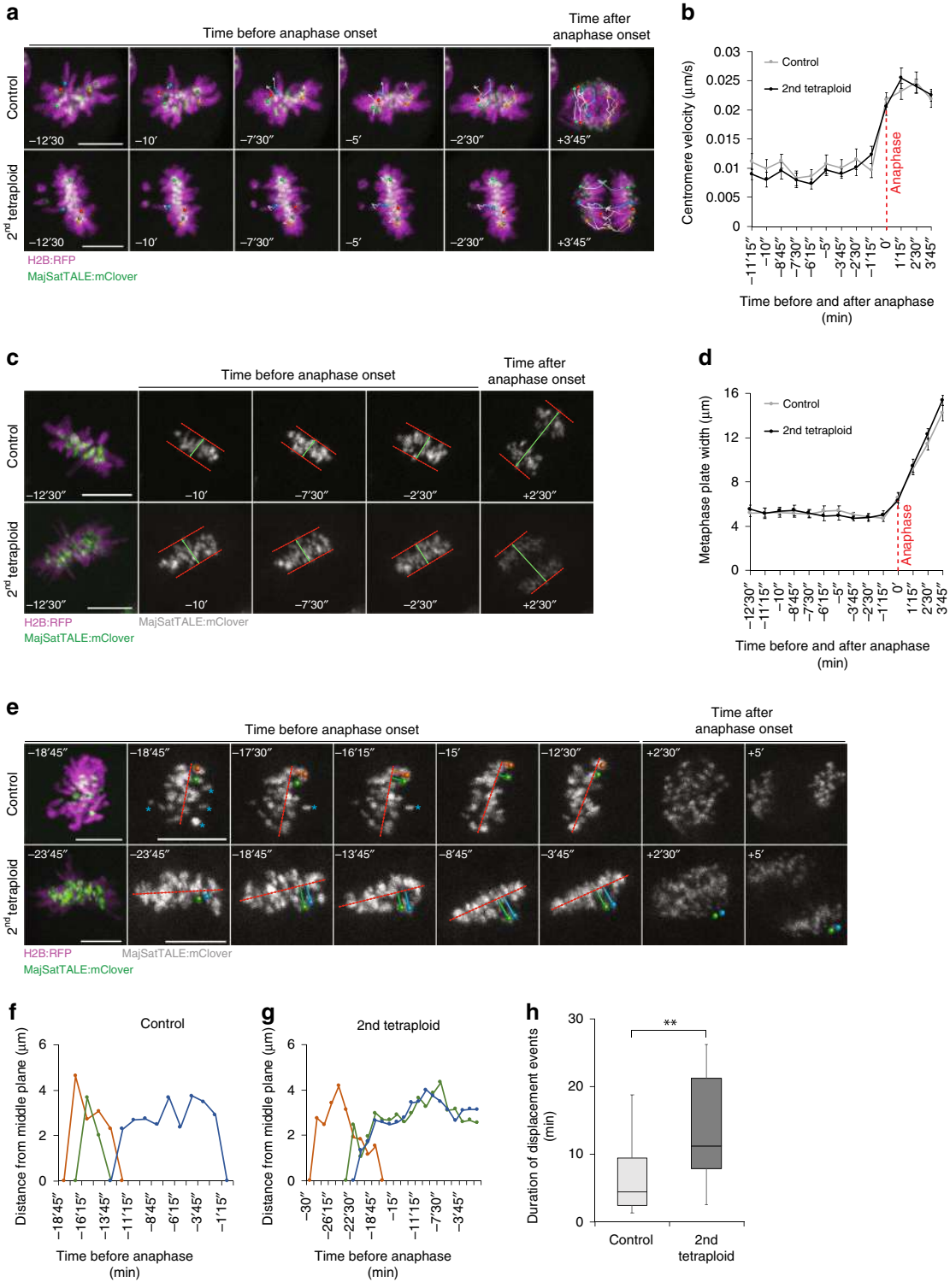

the same spindle pole (Supplementary Fig. 7). Thus, although formally distinguishing the proportional contribution of these two distinct defects to embryo aneuploidy is experimentally challenging, both likely contribute to the elevated rate of aneuploidy in the tetraploid embryo.

Tetraploidy is common in the early stages of tumorigenesis, and likely contributes to the CIN and aneuploidy associated with some cancers[5–9,54]. Genome doubling is thought to provide a permissive environment for the acquisition of CIN, as chromosome losses are more likely to be tolerated with multiple chromosome copies present[54]. Importantly, our data do not oppose the notion that centriole doubling can be a major driver of CIN, but rather add altered microtubule dynamics as a distinct mechanism that can also confer CIN immediately after tetraploidisation. In tetraploid somatic cells, the extra centrioles are lost after repeated passages[9,55], and it remains to be seen whether an analogous adaptation might occur with microtubule dynamics. Nonetheless our data adds altered MT dynamics to supernumerary centrosomes as two separate defects that emerge rapidly to drive CIN in the first cell cycles following tetraploidisation.

Fig. 4 Tetraploid embryos exhibit chromosome alignment defects. **a** Representative time-lapse images of centromere tracking in 16-cell controls and 8-cell tetraploid embryos co-expressing H2B:RFP and MajSatTALE:mClover. Coloured circles indicate centromere pairs that were tracked throughout mitosis and individualised centromeres at anaphase. Coloured lines represent the path covered by the centromere pairs during time. **b** Quantification of average centromere velocity in 16-cell control ($n = 24$ centromere pairs from five blastomeres) and 8-cell tetraploid embryos ($n = 21$ centromere pairs from five blastomeres). **c** Representative time-lapse images of 16-cell control and 8-cell tetraploid embryos co-expressing H2B:RFP and MajSatTALE:mClover, demonstrating the measurements of metaphase plate width throughout mitosis. Red dashed lines indicate the borders of the metaphase plate based on the MajSatTALE:mClover signal. Green lines indicate width measurements. **d** Quantification of metaphase plate width in 16-cell control ($n = 5$ blastomeres) and 8-cell tetraploid embryos ($n = 5$ blastomeres). **e** Representative time-lapse images of 16-cell control and 8-cell tetraploid embryos co-expressing H2B:RFP and MajSatTALE:mClover, demonstrating chromosome displacement events. In the control embryo, two chromosomes (orange and green circles—corresponding to the orange and green lines in figure **f**) that were previously aligned become displaced from the middle plane of the metaphase plate (red dashed lines) at mid-mitosis, returning to their original position before anaphase onset. In the tetraploid embryo, the two chromosomes that become displaced (green and blue circles—corresponding to the green and blue lines in figure **g**) fail to return to the metaphase plate, resulting in misaligned chromosomes at anaphase onset. Blue asterisks indicate chromosomes that were not yet aligned for the first time during the time sequence shown. **f** and **g** Quantification of the distance between centromere pairs and metaphase middle plane in a 16-cell control **f** and 8-cell tetraploid embryo **g**. **h** Quantification of average duration of displacement events in 16-cell controls ($n = 16$ displacement events from five blastomeres) and 8-cell tetraploid embryos ($n = 14$ displacement events from five blastomeres; $^{**}P = 0.0061$, unpaired two-tailed Mann–Whitney test). In the box plot, the centre line represents median, the bounds of box represent upper and lower quartiles and the whiskers represent minimum and maximum values. Scale bars = 10 µm. Error bars represent SEM

Methods

Embryo culture and microinjection. All experiments were performed in accordance with the guidelines for animal experimentation of the Comité Institutionnel de Protections des Animaux (CIPA). All experiments were approved by the Centre de Recherche du Centre Hospitaliaire de l'Université de Montréal (CRCHUM) Comité Institutionnel de Protections des Animaux (CIPA). Protocol number: IP18034GFs. Embryos were harvested from superovulated CD1 female mice (Crl: CD1(ICR) Charles River Laboratories) mated with CD1 male mice, and cultured in KSOM medium (EmbryoMax® KSOM; Millipore, MR-020P-5F) in 5% CO_2 at 37 °C. mRNA was manufactured using Ambion mMessage Machine T3 (AM1348) or T7 (AM1344) according to manufacturer's instructions. Plasmids used were H2B:RFP in pRN4 (gift from Alex McDougall), PCNA:EGFP in pcDNA3.1 + poly (A) (gift from Kazuo Yamagata), CDK5RAP2:GFP in pGEMHE (gift from Tomoya Kitajima), α-tubulin-human:PAGFP in pIRESHyg2 (Addgene, plasmid #12296), EB1:EGFP in pcDNA3.1 + poly(A) (gift from Lynne Cassimeris), MAD1:2EGFP in pIVT (gift from Michael Lampson), MajSatTALE:mClover in pTALYM3 (Addgene, plasmid #47878) and MCAK:GFP (purchased in the pEGFP-C1 vector from Addgene, #pYOY152 and subcloned into pcDNA.3.1/myc-His(–)A). Two-cell embryos were microinjected using a picopump (World Precision Instruments) and micromanipulators (Narishige) mounted on a Leica DMI4000 inverted microscope[45]. For the experiments in Fig. 3f, the embryos were microinjected at the 4-cell stage. For the experiments in Figs. 3g and 5h, the embryos were microinjected at late 4-cell binucleated stage (equivalent to 8-cell stage).

Drug treatments. To induce binucleation, late interphase 4-cell stage embryos (~64 h post-hCG) were treated for ~10 h with Latrunculin B (5 µM; EMD Millipore,428020). Embryos that did not display the four blastomeres with two visible nuclei by the end of the incubation period were excluded. Simultaneously, control embryos were treated with 1:1000 DMSO (Sigma Aldrich, D2650). After the incubation period, the embryos were thoroughly washed and cultured in KSOM media. For experiments in Supplementary Fig. 2a, b, either Cytochalasin B (5 µg/mL; Sigma-Aldrich C6762) or Blebbistatin (100 µM; Calbiochem/Millipore, 203391) were used to induce binucleation. For experiments in Supplementary Figs. 1e, f, 5g, h; Figs. 1f, g; 5f, g, the embryos were treated with 25 µM of MG 132 (Calbiochem 474790) to induce a metaphase arrest. For kinetochore counts in Supplementary Fig. 1e, f, after metaphase arrest the embryos were treated with 200 µM of Monastrol (Calbiochem, 475879) to induce monopolar spindle formation and allow better visualisation of individual kinetochores. For the SAC inhibition treatment in Fig. 3a, b, the embryos were live-imaged in the presence of AZ 3146 (Calbiochem, catalogue #531976). For experiments involving PAGFP:tubulin live imaging, embryos were arrested in metaphase using 100 µM of APCin (Tocris, 5747). For the photobleaching control experiments, MII eggs were live-imaged in the presence of 10 µM of Taxol (Paclitaxel; Sigma Aldrich, T402). Spindle labelling in live embryos was performed with a 2 h incubation in 300 nM of SiR Tubulin (Cytoskeleton Inc., CY-SC002). For the experiment in Supplementary Fig. 8f–h, the embryos were either exposed to 1 µM of SiR DNA (Cytoskeleton Inc., CY-SC007) alone for 3 h or to 300 nM of SiR Tubulin for 2 h followed by a 3 h exposure to 1 µM of SiR DNA.

Chromosome spreads. Chromosome spreads were performed using an air-drying method[56]. Metaphase arrested 32-cell diploid and 16-cell tetraploid embryos were exposed to 1% sodium citrate for 15 min and subsequently transferred to a grease-free slide. Three drops of methanol:acetic acid (3:1) were applied directly on top of the embryos and the slides were air-dried. For staining, air-dried slides were co-labelled with Hoechst 33342 (Sigma Aldrich, H6024, 1:500) and DRAQ5 (Thermo Fisher Scientific, 62254, 1:250) loaded in FluorSave™ Reagent (Calbiochem, 345789) in order to differentially label the chromosomes and centromeric regions.

Cold shock treatment. For assessment of kMT attachments in Fig. 5d, e, H2B:RFP-expressing embryos were exposed to a 10 min cold shock treatment in ice cold M2 media (Sigma Aldrich M7167) 35 min after NEBD was observed by live imaging and then immediately fixed.

Immunofluorescence and live Imaging. Embryos were fixed with 4% paraformaldehyde (PFA) in PBS for 40 min followed by 10 min permeabilization using 0.25% Triton X in PBS, and blocked with 3% bovine serum albumin (BSA) in PBS[57]. Where CREST antibodies were used, embryos were fixed with 2% PFA in PBS for 30 min. Where MAD2 antibodies were used, embryos were fixed with 2% PFA in PBS for 15 min. Primary antibodies used were: CREST anti-human (gift from Marvin J. Fritzler 1:100), β-tubulin anti-mouse (Sigma Aldrich catalogue #T4026 1:1000), MCAK anti-rabbit (gift from Duane Compton; 1:1000), pericentrin anti-mouse (BD Biosciences catalogue #611814 1:500), α-tubulin anti-rabbit (Abcam catalogue #AB18251 1:1000) and MAD2 anti-rabbit (Biolegend catalogue #924601; 1:300). Hoechst 33342 (1:1000) was used for DNA labelling. Alexa-labelled secondary antibodies (1:1000) were purchased from ThermoFisher.

Alexa Fluor® 555 Phalloidin-conjugated antibody (1:200) was purchased from Invitrogen (A34055). Immunofluorescence imaging was performed on either a Leica SP8 confocal microscope fitted with a 63 × 1.4 numerical aperture oil objective or a Leica SP5 confocal microscope fitted with a 100 × 1.4 numerical aperture oil objective and a HyD detector. Live cell imaging and FDAP was performed on a Leica SP8 confocal microscope fitted with a 20 × 0.75 numerical aperture air objective and a HyD detector and embryos were imaged on KSOM media, placed on a heated stage top incubator with 5% CO_2 supply at 37 °C. For the live imaging experiment performed in Supplementary Fig. 1a, the embryos were imaged in a Zeiss Axio observer, equipped with an Axiocam and Apotome and 20 × 0.8 numerical aperture air objective and LED light. For EB1:EGFP live imaging, embryos were imaged every 2.578 s for 2 min with a 63 × 1.4 numerical aperture oil objective. For live imaging in the presence of either Taxol (photobleaching control in Fig. 5a–c) or Latrunculin (Supplementary Fig. 2c, d), the embryos were live imaged in Ibidi micro-insert wells mounted in a glass-bottom dish with distilled water and our setup was modified for proper CO_2 supply[58].

Fluorescence dissipation after photoactivation. Photoactivation was performed by briefly exposing a defined rectangular region of interest positioned across one side of the metaphase spindle to 405-nm laser. Live imaging was performed at 30 s intervals for 15 min. For fluorescence decay curves and half-life analyses, the measurements of fluorescence intensity decay for each blastomere were plotted against time and fitted into a double exponential curve $f(t) = A \times \exp(-k_1 t) + B \times \exp(-k_2 t)$ using the cftool on MATLAB[43,59,60]. In this equation, t represents time; A, the less stable non-kMTs; B, the stable kMTs and k_1 and k_2 represent the decay rates of A and B, respectively. The half-life for each MT population was calculated as $\ln 2/k$. Photobleaching was corrected for each measurement by imaging MII eggs exposed to 10 µM of the MT-stabilising agent Taxol, where MT turnover is minimal. Poleward flux velocity was calculated by determining the distance between the fluorescent mark on the spindle and the corresponding spindle pole at each time point[45,60].

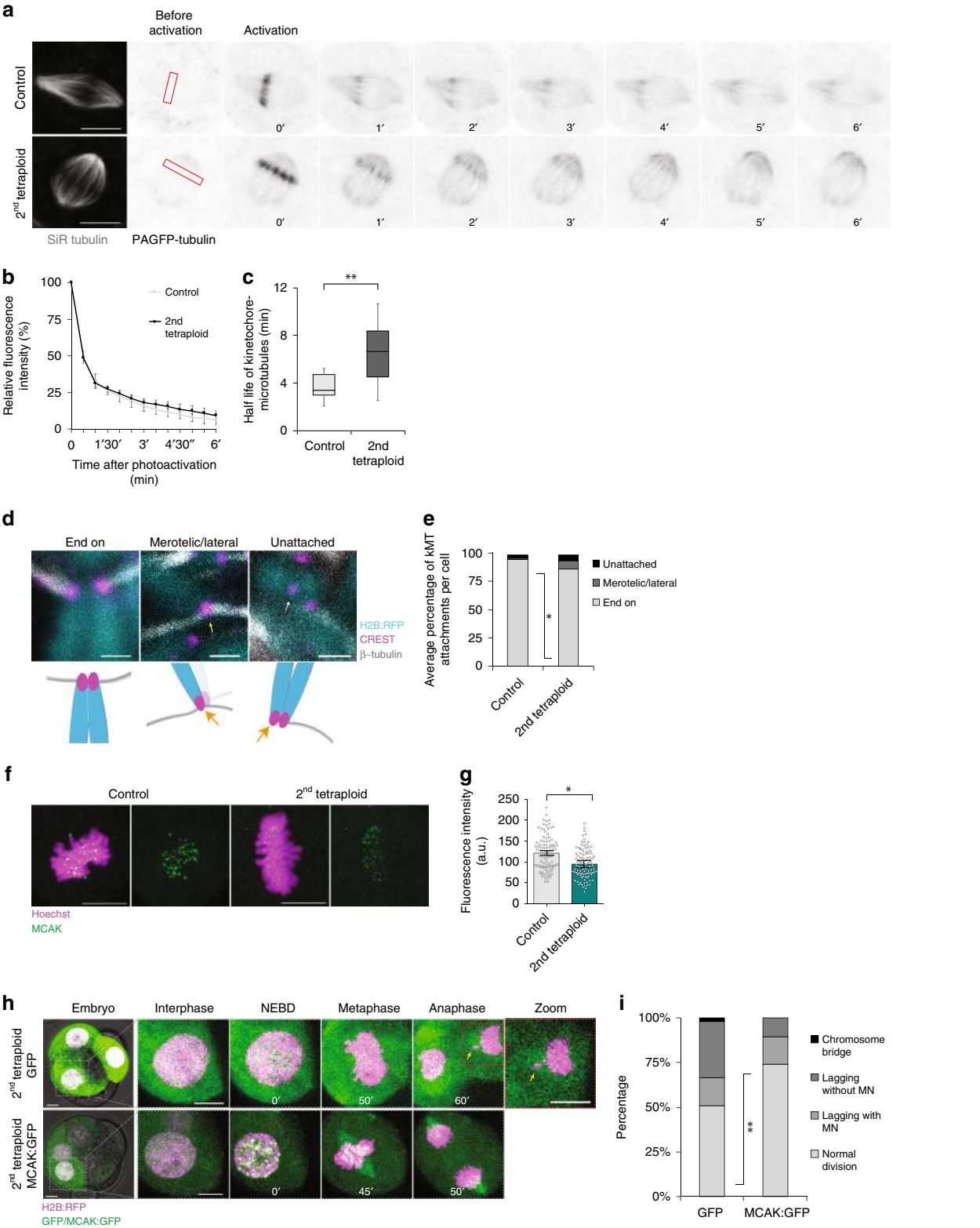

Imaging analysis and statistics. All image processing and analysis was performed using ImageJ/Fiji[61]. No thresholding or masking was applied to the images and LUT brightness varies linearly. For centromere tracking in Fig. 4a, b, manual tracking was performed using the "Manual Tracking with TrackMate" feature of TrackMate plugin[62] on Fiji. For metaphase plate width measurements in Fig. 4c, d, the distance between two lines drawn across each side of the metaphase plate was measured. The lines were drawn based on the MajSatTALE:mClover fluorescent signal and delimited the area occupied by all aligned chromosomes. Three dimensional reconstructions (Supplementary Fig. 5b; Supplementary Movies 1–3) and surface rendering (Supplementary Fig. 5b and Supplementary Movie 3) were generated using IMARIS 9.3. For MCAK fluorescence intensity analysis in Fig. 5f, g, background-subtracted fluorescence intensity values were obtained from a total of 100 kinetochores analysed from 10 embryos (10 kinetochores per embryo) for each group and statistical analysis was performed as an inter-embryo comparison using the average fluorescence intensity per embryo. All measurements analysed in this study were taken from distinct samples and samples were not measured repeatedly. Data were analysed using GraphPad Prism 7 software (GraphPad Software, La Jolla, CA, USA, www.graphpad.com). Shapiro–Wilk normality tests were applied where appropriate and either unpaired two-tailed *t* tests or two-tailed Mann–Whitney tests were applied. Statistical significance was considered when $P < 0.05$.

Fig. 5 Error correction mechanisms are defective in tetraploid embryos. **a** PAGFP-tubulin (inverted grey) was photoactivated at a rectangular region across one side of the metaphase spindle (red rectangles) and the time-course for fluorescence decay was monitored. Embryos were labelled with SiR Tubulin (grey) to identify the metaphase spindle. **b** and **c** Quantification of fluorescence decay values **b** and kinetochore–microtubule half-life (**c**; $^{**}P = 0.008$, unpaired, two-tailed *t* test) in 16-cell control ($n = 11$ blastomeres) and 8-cell tetraploid embryos ($n = 9$ blastomeres). In the box plot, the centre line represents median, the bounds of box represent upper and lower quartiles and the whiskers represent minimum and maximum values. **d** Representative z-projections of end-on, merotelic/lateral, and unattached kinetochores at 35 min after nuclear envelope breakdown (NEBD); and scheme illustrating the types of kinetochore–microtubule attachments analysed. Representative images were chosen to demonstrate the different types of attachments. For the merotelic/lateral attachment image, only the merotelically attached kinetochore is in focus (as represented in the illustration by a fainter colour of the sister chromatid). **e** Average percentage of end-on, merotelic/lateral and unattached kinetochores per cell in 16-cell ($n = 189$ kinetochores from five blastomeres) control and 8-cell tetraploid embryos ($n = 223$ kinetochores from five blastomeres; $^{*}P = 0.0148$, unpaired, two-tailed *t* test). **f** Representative z-projections of MCAK immunofluorescence in 16-cell control and 8-cell tetraploid embryos. **g** Quantification of fluorescence intensity in 16-cell control and 8-cell tetraploid embryos ($n = 100$ kinetochores from 10 blastomeres per group). Statistical analysis was performed as an inter-embryo comparison using the average from 10 individual kinetochores analysed per blastomere, $^{*}P = 0.0223$ (unpaired, two-tailed *t* test). **h** Representative time-lapse images of 8-cell tetraploid embryos co-expressing H2B:RFP and either GFP or MCAK:GFP. The yellow arrow indicates a lagging chromosome. **i** Percentage of cell divisions displaying chromosome segregation errors in 8-cell tetraploid embryos co-expressing H2B:RFP and either GFP ($n = 51$ divisions from 16 embryos) or MCAK:GFP ($n = 66$ divisions from 23 embryos) $^{**}P = 0.0093$ (two-tailed chi-square). Chromosome segregation errors observed included: lagging chromosomes resulting in micronuclei formation (lagging with MN); lagging chromosomes that did not result in micronuclei formation (lagging without MN); and chromosome bridges. Scale bars = 10 μm, except for **d**, where scale bars = 1 μm. Error bars represent SEM

Reporting summary. Further information on research design is available in the Nature Research Reporting Summary linked to this article.

Data availability

The data related to the findings of this study are available within the manuscript and Supplementary Information, or from the corresponding author upon request. The source data underlying Figs. 1c, e, g, 2c, 3a, b, d, e, 4b, d, f, g, h, 5c, e, g, i, Supplementary Figs. 1b, d, 2a, b, e, 3b, 4a, b, 5c, d, 5e, f, h, 6a–d, 8a, b, d, e, g, h are provided as a Source Data file.

Received: 1 February 2019; Accepted: 20 September 2019;
Published online: 23 October 2019

References

1. Compton, D. A. Spindle assembly in animal cells. *Annu. Rev. Biochem.* **69**, 95–114 (2000).
2. Heald, R. & Khodjakov, A. Thirty years of search and capture: the complex simplicity of mitotic spindle assembly. *J. Cell Biol.* **211**, 1103–1111 (2015).
3. Barr, F. A. & Gruneberg, U. Cytokinesis: placing and making the final cut. *Cell* **131**, 847–860 (2007).
4. Green, R. A., Paluch, E. & Oegema, K. Cytokinesis in animal cells. *Annu. Rev. Cell Dev. Biol.* **28**, 29–58 (2012).
5. Storchova, Z. & Kuffer, C. The consequences of tetraploidy and aneuploidy. *J. Cell Sci.* **121**, 3859–3866 (2008).
6. Storchova, Z. & Pellman, D. From polyploidy to aneuploidy, genome instability and cancer. *Nat. Rev. Mol. Cell Biol.* **5**, 45–54 (2004).
7. Fujiwara, T. et al. Cytokinesis failure generating tetraploids promotes tumorigenesis in p53-null cells. *Nature* **437**, 1043–1047 (2005).
8. Galipeau, P. C. et al. 17p (p53) allelic losses, 4N (G2/tetraploid) populations, and progression to aneuploidy in Barrett's esophagus. *Proc. Natl Acad. Sci. USA* **93**, 7081–7084 (1996).
9. Ganem, N. J., Godinho, S. A. & Pellman, D. A mechanism linking extra centrosomes to chromosomal instability. *Nature* **460**, 278–282 (2009).
10. Pfau, S. J. & Amon, A. Chromosomal instability and aneuploidy in cancer: from yeast to man. *EMBO Rep.* **13**, 515–527 (2012).
11. Silkworth, W. T., Nardi, I. K., Scholl, L. M. & Cimini, D. Multipolar spindle pole coalescence is a major source of kinetochore mis-attachment and chromosome mis-segregation in cancer cells. *PLoS ONE* **4**, e6564 (2009).
12. Quintyne, N. J., Reing, J. E., Hoffelder, D. R., Gollin, S. M. & Saunders, W. S. Spindle multipolarity is prevented by centrosomal clustering. *Science* **307**, 127–129 (2005).
13. Kwon, M. et al. Mechanisms to suppress multipolar divisions in cancer cells with extra centrosomes. *Genes Dev.* **22**, 2189–2203 (2008).
14. Delattre, M. & Gonczy, P. The arithmetic of centrosome biogenesis. *J. Cell Sci.* **117**, 1619–1630 (2004).
15. Howe, K. & FitzHarris, G. A non-canonical mode of microtubule organization operates throughout pre-implantation development in mouse. *Cell Cycle* **12**, 1616–1624 (2013).
16. Gueth-Hallonet, C. et al. Gamma-tubulin is present in acentriolar MTOCs during early mouse development. *J. Cell Sci.* **105**, 157–166 (1993).
17. Palacios, M. J., Joshi, H. C., Simerly, C. & Schatten, G. Gamma-tubulin reorganization during mouse fertilization and early development. *J. Cell Sci.* **104**, 383–389 (1993).
18. Andreassen, P. R., Lohez, O. D., Lacroix, F. B. & Margolis, R. L. Tetraploid state induces p53-dependent arrest of nontransformed mammalian cells in G1. *Mol. Biol. Cell* **12**, 1315–1328 (2001).
19. Ganem, N. J. et al. Cytokinesis failure triggers hippo tumor suppressor pathway activation. *Cell* **158**, 833–848 (2014).
20. Ueda, J. et al. Heterochromatin dynamics during the differentiation process revealed by the DNA methylation reporter mouse, MethylRO. *Stem Cell Rep.* **2**, 910–924 (2014).
21. Horii, T. et al. p53 suppresses tetraploid development in mice. *Sci. Rep.* **5**, 8907 (2015).
22. Eakin, G. S. & Behringer, R. R. Tetraploid development in the mouse. *Dev. Dyn.* **228**, 751–766 (2003).
23. Eakin, G. S., Hadjantonakis, A. K., Papaioannou, V. E. & Behringer, R. R. Developmental potential and behavior of tetraploid cells in the mouse embryo. *Dev. Biol.* **288**, 150–159 (2005).
24. Mogessie, B. & Schuh, M. Actin protects mammalian eggs against chromosome segregation errors. *Science* **357**, https://doi.org/10.1126/science.aal1647 (2017).
25. Vazquez-Diez, C., Yamagata, K., Trivedi, S., Haverfield, J. & FitzHarris, G. Micronucleus formation causes perpetual unilateral chromosome inheritance in mouse embryos. *Proc. Natl Acad. Sci. USA* **113**, 626–631 (2016).
26. Courtois, A., Schuh, M., Ellenberg, J. & Hiiragi, T. The transition from meiotic to mitotic spindle assembly is gradual during early mammalian development. *J. Cell Biol.* **198**, 357–370 (2012).
27. Fong, K. W., Choi, Y. K., Rattner, J. B. & Qi, R. Z. CDK5RAP2 is a pericentriolar protein that functions in centrosomal attachment of the gamma-tubulin ring complex. *Mol. Biol. Cell* **19**, 115–125 (2008).
28. Balboula, A. Z. et al. Haspin kinase regulates microtubule-organizing center clustering and stability through Aurora kinase C in mouse oocytes. *J. Cell Sci.* **129**, 3648–3660 (2016).
29. Lukinavicius, G. et al. Fluorogenic probes for live-cell imaging of the cytoskeleton. *Nat. Methods* **11**, 731–733 (2014).
30. Dumont, J. et al. Formin-2 is required for spindle migration and for the late steps of cytokinesis in mouse oocytes. *Dev. Biol.* **301**, 254–265 (2007).
31. Gatlin, J. C. et al. Spindle fusion requires dynein-mediated sliding of oppositely oriented microtubules. *Curr. Biol.* **19**, 287–296 (2009).
32. Reichmann, J. et al. Dual-spindle formation in zygotes keeps parental genomes apart in early mammalian embryos. *Science* **361**, 189–193 (2018).
33. Lara-Gonzalez, P., Westhorpe, F. G. & Taylor, S. S. The spindle assembly checkpoint. *Curr. Biol.* **22**, R966–R980 (2012).
34. Musacchio, A. The molecular biology of spindle assembly checkpoint signaling dynamics. *Curr. Biol.* **25**, R1002–R1018 (2015).
35. Bolton, H. et al. Mouse model of chromosome mosaicism reveals lineage-specific depletion of aneuploid cells and normal developmental potential. *Nat. Commun.* **7**, 11165 (2016).
36. Vazquez-Diez, C., Paim, L. M. G. & FitzHarris, G. Cell-size-independent spindle checkpoint failure underlies chromosome segregation error in mouse embryos. *Curr. Biol.* **29**, 865–873 e863 (2019).
37. Wei, Y. et al. Spindle assembly checkpoint regulates mitotic cell cycle progression during preimplantation embryo development. *PLoS ONE* **6**, e21557 (2011).

38. Miyanari, Y., Ziegler-Birling, C. & Torres-Padilla, M. E. Live visualization of chromatin dynamics with fluorescent TALEs. *Nat. Struct. Mol. Biol.* **20**, 1321–1324 (2013).
39. Cimini, D. et al. Merotelic kinetochore orientation is a major mechanism of aneuploidy in mitotic mammalian tissue cells. *J. Cell Biol.* **153**, 517–527 (2001).
40. Thompson, S. L. & Compton, D. A. Examining the link between chromosomal instability and aneuploidy in human cells. *J. Cell Biol.* **180**, 665–672 (2008).
41. Lampson, M. A. & Grishchuk, E. L. Mechanisms to avoid and correct erroneous kinetochore-microtubule attachments. *Biology* **6**, https://doi.org/10.3390/biology6010001 (2017).
42. Salmon, E. D., Cimini, D., Cameron, L. A. & DeLuca, J. G. Merotelic kinetochores in mammalian tissue cells. *Philos. Trans. R. Soc. Lond. B Biol. Sci.* **360**, 553–568 (2005).
43. Bakhoum, S. F., Genovese, G. & Compton, D. A. Deviant kinetochore microtubule dynamics underlie chromosomal instability. *Curr. Biol.* **19**, 1937–1942 (2009).
44. Zhai, Y., Kronebusch, P. J. & Borisy, G. G. Kinetochore microtubule dynamics and the metaphase–anaphase transition. *J. Cell Biol.* **131**, 721–734 (1995).
45. Fitzharris, G. A shift from kinesin 5-dependent metaphase spindle function during preimplantation development in mouse. *Development* **136**, 2111–2119 (2009).
46. Kline-Smith, S. L., Khodjakov, A., Hergert, P. & Walczak, C. E. Depletion of centromeric MCAK leads to chromosome congression and segregation defects due to improper kinetochore attachments. *Mol. Biol. Cell* **15**, 1146–1159 (2004).
47. Wordeman, L., Wagenbach, M. & von Dassow, G. MCAK facilitates chromosome movement by promoting kinetochore microtubule turnover. *J. Cell Biol.* **179**, 869–879 (2007).
48. Bakhoum, S. F., Thompson, S. L., Manning, A. L. & Compton, D. A. Genome stability is ensured by temporal control of kinetochore-microtubule dynamics. *Nat. Cell Biol.* **11**, 27–35 (2009).
49. Storchova, Z. et al. Genome-wide genetic analysis of polyploidy in yeast. *Nature* **443**, 541–547 (2006).
50. Stingele, S. et al. Global analysis of genome, transcriptome and proteome reveals the response to aneuploidy in human cells. *Mol. Syst. Biol.* **8**, 608 (2012).
51. Andrews, P. D. et al. Aurora B regulates MCAK at the mitotic centromere. *Dev. Cell* **6**, 253–268 (2004).
52. Lan, W. et al. Aurora B phosphorylates centromeric MCAK and regulates its localization and microtubule depolymerization activity. *Curr. Biol.* **14**, 273–286 (2004).
53. Zhang, C. Z. et al. Chromothripsis from DNA damage in micronuclei. *Nature* **522**, 179–184 (2015).
54. Davoli, T. & de Lange, T. The causes and consequences of polyploidy in normal development and cancer. *Annu. Rev. Cell Dev. Biol.* **27**, 585–610 (2011).
55. Baudoin, N. C. et al. Asymmetric clustering of centrosomes defines the early evolution of tetraploid cells. Prepint at https://www.biorxiv.org/content/10.1101/526731v1, https://doi.org/10.1101/526731 (2019).
56. Tarkowski, A. K. An air-drying method for chromosome preparations from mouse eggs. *Cytogenetics* **5**, 394–400 (1966).
57. FitzHarris, G. Anaphase B precedes anaphase A in the mouse egg. *Curr. Biol.* **22**, 437–444 (2012).
58. Vazquez-Diez, C. & FitzHarris, G. Correlative live imaging and immunofluorescence for analysis of chromosome segregation in mouse preimplantation embryos. *Methods Mol. Biol.* **1769**, 319–335 (2018).
59. Zhang, Q. H. et al. Cyclin A2 modulates kinetochore-microtubule attachment in meiosis II. *J. Cell Biol.* **216**, 3133–3143 (2017).
60. Cimini, D., Wan, X., Hirel, C. B. & Salmon, E. D. Aurora kinase promotes turnover of kinetochore microtubules to reduce chromosome segregation errors. *Curr. Biol.* **16**, 1711–1718 (2006).
61. Schindelin, J. et al. Fiji: an open-source platform for biological-image analysis. *Nat. Methods* **9**, 676–682 (2012).
62. Tinevez, J. Y. et al. TrackMate: an open and extensible platform for single-particle tracking. *Methods* **115**, 80–90 (2017).

Acknowledgements

Work funded by grants from the Natural Sciences and Engineering Research Council of Canada, Fondation Jean-Louis Lévesque, Canadian Foundation for Innovation and the Canadian Institutes of Health Research. LMGP is supported by a Fonds de Recherche du Québec—Santé Doctoral Scholarship. We thank Gilles Hickson, Jean-Claude Labbé, and Aleksandar Mihajlović for comments on the manuscript, Gaudeline Rémillard-Labrosse and Aurélie Cleret-Buhot for excellent technical support.

Author contributions

L.M.G.P. and G.F. conceptualised the study. L.M.G.P. performed the experiments and analysed the data. L.M.G.P. and G.F. wrote the manuscript.

Competing interests

The authors declare no competing interests.

Additional information

Supplementary information is available for this paper at https://doi.org/10.1038/s41467-019-12772-8.

Correspondence and requests for materials should be addressed to G.F.

Reprints and permission information is available at http://www.nature.com/reprints

Peer review Information *Nature Communications* thanks the anonymous reviewers for their contribution to the peer review of this work. Peer reviewer reports are available.

Publisher's note Springer Nature remains neutral with regard to jurisdictional claims in published maps and institutional affiliations.

Tetraploidy causes chromosomal instability in acentriolar mouse embryos

Paim and FitzHarris

Supplementary Figures

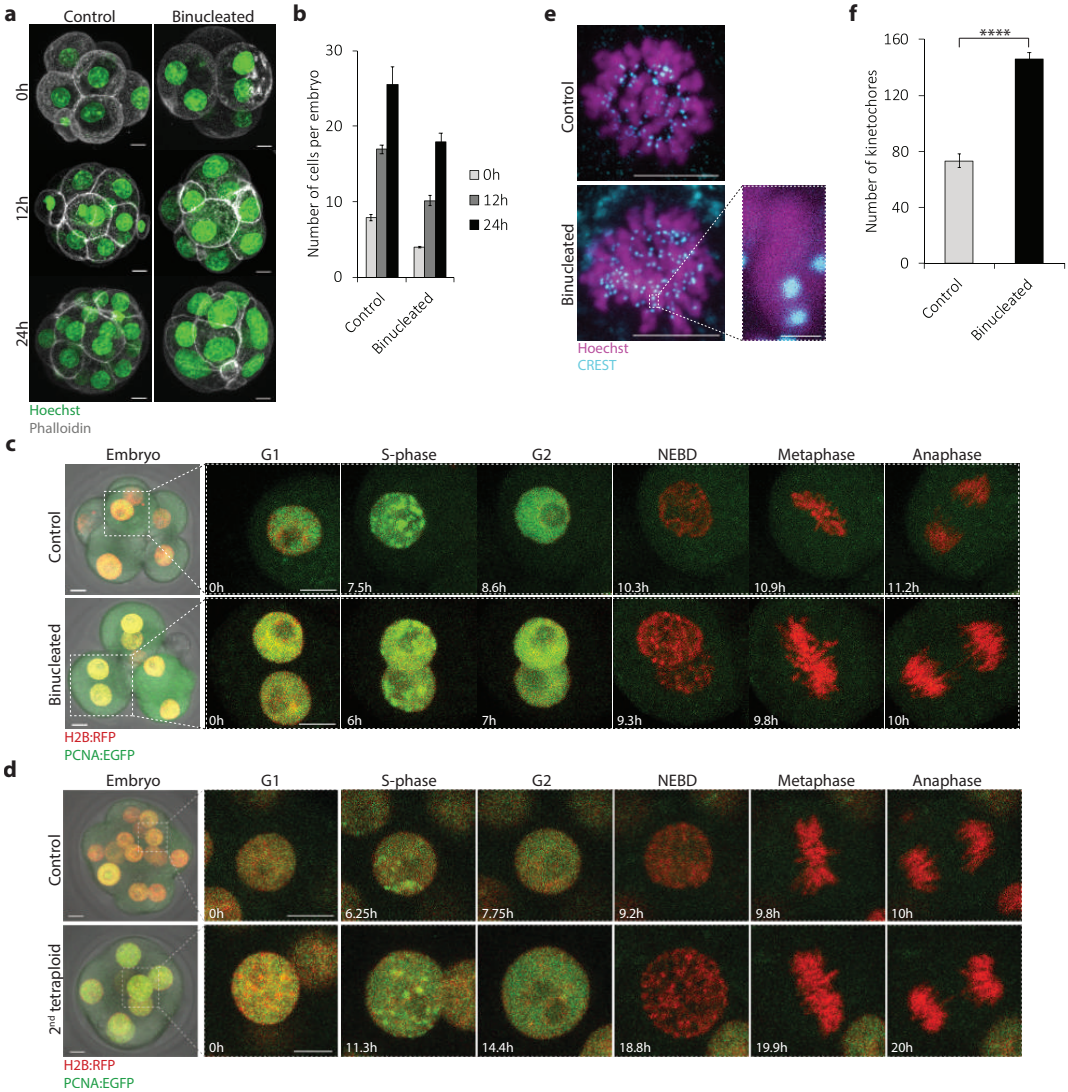

Supplementary Figure 1. The mouse embryo lacks a tetraploidy checkpoint. (a) Representative z-projections of embryos fixed 0h, 12h and 24h after exposure to either Latrunculin B (Binucleated) or DMSO (Control). **(b)** Quantification of number of cells per embryo 0h, 12h, and 24h after exposure to either DMSO (0h n=34 embryos; 12h n=31 embryos; 24h n=21 embryos) or Latrunculin B (0h n=27 embryos; 12h n=21 embryos; 24h n=23 embryos). **(c and d)** Representative z-projections of 8-cell control, 4-cell binucleated **(c)**, 16-cell control and 8-cell tetraploid embryos **(d)** expressing H2B:RFP (red) and PCNA:EGFP (green). Note that S-phase can be identified by the accumulation of PCNA foci at the nucleus demarking DNA replication. **(e)** Representative z-projections of metaphase-arrested controls and binucleated embryos. Note that treatment with Monastrol induces monopolar spindle formation, allowing for the better visualisation of individual kinetochores. **(f)** Quantification of number of kinetochores per cell in 8-cell control (n=5 blastomeres) and 4-cell binucleated embryos (n=8 blastomeres) ****P<0.0001 (unpaired, two-tailed t test). Note that this approach allows for an approximation of kinetochore numbers (close to 80 kinetochores in controls and close to 160 kinetochores in tetraploids). Scale bars = 10μm, except for the chromosome zoom in (**e**), where scale bar = 1μm. Error bars represent SEM. NEBD=nuclear envelope breakdown.

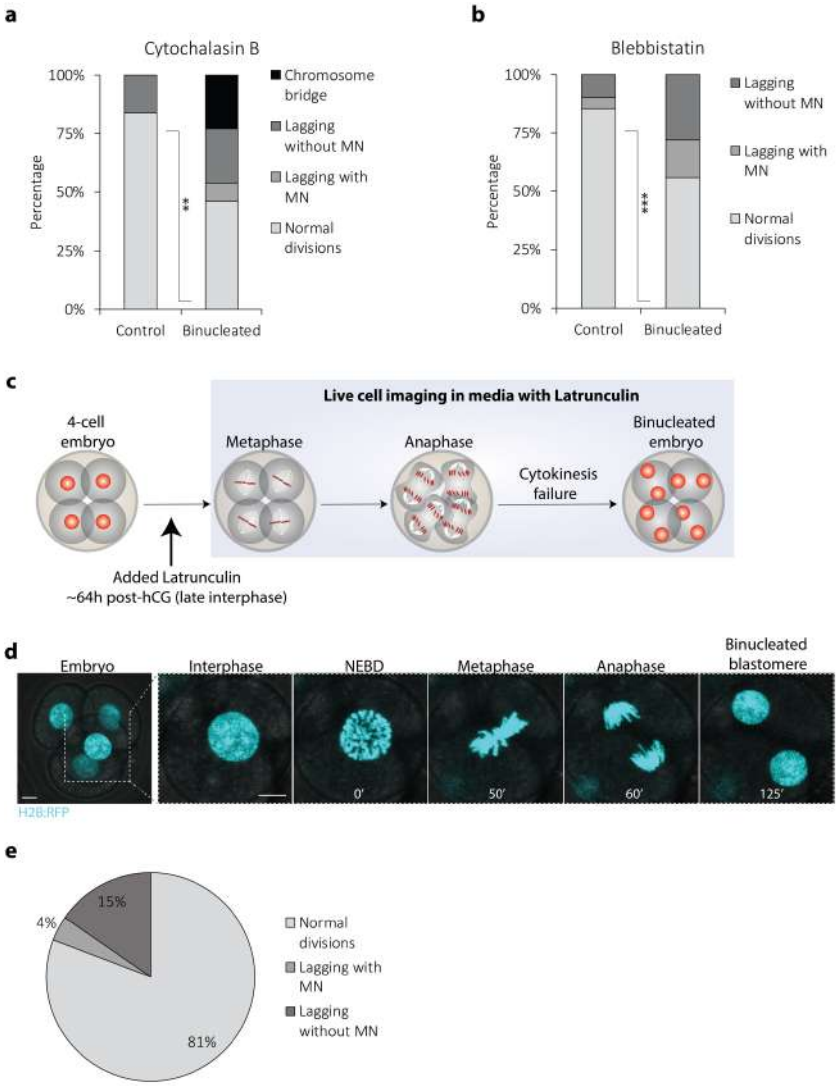

Supplementary Figure 2. The chromosome segregation errors observed after Latrunculin-induced binucleation are phenocopied by Cytochalasin B and Blebbistatin. (a and b) Percentage of chromosome segregation errors in 8-cell control and 4-cell binucleated embryos produced with either Cytochalasin B (control n= 62 divisions from 15 embryos; binucleated n=13 divisions from 7 embryos; ***P*=0.0072, unpaired, two-tailed Fisher's exact test) or Blebbistatin treatment (control n=90 divisions from 14 embryos; binucleated n=43 divisions from 16 embryos; ****P*=0.0004, unpaired, two-tailed Fisher's exact test). **(c)** Scheme illustrating the experimental design applied to assess the effects of actin depolymerization on chromosome segregation dynamics. 4-cell stage embryos at late interphase were live imaged in the presence of Latrunculin and the rate of chromosome segregation errors was assessed. **(d)** Representative z-projections of H2B:RFP-expressing 4-cell stage embryos live imaged in media containing Latrunculin B. **(e)** Percentage of chromosome segregation errors in 4-cell embryos imaged in media containing Latrunculin (n=26 divisions from 9 embryos). Chromosome segregation errors observed included: lagging chromosomes resulting in micronuclei formation (lagging with MN); lagging chromosomes that did not result in micronuclei formation (lagging without MN); and chromosome bridges. Scale bars = 10µm. NEBD=nuclear envelope breakdown.

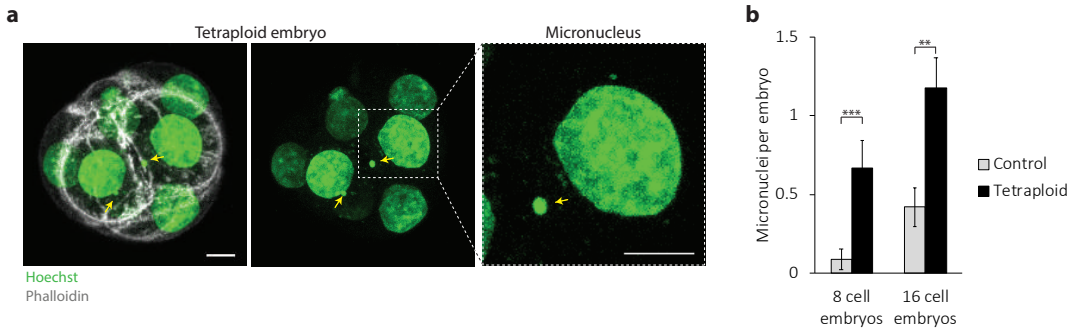

Supplementary Figure 3. Tetraploid embryos display high rates of micronuclei. (a) Representative z-projection of an 8-cell tetraploid embryo with two micronuclei (yellow arrows). **(b)** Rates of micronuclei per embryo in 8-cell controls (n=34 embryos), 8-cell tetraploid (n=21 embryos, ****P*=0.0006, unpaired, two-tailed t test), 16-cell controls (n=31 embryos) and 16-cell tetraploid embryos (n=23 embryos, ***P*=0.0011, unpaired, two-tailed t test). Scale bars = 10μm. Error bars represent SEM.

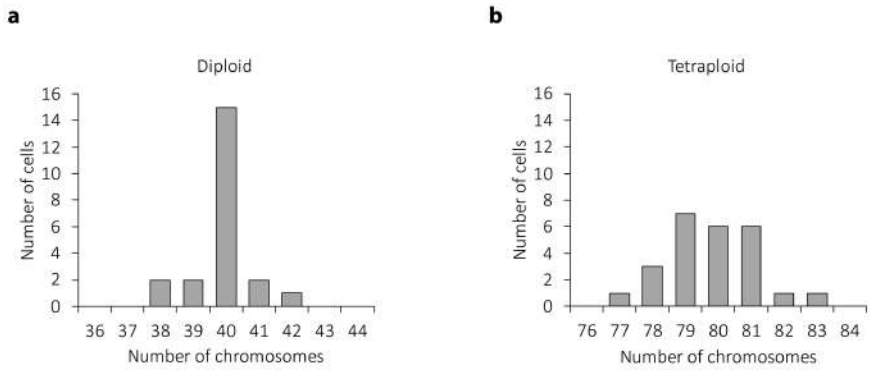

Supplementary Figure 4. Tetraploidy causes high levels of aneuploidy. (a) Histogram demonstrating the distribution of ploidy status in diploid blastomeres (n = 22 spreads). **(b)** Histogram demonstrating the distribution of ploidy status in tetraploid blastomeres (n= 25 spreads).

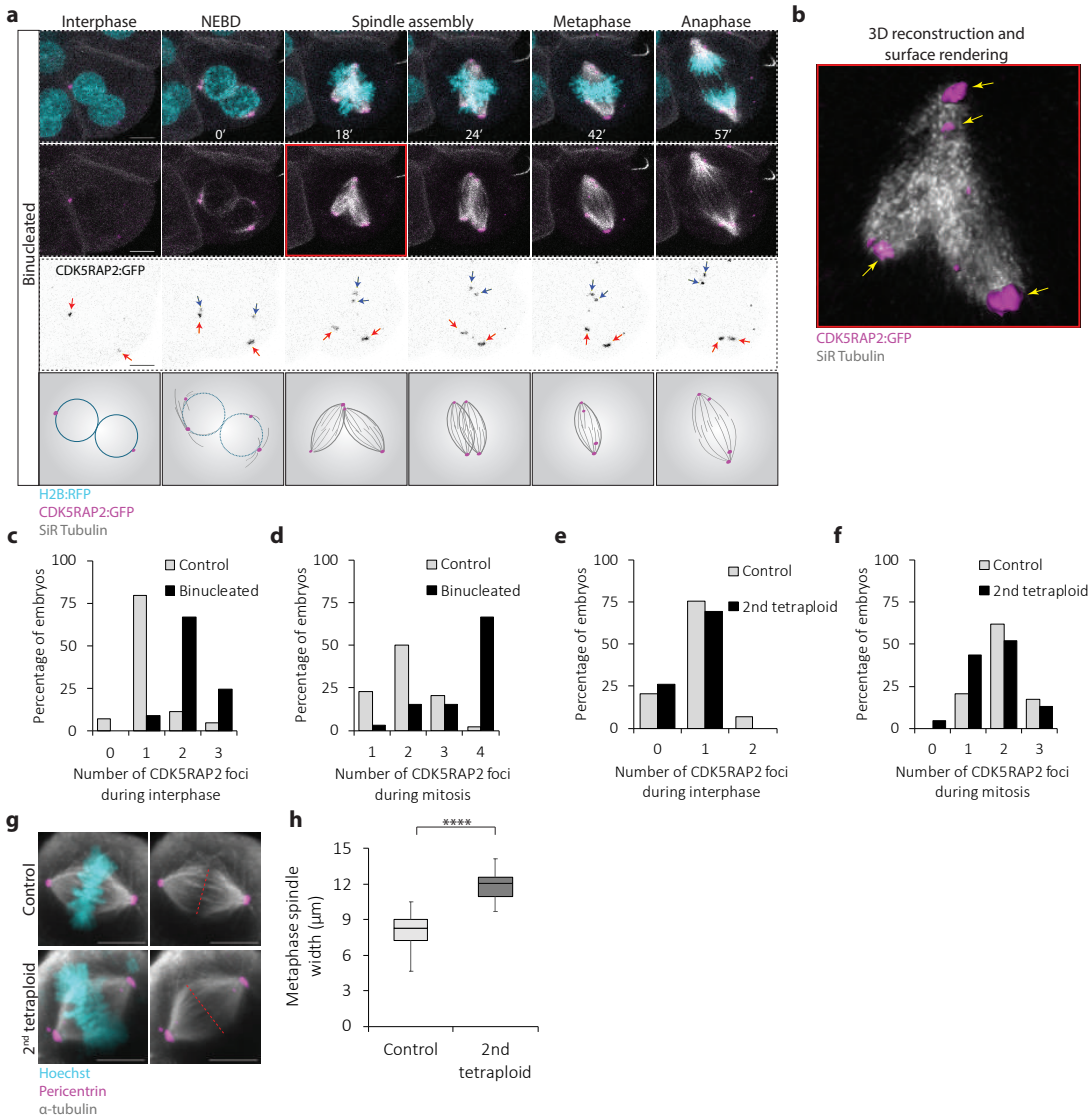

Supplementary Figure 5. Spindle assembly and MTOC dynamics in tetraploid embryos. (a) Representative z-projection and illustrations of a 4-cell binucleated embryo stained with SiR Tubulin (grey) and co-expressing H2B:RFP (cyan) and CDK5RAP2:GFP (magenta and inverted grey) chosen to illustrate an example of perpendicular spindle fusion. Two major microtubule organising centres (MTOCs) (red arrows) can be observed during interphase and two newly assembled MTOCs (blue arrows) can be observed during mitosis. **(b)** Three-dimensional reconstruction of the spindle fusion event in panel **(a)** (red square), with a surface rendering representation of spindle poles (magenta). Note the presence of four completely individualised spindle poles (yellow arrows), demarking the presence of two independent spindles during fusion. **(c and d)** Quantification of number of CDK5RAP2 foci during interphase **(c)** and mitosis **(d)** in 8-cell control (n=44 divisions from 11 embryos) and 4-cell binucleated embryos (n=33 divisions from 14 embryos). **(e and f)** Quantification of number of CDK5RAP2 foci during interphase **(e)** and mitosis **(f)** in 16-cell control (n=29 divisions from 9 embryos) and 8-cell tetraploid embryos (n=24 divisions from 9 embryos). **(g)** Representative immunofluorescence z-projections of a metaphase spindle of 16-cell control and 8-cell tetraploid embryo. **(h)** Quantification of metaphase spindle width in 16-cell controls (n= 31 spindles from 15 embryos) and 8-cell tetraploid embryos (n= 27 spindles from 14 embryos) ****P<0.0001 (unpaired, two-tailed t test). Scale bars = 10μm. Where box plots are shown, the centre line represents the median, the bounds of box represent the upper and lower quartiles and the whiskers represent minimum and maximum values. NEBD=nuclear envelope breakdown.

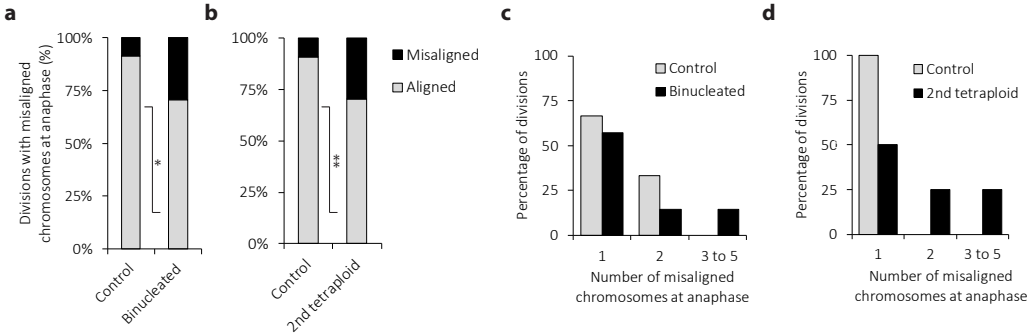

Supplementary Figure 6. High frequency of misaligned chromosomes in tetraploid embryos. (a and b) Percentage of divisions with severely misaligned chromosomes at anaphase onset in 8-cell controls (n= 47 divisions from 7 embryos), 4-cell binucleated embryos (n= 30 divisions from 8 embryos, **P*=0.0412, two-tailed Fisher's exact test) **(a)**, 16-cell controls (n= 66 divisions from 7 embryos) and 8-cell tetraploid embryos (n= 50 divisions from 9 embryos, ***P*=0.0012, two-tailed Fisher's exact test) **(b)**. **(c and d)** Quantification of number of severely misaligned chromosomes visible at anaphase onset per cell division in 8-cell controls, 4-cell binucleated embryos **(c)**; 16-cell controls and 8-cell tetraploid embryos **(d)**.

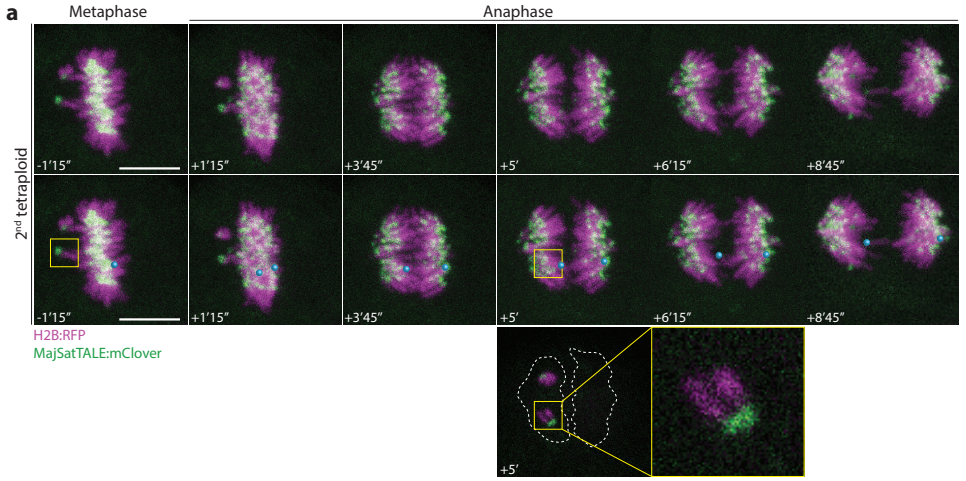

Supplementary Figure 7. Lagging chromosomes arise from fully aligned chromosomes. (a) A time-lapse image of mitosis in an 8-cell tetraploid embryo that exemplifies both anaphase chromosome lagging, and also misalignment at anaphase. Blue circles highlight a sister pair that was aligned at anaphase onset, but which gives rise to a lagging chromosome in anaphase. The yellow box indicates a sister pair that remains misaligned at the time of anaphase onset. The bottom row displays a reduced z-projection to clearly visualise the misaligned chromosome in mid anaphase. Note that both sister chromatids move towards the same spindle pole. Scale bars = 10μm.

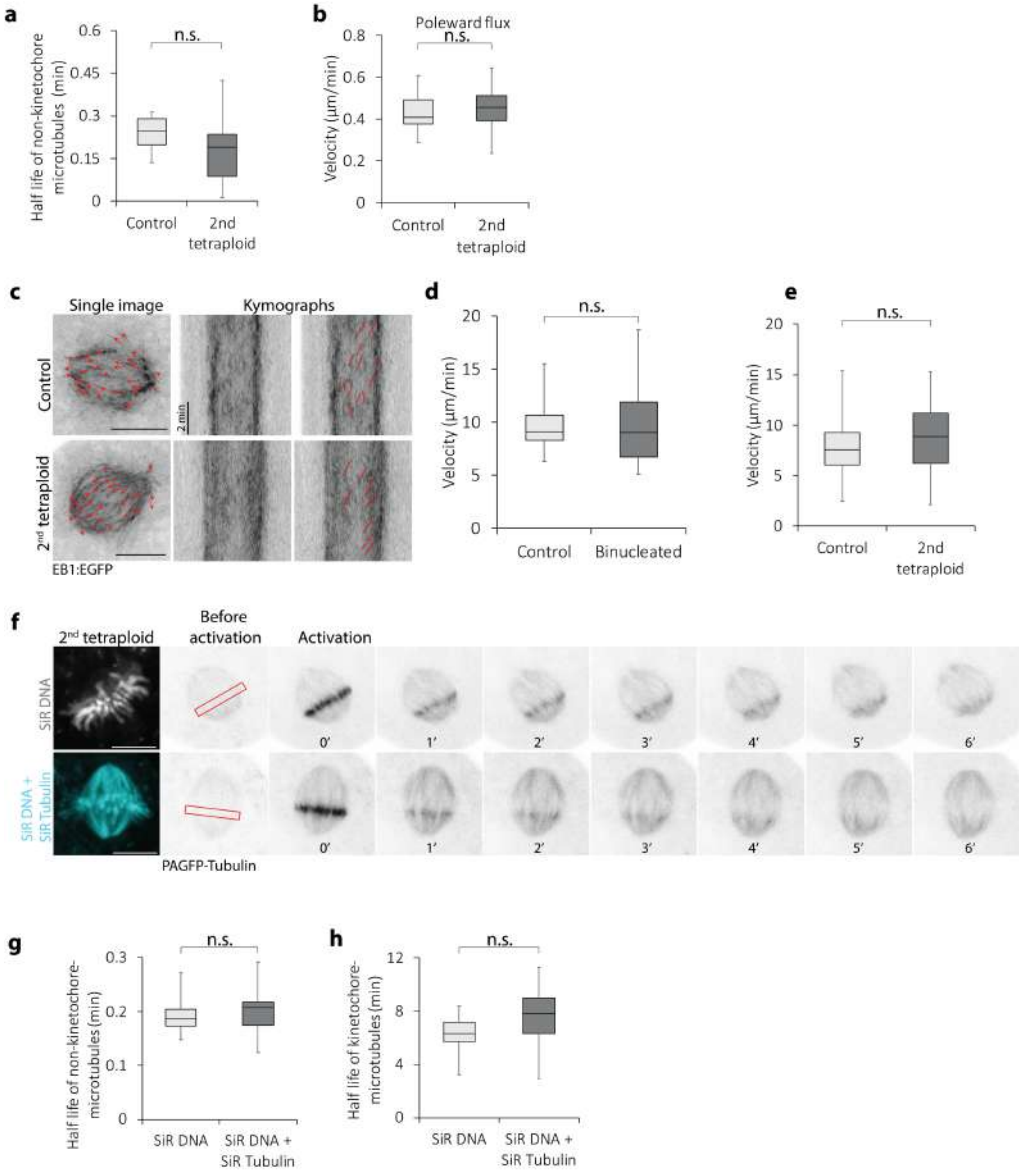

Supplementary Figure 8. Non-kinetochore-microtubule half-life, poleward flux and microtubule growth events are unchanged in tetraploid embryos. (a and b) Quantification of non-kinetochore-microtubule half-life in 16-cell control (n=11 blastomeres) and 8-cell tetraploid embryos (n=9 blastomeres) **(a)** and poleward flux in 16-cell control (n=11 blastomeres) and 8-cell tetraploid embryos (n=10 blastomeres) **(b)** (unpaired, two-tailed t test). **(c)** Representative z-projections and kymographs of control and tetraploid embryos expressing EB1:EGFP. **(d and e)** Quantification of microtubule growth velocity in 8-cell controls (n=36 tracks from 4 embryos), 4-cell binucleated (n=28 tracks from 3 embryos) (unpaired, two-tailed Mann-Whitney test) **(d)**, 16-cell controls (n=76 tracks from 8 embryos) and 8-cell tetraploid embryos (n=58 tracks from 6 embryos) (unpaired, two-tailed t test) **(e)**. **(f)** Representative time-lapse images of PAGFP-tubulin (inverted grey) in 8-cell tetraploid embryos labeled with either SiR DNA (grey) or SiR DNA + SiR Tubulin (cyan). **(g and h)** Quantification of non-kinetochore-microtubule half-life (unpaired, two-tailed Mann-Whitney test) **(g)** and kinetochore-microtubule half-life **(h)** in 8-cell tetraploid embryos labeled with either SiR DNA (n= 10 blastomeres) or SiR DNA + SiR Tubulin (n= 10 blastomeres) (unpaired, two-tailed Mann-Whitney test). Scale bars = 10µm. Where box plots are shown, the centre line represents the median, the bounds of box represent the upper and lower quartiles and the whiskers represent minimum and maximum values.

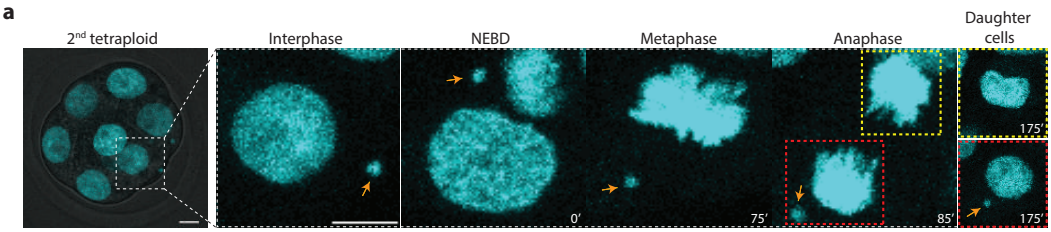

Supplementary Figure 9. Unilateral inheritance of micronuclei in tetraploid embryos. (a) Representative time-lapse images of mitosis in an 8-cell tetraploid embryo. A micronucleus originated from the previous cell division is observed (orange arrows). As anaphase takes place, the micronucleus is inherited by one of the daughter cells (red dashed square) without reincorporation in the principal nucleus, whereas the other daughter cell (yellow dashed square) remains without micronucleus. Note that the micronucleus remained visibly separate from the main chromosome mass throughout the process of cell division. The same unilateral inheritance pattern was observed in all 8 mitoses analysed. Scale bars = 10μm. NEBD=nuclear envelope breakdown.

Annexe 2

The following is the published version of Chapter 3 of this thesis, published in the journal PNAS in 2022.

PNAS RESEARCH ARTICLE | CELL BIOLOGY

Cell size and polarization determine cytokinesis furrow ingression dynamics in mouse embryos

Lia Mara Gomes Paim[a] and Greg FitzHarris[a,b,c,1]

Edited by Janet Rossant, Gairdner Foundation, Toronto, ON, Canada; received October 23, 2021; accepted February 7, 2022

Cytokinesis is the final step of cell division during which a contractile ring forms a furrow that partitions the cytoplasm in two. How furrow ingression is spatiotemporally regulated and how it is adapted to complex cellular environments and developmental transitions remain poorly understood. Here, we examine furrow ingression dynamics in the context of the early mouse embryo and find that cell size is a powerful determinant of furrow ingression speed during reductive cell divisions. In addition, the emergence of cell polarity and the assembly of the apical domain in outer cells locally inhibits the recruitment of cytokinesis components and thereby negatively regulates furrow ingression specifically on one side of the furrow. We show that this biasing of cytokinesis is not dependent upon cell–cell adhesion or shape but rather is cell intrinsic and is caused by a paucity of cytokinetic machinery in the apical domain. The results thus reveal that in the mouse embryo cell polarity directly regulates the recruitment of cytokinetic machinery in a cell-autonomous manner and that subcellular organization can instigate differential force generation and constriction speed in different zones of the cytokinetic furrow.

cytokinesis | cell polarity | embryo development | contractile ring | furrow ingression

Significance

The final step of cell division, termed cytokinesis, comprises the constriction of a furrow that divides the cytoplasm to form two daughter cells. Although cytokinesis is well studied in traditional cell systems, how cytokinesis is regulated in complex multicellular settings and during cell-fate decisions is less well understood. Here, using live imaging and physical and molecular interventions, we find that the emergence of cell polarity during mouse embryo morphogenesis dramatically impacts cytokinesis mechanisms. Specifically, the assembly of the apical domain in outer cells locally inhibits the cytokinetic machinery, leading to an unexpected laterally biased cytokinesis.

Cytokinesis is the final step of cell division, a multistep process initiated by signaling from the anaphase spindle midzone that induces the assembly and constriction of an actomyosin ring responsible for partitioning the cytoplasm in two (1, 2). Although many of the molecular players in furrow constriction have been identified, how furrow ingression is spatiotemporally regulated remains poorly understood. Moreover, little is known about how constriction is adapted to different cell contexts.

While many studies of cytokinesis use cultured cells, valuable insights can be gleaned from complex cellular systems. For instance, in epithelia cell–cell adhesion has been shown to mechanically regulate furrow ingression by anchoring the contractile ring to sites of cell adhesion, thereby restricting constriction on the apical side (3–6). Moreover, apical polarity has been proposed to contribute to furrow ingression positioning and dynamics during asymmetric cell divisions (7, 8), though how polarity controls cytokinesis, and how apical polarity and cell adhesion cooperate to regulate furrow ingression, are not well understood. One outstanding question to which complex systems have generated insight is how the contractile ring is organized and whether contractile forces are generated locally or globally throughout the ring. Interestingly, in the reductive cleavages of *Caenorhabditis elegans* embryos, it was found that cell-size reductions cause a progressive decline in contractile ring constriction speed (9–12). Based on this, a model was proposed wherein a greater number of locally regulated contractile units in bigger cells causes larger rings to constrict more rapidly than smaller ones (10). However, whether these observations extend to higher eukaryotes and what regulates furrow ingression dynamics in complex mammalian systems remain underexplored.

Here we address these questions in the niche context of early mouse embryo development, in which progressive cell-size reductions coincide with key morphogenetic events—such as the emergence of cell–cell adhesion patterns, apical polarity establishment, and cell-fate determination. In addition to a strong influence of cell size upon furrow ingression speed, we report that apical polarity limits the recruitment of cytokinesis components specifically on one side of the furrow, which serves as a cell-intrinsic mechanism for generating a laterally based cytokinesis.

Results

An Upper Limit to Cell-Size Scaling of Furrow Ingression in Mouse Embryos. Although many of the molecules essential for the constriction of the actomyosin ring that in turn drives furrow ingression are known, what determines the speed of ring constriction is poorly understood. We set out to perform four-dimensional live cell imaging during

Author affiliations: [a]Centre de Recherche du Centre Hospitalier de l'Université de Montréal, Montréal, QC H2X 0A9, Canada; [b]Département d'Obstétrique-Gynécologie, Université de Montréal, Montréal, QC H3C 3J7, Canada; and [c]Département de Pathologie et Biologie Cellulaire, Université de Montréal, Montréal, QC H3T 1J4, Canada

Author contributions: L.M.G.P. and G.F. designed research; L.M.G.P. performed research; L.M.G.P. and G.F. analyzed data; and L.M.G.P. and G.F. wrote the paper.

The authors declare no competing interest.

This article is a PNAS Direct Submission.

[1]To whom correspondence may be addressed. Email: greg.fitzharris@umontreal.ca.

This article contains supporting information online at http://www.pnas.org/lookup/suppl/doi:10.1073/pnas.2119381119/-/DCSupplemental.

Published March 16, 2022.

the 1–2, 2–4, 4–8, 8–16, 16–32, and 32–64 cell divisions in mouse embryos, using GAP43:GFP plasma membrane labeling to measure the perimeter of the contractile ring during furrowing (Fig. 1 *A* and *B* and see also *SI Appendix*, Fig. S1). The speed at which the cytokinetic furrow constricted ("speed of constriction," expressed as a decrease in furrow perimeter in micrometers per minute) was constant for the majority of the duration of furrow ingression in any given cell, similar to other cells studied (10, 13, 14). We found that constriction speed is similar between the 1–2 and 8–16 cell divisions in mouse embryos (Fig. 1*C*) and, consequently, the duration of cytokinesis (see *Materials and Methods*) decreases between the 1–2 and 8–16 cell divisions (Fig. 1*D*). However, furrowing speed decreased between the 8–16 and 16–32 cell division ($P < 0.05$), with a further nonsignificant decrease in speed observed between the 16–32 and 32–64 cell stages (Fig. 1 *C* and *D*).

To explore whether the differences in furrow ingression speed we observed from the 8–16 cell stage onward might be due to changing cell size, we first set out to artificially reduce cytoplasmic volume using micromanipulation (*SI Appendix*, Fig. S2 *A–I* and see *Materials and Methods*). Although furrowing speed was similar between sham-manipulated controls and blastomeres with reduced cytoplasmic size (~40% reduction by volume) at the 4–8 cell division (sham: 12.22 ± 0.43 μm/min; reduced cytoplasm: 11.78 ± 0.52 μm/min; $P = 0.5222$) (Fig. 1 *E* and *F*), furrowing speed was substantially reduced in blastomeres undergoing the 8–16 cell division with reduced cytoplasmic size (sham: 11.22 ± 0.55 μm/min; reduced cytoplasm: 8.55 ± 0.30 μm/min; $P = 0.0004$) (Fig. 1 *G* and *H*). Notably, the distribution of constriction speeds measured in sham-manipulated controls and blastomeres with reduced cytoplasmic size at the 8–16 cell division followed an inverse correlation with initial perimeter at anaphase onset ($R^2 = 0.4930$; *SI Appendix*, Fig. S2*J*), indicating that cytoplasmic removal impacted furrowing proportional to the amount of cytoplasm removed.

Next, to investigate the impact of increased cell size, we employed an approach we previously developed to increase cell volume while maintaining the correct ploidy and cell division count (15), wherein cytokinesis was blocked at the 2–4 cell stage, and micromanipulation was then employed to remove the additional nucleus, thereby creating an embryo comprising two double-sized four-cell-stage blastomeres (*SI Appendix*, Fig. S3). Analysis of these embryos later in development showed that constriction speed was similar at the 8–16 cell division between sham-manipulated controls (10.63 ± 0.35 μm/min) and double-sized blastomeres (11.52 ± 0.41 μm/min; $P = 0.1118$) (Fig. 1 *I* and *J*), consistent with a lack of impact of cell size upon furrowing speed prior to the 16–32 cell stage. Notably however, at the 16–32 cell division, constriction speed was increased in double-sized blastomeres (7.76 ± 0.25 μm/min) as compared to controls (5.44 ± 0.23 μm/min; $P < 0.0001$; Fig. 1 *K* and *L*). Thus, increasing or decreasing cytoplasmic volume changes furrowing speed accordingly from the 8–16 cell stage onward. Whether this effect is a direct impact of cell size on the cytokinesis machinery, as previously alluded to in *C. elegans* embryos (10, 12) and *Neurospora crassa* (13), or whether cell size impacts constriction speed indirectly by influencing other cellular systems that affect the cytoskeleton remains to be determined. Nonetheless, this series of experiments suggest that cytokinesis furrowing speed is strongly influenced by cell size from the 8–16 cell stage onward.

Apical Polarity Emergence Decreases Outer Cell Constriction Speed Independently of Cell Fate. Early embryonic development is marked not only by lessening cell size but also by well-defined morphogenetic events (Fig. 2*A*). At the 8-cell stage, pulsatile forces generated by the actomyosin cortex coupled with E-cadherin–dependent restriction of contractility away from cell–cell contacts drive the onset of compaction (16, 17). The subsequent cell division gives rise to a 16-cell embryo composed of approximately spherical/cuboidal nonpolarized inner blastomeres, and flatter, polarized outer blastomeres that possess a characteristic apical domain (16, 18–20) (Fig. 2*A*). By the late 16-cell stage, the first cell fate decision is initiated, wherein the transcription factor TEAD4 is expressed in outer cells and induces the expression of the trophectoderm determinant CDX2 exclusively in those cells (16) (Fig. 2*A*). To address whether any of these events might cooperate with cell size to influence furrowing speed in embryos, we first compared furrowing speeds in inner cells and outer cells and found that, both at the 16–32 and 32–64 cell divisions, outer cells had a significantly reduced furrowing speed compared to inner cells (16–32 outer: 5.39 ± 0.15 μm/min; 32–64 outer: 4.71 ± 0.67 μm/min; 16–32 inner: 7.71 ± 0.42 μm/min; 32–64 inner: 6.39 ± 0.24 μm/min; 16–32 $P = 0.0004$; 32–64 $P = 0.0081$) (Fig. 2 *B* and *C*). We wondered whether the slowed furrowing of outer cells might be a result of the different shapes of inner and outer cells, outer cells being predominantly more flattened than inner cells. To test this, we abolished cell adhesion in embryos undergoing the 16–32 cell division using Ca^{+2}-free media (*SI Appendix*, Fig. S4*A*). Importantly, removal of Ca^{+2} from the culture media did not prevent apical polarity establishment, as evidenced by the enrichment of the polarity marker PKCζ in the apical surface of outer cells (*SI Appendix*, Fig. S4 *B* and *C*) and embryos were able to undergo the 16–32C transition (*SI Appendix*, Fig. S4 *D* and *E* and Movie S1), but in the absence of cell–cell adherence all cells adopted a rounded shape. Notably, outer cells still displayed reduced speed of constriction (6.02 ± 0.39 μm/min) as compared to inner cells (7.42 ± 0.27 μm/min; $P = 0.0062$) (Fig. 2 *D* and *E*). Thus, the slower furrowing speed of outer cells relative to inner cells is not due to their flattened shape or cell–cell adhesion but is rather due to an intrinsic property of the cells.

We next wondered whether the emergence of cell polarity and the formation of the apical domain might be responsible for the decrease in speed of constriction of outer cells. To address this, we depleted the apical polarity protein PARD6B using short hairpin RNAs (shRNA). PARD6B shRNA efficiently disrupted apical polarity emergence, as evidenced by the absence of the apical domain marker PKCζ (Fig. 2 *F* and *G*), as previously described (21, 22). Strikingly, following PARD6B depletion, furrowing speed in outer cells increased to a velocity comparable to that of inner cells (7.04 ± 0.23 μm/min vs. 6.65 ± 0.20 μm/min, $P = 0.7127$) (Fig. 2 *H* and *I*), suggesting that the emergence of apical polarity in outer cells negatively impacts furrow dynamics. Formation of the apical domain contributes to cell-fate determination in the early embryo by allowing the transcriptional activation of TEAD4 in outer cells at the 16-cell stage (16, 23). Therefore, to determine whether the impact of the apical domain on furrowing speed might relate to cell fate, we depleted TEAD4 by double-stranded RNA (dsRNA) injections (23) and analyzed the speed of constriction of inner and outer cells at the 16–32 cell division. TEAD4 dsRNA knockdown efficiency was confirmed by the absence of TEAD4 nuclear localization with immunofluorescence (*SI Appendix*, Fig. S5 *A* and *B*), as previously described (23), and its depletion did not prevent apical polarity emergence at the 16-cell stage as evidenced by the enrichment of the polarity marker PKCζ in the apical surface of outer cells (*SI Appendix*, Fig. S5*C*). Notably, outer cells

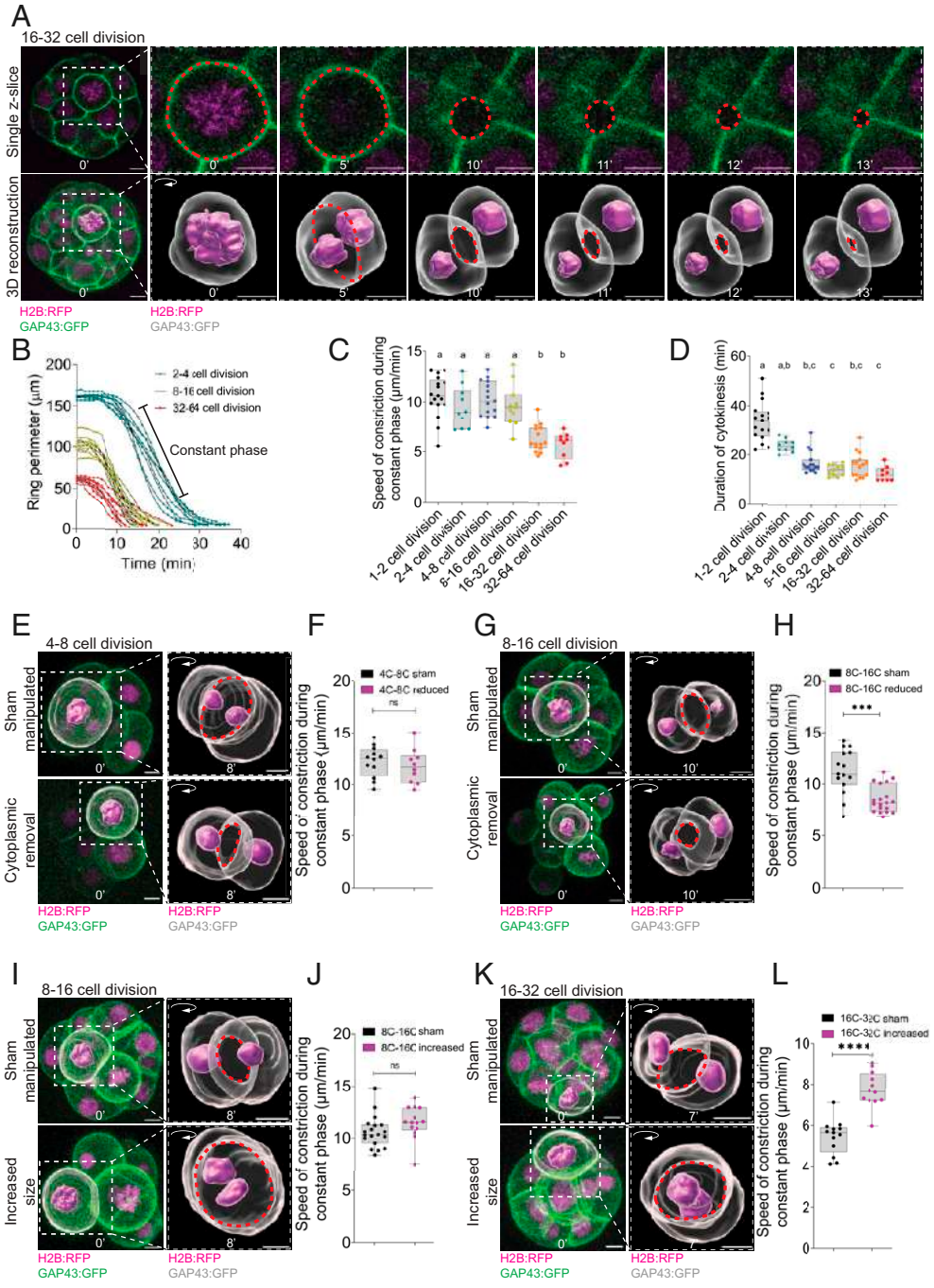

Fig. 1. Cell size determines furrowing speed from the eight-cell stage in mouse embryos. (*A*) Single z-slice (*Top*) and three-dimensional reconstructions (*Bottom*) of a cell undergoing the 16–32 cell division (example shown has 26 cells) coexpressing H2B:RFP (magenta) and GAP43:GFP (green/gray). Red dashed circles indicate where the measurements of contractile ring perimeter were performed. (*B*) Quantification of contractile ring perimeter in blastomeres undergoing the 2–4 (n = 10 blastomeres from 10 embryos), 8–16 (n = 11 blastomeres from 8 embryos), and 32–64 cell divisions (n = 9 blastomeres from eight embryos). Individual curves represent independent blastomeres. (*C* and *D*) Quantification of average speed of ring constriction during the constant phase of perimeter decrease (one-way ANOVA with multiple comparisons) (*C*) and duration of cytokinesis (Kruskal–Wallis with multiple comparisons) (*D*) at the 1–2 (n = 17 blastomeres from 17 embryos), 2–4 (n = 10 blastomeres from 10 embryos), 4–8 (n = 15 blastomeres from 12 embryos), 8–16 (n = 11 blastomeres from 8 embryos), 16–32 (n = 15 blastomeres from 11 embryos), and 32–64 cell divisions (n = 9 blastomeres from eight embryos). (*E* and *G* and see also *SI Appendix*, Fig. S2 *A*–*I*) Representative time-lapse three-dimensional reconstruction of a cell in a sham-manipulated and embryo with reduced cytoplasmic size undergoing the 4–8 (example in sham has seven cells and reduced size has six cells) (*E*) and 8–16 cell divisions (example in sham has 8 cells and reduced size has 13 cells) (*G*) coexpressing H2B:RFP (magenta) and GAP43:GFP (green/gray). (*F* and *H*) Quantification of average speed of constriction at the 4–8 (sham-manipulated n = 12 blastomeres from 11 embryos; cytoplasmic removal n = 10 blastomeres from 9 embryos; two-tailed unpaired t test, P = 0.5222) (*F*) and 8–16 cell divisions (sham-manipulated n = 15 blastomeres from 8 embryos; cytoplasmic removal n = 19 blastomeres from 10 embryos; two-tailed Mann–Whitney U test, ***P = 0.0004) (*H*). (*I* and *K*) Representative time-lapse three-dimensional reconstructions of cells undergoing the 8–16 cell division from sham-manipulated (*Top*; example shown has 12 cells) or embryos with increased cytoplasmic size (*Bottom*; example has six cells) (*I*) and cells undergoing the 16–32 cell division from sham-manipulated (*Top*; example has 18 cells) or embryos with increased cytoplasmic size (*Bottom*; example has 13 cells) (*K*). (*J* and *L*) Quantification of average speed of constriction of blastomeres from sham-manipulated or embryos with increased cytoplasmic size at the 8–16 (sham n = 19 blastomeres from 11 embryos; increased n = 14 blastomeres from 9 embryos; two-tailed unpaired t test nonsignificant (ns) P = 0.1118 (*J*) and outer blastomeres at 16–32 cell divisions (sham n = 13 blastomeres from 7 embryos; increased n = 12 blastomeres from 9 embryos; two-tailed unpaired t test ****P < 0.0001. Time is shown in minutes, where 0′ is anaphase onset. (Scale bars, 10 μm.) In the box plots, the center line represents the median, the bounds of the box represent upper and lower quartiles, the whiskers represent minimum and maximum values, and dots represent independent measurements. In multiple comparison analyses, different letters represent statistical significance at P < 0.05.

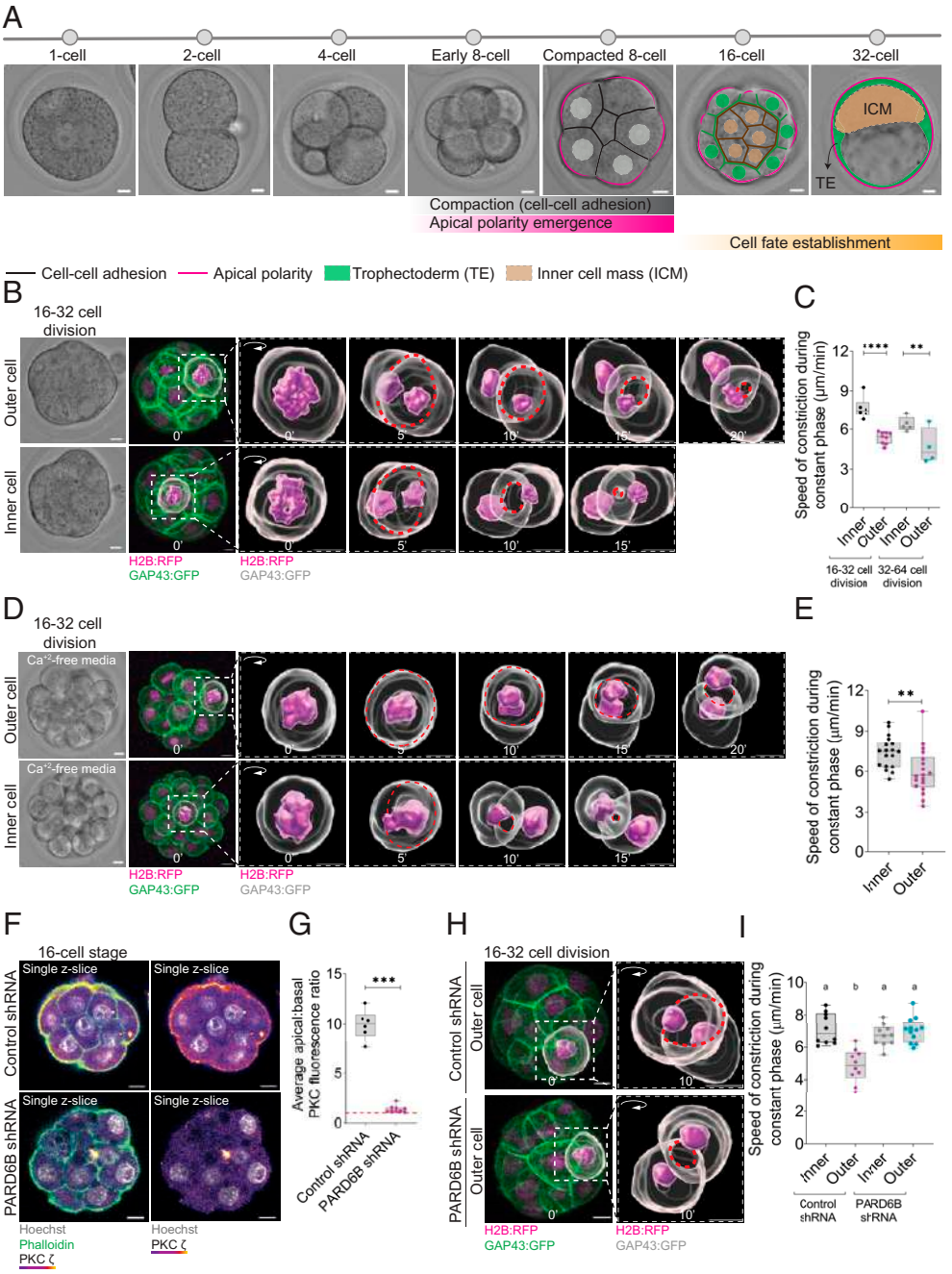

Fig. 2. Apical polarity reduces the speed of constriction of outer cells independently of cell shape and adhesion. (*A*) Illustration of morphogenetic events of mouse preimplantation development. E-cadherin accumulation at the basolateral surface drives compaction at the eight-cell stage, concomitantly with the emergence of apical polarity. The resulting 16-cell embryo displays outer cells that are polarized and flat and inner cells that are cuboidal and apolar and undergoes lineage specification, wherein most outer cells are destined to trophectoderm specification whereas inner cells are directed to the inner cell mass (ICM). (*B*) Representative bright-field and time-lapse three-dimensional (3D) reconstructions of outer and inner cells undergoing the 16–32 cell division (example shown for outer cell has 16 cells and for inner cell has 24 cells) coexpressing H2B:RFP (magenta) and GAP43:GFP (green/gray). (*C*) Quantification of average speed of constriction of inner and outer cells at 16–32 (inner $n = 6$ blastomeres; outer $n = 9$ blastomeres from 11 embryos) and 32–64 cell divisions (inner $n = 5$ blastomeres; outer $n = 4$ blastomeres from eight embryos; one-way ANOVA comparing means of preselected columns, $^{****}P < 0.0001$, $^{**}P = 0.0081$). The data quantified in *C* were obtained from the same embryos in Fig. 1 *B*–*D*. (*D*) Representative bright-field and time-lapse 3D reconstructions of outer and inner cells undergoing the 16–32 cell division (example for outer cell has 21 cells and for inner cell has 30 cells) coexpressing H2B:RFP (magenta) and GAP43:GFP (green/gray) cultured in Ca^{+2}-free media. (*E*) Quantification of average speed of constriction of inner ($n = 18$ blastomeres) and outer blastomeres ($n = 18$ blastomeres from total of 18 embryos; two-tailed unpaired *t* test, $^{**}P = 0.0062$) undergoing the 16–32 cell division from embryos cultured in Ca^{+2}-free media. (*F*) Representative immunofluorescence images of 16-cell embryos previously injected with either control shRNA (*Top*) or PARD6B shRNA (*Bottom*). (*G*) Quantification of average apical:basal PKCζ fluorescence ratio in 16-cell embryos previously injected with either control shRNA ($n = 6$ embryos) or PARD6B shRNA ($n = 9$ embryos; two-tailed Mann–Whitney *U* test, $^{***}P = 0.0004$). (*H*) Representative time-lapse 3D reconstructions of outer blastomeres undergoing the 16–32 cell division from embryos previously injected with control shRNA (*Top*; example has 17 cells) or PARD6B shRNA (*Bottom*; example has 20 cells) and coexpressing H2B:RFP (magenta) and GAP43:GFP (green/gray). (*I*) Quantification of average speed of constriction of inner and outer blastomeres undergoing the 16–32 cell division from embryos previously injected with control shRNA (inner $n = 10$ blastomeres; outer $n = 10$ blastomeres from a total of 12 embryos) or PARD6B shRNA (inner $n = 10$ blastomeres; outer $n = 12$ blastomeres from a total of 10 embryos; one-way ANOVA with multiple comparisons). Time is shown in minutes, where 0′ is anaphase onset. (Scale bars, 10 μm.) In the box plots, the center line represents the median, the bounds of the box represent upper and lower quartiles, the whiskers represent minimum and maximum values, and dots represent independent measurements.

from TEAD4-depleted embryos still displayed reduced speed of constriction (6.98 ± 0.23 μm/min) as compared to inner cells (9.75 ± 0.28 μm/min; $P = 0.0022$), similar to controls (inner: 9.06 ± 0.35 μm/min; outer: 6.47 ± 0.23 μm/min; $P = 0.0010$) (*SI Appendix*, Fig. S5 *D* and *E*). Thus, the emergence of the apical domain lessens furrowing speed in outer cells independently of the downstream impact on cell fate.

Apical Polarity Laterally Biases Furrow Ingression Independently of Cell Adhesion. In 16–32 cell-stage embryos, outer cell divisions are oriented either circumferentially or radially relative to the surface of the embryo (Fig. 3*A*). Circumferential cell divisions generate two new outer-residing cells immediately after cytokinesis completion, whereas radial cell divisions generate one inner-residing and one outer-residing cell (16, 24–26). Importantly, whereas radial divisions typically cause the apical domain to be asymmetrically inherited by the outer cell, circumferential divisions occur such that the contractile ring cuts through the apical domain and causes it to be symmetrically inherited by both daughter cells (Fig. 3*A*) (18). To better gauge the impact of polarity on cytokinesis in outer cells we therefore examined furrow ingression in relation to division orientation. Analysis of circumferential cell divisions demonstrated that the basal side of the furrow ingressed more quickly than the apical side (Fig. 3 *B–D*, *Top*), resulting in a total displacement of 17.37 ± 2.30 μm from the basal side and 8.71 ± 0.57 μm from the apical side (Fig. 3 *B–D*, first row; $P = 0.0327$). Strikingly, this basal-to-apical ingression bias was abolished in circumferential outer cell divisions upon PARD6B knockdown (total displacement apical side: 10.88 ± 0.73 μm; total displacement basal side: 13.28 ± 0.90 μm; $P = 0.1514$) (Fig. 3 *B–D*, third row and *SI Appendix*, Fig. S6). In contrast, in radial cell divisions both sides of the furrow ingressed similarly both in controls (total displacement side 1: 12.96 μm ± 1.44; total displacement side 2: 12.43 μm ± 1.77; $P = 0.8209$) as well as in PARD6B-depleted embryos (total displacement side 1: 12.37 μm ± 0.90; total displacement side 2: 13.73 μm ± 1.04; $P = 0.9290$) (Fig. 3 *B–D*, second and fourth rows and *SI Appendix*, Fig. S6).

A basal-to-apical cytokinesis ingression bias has previously been observed in both *Drosophila melanogaster* and mammalian epithelial cells (3–6, 27). Notably, however, in the case of *D. melanogaster* epithelial cells, cell–cell adhesion drives the bias via mechanical anchorage of the contractile ring to E-cadherin complexes, thus hampering furrow ingression on the apical side (3–6). Thus, to further probe whether the bias observed in outer blastomeres was indeed caused by an inhibitory effect of the apical domain on the cytokinesis machinery rather than cell–cell adhesion, we analyzed furrow ingression dynamics in circumferentially and radially dividing outer blastomeres at the 16–32 cell transition from embryos relieved of cell–cell adhesion via exposure to Ca^{+2}-free media (Fig. 3 *E–G*). Similarly to our previous results, a basal-to-apical bias of furrow ingression was detected exclusively in circumferentially dividing outer blastomeres of embryos devoid of cell–cell adhesion (total displacement apical side: 10.97 μm ± 0.94; total displacement basal side: 15.91 μm ± 0.98; $P = 0.0264$) and not in radially dividing blastomeres (total displacement side 1: 15.18 μm ± 0.92; total displacement side 2: 13.36 μm ± 0.65; $P = 0.2026$) (Fig. 3 *E–G*). We conclude that the overall slowing of ring constriction speed in outer cells is a result of reduced ingression specifically on the apical side during circumferential cell divisions, by a mechanism that is cell-intrinsic and not dependent on cell adhesion or shape.

Apical Polarity Disrupts the Recruitment of Furrowing Regulators in a Cell-Autonomous Manner. To understand why the apical domain might slow furrow ingression, we sought to visualize the distribution of cytokinesis components at the contractile ring during cytokinesis in circumferentially dividing outer cells. To do this, we applied a correlative live-fix imaging approach (28, 29), in which we first performed live imaging of control and PARD6B-depleted embryos at the 16–32 cell division expressing H2B:RFP to visualize cytokinesis and then fixed them specifically at midcytokinesis to further perform immunofluorescence of established cytokinesis regulators. Consistent with previous reports (18, 30), a focused apical domain was retained during M-phase in control embryos, as evidenced by the enrichment of polarity protein PKCζ in the apical surface at midcytokinesis (Fig. 4 *A* and *C*). Strikingly, in control embryos, Anillin and p-Myosin were asymmetrically distributed within the contractile ring, being enriched in regions where it overlapped with the basolateral domain, but substantially decreased where it overlapped with the PKCζ-positive apical domain (apical:basal ratio Anillin: 0.28 ± 0.05; p-Myosin: 0.31 ± 0.05; Fig. 4 *A–D* and *SI Appendix*, Fig. S7 *A* and *B*). This asymmetric distribution within the contractile ring was lost upon PARD6B knockdown, wherein the PKCζ-labeled apical domain was no longer evident, and Anillin and p-Myosin became evenly distributed (apical:basal ratio Anillin: 0.86 ± 0.04; p-Myosin: 0.96 ± 0.08; Fig. 4 *A–D*; *SI Appendix*, Fig. S7 *A* and *B*). The sum of fluorescence intensity of both apical and basal sides was similar between control (Anillin: 87.78 ± 16.41 arbitrary units [a.u.]; p-Myosin: 126.6 ± 12.86 a.u.) and PARD6B-depleted embryos (Anillin: 103.9 ± 22.48 a.u. $P = 0.6881$; p-Myosin: 118.7 ± 15.08 a.u. $P = 0.7006$; *SI Appendix*, Fig. S7 *C* and *D*), suggesting that the impact of polarity emergence was to bias the localization of Anillin and p-Myosin rather than affect their overall levels. To address whether asymmetric distribution of cytokinesis regulators could be mediated by cell adhesion rather than apical polarity, we performed correlative live-fix imaging of embryos at the 16–32 cell division treated with Ca^{+2}-free media to abolish cell adhesion and assessed the levels of Anillin at the contractile ring by immunofluorescence. Notably, Anillin was substantially underrepresented where the contractile ring overlapped with the apical domain and enriched at the basal side (Anillin apical:basal ratio: 0.35 ± 0.04; significant deviation from 1, $P < 0.0001$; Fig. 4 *E* and *F* and *SI Appendix*, Fig. S7*E*). These results corroborate the notion that the inhibitory effect of apical polarity on the cytokinetic machinery is a cell-autonomous effect that is not dependent on cell–cell contacts (Fig. 4*G*). The asymmetric localization of cytokinesis components was observed exclusively in dividing blastomeres undergoing cytokinesis, whereas interphase localization of Anillin (nuclear) and p-Myosin (undetectable/cytoplasmic) remained unaffected (Fig. 4 *A*, *C*, and *E*, third panels), suggesting that the apical domain most likely impacts the localization of cytokinesis components solely during cytokinesis. Thus, the emergence of the apical domain in outer cells prevents accumulation of cytokinesis components including Anillin and p-Myosin during cytokinesis, leading to an unbalanced furrow ingression which is slowed specifically on the apical side.

Discussion

Exploiting multiple well-characterized developmental transitions in the early mouse embryo, our work delineates two powerful influences on furrow ingression speed, both of which have

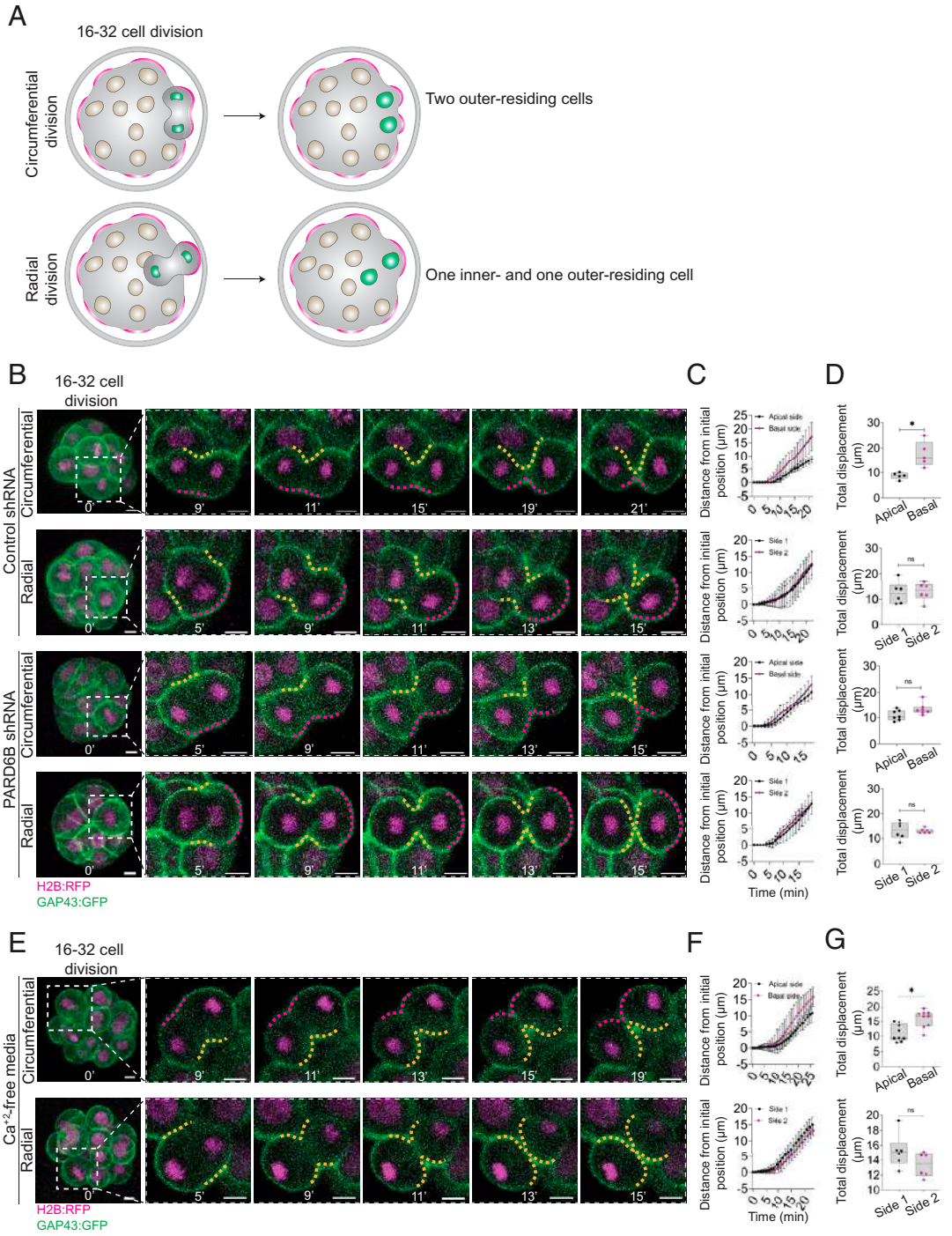

Fig. 3. Apical polarity biases furrow ingression independently of cell adhesion. (*A*) Illustration of cell division orientation in outer cells at the 16–32 cell transition. Outer cells divide either circumferentially, generating two new outer-residing cells, or radially, generating one inner-residing and one outer-residing cell. Note that circumferential cell divisions occur such that the contractile ring cuts through the apical domain and can lead to symmetric inheritance of the apical domain. (*B*) Representative time-lapse images of circumferentially and radially dividing blastomeres undergoing the 16–32 cell division from embryos previously injected with either control shRNA (examples shown for both circumferential and radial divisions have 23 cells) or PARD6B shRNA (example shown for circumferential division has 21 cells and for radial has 16 cells) and coexpressing H2B:RFP (magenta) and GAP43:GFP (green). Magenta dashed lines indicate the location of the apical domain, and yellow dashed lines indicate the regions that do not contain an apical domain. (*C*) Average distance from initial furrow position at anaphase onset in circumferentially or radially dividing blastomeres undergoing the 16–32 cell division from embryos previously injected with control (circumferential: $n = 5$ blastomeres from five embryos; radial: $n = 6$ blastomeres from five embryos) or PARD6B shRNA (circumferential: $n = 7$ blastomeres from five embryos; radial: $n = 6$ blastomeres from five embryos). (*D*) Total furrow displacement of blastomeres from embryos in *C*, dividing circumferentially (control: $^*P = 0.0327$; PARD6B: ns [not significant] $P = 0.1514$) or radially (control: ns $P = 0.8209$; PARD6B: ns $P = 0.9290$; two-tailed paired *t* tests). (*E*) Representative time-lapse images of circumferentially and radially dividing blastomeres undergoing the 16–32 cell division from embryos coexpressing H2B:RFP (magenta) and GAP43:GFP (green) and cultured in Ca^{+2}-free media (example shown for circumferential division has 21 cells and for radial has 19 cells). Magenta dashed lines indicate the location of the apical domain, and yellow dashed lines indicate the regions that do not contain an apical domain. (*F*) Average distance from initial furrow position at anaphase onset in circumferentially ($n = 9$ blastomeres from eight embryos) or radially dividing blastomeres ($n = 6$ blastomeres from six embryos) undergoing the 16–32 cell division from embryos cultured in Ca^{+2}-free media. (*G*) Total furrow displacement of blastomeres from embryos in *F*, dividing circumferentially (two-tailed paired *t* test, $^*P = 0.0264$) or radially (two-tailed paired *t* test, ns $P = 0.2026$). Time is shown in minutes, where 0′ is anaphase onset. (Scale bars, 10 μm.) In the box plots, the center line represents the median, the bounds of the box represent upper and lower quartiles, the whiskers represent minimum and maximum values, and dots represent independent measurements.

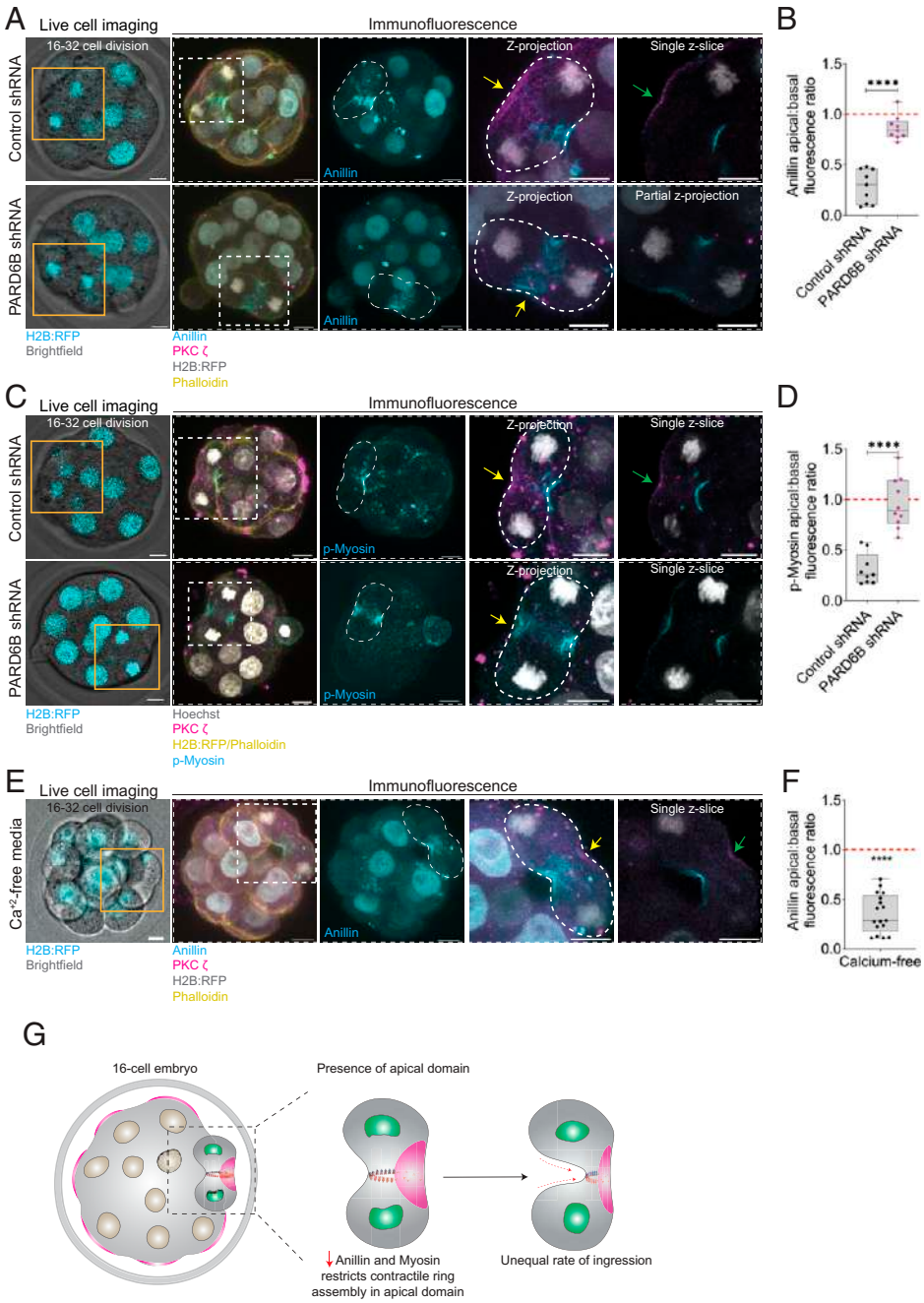

Fig. 4. Apical polarity disrupts the recruitment of furrowing regulators independently of cell adhesion. (*A* and *C*) Representative live and immunofluorescence images of circumferentially dividing blastomeres undergoing the 16–32 cell division from embryos previously injected with control (example shown in *A* has 19 cells and in *C* has 16 cells) or PARD6B shRNA (example shown in *A* has 16 cells and in *C* has 16 cells). Note that both Anillin (*A*) and p-Myosin (*C*) are underrepresented at the side of contractile ring that overlaps with the apical domain in controls, and this bias is abolished upon PARD6B depletion (yellow arrows). Also note that the apical domain is intact during division in controls (green arrows). (*B*) Apical:basal fluorescence ratio of Anillin in outer blastomeres undergoing the 16–32 cell division from embryos previously injected with control (n = 9 blastomeres from nine embryos) or PARD6B shRNA (n = 9 blastomeres from nine embryos; unpaired two-tailed t test, ****$P < 0.0001$). (*D*) Apical:basal fluorescence ratio of p-Myosin in outer blastomeres undergoing the 16–32 cell division from embryos previously injected with control (n = 9 blastomeres from nine embryos) or PARD6B shRNA (n = 10 blastomeres from 10 embryos; unpaired two-tailed t test, ****$P < 0.0001$). (*E*) Representative live and immunofluorescence images of a circumferentially dividing blastomere undergoing the 16–32 cell division from a H2B:RFP-expressing embryo cultured in Ca^{+2}-free media, in which the furrow overlaps with the apical domain (example has 16 cells). Note that Anillin was underrepresented at the apical side (yellow arrow) and the apical domain is intact during division (green arrow). (*F*) Apical:basal fluorescence ratio of Anillin in outer blastomeres undergoing the 16–32 cell division from embryos cultured in Ca^{+2}-free media (n = 17 blastomeres from 17 embryos, one-sample t test, ****$P < 0.0001$ significant deviation from 1). (*G*) Model for local regulation of ring constriction by the apical domain. In intact 16-cell embryos, apical polarity restricts the access of Anillin and p-Myosin to the contractile ring in circumferentially dividing outer cells, thereby slowing furrow ingression specifically on the side of the contractile ring that overlaps with the apical domain. Time is shown in minutes, where 0′ is anaphase onset. (Scale bars, 10 μm.) In the box plots, the center line represents the median, the bounds of the box represent upper and lower quartiles, the whiskers represent minimum and maximum values, and dots represent independent measurements.

broad ramifications for our understanding of the mechanism of ring ingression in diverse cell types. First, our data show a strong influence of cell size on furrow ingression from the 8–16 cell division onward. A similar cell-size to cytokinesis speed correlation in *C. elegans* (9–12) and *N. crassa* (13) was previously proposed as evidence that the contractile ring is locally

regulated, bigger rings contracting more quickly because they comprise larger numbers of locally regulated units that disassemble during furrowing. Our results extend the relationship between cell size and furrowing speed to the mouse preimplantation embryo. The insensitivity of furrowing speed to cell size from the 1–2 to 8–16 cell divisions suggests an upper limit of cell size beyond which furrowing speed cannot be further scaled up, and it is possible that this upper limit is not reached in one-cell *C. elegans* embryos which are more similar in volume to eight-cell-stage mouse blastomeres. An upper limit has been previously shown to restrict the scaling of spindle length in *Xenopus laevis* (31) and *C. elegans* embryos (32, 33). Given that the speed of chromosome separation and spindle elongation during anaphase is reduced from the eight-cell stage onward (34), altered furrowing speed may help avoid chromosome segregation error at later developmental stages.

Second, restricted furrowing in the apical domain was found to be the result of limited access of contractile ring components. This effect of the apical domain is independent of its role on cell fate determination, as determined by a lack of effect of TEAD4-knockdown (*SI Appendix*, Fig. S5), and consistent with this we also found a failure in the recruitment of Anillin and p-Myosin to the apical side of the contractile ring in circumferentially dividing blastomeres at the 8–16 cell division, in which apical polarity has already been established but cell fate is not yet determined (*SI Appendix*, Fig. S8). Limited myosin levels at the apical surface have also been observed in nondividing outer blastomeres and are thought to influence cell position and cell fate specification by reducing contractility to limit outer cell internalization and thus ensure adequate proportions of inner and outer blastomeres (35). Although the abundance of cytokinetic components has been previously correlated with ingression speed in asymmetrically ingressing furrows (5, 36, 37), our unexpected discovery that a similar bias in mouse embryos is due to the emergence of the apical domain allowed us to experimentally relieve that bias, and therein show directly that the abundance of Anillin and p-Myosin determines furrow ingression speed. Whether the inhibitory effect of polarity also affects other tissues in the mouse remains to be addressed. Nonetheless this series of experiments provide some of the strongest evidence that cell-autonomous subcellular organization can dictate local regulation of furrow ingression (Fig. 4*G*).

Our data also demonstrate that the inhibitory impact of the apical domain upon furrow ingression is not dependent on cell contacts, as embryos devoid of cell adhesion also display a basal-to-apical ingression bias and reduced Anillin localization to the apical side. This is distinct from previously noted links between furrowing and cell polarity described in *D. melanogaster* polarized epithelial cells, wherein cell adhesion promotes an anchoring of the contractile ring to E-cadherin complexes and reduce furrow ingression at the apical side independently of apical polarity (6). The phenomenon described herein is also distinct from that observed in *C. elegans* zygotes wherein apical PAR proteins promote the retention of Anillin and Septin at the anterior pole during an asymmetric division, possibly as a means to prevent an overload of cytokinesis regulators in the ingressing furrow in the first cell division (7). Why cytokinesis regulators are chased from the apical cortex during cytokinesis in mouse blastomeres remains to be seen, but an intriguing precedent is found in the observation that ECT2, the GEF responsible for activating cytokinesis master-regulator RhoA, and RhoA downstream effectors Rock1/2 can interact with polarity proteins (38, 39), albeit that whether these interactions might result in an inhibitory effect on cytokinesis components remains to be addressed. Alternatively, unidentified apical domain components may outcompete cytokinesis components for limited membrane binding sites. Our experiments highlight the complexity of furrow ingression regulation and underscore that cellular contexts and asymmetries can have stark impacts upon the mechanisms of cytokinesis.

Materials and Methods

Experimental Model. All experiments performed followed the guidelines for animal experimentation and were approved by the Comité Institutionnel de Protection des Animaux of the Centre de Recherche du Centre Hospitalier de l'Université de Montréal (protocol number: IP18034GFs). The female mice used in this study were 2- to 3-mo-old CD1 [Crl:CD1(ICR) 022CD1] and male mice were 3- to 12-mo-old BDF1 (B6D2F1/J 100006). All animals were kept in individually ventilated cages (up to five animals per cage for the females and one animal per cage for the males) at 22 ± 2 °C, 40 to 60% humidity in 12-h light/dark cycles with lights switched on from 6:30 AM to 6:30 PM and food and water available for ad libitum consumption.

Embryo Collection and Culture. Two-cell embryos were harvested from previously superovulated 2- to 3-mo-old female CD1 mice mated with BDF1 male mice, except for the experiment in Fig. 1 *A–D* (one-cell stage group), in which embryos were harvested at the zygote stage. Embryos were collected in homemade M2 media and cultured in KSOM (MR-020P-5F; EMD Millipore) in 5% CO_2 at 37 °C. For experiments in Figs. 2 *D* and *E*, 3 *E–G*, 4 *E* and *F*, and *SI Appendix*, Fig. S4, 16-cell embryos were exposed to either complete homemade KSOM or Ca^{+2}-free homemade KSOM (*SI Appendix*, Table S1) during the 16–32 cell division.

Messenger RNA, shRNA, and dsRNA production. Messenger RNA (mRNA) was synthesized using Ambion mMessage Machine T3 (AM1348) or SP6 (AM1340) according to the manufacturer's instructions from the following plasmids: H2B:RFP in pRN4 (gift from Alex McDougal, Observatoire Océanologique de Villefranche sur Mer, Villefranche sur Mer, France) and GAP43:GFP in psC2 (gift from Yojiro Yamanaka, McGill University, Montréal, Canada). Knockdown of PARD6B via shRNA and TEAD4 via dsRNA was performed following previously described protocols (21–23). shRNA plasmids were purchased from Millipore Sigma (Control shRNA SHC002; PARD6B shRNA SHCLND-NM_021409 TRCN0000054687) and purified using QIAGEN Miniprep kit (27106). For dsRNA production, a Tead4 specific PCR primer pair including T7-derived RNApol promoters was used to obtain the in vitro transcription template using mouse blastocyst cDNA (sense; TAATACGACTCACTATAGGGTGTTGGAGTTCTCGGCTTTC, antisense; TAATACGACTCACTATAGGGTCGGTAGATGTGGTGCTGAG, T7-promoter underlined) (23). For the control group, a GFP specific dsRNA was produced with PCR primers including a T7 promoter (sense; TAATACGACTCACTATAGGGAGAGTACA AATTTTCTGTCAGTGGAGAGG, antisense; TAATACGACTCACTATAGGGAGATGTATAGTTC ATCCATGCCATGTGTA, T7-promoter underlined) (23) using pcDNA3.1 plasmid vector containing a GFP sequence as a template. Tead4 and GFP specific double-stranded RNA synthesis was performed using Ambion mMessage Machine T7 (AM1344) according to the manufacturer's instructions.

Microinjection, Cytoplasmic Removal, and Enucleation. Cytoplasmic microinjection of mRNAs or dsRNAs in two-cell embryos or zygotes was performed in M2 media (M7167; Sigma) using a picopump (World Precision Instruments) and micromanipulators (Narishige) mounted on a Leica DMI4000 inverted microscope (40). For shRNA microinjections in Figs. 2 *F–I*, 3 *B–D*, 4 *A–D*, and *SI Appendix*, Figs. S6 and S7, shRNA plasmids were microinjected directly inside both nuclei of two-cell embryos. Prior to microinjection, shRNA plasmids were diluted to 20 ng/μL in homemade microinjection buffer (5 mM Tris pH 7.4 and 0.1 mM ethylenediaminetetraacetic acid) and Fluorescin Dextran 70 kDa (FD70S; Sigma) 0.01 mg/mL was added to the solution to confirm that the shRNA was successfully injected in the nucleus. Cytoplasmic removal in Fig. 1 *E–H* and *SI Appendix*, Fig. S2 was performed as previously described (41) and enucleation in Fig. 1 *I–L* and *SI Appendix*, Fig. S3 was adapted from a previous report (15). Hydraulic-controlled glass pipettes mounted on a Piezo-electric drill were used to perforate the zona pellucida of embryos and aspirate either the nucleus (for enucleation) or the cytoplasm without perturbing the nucleus. These procedures were performed in M2 media supplemented with Latrunculin A

5 μM (428021; EMD Millipore). After cytoplasmic removal, at the four-cell stage, sham-manipulated blastomeres displayed on average 32.61 ± 0.24 pL of volume, whereas blastomeres with reduced cytoplasmic size displayed 19.31 ± 0.57 pL (*SI Appendix*, Fig. S2*D*; average volume reduction of ∼40.8%). At the eight-cell stage, sham-manipulated blastomeres displayed on average 16.52 ± 0.74 pL of volume, whereas blastomeres with reduced cytoplasmic size displayed 10.02 ± 0.29 pL (*SI Appendix*, Fig. S2*G*; average volume reduction of ∼40.4%). Embryos were thoroughly washed through at least 10 drops of KSOM prior to being transferred to and cultured in clean KSOM drops prior to imaging.

Immunofluorescence and Live Imaging. Embryos were fixed in 2% paraformaldehyde (P6148; Sigma) diluted in phosphate-buffered saline (PBS) for 20 min followed by 10-min permeabilization using 0.25% Triton X-100 (T9284; Sigma) diluted in PBS and a blocking step with 3% bovine serum albumin (A7906; Sigma) diluted in PBS for either 1 h at 37 °C or overnight at 4 °C (41). Primary antibodies used were PKC ζ anti-mouse 1:100 (sc-17781; Santa Cruz), Anillin anti-rabbit 1:300 (gift from Alisa Piekny, Concordia University, Montréal, Canada); p-Myosin light chain II anti-rabbit 1:100 (3671T; Cell Signaling Technology), and TEAD4 anti-mouse 1:100 (ab58310; Abcam). Hoechst 33342 (1:1,000) (H1399; Invitrogen) was used for DNA labeling and Alexa-labeled secondary antibodies (1:1,000) were purchased from Thermo Fisher. Alexa Fluor 555 Phalloidin (A34055) and Alexa Fluor 647 Phalloidin (A22287) conjugated antibodies (1:200) were purchased from Invitrogen.

Immunofluorescence imaging was performed on a Leica SP8 confocal microscope fitted with a 63× 1.4 numerical aperture oil objective, HyD and PMT detectors and images were acquired using 1.5-μm optical sections and z-stack step size of 1.5 μm. Live imaging was performed on a Leica SP8 confocal microscope fitted with a 20× 0.75 numerical aperture air objective, HyD and PMT detectors and images were acquired with 1-min time intervals using 2.0-μm optical sections and z-stack step size of 2.0 μm. For experiments in Fig. 4, a correlative live and immunofluorescence imaging approach was used as described previously (28), wherein embryos expressing H2B:RFP were subjected to live imaging on either a Leica SP8 confocal microscope fitted with a 20× 0.75 numerical aperture air objective, HyD and PMT detectors or a Zeiss Axio observer equipped with an Axiocam and 20× 0.5 numerical aperture air objective and light-emitting diode light to observe ongoing cell divisions and fixed individually at midcytokinesis (∼9 min postanaphase onset) for further immunofluorescence imaging. For all live imaging, embryos were placed on a heated stage top incubator with 5% CO_2 supply at 37 °C and imaged in 3-μL drops of pre-equilibrated KSOM.

Image Analysis and Interpretation. Measurements of contractile ring perimeter were performed using IMARIS 9.3 (Bitplane; Oxford Instruments). Using the Oblique Slicer function of IMARIS, the images were slightly rotated and oriented such that the contractile ring was seen from a "face-on" position in a single z-slice and measurements were performed using the Measurement Point function to manually trace the outline of the contractile ring at each timepoint (every 1 min). The contractile ring perimeter was defined as the sum of distances between each Measurement Point outline around the contractile ring. For one-cell embryos, cell divisions always took place such that the contractile ring was parallel from the image plane, and therefore image rotation was deemed not appropriate due to limitations on z-step size resolution that caused deformations on the image and therefore, contractile ring perimeter was calculated based on measurements of ring diameter obtained from a single z-slice and applying the following formula $P = \pi \times d$, where P stands for perimeter, π stands for pi, and d stands for diameter. The duration of cytokinesis was measured as the time between the first frame at which a perimeter decrease was first observed (defined as 5% decrease), until the last frame at which a contractile ring was clearly visible and the perimeter reliably measurable.

Analysis of distance from initial furrow position in Fig. 3 was performed using a single middle z-slice where both sides of the furrow were visible simultaneously. Only blastomeres that were dividing parallel to the coverslip were analyzed. When furrow ingression rate was approximately equal between both sides of the furrow, the images were rotated in IMARIS, and the same analysis was performed using the portions of the furrow that were not visible in the original plane of analysis to confirm that no bias in furrow ingression was present from another plane (*SI Appendix*, Fig. S6). For measurements of furrow ingression of radial cell divisions in Fig. 3, since no apical and basal sides are present "side 1" was determined as the side of the furrow that was closer to the top of the image in the XY plane and side 2 as the side closer to the bottom of the image.

All experiments involving comparisons of fluorescence intensity between embryos were performed under strictly controlled conditions–simultaneous immunostaining of different samples, same antibody aliquots, concentrations, temperature, time of incubation, as well as confocal imaging performed simultaneously (on the same day) and with identical imaging settings. All fluorescence intensity measurements were performed using Fiji/ImageJ. Apical:basal fluorescence ratios presented in Figs. 2 *F* and *G* and 4 *A*–*F* and *SI Appendix*, Figs. S2 *H*–*I*, S4 *B* and *C*, and S8 were calculated using apical and basal maximum gray values from a single z-slice. Background-subtracted total fluorescence intensity (Raw Integrated Density) measurements obtained from a single middle z-slice were used for analysis of apical vs. basal levels of Anillin and p-Myosin in *SI Appendix*, Fig. S7. For confirmation of TEAD4 knockdown efficiency in *SI Appendix*, Fig. S5 *A* and *B*, nuclear:cytoplasmic ratios were calculated using total fluorescence intensity (Raw Integrated Density) measurements in the nucleus or cytoplasm. For analysis of apical vs. basal levels of PKC ζ and confirmation of TEAD4 knockdown, between 2 and 13 inner and outer blastomeres were quantified per embryo in each group and the data displayed is an average per embryo. For cell volume measurements in *SI Appendix*, Fig. S2 *D* and *G*, the areas delineated by the cell membrane (GAP43:GFP) were manually traced and measured in each z-slice in blastomeres prior to mitotic entry and the sum of areas was multiplied by the step size (2 μm) to obtain the volume in cubic micrometers and further converted to picoliters, as previously described (41).

For the live-imaging experiments, circumferential cell divisions were classified as those in which the dividing outer cell generated two new outer-residing cells immediately after cytokinesis completion, whereas radial cell divisions were considered as those in which the dividing outer cell generated one new outer-residing and one new inner-residing cell immediately following cytokinesis completion.

Statistical Analysis. All statistical analyses were performed using GraphPad Prism (https://www.graphpad.com/). Shapiro–Wilk normality tests were applied and either parametric or nonparametric statistical tests were applied accordingly. For data encompassing multiple comparisons, either unpaired one-way ANOVA or unpaired Kruskal–Wallis tests corrected for multiple comparisons were applied. For data encompassing two comparisons, either unpaired two-tailed *t* tests or unpaired two-tailed Mann–Whitney *U* tests were applied. For analyses of total furrow displacement (Fig. 3 *D* and *G* and *SI Appendix*, Fig. S6), background-subtracted fluorescence intensity of Anillin and p-Myosin (*SI Appendix*, Fig. S7), either paired two-tailed *t* test or paired Wilcoxon test were applied. For analyses in Fig. 4*F* and *SI Appendix*, Fig. S8 *B* and *D*, one-sample *t* test was applied for calculations of significant deviation from 1. For *SI Appendix*, Fig. S2*J*, simple linear regression analysis was applied. Statistical significance was considered when $P < 0.05$.

Data Availability. All study data are included in the article and/or supporting information.

ACKNOWLEDGMENTS. This work was funded by grants from the Natural Sciences and Engineering Research Council of Canada, Fondation Jean-Louis Lévesque, Canadian Foundation for Innovation, and the Canadian Institutes of Health Research. L.M.G.P. is supported by a Fonds de Recherche du Québec–Santé Doctoral Scholarship. We thank Drs. Jean-Claude Labbé, Gilles Hickson, and Tim Davies for comments on the manuscript as well as the members of the G.F., Labbé, Hickson, and Gerhold laboratories for constructive discussions. We also thank Gaudeline Rémillard-Labrosse and Aurélie Cleret-Buhot for excellent technical support.

1. F. A. Barr, U. Gruneberg, Cytokinesis: Placing and making the final cut. *Cell* **131**, 847–860 (2007).
2. R. A. Green, E. Paluch, K. Oegema, Cytokinesis in animal cells. *Annu. Rev. Cell Dev. Biol.* **28**, 29–58 (2012).
3. E. Morais-de-Sá, C. Sunkel, Adherens junctions determine the apical position of the midbody during follicular epithelial cell division. *EMBO Rep.* **14**, 696–703 (2013).
4. C. Thieleke-Matos, D. S. Osório, A. X. Carvalho, E. Morais-de-Sá, Emerging mechanisms and roles for asymmetric cytokinesis. *Int. Rev. Cell Mol. Biol.* **332**, 297–345 (2017).

5. N. Founounou, N. Loyer, R. Le Borgne, Septins regulate the contractility of the actomyosin ring to enable adherens junction remodeling during cytokinesis of epithelial cells. *Dev. Cell* **24**, 242–255 (2013).
6. C. Guillot, T. Lecuit, Adhesion disengagement uncouples intrinsic and extrinsic forces to drive cytokinesis in epithelial tissues. *Dev. Cell* **24**, 227–241 (2013).
7. S. N. Jordan *et al.*, Cortical PAR polarity proteins promote robust cytokinesis during asymmetric cell division. *J. Cell Biol.* **212**, 39–49 (2016).
8. C. Cabernard, K. E. Prehoda, C. Q. Doe, A spindle-independent cleavage furrow positioning pathway. *Nature* **467**, 91–94 (2010).
9. K. G. Bourdages, B. Lacroix, J. F. Dorn, C. P. Descovich, A. S. Maddox, Quantitative analysis of cytokinesis in situ during *C. elegans* postembryonic development. *PLoS One* **9**, e110689 (2014).
10. A. Carvalho, A. Desai, K. Oegema, Structural memory in the contractile ring makes the duration of cytokinesis independent of cell size. *Cell* **137**, 926–937 (2009).
11. R. N. KhaliuIlin *et al.*, A positive-feedback-based mechanism for constriction rate acceleration during cytokinesis in *Caenorhabditis elegans*. *eLife* **7**, e36073 (2018).
12. A. M. Silva *et al.*, Robust gap repair in the contractile ring ensures timely completion of cytokinesis. *J. Cell Biol.* **215**, 789–799 (2016).
13. M. E. Calvert *et al.*, Myosin concentration underlies cell size-dependent scalability of actomyosin ring constriction. *J. Cell Biol.* **195**, 799–813 (2011).
14. X. Ma *et al.*, Nonmuscle myosin II exerts tension but does not translocate actin in vertebrate cytokinesis. *Proc. Natl. Acad. Sci. U.S.A.* **109**, 4509–4514 (2012).
15. E. Tsichlaki, G. FitzHarris, Nucleus downscaling in mouse embryos is regulated by cooperative developmental and geometric programs. *Sci. Rep.* **6**, 28040 (2016).
16. C. Chazaud, Y. Yamanaka, Lineage specification in the mouse preimplantation embryo. *Development* **143**, 1063–1074 (2016).
17. J. L. Ma^ıtre, R. Niwayama, H. Turlier, F. Nédélec, T. Hiiragi, Pulsatile cell-autonomous contractility drives compaction in the mouse embryo. *Nat. Cell Biol.* **17**, 849–855 (2015).
18. R. Niwayama *et al.*, A tug-of-war between cell shape and polarity controls division orientation to ensure robust patterning in the mouse blastocyst. *Dev. Cell* **51**, 564–574.e6 (2019).
19. M. H. Johnson, J. C. Chisholm, T. P. Fleming, E. Houliston, A role for cytoplasmic determinants in the development of the mouse early embryo? *J. Embryol. Exp. Morphol.* **97** (suppl.), 97–121 (1986).
20. M. H. Johnson, C. A. Ziomek, Cell interactions influence the fate of mouse blastomeres undergoing the transition from the 16- to the 32-cell stage. *Dev. Biol.* **95**, 211–218 (1983).
21. V. B. Alarcon, Cell polarity regulator PARD6B is essential for trophectoderm formation in the preimplantation mouse embryo. *Biol. Reprod.* **83**, 347–358 (2010).
22. Y. Hirate *et al.*, Polarity-dependent distribution of angiomotin localizes Hippo signaling in preimplantation embryos. *Curr. Biol.* **23**, 1181–1194 (2013).
23. A. I. Mihajlović, V. Thamodaran, A. W. Bruce, The first two cell-fate decisions of preimplantation mouse embryo development are not functionally independent. *Sci. Rep.* **5**, 15034 (2015).
24. S. Anani, S. Bhat, N. Honma-Yamanaka, D. Krawchuk, Y. Yamanaka, Initiation of Hippo signaling is linked to polarity rather than to cell position in the pre-implantation mouse embryo. *Development* **141**, 2813–2824 (2014).
25. J. Rossant, P. P. Tam, Blastocyst lineage formation, early embryonic asymmetries and axis patterning in the mouse. *Development* **136**, 701–713 (2009).
26. T. Frum, A. Ralston, "Pluripotency–What does cell polarity have to do with it?" in *Cell Polarity in Development and Disease*, P. M. Conn, D. W. Houston, Eds. (Elsevier, 2018), chap. 2, pp. 31–60.
27. S. Reinsch, E. Karsenti, Orientation of spindle axis and distribution of plasma membrane proteins during cell division in polarized MDCKII cells. *J. Cell Biol.* **126**, 1509–1526 (1994).
28. C. Vázquez-Diez, G. FitzHarris, Correlative live imaging and immunofluorescence for analysis of chromosome segregation in mouse preimplantation embryos. *Methods Mol. Biol.* **1769**, 319–335 (2018).
29. C. Vázquez-Diez, K. Yamagata, S. Trivedi, J. Haverfield, G. FitzHarris, Micronucleus formation causes perpetual unilateral chromosome inheritance in mouse embryos. *Proc. Natl. Acad. Sci. U.S.A.* **113**, 626–631 (2016).
30. E. Korotkevich *et al.*, The apical domain is required and sufficient for the first lineage segregation in the mouse embryo. *Dev. Cell* **40**, 235–247.e7 (2017).
31. M. Wühr *et al.*, Evidence for an upper limit to mitotic spindle length. *Curr. Biol.* **18**, 1256–1261 (2008).
32. G. Greenan *et al.*, Centrosome size sets mitotic spindle length in *Caenorhabditis elegans* embryos. *Curr. Biol.* **20**, 353–358 (2010).
33. Y. Hara, A. Kimura, Cell-size-dependent spindle elongation in the *Caenorhabditis elegans* early embryo. *Curr. Biol.* **19**, 1549–1554 (2009).
34. K. Yamagata, G. FitzHarris, 4D imaging reveals a shift in chromosome segregation dynamics during mouse pre-implantation development. *Cell Cycle* **12**, 157–165 (2013).
35. J. L. Ma^ıtre *et al.*, Asymmetric division of contractile domains couples cell positioning and fate specification. *Nature* **536**, 344–348 (2016).
36. A. S. Maddox, L. Lewellyn, A. Desai, K. Oegema, Anillin and the septins promote asymmetric ingression of the cytokinetic furrow. *Dev. Cell* **12**, 827–835 (2007).
37. S. Herszterg, A. Leibfried, F. Bosveld, C. Martin, Y. Bellaiche, Interplay between the dividing cell and its neighbors regulates adherens junction formation during cytokinesis in epithelial tissue. *Dev. Cell* **24**, 256–270 (2013).
38. X. F. Liu, H. Ishida, R. Raziuddin, T. Miki, Nucleotide exchange factor ECT2 interacts with the polarity protein complex Par6/Par3/protein kinase Czeta (PKCzeta) and regulates PKCzeta activity. *Mol. Cell. Biol.* **24**, 6665–6675 (2004).
39. A. I. Mihajlović, A. W. Bruce, Rho-associated protein kinase regulates subcellular localisation of Angiomotin and Hippo-signalling during preimplantation mouse embryo development. *Reprod. Biomed. Online* **33**, 381–390 (2016).
40. G. Fitzharris, A shift from kinesin 5-dependent metaphase spindle function during preimplantation development in mouse. *Development* **136**, 2111–2119 (2009).
41. C. Vázquez-Diez, L. M. G. Paim, G. FitzHarris, Cell-size-independent spindle checkpoint failure underlies chromosome segregation error in mouse embryos. *Curr. Biol.* **29**, 865–873.e3 (2019).

PNAS
www.pnas.org

Supplementary Information for

Cell size and polarisation determine cytokinesis furrow ingression dynamics in mouse embryos

Lia Mara Gomes **Paim**[1]; Greg **FitzHarris**[1,2,3*]

*Corresponding author: Greg FitzHarris
Email: greg.fitzharris@umontreal.ca

This PDF file includes:

Figures S1 to S8
Table S1
Supplementary Video 1 legend

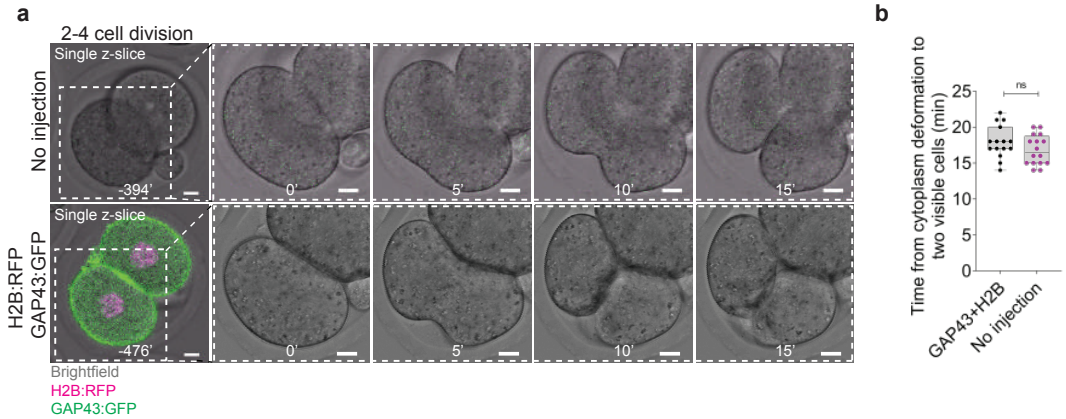

Fig. S1. H2B:RFP and GAP43:GFP imaging does not affect cytokinesis dynamics. (a) Representative time-lapse images of a cell undergoing the 2-4 cell division from non-injected embryos (top; example shown has 2 cells) or expressing H2B:RFP (magenta) and GAP43:GFP (green) (bottom; example has 2 cells). **(b)** Quantification of average time from initial cytoplasm deformation until two individualised blastomeres are visible in blastomeres undergoing the 2-4 cell division from embryos without microinjection (n=15 blastomeres from 11 embryos) or microinjected with H2B:RFP and GAP43:GFP (n=16 blastomeres from 14 embryos; two-tailed unpaired t test, *P*=0.1596). Quantification was performed using only the brightfield channel in both groups for visualisation of cytoplasm deformation and cell separation. Time is shown in minutes, where 0' is the first frame of visible cytoplasm deformation. Scale bars = 10μm. In the box plots, the centre line represents the median, the bounds of the box represent upper and lower quartiles, the whiskers represent minimum and maximum values, and dots represent independent measurements. See also Figure 1.

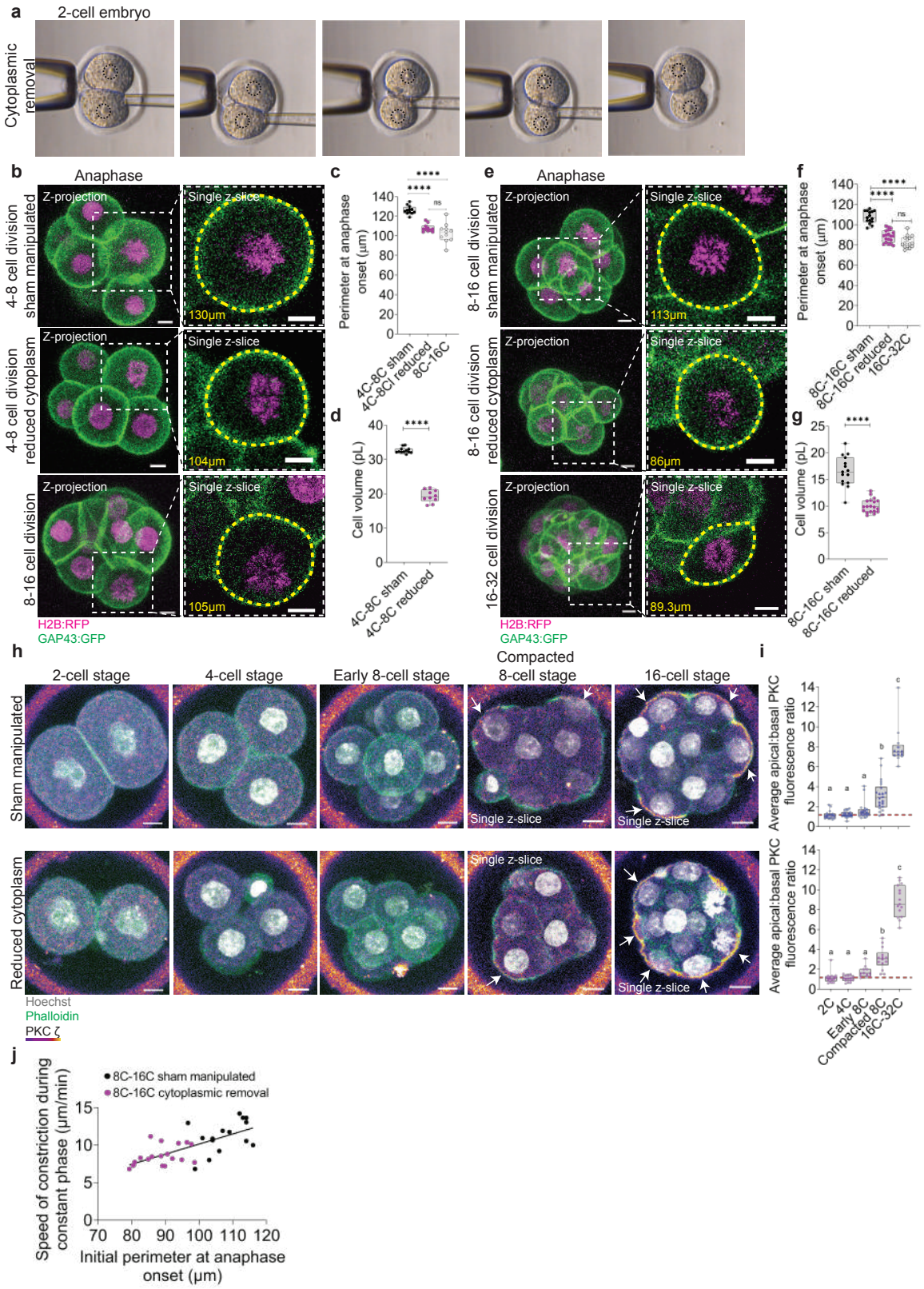

Fig S2. Cytoplasmic removal to reduce blastomere size. (a) Representative brightfield time-lapse images of cytoplasmic removal procedure in a 2-cell embryo. Dashed black circles indicate the location of the nuclei. Note that upon cytoplasmic removal, cell volume decreases

approximately 40% **(b and e)** Representative z-projections of cells undergoing the 4-8 cell division in sham manipulated embryos (top; example shown has 7 cells), embryos with reduced cytoplasm (middle; example has 5 cells) and a cell undergoing the 8-16 cell division (bottom; example has 8 cells) **(b)**; cells undergoing the 8-16 cell division in sham manipulated embryos (top; example shown has 8 cells), embryos with reduced cytoplasm (middle; example has 9 cells) and a cell undergoing the 16-32 cell division (bottom; example has 22 cells) **(e)** from embryos co-expressing H2B:RFP (magenta) and GAP43:GFP (green). The yellow dashed lines and values indicate the measurements of cell perimeter at anaphase onset. **(c and f)** Quantification of average perimeter measured at anaphase onset in sham manipulated embryos at the 4-8 cell transition (n=12 blastomeres from 11 embryos), embryos with reduced cytoplasm at the 4-8 cell transition (n=11 blastomeres from 9 embryos) and embryos at the 8-16 cell transition (n =11 blastomeres from 8 embryos; one-way ANOVA with multiple comparisons, ****P<0.0001, ns P=0.5365) **(c)**; sham manipulated embryos at 8-16 cell transition (n=15 blastomeres from 8 embryos), embryos with reduced cytoplasm at 8-16 cell transition (n=19 blastomeres from 10 embryos) and embryos at the 16-32 cell transition (n=15 blastomeres from 11 embryos; Kruskal-Wallis with multiple comparisons, ****P<0.0001, ns P= 0.1734) **(f)**. **(d and g)** Quantification of average blastomere volume in sham manipulated embryos at the 4-8 cell transition (n=12 blastomeres from 11 embryos), embryos with reduced cytoplasm at the 4-8 cell transition (n=11 blastomeres from 9 embryos; unpaired t test, ****P<0.0001) **(d)**; sham manipulated embryos at 8-16 cell transition (n=15 blastomeres from 8 embryos), embryos with reduced cytoplasm at 8-16 cell transition (n=19 blastomeres from 10 embryos, unpaired t test ****P<0.0001) **(g)**. The data from 8-16 in (c) and 16-32 cell divisions in (f) was obtained from the same embryos in figure 1B-D. (**h**) Evidence that polarity emerges at the compacted 8-cell stage even in embryos with reduced cytoplasmic size. Representative immunofluorescence images of 2-cell, 4-cell, early 8-cell, compacted 8-cell and 16-cell stage sham manipulated (top) and embryos with reduced cytoplasm (bottom). Note that apical localization of PKCζ is only clearly visible from the compacted 8-cell stage onwards in both sham-manipulated and embryos with reduced cytoplasm (white arrows). (**i**) Quantification of average apical:basal PKC ζ fluorescence ratio in sham manipulated (top) 2-cell (n = 17 embryos), 4-cell (n = 20 embryos), early 8-cell (n = 19 embryos), compacted 8-cell (n = 22 embryos) and 16-32 cell stage embryos (n = 13 embryos; One-way ANOVA) and embryos with reduced cytoplasm (bottom) at the 2-cell (n = 17 embryos), 4-cell (n = 15 embryos), early 8-cell (n = 12 embryos), compacted 8-cell (n = 14 embryos) and 16-32 cell stage (n = 15 embryos; One-way ANOVA). (**j**) Scatterplot demonstrating the distribution of average speed of constriction during constant phase of perimeter decrease relative to the initial perimeter at anaphase onset in sham-manipulated (black dots; n=15 blastomeres from 8 embryos) and embryos with reduced cytoplasm at the 8-16 cell transition (pink dots; n=19 blastomeres from 10 embryos; simple linear regression analysis R^2 = 0.4930, slope is significantly non-zero p<0.0001). Scale bars = 10μm. In box plots, the center line represents the median, the bounds of the box represent upper and lower quartiles, the whiskers represent minimum and maximum values, and dots represent independent measurements. In multiple comparison analyses, different letters represent statistical significance at P<0.05. See also Figure 1.

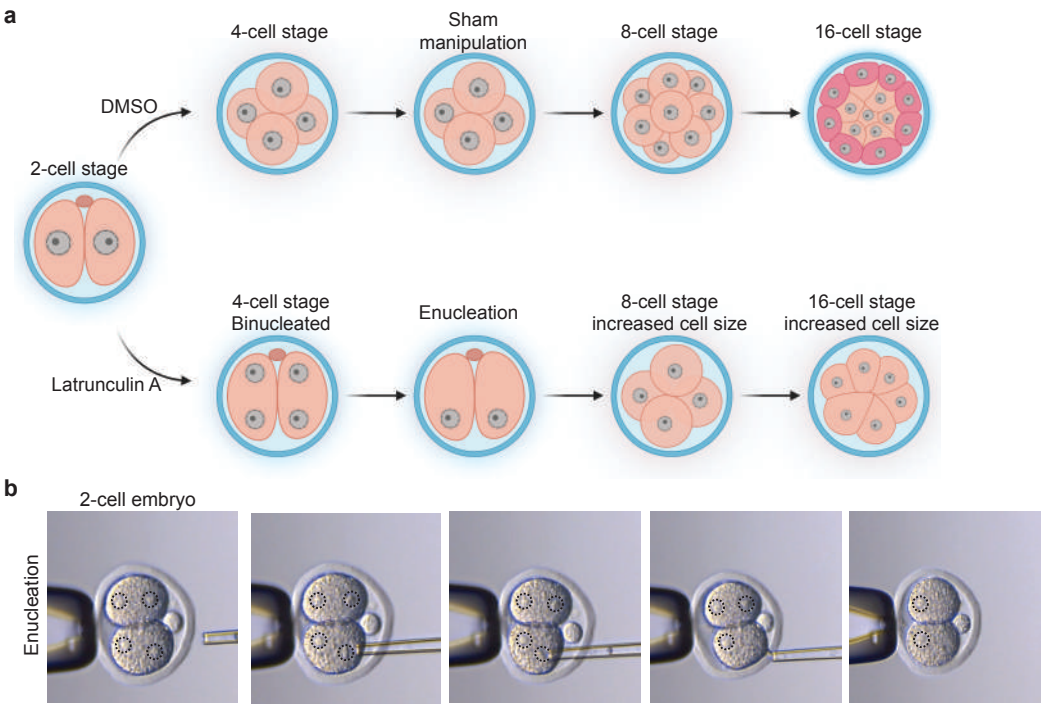

Fig S3. Procedure to artificially increase blastomere size. (a and b) Scheme illustrating the experimental design to increase cytoplasmic size. Two-cell embryos were treated Latrunculin A during the 2- to 4-cell transition to generate binucleated embryos. Binucleated embryos were then subjected to micromanipulation to remove one of the extra nuclei generated as a result of cytokinesis failure (enucleation; **b**) and allowed to divide to the 8-cell or 16-cell stages prior to live cell imaging. Figure S3A was created with BioRender. See also Figure 1.

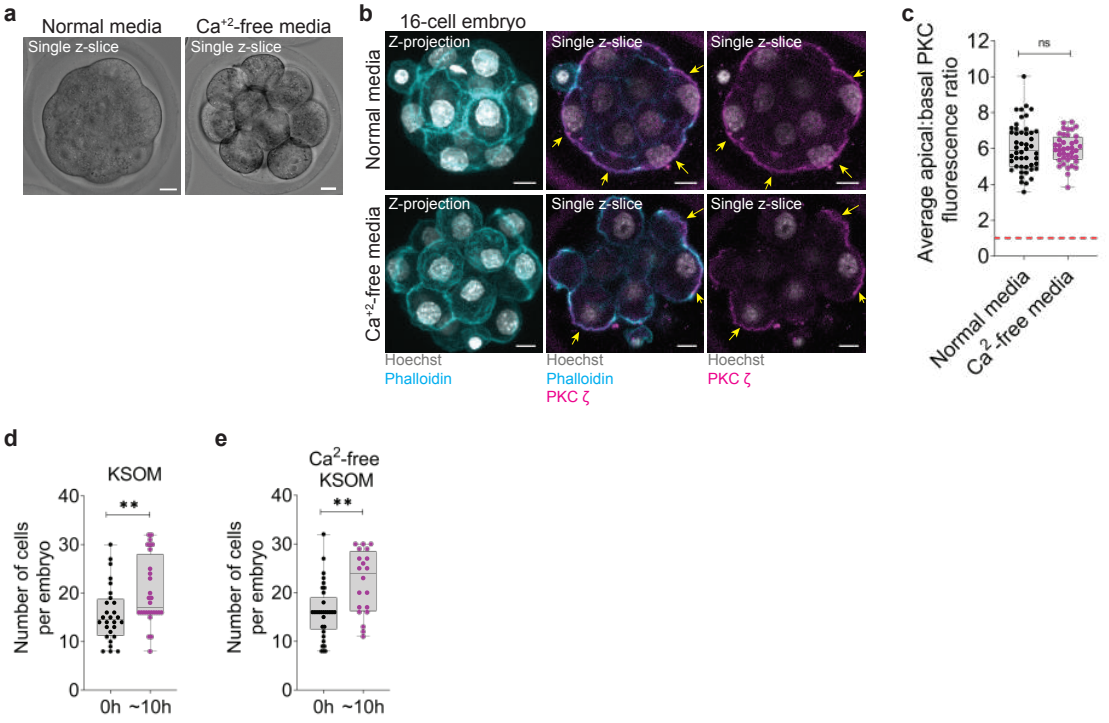

Fig S4. Embryos treated with Ca^{+2}-free media form apical domains and undergo cell division. **(a)** Representative brightfield images of 16-cell embryos exposed to either normal (left) or Ca^{+2}-free media (right). Note that upon treatment with Ca^{+2}-free media, compaction is abolished and all blastomeres have a nearly identical round shape. **(b)** Representative immunofluorescence images of 16-cell embryos exposed to either normal (top) or Ca^{+2}-free media (bottom). Note that in both groups, the apical domain (PKC ζ staining, magenta) is present in outer cells (yellow arrows). **(c)** Quantification of average PKC ζ apical:basal fluorescence ratio of outer cells in 16-cell embryos exposed to normal (n=48 embryos) or Ca^{+2}-free media (n=40 embryos; unpaired two-tailed t test, *P*=0.6809). **(d)** Quantification of average cell number per embryo before (n=28 embryos) and after ~10h exposure to normal media (n=28 embryos; two-tailed Mann-Whitney test, ***P*=0.0044). **(e)** Quantification of average cell number per embryo before (n=33 embryos) and after ~10h exposure to Ca^{+2}-free media (n=20 embryos; two-tailed Mann-Whitney test, ***P*=0.0010). Scale bars = 10μm. In the box plots, the centre line represents the median, the bounds of the box represent upper and lower quartiles, the whiskers represent minimum and maximum values, and dots represent independent measurements. See also Figure 2.

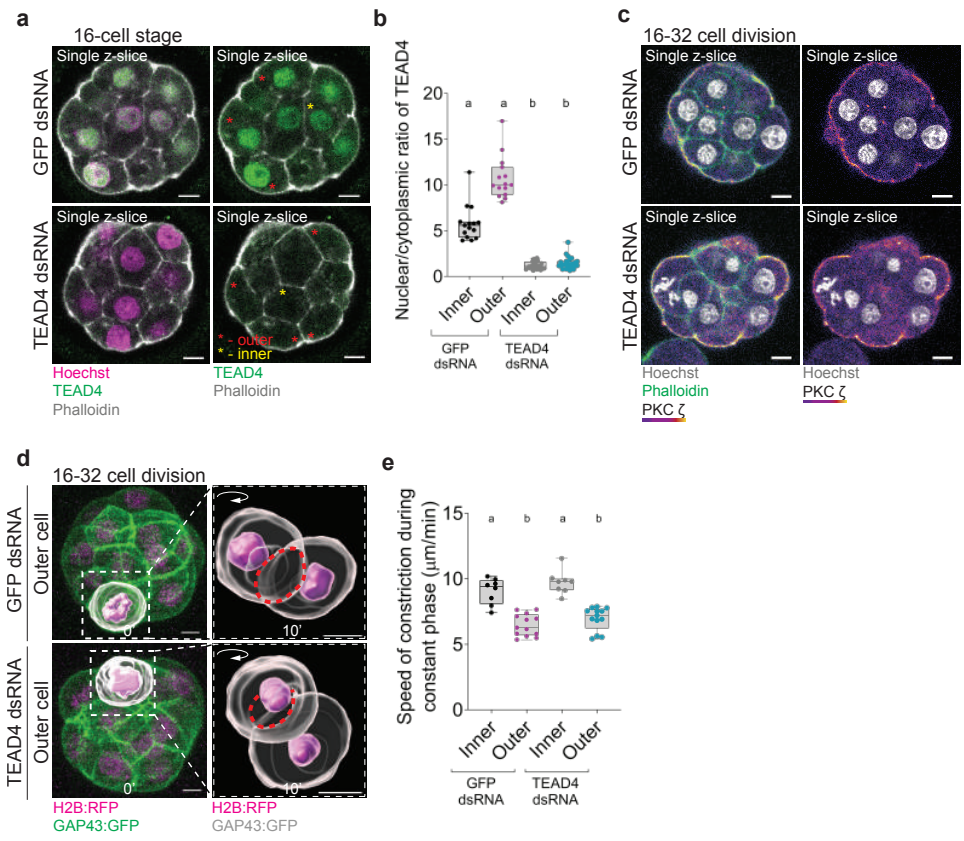

Fig S5. TEAD4 knockdown does not affect apical polarity emergence and does not alter the speed of constriction of outer cells. (a) Representative immunofluorescence images of 16-cell embryos previously injected at the 2-cell stage with either GFP dsRNA (top) or TEAD4 dsRNA (bottom). **(b)** Quantification of nuclear/cytoplasmic ratio of TEAD4 in 16-cell embryos previously injected with either GFP dsRNA (n=15 embryos) or TEAD4 dsRNA (n=26 embryos; Kruskal-Wallis test with multiple comparisons). **(c)** Representative immunofluorescence images of embryos undergoing the 16-32 cell division previously injected with either GFP dsRNA (top; example shown has 26 cells) or TEAD4 dsRNA (bottom; example has 25 cells). Note that in both groups, the apical polarity marker PKC ζ (magenta) is present in outer cells. **(d)** Representative time-lapse 3D reconstructions of outer blastomeres undergoing the 16-32 cell division from embryos previously injected with GFP dsRNA (example has 18 cells) or TEAD4 dsRNA (example has 21 cells) and co-expressing H2B:RFP (magenta) and GAP43:GFP (green/grey). **(e)** Quantification of average speed of constriction of inner and outer blastomeres undergoing the 16-32 cell division from embryos previously injected with GFP dsRNA (inner n=8 blastomeres; outer n=13 blastomeres from a total of 12 embryos) or TEAD4 dsRNA (inner=8 blastomeres; outer n=13 blastomeres from a total of 13 embryos; Kruskal-Wallis with multiple comparisons). Time is shown in minutes, where 0' is anaphase onset. Scale bars = 10µm. In the box plots, the centre line represents the median, the bounds of the box represent upper and lower quartiles, the whiskers represent minimum and maximum values, and dots represent independent measurements. In multiple comparison analyses, different letters represent statistical significance at $P<0.05$. See also Figure 2.

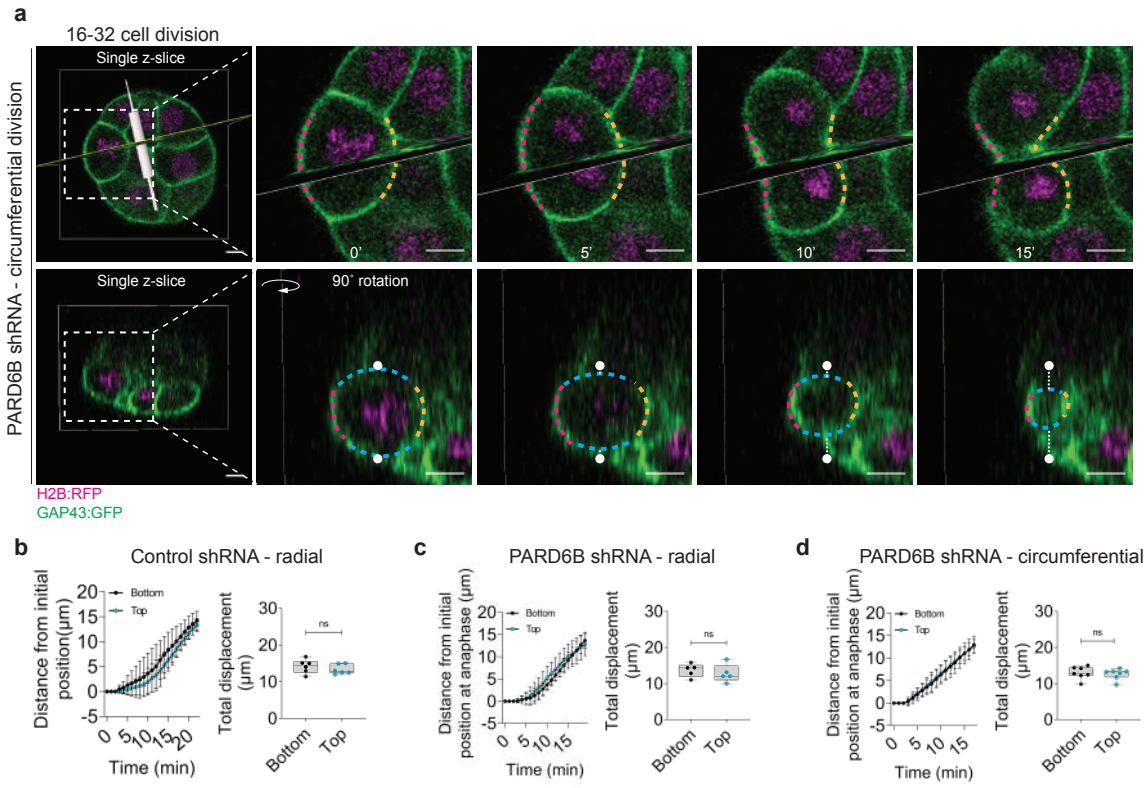

Fig S6. Three-dimensional analysis of furrow ingression rate. (a) Representative time-lapse images of a circumferentially-dividing outer blastomere undergoing the 16-32 cell division (example shown has 20 cells) from an embryo previously injected with PARD6B shRNA. In the top row, note that when 2D furrow ingression analysis revealed furrow ingression rate to be approximately equal in both sides of the furrow, the images were rotated 90º in IMARIS and the same analysis was performed using the portions of the furrow that were not originally visible in the 2D plane of image (blue dashed lines). **(b-d)** Average distance from initial furrow position at anaphase onset and total furrow displacement in radially dividing outer blastomeres undergoing the 16-32 cell division from embryos previously injected with control shRNA (n=6 blastomeres from 5 embryos; two-tailed paired t test, ns *P*=0.3096) **(b)**; radially dividing outer blastomeres undergoing the 16-32 cell division from embryos previously injected with PARD6B shRNA (n=5 blastomeres from 5 embryos; two-tailed paired t test, ns *P*=0.4402) **(c)**; and circumferentially dividing outer blastomeres undergoing the 16-32 cell division from embryos previously injected with PARD6B shRNA (n=7 blastomeres from 5 embryos; two-tailed paired t test, ns *P*=0.4394) **(d)**. Time is shown in minutes, where 0' is anaphase onset. Scale bars = 10μm. In the box plots, the centre line represents the median, the bounds of the box represent upper and lower quartiles, the whiskers represent minimum and maximum values, and dots represent independent measurements. See also Figure 3.

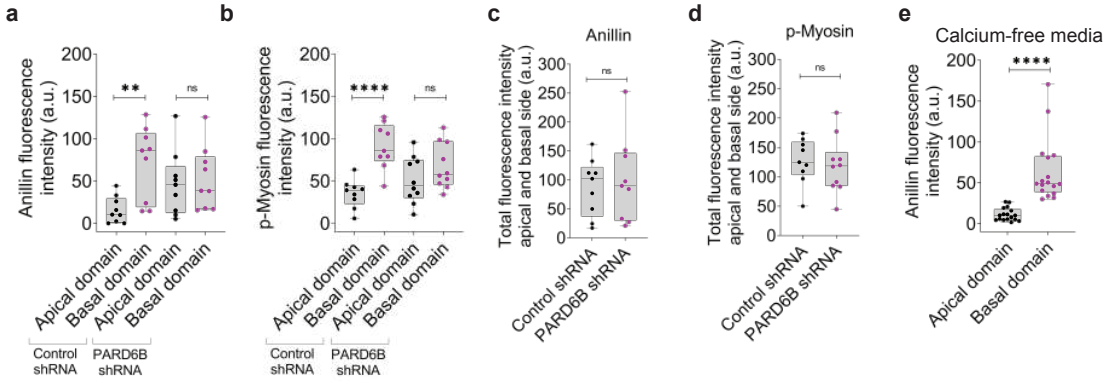

Fig S7. Anillin and p-Myosin are asymmetrically distributed in outer blastomeres. (a) Background-subtracted fluorescence intensity of Anillin in apical vs basal sides in outer blastomeres undergoing the 16-32 cell division from embryos previously injected with control (n=9 blastomeres from 9 embryos two-tailed paired t test, ***P*=0.004) or PARD6B shRNA (n=9 blastomeres from 9 embryos; two-tailed paired t test, *P*=0.2946). **(b)** Background-subtracted fluorescence intensity of p-Myosin in apical vs basal sides in outer blastomeres undergoing the 16-32 cell division from embryos previously injected with control (n=9 blastomeres from 9 embryos; two-tailed paired t test, *****P*<0.0001) or PARD6B shRNA (n=10 blastomeres from 10 embryos; two-tailed paired t test, *P*=0.0706). **(c)** Total (sum) Anillin fluorescence intensity in apical and basal sides of the contractile ring in blastomeres undergoing the 16-32 cell division from embryos previously injected with either control (n = 9 blastomeres from 9 embryos) or PARD6B shRNA (n = 9 blastomeres from 9 embryos; two-tailed unpaired t test, *P*=0.6881). **(d)** Total (sum) p-Myosin fluorescence intensity in apical and basal sides of the contractile ring in blastomeres undergoing the 16-32 cell division from embryos previously injected with either control (n = 9 blastomeres from 9 embryos) or PARD6B shRNA (n =10 blastomeres from 10 embryos; two-tailed unpaired t test, *P*=0.7006). **(e)** Background-subtracted fluorescence intensity of Anillin in apical vs basal sides in outer blastomeres undergoing the 16-32 cell division from embryos cultured in Ca^{+2}-free media (n= 17 blastomeres from 17 embryos, two-tailed paired Wilcoxon test, *****P*<0.0001). In the box plots, the centre line represents the median, the bounds of the box represent upper and lower quartiles, the whiskers represent minimum and maximum values, and dots represent independent measurements. See also Figure 4.

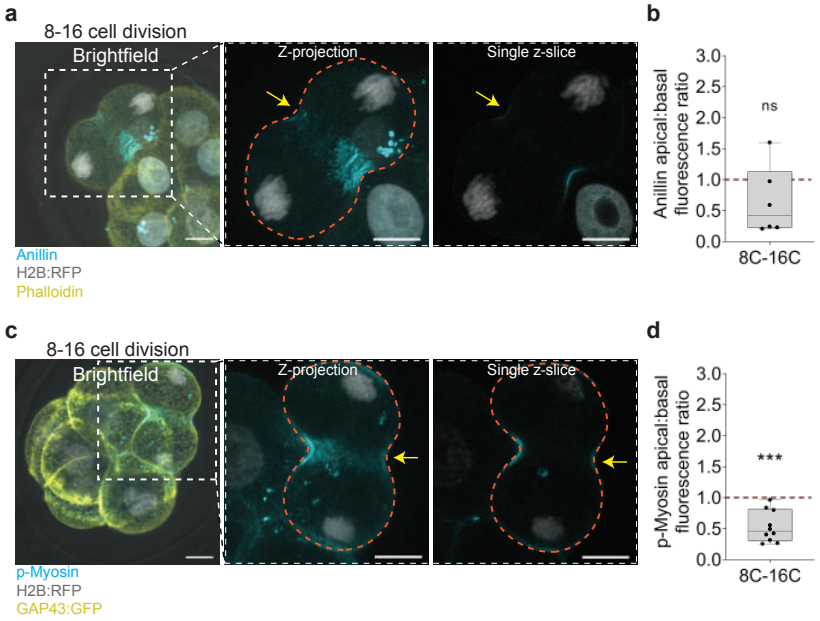

Fig S8. Anillin and p-Myosin are underrepresented in the apical side of the contractile ring in circumferentially dividing 8-cell blastomeres. (a and c) Representative immunofluorescence images of circumferentially dividing blastomeres undergoing the 8-16 cell division (examples shown both in (a) and (c) have 8 cells each). Note that both Anillin **(a)** and p-Myosin **(c)** are underrepresented at the side of contractile ring that overlaps with the apical domain (yellow arrows). **(b)** Anillin apical:basal fluorescence ratio in blastomeres undergoing the 8-16 cell division (n=6 blastomeres from 6 embryos; one-sample t test, *P*=0.1762). **(d)** p-Myosin apical:basal fluorescence ratio in blastomeres undergoing the 8-16 cell division (n=10 blastomeres from 10 embryos; one-sample t test, ****P*=0.0003, significant deviation from 1). Scale bars = 10μm. In the box plots, the centre line represents the median, the bounds of the box represent upper and lower quartiles, the whiskers represent minimum and maximum values, and dots represent independent measurements.

Table S1. Composition of Ca^{+2}-free KSOM media.

Component	Concentration (mM)	Source	Observation
NaCl	95	Sigma – S9625	
KCl	2.5	Sigma – P5405	
KH_2PO_4	0.35	Sigma – P5655	
$MgSO_4.7H_2O$	0.2	Sigma – 230391	
Na lactate	10	Sigma – L1375	
D-glucose	0.2	Sigma – G8270	
Na pyruvate	0.2	Sigma – P3662	
$NaHCO_3$	25	Sigma – S5761	
L-glutamine	1	Sigma – G7513	
$EDTA.2H_2O$	0.01	Sigma – E5134	pH = 7.3
K Penicillin G	0.16	Sigma – P7799	
Streptomycin SO_4	0.03	Sigma – S6501	
BSA	1 mg/mL	Sigma – A7906	Added before usage

The media was equilibrated in incubator (37˚C, 5% CO_2) for 24h, followed by pH adjustment to 7.3.

Supplementary Video 1: Mouse embryos cultured in Ca^{+2}-free media.
Time-lapse video of mouse embryos co-expressing H2B:RFP (magenta) and GAP43:GFP (green) and undergoing the 16- to 32-cell division in Ca^{+2}-free KSOM. Brightfield images are shown on the right. Live embryos were imaged for 16h with 1min interval image acquisitions on the confocal microscope. This video shows images every 30min. Note that embryos successfully undergo the 16- to 32-cell transition and cells appear heathy in Ca^{+2}-free media for 16h. Scale = 20μm.

Annexe 3

The following is the published version of Chapter 4 of this thesis, published in the journal Reproduction in 2020.

REPRODUCTION
POINT OF VIEW

The impact of embryo binucleation depends upon its origin

Lia Mara Gomes Paim[1] and Greg FitzHarris[1,2]

[1]*Centre de Recherche du Centre Hospitalier de l'Université de Montréal, Montréal, Québec, Canada and*
[2]*Département d'Obstétrique-Gynécologie, Université de Montréal, Montréal, Québec, Canada*

Correspondence should be addressed to G FitzHarris; Email: greg.fitzharris@umontreal.ca

Summary

Preimplantation embryos frequently contain binucleated cells, but reports differ as to whether binucleation affects development and whether such embryos should be used clinically. In this Point Of View article, we propose a possible explanation for this disparity: binucleation can arise by distinct routes, one that produces healthy blastomeres and one that directly threatens embryo viability.
Reproduction (2020) **160** V1–V4

The success of *in vitro* fertilisation cycles relies heavily on the choice of the most suitable embryo to be transferred to patients. Despite the emergence in recent years of a myriad of exotic means of embryo testing, embryo selection remains mainly based on morphological features observable under the light microscope, such as stage appropriate cell numbers, cytoplasmic fragmentation patterns, and nucleus configuration. Binucleation is the scenario wherein a blastomere within an embryo contains two evenly sized nuclei and is an example of a feature of nuclear morphology that can be seen under a microscope. Note that, in this Point of View article, we refer principally to truly binucleated embryos and not to other types of nuclear aberration such as micronucleation, where cells contain an extra 'mini' nucleus, or multinucleation, where three or more nuclei are seen in a blastomere. Binucleation is a relatively common phenomenon in human embryos in *in vitro* fertilisation cycles, with frequencies ranging from 7 to 65% of embryos depending on the stage of development examined (Hardy *et al.* 1993, Meriano *et al.* 2004, Aguilar *et al.* 2016, Seikkula *et al.* 2018). Although it is perhaps intuitive that to have two nuclei in a given cell should be indicative of poor prognosis for the embryo, contrasting and perhaps puzzling results as to the developmental potential and clinical outcomes of these embryos have been reported. Some studies report that the presence of binucleated blastomeres causes decreased developmental potential and implantation rates (Hardy *et al.* 1993, Aguilar *et al.* 2016, Seikkula *et al.* 2018). On the other hand, perhaps surprisingly, other reports seem to suggest that embryos containing binucleated blastomeres have relatively normal developmental potential (Staessen & Van Steirteghem 1998, Meriano *et al.* 2004). An explanation for the apparently divergent reports is not apparent, and thus the use of binucleation as a means of embryo selection is not widely implemented. Here, following recent mechanistic studies of cell divisions and nuclear morphology in mouse embryos, we propose that binucleation can originate by two mechanistically distinct routes, depending on whether it occurs at the 2-cell stage or at later stages of development, and that these two routes to binucleation have contrasting implications for embryo health that explain the apparent conflicting reports.

The origins of binucleation in mid-preimplantation development (~16-cell stage) human embryos were studied by Hardy *et al.* (1993), who found that binucleated blastomeres at the 16-32 cell stage had double the amount of cytoplasm compared to mononucleated counterparts, and thus concluded that binucleated blastomeres arise as a result of a failure of cytokinesis, the final step of cell division. Although other routes to binucleation can be envisaged, such as cell fusion, cytokinesis failure is generally considered the most common route to binucleation in somatic cells, and thus the conclusions of Hardy *et al.* appear very likely. Cytokinesis failure (or indeed cell fusion) means that the resulting blastomere contains an entire duplicated genome complement (i.e. tetraploid). Consistent with this, complete tetraploidy has been described in spontaneous abortions (Genest *et al.* 1995), as well as in embryos undergoing preimplantation genetic screening (Bielanska *et al.* 2002), and the rare cases of tetraploid live-born infants display severe developmental abnormalities, with a lifespan limited to months (Stefanova *et al.* 2010), indicative that tetraploidy is indeed a feature of early embryo development and poses severe consequences for fertility and life. Recent mechanistic studies in mouse embryos have uncovered at least two reasons why tetraploid blastomeres in mid-preimplantation development should jeopardise the likelihood of a successful pregnancy. First, it was shown

ISSN 1470–1626 (paper) 1741–7899 (online)
https://doi.org/10.1530/REP-20-0188
Online version via https://rep.bioscientifica.com

that tetraploidy resulting from cytokinesis failure at the 4–8 cell division increases the rates of chromosome segregation errors and consequently favors the development of further aneuploidy (Paim & FitzHarris 2019) (Fig. 1). Such errors could lead to the complex and chaotic karyotypes seen in embryo blastomeres which are widely associated with embryonic failure (Bielanska *et al*. 2002). Second, tetraploidy in early mouse embryos has been shown to reduce the number of cells available to form the inner cell mass within the blastocyst that forms the embryo proper (Eakin *et al*. 2005, LMG Paim and G FitzHarris, unpublished observations). Why this decrease in the number of cells takes place is not entirely clear, but it is likely that fewer but larger cells at the time of blastocoel formation reduce the availability of 'inner' cells to form the ICM. Thus, binucleation in later stage embryos likely occurs by cytokinesis failure and threatens embryo viability in at least two ways (Fig. 1).

In contrast, a recent examination of the first mitosis (1-cell to 2-cell transition) in mouse leads us to suggest that binucleation at the 2-cell stage in human embryos may arise by an entirely different means. Reichmann *et al*. (2018) demonstrated that each pronucleus in the mouse zygote originates two spatially separate parental genomes that initially remain individualised during the first mitotic division (Fig. 1). As the first mitosis progresses, two independent spindles are assembled (one for each parental genome), which eventually fuse to align the maternal and paternal genome before anaphase. Interestingly, experimentally induced failure to align the two zygotic spindles leads to the formation of perfectly binucleated 2-cell embryos (Reichmann

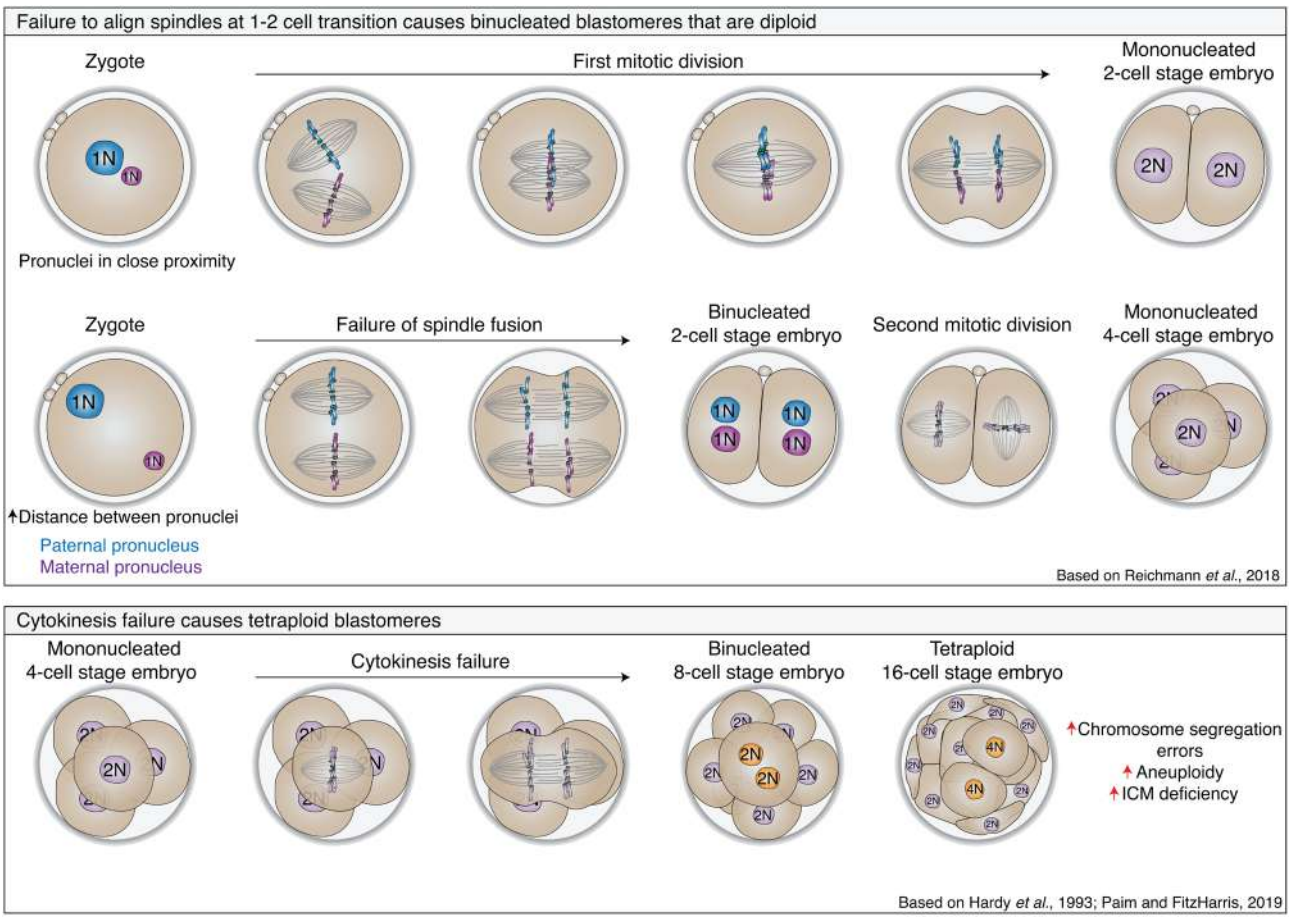

Figure 1 Two mechanistically distinct modes of binucleation might explain divergent clinical outcomes. Top panel: At the zygote stage, the paternal and maternal pronuclei are maintained physically separated due to the assembly of two individualized mitotic spindles. Further into the first mitotic division, the spindles fuse such that the parental genome is aligned in a single metaphase plate, allowing cell division to take place, and a diploid mononucleated 2-cell stage embryo is formed. Middle panel: In cases where the two parental pronuclei are too distant from each other, the two individualized spindles fail to fully fuse and cell division takes place without alignment of the parental genomes, resulting in a 2-cell stage embryo with two haploid nuclei. This scenario is likely not deleterious to development, since the resulting 2-cell embryo remains with a diploid genome complement. Bottom panel: Binucleation later in development more likely indicates cytokinesis failure or regression (which may be mistaken optically for cell fusion), which would lead to tetraploidy. This is followed by an increase in the levels of chromosomes segregation errors, allowing for the accumulation of highly aneuploid blastomeres that potentially lead to low implantation rates.

et al. 2018) (Fig. 1). Although the implications of this were not explored, each nucleus would be haploid and thus each cell should logically be overall diploid. Since binucleated cells can assemble a single spindle and form mononucleated daughter cells (Paim & FitzHarris 2019), resulting 4-cell embryos would be expected to be mononucleated, euploid (overall correct chromosome complement), and as such be identical to other 'normal' embryos that were never binucleated (Fig. 1). Thus, although it remains to be formally tested, we propose that binucleation at the 2-cell stage under these circumstances likely has minimal impact upon developmental potential.

To our knowledge, this explanation to the varied results of clinical binucleation studies mentioned has not previously been proposed. And while the tendency of many clinical studies to group binucleation in conjunction with other forms of nuclear aberration (micronucleation, multinucleation – which themselves very likely have severe consequences for embryo development (Vazquez-Diez *et al.* 2016)) muddies the issue in some cases, close examination of a few key papers lends some support for our proposal. Specifically, Staessen and Van Steirteghem (1998) showed that blastomeres karyotyped at the 3–8 cell stage from embryos previously scored as binucleated at the 2-cell stage are frequently diploid. This strongly supports the notion that the binucleated 2-cell blastomere can be diploid. Perhaps most intriguingly, one study that carefully distinguished binucleated embryos from multinucleated and mononucleated, and then by developmental stage, found that embryos displaying 2/4 binucleated blastomeres at the 4-cell stage never implanted, whereas implantation rates were normal in embryos binucleated at the 2-cell stage (Aguilar *et al.* 2016). The studies described previously (Staessen & Van Steirteghem 1998, Bielanska *et al.* 2002) used karyotyping techniques now considered outdated such as FISH, and further analyses of the ploidy status of binucleated embryos using more reliable modern approaches are certainly warranted. Nevertheless, the findings described by Aguilar *et al.* (2016), Reichmann *et al.* (2018), and Paim and FitzHarris (2019) support the notion that binucleation at different stages of development might affect embryo health differently. Therefore, we hypothesise that the discordant conclusions on the impact of binucleation are a result of the different impacts of binucleation at different developmental stages; whereas binucleation in mid- to late-preimplantation development very likely indicates an error of chromosomal content, binucleation at 2-cell stage may not.

How and why cytokinesis failure comes about, whether a single binucleated/tetraploid blastomere is sufficient to significantly disrupt embryonic development at a given developmental stage, and to what extent embryos can tolerate binucleation/tetraploidy and still give rise to healthy live births, all remain unknown. However, the developments discussed here underscore the importance of foundational molecular research to understand and interpret the biological basis of phenomena observed in the clinic. Non-invasive means of selecting the best embryo(s) for transfer in the clinic remains one of the holy grails of reproductive medicine, and it is our hope that this re-interpretation of the impact of binucleation, paired with improvements in time-lapse microscopy, may ultimately lead to better paradigms and tools for embryo sorting. Essential in this will be further studies that carefully distinguish the developmental stage at which true binucleation occurs.

Declaration of interest

G FitzHarris is on the editorial board of *Reproduction*. G FitzHarris was not involved in the review or editorial process for this paper, on which he is listed as an author. L M Gomes Paim has nothing to disclose.

Funding

This work did not receive any specific grant from any funding agency in the public, commercial, or not-for-profit sector.

Author contribution statement

L M G P and G F wrote the manuscript. L M G P produced the figure.

Acknowledgements

The authors thank Drs Alexander Bruce and Jim Meriano for comments on the manuscript. Work in G F's lab is supported by grants from the Natural Sciences and Engineering Research Council of Canada, Fondation Jean-Louis Lévesque, Canadian Foundation for Innovation, and the Canadian Institutes of Health Research. L M G P is supported by a Fonds de Recherche du Québec – Santé Doctoral Scholarship.

References

Aguilar J, Rubio I, Munoz E, Pellicer A & Meseguer M 2016 Study of nucleation status in the second cell cycle of human embryo and its impact on implantation rate. *Fertility and Sterility* **106** 291.e2–299.e2. (https://doi.org/10.1016/j.fertnstert.2016.03.036)

Bielanska M, Tan SL & Ao A 2002 Chromosomal mosaicism throughout human preimplantation development in vitro: incidence, type, and relevance to embryo outcome. *Human Reproduction* **17** 413–419. (https://doi.org/10.1093/humrep/17.2.413)

Eakin GS, Hadjantonakis AK, Papaioannou VE & Behringer RR 2005 Developmental potential and behavior of tetraploid cells in the mouse embryo. *Developmental Biology* **288** 150–159. (https://doi.org/10.1016/j.ydbio.2005.09.028)

Genest DR, Roberts D, Boyd T & Bieber FR 1995 Fetoplacental histology as a predictor of karyotype: a controlled study of spontaneous first trimester abortions. *Human Pathology* **26** 201–209. (https://doi.org/10.1016/0046-8177(95)90038-1)

Hardy K, Winston RM & Handyside AH 1993 Binucleate blastomeres in preimplantation human embryos in vitro: failure of cytokinesis during

early cleavage. *Journal of Reproduction and Fertility* **98** 549–558. (https://doi.org/10.1530/jrf.0.0980549)

Meriano J, Clark C, Cadesky K & Laskin CA 2004 Binucleated and micronucleated blastomeres in embryos derived from human assisted reproduction cycles. *Reproductive Biomedicine Online* **9** 511–520. (https://doi.org/10.1016/s1472-6483(10)61635-5)

Paim LMG & Fitzharris G 2019 Tetraploidy causes chromosomal instability in acentriolar mouse embryos. *Nature Communications* **10** 4834. (https://doi.org/10.1038/s41467-019-12772-8)

Reichmann J, Nijmeijer B, Hossain MJ, Eguren M, Schneider I, Politi AZ, Roberti MJ, Hufnagel L, Hiiragi T & Ellenberg J 2018 Dual-spindle formation in zygotes keeps parental genomes apart in early mammalian embryos. *Science* **361** 189–193. (https://doi.org/10.1126/science.aar7462)

Seikkula J, Oksjoki S, Hurme S, Mankonen H, Polo-Kantola P & Jokimaa V 2018 Pregnancy and perinatal outcomes after transfer of binucleated or multinucleated frozen-thawed embryos: a case-control study. *Reproductive Biomedicine Online* **36** 607–613. (https://doi.org/10.1016/j.rbmo.2018.02.003)

Staessen C & Van Steirteghem A 1998 The genetic constitution of multinuclear blastomeres and their derivative daughter blastomeres. *Human Reproduction* **13** 1625–1631. (https://doi.org/10.1093/humrep/13.6.1625)

Stefanova I, Jenderny J, Kaminsky E, Mannhardt A, Meinecke P, Grozdanova L & Gillessen-Kaesbach G 2010 Mosaic and complete tetraploidy in live-born infants: two new patients and review of the literature. *Clinical Dysmorphology* **19** 123–127. (https://doi.org/10.1097/MCD.0b013e3283353877)

Vazquez-Diez C, Yamagata K, Trivedi S, Haverfield J & Fitzharris G 2016 Micronucleus formation causes perpetual unilateral chromosome inheritance in mouse embryos. *PNAS* **113** 626–631. (https://doi.org/10.1073/pnas.1517628112)

Received 2 April 2020
First decision 9 April 2020
Revised manuscript received 10 April 2020
Accepted 24 April 2020

Annexe 4

The following is a collaborative publication developed during my Ph.D. published in the journal Current Biology in 2019, where I performed some of the experiments that demonstrate that the Spindle Assembly Checkpoint is ineffective in early embryos.

Report

Current Biology

Cell-Size-Independent Spindle Checkpoint Failure Underlies Chromosome Segregation Error in Mouse Embryos

Highlights

- The spindle assembly checkpoint is ineffective in early mouse embryos
- Checkpoint fallibility is not attributable to the large size of early embryo cells
- APC/C partial inhibition can reduce the number of segregation errors in embryos

Authors

Cayetana Vázquez-Diez, Lia Mara Gomes Paim, Greg FitzHarris

Correspondence

greg.fitzharris@umontreal.ca

In Brief

Chromosome segregation errors following fertilization lead to so-called mosaic-aneuploid embryos, which are thought to reduce the chance of a successful pregnancy. Here, Vázquez-Diez et al. provide evidence that the error-prone nature of those first few mitotic divisions may be attributable to an unusual weakness in the spindle assembly checkpoint.

Vázquez-Diez et al., 2019, Current Biology *29*, 865–873
March 4, 2019
https://doi.org/10.1016/j.cub.2018.12.042

CellPress

Current Biology
Report

Cell-Size-Independent Spindle Checkpoint Failure Underlies Chromosome Segregation Error in Mouse Embryos

Cayetana Vázquez-Diez,[1] Lia Mara Gomes Paim,[1] and Greg FitzHarris[1,2,3,*]
[1]Centre de Recherche du Centre Hospitalier de l'Université de Montréal, 900 Rue St-Denis, Montréal, QC H2X 0A9, Canada
[2]Département d'Obstétrique-Gynécologie, Faculté de Médecine, Université de Montréal, 175 chemin de la Côte-Sainte-Catherine, Montréal, QC H3T 1C5, Canada
[3]Lead Contact
*Correspondence: greg.fitzharris@umontreal.ca
https://doi.org/10.1016/j.cub.2018.12.042

SUMMARY

Chromosome segregation errors during mammalian preimplantation development cause "mosaic" embryos comprising a mixture of euploid and aneuploid cells, which reduce the potential for a successful pregnancy [1–5], but why these errors are common is unknown. In most cells, chromosome segregation error is averted by the spindle assembly checkpoint (SAC), which prevents anaphase-promoting complex (APC/C) activation and anaphase onset until chromosomes are aligned with kinetochores attached to spindle microtubules [6, 7], but little is known about the SAC's role in the early mammalian embryo. In *C. elegans*, the SAC is weak in early embryos, and it strengthens during early embryogenesis as a result of progressively lessening cell size [8, 9]. Here, using live imaging, micromanipulation, gene knockdown, and pharmacological approaches, we show that this is not the case in mammalian embryos. Misaligned chromosomes in the early mouse embryo can recruit SAC components to mount a checkpoint signal, but this signal fails to prevent anaphase onset, leading to high levels of chromosome segregation error. We find that failure of the SAC to prolong mitosis is not attributable to cell size. We show that mild chemical inhibition of APC/C can extend mitosis, thereby allowing more time for correct chromosome alignment and reducing segregation errors. SAC-APC/C disconnect thus presents a mechanistic explanation for frequent chromosome segregation errors in early mammalian embryos. Moreover, our data provide proof of principle that modulation of the SAC-APC/C axis can increase the likelihood of error-free chromosome segregation in cultured mammalian embryos.

RESULTS AND DISCUSSION

SAC Is Ineffective and Cell-Size Independent in the Early Mouse Embryo

The major cellular safeguard preventing chromosome segregation errors in many cell types is the spindle assembly checkpoint (SAC), a near-ubiquitous signaling pathway that delays anaphase onset. Unattached kinetochores catalyze the generation of the mitotic checkpoint complex (MCC), a diffusible signal that inhibits the anaphase-promoting complex (APC/C), preventing anaphase until correct attachment is achieved [6, 7]. In mouse embryos, the level of aneuploidy can be exacerbated by SAC inhibition, and thus, to date, it has been assumed that the SAC is in operation in the early embryo [1, 10]. However, a detailed examination of SAC function, or an explanation as to why segregation errors are normally common in the early embryo, is yet to be presented. In *C. elegans* embryos, the SAC is ineffective during the initial cell divisions after fertilization, and it becomes more stringent as cells reduce in size during early development, an effect attributed to limited amounts of diffusible MCC to inhibit APC/C throughout the cytoplasm in larger cells [8, 9]. Consistent with this notion, it is well established that the SAC is relatively inefficient in preventing segregation errors in the mammalian oocyte [11–14], and experimental manipulations that reduce oocyte size can strengthen the SAC [15, 16]. Based on these observations, we hypothesized that the SAC might be particularly weak in early mammalian embryos and that a similar cell-size-dependent strengthening of the SAC-APC/C axis might occur as cells lessen in size during preimplantation development.

To test our hypothesis, we first performed live imaging of H2B:RFP-expressing embryos in the presence and absence of a mild spindle challenge (10 nM nocodazole), and we used the resulting increase in mitotic duration as a measure of SAC strength at different developmental stages. Mouse embryos progress from a fertilized 1-cell embryo to an 8- to 32-cell stage morula and a 64- to 128-cell blastocyst over the course of 4–5 days. Blastomeres approximately halve in size at each cell division, causing cells to decrease in size ~40-fold from ~200 pL at the 1-cell stage, similar to the oocyte, to ~5 pL at the blastocyst stage [17, 18]. Low-dose nocodazole prolonged mitosis significantly at the 2-cell stage and in blastocysts, but not in embryos at the 4- to 8-cell stage or in morulae (Figure S1), suggesting no direct relationship between cell size and SAC efficiency. In mouse embryos, the mechanism of spindle assembly is modulated during preimplantation development [17, 19]. Therefore, we sought a second approach to examine the SAC and cell size that would dissociate any potential impacts of the developmental stage, and we chose to use embryo micromanipulation to directly alter cell size (Figure 1A). Up to 40% of cytoplasm was

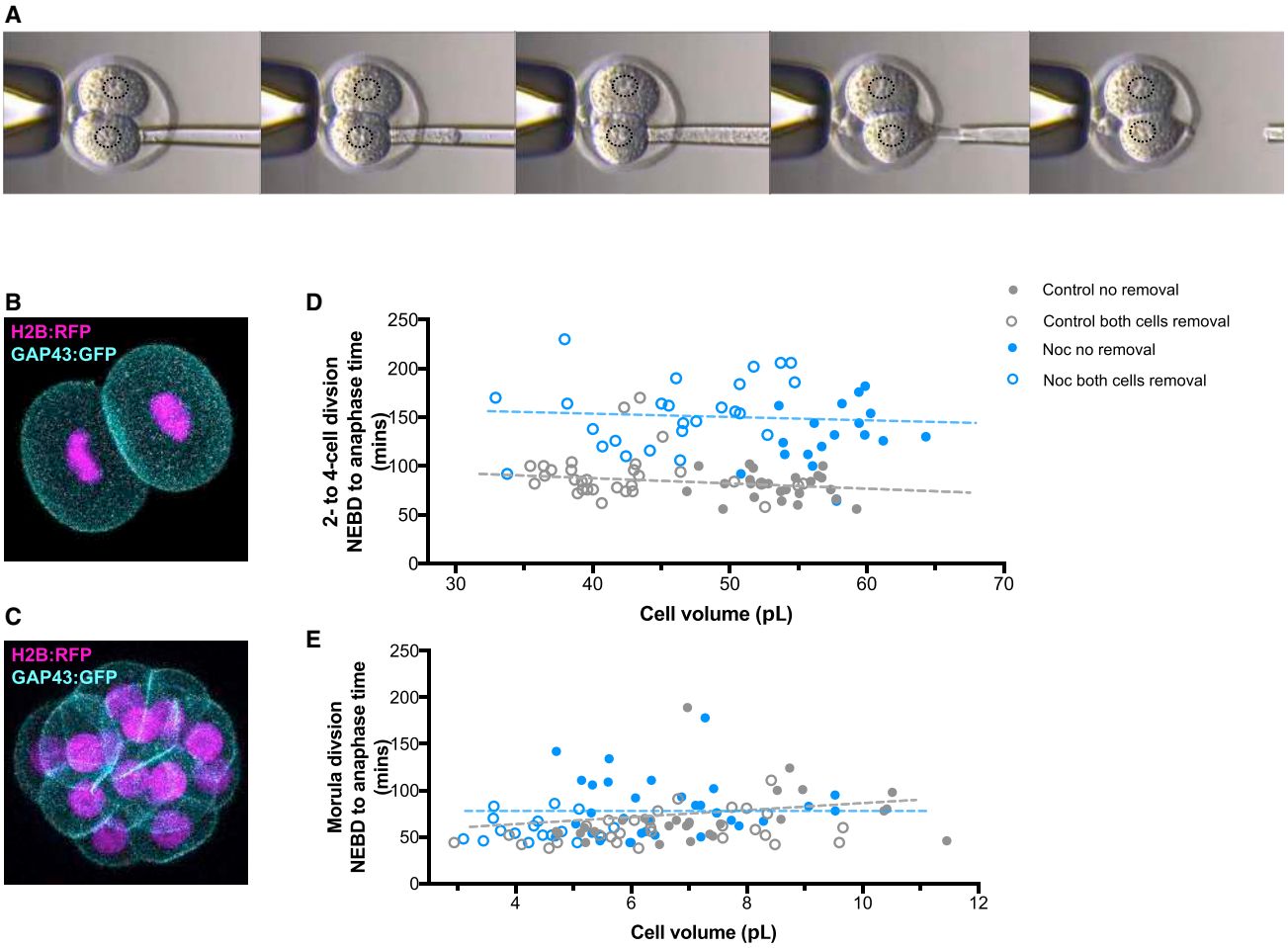

Figure 1. SAC Strength Is Cell-Size Independent

(A) Representative images of cytoplasmic removal technique in 2-cell embryos.

(B and C) Representative images of 2-cell (B) and morula H2B:RFP-GAP43:GFP-expressing (C) embryos, respectively.

(D and E) Scatterplot of mitosis duration and cell volume measured at metaphase for individual cells from embryos that were either un-manipulated or had been subjected to cytoplasmic reduction in both cells at the 2-cell stage. Experiments were performed for both groups in control or 10 nM nocodazole conditions at the 2- to 4-cell stage and morula divisions ($n \geq 17$ divisions/group, correlation analysis, $r = -0.11$ and -0.17 at 2–4C, $r = 0.33$ and -0.24 at morula, in control, and 10 nM nocodazole, respectively).

See also Figure S1.

removed from interphase 2-cell embryos using a cytoplasm-aspiration pipette. Mitosis was then examined in the presence and absence of nocodazole at the 2- to 4-cell transition and in morulae (Figures 1B–1E). Importantly, embryos co-expressed H2B:RFP (chromosomes) and GAP43:GFP (plasmalemma) during live imaging, allowing mitosis duration and cell volume to be simultaneously analyzed on a cell-by-cell basis. Blastomeres in cytoplasm-reduced morulae were as small as 3 pL in volume, smaller than many cultured cells, which are generally ~2–5 pL in volume [20]. As in the previous experiment (Figure S1), nocodazole extended mitosis at the 2-cell stage, but did not extend mitosis in morulae (Figures 1B–1E). However, regression analysis showed no association between cell size and mitosis duration at either developmental stage, regardless of the presence or absence of nocodazole. Similar results were obtained in a separate series of experiments in which only a single blastomere was manipulated per embryo (Figure S1). Thus, unexpectedly, these experiments suggest that SAC strength varies during development in a manner unrelated to cell size.

SAC Signaling Fails to Prevent Chromosome Segregation Errors in Embryos

We next set out to perform a more detailed examination of the SAC in morula-stage embryos, which showed little to no increase in mitosis duration in response to low-dose nocodazole in the previous experiments. Classically, in somatic cells, a single misaligned chromosome is sufficient to sustain robust SAC signaling and prevent anaphase [21]. We examined 102 cell divisions in morulae using live imaging in the absence of any treatments, and we found that chromosomes were fully aligned at the time of anaphase onset in 76% of divisions. However, a significant subset of divisions progressed into anaphase despite

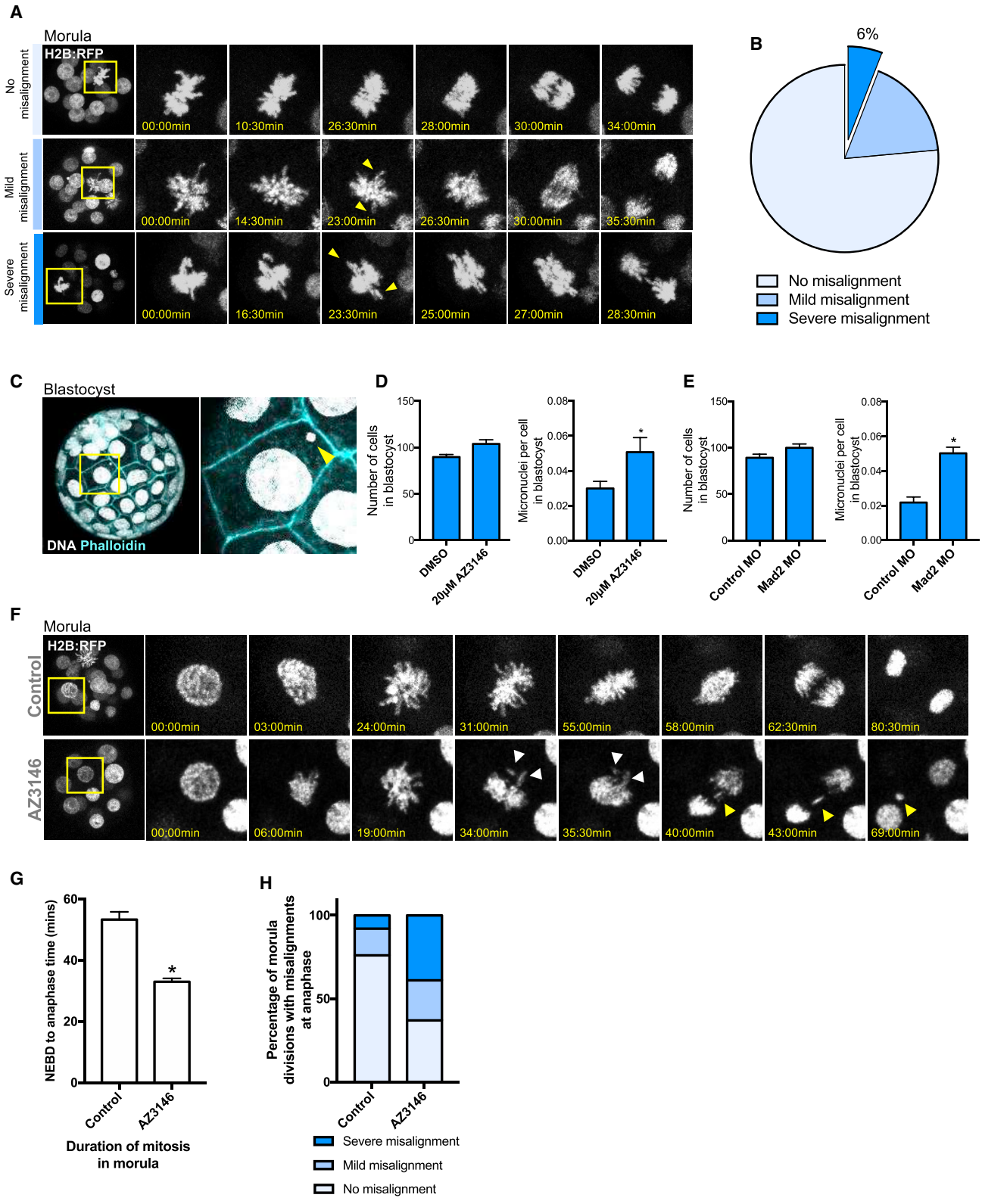

Figure 2. SAC Signaling Fails to Prevent Mitotic Errors

(A and B) Representative confocal images of H2:BRFP-expressing embryos (A) and analysis of chromosome alignment (B) prior to anaphase (n = 102 divisions in morulae). Yellow arrows indicate misaligned chromosomes prior to anaphase onset.

(legend continued on next page)

the presence of mildly (18%) or severely (6%) misaligned chromosomes (Figures 2A and 2B). Notably, the duration of mitosis was similar in blastomeres with misalignments and those with complete alignment at anaphase (Figure S2). To begin to assess the involvement of SAC signaling in embryos, we immunolabelled the kinetochore SAC component Mad2 at 10-min intervals after nuclear envelope breakdown (NEBD), finding that Mad2 is recruited to kinetochores after NEBD and is extinguished as chromosomes align at the metaphase plate, as in other cell types (Figure S2). To functionally address whether SAC signaling plays a role in morulae, we inhibited the SAC using two complimentary approaches: AZ3146, a highly specific inhibitor of Mps1 kinase [22], and morpholino oligonucleotides (MOs) against Mad2 (Figure S2). Neither treatment prevented development to blastocyst or altered cell numbers (Figures 2C–2E). Analysis of chromosome segregation dynamics in live morula-stage embryos revealed that 20 μM AZ3146 shortened mitosis from 53 ± 3 min to 33 ± 1 min ($p < 0.0001$) and caused a marked increase in chromosomes remaining misaligned at anaphase onset (63% compared to 24%; $p < 0.0001$) (Figures 2F–2H). The number of micronuclei, which in mouse embryos is a direct indication of accumulated segregation errors [23], doubled in AZ3146-treated and Mad2-MO-injected embryos compared to controls ($p < 0.01$; Figures 2D and 2E). Together, these data suggest that SAC signaling is in effect and serves to prolong mitosis in morulae, thereby allowing more time for complete chromosome alignment prior to anaphase onset. However, blastomeres in normally cultured embryos nonetheless frequently enter anaphase before chromosome alignment is complete, suggesting that the SAC is unresponsive to misaligned chromosomes.

To explore this notion further, we examined the effect of introducing spindle errors in early embryos. Treating embryos with high concentrations of nocodazole caused a pronounced mitotic arrest (mitotic index 40% and 95% in 100 nM and 1 μM nocodazole, respectively) (Figure S2). Mad2 was evident at kinetochores in nocodazole-treated cells, and the arrest was reversible by AZ3146 (Figure S2). Thus, severe spindle damage can elicit a classic SAC-dependent mitotic arrest in early embryos, much as it does in other cell types [24–26]. To more discerningly appraise the SAC's capacity to prevent anaphase, we employed GSK923295, a specific inhibitor of motor protein CENP-E, which in mammalian somatic cells prevents chromosome alignment, leading to SAC activation and mitotic arrest [27]. Fixed-cell analysis revealed that 500 nM GSK923295 resulted in multiple misaligned chromosomes in almost all metaphase cells in morulae (93%) without obviously disrupting spindle architecture (Figures 3A and 3B). However, embryos displayed only a moderate increase in mitotic index (23%), suggesting a failure of cells to arrest in mitosis (Figure 3C). Live imaging of morula-stage embryos in 500 nM GSK923295 confirmed the failure to arrest in mitosis and revealed that anaphase onset occurred with at least one, and as many as nine, severely misaligned chromosomes in all cases (mean of 3.6 ± 0.3 per cell) (Figures 3D, 3E, and S3). Embryos treated simultaneously with nocodazole and GSK923295 mounted a robust mitotic arrest with Mad2-positive kinetochores, revealing that GSK923295 had not unexpectedly inactivated the SAC (Figure S3). Thus, SAC signaling is in operation and is capable of preventing mitosis completion in the face of very severe spindle disruption, but it is unresponsive to the presence of even large numbers of misaligned chromosomes.

We wondered whether the failure of misaligned chromosomes to enforce a mitotic arrest could be attributable to a defect in kinetochore-SAC component recruitment. Fixed-cell analysis showed that Mad2 immunolocalized on kinetochores of misaligned, but not aligned, chromosomes in prometaphase in GSK923295-treated embryos (Figure S3), as in control embryos (Figure S2), confirming that misaligned chromosomes can recruit SAC components. To determine whether recruitment of SAC components to the kinetochore persists at the time of anaphase onset, we employed Mad1:EGFP, an extensively used reporter of SAC activity at kinetochores [28–32]. Mad1:EGFP overexpression did not affect development of embryos to the blastocyst stage. Mad1:EGFP displayed expected spatiotemporal dynamics in GSK923295-treated embryos, accumulating at the nuclear periphery in interphase and then on kinetochores shortly after nuclear breakdown, leaving kinetochores as chromosomes align [28, 31, 33] (Figure S3). Live imaging of H2B:RFP- and Mad1:EGFP-expressing embryos in 500 nM GSK923295 again revealed multiple misaligned chromosomes at anaphase onset (mean 3.5 ± 0.4 per cell). Notably, 80% of severely misaligned chromosomes at anaphase onset clearly harbored Mad1:EGFP at kinetochores (Figures 3F and 3G). Together, these data suggest that misaligned chromosomes can mount a SAC signal but that SAC signaling from even a large number of kinetochores cannot usually prevent anaphase onset in mid-preimplantation development embryos.

Partial APC/C Inhibition Can Reduce Chromosome Segregation Errors

Our data show that, in embryos, misaligned chromosomes fail to inhibit anaphase onset, leading to chromosome segregation error. Recent screens in *Xenopus* extracts have led to the identification of specific small-molecule inhibitors of the APC/C [34, 35]. In experimentally SAC-compromised somatic cells, moderate concentrations of the cell-permeable APC/C inhibitor proTAME can extend mitosis and reduce chromosome segregation errors [35, 36]. We thus wondered whether low concentrations of

(C) Representative images of a blastocyst and a micronucleus (indicated by the yellow arrowhead).
(D and E) Quantification of cell numbers and micronuclei per cell in blastocyst stage embryos that were treated with DMSO (control) or AZ3146 at the 2-cell stage through to blastocyst (D) (mean ± SEM; $n \geq 20$ embryos per group; t test, $p < 0.05$), or injected with Mad2 or control MO at the 2-cell stage (E) (mean ± SEM; $n \geq 20$ embryos per group; t test, $p < 0.05$).
(F) Representative images of chromosome segregation dynamics in H2B:RFP morulae that were treated with DMSO (control) or 20 μM AZ3146. White arrows indicate pre-anaphase misaligned chromosomes; yellow arrows indicate anaphase lagging chromosomes resulting in the formation of a micronucleus.
(G and H) Duration of mitosis (G; mean ± SEM; t test, $p < 0.05$) and incidence of pre-anaphase misaligned chromosomes (H) in DMSO and 20 μM AZ3146 ($n \geq 40$ divisions per group).
See also Figure S2.

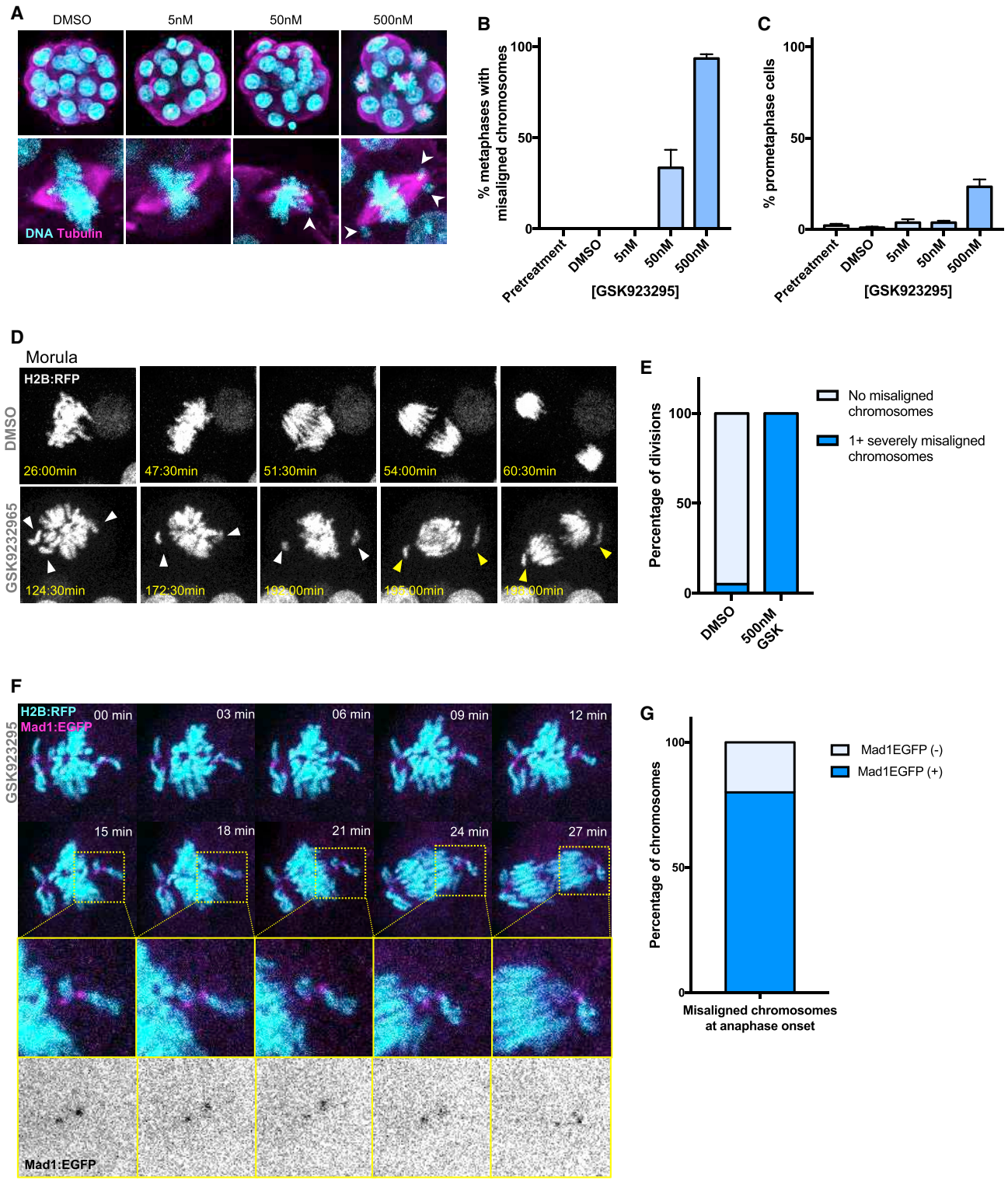

Figure 3. SAC-Active Misaligned Chromosomes Fail to Prevent Anaphase

(A) Representative images of embryos and metaphase spindles after a 16-h exposure to GSK923295. White arrowheads indicate misaligned chromosomes

(B) Mean percentage of metaphases containing severely misaligned chromosomes (mean ± SEM; n ≥ 7 metaphases per group).

(C) Percentage of prometaphase cells in embryos exposed to GSK923295 (mean ± SEM; n = 129 embryos with n ≥ 7 embryos per group).

(D) Representative confocal images of chromosome segregation dynamics of H2B:RFP-expressing morulae in DMSO and 500 nM GSK923295. White and yellow arrowheads indicate misaligned chromosomes prior to and during anaphase, respectively.

(legend continued on next page)

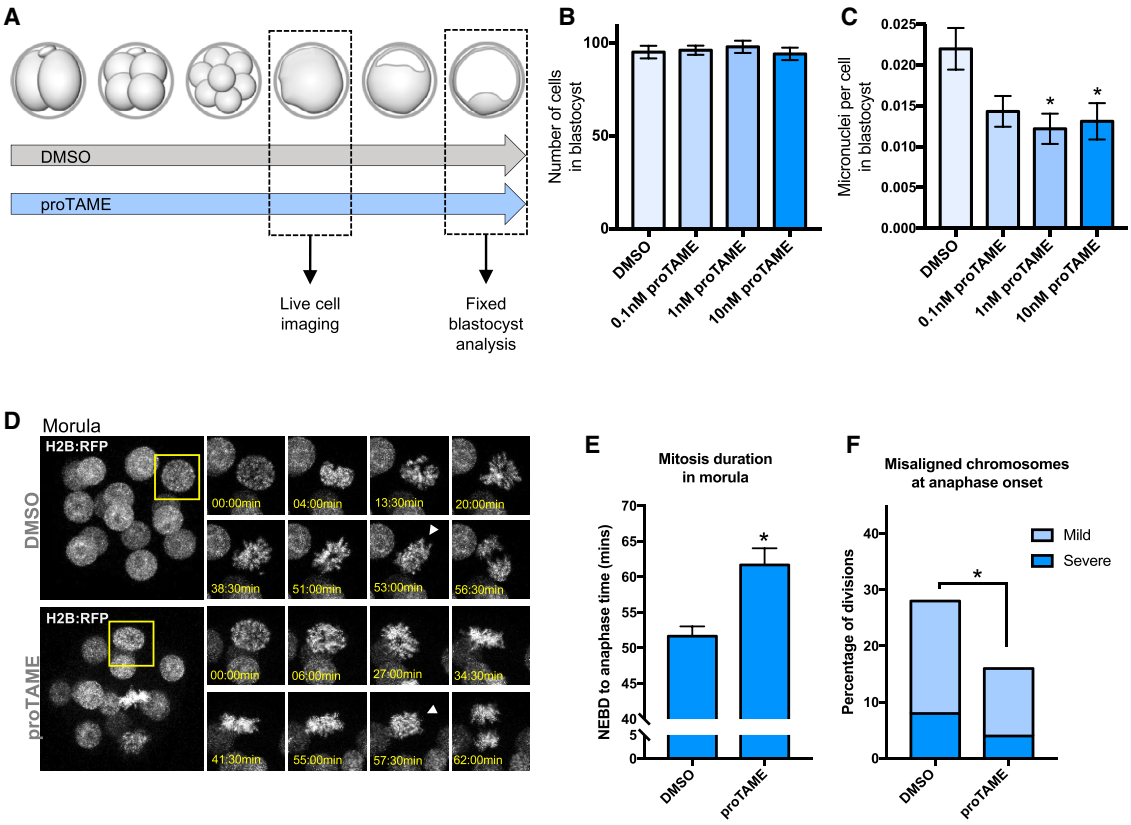

Figure 4. Mild APC/C Inhibition Reduces Chromosome Segregation Errors

(A) Diagrammatic representation of the experimental design. 2-cell embryos were cultured to blastocyst in DMSO or different concentrations of proTAME for immunofluorescence analysis or were previously microinjected with H2B:RFP for live-cell imaging at morula stage.

(B) Number of cells in blastocysts treated with proTAME (mean ± SEM; n ≥ 26 embryos per group).

(C) Number of micronuclei per cell in blastocysts exposed to different proTAME concentrations (mean ± SEM; n ≥ 26 embryos per group; one-way ANOVA, p = 0.006; Tukey's multiple comparisons test, asterisks denote p < 0.01).

(D) Representative confocal images of H2B:RFP-expressing morulae in DMSO and 10 nM proTAME. Yellow squares delineate cells that are zoomed in on in the panels, and white arrowheads indicate anaphase onset.

(E) Quantification of mitosis duration in DMSO and 10 nM proTAME (mean ± SEM; n ≥ 150 divisions per group; Mann-Whitney test, p < 0.05).

(F) Analysis of incidence of mild and severely misaligned chromosomes at anaphase onset in DMSO and 10 nM proTAME (n ≥ 150 divisions per group; Fisher's exact test, p < 0.05).

See also Figure S4.

proTAME would improve chromosome segregation outcomes in otherwise normally cultured embryos. Embryos were cultured in various concentrations of proTAME from the 2-cell stage onward. Micromolar concentrations (1–10 μM) of proTAME prevented embryo development to blastocyst (Figure S4). In contrast, nanomolar proTAME (0.01–100 nM) was permissive of development to blastocyst (Figures 4A and S4) and did not affect the blastocyst cell number (Figure 4B). Live H2B-RFP imaging revealed that 10 nM proTAME increased the duration of mitosis in morulae by ~10 min (from 51.7 ± 1.4 to 61.7 ± 2.3 min, p < 0.0001). Simultaneously, the incidence of misaligned chromosomes at anaphase onset was reduced from 28% to 16% (p = 0.025) (Figures 4D–4F), suggesting that the increased duration of mitosis allowed more chromosomes to align prior to anaphase onset. Strikingly, blastocysts cultured from the 2-cell stage to blastocyst in 1 nM and 10 nM proTAME exhibited a substantial reduction in micronuclei number, from 0.022 micronuclei per cell in controls to 0.012 and 0.013, respectively (p < 0.05) (Figure 4C). A reduction in micronuclei number in blastocysts was also observed in experiments employing low concentrations of APCin (10 μM), a second APC/C inhibitor that acts by binding the mitotic APC/C cofactor Cdc20 [37] (Figure S4). These data suggest that mild pharmacological APC/C inhibition can extend mitosis in embryos, allowing time

(E) Proportion of divisions initiating anaphase in the presence of at least one severely misaligned chromosome (n ≥ 50 divisions per group).

(F) Representative images of a misaligned chromosome at anaphase onset (denoted by black arrowhead) in the 4- to 8-cell mitosis in H2B:RFP/Mad1:EGFP-expressing embryos. The white arrowhead indicates sister chromatid separation.

(G) Proportion of misaligned chromosomes displaying detectable Mad1:EGFP signal at anaphase onset (n = 59 misaligned chromosomes from 17 divisions).

See also Figure S3.

for more chromosomes to align before anaphase, and reducing the incidence of segregation error.

Why mammalian embryos exhibit such staggering levels of mosaic aneuploidy was unknown, and a detailed interrogation of the SAC in a mammalian embryo had not been presented [2, 38]. Our data show that misaligned chromosomes fail to prevent anaphase, despite apparent SAC signaling at their kinetochores. This is in stark contrast with somatic cells, where signaling from a single misaligned and mis-attached kinetochore can delay anaphase [21, 39]. As a result, early embryo blastomeres initiate anaphase before chromosome alignment is complete, leading to chromosome segregation errors. That MCC can be generated and can inhibit APC/C activity in embryos is supported by our observations that SAC inhibition shortens mitosis and that nocodazole elicits a SAC-dependent arrest. Why, therefore, should the early embryo be insensitive to SAC-signaling kinetochores? Perhaps unexpectedly, given recent reports [15, 16], we find that cell volume is not directly responsible for this SAC-APC/C disconnect. Rather, we speculate that mismatched stoichiometry of SAC-APC/C-signaling components could arise as maternal and embryonic transcripts and proteins are differentially synthesized and destroyed during the first few embryonic mitoses [40]. Protein-level analyses to date in mice have detected several SAC components that are expressed throughout embryo development [41] (Figure S4), and we speculate that that SAC-APC/C disconnect may not constitute a simple absence of any one factor. Further analysis will benefit from pairing live imaging with single-cell sequencing and quantitative proteomics approaches [42, 43].

A SAC-APC/C disconnect is further supported by the observation that low doses of the APC/C inhibitors proTAME and APCin can extend embryo mitosis and reduce segregation errors. To our knowledge, these studies provide the first example of a specific chemical intervention improving chromosome segregation outcomes in cultured embryos. While the data allude that modulation of the cell cycle may in the future present a viable approach for improving embryo quality in some specific scenarios, such an approach should not be applied clinically prior to exhaustive testing of safety and efficacy [44–46].

Preventing anaphase until all chromosomes are aligned is a key SAC function. Notably, even many chromosomally unstable cancer cells await full chromosome alignment before anaphase onset is triggered [47, 48], suggesting that severe SAC dysfunction is not commonly the cause of segregation error in cultured cells [49, 50]. In contrast, our data show that early embryos sometimes fail to await complete alignment despite SAC-active kinetochores. A similar scenario is observed in oocyte meiosis I [11–14], where recent work suggests that SAC signaling may play an unexpected additional role in sensing DNA damage [51, 52]. Whether DNA damage activates the SAC in embryos is yet to be explored, but mounting evidence suggests that non-canonical SAC function is a feature of early mammalian development. Landmark studies revealed that early embryos harboring a moderate number of aneuploid cells may still have potential to produce a viable offspring, suggesting that the embryo can tolerate mosaicism up to a threshold level [1, 53]. Detailed studies of other cell-cycle checkpoints in embryos are warranted, but it appears that the preimplantation development prioritizes survival over genetic integrity, and post-implantation selection mechanisms determine the embryo's fate.

STAR★METHODS

Detailed methods are provided in the online version of this paper and include the following:

- KEY RESOURCES TABLE
- CONTACT FOR REAGENT RESOURCE SHARING
- EXPERIMENTAL MODEL AND SUBJECT DETAILS
  - Embryo collection and culture
- METHOD DETAILS
  - Embryo chemical treatments
  - Cytoplasmic removal and microinjection
  - Live cell imaging and immunofluorescence
- QUANTIFICATION AND STATISTICAL ANALYSIS
  - Image analysis and statistics

SUPPLEMENTAL INFORMATION

Supplemental Information includes four figures and can be found with this article online at https://doi.org/10.1016/j.cub.2018.12.042.

ACKNOWLEDGMENTS

We thank Abby Gerhold, Hugh Clarke, and Aleksandar Mihajlovic for valuable discussions; Michael Lampson for the pIVT-Mad1:2xEGFP plasmid; and Yojiro Yamanaka for the pCS2-GAP43:GFP plasmid. This research was supported by grants to G.F. from Fondation Jean-Louis Lévesque, CFI, CIHR, and NSERC.

AUTHOR CONTRIBUTIONS

G.F. and C.V.-D. designed the study and wrote the paper. C.V.-D. and L.M.G.P. performed experiments, analyzed the images and data, and produced the figures.

DECLARATION OF INTERESTS

The authors declare no competing interests.

Received: September 27, 2018
Revised: November 23, 2018
Accepted: December 21, 2018
Published: February 14, 2019

REFERENCES

1. Bolton, H., Graham, S.J.L., Van der Aa, N., Kumar, P., Theunis, K., Fernandez Gallardo, E., Voet, T., and Zernicka-Goetz, M. (2016). Mouse model of chromosome mosaicism reveals lineage-specific depletion of aneuploid cells and normal developmental potential. Nat. Commun. *7*, 11165.
2. van Echten-Arends, J., Mastenbroek, S., Sikkema-Raddatz, B., Korevaar, J.C., Heineman, M.J., van der Veen, F., and Repping, S. (2011). Chromosomal mosaicism in human preimplantation embryos: a systematic review. Hum. Reprod. Update *17*, 620–627.
3. McCoy, R.C. (2017). Mosaicism in preimplantation human embryos: when chromosomal abnormalities are the norm. Trends Genet. *33*, 448–463.
4. Vanneste, E., Voet, T., Le Caignec, C., Ampe, M., Konings, P., Melotte, C., Debrock, S., Amyere, M., Vikkula, M., Schuit, F., et al. (2009). Chromosome instability is common in human cleavage-stage embryos. Nat. Med. *15*, 577–583.

5. Vázquez-Diez, C., and FitzHarris, G. (2018). Causes and consequences of chromosome segregation error in preimplantation embryos. Reproduction *155*, R63–R76.
6. Lara-Gonzalez, P., Westhorpe, F.G., and Taylor, S.S. (2012). The spindle assembly checkpoint. Curr. Biol. *22*, R966–R980.
7. Musacchio, A. (2015). The molecular biology of spindle assembly checkpoint signaling dynamics. Curr. Biol. *25*, R1002–R1018.
8. Galli, M., and Morgan, D.O. (2016). Cell size determines the strength of the spindle assembly checkpoint during embryonic development. Dev. Cell *36*, 344–352.
9. Gerhold, A.R., Poupart, V., Labbé, J.-C., and Maddox, P.S. (2018). Spindle assembly checkpoint strength is linked to cell fate in the C. elegans embryo. Mol. Biol. Cell *29*, 1435–1438.
10. Wei, Y., Multi, S., Yang, C.-R., Ma, J., Zhang, Q.-H., Wang, Z.-B., Li, M., Wei, L., Ge, Z.-J., Zhang, C.-H., et al. (2011). Spindle assembly checkpoint regulates mitotic cell cycle progression during preimplantation embryo development. PLoS ONE *6*, e21557.
11. Gui, L., and Homer, H. (2012). Spindle assembly checkpoint signalling is uncoupled from chromosomal position in mouse oocytes. Development *139*, 1941–1946.
12. Jones, K.T., and Lane, S.I.R. (2013). Molecular causes of aneuploidy in mammalian eggs. Development *140*, 3719–3730.
13. Kolano, A., Brunet, S., Silk, A.D., Cleveland, D.W., and Verlhac, M.-H. (2012). Error-prone mammalian female meiosis from silencing the spindle assembly checkpoint without normal interkinetochore tension. Proc. Natl. Acad. Sci. USA *109*, E1858–E1867.
14. Nagaoka, S.I., Hassold, T.J., and Hunt, P.A. (2012). Human aneuploidy: mechanisms and new insights into an age-old problem. Nat. Rev. Genet. *13*, 493–504.
15. Kyogoku, H., and Kitajima, T.S. (2017). Large cytoplasm is linked to the error-prone nature of oocytes. Dev. Cell *41*, 287–298.e4.
16. Lane, S.I.R., and Jones, K.T. (2017). Chromosome biorientation and APC activity remain uncoupled in oocytes with reduced volume. J. Cell Biol. *216*, 3949–3957.
17. Courtois, A., Schuh, M., Ellenberg, J., and Hiiragi, T. (2012). The transition from meiotic to mitotic spindle assembly is gradual during early mammalian development. J. Cell Biol. *198*, 357–370.
18. Tsichlaki, E., and FitzHarris, G. (2016). Nucleus downscaling in mouse embryos is regulated by cooperative developmental and geometric programs. Sci. Rep. *6*, 28040.
19. Fitzharris, G. (2009). A shift from Kinesin 5-dependent metaphase spindle function during preimplantation development in mice. Development *136*, 2111–2119.
20. Zlotek-Zlotkiewicz, E., Monnier, S., Cappello, G., Le Berre, M., and Piel, M. (2015). Optical volume and mass measurements show that mammalian cells swell during mitosis. J. Cell Biol. *211*, 765–774.
21. Rieder, C.L., Cole, R.W., Khodjakov, A., and Sluder, G. (1995). The checkpoint delaying anaphase in response to chromosome monoorientation is mediated by an inhibitory signal produced by unattached kinetochores. J. Cell Biol. *130*, 941–948.
22. Hewitt, L., Tighe, A., Santaguida, S., White, A.M., Jones, C.D., Musacchio, A., Green, S., and Taylor, S.S. (2010). Sustained Mps1 activity is required in mitosis to recruit O-Mad2 to the Mad1-C-Mad2 core complex. J. Cell Biol. *190*, 25–34.
23. Vázquez-Diez, C., Yamagata, K., Trivedi, S., Haverfield, J., and FitzHarris, G. (2016). Micronucleus formation causes perpetual unilateral chromosome inheritance in mouse embryos. Proc. Natl. Acad. Sci. USA *113*, 626–631.
24. Brito, D.A., Yang, Z., and Rieder, C.L. (2008). Microtubules do not promote mitotic slippage when the spindle assembly checkpoint cannot be satisfied. J. Cell Biol. *182*, 623–629.
25. Chen, R.H., Waters, J.C., Salmon, E.D., and Murray, A.W. (1996). Association of spindle assembly checkpoint component XMAD2 with unattached kinetochores. Science *274*, 242–246.
26. Meraldi, P., Draviam, V.M., and Sorger, P.K. (2004). Timing and checkpoints in the regulation of mitotic progression. Dev. Cell *7*, 45–60.
27. Bennett, A., Bechi, B., Tighe, A., Thompson, S., Procter, D.J., and Taylor, S.S. (2015). Cenp-E inhibitor GSK923295: novel synthetic route and use as a tool to generate aneuploidy. Oncotarget *6*, 20921–20932.
28. Emre, D., Terracol, R., Poncet, A., Rahmani, Z., and Karess, R.E. (2011). A mitotic role for Mad1 beyond the spindle checkpoint. J. Cell Sci. *124*, 1664–1671.
29. Heinrich, S., Sewart, K., Windecker, H., Langegger, M., Schmidt, N., Hustedt, N., and Hauf, S. (2014). Mad1 contribution to spindle assembly checkpoint signalling goes beyond presenting Mad2 at kinetochores. EMBO Rep. *15*, 291–298.
30. Kruse, T., Larsen, M.S.Y., Sedgwick, G.G., Sigurdsson, J.O., Streicher, W., Olsen, J.V., and Nilsson, J. (2014). A direct role of Mad1 in the spindle assembly checkpoint beyond Mad2 kinetochore recruitment. EMBO Rep. *15*, 282–290.
31. Lane, S.I.R., Morgan, S.L., Wu, T., Collins, J.K., Merriman, J.A., Ellnati, E., Turner, J.M., and Jones, K.T. (2017). DNA damage induces a kinetochore-based ATM/ATR-independent SAC arrest unique to the first meiotic division in mouse oocytes. Development *144*, 3475–3486.
32. Matson, D.R., and Stukenberg, P.T. (2014). CENP-I and Aurora B act as a molecular switch that ties RZZ/Mad1 recruitment to kinetochore attachment status. J. Cell Biol. *205*, 541–554.
33. Howell, B.J., Moree, B., Farrar, E.M., Stewart, S., Fang, G., and Salmon, E.D. (2004). Spindle checkpoint protein dynamics at kinetochores in living cells. Curr. Biol. *14*, 953–964.
34. Verma, R., Peters, N.R., D'Onofrio, M., Tochtrop, G.P., Sakamoto, K.M., Varadan, R., Zhang, M., Coffino, P., Fushman, D., Deshaies, R.J., and King, R.W. (2004). Ubistatins inhibit proteasome-dependent degradation by binding the ubiquitin chain. Science *306*, 117–120.
35. Zeng, X., Sigoillot, F., Gaur, S., Choi, S., Pfaff, K.L., Oh, D.-C., Hathaway, N., Dimova, N., Cuny, G.D., and King, R.W. (2010). Pharmacologic inhibition of the anaphase-promoting complex induces a spindle checkpoint-dependent mitotic arrest in the absence of spindle damage. Cancer Cell *18*, 382–395.
36. Sansregret, L., Patterson, J.O., Dewhurst, S., López-García, C., Koch, A., McGranahan, N., Chao, W.C.H., Barry, D.J., Rowan, A., Instrell, R., et al. (2017). APC/C dysfunction limits excessive cancer chromosomal instability. Cancer Discov. *7*, 218–233.
37. Sackton, K.L., Dimova, N., Zeng, X., Tian, W., Zhang, M., Sackton, T.B., Meaders, J., Pfaff, K.L., Sigoillot, F., Yu, H., et al. (2014). Synergistic blockade of mitotic exit by two chemical inhibitors of the APC/C. Nature *514*, 646–649.
38. Taylor, T.H., Gitlin, S.A., Patrick, J.L., Crain, J.L., Wilson, J.M., and Griffin, D.K. (2014). The origin, mechanisms, incidence and clinical consequences of chromosomal mosaicism in humans. Hum. Reprod. Update *20*, 571–581.
39. Li, X., and Nicklas, R.B. (1995). Mitotic forces control a cell-cycle checkpoint. Nature *373*, 630–632.
40. Lee, M.T., Bonneau, A.R., and Giraldez, A.J. (2014). Zygotic genome activation during the maternal-to-zygotic transition. Annu. Rev. Cell Dev. Biol. *30*, 581–613.
41. Gao, Y., Liu, X., Tang, B., Li, C., Kou, Z., Li, L., Liu, W., Wu, Y., Kou, X., Li, J., et al. (2017). Protein expression landscape of mouse embryos during pre-implantation development. Cell Rep. *21*, 3957–3969.
42. Guo, G., Huss, M., Tong, G.Q., Wang, C., Li Sun, L., Clarke, N.D., and Robson, P. (2010). Resolution of cell fate decisions revealed by single-cell gene expression analysis from zygote to blastocyst. Dev. Cell *18*, 675–685.
43. Petropoulos, S., Edsgärd, D., Reinius, B., Deng, Q., Panula, S.P., Codeluppi, S., Plaza Reyes, A., Linnarsson, S., Sandberg, R., and Lanner, F. (2016). Single-cell RNA-seq reveals lineage and X chromosome dynamics in human preimplantation embryos. Cell *165*, 1012–1026.

44. Brison, D.R., Roberts, S.A., and Kimber, S.J. (2013). How should we assess the safety of IVF technologies? Reprod. Biomed. Online *27*, 710–721.
45. Ventura-Juncá, P., Irarrázaval, I., Rolle, A.J., Gutiérrez, J.I., Moreno, R.D., and Santos, M.J. (2015). In vitro fertilization (IVF) in mammals: epigenetic and developmental alterations. Scientific and bioethical implications for IVF in humans. Biol. Res. *48*, 68.
46. Young, L.E., and Fairburn, H.R. (2000). Improving the safety of embryo technologies: possible role of genomic imprinting. Theriogenology *53*, 627–648.
47. Gascoigne, K.E., and Taylor, S.S. (2008). Cancer cells display profound intra- and interline variation following prolonged exposure to antimitotic drugs. Cancer Cell *14*, 111–122.
48. Thompson, S.L., and Compton, D.A. (2010). Proliferation of aneuploid human cells is limited by a p53-dependent mechanism. J. Cell Biol. *188*, 369–381.
49. Thompson, S.L., Bakhoum, S.F., and Compton, D.A. (2010). Mechanisms of chromosomal instability. Curr. Biol. *20*, R285–R295.
50. Tighe, A., Johnson, V.L., Albertella, M., and Taylor, S.S. (2001). Aneuploid colon cancer cells have a robust spindle checkpoint. EMBO Rep. *2*, 609–614.
51. Collins, J.K., Lane, S.I.R., Merriman, J.A., and Jones, K.T. (2015). DNA damage induces a meiotic arrest in mouse oocytes mediated by the spindle assembly checkpoint. Nat. Commun. *6*, 8553.
52. Marangos, P., Stevense, M., Niaka, K., Lagoudaki, M., Nabti, I., Jessberger, R., and Carroll, J. (2015). DNA damage-induced metaphase I arrest is mediated by the spindle assembly checkpoint and maternal age. Nat. Commun. *6*, 8706.
53. Lightfoot, D.A., Kouznetsova, A., Mahdy, E., Wilbertz, J., and Höög, C. (2006). The fate of mosaic aneuploid embryos during mouse development. Dev. Biol. *289*, 384–394.
54. Taylor, S.S., Hussein, D., Wang, Y., Elderkin, S., and Morrow, C.J. (2001). Kinetochore localisation and phosphorylation of the mitotic checkpoint components Bub1 and BubR1 are differentially regulated by spindle events in human cells. J. Cell Sci. *114*, 4385–4395.
55. Prodon, F., Chenevert, J., Hébras, C., Dumollard, R., Faure, E., Gonzalez-Garcia, J., Nishida, H., Sardet, C., and McDougall, A. (2010). Dual mechanism controls asymmetric spindle position in ascidian germ cell precursors. Development *137*, 2011–2021.
56. Anani, S., Bhat, S., Honma-Yamanaka, N., Krawchuk, D., and Yamanaka, Y. (2014). Initiation of Hippo signaling is linked to polarity rather than to cell position in the pre-implantation mouse embryo. Development *141*, 2813–2824.
57. Miyanari, Y., Ziegler-Birling, C., and Torres-Padilla, M.-E. (2013). Live visualization of chromatin dynamics with fluorescent TALEs. Nat. Struct. Mol. Biol. *20*, 1321–1324.
58. Schindelin, J., Arganda-Carreras, I., Frise, E., Kaynig, V., Longair, M., Pietzsch, T., Preibisch, S., Rueden, C., Saalfeld, S., Schmid, B., et al. (2012). Fiji: an open-source platform for biological-image analysis. Nat. Methods *9*, 676–682.
59. Nakagawa, S., and FitzHarris, G. (2016). Quantitative microinjection of morpholino antisense oligonucleotides into mouse oocytes to examine gene function in meiosis-I. Methods Mol. Biol. *1457*, 217–230.
60. Vázquez-Diez, C., and FitzHarris, G. (2018). Correlative live imaging and immunofluorescence for analysis of chromosome segregation in mouse preimplantation embryos. Methods Mol. Biol. *1769*, 319–335.
61. Nakagawa, S., and FitzHarris, G. (2017). Intrinsically defective microtubule dynamics contribute to age-related chromosome segregation errors in mouse oocyte meiosis-I. Curr. Biol. *27*, 1040–1047.
62. Illingworth, C., Pirmadjid, N., Serhal, P., Howe, K., and Fitzharris, G. (2010). MCAK regulates chromosome alignment but is not necessary for preventing aneuploidy in mouse oocyte meiosis I. Development *137*, 2133–2138.

STAR★METHODS

KEY RESOURCES TABLE

REAGENT or RESOURCE	SOURCE	IDENTIFIER
Antibodies		
Rabbit anti-Mad2	Biolegend	Cat# 924601; RRID: AB_2565454
Sheep anti-BubR1	[54]	N/A
Mouse anti-Bub3	BD Biosciences	Cat# 611730; RRID: AB_2243620
Mouse anti-β-Tubulin	Sigma	Cat# T4026; RRID: AB_477577
Alexa Fluor 488 anti-Rabbit	ThermoFisher	Cat# A-11008; RRID: AB_2540618
Alexa Fluor 488 anti-Sheep	ThermoFisher	Cat# A-11015; RRID: AB_2534082
Alexa Fluor 488 anti-Mouse	ThermoFisher	Cat# A-11029; RRID: AB_2534088
Alexa Fluor 568 anti-Mouse	ThermoFisher	Cat# A-11031; RRID: AB_144696
Chemicals, Peptides, and Recombinant Proteins		
Alexa Fluor 555 Phalloidin	ThermoFisher	Cat# A-34005
Hoechst	ThermoFisher	Cat# H-2399
Pregnant Mare's Serum Gonadotrophin	Genway Biotech	Cat# GWB-2AE30A
Human Chorionic Gonadotrophin	Sigma	Cat# CG10
M2 Media	Sigma	Cat# M7167
KSOM Embryo Culture Media	Millipore Sigma	Cat# MR-020P-5F
AZ3146	Calbiochem	Cat# 531976; CAS: 1124329-14-1
Nocodazole	Calbiochem	Cat# 487928; CAS: 31430-18-9
GSK923295	Cayman Chemical	Cat# 18389; CAS: 1088965-37-0
Cytochalasin B	Sigma	Cat# C6762; CAS: 14930-96-2
MG-132	Calbiochem	Cat# 474790; CAS: 133407-82-6
proTAME	R&D Systems Inc.	Cat# I-440-01M; CAS: 1362911-19-0
APCin	Tocris	Cat# 5747; CAS: 300815-04-7
Critical Commercial Assays		
mMessage Machine Kit (SP6, T3 and T7)	Ambion	Cat# AM1336, AM1348, AM134
Experimental Models: Organisms/Strains		
Mouse: CD-1 IGS	Charles River Laboratories	Crl:CD1(ICR)
Oligonucleotides		
Control Morpholino Oligonucleotide CCTCTTACCTCAGTTACAATTTATA	Gene Tools	N/A
Mad2 Morpholino Oligonucleotide GCTCTCGGGCGAGCTGCTGTGCCAT	Gene Tools	N/A
Recombinant DNA		
pRNA-H2B:RFP	[55]	N/A
GAP43:GFP	[56]	N/A
MajSatTALEmClover (pTALYM3B15)	[57]	Addgene Plasmid # 47878
pIVT-Mad1:2xEGFP	[31]	N/A
Software and Algorithms		
Fiji	[58]	https://imagej.net/Fiji
GraphPad Prism	GraphPad Prism7 GraphPad Software, La Jolla California USA	https://www.graphpad.com
Other		
4-well micro-insert	Ibidi	Cat# 80489

CONTACT FOR REAGENT RESOURCE SHARING

Further information and requests for resources and reagents should be directed to and will be fulfilled by the Lead Contact, Greg FitzHarris (greg.fitzharris@umontreal.ca).

EXPERIMENTAL MODEL AND SUBJECT DETAILS

Embryo collection and culture

All experiments were approved by the Centre de Recherche du Centre Hospitalier de l'Université de Montréal (CRCHUM) Comité Institutionnel de Protection des Animaux (CIPA). Two cell embryos were obtained from superovulated 2-3 month old CD-1 female mice mated with CD-1 males. Embryos were collected in M2 media and cultured in KSOM media drops covered in mineral oil at 37°C in 5%CO_2.

METHOD DETAILS

Embryo chemical treatments

For chemical treatments, media was supplemented with the following compounds: AZ3146 (20μM), GSK923295 (various concentrations), Nocodazole (various concentrations), Cytochalasin B (5μg/mL), MG-132 (25μM), proTAME (various concentrations), APCin (various concentrations). All drug stocks are dissolved in DMSO. For experiments involving proTAME and APCin, embryos were cultured without oil in 500μL of media in 4-well plates.

Cytoplasmic removal and microinjection

All micromanipulations were performed on an Leica inverted microscope fitted with Narashige micromanipulators. Cytoplasmic aspiration and removal was achieved with hydraulic-controlled glass pipettes mounted on a piezo-electric drill, to perforate the *zona pellucida,* in two-cell embryos treated with 10 μM Nocodazole and 5μg/mL Cytochalasin B. Embryos were thoroughly washed in over a dozen drops of M2 media prior to transfer to and incubation in equilibrated KSOM medium for at least 2 hours prior to imaging to allow them to recover from the cytoplasmic removal procedure. Microinjections were performed as described previously [23, 59, 60]. cRNA was synthesized using mMessenger Machine kit (Ambion) as previously [60, 61], from the following plasmids; pRN4-H2B:RFP, psC2-GAP43:GFP, MajSatTALE:mClover. Morpholino antisense oligonucleotides were microinjected to an estimated final concentration of 50-100uM, as previously [62].

Live cell imaging and immunofluorescence

All imaging was performed on a Leica SP8 confocal microscope fitted with a HyD detector. For live imaging embryos were placed in a heated stage top incubator with 5% CO_2 supply and imaged with a 20x 0.75NA objective as previously [23]. All imaging was performed in ~2μL drops under mineral oil as previously described in detail [60], except for live cell imaging experiments involving proTAME, in which embryos were cultured in Ibidi micro-insert wells mounted on a glass-bottom dish with distilled water supplied with humidified CO_2 gas supply. Z stack images of embryos (~50μm) were obtained at a time interval of 30 s for experiments concerning H2B:RFP only, 2 min for H2B:RFP-GAP43:GFP, and 3 min H2B:RFP-Mad1:EGFP experiments. For experiments involving chemical treatments, embryos were washed through three 50μL drops of pre-equilibrated KSOM supplemented with DMSO, Nocodazole, GSK923295 or AZ3146 and placed in a ~2μL drop in a glass-bottom dish for imaging. Live imaging at the 2-4C, 4-8C, 16-32C and 32-64C cell transitions began at ~48h, ~60h, 72h-84h and ~96h post-hCG administration and mating (hCG+m), respectively. Note that all morula experiments were performed at the 16-to-32C transition, except those involving GSK923295 and its control which were done at the 8-to-16C transition, however we find mitosis duration, incidence of severe pre-anaphase misalignments and severely lagging chromosomes during cell division did not differ significantly between these developmental stages ($p = 0.67$, 0.57 and 0.37, respectively). Chromosomes were classified as mildly or severely misaligned as previously [62]: chromosomes protruding from the metaphase plate were classified as mildly misaligned, whereas those spatially separated from the metaphase plate were considered severely misaligned. For immunolocalization of Mad2 during mitosis presented in Figure S2, H2B:RFP-expressing morula stage embryos were live-imaged and embryos fixed either 10, 20 or 30 min following NEBD for immunoprocessing.

For immunofluorescence embryos were fixed in 2% PFA in PBS (20min) and permeabilized in 0.25% Triton X-100 in PBS (10min). For Mad2 and BubR1 immunofluorescence embryos were fixed for 15 min in PHEM buffer containing 2% PFA and 0.05% Triton X-100, and permeabilized in 0.05% Triton-X in PHEM buffer for 15min. For immunofluorescence of Bub3, embryos were treated with acidic Tyrode for < 1 min at 37°C to remove the zona pellucida. Fixation was performed in PBS containing 2% PFA for 30 min followed by permeabilization with 0.25% Triton X in PBS for 10 min. Blocking was performed in 3% bovine serum albumin in PBS, for 1 hr at 37°C or overnight at 4°C. Primary antibodies used are rabbit anti-Mad2 (1:300), mouse anti-beta-Tubulin (1:1000), sheep anti-BubR1 (1:100), mouse anti-Bub3 (1:100), anti- rabbit, anti-mouse and anti-sheep AlexaFluor secondaries were used at 1:1000 dilution. Alexa-555-Phalloidin (1:300) and Hoechst (1:1000) were used to visualize F-actin and DNA, respectively. Briefly, immunofluorescence confocal imaging was performed on a Leica SP8 microscope using a 63x 1.4 NA oil objective lens, using a 1.5μm optical section and acquiring Z stacks with a step size of 1.5μm, described in more detail in [60]. For immunofluorescence

experiments of SAC components (Mad2, BubR1 and Bub3) during development presented in Figure S4, images were acquired on a Leica SP8 microscope using a 20x0.75 NA objective lens, using a 2.0μm optical section and acquiring Z stacks with a step size of 2.0μm. For immunofluorescence experiments in morulae, embryos were cultured in the indicated concentrations of Nocodazole and/or from the 8C stage (at ~72hrs post hCG+m) for 16hrs. For blastocyst examination, embryos were cultured from the 2C stage in control vehicle (DMSO), AZ3146, proTAME or APCIN until blastocyst stage and fixed at ~120hrs post hCG+m.

QUANTIFICATION AND STATISTICAL ANALYSIS

Image analysis and statistics

All image analysis was performed using Fiji software. Time-lapse Z stacks were examined to determine mitosis duration and identify chromosome alignment and segregation errors. Spindle length measurements were performed measuring the distance between spindle poles, using Pythagoras' theorem when spindle poles were located on different Z-slices. Mad2 Immunofluorescence was quantified by measuring maximum gray values of the Mad2 signal at the nuclear envelope and in the image background for each Z-plane and subsequently subtracting the background values. To calculate cell volume for each cell at metaphase, areas delineated by the cell membrane (GAP43:GFP signal) were manually traced and measured at each Z-slice, the sum of the areas was multiplied by the step size (2μm). All data analysis was performed using GraphPad Prism, statistical tests used are accordingly noted in figures.

Current Biology, Volume *29*

Supplemental Information

Cell-Size-Independent Spindle Checkpoint Failure Underlies Chromosome Segregation Error in Mouse Embryos

Cayetana Vázquez-Diez, Lia Mara Gomes Paim, and Greg FitzHarris

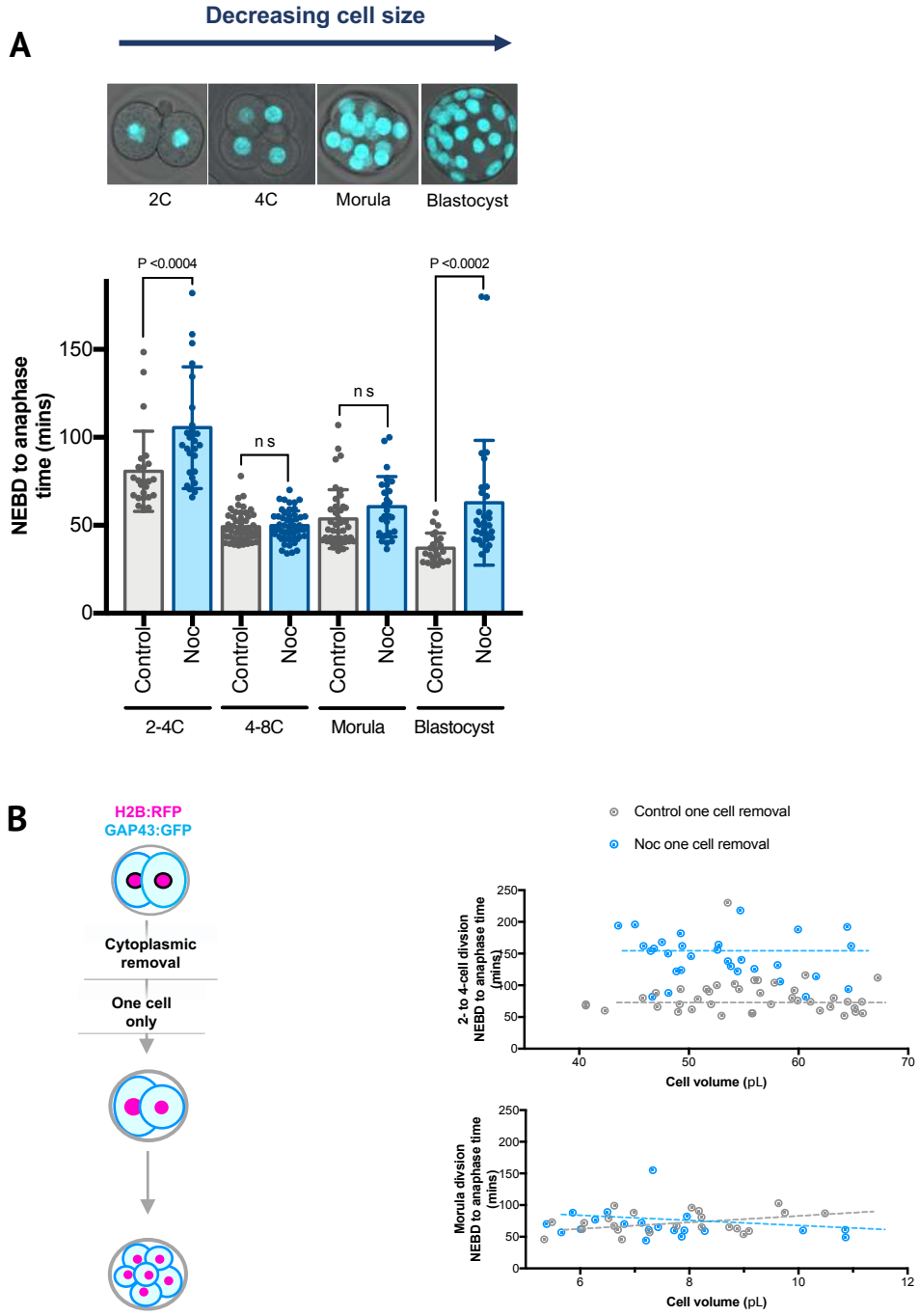

Figure S1. Cell-size-independent SAC. Relates to Figure 1.

A: H2B:RFP-expressing embryos were imaged live in the presence or absence of 10nM nocodazole. Embryos were cultured to the desired developmental stage in nocodazole-free media, and transferred to nocodazole-containing media shortly prior to imaging. Representative images of H2B:RFP-expressing embryos at two-cell (2C), four-cell (4C), morula (16-32C) and blastocyst stages are shown. Quantification of mitosis duration at the different stages examined in control and 10nM of nocodazole (mean ± SD, n ≥ 24 divisions/group) is shown. Note that 10nM nocodazole significantly extends the duration of mitosis (NEBD to anaphase) at the 2-4 cell transition and in blastocysts, but not at the 4-8 cell transition or in 16-32 cell stage morulae.

B: Cytoplasmic removal was performed in one cell of two-cell embryos expressing H2B:RFP and GAP43:GFP as per the experimental design cartoon shown. Analysis of cell volume measured at metaphase, and mitosis duration in control or 10nM nocodazole conditions is shown at the two-cell and morula- stages, respectively (n ≥ 24 divisions per group).

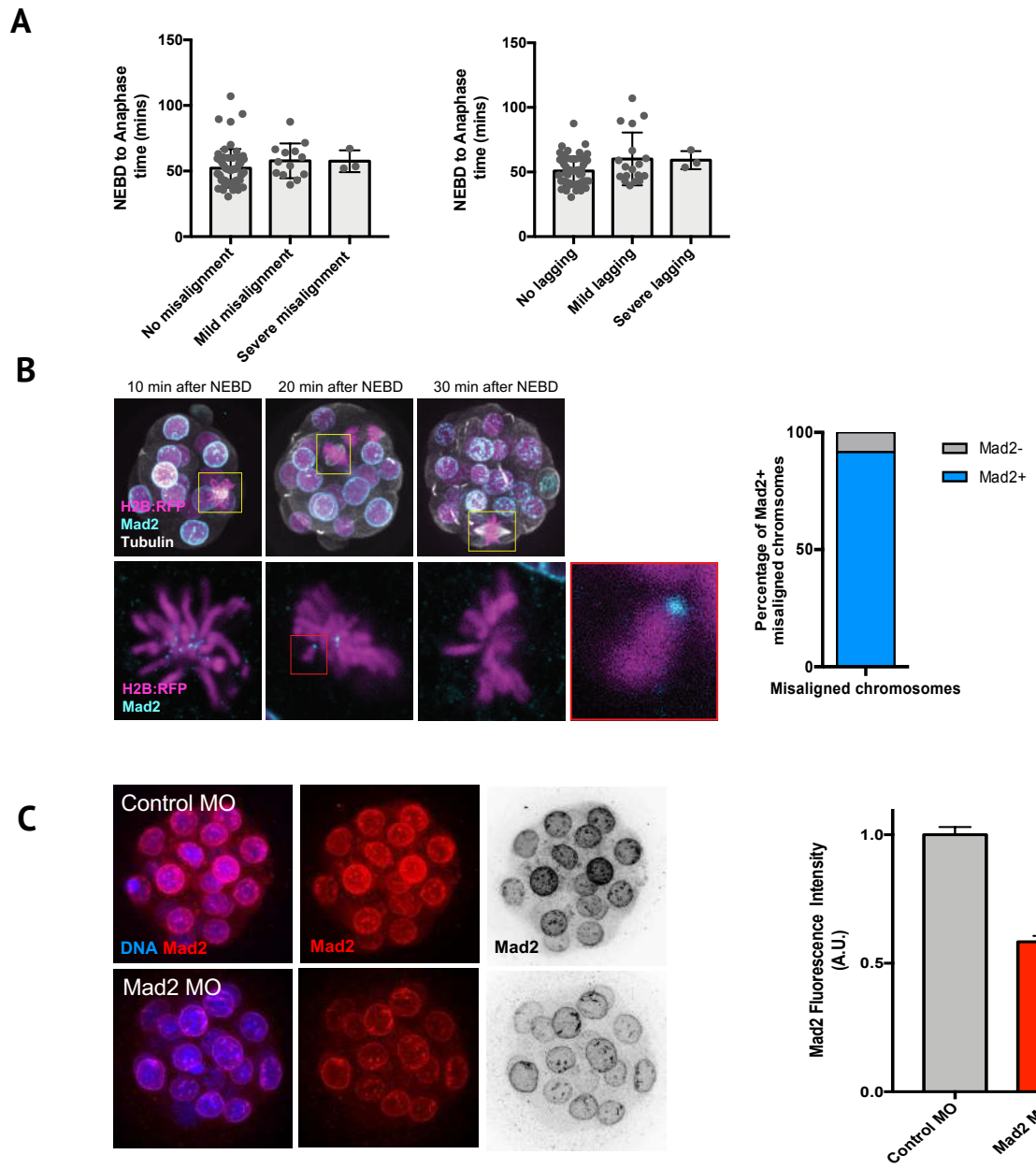

Figure S2. Weak spindle assembly checkpoint in morulae. Relates to Figure 2.

A: Mitosis duration does not correlate with the presence of misaligned chromosomes at anaphase onset, nor lagging anaphase chromosomes. Quantification of NEBD to Anaphase time in divisions with or without misalignments at anaphase onset (left) and with or without lagging chromosomes during anaphase (right) in H2B:RFP-expressing embryos (mean and SD, n=75 divisions).

B: Immunolocalisation of Mad2 during mitosis in morulae. Representative z-projections (top) and single z-slices (bottom) of Mad2 and Tubulin immunofluorescence at 10, 20 and 30 minutes after nuclear envelope breakdown (NEBD) in morula stage embryos. Note that 10 minutes after NEBD the majority of chromosomes are positively stained for Mad2 at kinetochores. At 20 and 30 minutes after NEBD the majority of chromosomes are aligned at the metaphase plate and do not display Mad2 staining. Note however that, in 15 of 16 cases, misaligned chromosomes 20-30 mins after NEBD harbour prominent Mad2 signals. One such example of a misaligned chromosome harbouring clear Mad2 signal when most aligned chromosomes have extinguished Mad 2 is highlighted by the zoomed inset (red box).

C: Mad2 knockdown with Morpholino Oligonucleotides. Representative confocal images and fluorescence intensity quantification of Mad2 immunofluorescence in embryos microinjected with Control and Mad2 morpholino oligonucleotides (MO) (mean and SEM, n ≥ 108 cells/group, t-test, P<0.0001).

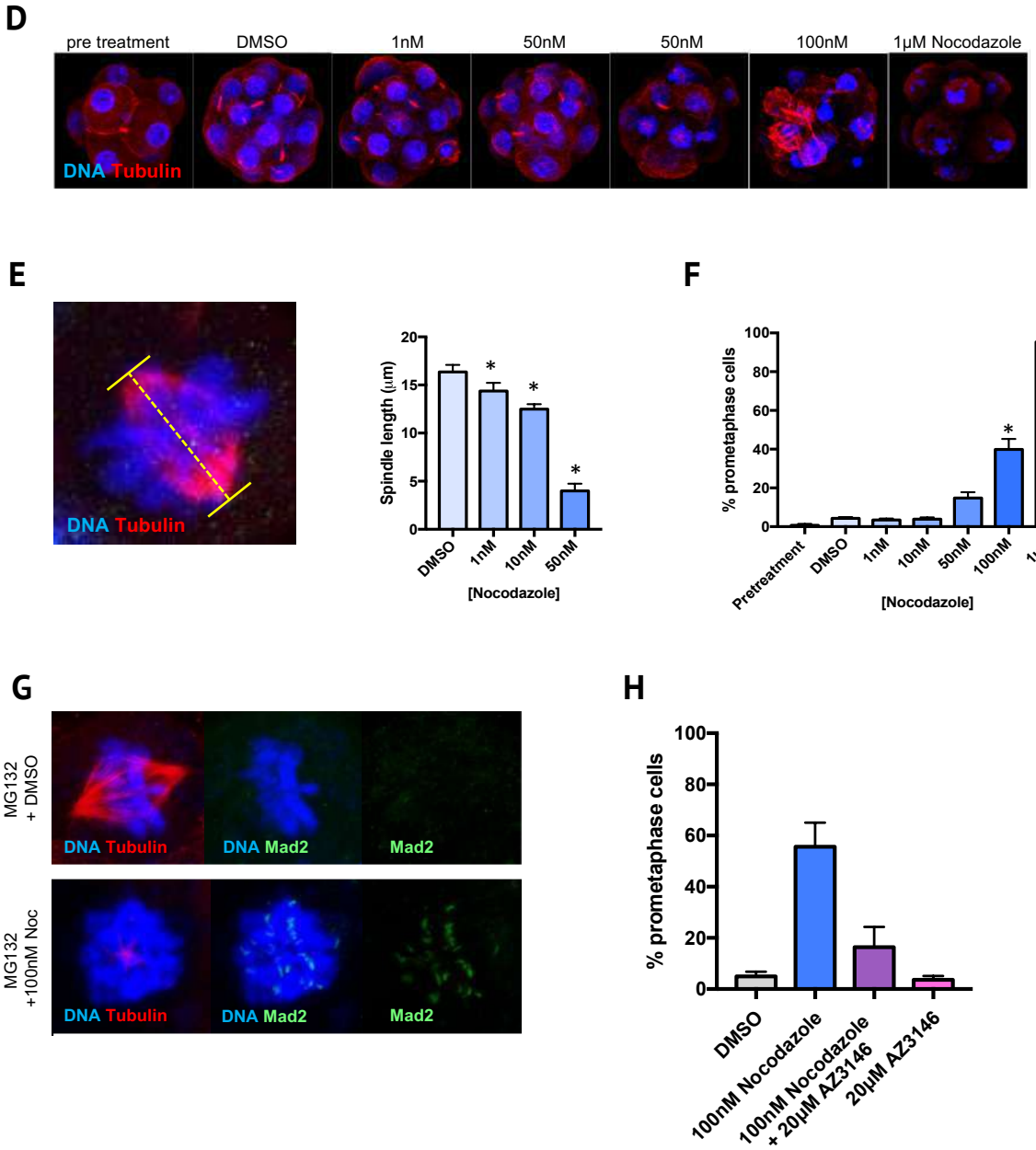

Figure S2. Weak spindle assembly checkpoint in morulae. Relates to Figure 2.
D: Severe spindle damage induces a SAC-mediated mitotic arrest. Representative images of embryos before and after a 16 hour exposure to vehicle (DMSO) or different concentrations of the spindle poison nocodazole. **E:** Representative image and example of measurement of spindle length, and measurements of spindle length in DMSO and nocodazole-treated embryos (mean and SEM, n ≥ 7 metaphases per group). Note that increasing nocodazole concentrations cause the spindle to shorten. **F:** Percentage of prometaphase cells in embryos exposed to different nocodazole concentrations (mean and SEM, n ≥ 20 embryos/group, one-way ANOVA, $P<0.05$). **G:** Representative images of Mad2 recruitment to metaphase spindles in the presence of Nocodazole. **H:** Quantification of the percentage of mitotic cells in embryos treated with DMSO or 100nM nocodazole and/or 20µM AZ3146 (mean and SEM, n ≥ 13 embryos/group, one-way ANOVA, $P<0.0001$).

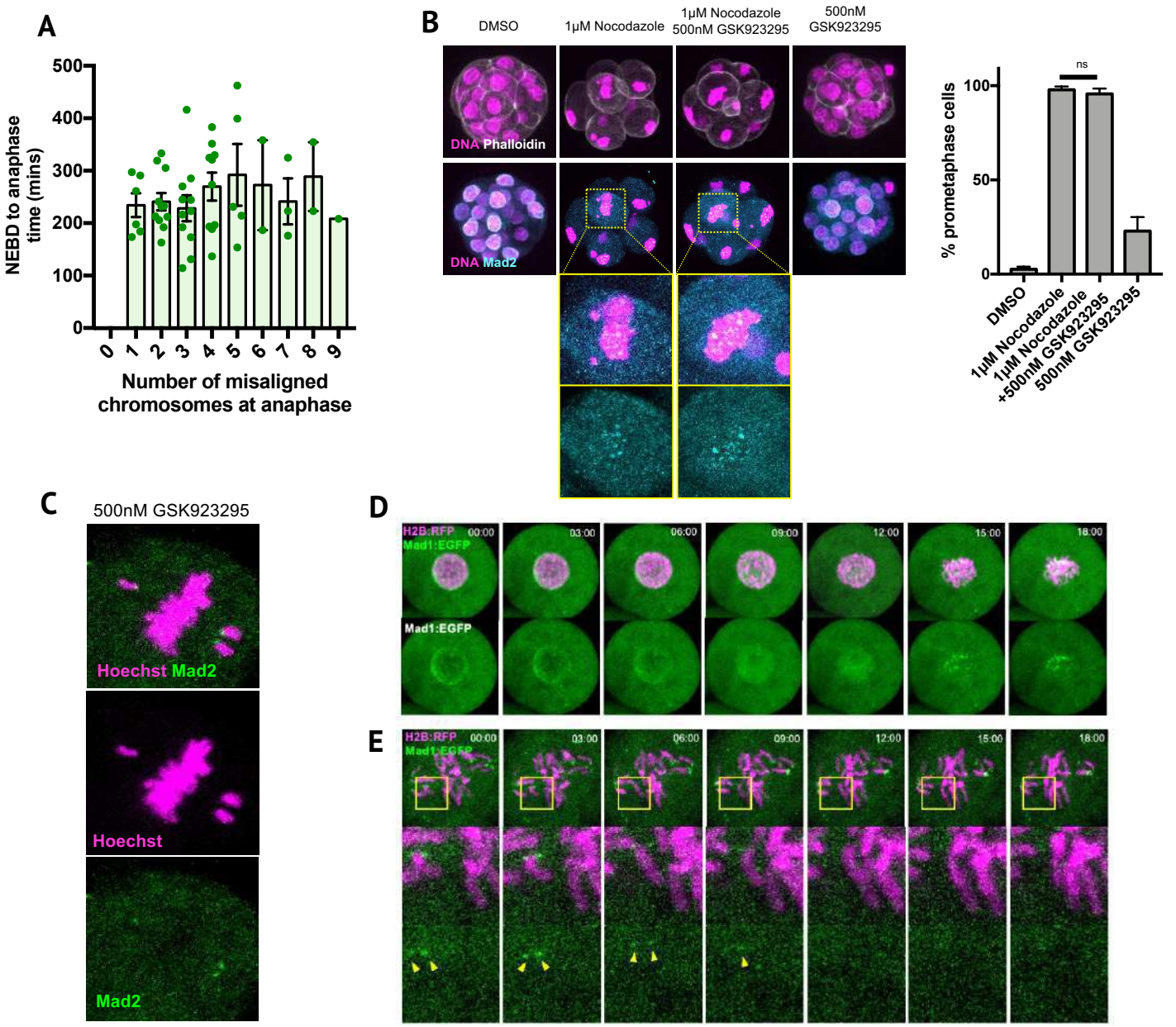

Figure S3. Chromosome segregation in CENPE-inhibited embryos. Relates to Figure 3.

A: Quantification of NEBD to anaphase time and number of misaligned chromosomes at anaphase onset during the eight- to sixteen-cell division of H2B:RFP-expressing embryos in 500nM GSK (mean and SEM, n=51 divisions, one-way ANOVA, P=0.86). Note both NEBD to metaphase and metaphase to anaphase times are extended in the presence of GSK923295.

B: SAC response to nocodazole is unaffected by CENP-E inhibition. Representative confocal images are shown; note GSK923295 does not reduce nocodazole-induced Mad2 localization. Right, analysis of percentage of prometaphase cells in fixed embryos following a 16hr treatment with 1μM nocodazole ± 500nM GSK923295 and immuno-stained with Mad2 (mean and SEM, one-way ANOVA, P<0.0001, Tukey's multiple comparisons test, P=0.981).

C: Mad2 is recruited to misaligned chromosomes during CENP-E inhibition. Representative confocal images of Mad2 immunofluorescence in 8-cell embryos treated with 500nM GSK923295.

D: Mad1:EGFP is recruited to chromosomes following nuclear envelope breakdown. Consecutive time-points of confocal time-lapse imaging of the four- to eight-cell division in H2B:RFP/Mad1:EGFP expressing embryos in GSK923295. Note that Mad1:EGFP localises to the nuclear lamina prior to NEBD, is lost from the envelope during NEBD, and forms puncta on chromosomes in prometaphase.

E: Mad1:EGFP (yellow arrowheads) is lost from chromosomes as they become aligned.

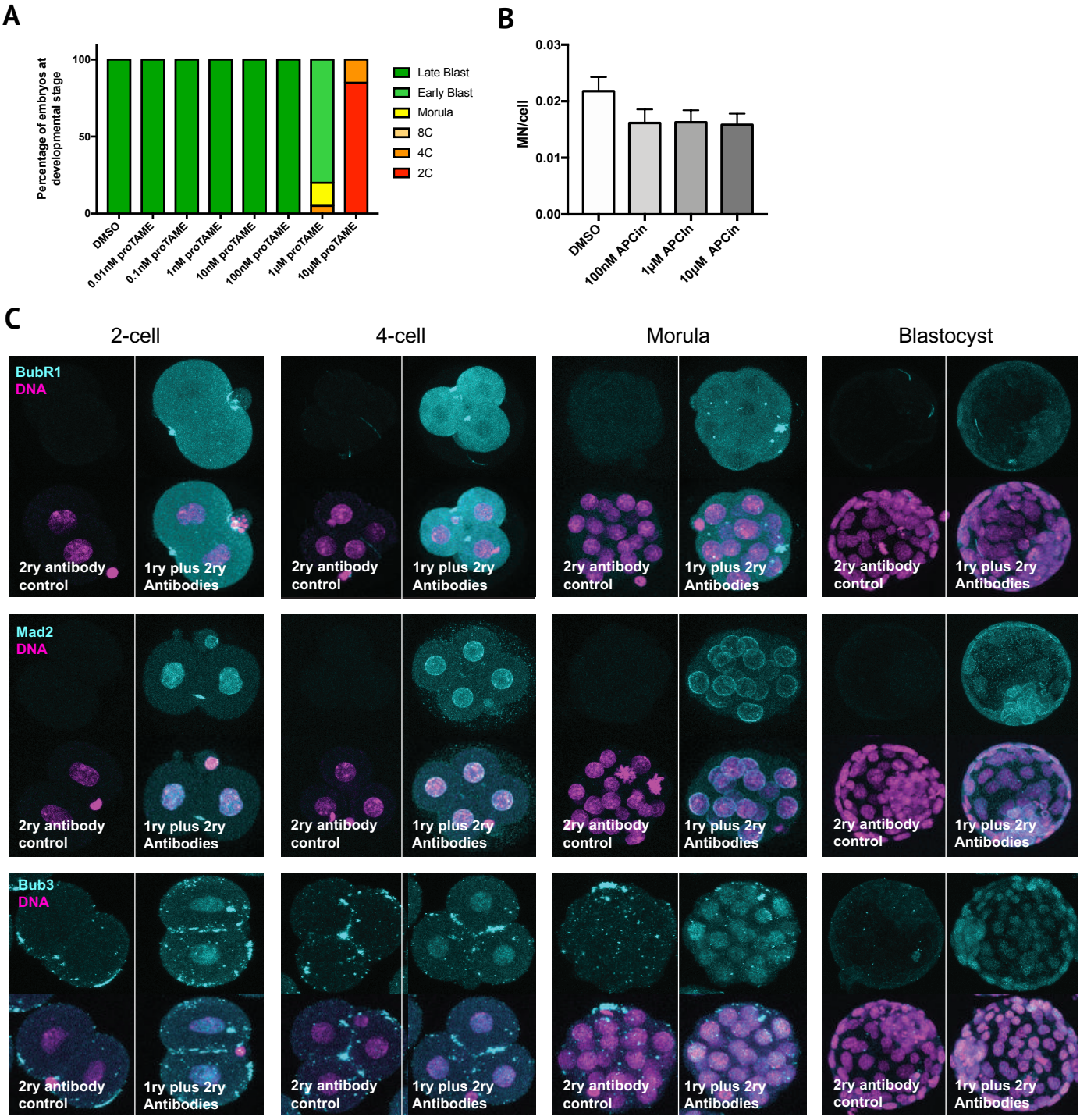

Figure S4. Effect of APC inhibition upon blastocyst development. Relates to Figure 4.

A: Scoring of developmental stages of embryos at E4.5 following culture in various concentrations of proTAME from the two-cell stage (n ≥ 17 embryos per group).

B: APCin reduces micronucleus frequency in embryos (mean ± SEM, n ≥ 28 embryos/group, one-way ANOVA P=0.21).

C: Immunofluorescence detection of SAC components during preimplantation development. Representative confocal images of BubR1 (top), Mad2 (middle) and Bub3 (bottom) immunofluorescence in 2-cell, 4-cell, morula and blastocyst stage embryos. Embryos stained only with secondary antibody are displayed on the left side of each developmental stage for comparison. Note that immunofluorescence is readily detectable at all developmental stages for all three proteins tested.

Annexe 5

The following is a collaborative publication developed during my Ph.D. published in the journal PNAS in 2018, where I performed some of the experiments that demonstrate that the treatment of mouse oocytes with Cytochalasin B disrupts the cytoskeleton, which thus affect cell elasticity.

Ultrafast imaging of cell elasticity with optical microelastography

Pol Grasland-Mongrain[a], Ali Zorgani[b], Shoma Nakagawa[c], Simon Bernard[a], Lia Gomes Paim[c], Greg Fitzharris[c,d], Stefan Catheline[b,1], and Guy Cloutier[a,e,f,1,2]

[a]Laboratory of Biorheology and Medical Ultrasonics, University of Montreal Hospital Research Center, Montreal, QC, Canada H2X 0A9; [b]LabTAU, INSERM u1032, University of Lyon, F-69003 Lyon, France; [c]Oocyte and Embryo Research Laboratory, University of Montreal Hospital Research Center, Montreal, QC, Canada H2X 0A9; [d]Department of Obstetrics and Gynecology, University of Montreal, Montreal, QC, Canada H3T 1J4; [e]Department of Radiology, Radio-Oncology and Nuclear Medicine, University of Montreal, Montreal, QC, Canada H3T 1J4; and [f]Institute of Biomedical Engineering, University of Montreal, Montreal, QC, Canada H3T 1J4

Edited by David A. Weitz, Harvard University, Cambridge, MA, and approved December 20, 2017 (received for review July 28, 2017)

Elasticity is a fundamental cellular property that is related to the anatomy, functionality, and pathological state of cells and tissues. However, current techniques based on cell deformation, atomic force microscopy, or Brillouin scattering are rather slow and do not always accurately represent cell elasticity. Here, we have developed an alternative technique by applying shear wave elastography to the micrometer scale. Elastic waves were mechanically induced in live mammalian oocytes using a vibrating micropipette. These audible frequency waves were observed optically at 200,000 frames per second and tracked with an optical flow algorithm. Whole-cell elasticity was then mapped using an elastography method inspired by the seismology field. Using this approach we show that the elasticity of mouse oocytes is decreased when the oocyte cytoskeleton is disrupted with cytochalasin B. The technique is fast (less than 1 ms for data acquisition), precise (spatial resolution of a few micrometers), able to map internal cell structures, and robust and thus represents a tractable option for interrogating biomechanical properties of diverse cell types.

elastography imaging | cell elasticity imaging | shear wave imaging | cell biomechanics | cell biophysics

The ability to measure the elasticity of a cell provides information about its anatomy, function, and pathological state. For example, cell biomechanical properties are related to the cytoskeletal network arrangement and water content (1). The cell membrane can harden or soften to modulate passage of biomolecules (2). Electrochemical activation can induce rapid contraction and mechanical modulation of cell properties in electrophysiology and neurology. Notably, tumor cells are characterized by a change of elasticity (3) and therapies inducing fibrosis, necrosis, and apoptosis are also accompanied by changes in tissue elasticity. Cytoskeleton reorganization is also linked to the activation process of immune cells and critical for effective cell–cell interactions, formation of immunological synapses, and migration processes (4). These are just a few examples that emphasize the importance of cell biomechanics in biology.

Many techniques have been proposed to measure a cell's mechanical properties, especially its elasticity. Most need a very accurate model of the cell characteristics but the chosen model may impact the measurement accuracy. Moreover, current measurements take seconds to hours to perform, during which biological processes can modify the cell elasticity, and they necessitate fixing the cell on a substrate. Variations in elasticity by a factor of two can occur within a few seconds (5).

In this study we propose an elasticity measurement technique based on elastic wave propagation. This technique performs local measurement of the speed c_s of a shear wave, a type of elastic wave. The shear modulus μ (elasticity) is given by ρc_s^2, with ρ the medium density, by assuming a purely linear elastic medium and negligible preloads. Here, we show that the shear wave elastography technique can perform micrometer-scale measurements and that it can extract local elasticity on a whole cell. Three main technological challenges needed to be met to achieve this: (*i*) developing an efficient way to induce kilohertz-range high-frequency shear waves in cells, (*ii*) finding a robust method to track these waves, and (*iii*) extracting elasticity from the observed traveling elastic waves.

Results

We first set out to demonstrate that high-frequency shear waves can be induced in cells. The key components of the experimental setup are as follows (Fig. 1): a cell held by a first micropipette and excited by contact with a second micropipette vibrating at 15 kHz, a 100× microscope magnification to observe the cell, and a 200,000-frames-per-second camera fixed on the microscope to acquire optical images over time. The 15-kHz vibration represents a compromise between a high-frequency stimulation to have a wavelength smaller than the cell size and a low-frequency excitation to reduce wave attenuation, especially in such a soft medium. The experiment was applied on spherical mouse oocytes (80 μm in diameter), which are well-characterized and easy to manipulate ex vivo. A finite element simulation with a 15-kHz vibration occurring on the side of a soft solid was also built to validate the technique.

Using an optical flow algorithm (6), displacements can be seen propagating left to right, with good agreement between experiment (Fig. 2*A*) and simulation (Fig. 2*B*). Attenuation is strong but displacements can nevertheless be observed on the right side

Significance

In wave physics, and especially seismology, uncorrelated vibrations could be exploited using "noise correlation" tools to reconstruct images of a medium. By using a high-frequency vibration, a high-speed tracking device, and a reconstruction technique based on temporal correlations of travelling waves we conceptualized an optical microelastography technique to map elasticity of internal cellular structures. This technique, unlike other methods, can provide an elasticity image in less than a millisecond, thus opening the possibility of studying dynamic cellular processes and elucidating new mechanocellular properties. We call this proposed technique "cell quake elastography."

Author contributions: P.G.-M., S.C., and G.C. designed research; P.G.-M., S.N., S.B., and L.G.P. performed research; G.F. and G.C. contributed new reagents/analytic tools; P.G.-M., A.Z., and S.C. analyzed data; and P.G.-M., G.F., S.C., and G.C. wrote the paper.

Conflict of interest statement: G.C., S.C., P.G.-M., and A.Z. filed a patent supported jointly by the University of Montreal and University of Montreal Hospital and INSERM on the technology reported in this manuscript.

This article is a PNAS Direct Submission.

[1]S.C. and G.C. contributed equally to this work.

[2]To whom correspondence should be addressed. Email: guy.cloutier@umontreal.ca.

This article contains supporting information online at www.pnas.org/lookup/suppl/doi:10.1073/pnas.1713395115/-/DCSupplemental.

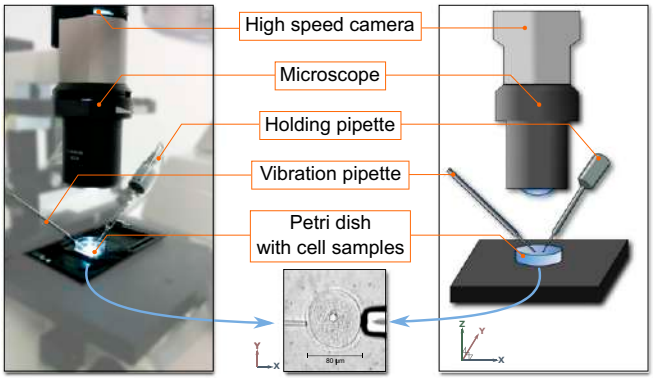

Fig. 1. Illustration of the experiment (*Left*: picture; *Right*: scheme). A cell placed in a Petri dish is held by a holding pipette and vibration is applied using a second pipette attached to a piezo-drive unit. Vibration is applied to the zona pellucida of the oocyte. Images of the cell are acquired by a high-speed camera through a microscope.

of the cell. Almost no displacement is seen in the surrounding fluid. These displacements propagate at a speed of 1.1 ± 0.1 m/s, under the form of elastic waves. Elastic waves are often decomposed in bulk waves (i.e., compression and shear waves) and surface waves (i.e., Rayleigh and Love waves). Any compression waves cannot be seen here, as a 15-kHz compression wave has a wavelength of $\sim 10^5$ μm in such a medium, which is 1,000 times larger than the oocyte diameter. As the oocyte is surrounded by a fluid of similar density, we made the hypothesis of an infinite medium, a common hypothesis in shear wave elastography. Besides, Rayleigh and Love waves typically propagate at a speed close to the shear wave speed (about 10% slower depending on conditions). Consequently, we approximated observed elastic waves as shear waves propagating at a speed c_s.

To map cell elasticity from observed shear waves we explored methods proposed in the field of shear wave elastography, such as time of flight (7), elastodynamic equation inversion (8, 9), and optimal control (10). In this study the best reconstruction was obtained using the "passive" elastography algorithm (11, 12), inspired by the seismology field (see *Materials and Methods* for details). It primarily calculates the shear wave speed, which then allows estimating the shear elasticity modulus.

On experimental elasticity maps (Fig. 3*A*), for analysis purposes, we segmented the oocyte into three functionally distinct zones: the zona pellucida (median of 0.31 kPa), the cytoplasm (median of 0.76 kPa), and the nucleus (median of 0.59 kPa). A median shear modulus was estimated at 0.21 kPa for the extracellular fluid (which should theoretically be zero), but this is attributed to displacements surrounding the cell interpreted by the elastography algorithm as shear waves. Each of these values is pairwise significantly different ($P < 0.05$, Mann–Whitney U test). Displacements could, however, not be properly estimated by the particle imaging velocimetry algorithm near the pipettes due to the high mechanical contrast of these objects. Consequently, the elasticity could not be calculated in a 10- to 20-μm layer around the holding pipette and the actuator.

These elasticity values were used as inputs of a simulated medium comprising four concentric circles (Fig. 3*B*) representing the different cellular zones. The nucleus is quite homogeneous and has a median elasticity of 0.66 kPa (10% difference with input); the cytoplasm is not homogeneous along the x axis, especially around the actuator, but has a median elasticity of 0.7 kPa (10% difference with input); the zona pellucida is around the resolution limit and has some artifacts around the actuator and the holding pipette and has a median elasticity of 0.41 kPa (difference of 25% with input); finally, apart from some specific outliers, the extracellular fluid elasticity is very small (0.04-kPa median value). Hence, we can state that the reconstruction process leads to a few artifacts, mainly in the vicinity of the actuator and the holding pipette, but it can nevertheless estimate shear moduli in four different zones, with medians close to input values.

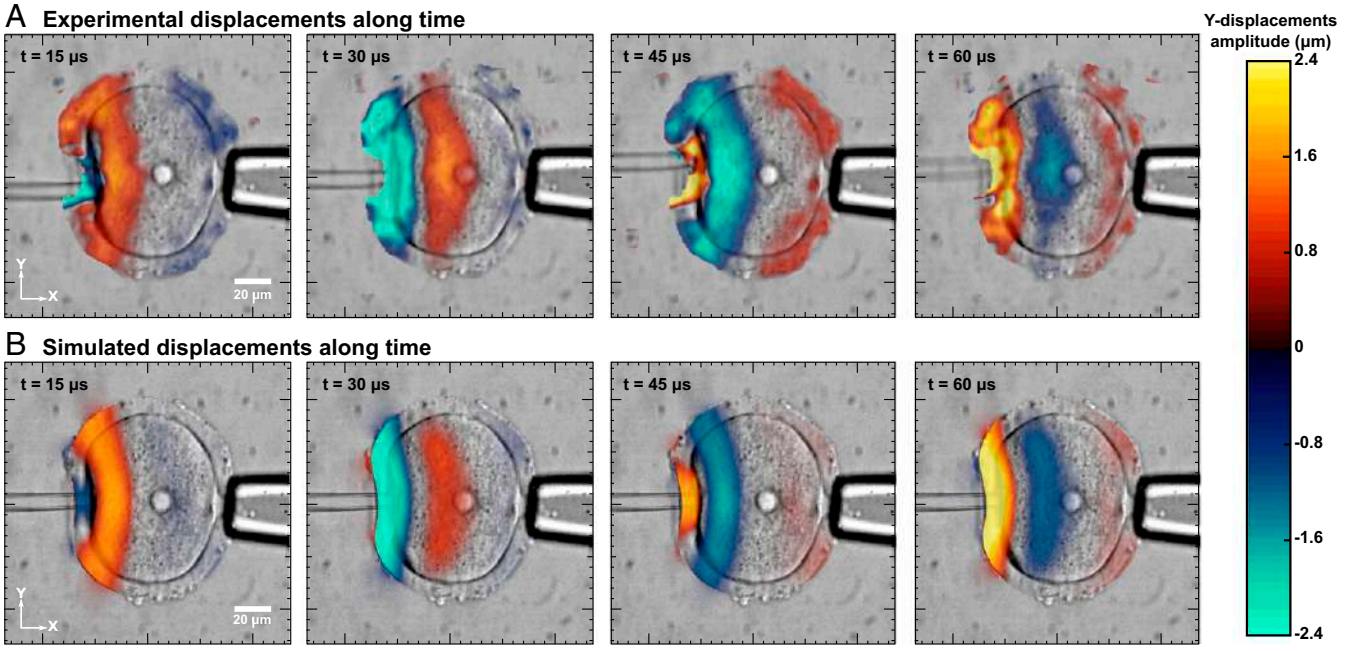

Fig. 2. Experimental (*A*) and simulated (*B*) Y-displacement maps, at $t = 15$, 30, 45, and 60 μs, respectively, superimposed on the optical images of the cell. Displacements with amplitude approximately from −2.4 to 2.4 μm propagating from the left vibrating pipette toward the right side of the cell can be observed.

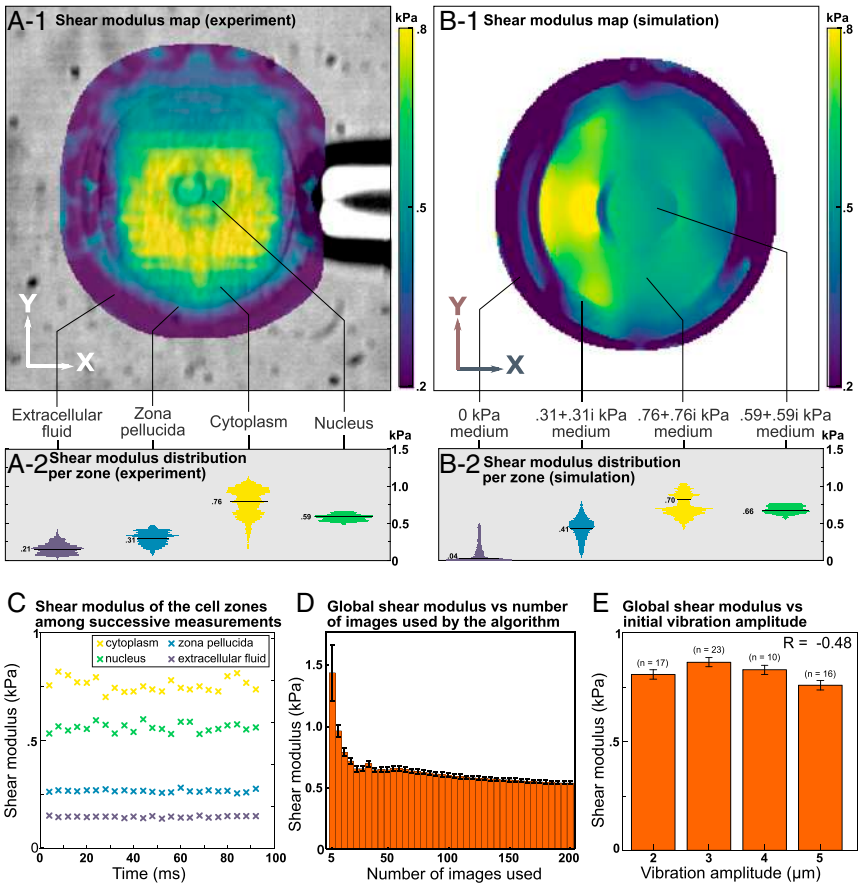

Fig. 3. (*A*) Elasticity map estimated from experimental displacements superimposed on the microscopy image (*A-1*) and corresponding distribution of elasticity with median values (*A-2*) of a mouse oocyte. (*B*) Elasticity map estimated from simulated displacements superimposed on the microscopy image (*B-1*) and corresponding distribution of elasticity with median values (*B-2*) of a soft medium mimicking a mouse oocyte. Nucleus, cytoplasm, zona pellucida, and extracellular fluid can be easily distinguished on both images; artifacts are observed in the zona pellucida. (*C*) Median shear moduli for successive measures within different zones (cytoplasm, nucleus, zona pellucida, and extracellular fluid). No time evolution is observed. (*D*) Average median shear moduli of the whole cell among 23 successive measurements as a function of the number of optical images used. Error bars correspond to the SD among successive measurements. (*E*) Effect of the vibration amplitude on oocyte shear modulus median, obtained by averaging 10–23 measures. Error bars correspond to the SD among successive measurements. Pearson's correlation coefficient R is too low to show any correlation between the measured shear modulus and the vibration amplitude.

To assess reproducibility of the technique, 23 successive measurements were made every 2.5 ms (with 200 images per measurement). Such quick repetition of the measure ensured absence of confounding time-dependent hardening or softening of the cell. Fig. 3*C* illustrates the median shear modulus within different zones (cytoplasm, nucleus, zona pellucida, and extracellular fluid). No time evolution could be observed in any part of the cell, indicating excellent reproducibility of the technique.

Next, we applied the elasticity reconstruction algorithm using 5–200 frames for each of the 23 measurements to test robustness. Mean elasticity quickly decreased by using 5–50 images then continued to slowly decrease (<10%) with 50–160 images, to reach a plateau with around 160 images (Fig. 3*C*). This implies that at 200,000 frames per second reliable measures of cell elasticity require ∼0.8 ms.

Finally, we studied the impact of the vibration amplitude on the elasticity estimation. With four pipette vibration amplitudes (as measured on optical images) we estimated the shear modulus of one oocyte (Fig. 3*E*). The shear modulus did not depend on the cell vibration amplitude within the range of 2–5 μm. This result may facilitate future implementation of the technique as it demonstrates that the vibration amplitude is not a critical parameter to consider.

Next, we studied the effect of disrupting the actin cortex of the oocyte upon cell elasticity. Cytochalasin B is a toxin known to block polymerization and the elongation of actin, and we thus expected oocyte softening. Examination of the cortex using Alexa-labeled phalloidin and confocal microscopy revealed a major reduction in actin labeling in the oocyte cortex, confirming the expected action of the drug (*SI Materials and Methods*). Notably, using optical microelastography, a decrease in shear modulus (softening) was observed when comparing normal and cytochalasin-treated oocytes, both in the cytoplasm and nucleus (Fig. 4 *A* and *B*). An artifactual decrease in elasticity within the zona pellucida was observed due to the proximity with the cytoplasm. With a total of 90 measurements on five normal cells and four cytochalasin-treated cells we observed a significant decrease ($P < 0.02$ with a Mann–Whitney rank sum test) of the mean shear modulus of the whole cells (Fig. 4*C*).

We also observed the shear modulus of cells at different stages of maturation: a germinal vesicle-stage oocyte (Fig. 4*D*), a two-cell embryo (Fig. 4*E*), and a four-cell embryo (Fig. 4*F*). The four-cell embryo cytoplasm was difficult to segment, as the fourth cell in the background degraded the shear wave displacement estimation. We could nevertheless measure almost the same elasticity at the three stages.

Discussion

Compared with existing elasticity mapping techniques the cellular imaging method presented in this study may become a viable alternative. Indeed, most cell elasticity measurement techniques are

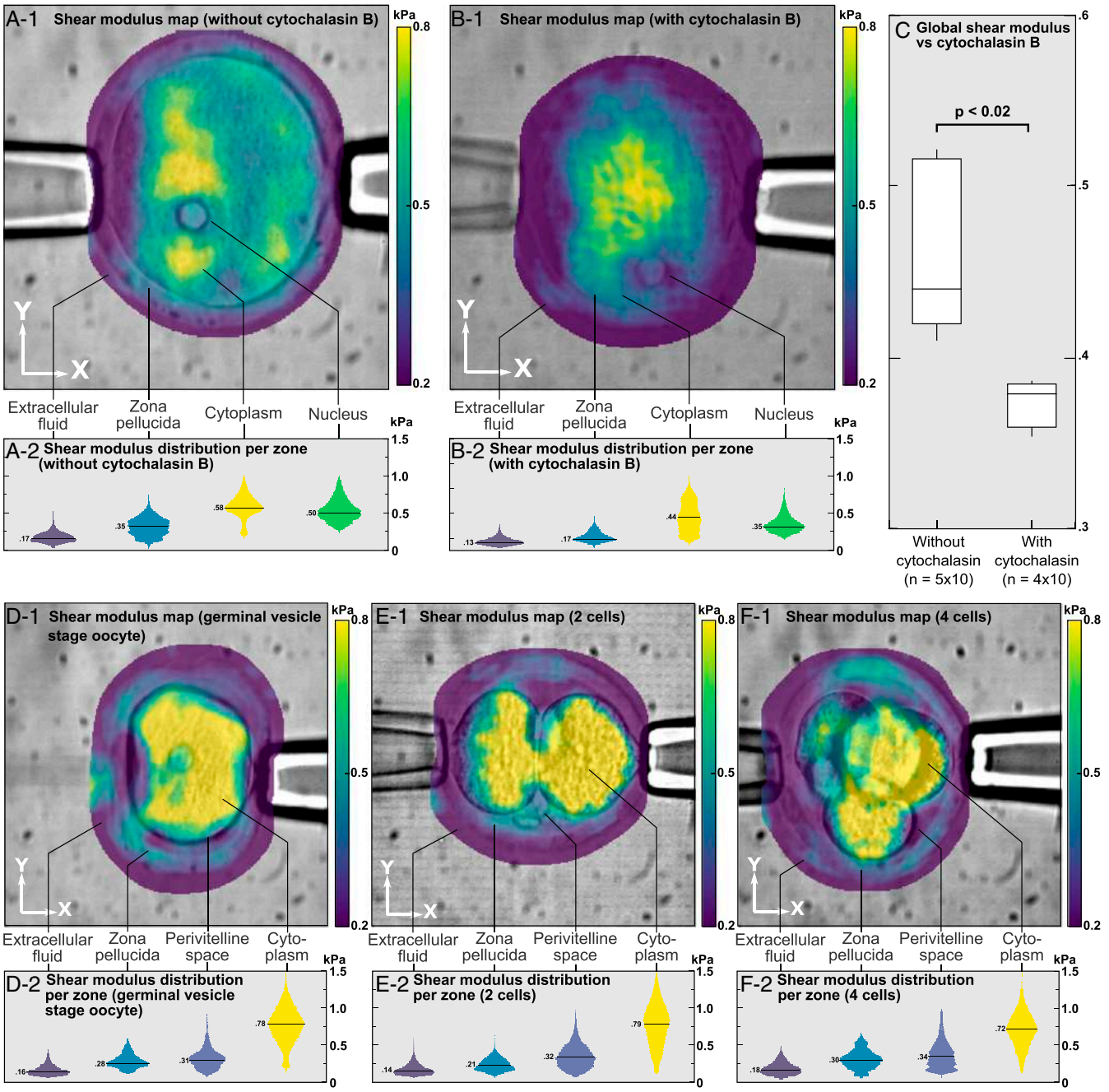

Fig. 4. Elasticity map superimposed on the microscopy image (*A-1* and *B-1*) and corresponding distribution of elasticity with median values (*A-2* and *B-2*) of a normal mouse oocyte (*A*) and a mouse oocyte softened by cytochalasin B (*B*). Elasticity decreased in all functional areas. (*C*) Box plot of whole oocyte shear modulus without and with cytochalasin B, showing a significant decrease in elasticity. Elasticity map superimposed on the microscopy image (*1*) and corresponding distribution of elasticity with median values (*2*) of a germinal vesicle-stage oocyte (*D*), a two-cell mouse embryo (*E*), and a four-cell mouse embryo (*F*).

based on static cell deformation under an external force, using aspiration micropipettes (13), magnetic bead twisting (14), and optical tweezers or stretcher (15). The deformation is estimated from optical images acquired before and after applying the force. While global elasticity is easily calculated by dividing the applied force intensity by the measured deformation, localized internal cell structure elasticity is more difficult, because the local deformation depends strongly on the internal distribution of stress. Thus, localized elasticity estimation needs a descriptive model of the cell mechanics, which is difficult to validate and may explain the variability observed among different studies (16–18).

In atomic force microscopy, local elasticity is estimated from the penetration depth of a small probe (19–21). This technique is able to map elasticity with a submicrometric spatial resolution. However, measurements are performed at the cell surface only, so that elasticity of internal structures cannot be determined. Besides, elasticity estimation highly depends on the chosen model. In particular, the probe shape must be precisely calibrated, as a change of shape due to probe aging, for example, can have an important impact. In most implementations, acquisitions are rather slow, taking typically at least a few minutes to acquire a full set of data, thus potentially increasing susceptibility to time-dependent confounding biological processes. Moreover,

one needs to attach the cell on a substrate to avoid its displacement, thus imposing boundary conditions that must be taken into account in the model to avoid biased elasticity measures.

An alternative strategy is to inject fluorescent nanoparticles within the cell and to measure the mean random displacement of these particles when the cell is subjected to a shear motion (22). This technique gives access to elasticity and viscosity, but at the location of nanoparticles only, so it does not produce images of the cell's viscoelasticity. It also requires a few minutes to make a measurement, and this approach is invasive by nature.

Brillouin scattering microscopy, more recently introduced (23, 24), consists of transmitting a laser beam through the cell, where internal mechanical waves shift the laser frequency. Measurement of this shift allows estimating the medium bulk modulus. However, the bulk modulus offers a much smaller contrast than Young's or shear modulus for similar changes in cell elasticity. For example, Scarcelli et al. (23) found a bulk modulus increase of only 16% when the Young's modulus raised by about 500% for the same experimentation. As for abovementioned technologies, acquisitions are rather slow, on the order of an hour.

Contrary to existing methods, the proposed technique does not require a stress distribution model and allows localized absolute elasticity measures (i.e., elasticity in kilopascals). As is done in shear wave elastography of whole organ systems, our method may be expanded to provide viscous properties (25, 26). Although we observed some artifacts on reconstructed elasticity maps, median values in each zone can be considered as accurate (differences of about 10% with input values in the simulation). This accuracy could nevertheless be improved, notably by working on the reconstruction process.

Reported measurements could distinguish internal structures of an oocyte based on their elasticity differences. To our knowledge, no measurement of oocyte elasticity has been previously reported at the frequency we used (15 kHz). Most biological tissues exhibit a frequency-dependent elasticity behavior (27), so our measurements lack a gold standard to be compared with. We can nevertheless state that elasticity values reported in our study are reproducible and consistent with finite element simulations. The closest measurement found in the literature has been done by Othman et al. (28) using a 550-Hz vibration frequency (one order of magnitude lower than in our experiments). They measured a global shear modulus of 0.3 kPa for a frog oocyte, which is in the same order of magnitude as our experiments.

An important advantage of the proposed method is the speed of acquisition, on the order of a millisecond. No confounding biological processes, such as cross-linking, could occur during the acquisition time. Future validations of the ultrafast optical microelastography technique may allow demonstrating the capability of this method to follow dynamic cellular processes inducing elasticity changes.

Spatial resolution in shear wave elastography is not directly related to the shear wavelength but depends on many parameters, such as the frame rate, reconstruction algorithm, and shear wave shape. In the current implementation, variations of elasticity could be observed in the nucleus or in the perivitelline space—so we estimate an average resolution on the order of 10 μm. The spatial resolution could be improved, for example with higher vibration frequencies or better imaging analysis algorithms, with the imaging apparatus resolution as the highest achievable—in this case the pixel size (0.57 μm). Different vibrating devices could be conceptualized as multiple harmonic sources and would facilitate the elasticity map reconstruction with the proposed method (11, 12). Three-dimensional mapping is also achievable simply by repeating the experiment at different microscope focusing depths.

Finally, the experimental apparatus is rather simple, consisting of a standard microscope, micropipettes, and a high-speed camera. Phase-contrast optical methods might be used for better contrast and resolution. It may also improve displacement estimation because phase information is available. The resolution of the microscope is not a critical parameter: The technique needs mainly to observe and track displacements inside the cell. The camera minimum speed of acquisition has to be tuned to the experiment as the shear wave velocity is related to the cell elasticity: We have to observe the shear wave propagation over a few images. A slower, less expensive camera could also be employed using a stroboscopic effect (i.e., by repeating synchronized image acquisitions and taking pictures with increasing delays).

Thanks to its speed, robustness, and relative simplicity, we therefore envision that this optical microelastography technique could become an alternative for mapping biomechanical properties of cells. It could open the possibility of studying dynamic cellular processes and elucidating new mechanobiology cellular properties, including cell division and migration.

Materials and Methods

Experimental Setup. The ultrafast camera (model v2512; Phantom Research) acquired 256- × 256-pixel windows at 200,000 images per second. The frame rate could be lowered down to 30,000 images per second (Nyquist–Shannon limit for a 15-kHz vibration), but oversampling allowed a better tracking of the shear wave propagation. With microscope amplification (Leica DMi1 with 100× lens), each square pixel had a lateral size of 0.57 μm. Cells used were mouse germinal vesicle-stage oocytes. Oocytes were collected as described previously (29) and kept in M2 medium (M-7167; Sigma Aldrich) supplemented with 200 nM 3-isobotyl-1-methyl-xanthine (I-5879; Sigma Aldrich) during observation. Experiments were performed shortly after oocytes were harvested. Cytochalasin B toxin (C-6762; Sigma-Aldrich) was used to depolymerize the actin cortex in some experiments, as described. Experimental procedures were conducted in accordance with guidelines of the Institutional Animal Care Committee of the University of Montreal Hospital Research Center. The investigation conformed with guidelines of the Canadian Council on Animal Care and the Guide for the Care and Use of Laboratory Animals.

To apply vibration, the oocyte was immobilized using a standard holding pipette. A glass vibration pipette was positioned on the zona pellucida of the oocyte, in an area where the zona pellucida was contacting the plasmalemma. The vibration was created by a piezoelectric device (piezo impact drive unit; Prime Tech Ltd.), moving along the *y* axis with a peak-to-peak amplitude of 20 μm at 15 kHz. The pipette was "rubbing" the cell, so the transmitted displacement was much lower, at about 5.0 ± 0.1 μm (in the Y direction), at the pipette contact. The point here is to induce in-plane pipette displacement with sufficient amplitude to allow tracking vibrations all over the cell.

It would be difficult to use a lower vibration frequency because it would lead to a shear wavelength close to the medium size (around 100 μm), making reconstruction more difficult. However, using a higher vibration frequency to improve resolution would lead to a stronger attenuation and more difficult displacement tracking.

Finite Element Simulation. The wave equations were solved using COMSOL (version 3.5a) with a structural mechanics module, assuming plane strain. The Navier equation was solved in the frequency domain. We used a 2D model with a manual segmentation of internal structures based on one optical image. The oocyte has an almost spherical shape, symmetrical along the *z* axis, surrounded by fluid of almost equal density, and we assumed that any out-of-plane border effect had minimal impact. Three zones were segmented: the nucleus, a 20-μm-diameter circle; the cytoplasm, an 80-μm-diameter circle around the nucleus; and the zona pellucida, a 10-μm layer around the cytoplasm. The whole simulated cell was placed in a 200- × 200-μm^2 space filled with isotonic saline water. We set the bulk modulus for all zones to 2.2 GPa (water compressibility) and the shear modulus elasticity at 0.59 + 0.59i kPa for the nucleus, 0.76 + 0.76i kPa for the cytoplasm, 0.31 + 0.31i kPa for the zona pellucida, and 0 Pa for the surrounding fluid. The shear moduli were extracted from the experimental results, and the loss moduli were set to the same values—we found that this selection gave wave attenuation very comparable to experiments. We tested different sets of parameters but simulated displacements were very different. The nodes on the left side of the zona pellucida were fixed (no displacement in X and Y directions) to simulate the holding pipette, and a vertical prescribed 10-μm harmonic displacement at 15 kHz was applied to the nodes on the left side of the zona pellucida. The continuity of displacement and strain was ensured by the finite element model code at all other interfaces. The model converged using 330,000 degrees of freedom using 75,000 quadratic triangular elements, with a low dependence on the number of elements or degrees of freedom.

Elasticity Derived from Shear Wave Speed. The proposed technology is inspired by pioneering work in shear wave elastography developed for organ

elasticity imaging (7, 8, 30, 31). Considering a medium as elastic, linear, isotropic, and infinite with respect to the wavelength, Navier's equation governs the displacement $\mathbf{u}$ at each point of the cell:

$$\rho\frac{\partial^2\mathbf{u}}{\partial t^2}=\left(K+\frac{4}{3}\mu\right)\nabla(\nabla.\mathbf{u})+\mu\nabla\times(\nabla\times\mathbf{u}),$$

where ρ is the medium density, $\mathbf{u}$ the local displacement, K the bulk modulus, and μ the shear modulus. Using Helmholtz decomposition $\mathbf{u}=\mathbf{u_p}+\mathbf{u_s}$, where $\mathbf{u}_\mathrm{p}$ and $\mathbf{u}_\mathrm{s}$ are, respectively, curl-free and divergence-free vector fields, two elastic waves can be retrieved: (*i*) a compression wave, which obeys the equation $\rho\partial^2\mathbf{u}_\mathrm{p}/\partial t^2=c_\mathrm{p}^2\Delta\mathbf{u_p}$, where $c_p=\sqrt{(K+4/3\mu)/\rho}$ is the compression wave speed; and (*ii*) a shear wave, which obeys the equation $\rho\partial^2\mathbf{u}_\mathrm{s}/\partial t^2=c_\mathrm{s}^2\Delta\mathbf{u_s}$, where $c_\mathrm{s}=\sqrt{\mu/\rho}$ is the shear wave speed. Hence, measuring the shear wave speed locally allows the estimation of the shear modulus (i.e., elasticity).

Shear Wave Speed Estimation. Once optical images were acquired, displacements along X and Y were estimated using a 2D particle image velocimetry algorithm (6). This algorithm is based on a Lucas–Kanade-based optical flow method with an affine displacement in each block. Shear wave speed was then estimated on the Y-displacement maps using a "passive" elastography algorithm (11, 12). In this algorithm, the temporal cross-correlation between a point (x_0, y_0) and all other points (x, y) of the image is calculated to create a 2D+t image $C_{(x_0,y_0)}(x, y; t)$ for each position considered (x_0, y_0). Cross-correlation images typically look like a cross, showing a converging wave for $t<0$, a refocusing at $t=0$ with a maximum of amplitude, and a diverging wave for $t>0$. Curvature of the focal spot is then evaluated on the resulting image, as the focal spot size is directly linked to the wavelength λ of the shear wave. Shear wave speed c_s is then estimated by multiplying the wavelength with the shear wave frequency f: $c_s=\lambda\times f$ (see *SI Materials and Methods* for an illustration of the algorithm). The wave correlation technique used here for the inverse problem solution (11, 12) is advantageous because the more diffuse the wavefield the better the reconstruction quality.

ACKNOWLEDGMENTS. We thank Sylvain Bossé (Phantom Research) for information on how to use the high-speed camera and Julian Garcia-Duitama and Marie-Hélène Roy Cardinal for help with statistics. This work was supported by a postdoctoral fellowship award from the Natural Sciences and Engineering Research Council of Canada (NSERC) (P.G.-M.), a MEDITIS postdoctoral fellowship from NSERC provided by the Institute of Biomedical Engineering of the École Polytechnique and University of Montréal (to S.B.), Fonds de Recherche du Québec – Nature et Technologies Grant PR-174387, and Canadian Institutes of Health Research Grants MOP-84358 and MOP-142334.

1. Charras GT, Mitchison TJ, Mahadevan L (2009) Animal cell hydraulics. *J Cell Sci* 122: 3233–3241.
2. Bleil JD, Wassarman PM (1980) Structure and function of the zona pellucida: Identification and characterization of the proteins of the mouse oocyte's zona pellucida. *Dev Biol* 76:185–202.
3. Cross SE, Jin Y-S, Rao J, Gimzewski JK (2007) Nanomechanical analysis of cells from cancer patients. *Nat Nanotechnol* 2:780–783.
4. Bufi N, et al. (2015) Human primary immune cells exhibit distinct mechanical properties that are modified by inflammation. *Biophys J* 108:2181–2190.
5. Liu X, Shi J, Zong Z, Wan KT, Sun Y (2012) Elastic and viscoelastic characterization of mouse oocytes using micropipette indentation. *Ann Biomed Eng* 40:2122–2130.
6. Porée J, Garcia D, Chayer B, Ohayon J, Cloutier G (2015) Noninvasive vascular elastography with plane strain incompressibility assumption using ultrafast coherent compound plane wave imaging. *IEEE Trans Med Imaging* 34:2618–2631.
7. Catheline S, Wu F, Fink M (1999) A solution to diffraction biases in sonoelasticity: The acoustic impulse technique. *J Acoust Soc Am* 105:2941–2950.
8. Muthupillai R, et al. (1995) Magnetic resonance elastography by direct visualization of propagating acoustic strain waves. *Science* 269:1854–1857.
9. Sandrin L, Tanter M, Catheline S, Fink M (2002) Shear modulus imaging with 2-D transient elastography. *IEEE Trans Ultrason Ferroelectr Freq Control* 49:426–435.
10. Ammari H (2008) *An Introduction to Mathematics of Emerging Biomedical Imaging* (Springer, Berlin).
11. Gallot T, et al. (2011) Passive elastography: Shear-wave tomography from physiological-noise correlation in soft tissues. *IEEE Trans Ultrason Ferroelectr Freq Control* 58: 1122–1126.
12. Zorgani A, et al. (2015) Brain palpation from physiological vibrations using MRI. *Proc Natl Acad Sci USA* 112:12917–12921.
13. Evans E, Yeung A (1989) Apparent viscosity and cortical tension of blood granulocytes determined by micropipet aspiration. *Biophys J* 56:151–160.
14. Wang N, Butler JP, Ingber DE (1993) Mechanotransduction across the cell surface and through the cytoskeleton. *Science* 260:1124–1127.
15. Guck J, et al. (2001) The optical stretcher: A novel laser tool to micromanipulate cells. *Biophys J* 81:767–784.
16. Khalilian M, Navidbakhsh M, Valojerdi MR, Chizari M, Yazdi PE (2010) Estimating Young's modulus of zona pellucida by micropipette aspiration in combination with theoretical models of ovum. *J R Soc Interface* 7:687–694.
17. Murayama Y, et al. (2008) Elasticity measurement of zona pellucida using a micro tactile sensor to evaluate embryo quality. *J Mamm Ova Res* 25:8–16.
18. Sun Y, Wan K-T, Roberts KP, Bischof JC, Nelson BJ (2003) Mechanical property characterization of mouse zona pellucida. *IEEE Trans Nanobioscience* 2:279–286.
19. A-Hassan E, et al. (1998) Relative microelastic mapping of living cells by atomic force microscopy. *Biophys J* 74:1564–1578.
20. Putman CA, van der Werf KO, de Grooth BG, van Hulst NF, Greve J (1994) Viscoelasticity of living cells allows high resolution imaging by tapping mode atomic force microscopy. *Biophys J* 67:1749–1753.
21. Radmacher M, Tillamnn RW, Fritz M, Gaub HE (1992) From molecules to cells: Imaging soft samples with the atomic force microscope. *Science* 257:1900–1905.
22. Tseng Y, Lee JS, Kole TP, Jiang I, Wirtz D (2004) Micro-organization and visco-elasticity of the interphase nucleus revealed by particle nanotracking. *J Cell Sci* 117:2159–2167.
23. Scarcelli G, et al. (2015) Noncontact three-dimensional mapping of intracellular hydromechanical properties by Brillouin microscopy. *Nat Methods* 12:1132–1134.
24. Scarcelli G, Yun SH (2007) Confocal Brillouin microscopy for three-dimensional mechanical imaging. *Nat Photonics* 2:39–43.
25. Bernard S, Kazemirad S, Cloutier G (2017) A frequency-shift method to measure shear-wave attenuation in soft tissues. *IEEE Trans Ultrason Ferroelectr Freq Control* 64:514–524.
26. Kazemirad S, Bernard S, Hybois S, Tang A, Cloutier G (2016) Ultrasound shear wave viscoelastography: Model-independent quantification of the complex shear modulus. *IEEE Trans Ultrason Ferroelectr Freq Control* 63:1399–1408.
27. Lakes RS (2009) *Viscoelastic Materials* (Cambridge Univ Press, Cambridge, UK).
28. Othman SF, Xu H, Royston TJ, Magin RL (2005) Microscopic magnetic resonance elastography (microMRE). *Magn Reson Med* 54:605–615.
29. Nakagawa S, FitzHarris G (2017) Intrinsically defective microtubule dynamics contribute to age-related chromosome segregation errors in mouse oocyte meiosis-I. *Curr Biol* 27:1040–1047.
30. Sarvazyan AP, Rudenko OV, Swanson SD, Fowlkes JB, Emelianov SY (1998) Shear wave elasticity imaging: A new ultrasonic technology of medical diagnostics. *Ultrasound Med Biol* 24:1419–1435.
31. Krouskop TA, Dougherty DR, Vinson FS (1987) A pulsed Doppler ultrasonic system for making noninvasive measurements of the mechanical properties of soft tissue. *J Rehabil Res Dev* 24:1–8.

Supporting Information

Grasland-Mongrain et al. 10.1073/pnas.1713395115

SI Materials and Methods

Validation of Cytochalasin B Experiment. Fig. S1 demonstrates the action of cytochalasin B in disrupting the actin cortex of germinal vesicle-stage oocytes.

Displacements Along the Horizontal Direction. Similarly to the Y-displacement maps in Fig. 2, X displacements over time are illustrated in Fig. S2 for the same excitation by the micropipette. We can see a good agreement between simulation and experiment, with comparable amplitudes and similar wavelength. The displacements are propagating mainly from the vibration pipette through the zona pellucida, because of the cell geometry. The experimental and simulated results nevertheless have some differences, especially at the vibration pipette location, mainly due to two reasons: (*i*) Experimental displacements calculated in the vicinity of the pipette are highly unreliable, whereas the simulation considered accurate displacements, and (*ii*) X displacements are about two times lower in amplitude than Y ones, leading to a lower signal-to-noise ratio.

X-displacement maps were, however, not used to compute elasticity, as the amplitude was smaller, especially in the middle of the cell, which could lead to unreliable results.

Passive Elastography Algorithm Principle. The "passive" elastography algorithm consists of a few steps, as illustrated in Fig. S3. It is based on (*i*) estimating the displacement between each image over time, using the 2D particle image velocimetry algorithm; (*ii*) calculating the temporal cross-correlation between a point (x_0, y_0) and all other points (x, y) of the image; and (*iii*) measuring the focal spot size using the local curvature to obtain the local shear wavelength, so that by multiplying this wavelength with the shear wave frequency one can calculate the shear wave speed, and hence the shear modulus. If the frame rate is under the Nyquist–Shannon limit (i.e., 30,000 frames per second for a 15-kHz vibration), the passive elastography algorithm is able to produce an elasticity map but the results would not be quantitative (12).

Segmentation Illustration. Fig. S4 illustrates the segmentation of the oocyte constituents.

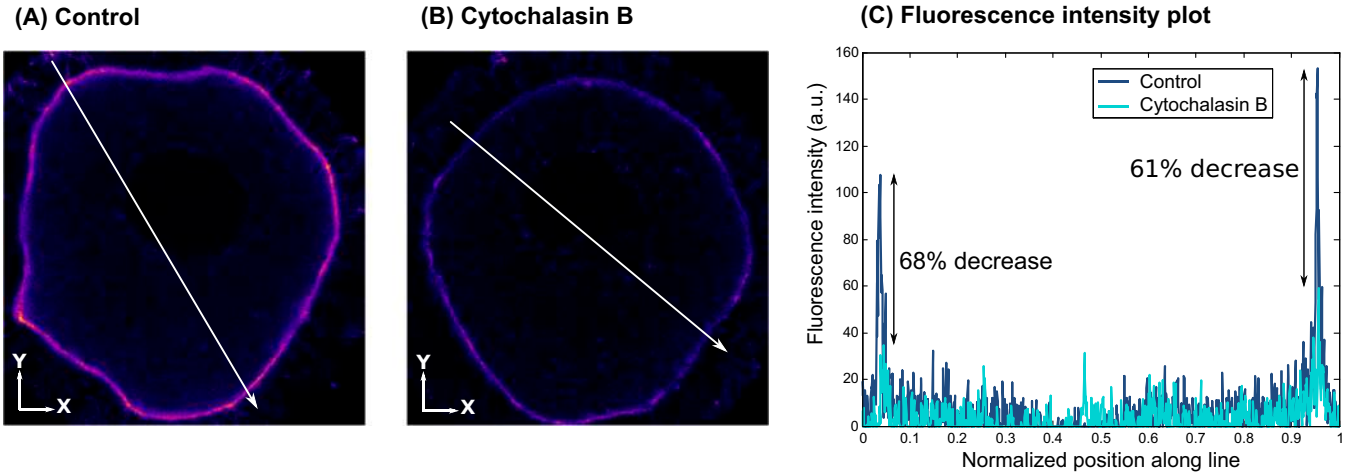

Fig. S1. Demonstration that cytochalasin B disrupts the actin cortex in germinal vesicle-stage oocytes. Images show typical examples of (*A*) control and (*B*) cytochalasin B-treated oocytes that were subsequently fixed and permeabilized, and the actin cortex labeled with Alexa-phalloidin. The actin cortex, concentrated under the plasmalemma, is indicated as a pseudocolor image, warmer colors indicating greater Alexa-phalloidin signal. Note that cytochalasin substantially diminishes but does not completely remove the actin cortex. (*C*) A line intensity plot of fluorescence measured along the white lines, providing a quantitative readout of the loss of cortical actin.

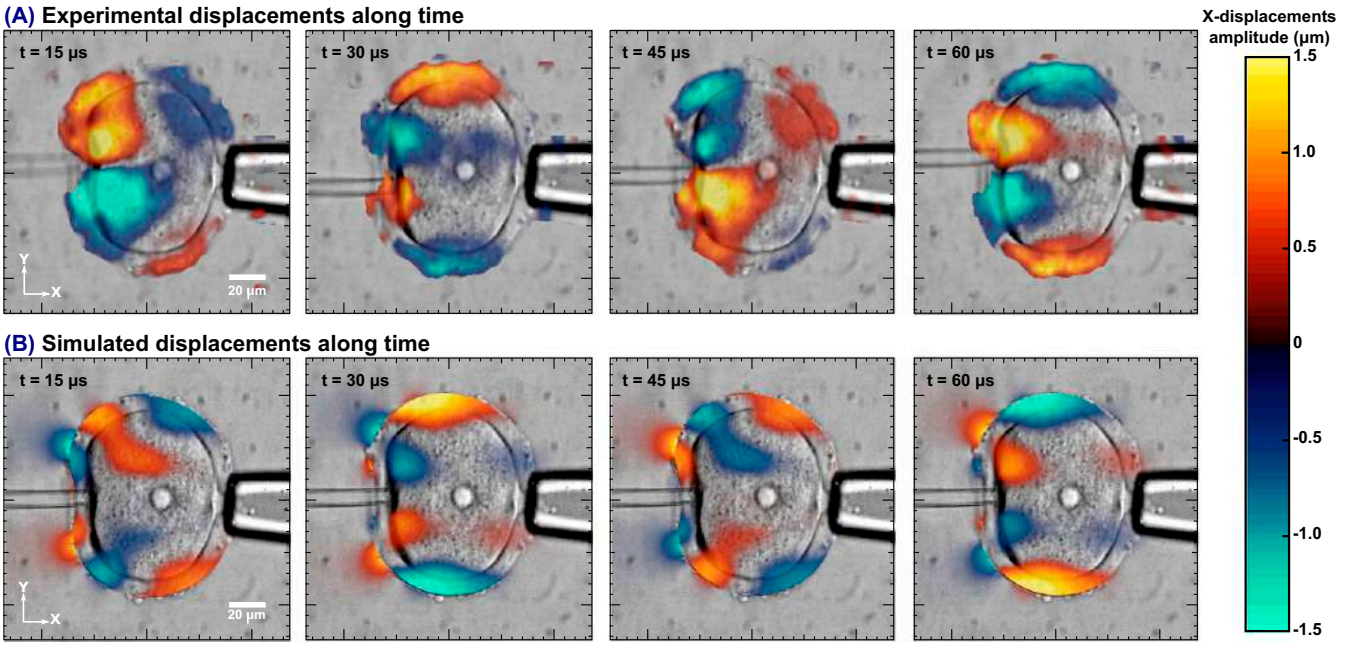

Fig. S2. Experimental (*A*) and simulated (*B*) X-displacement maps, at t = 15, 30, 45, and 60 µs, superimposed on the optical images of the cell. We can see displacements with an amplitude approximately from −1.5 to 1.5 µm, propagating from the vibrating pipette through the external layer of the cell. (Scale bars, 20 µm.)

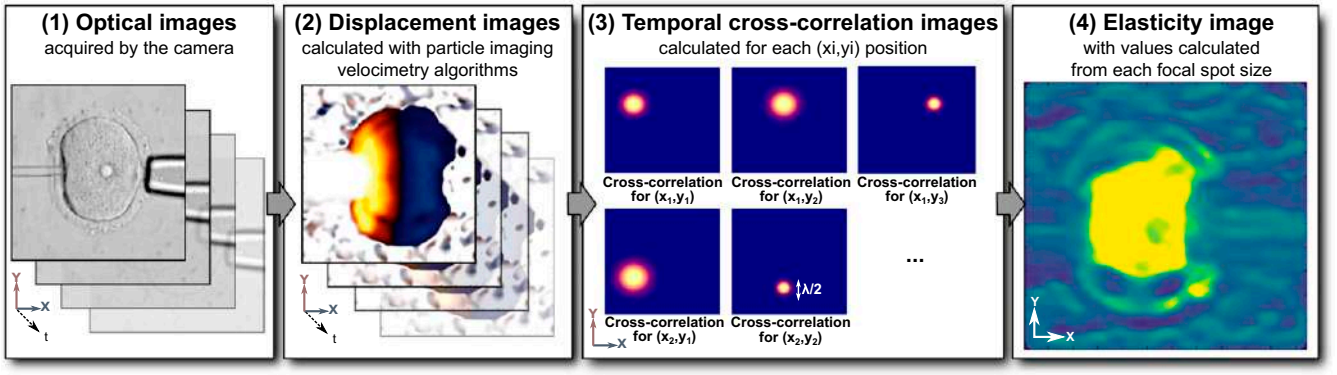

Fig. S3. Illustration of the passive elastography algorithm applied on cells. The elasticity estimation consists of four steps: (1) acquisition of the optical images, (2) estimation of the displacements between images, (3) computation of the temporal cross-correlation of each image, and (4) estimation of the elasticity from the focal spot size.

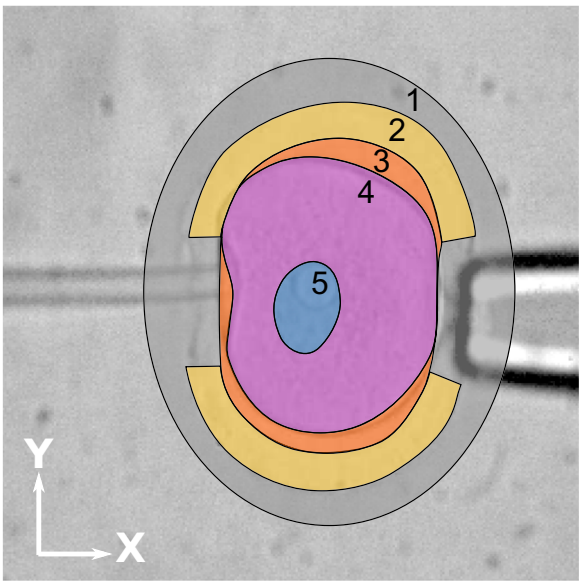

Fig. S4. Illustration of the segmentation. 1: extracellular fluid; 2: zona pellucida; 3: perivitelline space; 4: cytoplasm; 5: nucleus; 2 + 3 + 4 + 5: whole cell.